

Photoanode engineering of dye-sensitized photovoltaic cells using zinc oxide microstructures for efficient light harvesting applications

by

Anooja J.
10PP17A39032

A thesis submitted to the
Academy of Scientific & Innovative Research
for the award of the degree of
DOCTOR OF PHILOSOPHY
in
Science

Under the supervision of

Dr. Suraj Soman



**CSIR-National Institute for Interdisciplinary
Science and Technology (CSIR-NIIST),
Thiruvananthapuram - 695 019**



Academy of Scientific and Innovative Research
AcSIR Headquarters, CSIR-HRDC campus
Sector 19, Kamla Nehru Nagar,
Ghaziabad, U. P. - 201 002, India

April, 2024

Dedicated to ...

My family, for their sacrifices, patience, and support...



राष्ट्रीय अंतर्विषयी विज्ञान तथा प्रौद्योगिकी संस्थान
NATIONAL INSTITUTE FOR INTERDISCIPLINARY SCIENCE AND TECHNOLOGY

वैज्ञानिक तथा औद्योगिक अनुसंधान परिषद्
इंडस्ट्रियल एस्टेट पी ओ, पाप्पनमकोड, तिरुवनंतपुरम, भारत – 695 019

Council of Scientific and Industrial Research
Industrial Estate P O, Pappanamcode, Thiruvananthapuram, India – 695 019


डॉ. सूरज सोमन
वैज्ञानिक
फोटो विज्ञान और फोटोनिक्स अनुभाग

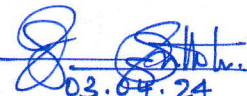
Dr. Suraj Soman
Scientist
Photosciences and Photonics Section

April 03, 2024

CERTIFICATE

This is to certify that the work incorporated in this Ph.D. thesis entitled, ***“Photoanode engineering of dye-sensitized photovoltaic cells using zinc oxide microstructures for efficient light harvesting applications”*** submitted by ***Ms. Anooja J.*** to the Academy of Scientific and Innovative Research (AcSIR) in fulfilment of the requirements for the award of the Degree of ***Doctor of Philosophy in Science***, embodies original research work carried out by the student. We further certify that this work has not been submitted to any other University or Institution in part or full for the award of any degree or diploma. Research materials obtained from other sources and used in this research work have been duly acknowledged in the thesis. Images, illustrations, figures, tables etc., used in the thesis from other sources, have also been duly cited and acknowledged.



03/04/2024
Anooja J.


03.04.24
Dr. Suraj Soman
(Supervisor)


3/4/24
Dr. Narayanan Unni K. N.
(Co-Supervisor)

STATEMENTS OF ACADEMIC INTEGRITY

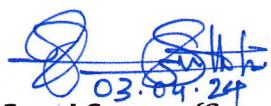
I Anooja J., a Ph.D. student of the Academy of Scientific and Innovative Research (AcSIR) with Registration No. 10PP17A39032 hereby undertake that, the thesis entitled "*Photoanode engineering of dye-sensitized photovoltaic cells using zinc oxide microstructures for efficient light harvesting applications*" has been prepared by me and that the document reports original work carried out by me and is free of any plagiarism in compliance with the UGC Regulations on "*Promotion of Academic Integrity and Prevention of Plagiarism in Higher Educational Institutions (2018)*" and the CSIR Guidelines for "*Ethics in Research and in Governance (2020)*".

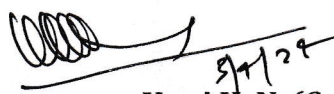

03/04/2024
Anooja J.

April 03, 2024

Thiruvananthapuram

It is hereby certified that the work done by the student, under my supervision, is plagiarism-free in accordance with the UGC Regulations on "*Promotion of Academic Integrity and Prevention of Plagiarism in Higher Educational Institutions (2018)*" and the CSIR Guidelines for "*Ethics in Research and in Governance (2020)*".


03.04.24
Dr. Suraj Soman (Supervisor)


9/4/24
Dr. Narayanan Unni K. N. (Co-supervisor)


April 03, 2024

Thiruvananthapuram

DECLARATION

I, Anooja J., AcSIR Registration No. 10PP17A39032 declare that my thesis entitled, "***Photoanode engineering of dye-sensitized photovoltaic cells using zinc oxide microstructures for efficient light harvesting applications***" is plagiarism-free in accordance with the UGC Regulations on "*Promotion of Academic Integrity and Prevention of Plagiarism in Higher Educational Institutions (2018)*" and the CSIR Guidelines for "*Ethics in Research and in Governance (2020)*".

I would be solely held responsible if any plagiarised content in my thesis is detected, which is violative of the UGC regulations 2018.


Anooja J.

April 03, 2024

Thiruvananthapuram

ACKNOWLEDGEMENTS

Firstly, I would like to express my deep sense of gratitude to Dr. Suraj Soman and Dr. Narayanan Unni K. N., my thesis supervisors, for their valuable guidance, constant support, and encouragement, leading to the successful completion of this research work.

I am grateful to Dr. C. Anandharamakrishnan, Dr. Ashish Lele and Dr. A. Ajayaghosh, the present and former Directors of CSIR-National Institute for Interdisciplinary Science and Technology (CSIR-NIIST), Thiruvananthapuram, for providing me the necessary facilities for carrying out the work.

My heartfelt gratitude to:

- *Dr. Manoj Raama Verma, Dr. Biswapriya Deb and Dr. Hareesh U. S., Doctoral Advisory Committee (DAC) members for their thoughtful discussions and suggestions in the DAC meetings.*
- *Dr. Jayamurthy P., Dr. V. Karunakaran, Dr. C. H. Suresh, Dr. R. Luxmi Varma and Dr. Mangalam S. Nair, the present and former AcSIR co-ordinators for the timely help and advice for the academic procedures of AcSIR.*
- *Dr. K. V. Radhakrishnan, Dr. P. Sujatha Devi, and Dr. R. Luxmi Varma, the present and former Heads, Chemical Sciences and Technology Division (CSTD) for their support.*
- *Dr. Narayanan Unni K. N., Head, Centre for Sustainable Energy Technologies (C-SET) for his support.*
- *All the AcSIR faculty members of CSIR-NIIST for their help and support during the course work period.*
- *All the present and former scientists at Chemical Sciences and Technology Division, Material Sciences and Technology Division and Centre for Sustainable Energy Technologies, for all the help and support extended to me.*
- *Dr. Rakhi R. B., Mr. Visakh M., Dr. Hareesh U. S., Dr. Swetha S., Dr. P. Sujatha Devi, Dr. L. Giribabu (IICT, Hyderabad), Dr. V. Ganpathy (ACRI, Hyderabad) for their contributions towards various research publications.*
- *Mr. Robert Philip, Mr. Kiran Mohan, Ms. Aswathi, Mr. Merin, Ms. Gayathri, Mr. Prasad, Mr. Peer Mohammed, Mr. Hareesh, and Mr. Kiran J. S. for the general help and for helping with various characterizations.*

- *Dr. Sourav Chandra Pradhan, Mr. Lingamoorthy S., Dr. Jayadev V., Mr. Gokul, Mr. Sabu, Ms. Ramees Jebin P., Ms. Sruthi M. M., Mr. Sreenandu P. H., Ms. Nisha, Mr. Vipin C. K., Mr. Andrew Simon George, Ms. Sreelekshmy M. R., Dr. Anantharaj, Ms. Kanishga L., Mr. Manikandan, Ms. Aneesha V. P., Mr. Soumalya Banerjee, Mr. Akshay, Ms. Aswathi, Mr. Hari, Ms. Varsha M. Vijay, Ms. Greeshma Mohan T. P., Mr. Udith Unnikrishnan P., and all other former group members for their good cooperation and companionship in the lab.*
- *Dr. Rajeev, Dr. Anjali Soman, Dr. Hanna B., Dr. Manuraj, Mr. Vibhu Darshan, Ms. Anjali Sajeev, Ms. Kavya Rajeev, Mr. Rishad, and Ms. Swathilekshmy for their companionship and support throughout my PhD period.*
- *M. Sc. project students for all the help and love*
- *All other friends at CSIR-NIIST for their good companionship, care, love, and support throughout my PhD period.*
- *CSIR and DST for financial assistance.*

I am deeply indebted to my family, especially my parents, for their unconditional love, endearing care, and support throughout my life. I am greatly obliged to my partner, Vineesh, for all the patience, understanding, love and trust. Last, but not the least, I would like to extend my thanks and appreciation to all my teachers and friends who are an inevitable part of my growth in life.

Anooja J.
03/04/2024
Anooja J.

TABLE OF CONTENTS

Certificate		i
Statements of Academic Integrity		ii
Declaration		iii
Acknowledgments		iv
Table of Contents		vi
List of Abbreviations		xi
Preface		xvi
Chapter 1	Introduction to dye-sensitized photovoltaic cells	1-72
	Abstract	1
1.1.	Global energy scenario	2
1.2.	Internet of things and indoor photovoltaics	3
1.3.	Dye-sensitized photovoltaic cells: Structure and working	6
1.3.1.	Structure of DSCs	7
	(a) Photoanode/working electrode	7
	(b) Counter electrode	9
	(c) Redox mediator	9
1.3.2.	Working of DSCs	10
1.4.	Photoanode engineering strategies for enhancing the performance of DSCs	15
1.4.1.	Development of various nanostructures	16
	(a) TiO ₂ nanostructures	16
	(b) ZnO nanostructures	19
	(c) Nanostructures of other materials & hybrid nanocomposites	22
1.4.2.	Inclusion of light scattering entities	23
	(a) Scattering particles	24
	(b) Scattering voids and surface roughness	25
	(c) Plasmonic nanoparticles	27
1.4.3.	Doping with ions	28
1.4.4.	Interfacial modification by depositing blocking layers	29
1.4.5.	Interfacial engineering by co-sensitization strategy	30
1.4.6.	Interfacial modification by co-adsorption and pre-adsorption strategy	32
1.5.	Copper complex based redox mediators for DSCs	34
1.5.1.	Emergence of copper complex redox shuttles	34
1.5.2.	Charge transfer dynamics at photoanode/electrolyte interface	37
1.5.3.	Mass transport limitations	39
1.6.	Statement of the problem	41

1.7.	Objectives of the present thesis work	42
1.8.	Experimental and theoretical background	44
1.8.1.	Steps for fabricating DSCs	45
	(a) Photoanode fabrication	45
	(b) Counter electrode preparation	46
	(c) Assembling of photoanode and counter electrode	48
	(d) Electrolyte preparation and filling	49
1.8.2.	Basic characterization techniques for DSCs	49
	(a) Current density versus voltage characterization	49
	(b) Incident photon-to-current conversion efficiency measurement	50
1.8.3.	Detailed interfacial charge transfer analysis in DSCs	51
	(a) Open circuit voltage decay measurement	52
	(b) Charge extraction measurement	52
	(c) Transient photovoltage decay measurement	53
	(d) Transient photocurrent decay measurement	54
	(e) Current transient measurement	55
	(f) Electrochemical impedance spectroscopy	56
	(g) Intensity modulated photovoltage and photocurrent spectroscopy	59
1.8.4.	Mott-Schottky analysis of the semiconductor/electrolyte interface	60
	References	63
Chapter 2A	ZnO microstructures as photoanode materials in copper electrolyte based dye-sensitized photovoltaic cells	73-104
	Abstract	73
2A.1.	Introduction	74
2A.2.	Experimental procedures	75
2A.2.1.	Material synthesis and characterization	75
2A.2.2.	Photoanode preparation and characterization	77
2A.2.3.	DSC fabrication and characterization	79
2A.3.	Results and discussions	80
2A.3.1.	Effect of redox mediator on the performance of ZnO based DSCs	80
	(a) Synthesis and characterization of ZnO hierarchical microstructures	80
	(b) Characterization of ZnO based DSCs using different redox mediators	86
2A.3.2.	Effect of TiO ₂ post blocking layer on the performance of ZnO based DSCs	91
	(a) Characterization of ZnO based photoanodes with and without TiO ₂ blocking layer	91

	(b) PV performance of ZnO based DSCs with and without TiO ₂ blocking layer	95
	(c) Detailed interfacial charge transfer analysis	98
2A.4.	Conclusions	100
	References	101
Chapter 2B	Addressing mass transport issue in copper electrolyte based dye-sensitized photovoltaic cells using surface textured photoanodes	105-129
	Abstract	105
2B.1.	Introduction	106
2B.2.	Experimental procedures	107
2B.2.1.	Surface texturing of TiO ₂ photoanodes using ZnO microstructure as templates	107
2B.2.2.	Characterization of the TiO ₂ photoanodes	109
2B.2.3.	DSC fabrication and characterization	110
2B.3.	Results and discussions	111
2B.3.1.	Characterization of surface textured TiO ₂ photoanode	111
	(a) Effect of surface texturing on light harvesting efficiency of TiO ₂ photoanode	111
	(b) Presence of ZnO in surface textured TiO ₂ photoanodes	114
2B.3.2.	Effect of surface textured TiO ₂ photoanodes on the DSC performance	115
	(a) Basic photovoltaic and mass transport studies	115
	(b) Detailed interfacial electron transfer studies	121
2B.4.	Conclusions	126
	References	127
Chapter 3	ZnO templated scattering layers for enhanced performance in copper electrolyte based dye-sensitized photovoltaic cells	130-158
	Abstract	130
3.1.	Introduction	131
3.2.	Experimental procedures	133
3.2.1.	Preparation and characterization of ZnO templated TiO ₂ photoanodes	133
3.2.2.	DSC fabrication and characterization	135
3.3.	Results and discussions	137
3.3.1.	ZnO templated TiO ₂ photoanodes for DSCs	137
	(a) Characteristics of ZnO templated photoanodes	137
	(b) Photovoltaic performance and mass transport studies	141

	(c) Advanced characterizations for interfacial charge transfer studies	145
3.3.2.	Optimizing the weight percentage of ZnO templates for enhanced DSC performance	148
	(a) Effect of ZnO content on the LHE of templated photoanodes	148
	(b) Photovoltaic performance evaluation under various light conditions and interfacial charge dynamics studies	150
3.4	Conclusions	155
	References	156
Chapter 4	Synergetic effect of TiO₂/ZnO bilayer photoanodes realizing exceptionally high V_{OC} in DSCs under outdoor and indoor illuminations	159-192
	Abstract	159
4.1.	Introduction	160
4.2.	Experimental procedure	162
4.2.1.	Synthesis and characterization of ZnO hierarchical structures	162
4.2.2.	Photoanode preparation and characterization	163
4.2.3.	Fabrication and characterization of DSCs	164
4.3.	Results and Discussion	166
4.3.1.	Characterization of materials and photoanodes	166
4.3.2.	Photovoltaic and advanced characterization of DSCs	169
4.3.3.	Effect of ZnO layer thickness and TiO ₂ blocking layers on the performance of bilayer DSCs	176
4.3.4.	Achieving record V_{OC} by using TiO ₂ /ZnO bilayer photoanodes	185
4.4.	Conclusions	188
	References	189
Chapter 5	Dye-sensitized TiO₂/ZnO bilayer photoanode based photocapacitors for outdoor/indoor light harvesting and storage applications	193-219
	Abstract	193
5.1.	Introduction	194
5.2.	Experimental procedure	197
5.2.1.	Dye sensitized photovoltaic cell fabrication and characterization	197
5.2.2.	Photocapacitor fabrication and characterization	199
5.3.	Results and Discussion	201
5.3.1.	Optimizing the TiO ₂ layer thickness for dye sensitized light harvesters	201
5.3.2.	Characterization of the EDLC	210
5.3.3.	Photocapacitor characterization and application	212

5.4.	Conclusions	216
	References	217
	Summary & Future Perspectives	220
	Abstract of the Thesis	224
	List of Publications	225
	List of Conference Presentations	226
	Abstracts of Conference Presentations	227
	SCI Publications Emanating from the Thesis	233

LIST OF ABBREVIATIONS

A	Ampere
A	Area (cm ²)
Å	Angstrom
AC	Alternating current
ACN	Acetonitrile
AFM	Atomic force microscopy
Ag	Silver
Al	Aluminium
Al ₂ O ₃	Aluminium oxide
ALD	Atomic layer deposition
AM 1.5G	Air mass 1.5 global
Au	Gold
BIPV	Building integrated photovoltaics
CB	Conduction band
CE	Charge extraction
Co	Cobalt
[Co(bpy) ₃] ^{3+/2+}	Cobalt (III/II) tris(2,2'-bipyridyl)
CT	Current transient
Cu	Copper
[Cu(dmp) ₂] ^{2+/+}	bis-(2,9-dimethyl-1,10-phenanthroline) copper
[Cu(tmby) ₂] ^{2+/+}	bis-(4,4',6,6'-tetramethyl-2,2'-bipyridine) copper
CV	Cyclic Voltammetry
CVD	Chemical vapour deposition
D-π-A	Donor-pi-acceptor
D35	(E)-3-(5-(4-(bis(2',4'-dibutoxy-[1,1'-biphenyl]-4-yl)amino)phenyl)thiophen-2-yl)-2-cyanoacrylic acid
D _n	Diffusion coefficient

d	Semiconductor layer thickness
DC	Direct current
DFT	Density functional theory
DL	Dye loading
DLS	Dynamic light scattering
DSC	Dye-sensitized solar cell
e	Electron charge
E_F	Fermi level
E_g	Energy band gap
EIS	Electrochemical impedance spectroscopy
EQE	External quantum efficiency
FF	Fill factor
FTO	Fluorine doped tin oxide
G	Generation rate
Ga	Gallium
GaAs	Gallium arsenide
h	Plank's constant
H ₂ O	Water
HOMO	Highest occupied molecular orbital
HRTEM	High resolution transmission electron microscope
I	Current
I^-/I_3^-	Iodide/triiodide
I_{dark}	Dark current
IMPS	Intensity modulated photocurrent decay
IMVS	Intensity modulated photovoltage decay
InAlGa ₂ N	Indium aluminium gallium nitride
InGa ₂ N	Indium gallium nitride
InN	Indium nitride
IoT	Internet of things

IPA	Isopropyl alcohol
IPCE	Incident photon to current conversion efficiency
I_{ph}	Photocurrent
IR	Infrared
J_{dark}	Dark current density
J_{sc}	short-circuit current density
$J-V$	Current density vs. voltage
K_B	Boltzmann constant
LED	Light emitting diode
L	Semiconductor thickness
LEG4	3-{6-{4-[bis(2',4'-dibutyloxybiphenyl-4-yl)amino-]phenyl}-4,4-dihexyl-cyclopenta-[2,1-b:3,4-b']dithiophene-2-yl}-2-cyanoacrylic acid
LHE	Light harvesting efficiency
L_n	Diffusion length
Li	Lithium
LUMO	Lowest unoccupied molecular orbital
MPP	Maximum power point
MS5	N-(2',4'-bis(dodecyloxy)-[1,1'-biphenyl]-4-yl)-2',4'-bis(dodecyloxy)-N-phenyl-[1,1'-biphenyl]-4-amine-4-(benzo[c][1,2,5]thiadiazol-4-yl)benzoic acid
n	Ideality factor
N	Nitrogen
NHE	Normal hydrogen electrode
OCVD	Open circuit voltage decay
PCE	Power conversion efficiency
PEDOT	Poly(3,4-ethylenedioxythiophene)
P_{in}	Input power
Pt	Platinum
PV	Photovoltaic

q	Elemental charge
QDs	Quantum dots
SEM	Scanning electron microscope
SHE	Standard hydrogen electrode
Si	Silicon
SnO ₂	Tin (IV) oxide
T	Temperature
t	Time
tbp	Tert-butyl pyridine
TCO	Transparent conducting oxide
TiCl ₄	Titanium (IV) chloride
TiO ₂	Titanium dioxide
UV	Ultraviolet
V	Bias voltage
VB	Valance band
$V_{applied}$	Applied voltage
V_F	Fermi voltage
V_{oc}	Open-circuit voltage
V_{fb}	Flat band potential
XRD	X-ray diffraction
XPS	X-ray Photo-electron Spectroscopy
XY1b	(E)-3-(4-(6-(7-(4-(bis(2',4'-dibutoxy-[1,1'-biphenyl]-4-yl)amino)phenyl)benzo[c] [1,2,5]thiadiazol-4-yl)-4,4-bis(2-ethylhexyl)-4H-cyclopenta[2,1-b:3,4-b']dithiophen-2-yl)phenyl)-2-cyanoacrylic acid
Y123	3-{6-{4-[bis(2',4'-dihexyloxybiphenyl-4-yl)amino-]phenyl}-4,4-dihexyl-cyclopenta-[2,1-b:3,4-b']dithiophene-2-yl}-2-cyanoacrylic acid
Zn	Zinc
ZnO	Zinc oxide
ε	Molar extinction coefficient

η	Power conversion efficiency
η_{cc}	Charge collection efficiency
η_{inj}	Injection efficiency
η_{LHE}	Light harvesting efficiency
η_{reg}	Regeneration efficiency
τ_n	Lifetime
τ_{tr}	Transport time
τ_d	Diffusion time
C_{μ}	Chemical capacitance
R_{rec}	Recombination resistance
R_{ct}	Charge transfer resistance
α	Absorption coefficient, power constant
λ	Wavelength
ν	Frequency

PREFACE

Several research activities are being pursued to enhance the efficiency of dye-sensitized photovoltaic cells (DSCs) by designing and synthesizing new sensitizer molecules and electrolyte species, by adopting co-sensitization and co-adsorption or pre-adsorption strategies, and by utilizing different photoanode and counter electrode materials. However, in majority of the breakthrough works, the DSCs utilize conventional bilayer photoanodes constituted by an active layer (AL) containing ~20-30 nm sized TiO₂ nanoparticles and a scattering layer (SL) made up of larger sized (~200-400 nm) TiO₂ nanoparticles. Meanwhile, several novel dye and electrolyte systems were investigated for DSCs to realize remarkable performances. Recently, the earth abundant copper (Cu(II/I)) metal complexes have been successfully employed in DSCs as electrolytes for achieving remarkable open circuit potentials (V_{oc}) owing to their highly positive redox potential. DSCs employing Cu(II/I) electrolyte could achieve appreciable power conversion efficiencies ($PCEs$) and voltages ($> 1V$) not only under one sun irradiation (AM 1.5G, 100 mW/cm²), but also under indoor/ambient light illuminations. Since voltage output is crucial for powering smart electronic devices involving sensors and actuators, the Cu(II/I) electrolyte based DSCs can be extensively utilized for indoor photovoltaic and internet of things (IoT) applications. So far, several organic sensitizer molecules have been developed to be used along with Cu(II/I) complex based electrolytes. Nevertheless, the compatibility of Cu(II/I) electrolyte with other photoanode materials and architectures are seldom explored. The present thesis work aims to design and develop novel photoanode architectures for DSCs using ZnO microstructures for attaining enhanced V_{oc} and PCE under indoor (ambient) as well as outdoor (one sun) illumination conditions.

The thesis is organized into five chapters, of which the Chapter 1 provides an overview on dye sensitized photovoltaic cells (DSCs). It includes the working principle and characterization techniques for DSCs. It also discusses the properties and uses of zinc oxide as photoanode material in DSCs. The advantages and disadvantages of ZnO when compared to conventional DSC photoanode material, *viz.* TiO₂, are also discussed. The photoanode design and fabrication strategies adopted within the thesis work are also incorporated in this chapter. Chapter 2 is divided into two parts 2A and 2B. Chapter 2A includes the synthesis method and characterization of a ZnO hierarchical microstructure

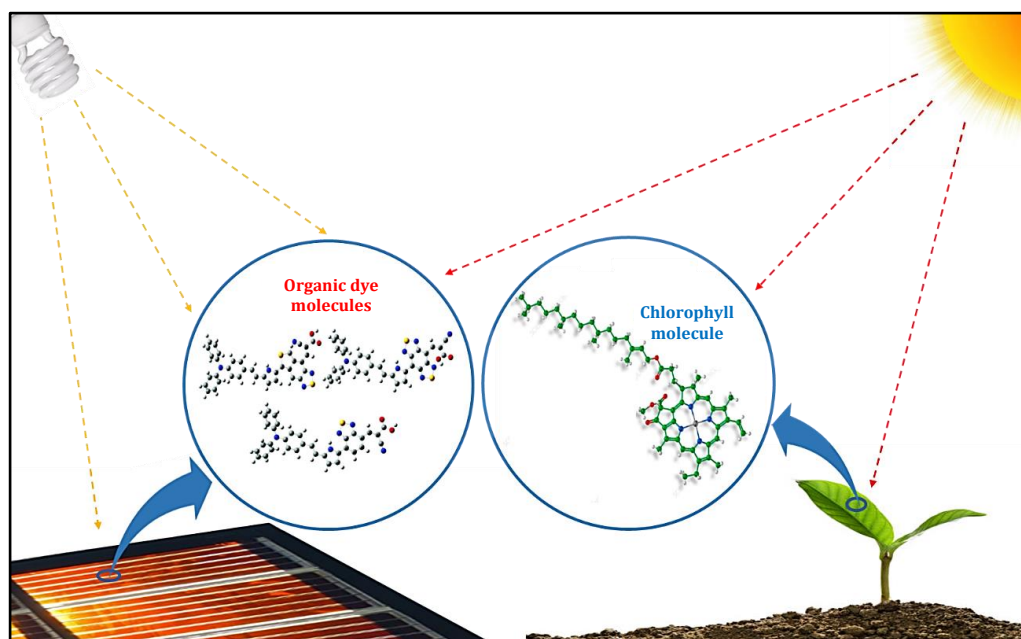
(designated as Z0) and its application as the photoanode active layer material in DSC utilizing standard organic dye Y123 and two different electrolyte systems, viz. iodide/triiodide (I^-/I_3^-) and copper dimethyl phenanthroline ($[Cu(dmp)_2]^{2+/+}$) based redox mediators. The copper electrolyte based DSC exhibited better power conversion efficiency (*PCE*) when compared to the iodine based one. The *PCE* of copper electrolyte based device was further improved by depositing a TiO_2 post-blocking layers (BL) which suppress the electron recombination in ZnO photoanode based DSCs. Chapter 2B discusses the implementation of the Z0 microstructure as a sacrificial layer for surface texturing the conventional TiO_2 photoanodes in DSCs. It was observed that the surface texturing of TiO_2 layer increased its surface roughness which enhanced the light scattering properties and hence resulted in improved light harvesting efficiency (*LHE*). The DSCs utilizing the surface textured TiO_2 photoanodes (T-Z) sensitized with Y123 dye along with $[Cu(dmp)_2]^{2+/+}$ electrolyte outperformed the standard device (std) employing conventional AL/SL bilayer TiO_2 photoanode, both under outdoor and indoor illumination conditions. With reduced layer thickness, the T-Z device could address the mass transport limitation in $Cu(II/I)$ electrolyte based DSCs. Chapter 3 further extends the application of the ZnO microstructures as templates by utilizing them to incorporate light scattering voids within the TiO_2 scattering layer of DSCs. The resulting photoanode, designated as T-M, co-sensitized with two organic sensitizers, D35:XY1b (1:1), having complimentary absorption profiles were utilized in DSCs along with $[Cu(dmp)_2]^{2+/+}$ based electrolyte to achieve a *PCE* of 8.9% under one sun condition and 32.3% under 1000 lux CFL illumination. The improved performance of T-M under indoor illumination may be attributed to its better *LHE* owing to better light scattering and higher dye loading owing to thicker film. However, under one sun irradiation, T-M suffered from mass transport limitation, which could be resolved by optimizing the weight percentage of ZnO templates used for creating the voids. Using 20 wt% of ZnO template particles, we could achieve a *PCE* of 10.1% under one sun and 33.8% under 1000 lux CFL illumination. Finally, we were able to power a temperature sensor by connecting two of the fabricated small area devices ($\sim 0.24\text{ cm}^2$ each) in series, under 1000 lux CFL illumination.

In chapter 4, we present a novel photoanode architecture for DSCs, which involves the implementation of a layer of ZnO hierarchical microstructures over the conventional TiO_2 active layer, resulting in a TiO_2/ZnO bilayer photoanode. Our design aims to enhance the V_{oc} of DSCs under one sun and indoor/ambient lighting conditions by controlling the

conduction band (CB) position of the semiconductor layer. For this, we synthesized three different ZnO microstructures, namely mimosa flower-like (Z1), dandelion flower-like (Z2) and rose flower-like (Z3) microstructures and deposited them as an additional layer over the TiO₂ active layer to obtain T+Z1, T+Z2 and T+Z3 DSC photoanode, respectively. Initially, the photoanodes were sensitized with Y123 dye and utilized in DSC along with [Cu(dmp)₂]^{2+/+} electrolyte. The V_{oc} of the T+Z1 based device was found to be about 100 mV higher than that of reference device (consisting TiO₂ active layer only). This improvement in V_{oc} of bilayer DSCs was attributed to the negative shift in CB edge and reduced recombination kinetics. TiO₂ BL was introduced over the T+Z1 electrode to further improve the device performance and to slow down the degradation process associated with ZnO. Further, by using the optimized bilayer electrode with blocking layer (T+Z1+BL) in combination with the MS5 sensitizer and [Cu(dmp)₂]^{2+/+} redox electrolyte, we achieved a record V_{oc} of 1.27 V under one sun illumination and 1.025 V under 1000 lux CFL and LED illumination. Finally, we developed a battery-free temperature sensor that was powered autonomously by a single TiO₂/ZnO bilayer DSC under outdoor as well as indoor illumination. In chapter 5, we utilized the best performing photoanode architecture (T+Z1) and optimized the TiO₂ layer thickness to further improve the PCE , particularly under indoor illumination. Under one sun condition, the DSC utilizing 6 μm thick TiO₂ showcased the best performance while under indoor light (1000 lux CFL) the device using 9 μm thick TiO₂ delivered the best PCE . Further, by implementing co-sensitization strategy [XY1b:MS5, (2:1)], in our best optimized photoanode architecture (T+Z1+BL with 9 μm thick TiO₂ layer) we achieved a PCE of 34.5% under 1000 lux CFL and 39.5% under 6000 lux CFL illumination. The co-sensitization strategy was adopted to enhance the power output of DSCs without compromising the V_{oc} . Finally, we developed a photocapacitor by integrating an activated charcoal based electric double layer capacitor (EDLC) device to the DSC employing our best optimized photoanode architecture. Upon photocharging under AM 1.5G solar irradiation, the photocapacitor could attain a maximum voltage (V_m) of 1.1 V in 3 min. Whereas under 6000 lux CFL illumination the V_m acquired was 1.0 V after 20 min of photocharging. The V_m obtained was 0.98 V (after 30 min of photocharging) and 0.95 V (after 40 min of photocharging) respectively, under 4000 lux and 2000 lux illumination. Under indoor illumination conditions, there was a reduction in the voltage acquired by photocharging even after prolonged exposure to CFL illumination and the photocharging

curves tend to show saturation after the specified photocharging time. Nevertheless, we were successful in charging the EDLC part with the small area DSC ($\sim 0.24 \text{ cm}^2$ active area) with a maximum overall photoelectric conversion and storage efficiency (*OPCSE*) of 4.1% under one sun irradiation. Under CFL illumination of 2000 lux, 4000 lux and 6000 lux, the PC could exhibit a remarkably high maximum OPCSE of 8.2%, 11.4% and 15.5%, respectively. Finally, we succeeded in powering a temperature sensor/digital clock device by using the PC, under outdoor as well as indoor illumination. The PC was able to power the device for more than 20 minutes, even after the illumination was cut-off.

Introduction to dye-sensitized photovoltaic cells



Abstract: *The concurrent energy scenario and concomitant environmental impacts have urged global scientific community to invest their efforts on augmenting alternate energy sectors, essentially the photovoltaic (PV) technology. Dye-sensitized photovoltaic cells (DSCs) have been identified as one among the most prominent PV technologies, owing to their beneficial economical as well as environmental aspects. Moreover, DSCs impart exceptional performance under ambient/indoor light conditions and can be easily integrated to other electronic devices and storage devices, which make them a convenient candidate for smart electronics applications like internet of things (IoT), building-integrated photovoltaic systems (BIPV), etc. In order to enhance the power conversion efficiency (PCE) of DSCs enormous researches on different device components such as sensitizers, semiconducting layer, blocking layer, counter electrode and electrolyte are being pursued worldwide. The present chapter includes an overview of DSCs, various strategies of photoanode engineering reported so far for enhancing DSC performance, mass transport limitation in copper electrolyte based DSCs and experimental methods utilized for DSC fabrication and characterization. It also discusses the main objectives of the thesis which focuses on improving the performance of copper electrolyte based DSCs via photoanode modifications.*

1.1. Global energy scenario

Technological breakthroughs, population growth, and economic expansion have all contributed to an unavoidable surge in energy consumption rates, which has had a disastrous effect on the environment and human well-being. **(Figure 1.1)** The international energy agency (IEA) suggested that the world net electricity generation is expected to rise beyond ten thousand tera watt-hour by the year 2050.^[1] More than 70% of the global energy demands are currently satisfied by non-renewable resources including coal, oil, and natural gas, which has resulted in serious environmental degradation and associated issues like global warming, climate change, melting glaciers, sea-level rise, etc.^[2-4] According to the world climate clock, we are now left with less than six years to limit the global warming to 1.5°C when compared to the pre-industrial levels, exceeding which may lead to devastating consequences. Henceforth, it is an immensely critical requirement that we switch to renewable sources, such as geothermal, biomass, wind, solar or hydro-electric power sources.

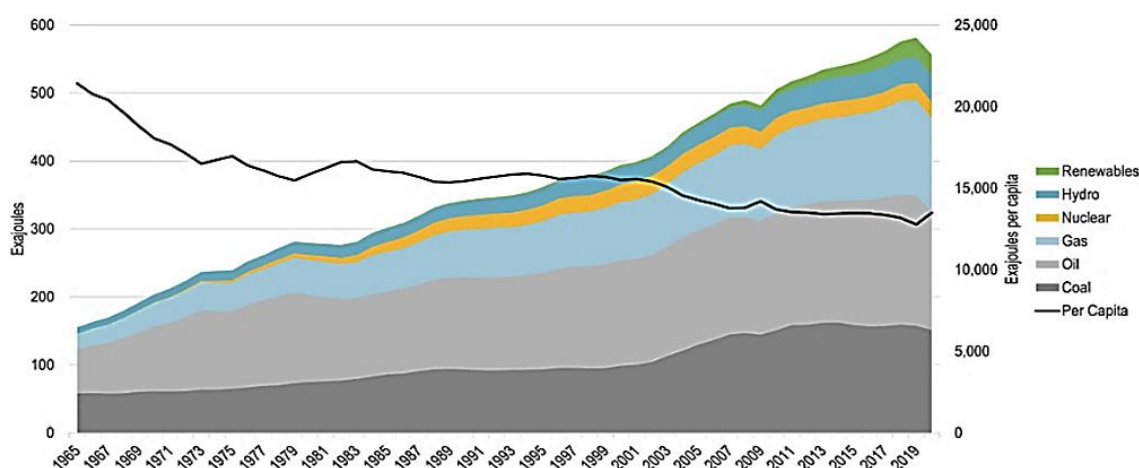


Figure 1.1. World energy consumption 1965-2020 (Source: BP Statistical Review of World Energy. Population data from World Bank).^[5]

The solar photovoltaics is expected to occupy more than 20% of the global electric energy generation sector in the coming decades, as solar energy is the cleanest, most abundant, and readily available source accessible to us. Moreover, the advent of technologies like internet of things, machine-to-machine communication, cyber physical systems etc. have rendered significance to indoor photovoltaics as well. Consequently, researchers worldwide have started working to improve the energy conversion efficiency of photovoltaic (PV) devices and to integrate them with other systems.^[6-9] In general, PV

technologies can be categorized into three generations (**Figure 1.2**): first, there are traditional p-n junction solar cells based on silicon (mono- or polycrystalline); second, there are thin-film solar cells (based on amorphous Si, gallium arsenide, cadmium telluride, etc.); and third, there are emerging molecular PV technologies, such as dye-sensitized solar cells (DSCs), organic solar cells (OSCs), perovskite solar cells (PSCs), etc.^[10–12] The high cost, intricate production process, and need for substantial quantities of high-purity silicon are some of the drawbacks of the first generation solar cells. When compared to the first generation solar cells, the second generation solar cells, which are based on thin film technology, have a number of advantages like requirement of fewer materials and processing steps, appreciable performance under outdoor as well as indoor illumination conditions, etc. However, they are having several disadvantages, including a higher rate of amorphous silicon degradation, a higher toxicity level for materials like cadmium, arsenic, etc., a lower availability of materials like tellurium, and a lower performance when compared to first generation. Some of the major drawbacks of the first two generations of solar PV cells are addressed by the third generation, which offers highly effective, less hazardous, and economically viable alternatives. However, they are limited by stability issues and lower performance under outdoor conditions.

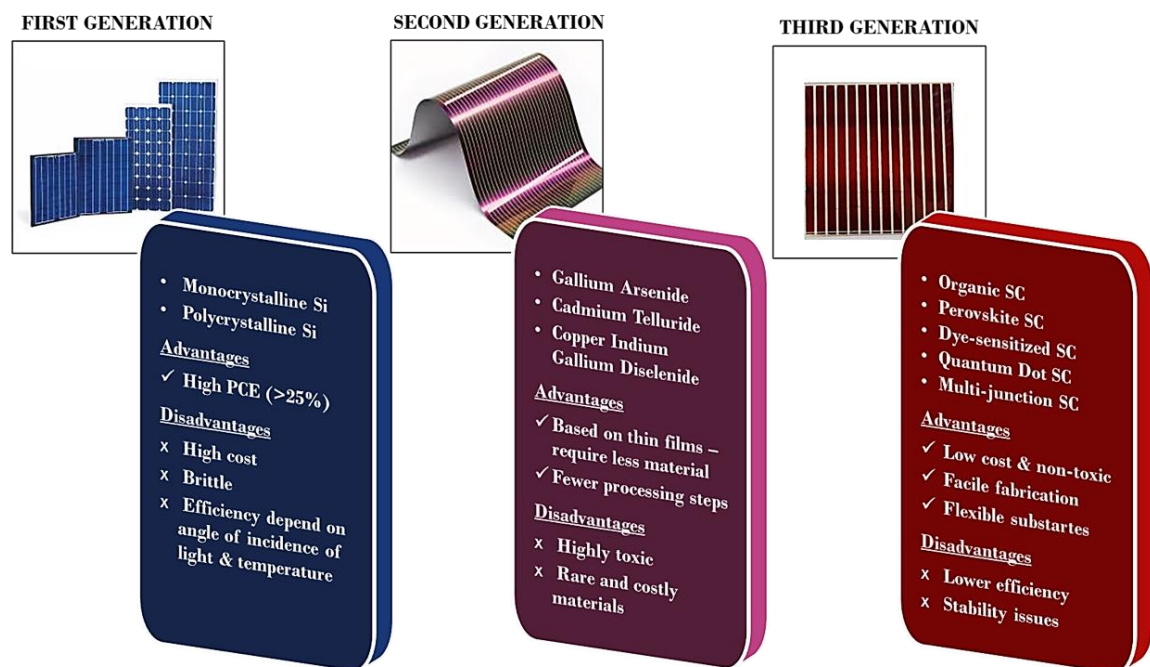


Figure 1.2. Different generations of photovoltaic technology.

1.2. Internet of things and indoor photovoltaics

The emergence of industry 4.0 has led to the promotion of automation and digitalization through the use of internet of things (IoT) networks (**Figure 1.3**) in smart

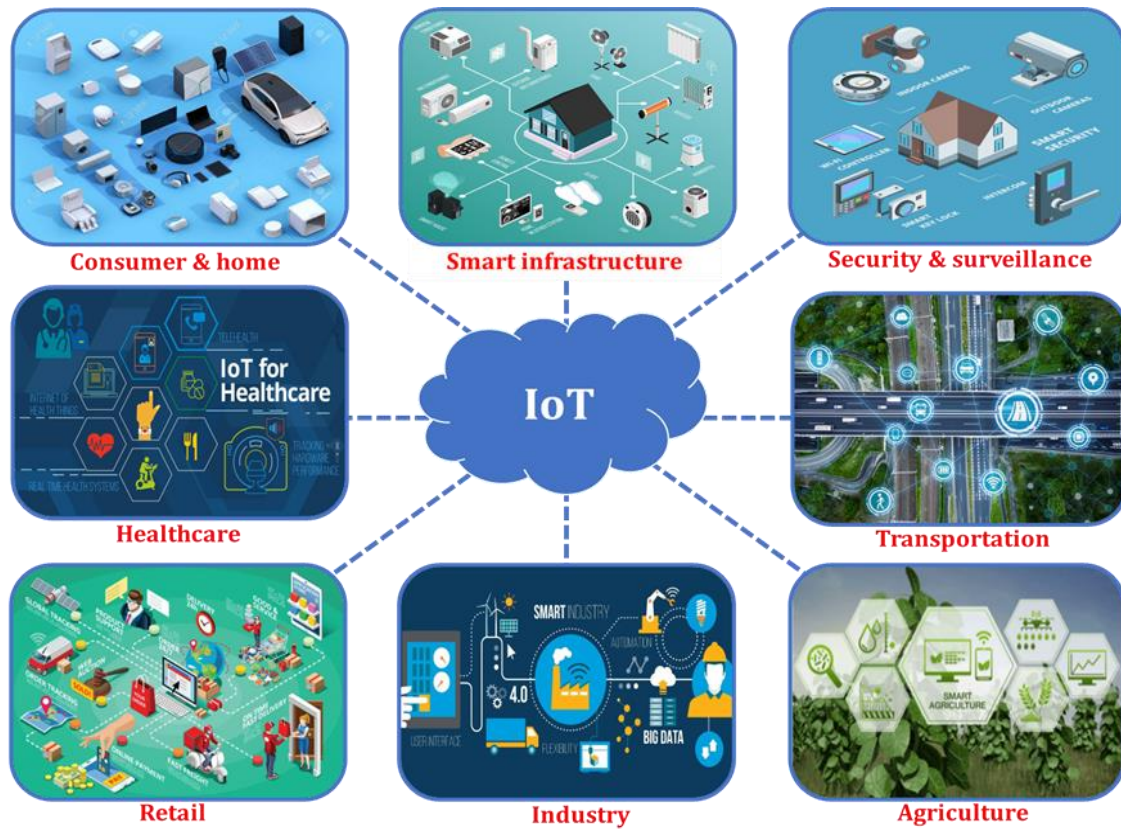


Figure 1.3. Various application domains of Internet of Things (IoT).

manufacturing technologies and related industries, as well as at homes, offices, shopping centres, hospitals and nearly every other sectors that we encounter in our daily lives.^[13] Batteries power the sensors and actuators that are implicit part of these IoT systems, whose deployment is expected to peak in the upcoming years.^[14,15] This creates a significant environmental risk as batteries impose large carbon footprint during their production as well as disposal. Overall, it is imperative that we combine our efforts to create ecologically friendly and self-sustaining energy harvesting technologies. This has paved the way for inception of integrated smart electronics that are self-powered and require no batteries, thus helping to decarbonize the energy industry. The necessity of sustainable energy harvesting for a circular economy has been emphasized by extensive research conducted in the alternative energy industries in recent years.^[16–19] The energy conversion efficiencies rendered by ambient energy harvesters, such as PV cells, piezo-electric devices, thermo-electric devices etc. need to be boosted, in order to accomplish our concurrent interest for building battery-free smart gadgets and IoT systems, as most of these systems are implemented indoors. Among the various ambient energy harvesters, the PV cells that can capture and recycle the omnipresent ambient light energy (which might be coming from diffused sunlight or from indoor/artificial light sources) into useful form, seems to be the

most suitable option for developing battery-free electronic systems. Hence indoor photovoltaics (IPV) will certainly have a significant role in the future IoT applications.

The most widely used indoor light sources are compact fluorescent light (CFL), light emitting diode (LED), incandescent, and halogen bulbs. At the same illuminance, each of these artificial light sources has a unique irradiance power density, irradiance spectrum, and light wavelength distribution.^[20] The same PV cell's spectral response will therefore differ at the same illuminance levels of various light sources. Until now, there has not been a standard method for gauging the indoor performance of PV devices. Environmental stability, large-area fabrication, mechanical flexibility, and spectral matching between the PV active material and the irradiance of the indoor light source are a few further difficulties in applying PV technology for indoor use. With an optimum band gap of 1.1-1.3 eV, the active materials designed for conventional PV systems are intended to absorb light in the 300 - 2500 nm window (covering the entire solar spectrum).^[21] Nonetheless, majority of the artificial light sources have irradiance spectra that fall in the visible region between 300 and 800 wavelengths. Therefore, thermalization and non-absorption of light energy might cause energy loss while using regular PV cells indoors. According to Teran et al., PV materials having a theoretical band gap energy of 1.8 - 2 eV are best suited for indoor light harvesting applications.^[21] Despite having a remarkable power conversion efficiency ($PCE > 26\%$) under full sun irradiation (AM 1.5G), the low band gap energy (~ 1.1 eV) of the first generation solar cells prevents them from performing well when exposed to indoor/ambient light. Second generation PV devices using III-IV compound semiconducting materials with tunable, larger band gap energies could achieve a higher PCE indoors. However, the high cost of these materials limits their use in the large-scale fabrication of interior PV modules.^[22] Soft materials with adjustable energy gaps are the foundation of third-generation photovoltaic cells, which include OSCs, PSCs, and DSCs. These devices offer several benefits, including increased flexibility, low weight, appreciable open circuit voltage, and easy spectral overlap with artificial light sources, making them appropriate candidates for indoor PV applications.

As compared to the other PV technologies, DSC has superior performance in indoor and ambient light settings, making it the most attractive option for light harvesting applications within buildings (**Figure 1.4**).^[23-25] Additionally, considering the use of inexpensive and environmentally safe components, ability to be fabricated on flexible substrates, and possibility to include visually appealing designs, DSCs can be integrated into wearable and portable smart devices as well as light-harvesting infrastructures like

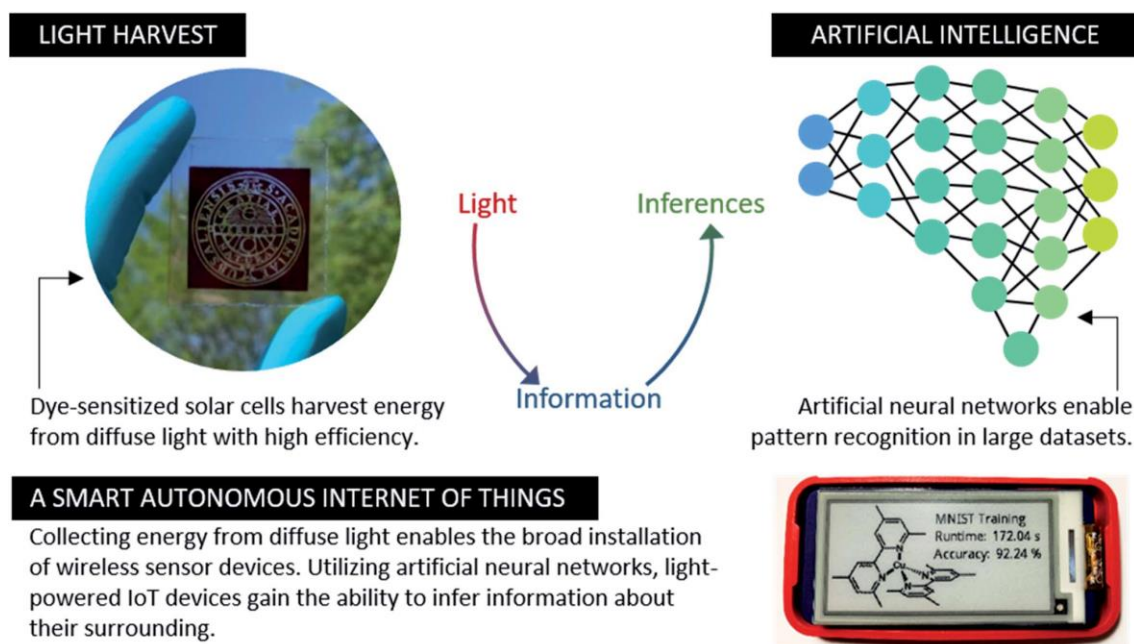


Figure 1.4. Demonstration of using dye-sensitized diffuse/ambient light harvesters (DSC) for powering automated IoT devices.^[26]

windows, roofs, and facades. The development of indoor dye-sensitized cells (I-DSCs) for powering low-power electronic devices has been aided by the enhanced PV performance of DSCs under indoor/ambient/diffused light conditions compared to the traditional first and second generation PV cells. One possible explanation for the improved *PCE* s of DSC in indoor environments is the convenient overlap between the emission spectra of indoor light sources and the absorption profile of the sensitizers utilized in these devices. In this regard, creating new dyes whose absorption matches the emission spectra of artificial or indoor light sources and utilizing dyes with complementary absorption for co-sensitizing the DSC photoanode have gained significant attraction in recent years. Other factors that contribute towards the better performance of I-DSCs are their higher shunt resistance and lower thermalization losses under low intensity indoor/ambient light illuminations.^[27] Altogether, DSCs are among the best PV options available for indoor/ambient light harvesting and hence IoT applications.

1.3. Dye-sensitized photovoltaic cells: Structure and working

Dye-sensitized photovoltaic cells (DSCs or DSPVs) are electrochemical devices which imitate the natural process of photosynthesis to convert light energy to electrical energy. Unlike the conventional solar cells, dye molecules are used to harvest light in DSCs. By tuning the energy levels of dye molecules, absorption in any desirable wavelength range can be achieved. Hence, DSCs can achieve better power conversion

efficiency under indoor/ambient light conditions. DSCs were first introduced by Michael Grätzel and Brian O'Regan in 1991, wherein they could achieve a power conversion efficiency of $\sim 7\%$ under simulated sunlight and $\sim 15\%$ under diffused daylight condition.^[28] Ever since then, numerous researches are being done on various components of DSCs to enhance the device performance under outdoor as well as indoor conditions. Till date, a highest efficiency of 15.2% under one sun condition (AM 1.5G simulated solar irradiation)^[29] and 35.6% under indoor condition (1000 lux fluorescent light) has been realized.^[30]

1.3.1. Structure of DSCs

The basic device components of DSCs are illustrated in **Figure 1.5**. A dye-adsorbed photoanode, a counter electrode, and a redox mediator make up the three primary parts of a DSC.^[28,31]

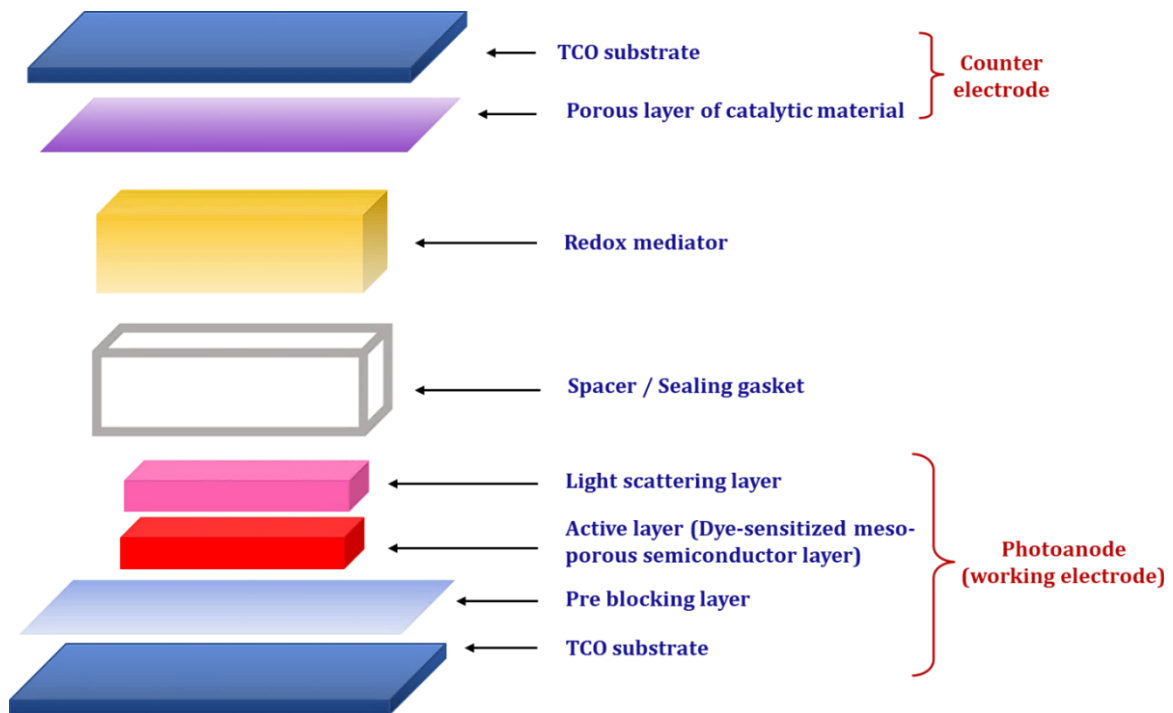


Figure 1.5. Typical components used in DSCs.

(a) **Photoanode/working electrode.** Traditionally, a mesoporous layer of semiconductor deposited over a transparent conducting oxide (TCO) substrate and sensitized with dye molecules, serves as the photoanode or working electrode (WE) of DSC. TCO substrates for the fabrication of DSCs have been made of glass plates deposited with fluorine doped tin oxide (FTO) or plastic substrates, such as polyethylene terephthalate (PET), polyethylene naphthalate (PEN) etc., coated with indium doped tin oxide (ITO) or FTO. The conventional photoanode materials for DSCs are wide band gap, n-type metal oxide

semiconductors, such as TiO_2 , ZnO , Nb_2O_5 , SnO_2 , and so on. Some of the ideal characteristics for a semiconductor layer to be utilized as photoanode in DSCs are listed below.^[32,33]

- High specific surface area for maximum dye adsorption.
- Optimal conduction band edge position to achieve higher open circuit voltage and to facilitate efficient electron injection from dye to semiconductor layer.
- Optimum thickness to guarantee maximum dye adsorption, thereby enhancing light absorption and better charge collection.
- Appreciable connectivity between particles to facilitate faster electron diffusion.
- Minimum amount of defects to minimize recombination.
- High porosity for efficient electrolyte penetration and diffusion, to enable efficient dye regeneration.
- Sufficient mechanical strength to avoid detachment of the semiconductor film from TCO.

TiO_2 is the most popular photoanode material for DSCs, owing to its desirable properties. In DSC, the semiconductor layer acts as a platform for adsorption of sensitizer or dye molecules, while the dye molecules perform the function of photon absorption and charge separation. Hence, the long-term stability and the light harvesting efficiency of DSC are substantially influenced by the electrochemical and photophysical properties of the dye. An ideal sensitizer for DSC should possess following properties.^[34]

- Broader absorption in the visible range.
- Ground state and excited state energy levels appropriately matching with the electrolyte's redox potential and the semiconductor's conduction band edge, respectively.
- Suitable anchoring groups with a strong binding coefficient, such as carboxylate or phosphonate for firmly binding on to the semiconductor oxide surface.
- Long alkyl chains to retard the recombination processes
- Photochemical and electrochemical stability under light exposure.

Photovoltaic performance of DSCs can be improved by improving its light harvesting efficiency via photoanode modifications, such as introduction of blocking layers, inclusion of plasmonic nanoparticles or scattering particles, incorporation of voids or surface roughness, development of hybrid nanostructures and so on, or by designing new

sensitizers with broader absorption profile or by adopting co-sensitization strategy, wherein different dyes with complementary absorption are anchored on to the semiconducting layer for achieving panchromatic absorption.

(b) Counter electrode. A porous layer of catalyst material coated over a TCO substrate makes up the counter electrode (CE). In DSC, the CE performs the function of reducing the oxidized electrolyte species, which in turn regenerates the oxidized dye molecules. The charge transfer kinetics at the CE/electrolyte interface influence the series resistance (R_s) and hence the fill factor of the device. A good CE material should possess the following characteristics.

- High catalytic activity to enhance the redox reaction at the CE.
- High surface area to reduce the charge transfer resistance.
- High porosity to enable better electrolyte penetration.
- Good mechanical, electrochemical and chemical stability.
- Minimal light absorption, particularly in case of bifacial devices.
- Inexpensiveness, non-toxicity and environment friendliness.

Platinum is the most commonly used CE material in conventional DSCs owing to its high conductivity, stability, and catalytic property. However, it is costly and less abundant, which creates a need for development of other CE materials such as carbonaceous materials (graphene, carbon black, carbon nanotubes, etc.), conducting polymers (poly (3,4-ethylene dioxythiophene) or PEDOT, polyaniline or PANI, etc.), transition metal compounds, heteroatom-doped materials, noble metal-free chalcogenides and other composite materials, in order to realize economically feasible DSCs.^[35,36]

(c) Redox mediator. Redox mediators, also known as electrolytes, is one of the vital components of DSC.^[37] It is composed of both oxidized and reduced species, the later aid in the regeneration of oxidized dye molecules. Also. the concentration and diffusion kinetics of different electrolyte species regulate the charge transfer between WE and CE. The incident photon-to-current conversion efficiency and hence the short circuit current density of DSCs are concomitantly dependent on light harvesting, electron injection, charge collection, and dye regeneration efficiencies. Whereas, the dye regeneration is predominantly determined by the ion mobility and mass transport within the electrolyte system. As a result, the redox mediator plays an inevitable role in determining the short circuit current density of DSC. In addition to this, the open circuit voltage of the DSCs is influenced by the redox potential of the redox system. In short, the electrolyte plays a vital role in determining the power conversion efficiency of DSCs. Moreover, the long-term

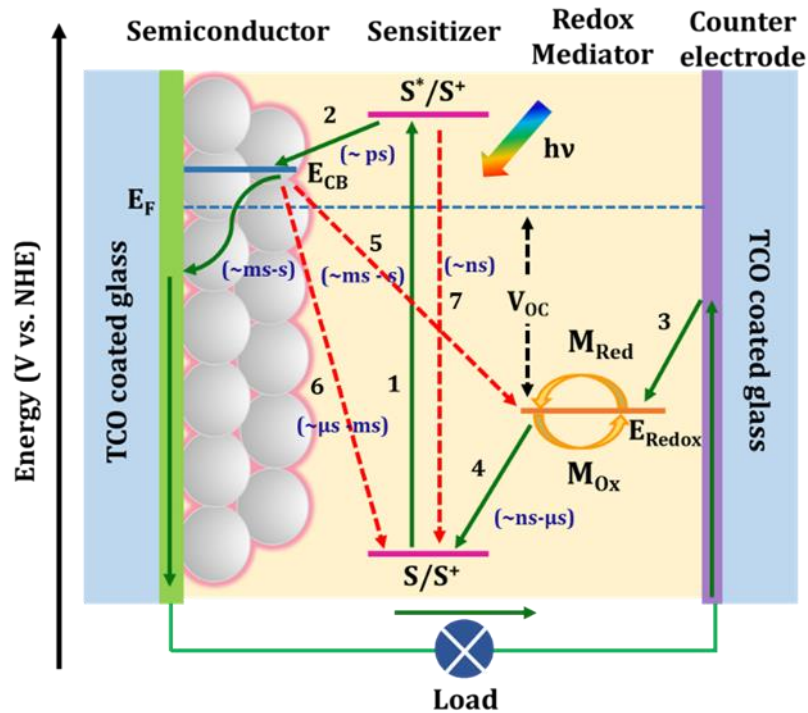
stability of DSC also depends on the electrolyte. In order to function efficiently as a redox mediator in DSCs, the electrolyte system must ensure some essential properties as mentioned below.

- High solubility in organic solvents.
- High photochemical and electrochemical inertness.
- Less bulkiness to enable sufficient mass transport in the electrolyte as well as within the mesoporous semiconductor matrix.
- Positive redox potentials to ensure higher open circuit voltage with minimum over potential loss and sufficient driving force for regeneration.
- Faster charge transfer at the CE interface to promote rapid dye regeneration.
- Slower charge transfer dynamics at the semiconductor interface to suppress the recombination.
- Minimal competitive light absorption with the sensitizer.
- Less corrosive towards components such as sensitizer, semiconductor, silver interconnection, sealing materials, etc. to ensure long term stability.

In addition to the redox species, some additives are added in the electrolyte system to achieve precise control over conduction band position and recombination rates, which are inevitable to achieve higher DSC performance. The traditional usage of iodide-triiodide redox system as electrolytes is being replaced by metal complex redox shuttles based on cobalt and copper, which provided higher positive redox potentials. On the other hand, quasi solid-state and solid-state electrolytes are being investigated lately in order to rectify the issues normally associated with the liquid state electrolytes, such as leakage, solvent evaporation, corrosion of sealing materials and CE materials, photodegradation and desorption of dye molecules.

1.3.2. Working of DSCs

The basic working principle of DSCs involves a number of interfacial charge transfer processes as provided in **Figure 1.6**. The forward or gain mechanisms that determine DSC performance include photon absorption, which excite the dye molecules at the photoanode (1); electron injection to the conduction band (CB) of the semiconductor (2), which is followed by electron diffusion through the mesoporous semiconductor matrix to reach the TCO and the external circuit; reduction of oxidized species in the electrolyte by electrons at the counter electrode (3); and regeneration of oxidized dye molecules by



Forward or Gain processes:

- (1) Dye excitation: $S + hv \rightarrow S^*$
- (2) Electron injection and diffusion: $S^* \rightarrow S^+ + e_{CB}^-$
- (3) Reduction of electrolyte species: $M_{Ox} + e_{Pt}^- \rightarrow M_{Red}$
- (4) Dye regeneration: $S^+ + M_{Red} \rightarrow S + M_{Ox}$

Backward or Loss processes:

- (5) Recombination with redox species: $M_{Ox} + e_{CB}^- \rightarrow M_{Red}$
- (6) Recombination with oxidized dye: $S^+ + e_{CB}^- \rightarrow S$
- (7) De-excitation of dye: $S^* \rightarrow S$

Figure 1.6. Working principle of DSCs.

reduced species in the redox shuttle (4). The photovoltaic performance of DSCs can be enhanced by judiciously tuning the energy levels of various device components, such as dye, semiconductor and electrolyte, so as to affirm ample driving force for different interfacial electron transfer gain processes without major overpotential losses. On the other hand, the conduction band (CB) and sub-bandgap electrons undergo recombination with the oxidized dye molecules (5) and the oxidized species in the electrolyte (6), as well as the excited dye molecules decay (7). These backward or loss processes limit the DSC performance, the former being more detrimental. The quantum yield and photovoltaic

performance of these devices are determined by the dynamic competition between these forward and backward processes under operating conditions.^[38] For optimal performance, the forward processes' kinetics need to be faster than the backward processes. For example, to avoid spontaneous de-excitation of the sensitizer, the injection of electrons into the semiconducting matrix should be rapid. Likewise, the dye regeneration and charge diffusion within the semiconductor should occur more quickly ($\sim \mu\text{s} - \text{ns}$) than the recombination rates, which are typically in $\sim \text{ms}$ range. An ideal equilibrium between the kinetics of these charge transfer processes should be realized to achieve desired DSC performance; which might be accomplished by carefully designing the different device components.

The photovoltaic performance of a DSC or any PV device is evaluated by estimating its power conversion efficiency (*PCE*) under constant illumination. The *PCE* of a PV device is defined as the ratio of the maximum output power density (P_{max}) of the device to the input power density of the incident light (P_{in}). Whereas, the P_{max} of the device depends on open circuit voltage (V_{OC}), short circuit current density (J_{SC}) and fill factor (*FF*). V_{OC} is the maximum voltage output of the cell that can be realized by connecting infinite load across the device, known as open circuit condition (**Figure 1.7(a)**). While J_{SC} is the maximum current output flowing out of the device when it is short circuited, by connecting zero load across it (**Figure 1.7(b)**). On the other hand, *FF* is a parameter (with ideal value of 1) which is determines the quality of the PV cell. It depends on the series resistance and shunt resistance of the device. The V_{OC} of DSC is predominantly influenced by the energy difference between the semiconductor's Fermi level (E_F) and the electrolyte's redox potential (E_{redox}), as stated in equation 1.1.

$$V_{OC} = \frac{E_F - E_{redox}}{q} \quad (1.1)$$

where q is the electronic charge. The V_{OC} of DSC is further affected by the charge transfer kinetics at the semiconductor/electrolyte. Meanwhile, the J_{SC} is determined by its incident photon-to-current conversion efficiency (*IPCE*), which in turn depends on the performance determining parameters of DSCs, such as light harvesting efficiency (*LHE*), electron injection efficiency (η_{inj}), charge collection efficiency (η_{CC}), and dye regeneration efficiency (η_{reg}) as,

$$IPCE = LHE \eta_{inj} \eta_{CC} \eta_{reg} \quad (1.2)$$

The combined impact of all these factors determines how well the DSC performs.^[39]

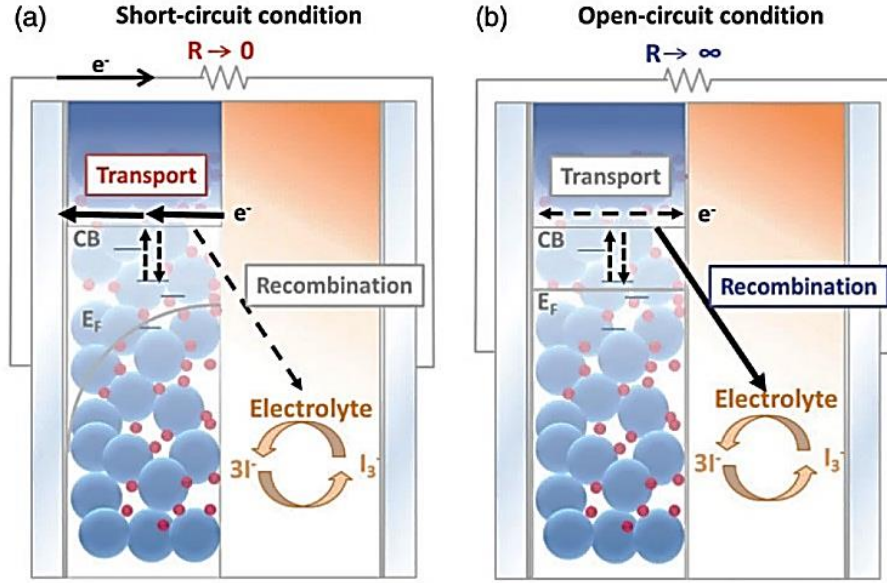


Figure 1.7. DSC connected under (a) short circuit and (b) open circuit condition.^[40]

The *LHE* of the photoelectrode is one of the significant factors that influence the performance of DSCs. *LHE* is predominantly related to the amount of light absorbed by the active layer of the solar cell. *LHE* of a DSC photoanode film can be expressed as,

$$LHE = 1 - 10^{-A(\lambda)} \quad (1.3)$$

where $A(\lambda)$ is the absorbance of the dye sensitized photoanode film at wavelength λ . The extinction coefficient, the absorption profile and the amount of sensitizer molecules adsorbed on the mesoporous layer, and the optical path length of the incident light within the active layer are the major factors affecting the *LHE* of a DSC photoanode. According to Marcus theory, the rate of injection (k_{inj}) of photo-generated electrons from the dye molecules to the semiconductor is determined predominantly by the relative position of lowest unoccupied molecular orbital (LUMO) of the dye and the CB states of the semiconductor.^[41] In addition, the nature of the anchoring group in the dye, mode of adsorption of dye to the semiconductor, other adsorbed species on the semiconductor surface and the surrounding medium, i.e. the electrolyte solution including the additives also influence the k_{inj} .^[42] Whereas the rate of de-excitation or relaxation (k_{relax}) of the excited dye molecules depends on their HOMO/LUMO levels' nature and position, and also on nature of the surrounding electrolyte. Assuming the rate constants of all the processes in DSCs to be of pseudo first order, the injection efficiency (η_{inj}) of DSCs can be estimated as,

$$\eta_{inj} = \frac{k_{inj}}{k_{inj} + k_{relax}} = \frac{\tau_{relax}}{\tau_{inj} + \tau_{relax}} \approx 1 - (\tau_{inj}/\tau_{relax}) \quad (1.4)$$

where τ_{inj} is the time constant for injection, and τ_{relax} is the relaxation or luminescence lifetime of the dye. For better DSC performance, shorter τ_{inj} and longer τ_{relax} is favourable. The τ_{relax} of typical sensitizer molecules used in DSCs lie in the ns range, while the injection occurs in ~fs – ps timescale, giving rise to a η_{inj} of more than 90%.

The charge collection and extraction occur effectively only when the injected electrons diffuse through the mesoporous semiconductor layer to reach the back contact, which can be described by a random walk model, and this extracted charge do the electrical work. The charge collection efficiency (η_{CC}) of DSC is contingent upon the diffusion length and diffusion time of electrons within the semiconductor layer. The diffusion or transport of electrons within the semiconductor network is driven by the charge concentration gradient created by photoelectron injection and hence depend on the intensity of incident light. The electron diffusion process is further dictated by the nanostructure, thickness and inter-particle connectivity in the mesoporous semiconducting layer. The grain boundaries and sub band gap states present within the nanoporous semiconducting film act as electron traps, and hinder the diffusion process. During the diffusion process, the electrons in the conduction band get continuously trapped and de-trapped, whereas the diffusion current is constituted by the conduction band electrons only.^[43] This is called the multiple trapping/detrapping model for electron diffusion. There is a persistent probability for the electrons in the conduction band states and the sub-bandgap states (trap states) to recombine with the oxidized dye molecules or the oxidized species present in the electrolyte as well. Hence, a combined effect of electron diffusion and recombination determines the η_{CC} of DSC, as

$$\eta_{CC} = \frac{k_{tr}}{k_{tr} + k_{rec}} = \frac{\tau_{rec}}{\tau_{tr} + \tau_{rec}} \approx 1 - (\tau_{tr}/\tau_{rec}) \quad (1.5)$$

where k_{tr} and k_{rec} are the diffusion/transport rate and recombination rate, respectively, while τ_{tr} and τ_{rec} are the corresponding time constants. The transport time (τ_{tr}), also known as diffusion time (τ_d), refers to the time taken by the electrons to diffuse through the semiconductor matrix before they get collected at the back contact. On the other hand, the time for which the electron remains in the semiconductor layer before recombining with the oxidized species in the electrolyte or with the oxidized dye, is referred to as the recombination time (τ_{rec}) or lifetime (τ_n). τ_d is generally determined under short circuit condition when most of the injected electrons are collected at the back contact (**Figure 1.7(a)**). Typical values of τ_d for a nanostructured TiO₂ film lies in the ms to s range. τ_n is obtained under open circuit condition, when no charge is extracted at the back contact and

the only pathway for the injected electrons to decay is via recombination (**Figure 1.7(b)**).

The η_{CC} of DSC, given in equation 1.5, can also be expressed as,

$$\eta_{CC} = \frac{1}{1 + \tau_d/\tau_n} \approx 1 - (\tau_d/\tau_n) \quad (1.6)$$

Efficient charge collection requires faster electron diffusion and slower recombination kinetics (i.e. $\tau_d < \tau_n$). The diffusion length (L_n) refers to the distance covered by the electrons within the mesoporous semiconductor layer before recombining with the oxidized species.

L_n can be expressed as,

$$L_n = d\sqrt{\tau_n/\tau_d} = \sqrt{D_n \tau_n} \quad (1.7)$$

where d is the semiconductor layer thickness, and D_n ($\approx d^2/\tau_d$) is the coefficient of electron diffusion. L_n must be higher than d for effective charge collection and hence higher current output.

On one hand, the dye regeneration process dynamically competes with the charge recombination with oxidized dye molecules to realize effective charge collection, while on the other hand, the regeneration efficiency (η_{reg}) is affected by the rate of recombination of electrons with the oxidized electrolyte species (k_{rec}) as,

$$\eta_{reg} = \frac{k_{reg}}{k_{reg} + k_{rec}} = \frac{\tau_{rec}}{\tau_{reg} + \tau_{rec}} \approx 1 - (\tau_{reg}/\tau_{rec}) \quad (1.8)$$

where k_{reg} is the rate and τ_{reg} is the time constant corresponding to the dye regeneration process. Again, the Marcus theory suggests that k_{reg} , and subsequently τ_{reg} , depends on the position and nature of the energy states of the redox species as well as the highest occupied molecular orbital (HOMO) level of the dye.^[44,45] It is also influenced by the surrounding medium, i.e. the solvent of electrolyte. The rate of regeneration further relies on the rate at which electrolyte species diffuse between the photoanode and counter electrode as well as the rate at which redox species seep into the nanoporous semiconductor matrix.

1.4. Photoanode engineering strategies for enhancing the performance of DSCs

Photoanode, made up of dye sensitized nanoporous semiconducting layer, is an imperative part of DSC, as various crucial processes such as photoelectron generation, charge separation, electron transportation, and dye regeneration occur at the photoanode interface. The semiconductor layer of photoanode plays a prominent role in determining the DSC performance. DSCs which bestowed record breaking performance under outdoor

(15.2% under AM 1.5G simulated solar irradiation) and indoor (35.6% under 1000 Lux CFL illumination) conditions, have employed photoanodes based on mesoporous titania (TiO_2) nanoparticles network co-sensitized with various organic dye molecules.^[29,30] Over the past few decades, several strategies have been explored to enhance the DSC performance by improving its *LHE* by engineering the nanostructured semiconducting layer as well as sensitizers. Some of them are detailed in this section.

1.4.1. Development of various nanostructures

Though nanoparticulate films made of TiO_2 nanoparticles are recognized to be the most suitable material for DSC working electrode, many other metal oxide semiconductors like ZnO , SnO_2 , Nb_2O_5 , WO_3 , CeO_2 , In_2O_3 , SrTiO_3 , Zn_2SnO_4 , and so on were also being employed as photoanode materials in DSCs.^[46] Due to the existence of a large number of grain boundaries, nanoparticle films exhibit quite smaller electron diffusion coefficient than that of bulk materials, resulting in shorter electron diffusion length. This drawback of nanoparticle thin films could be rectified by using other nanostructures like nanorods, nanotubes etc. which offer longer electron diffusion lengths owing to their lesser grain boundaries. However, they are compromised with a decreased dye adsorption due to reduced specific surface area. The nanostructures of various semiconducting metal oxides and hybrid materials, developed for DSC photoanodes are discussed below.

(a) ***TiO₂ nanostructures.*** Owing to its favourable optical absorption, suitably positioned CB edge, good chemical stability, non-toxicity, low cost, and environment friendliness, TiO_2 is the widely accepted semiconducting material for DSC application. The first ever successful DSC, reported by Michael Grätzel and Brian O'Regan, used spherical TiO_2 nanoparticles sensitized with ruthenium dyes, iodide/triiodide electrolyte and platinum CE.^[28] Later, Hu et al. exhibited the use of polyvinylpyrrolidone (PVP, 1.5 wt%) as a pore-forming agent in the TiO_2 matrix to increase the surface area for dye adsorption, thereby attaining an elevated efficiency of 9.86% with N719 dye and I^-/I_3^- electrolyte.^[47] Many other morphologies of TiO_2 nano- and micro-structures were explored to achieve improvement in DSC performance. For instance, Pazoki et al. introduced mesoporous TiO_2 microbeads based electrode for improving the performance of DSC using cobalt complex based electrolyte.^[48] Endowed with larger pore size, microbeads reduced the mass transport issues in cobalt electrolyte and facilitated faster electron diffusion along with enhanced dye adsorption and light scattering, leading to ~ 28% improvement in *PCE*. Hwang et al. utilized multi-shell hollow TiO_2 nanoparticles in DSC photoanode, which enabled multiple

light reflection within the photoanode, in addition to high dye loading and faster electrolyte diffusion, leading to improved current density and hence *PCE*.^[49] TiO₂ nanoparticles based photoanode films have several disadvantages, viz. large electron recombination kinetics, low electron diffusion coefficient ($\sim 5 \times 10^{-5}$ cm²/s) and shorter diffusion length, which is attributed to the large number of grain boundaries and defects acting as recombination centers.^[50]

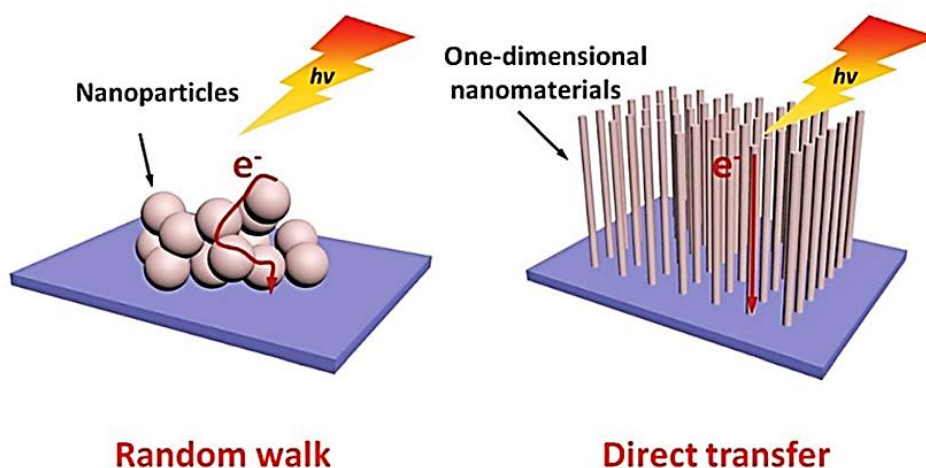


Figure 1.8. Electron transfer pathways in traditional photoanodes made up of spherical semiconductor nanoparticles and the ones using one-dimensional nanostructures.^[51]

One dimensional (1-D) nanostructures have better connectivity and hence offer direct path ways for electron diffusion, which leads to larger electron diffusion lengths and better charge collection (**Figure 1.8**). Recombination rate may also be decreased due to reduced grain boundaries. Hence 1-D TiO₂ nanostructures, such as nanorods, nanotubes, nanofiber, nanowire etc., ought to be used as replacement for conventional spherical nanoparticles in DSC photoanodes.^[51] However, most of them have lesser surface area compared to nanoparticles, which affects the dye adsorption and hence the current density in DSC. This problem could be overcome by employing surface treated 1-D materials with increased porosity or by using hybrid photoanode architectures.^[52,53] Zhang et al. utilized randomly oriented TiO₂ nanorods having varying lengths to fabricate DSCs and concluded that longer nanorods with lesser grain boundaries gave rise to higher charge collection efficiency compared to shorter ones and resulted in a *PCE* of 8.87%, using Z907 dye along with iodine redox shuttle.^[54] TiO₂ nanotubes render more internal surface area for dye adsorption compared to the nanorods, owing to their hollow architecture.^[55] TiO₂ nanowires and fibers were also explored as DSC photoelectrodes.^[56,57] Ni et al. found that the dye loading in TiO₂ nanowires could be enhanced by improving their surface roughness

by prolonged etching treatment using hydrochloric acid (HCl).^[58] Using the rough surface TiO₂ nanowires along with a scattering layer as photoanode in DSC, they could achieve 9.39% *PCE*. Gnida et al. compared the performance of DSCs using different photoanodes with TiO₂ nanoparticles, mixture of TiO₂ nanoparticles and nanotubes, and mixture of TiO₂ nanoparticles and nanowires, and observed that the latter one delivered the best *PCE*, owing to better surface area and facile charge transport.^[59] Chatterji et al. employed a 1:1 wt% composite of TiO₂ nanorod (hydrothermally synthesized) and nanoparticle (commercial) as the photoanode material in DSC to realize a *PCE* of 8.61%, owing to the improved charge carrier transport and reduced recombination.^[60] In a similar approach, Shobana et al. constructed a bi-layered photoanode with hydrothermally prepared rutile TiO₂ nanorod and nanoparticle, which could outperform the ones using the nanorod alone. The bi-layer device could deliver better current density as the nanoparticles impart better dye loading while the nanorods provide easy electron diffusion pathways.^[61] Wu et al. developed a multilayered TiO₂ nanowire array, made up of a bottom layer of densely packed TiO₂ nanowire array (DTNW), intermediate layer of hierarchically branched TiO₂ nanowire arrays (HTNW) and a top layer of loosely packed TiO₂ nanowire arrays (LTNW), via repeated hydrothermal cycles, and utilized it in DSC to obtain better performance than the standard TiO₂ nanoparticle (P25) based DSC.^[56] The DSC based on this multilayered assembly delivered a *PCE* of 9.4%. Increment in light scattering and suppressed electron recombination were regarded as the reason for this impressive performance. Several other hierarchical TiO₂ structures were also widely explored as DSC photoanode materials (some of them are given in **Figure 1.9**), owing to their appreciable surface area, porosity and light scattering properties.^[62–64] Zhao et al. demonstrated hierarchically structured 3-D ordered macroporous TiO₂ (HS-3DOM) samples synthesized with the help of well arrayed polymethyl methacrylate (PMMA) microsphere templates with pore size ranging from 85–155 nm. When used in DSC, the HS-3DOM with an optimum pore size of ~105 nm provided the highest energy conversion efficiency of ~ 9.4%.^[65] This *PCE* could be further increased to ~ 10.3% by Xu et al. via introduction of micropores into the macroporous 3-D inverse opal (3D-IO) TiO₂ structure, which increased the specific surface area of the structure by ~ 47%.^[66] The resultant increase in dye adsorption improved the current density and *PCE* for devices while employing a ruthenium based dye (N719) and an organic dye (YKP-88) along with liquid iodine electrolyte. These structures have highly interconnected and uniformly distributed pores that ensure faster diffusion of charges leading to better charge collection and hence enhanced current density. In addition to this,

the highly porous nature of these structures make them suitable for DSCs based on mass transport limited metal complex based electrolyte systems.

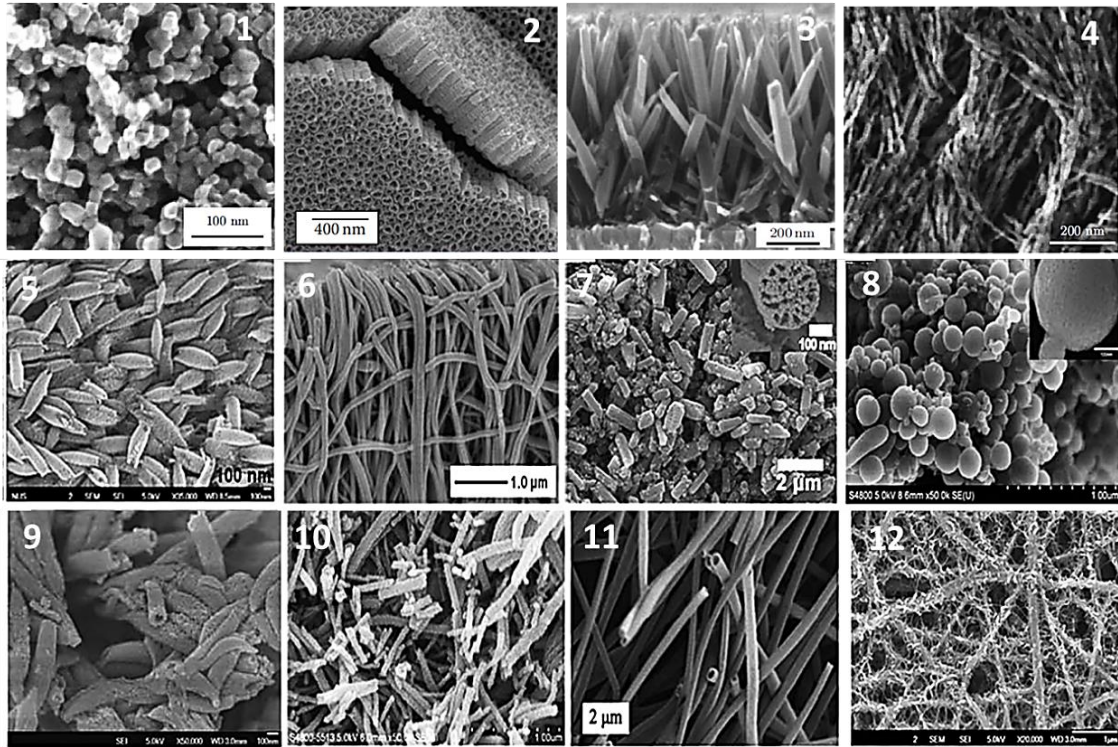


Figure 1.9. SEM images of some of the widely used morphologies of TiO₂ nanostructures used in DSC photoanodes.

(b) ZnO nanostructures. Zinc oxide (ZnO) is considered to be the most suitable alternative for TiO₂ to be used in DSC photoanode, considering their similar energy band structures, electron transfer process and injection dynamics.^[67] In addition, ZnO possess similar trap state distribution, but higher electron mobility when compared to TiO₂. In spite of these favourable characteristics, ZnO based DSCs exhibit considerably lower photovoltaic performance than the TiO₂ devices due to poor dye adsorption and faster degradation of dye molecules. In addition, it is reported that the faster electron transport in ZnO layer is compensated by its higher recombination rate, which makes it less efficient candidate for DSC photoanode comparative to TiO₂.^[68] Also, the lower dielectric constant of ZnO makes the charge separation difficult, as a result of which the injected electrons recombine with the oxidized dye molecules before they could be regenerated by the electrolyte species.^[69] The lower electrochemical stability of ZnO under acidic environment and the working conditions of DSC, affects the long-term stability of the ZnO based devices. There are two major degradation processes involved in ZnO based DSCs. First one occurs during the dye soaking. When immersed in the acidic dye solution, the ZnO degrades and releases Zn²⁺

ions which form Zn^{2+} /dye aggregates.^[70] ZnO also undergoes chemical degradation under illumination in the presence of electrolyte.^[71] These degradation processes result in injection limitations caused by dye aggregation, decrease in number of dye molecules available for photoelectron generation, and defects on ZnO surface, thereby affecting the J_{SC} of the device. Reducing the time for dye soaking and usage of blocking layers are two effective strategies for suppressing such degradation. It is anticipated that ZnO photoanodes can render improved DSC performance by using appropriate dye-electrolyte combinations and interfacial treatments, while reducing the cost of fabrication. A wide variety of ZnO nanostructures, such as nanoparticles, nanoforest, nanoflowers etc. (few of them shown in **Figure 1.10**) prepared via facile synthesis techniques were studied for improving the performance of DSCs.^[72–75]

Lin et al. achieved an appreciable *PCE* of 6.06% using ZnO nanosheets (ZnO-NS) which possess better electron diffusion coefficient and higher dye loading when compared to ZnO nanoparticles.^[76] Furthermore, they obtained a *PCE* of 7.07% by utilizing a bilayer TiO_2 -NP/ZnO-NS film sensitized with a metal free organic dye D149. Later on, He et al. observed that hydrogen related defects in ZnO lead to electron recombination and hence affected the J_{SC} of ZnO based DSCs.^[77] They could effectively resolve this problem by treating the $\text{Zn}(\text{OH})_2$ precursor with low temperature plasma, which reduced the hydrogen related defects in the synthesized ZnO NPs, hence suppressing recombination in ZnO based DSCs and delivering a remarkable *PCE* of 8.03%. The grain boundary problems of these 0-D nanostructures could be rectified using 1-D nanostructures, like nanorods and nanowires, which provide direct pathways for electron conduction.^[78–80] Wijeratne et al. studied the influence of aspect ratio of ZnO nanorods (NRs) on the electron transport properties in DSC photoanodes and observed that the *PCE* of DSC improved with the increase in aspect ratio of ZnO NRs upto an optimum value. This increase was attributed to the enhanced J_{SC} owing to the increase in dye loading and reduced electron transport resistance. However, increasing the aspect ratio beyond the optimum value (~ 6.8) resulted in more electron recombination resulting in reduced *PCE*.^[81] Yuliasari et al. reported that DSCs based on ZnO nanorods with hedgehog structure could perform better when compared to the vertically aligned ZnO nanorods.^[78] Hedgehog shaped ZnO NRs were endowed with better dye loading, electrolyte penetration and faster electron transport, which assisted them in attaining better DSC performance. It is also observed that the larger electron diffusion length ($\sim 100 \mu\text{m}$) of vertically aligned ZnO NWs is advantageous to

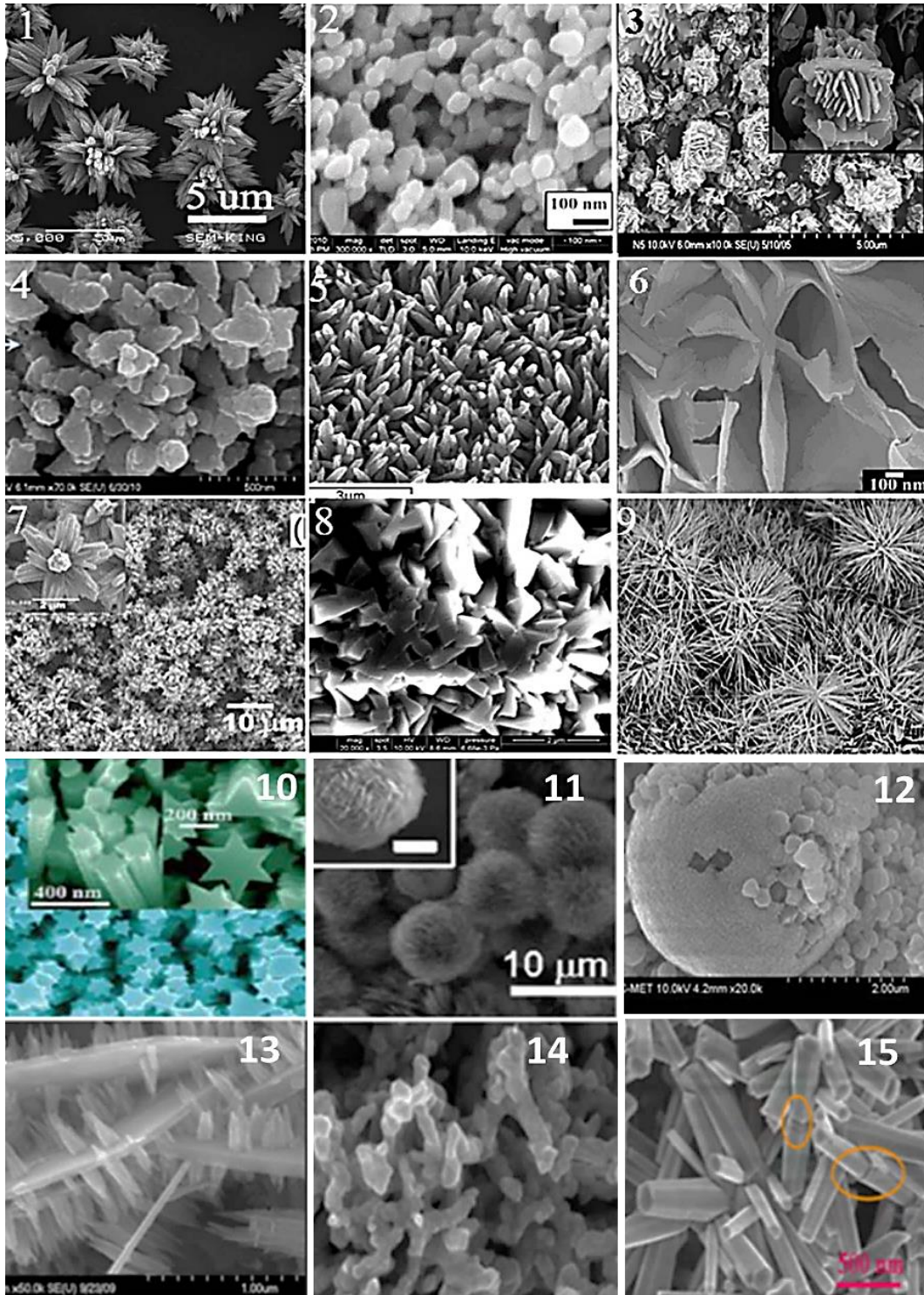


Figure 1.10. SEM micrographs of some of the various morphologies of ZnO nanostructures synthesized for DSC photoanodes. ^[82]

DSCs working with organic dyes and alternative redox shuttles. ^[83,84] Various hierarchical ZnO aggregates and 3-D structures were also explored to increase J_{sc} by improving dye loading and scattering effect in addition to the enhancement in diffusion length and thereby enhancing the device performance. ^[85–87] Recently, Yang et al. electrodeposited an array of

ZnO hierarchical nanorods on stainless steel meshes and employed them as photoanodes in flexible DSCs.^[86] The hierarchical nanorod arrays based device exhibited better J_{SC} and hence higher PCE when compared to the ones using primary nanorod arrays.

(c) Nanostructures of other materials & hybrid nanocomposites. Besides the above-mentioned metal oxide semiconductors, i.e. TiO_2 and ZnO , many other materials have been investigated to be incorporated as the active layer in DSC photoanodes. Tin oxide (SnO_2), a transparent conducting oxide with a wider energy gap (~ 3.6 eV) and higher electron mobility, is one such material. SnO_2 with a more positive CB edge, happens to be a suitable choice for DSCs employing potential sensitizers, like porphyrin based dyes, having excited state energy lying below the CB minimum of TiO_2 .^[88] Nevertheless, DSCs based on SnO_2 have lower PCE than those made of TiO_2 photoelectrodes, because of its low dye adsorption and lower V_{OC} owing to its more positive CB position. Dimarco et al. did a comparison of charge kinetics in TiO_2 and SnO_2 based DSCs and revealed that the poor performance of the latter was due to the dynamic competition between the electron recombination with the oxidized sensitizer and the regeneration mechanism.^[89] It was observed by Cheema et al. that surface modification of SnO_2 nanoparticle films by $TiCl_4$ treatment effectively reduced the back electron transfer and improved the DSC performance.^[90] Mesoporous niobium oxide (Nb_2O_5) is another promising alternative to TiO_2 in DSC photoanodes, as it has wider band gap (3.2 - 4eV) and a more negatively placed conduction band edge which ensure higher V_{OC} .^[91] Panetta et al. synthesized peanut shaped Nb_2O_5 nanoparticles and used it along with N719 dye and iodine electrolyte to obtain a PCE of 3.4% under one sun.^[92] This was further enhanced to 4.4% by Latini et al. using organic dye (C106) sensitized Nb_2O_5 nanostructures.^[93] It was found that DSCs made up of single crystalline $Nb_3O_7(OH)$ based photoanodes could outperform the ones employing Nb_2O_5 nanostructures, owing to their high dye loading capacity, better optoelectronic and electron transport properties.^[94,95] Tungsten oxide (WO_3), with a narrower band gap of 2.6 - 3.0 eV, is another semiconductor oxide which is explored for DSC photoanode materials.^[96] Recently, Patil et al. fabricated a surfactant (sodium dodecyl sulfate) assisted WO_3 nanostructures based photoanode for DSCs employing natural dyes and achieved a $PCE \sim 3.5\%$.^[97] Zn_2SnO_4 is another ternary oxide semiconductor with tunable band gap, which finds application in DSC photoelectrode, because of its wider bandgap, better electron mobility and more negative CB edge compared to TiO_2 .^[98,99] Nanostructures of other metal oxides like cerium oxide (CeO_2), indium oxide (In_2O_3), strontium titanate ($SrTiO_3$) etc. are also attempted in DSC as photoanode materials.^[100-102]

Numerous hybrid nanocomposites have also been explored and developed for application as working electrode materials in DSCs. Metal oxides incorporated with carbonaceous materials are widely used for DSC photoanode preparation. High electrical conductivity and large surface area of carbon nanotubes (CNT) help in improving the electron transport in TiO₂/CNT and ZnO/CNT nanocomposite based photoanodes.^[103–106] Introduction of highly conducting graphene or reduced graphene oxide (rGO) into the semiconducting active layer also help to reduce recombination by creating direct path ways for electron diffusion, owing to the higher electron mobility in these materials. Hence, DSCs employing TiO₂/graphene or ZnO/graphene nanocomposite photoanodes exhibit an efficiency enhancement when compared to the devices using pristine TiO₂ or ZnO photoanodes.^[107–109] A similar performance improvement is observed in DSCs utilizing rGO nanocomposite based hybrid photoanodes.^[110–112] An increase in the amount of the aforementioned carbonaceous materials in the metal oxide semiconductor layers of DSC photoanodes contribute towards better J_{SC} , owing to their highly conducting nature. However, after an optimum amount, further increase in content of these carbonaceous materials, like graphene, rGO etc., tend to diminish the performance, which could be attributed to agglomeration of these materials on the semiconductor surface, leading to increase in defects for recombination, lower dye adsorption and light absorption. DSCs employing TiO₂/ZnO nanocomposites are found to have better PCE than both pristine TiO₂ and ZnO based DSCs.^[113–115] Hybrid composites of TiO₂ with other materials like WO₃, Nb₂O₅, SnO₂, etc. are also studied recently for implementing them as photoanode in DSCs.^[116–118] In addition to this, various two dimensional nanolayers (2D NLs) of materials such as graphene, reduced graphene oxide, TiO₂, ZnO, MXene, black phosphorus, WS₂, MOS₂, etc., are also implemented in the DSC photoanodes for improving dye adsorption, mesoporosity and conductivity, thereby achieving enhanced DSC performance and stability.^[119–130]

1.4.2. Inclusion of light scattering entities

A typical DSC photoanode film uses nanoparticles of smaller size (~ 20-40 nm), which provide appreciable surface area for dye adsorption, though most of the incident light photons are transmitted through the film without absorption by sensitizer. By improving the light scattering properties of the active layer, the optical path length of incident light within the film can be elongated, thereby enhancing the probability of light absorption by the adsorbed dye molecules. This will improve the LHE of the DSC

photoanode, which in turn appears as an improvement in J_{SC} of the device. Various strategies for improving the light scattering properties of DSC photoanodes have been adopted so far, which are discussed under the following sub-headings.

(a) Scattering particles. The light absorbing layer or active layer in DSC photoanodes are conventionally constituted by nanoparticles of semiconducting materials. Larger particles of the same material, having sizes comparable to the wavelength of incident light, can scatter light effectively, as suggested by Mie theory.^[131] Such scattering particles can be incorporated into the photoanode in two ways (as shown in **Figure 1.11**): (a) by uniformly embedding them within the active layer to form a mixture structure, or (b) by depositing them as a separate layer over the active layer to form a bi-layer or double-layer structure.^[51,132] The effect of incorporating submicron sized TiO_2 particles on the light scattering properties of DSC based on TiO_2 nanoparticle films have been investigated thoroughly, and the bi-layer or multi-layer structure with larger particles as over layers was found to be the best choice.^[133–135] TiO_2 based bi-layered photoanode films developed by Balu et al. was able to achieve an efficiency of $\sim 10\%$.^[135] They constructed bilayer films with TiO_2 nanoparticle as under layer and various TiO_2 nanostructures, viz. nanowire, core-shell microsphere and hierarchical nanorods, as well as commercial nanocrystalline TiO_2 (WER2-O) as scattering overlayers. The device utilizing the nanowire based scattering layer gave the best performance. Various hierarchical micro-nanostructures of TiO_2 , such as flower-shaped, rice grain-shaped, star-shaped, dice-shaped, hollow microsphere, and core-shell structures have been successfully employed as over layer for enhancing DSC performance by improving the light scattering.^[136–139] Implementation of 1-D nanostructures as scattering over layer has also proved to be effective.^[140,141] Inclusion of larger sized nanostructures within the nanoparticle film was also reported to be an efficient method for improving the light scattering properties of photoanodes.^[142,143]

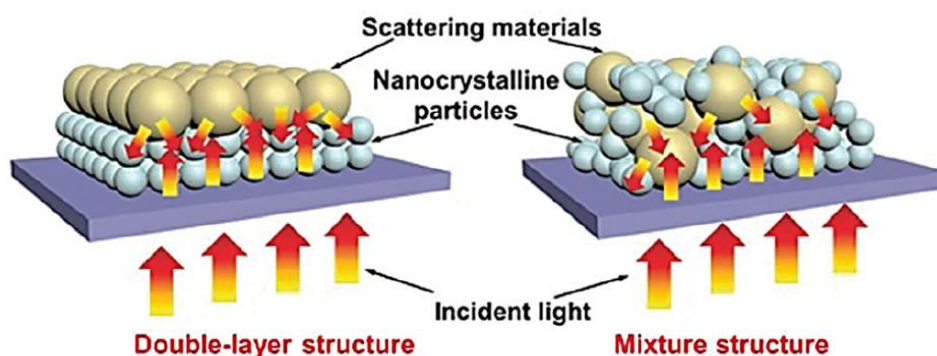


Figure 1.11. Schematic diagram representing the incorporation of larger light scattering particles into the nanoparticulate active layer in DSC photoanode.^[51]

Another means for achieving effective light scattering in DSC photoanode is by inclusion of particles with different refractive index than that of the active layer material or by implementing core-shell structures with different indices of refraction for the core and shell materials.^[144] Son et al. fabricated TiO₂ nanocrystalline films incorporated with SiO₂/TiO₂ core/shell nanoparticles (STCS-NPs), as provided in **Figure 1.12**.^[145] They employed the hybrid film as photoanode of DSC and studied the effect of STCS-NPs size and refractive index on the light scattering properties. It was observed that the *PCE* of the devices got enhanced with increasing particle size, up to a maximum value of 7.9% using particle size of ~ 240 nm, taking advantage of the increased light scattering efficiency. However, further increase in particle size affected the dye loading. It was also concluded that the usage of low refractive index core (SiO₂) and high refractive index shell (TiO₂), induced optical confinement, thus contributed to the strong optical scattering.

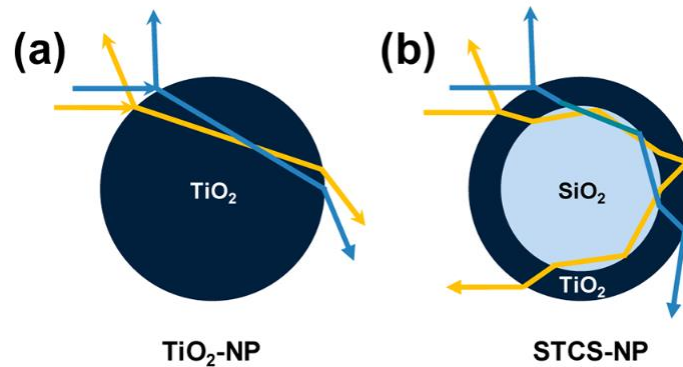


Figure 1.12. Schematic illustration of light scattering by (a) TiO₂ nanoparticles (TiO₂-NPs) and (b) SiO₂/TiO₂ core/shell nanoparticles (STCS-NPs).^[145]

(b) Scattering voids and surface roughness. The method of including scattering particles in the DSC photoanode for improving scattering efficiency have certain drawbacks. The larger particles included in the nanocrystalline film reduces the internal surface area for dye loading. Also, the charge transport resistance becomes higher in case of bi-layer films.^[132] Scattering of light can also be achieved by creating vacant spaces or voids within the active layer. The variation in refractive indices when going from semiconducting material to the void region, filled with electrolyte, induces scattering effect in such photoanodes. Hore et al. used carboxyl stabilized polystyrene spheres to create spherical voids in TiO₂ film.^[146] These voids acted as scattering centers and increased the current density, resulting in an improvement in *PCE* by 25%. Similarly, polystyrene microspheres were used to induce voids in the TiO₂ film of DSC photoanode in order to attain an improved *PCE* of ~ 7.44% by Peng et al. A multiscale bilayer inverse opal (IO) structure

was introduced by Lee et al., which utilized IO layers of smaller diameter (~ 70 nm) pores as under layer and that with larger diameter ($\sim 215 - 250$ nm) pores as over layer (**Figure 1.13**).^[147] The pores were realized by using polystyrene colloidal crystal templates. The mesoscopic IO under layer endowed high surface area for dye adsorption while the microporous top IO layer provided better light scattering, since their photonic bandgap (PBG) lie in the visible wavelength range. Therefore, by utilizing this novel structure as photoanode in DSCs along with N719 dye, they could realize a *PCE* of $\sim 6.5\%$. They observed that by varying the pore size in the top layer from 215 nm to 250 nm, there was an enhancement in J_{SC} and hence *PCE* of the device. This was attributed to the improved matching between the wavelength corresponding to PBG and the wavelength range in which N719 dye possesses the least absorption. In another report, Yang et al. utilized carbon spheres for inclusion of scattering voids into anatase TiO_2 nanoparticles based photoanode and studied the effect of varying pore size and concentration of carbon in the film.^[148] It was observed that photoanode made from 500 nm and 15 wt% carbon spheres provided the highest *PCE* of 7.2%. Han et al. employed quasi-inverse opal (QIO) layers with imperfect periodicity of voids as scattering layers to obtain high dye loading and better light scattering over the wavelength range of 600 - 750 nm.^[149]

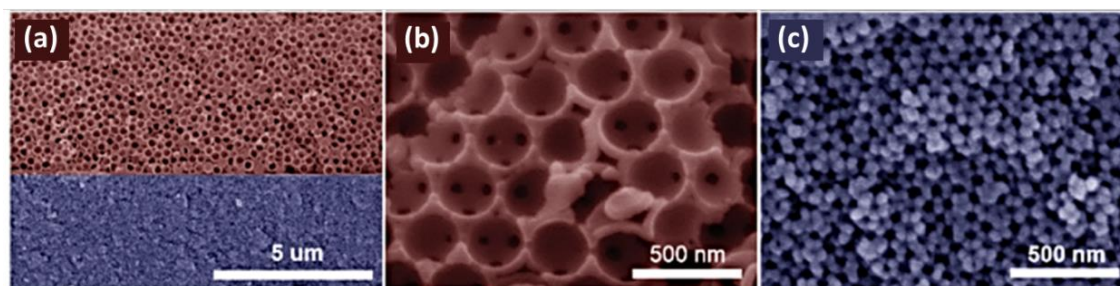


Figure 1.13. SEM images of (a) the multiscale bilayer inverse opal structure, (b) the IO over layer created using larger diameter ($\sim 215 - 250$ nm) template particles and (c) the IO under layer created using smaller diameter (~ 70 nm) template particles.^[147]

Pham et al. introduced a novel strategy for creating scattering voids by including ZnO template particles into the TiO_2 photoanode film and then selectively etching off ZnO by simple TiCl_4 treatment (**Figure 1.14(a-c)**).^[150] They were able to obtain a remarkable efficiency of 9.4% for DSC by employing the templated films with a gel type electrolyte. The same group further investigated the influence of ZnO template particle size on the device performance and concluded that 380 nm sized ZnO particles gave the best result.^[151] Sasidharan et. al. adopted a similar strategy to induce surface roughness over TiO_2

films.^[152,153] They introduced various ZnO microstructures as sacrificial layers (**Figure 1.14(d)**) over the conventional TiO₂ active layer. When the ZnO over layer was etched off by TiCl₄ treatment, imprints or grooves were formed on the TiO₂ film surface, which paved way for enhanced film roughness (**Figure 1.14(e)**). This rough film resulted in better light scattering leading to improved DSC performance.

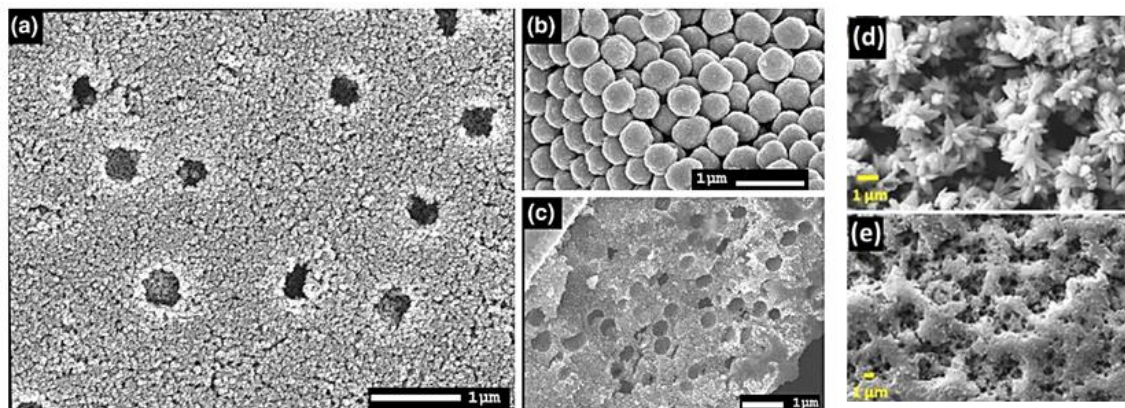


Figure 1.14. SEM images of (a) surface of ZnO templated TiO₂ film, (b) ZnO template nanoparticles, and (c) cross section of ZnO templated TiO₂ film with voids created by etching off ZnO template nanoparticles, reported by Pham et al.^[150] SEM images of (d) ZnO nanoflowers used as sacrificial overlayer and (e) surface of rough TiO₂ film obtained by etching off ZnO overlayer using TiCl₄ treatment, reported by Sasidharan et al.^[152]

(c) **Plasmonic nanoparticles.** Another strategy for enhancing the light harvesting efficiency of DSC is by decorating the photoanode films with metal nanoparticles (NPs). The optical properties of metals, like gold and silver, are dependent on the phenomenon of Surface Plasmon Resonance (SPR), which is the collective oscillation of conduction electrons induced by electromagnetic radiations, at the characteristic resonant frequency of the material.^[154] In case of metal NPs, the plasmonic resonance becomes localized (LSPR), which induces a dipole moment in the NPs. As a result there occurs a magnification of local electromagnetic field in the vicinity of the metal NPs, which subsequently paves way for an increment in optical absorption and scattering. Hence, the presence of metal NPs in the photoanode of DSC may enhance its performance.^[155,156] The inclusion of metal NPs into the DSC photoanode can also affect the CB position of the semiconductor. In many reports, NPs are implemented in the form of core-shell structure in which the metal NP core will be covered by the metal oxide shell, in order to prevent the corrosion of metal NPs by the electrolyte. Nbelayim et al. came up with Ag@TiO₂ core-shell structure for fabricating DSC and studied the effect of varying concentration of Ag in the device performance.^[157]

When the Ag concentration was increased from 0 to 0.1%, the *PCE* improved from 4.66% to 4.88%, owing to the improved charge injection and transfer induced by positive shift in CB of TiO₂. Further increase in concentration from 0.25% to 1% again showed a hike in *PCE* to reach 5.0%, which was attributed to the electron sink effect. A similar study was conducted by Lim et al. wherein they observed an enhancement of optical absorption and electron lifetime by incorporation of Ag NPs in TiO₂ photoanode.^[158] Liu et al. successfully incorporated Au@ZnO core-shell structures into the TiO₂ active layer of DSC photoanode and obtained an enhancement in *PCE* from 7.5% (for bare TiO₂) to 8.91%.^[159] The improvement in *J_{SC}* was attributed to the SPR induced optical extinction (absorption or scattering). Certain reports demonstrate the simultaneous incorporation of both Ag and Au nanoparticles into the active layer.^[160,161] Compact blocking layers doped with plasmonic nanoparticles are also employed in DSC photoanodes to improve light harvesting in addition to the suppression of back transfer of electrons.^[162,163]

1.4.3. Doping with ions

Conventionally, the conduction band (CB) and valence band (VB) edges of semiconductors are modulated by doping them with ions for photocatalytic applications. This method can be adopted in DSCs to modulate the injection and recombination rates, by tuning the CB of the semiconducting material. The change in the conduction band position of the semiconductor with the introduction of dopants will be reflected in the *V_{OC}* of the device. It will also affect the *J_{SC}* due to change in driving force for electron injection and recombination. Numerous literatures have reported the doping of DSC photoanode materials with metallic as well as non-metallic ions. The metallic dopants such as ions of niobium (Nb), magnesium (Mg), zinc (Zn), tin (Sn), chromium (Cr), nickel (Ni), copper (Cu), iron (Fe), cobalt (Co), silver (Ag), vanadium (V) etc. can be used for altering the charge transfer processes in TiO₂ photoanode based DSC.^[164–167] These dopants shift the conduction band edge of TiO₂ to a more positive position with respect to that of the undoped TiO₂, which leads to higher *J_{SC}* owing to increase in driving force for electron injection and decrease in driving force for recombination. In spite of this, cation doping may lead to a decrease in *V_{OC}* as the energy difference between the Fermi level of TiO₂ and the redox potential of electrolyte is reduced due to the downward CB shift. Also there may be a lowering of *J_{SC}* due to minimized dye loading caused by particle agglomeration in such systems. Similar observations are reported for ZnO and SnO₂ based photoanode films doped with metallic cations.^[168,169] Apart from the metallic cations, doping of

semiconductor film of DSC working electrode with anions of non-metals like nitrogen (N), boron(B), carbon (C), sulfur (S) etc. are also reported in many literatures.^[170–174] The DSCs employing anion doped electrodes generally displayed increase in V_{OC} ascribed to the upward shift in CB edges and reduced recombination due to surface trap state passivation by the dopant ions. Though the driving force for injection was limited by this CB shift, improvement in J_{SC} could be observed for DSCs using such anion doped semiconductors. This elevated J_{SC} was attributed to the faster charge diffusion rate and reduced internal resistance induced by the dopant ions in the photoanode.

1.4.4. Interfacial modification by depositing blocking layers

The two major performance limiting processes of DSCs are the electron back transfer at the TCO/electrolyte interface and the semiconductor/dye/electrolyte. The photoanodes employing nanocrystalline semiconductor films offer a large number of surface trap states or recombination sites which adversely affect the device performance. An appropriate method to deal with this issue is the passivation of these trap states by using blocking layers. Blocking layers (BLs) are usually ultra-thin compact layers of materials like TiO_2 , ZnO , Nb_2O_5 , Al_2O_3 , SnO_2 etc., which have semiconducting or insulating nature.^[175,176] Pre-blocking layers (pre BL) or buffer layers coated on the TCO prevents electron back transfer from TCO (**Figure 1.15(a)**) to electrolyte, whereas post-blocking layer (post BL), which is a conformal barrier layer deposited over the mesoporous photoanode film that resists recombination of electron from semiconductor's CB to the electrolyte (**Figure 1.15(b)**).^[177–179] A mesoporous layer of core-shell nanostructures is obtained as a result of post BL deposition on nanoporous films. BL can be deposited via various deposition techniques like, chemical bath deposition, spin, atomic layer deposition (ALD), spray pyrolysis, electrochemical deposition, dip coating, electron beam evaporation etc. The interfacial electron transfer dynamics in the TiO_2 based DSCs could be regulated by means of compact barrier layers constituted of other metal oxides like Nb_2O_5 , Al_2O_3 , ZrO_2 , Ga_2O_3 , MgO , and so on.^[179] The improvement in efficiency of DSCs employing these BLs were attributed to the increment in V_{OC} , which in turn relates to the enhanced electron lifetime caused by suppressed recombination.

With an increase in the thickness of BL, an enhancement in the recombination resistance occurs, that leads to an elevated DSC performance. However, increase in BL thickness beyond an optimum limit affects the process of injection of photoelectrons from the dye to the semiconductor, hence oppressing the device performance. This was verified

by Chandiran and co-workers, who could achieve V_{OC} above 1 V using an organic dye (Y123) sensitized TiO_2 photoanodes employing passivating post BL of Ga_2O_3 deposited by ALD in conjugation with Co based electrolyte.^[180] They observed that upon thickening of the barrier layer, there was a decrease in recombination rate leading to enhanced V_{OC} (up to 1118 mV for 6 ALD cycles). However, the J_{SC} and PCE began to diminish after an optimum thickness (4 ALD cycles), due to the injection limitations caused by thickened blocking layer. TiO_2 BL is the most frequently used one in DSCs along with different photoanode materials such as TiO_2 , ZnO , SnO_2 , CeO_2 etc. to improve the device performance by suppressing recombination processes.^[178,181–183] TiCl_4 treatment, which is a simple chemical bath deposition technique, is the most effective method for depositing TiO_2 blocking layers in DSC photoanodes.^[184–186] In this technique, the specimen (either the bare TCO substrate or the TCO coated with mesoporous semiconducting layer) is immersed in an aqueous solution of TiCl_4 , which is maintained at a temperature of 70°C - 80°C for a specific period of time, so that the TiCl_4 hydrolyses and produces TiO_2 nanoparticles that are deposited on the specimen to form BL. Till date, majority of the significant reports on TiO_2 photoanode based DSCs elaborately use this method for depositing TiO_2 pre and/or post BLs, for efficient performance under standard one sun as well as ambient light conditions.

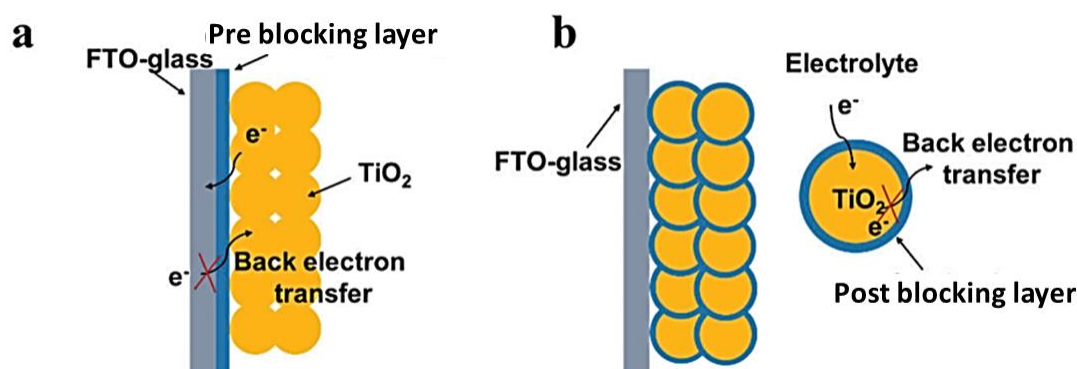


Figure 1.15. Schematic diagram of prevention of back electron transfer by (a) the pre blocking layer deposited over FTO substrate and (b) the post blocking layer deposited over the TiO_2 mesoporous network to form core-shell structure^[179]

1.4.5. Interfacial engineering by co-sensitization strategy

Dye molecules adsorbed on the semiconductor surface have a significant impact on the electron transfer kinetics at the semiconductor/electrolyte interfaces in DSCs.^[187] By depositing a pinhole-free monolayer of small sensitizer molecules over the semiconductor surface, the recombination of photoelectrons with the electrolyte species can be effectively

blocked. Whereas, the steric hindrance offered by the long alkyl chains and twisted geometry of the bulky organic dye molecules prevent the approach of oxidized electrolyte species to the semiconductor surface, thereby retarding the electron back transfer. In co-sensitization method, the DSC photoanode is sensitized using two or more dye molecules having different sizes and complementary absorption profile, in order to achieve a panchromatic light absorption. Moreover, this strategy helps in achieving a highly ordered and dense molecular packing of dye molecules over the semiconductor surface, which helps in suppressing the recombination at the semiconductor/electrolyte interface, as discussed before.^[188,189] Usually, co-sensitization is done in two ways: (a) by soaking the photoanode in a cocktail dye solution containing different dye molecules (having different molecular sizes), for a specific interval of time, or (b) by successively immersing the photoanode in different dye solutions for different time periods (step-wise co-sensitization). In the step-wise co-sensitization, the mesoporous semiconductor layer coated over TCO is initially immersed in the solution containing bulky dye molecules (with large number of branches and long alkyl chains or with large dihedral angles), followed by sensitization with smaller dye molecules. In both the cases, the small sized dye molecules occupy the vacant spaces between the bulky dye molecules anchored on to the semiconductor surface. Consequently, co-sensitization gives rise to a tightly packed monolayer of different sensitizer molecules on the semiconductor surface, which effectively hinders the oxidized electrolyte species from approaching the semiconductor, thereby retarding the recombination process. This helps in improving the V_{OC} of DSCs. In addition to this, the co-sensitization strategy prevents dye aggregation possibilities and ensures light harvesting over a wider spectral domain, both of which contribute towards improvement in J_{SC} . Co-sensitization of organic dyes in conjugation with copper complex based electrolytes opened a new realm of indoor DSCs (I-DSCs), which could attain larger V_{OC} values and outstanding PCE under indoor/ambient light conditions. Freitag et al. realized a higher PCE of 28.9% under 1000 lux fluorescent light illumination, by the judiciously co-sensitizing the TiO_2 photoanode with two organic dyes (XY1 and D35) having complementary absorption profiles and compatible with copper complex based redox mediators (**Figure 1.16**).^[23] Later on Cao et al. developed a direct contact devices (DCD) employing Y123/XY1b co-sensitized TiO_2 layer along with copper based redox mediator delivered an exceptional PCE of 13.1% under one sun and 31.8% under 1000 lux fluorescent light.^[190] Similarly, two organic dyes, namely XY1 and L1, which complement each other in terms of steric hindrance and absorption profile, were utilized by Michaels et al. along with a copper electrolyte to obtain

an outstanding *PCE* of 34% under 1000 lux fluorescent illumination and 11.5% under one sun condition.^[26] The size difference of the two dye molecules facilitated the formation of a densely packed monolayer on the TiO₂ surface, which led to *V_{OC}* improvement, while the perfect overlapping of the complementary absorption profile of the selected dyes with the emission spectra of the indoor light source resulted in enhanced *J_{SC}*. Subsequently, a remarkable *PCE* of 34.5% for DSCs under 1000 lux fluorescent light illumination and 13.5% under full sun irradiation was realized by Zhang et al. by co-sensitization of TiO₂ mesoporous layer with organic dyes namely XY1b and MS5, and employing copper based electrolyte.^[191]

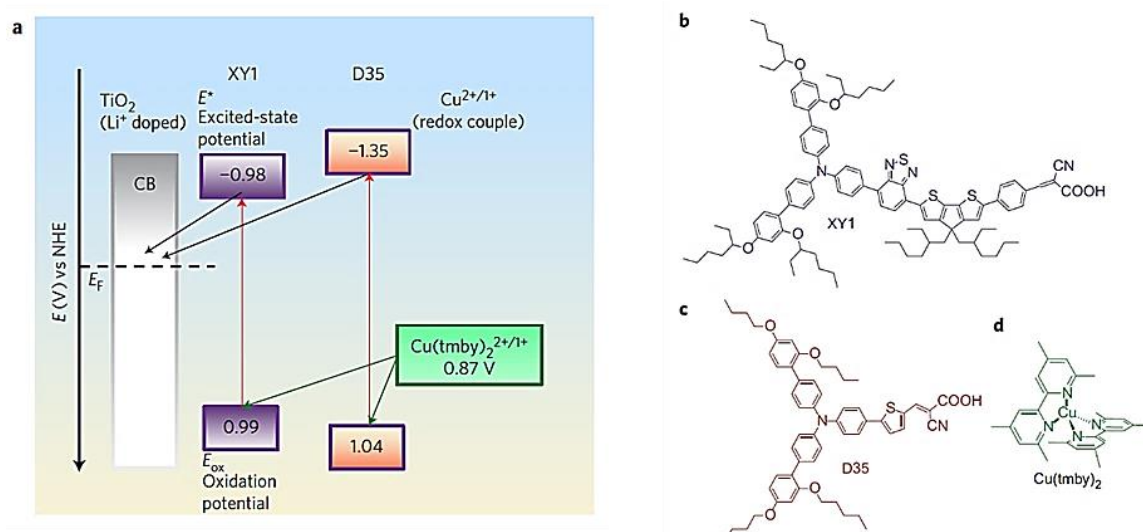


Figure 1.16. (a) The energy level diagram, (b) structure of XY1 dye molecule, (c) structure of D35 dye molecule and (d) structure of the copper complex ($[\text{Cu}(\text{tmby})_2]^{2+/+}$) utilized by Frietag et al.^[23]

1.4.6. Interfacial modification by co-adsorption and pre-adsorption strategy

Another widely adopted method for suppressing recombination at semiconductor/electrolyte interface and to prevent dye aggregation in DSCs is the adsorption of semiconductor surface with other molecules, known as the co-adsorbents, in addition to the dye molecules. The co-adsorbents used in DSC photoanodes are usually simple and small organic molecules having carboxylic or phosphonic groups, having very low optical absorption in the visible region when compared to the sensitizer molecules.^[192,193] These molecules bind weakly on the semiconductor surface so that the dye molecules can easily replace them. Conventionally, the co-adsorbent molecules are added into the dye solution itself and get anchored onto the semiconductor surface during the dye soaking process. The co-adsorbent molecules occupy the vacant sites on the

semiconductor surface, and help in organizing and orienting the adsorbed dye molecules, hence spatially separating the oxidized electrolyte species from the semiconductor and preventing dye aggregation. [194,195] This effect can be enhanced by using the co-adsorbent molecules endowed with long hydrophobic alkyl chains. [196] In addition to this, the use of co-adsorbent molecules can bring about changes in the CB edges of the semiconductor, thereby influencing the V_{OC} of DSCs. Various organic acid derivatives like those of deoxycholic acid, phosphonic acid, benzoic acid, acetic acid etc. can be employed in DSC photoanodes as co-adsorbents. [193] Chenodeoxycholic acid (CDCA) is the most widely used substance for co-adsorption of DSC photoanodes.

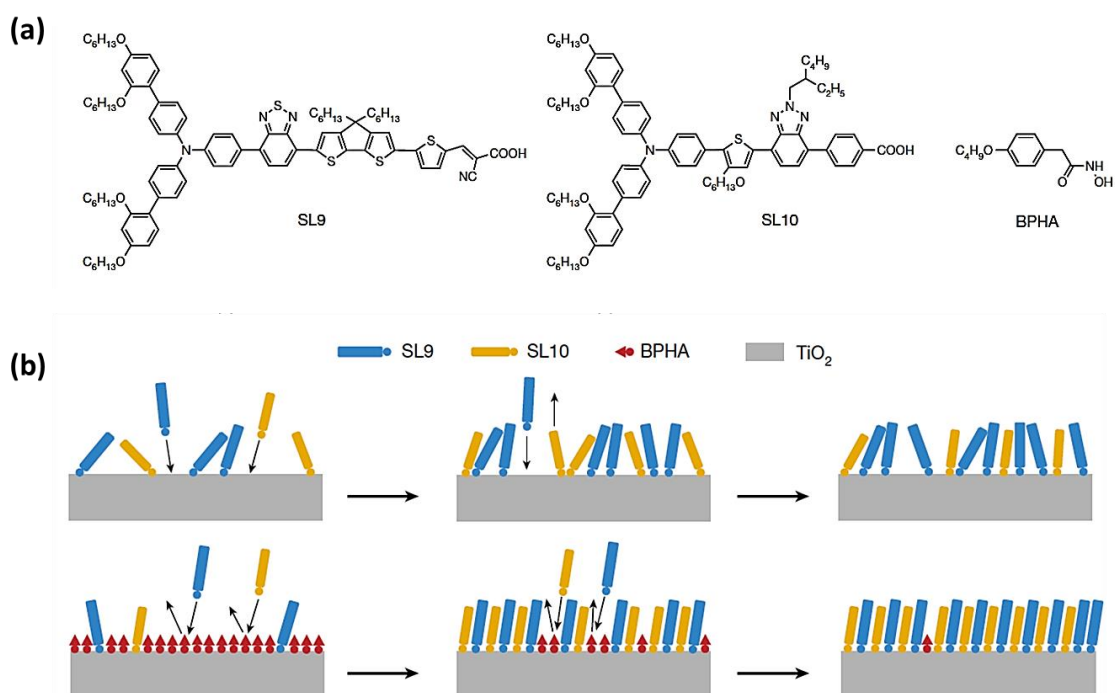


Figure 1.17. (a) The molecular structures of SL9, SL10 and BPHA molecules, and (b) the schematic representation of dye adsorption on the surface of untreated and BPHA pre-treated TiO_2 layer, reported by Ren et al. [29]

A similar but a novel surface treatment strategy utilizing pre-adsorbents was adopted by Ren et al., in 2023, to render an all-time record PCE of 15.2% under standard AM 1.5G solar irradiation for DSC fabricated with co-sensitized TiO_2 photoanode and copper electrolyte. [29] In this approach, the surface of TiO_2 mesoscopic layer was adsorbed with the hydroxamic acid derivative, namely 2-(4-butoxyphenyl)-hydroxyacetamide (BPHA), even before dye loading. The TiO_2 photoanode, pre-adsorbed with BPHA molecules, were then immersed in the cocktail dye solution containing two novel organic dyes (SL9 and SL10, shown in **Figure 1.17(a)**) having complementary absorption to cover

the entire visible light spectrum. Apparently, upon dye soaking, the dye molecules replaced the BPHA molecules from the TiO₂ surface, which was confirmed using FTIR analysis. It was observed that the BPHA pre-treated TiO₂ layer was having a well ordered and denser molecular packing of sensitizers (**Figure 1.17(b)**) when compared to the untreated one. Subsequently the DSC employing the BPHA pre-treated films exhibited enhanced J_{SC} and hence showcased better performance not only under outdoor but also under indoor illumination conditions (30.1% under 1479 lux illumination using a 4000K LED lamp).

1.5. Copper complex based redox mediators for DSCs

1.5.1. Emergence of copper complex redox shuttles

Iodine-based redox mediators marked an era of low-cost and efficient electrolytes for dye-sensitized electrochemical cells since its beginning back in 1990s. The DSC arena was dominated by iodide/triiodide electrolytes owing to their significant stability and favourable charge transfer mechanism. The two-electron reaction mechanism followed by the iodide/triiodide redox couple consists of a sequence of rapidly occurring one-electron reactions that involve multiple intermediate species. Iodide/triiodide redox couples are the best candidates for DSC electrolyte because of their faster ion diffusion capabilities, asymmetric charge transfer kinetics behavior prompted by faster oxidation of I⁻ ions ensuring faster dye regeneration, and relatively slower reduction of I₃⁻ ions enabling better charge collection. Despite its excellent performance both indoors and outdoors, a number of issues prevent the widespread use of iodine electrolyte in the manufacturing and commercialization of large area dye-sensitized PV modules (DSMs). Triiodide ions are very corrosive towards silver electrodes, that are used in large area DSMs for effective current collection. Additionally, it corrodes the sealing materials that are commonly used to assemble the working and the counter electrodes. Large regeneration overpotential loss owing to less positive redox potential, which restricts the maximum achievable V_{OC} , and competitive light absorption in the lower wavelength region, which lessens the light harvesting by the photoanode and affects J_{SC} , are two other drawbacks of iodine-based electrolytes. Another demerit of the iodide/triiodide redox couple is its intricate, multistep dye regeneration mechanism, which is still poorly understood. Furthermore, the organic sensitizers that are being developed for improved light absorption and charge separation have been found to be incompatible with the iodide/triiodide electrolyte. This created a requirement for exploring alternative redox systems to be employed in DSCs for efficient dye regeneration and hole transport, without affecting other device components. Because

of their less corrosive nature and higher positive redox potential, one-electron outer sphere redox systems based on transition metal complexes like copper and cobalt based ones account for the most viable alternatives. Also, it is possible to tune the redox potentials of these metal complexes to a desired degree by altering the ligands attached. Though cobalt based redox shuttles have several advantages over the copper based ones, such as less competitive light absorption, non-corrosiveness, non-volatile nature, etc., DSCs employing cobalt redox shuttles suffer from higher recombination losses especially at FTO/electrolyte interface, and slow ion diffusion leading to mass transport limitations.^[197–200] Copper complexes are less bulky when compared to cobalt species, as a result of which the diffusion of the later in the bulk electrolyte as well as within the semiconductor layer is slower, and hence is highly prone to mass transport issues. Moreover, copper complex based redox systems have more positive redox potentials, which minimize the overpotential loss for dye regeneration and thence contribute towards better voltage (**Figure 1.18**).^[201]

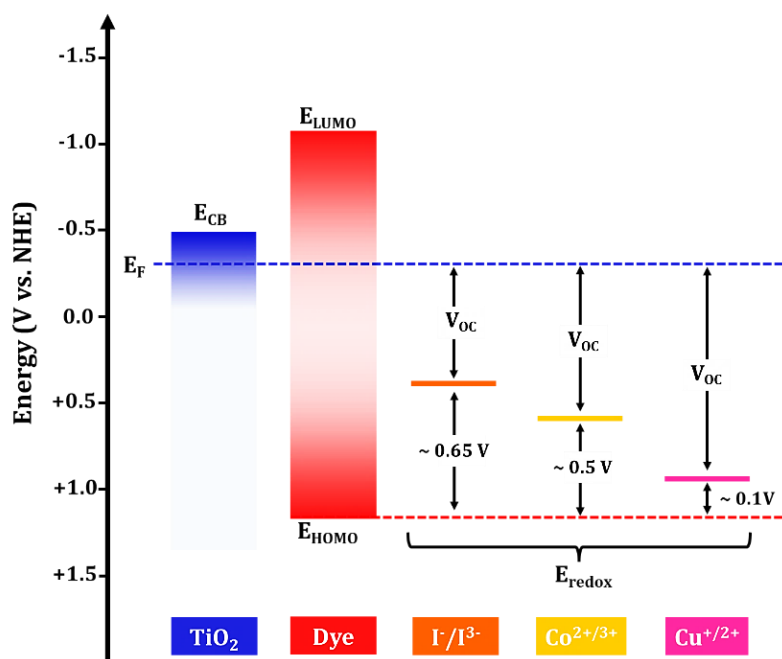


Figure 1.18. Schematic representation of energy level alignment of different components of an organic dye sensitized TiO_2 based DSC with respect to three different redox mediators, viz. iodine, cobalt and copper based ones.

Copper complex based electrolytes are more advantageous for DSC applications considering its smaller sized species which contribute towards higher ion diffusion rates along with more positive redox potential compared to cobalt complex based redox shuttles. Also, the commercialization of copper electrolyte based DSCs is more appropriate due to the abundance, low cost, and reduced toxicity of copper species. The pioneering work done

by Hattori et al. (in 2005) marked the beginning of copper electrolyte based DSCs. They synthesized a series of copper complexes and employed them as redox mediators in DSCs along with N719 dye sensitized photoanodes. Among them, the DSC based on the copper(II/I)bis(2,9-dimethyl-1,10-phenanthroline) complex ($[\text{Cu}(\text{dmp})_2]^{2+/+}$), with a redox potential of 0.66 V vs. SHE, delivered the highest *PCE* of 1.4% under 100 mW/cm² and 2.2% under 20 mW/cm² simulated solar irradiation.^[202] Six years later, Bai et al. observed that copper complex based electrolytes were more compatible with organic dyes.^[203] By utilizing $[\text{Cu}(\text{dmp})_2]^{2+/+}$ complex based electrolytes in conjugation with an organic dye (C218) sensitized DSC photoanode, they could achieved a *PCE* of 7% under 100 mW/cm² and 8.3% under 23 mW/cm² illumination. This was further established by Saygili et al. by utilizing copper bipyridyl based redox mediators, viz. Cu(II/I)(4,4',6,6'-tetramethyl-2,2'-bipyridine) ($[\text{Cu}(\text{tmbpy})_2]^{2+/+}$) (0.87 V vs. SHE) and Cu(II/I)(6,6'-dimethyl-2,2'-bipyridine) ($[\text{Cu}(\text{dmby})_2]^{2+/+}$) (0.97 V vs. SHE) complexes, in addition to $[\text{Cu}(\text{dmp})_2]^{2+/+}$ (0.93 V vs. SHE), in DSCs along with an organic dye named Y123 (**Figure 1.19**).^[204] They could achieve an impressive *PCE* of ~ 10% with V_{OC} above 1V, under 100 mW/cm² simulated sunlight, by employing these copper bipyridyl complexes as redox mediators. Although the energy levels in case of copper redox shuttles are closer to the HOMO of the sensitizers, efficient dye regeneration is still possible as a very small driving force (less than 0.1 eV) is required for the same, thanks to its lower reorganizational energy between the Cu(I) and Cu(II) complexes leading to faster charge transfer kinetics. Consequently, the copper electrolyte based DSCs could outclass the conventional iodine electrolyte as well as the cobalt electrolyte based devices, paving way for a new generation of DSCs with remarkable performances not only under outdoor, but also under indoor illumination conditions.

[201,205,206]

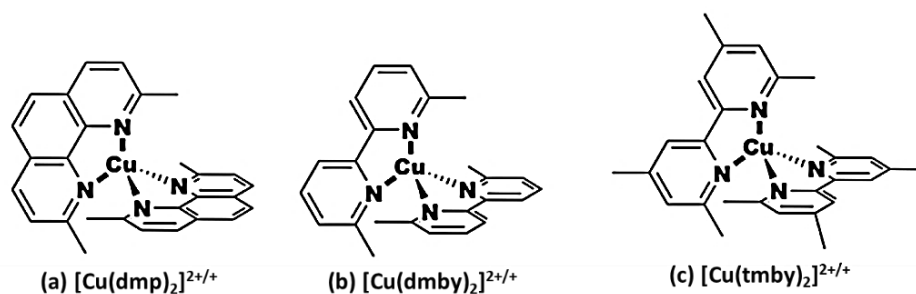


Figure 1.19. Molecular structure of (a) $[\text{Cu}(\text{dmp})_2]^{2+/+}$, (b) $[\text{Cu}(\text{dmby})_2]^{2+/+}$ and (c) $[\text{Cu}(\text{tmbpy})_2]^{2+/+}$ complexes.

Majority of the recent reports unveiling exceptional DSC performances with V_{OC} above 1V and PCE surpassing 10% under standard AM 1.5G simulated sunlight are based on $[\text{Cu}(\text{tmby})_2]^{2+/+}$ copper complex based redox mediators coupled with various organic sensitizer molecules. In 2017, Freitag et al. made a quantum leap in the I-DSC realm by attaining exceptional PCE of 28.9% under indoor condition (1000 lux fluorescent light) by utilizing $[\text{Cu}(\text{tmby})_2]^{2+/+}$ redox shuttle along with two organic dyes (XY1 and D35).^[23] The $[\text{Cu}(\text{tmby})_2]^{2+/+}$ redox mediator could successfully regenerate both the dyes with the driving forces as low as 0.1 - 0.2 eV. In a similar manner, $[\text{Cu}(\text{tmby})_2]^{2+/+}$ redox mediator was used in conjunction with various co-sensitized systems to obtain outstanding DSC performances under outdoor and indoor conditions.^[26,29,190,191,207] DSCs employing $[\text{Cu}(\text{dmp})_2]^{2+/+}$ based electrolytes are also explored intensely, because of the favourable structural, electrochemical and optoelectronic properties of these copper complexes, in addition to the low cost and more availability of the 2,9-disubstituted-1,10-phenanthroline (dmp) ligand.^[204,208,209] Recently, Jagadeesh et. al. could achieve a breakthrough V_{OC} of 1.27 V under one sun and 1.02 V under 1000 lux CFL illumination, by fabricating DSCs using a TiO_2/ZnO bilayer photoanode along with $[\text{Cu}(\text{dmp})_2]^{2+/+}$ complex based electrolyte.^[30,210] Later, by employing a modified $[\text{Cu}(\text{dmp})_2]^{2+/+}$ complex synthesized using the novel concept of asymmetric dual species copper electrolyte, Meethal et. al. realized a record efficiency of 35.6% under 1000 lux CFL illumination.^[30,210]

1.5.2. Charge transfer dynamics at photoanode/electrolyte interface

Since most of the crucial charge transfer processes in DSCs occur at the photoanode/electrolyte junction, it has a pivotal role in governing the photovoltaic performance of the device. As already discussed, the photoanode is made up of a semiconductor layer coated with dye molecules, and therefore the photoanode/electrolyte interface is constituted by the semiconductor/dye, the dye/electrolyte and the semiconductor/electrolyte interfaces. Since the injection process occurs at the semiconductor/dye interface, the injection rate (k_{inj}) is determined by the energy level alignment and overlap at the semiconductor/dye interface, as suggested by the Marcus theory. Besides, k_{inj} is also influenced by the surrounding medium, that is the electrolyte. There are several reports endorsing that in the presence of copper complex based electrolyte, organic dye sensitized TiO_2 photoanodes experience a shift in CB edges, so as to increase the driving force for injection or to establish better energy level overlapping

between the semiconductor's CB and the molecular orbitals of the dye, which in turn contribute towards enhanced η_{inj} (more than 90%).^[203,209,211]

Similarly, the energetic distribution at the dye/electrolyte interface influences the dye regeneration rate (k_{reg}). Saygili et al. studied the regeneration kinetics at TiO₂/Y123 dye interface in the presence of various copper complex based electrolytes having different redox potentials.^[204] They found that there was a decrease in regeneration lifetime with increase in regeneration driving force, which is determined by the redox potential (E_{redox}) of the copper complex with respect to the ground state energy of the dye. The [Cu(tmby)₂]^{2+/+} complex with the most negative redox potential rendered the fastest regeneration (with regeneration half lifetime of 1.8 μ s). Further, it is set forth by many reports that in case of DSCs employing copper complex based electrolyte and organic dyes, an energy difference of less than 0.1 eV between the Fermi level of the redox shuttle and the HOMO of the dye, is sufficient to drive dye regeneration with $\eta_{reg} \sim 100\%$.^[23,209,212]

The kinetics of electron transfer at the semiconductor/electrolyte interface determines the rate of the performance limiting charge recombination (k_{rec}) in DSCs. Thus, the recombination kinetics depend not only on the driving force rendered by the difference in E_F and E_{redox} , but also on the degree of overlap of the CB states and sub band gap states of the semiconductor with the oxidized energy levels of the electrolyte. In case of copper electrolyte based DSCs, the dependence of the recombination rate, and hence the lifetime, on the driving force ($E_F - E_{redox}$) was elucidated by Saygili et al. ^[204] The [Cu(tmby)₂]^{2+/+} complex with the more negative E_{redox} comparative to [Cu(dmp)₂]^{2+/+} and [Cu(dmby)₂]^{2+/+} complexes, apparently carried the least driving force for recombination, and hence exhibited better lifetime. The charge transfer kinetics at semiconductor/electrolyte interface is further influenced by the molecular structure and size of the sensitizer molecules anchored to the semiconductor surface. Several authors have reported that bulky dye molecules with long alkyl chains and twisted structure are capable of hindering the oxidized electrolyte species from coming close to the semiconductor surface.^[213,214] As we have discussed in the previous section 1.4.5., co-sensitization, wherein a combination of bulky dye and small sized dye is used to sensitize the photoanode, is a successful approach for suppressing recombination at the semiconductor/electrolyte interface leading to better lifetime.^[23,26,188] The use of different sized dye molecules is effective in achieving sufficient surface coverage to block the approach of oxidized electrolyte species to the semiconductor. The use of blocking layer (post BL), as mentioned in the section 1.4.4., is

also an efficient method for blocking the back electron transfer at the semiconductor/electrolyte interface.

1.5.3. Mass transport limitations

In electrochemical systems, the mass transport refers to the process by which the electrically active particles, i.e., the species involved in the charge transfer process, are transferred towards the electrode, where the charge transfer takes place, while the products formed move in the opposite direction, away from the electrode to the solution volume.^[215] Mass transport can occur via diffusion, migration, or convection mechanism. In DSCs, the electrochemical charge transfer processes occur at the photoanode/electrolyte interface and the active particles involved are the reduced species in the electrolyte. Upon optical irradiation of the photoanode, the dye molecules get excited and subsequently inject the excited electrons into the CB of the semiconductor onto which they are anchored. The oxidized dye molecules are immediately regenerated by the reduced electrolyte species in the close vicinity of the photoanode. At the same time, the oxidized species in the electrolyte are reduced at the CE/electrolyte junction. This creates a concentration gradient within the system, as a result of which oxidized species in the electrolyte diffuse away from the photoanode while the reduced ones diffuse towards it, which is essential for the electrochemical process to continue. The mass transport or diffusion of these species in the bulk of the electrolyte as well as within the mesoporous semiconductor matrix is affected

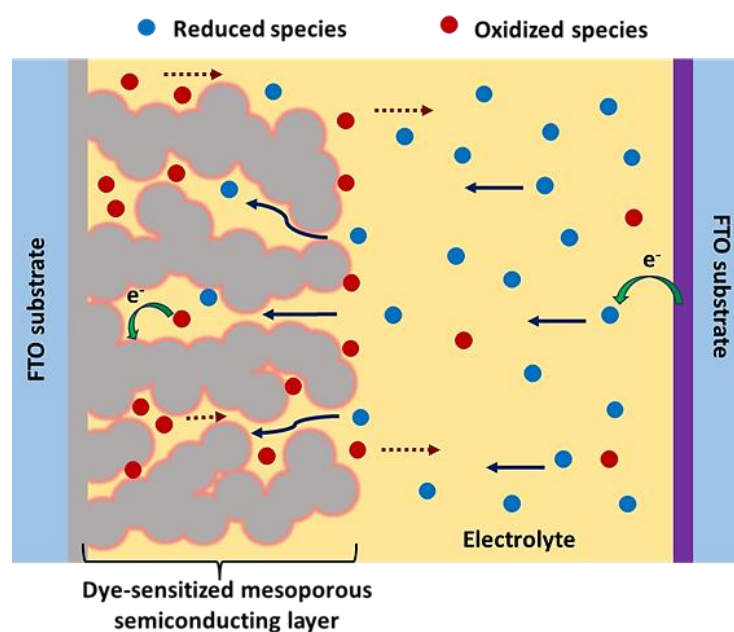


Figure 1.20. Schematic illustration of mass transport of oxidized and reduced electrolyte species in the bulk of the electrolyte and within the semiconductor matrix in DSCs.

by their bulkiness (**Figure 1.20**). The bulkier the redox species, the more limited will be their mass transport. Mass transport limitation in DSCs employing bulky electrolyte species can be easily detected using current transient curves as well as by plotting the current output (I_{SC} or J_{SC}) of the device against incident light intensity.

The current transient curves of diffusion limited devices show a peak current which decays with time and then saturates. **Figure 1.21(a)** shows the dependence of mass transport of a copper electrolyte based DSC on incident light intensity.^[201] At higher intensities (0.6 – 1 sun illuminations) mass transport issues are highly pronounced, as a result of which the current transient curves shows a decay in current density. At lower intensities, the current transients do not show any decay, indicating that mass transport issues are not significant. This is because, at lower light intensities the number of photoelectrons generated are very less, as a result of which all the charge transfer processes occur at a slower rate, which compensates the slow diffusion of bulky copper species in the electrolyte. Hence, the mass transport limited systems show sub-linear deviations in the stable state J_{SC} versus intensity curves (**Figure 1.21(b)**). The J_{SC} of iodide/triiodide electrolyte based DSC are linearly dependent on the incident intensity, while those for cobalt ($[\text{Co}(\text{bpy})_2]^{3+/2+}$) and copper ($[\text{Cu}(\text{dmp})_2]^{2+/+}$) based electrolyte deviate from the linear behaviours owing to their bulkiness. The cobalt complex being bulkier than copper species, shows the highest non-linearity in J_{SC} vs intensity plot.

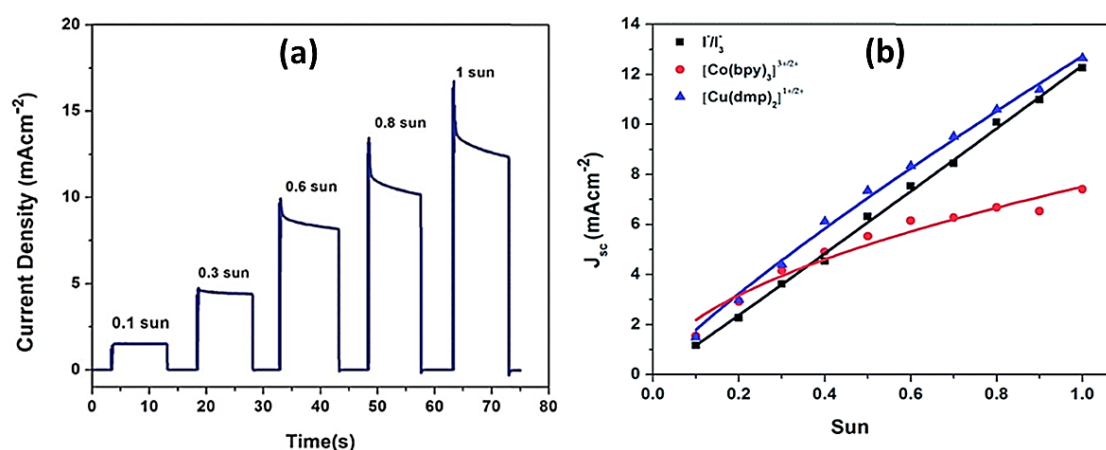


Figure 1.21. (a) current transient curves for $[\text{Cu}(\text{dmp})_2]^{2+/+}$ based DSCs under different illumination conditions (from 0.1 to 1 sun), and (b) J_{SC} versus intensity curves for DSCs employing different electrolytes viz. I^-/I_3^- , $[\text{Co}(\text{bpy})_2]^{3+/2+}$ and $[\text{Cu}(\text{dmp})_2]^{2+/+}$ based electrolytes.^[201]

The structural characteristics of the dye molecules adsorbed as well as the thickness of semiconductor layer were also observed to affect the mass transport properties of copper electrolyte based DSCs by Velore et al.^[216] They utilized TiO₂ films sensitized with D35 dye alone, XY1 dye alone and co-sensitized with D35:XY1 (1:1) dye combination to fabricate DSCs along with [Cu(tmby)₂]^{2+/+} complex based electrolyte and found that even though the XY1 based and co-sensitized systems exhibited better *IPCE* owing to better light absorption, the D35 based device delivered the best *J_{SC}* and *PCE* under one sun illumination. It was inferred that under one sun intensity, when the mass transport limitation is prominent, the D35 sensitized TiO₂ layer provide an easier path for the diffusion of copper species within the photoanode when compared to the other two photoanodes. This was clear from the current transients at one sun condition, as shown in **Figure 1.22(a)**. Further, they could diminish the mass transport limitation in D35:XY1 co-sensitized system by reducing the TiO₂ layer thickness from 8 μm to 4 μm (**Figure 1.22(b)**).

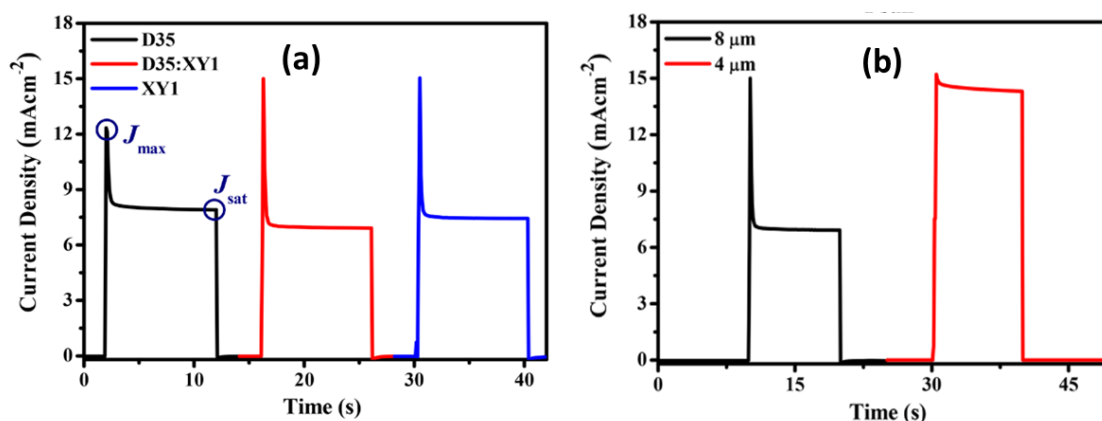


Figure 1.22. Current transients under one sun condition for (a) different DSCs with photoanodes sensitized with D35 dye, XY1 dye, and co-sensitized with 1:1 D35:XY1, and (b) D35:XY1 co-sensitized devices with different TiO₂ layer thickness.^[216]

1.6. Statement of the problem

Copper complex based redox shuttles are identified to be the most suitable electrolyte candidates for DSCs, owing to their more positive redox potential and compatibility to be used in conjugation with organic dye molecules. The highly positive redox potentials (E_{redox}) of copper species, ranging from 0.59 V - 0.97 V vs. NHE, not only minimize the over potential loss for dye regeneration, but also enlarge the energy difference between E_{redox} and E_F of the semiconductor, together contributing towards higher open circuit voltage (V_{OC}). The higher V_{OC} in copper electrolyte based DSCs enable them to achieve exceptional performance not only under standard one sun condition but also under

indoor/ambient light conditions as well. However, the positive redox potentials may lead to higher driving force for recombination at the semiconductor/electrolyte interface, leading to reduction in electron lifetime and hence affecting the V_{OC} of the DSC. Also, the bulky nature of copper species limits their diffusion in the electrolyte solution and within the mesoporous photoanode layer, which in turn affect the J_{SC} of the device. A comparison of performance of DSCs employing different electrolyte systems and different photoanode materials are provided in **Table 1.1.** for further reference.

So far, most of the studies done for improving the PCE of copper electrolyte based DSCs relied on developing novel organic dyes or other organic molecules for sensitizing standard TiO_2 photoanodes (constituted by an active layer made up of 20-30 nm sized TiO_2 particles and a scattering layer containing 200-400 nm sized TiO_2 particles). Other photoanode modification methods are yet to be explored in case of copper redox mediator based DSCs. Modification techniques for enhancing the light harvesting properties of photoanode along with improvement in mass transport of copper species within the photoanode ought to be an effective strategy for elevating the J_{SC} of these DSCs. Whereas, photoanode engineering strategies that can improve the electron lifetime by precisely regulating the recombination kinetics at the semiconductor/electrolyte interface, by modulating the E_F level, can help in attaining the maximum achievable V_{OC} in copper complex based devices.

Table 1.1. Comparison of performance (best ones reported in the past few years) of DSCs employing different electrolyte systems, photoanode materials, and sensitizers.

Electrolyte system	Photoanode material	Sensitizer/s	PCE (%) under AM 1.5G solar irradiation	PCE (%) under ~1000 lux indoor light illumination	Reference
Iodide/triiodide electrolyte (I^-/I_3^-)	TiO_2 nanoparticles	N719	9.86	-	[47]
	Multi-shell hollow TiO_2 nanoparticles	N719	9.4	-	[49]
	TiO_2 nanorods	Z907	8.87	-	[54]
	TiO_2 nanowires	N719	9.4	-	[56]
	Macroporous 3D inverse opal TiO_2 nanostructures	YKP-88	10.3	-	[66]

Iodide/triiodide electrolyte (I ⁻ /I ₃ ⁻)	TiO ₂ nanoparticles / TiO ₂ nanowires bilayer	N719	9.9	-	[135]
	ZnO nanoparticles	N719	8.03	-	[77]
	ZnO nanorods	N719	4.7	-	[81]
	ZnO nanowires	SK1	5.0	-	[84]
	Hierarchically Structured ZnO Nanorods	N719	4.13	-	[85]
	TiO ₂ nanoparticles layer surface textured using ZnO templates	N719	6.82	11.8	[152]
	TiO ₂ nanoparticles layer surface textured using ZnO templates	N719	7.32	15.5	[153]
	TiO ₂ nanoparticles/ 2D TiO ₂ nanosheet bilayer	N3	7.54	-	[121]
	2D TiO ₂ nanosheets grown on ZnO nanowires	N719	7.5	-	[122]
	g-C ₃ N ₄ modified TiO ₂ nanosheets	N719	7.34	-	[120]
	Nb doped TiO ₂ nanosheets	N719	10.0	-	[123]
	Black phosphorus nanosheet / TiO ₂ nanocomposite	N719	9.73	-	[126]
	MoS ₂ nanoparticles / graphene nanosheets	N719	8.92	-	[127]
	WS ₂ nanoparticles / graphene nanosheets	N719	9.6	-	[129]

Cobalt bipyridine based electrolyte ([Co(bpy) ₃] ^{3+/2+})	Mesoporous TiO ₂ microbeads	D35	6.4	-	[48]
	TiO ₂ nanoparticles	MK-2	7.3	15.3	[200]
	TiO ₂ nanoparticles	YD2-o-C8	9.5	21.9	[199]
	TiO ₂ nanoparticles	Y123	2.7	26.9	[197]
	TiO ₂ nanoparticles	YD2-o-C8	11.0	32.0	[198]
Copper tetramethyl bipyridine based electrolyte ([Cu(tmby) ₂] ^{2+/+})	TiO ₂ nanoparticles	XY1 + D35	11.3	28.9	[23]
	TiO ₂ nanoparticles	XY1 + 5T	9.1	29.2	[188]
	TiO ₂ nanoparticles	Y123 + XY1b	13.1	32.0	[190]
	TiO ₂ nanoparticles	XY1 + L1	11.5	34.0	[26]
	TiO ₂ nanoparticles	MS5 + XY1b	13.5	34.5	[191]
	TiO ₂ nanoparticles	SL9 + SL10	15.2	29.5	[217]
Copper dimethyl phenanthroline based electrolyte ([Cu(dmp) ₂] ^{2+/+})	TiO ₂ nanoparticles	XY1 + D35	8.0	35.6	[30]

1.7. Objectives of the present thesis work

Till date, literature reports on modification of photoanode architecture and semiconducting layer for enhancing the performance of copper electrolyte based DSCs are rarely encountered. It is already known that except for TiO₂, ZnO is a suitable semi-conducting material for DSC photoanode, owing to its favourable energy band structure and charge transfer dynamics, which are similar to those of TiO₂, and higher electron mobility when compared to TiO₂. In addition, ZnO is a cheap, abundant and viable material which can be easily synthesized into a wide variety of morphologies and nano- or micro-structures, using facile methods. Also, the poor chemical stability of ZnO enables it to be used as templates which can be easily etched off by acidic treatments. The present thesis work aims to take advantage of these benefits of ZnO, by designing and developing novel photoanode architectures using ZnO microstructures for copper electrolyte based DSCs, in

order to improve their power conversion efficiencies by tackling the mass transport issues within the photoanode and by curtailing the charge recombination at the photoanode/electrolyte interface.

The initial studies involve the synthesis and characterization of ZnO microstructures, which are not only utilized as the photoanode material in DSCs but also employed as sacrificial layers or templates for creating surface roughness or scattering voids in conventional TiO₂ photoanodes, in order to achieve better light scattering properties along with improved mass transport for copper electrolyte species. We also aim to investigate the synergetic effect of TiO₂/ZnO bilayer photoanodes on the CB position and interfacial charge transfer dynamics in copper electrolyte based DSCs, for achieving exceptionally high open circuit voltages, even under low intensity illumination. Such small area DSCs delivering high voltages can be effectively implemented in self-powered small electronics and IoT systems. We further target to extend the applicability of our small area DSC by integrating it to a standard electric double layer capacitor (EDLC), hence developing an indoor light harvesting photo-capacitor.

1.8. Experimental and theoretical background

1.8.1. Steps for fabricating DSCs

The various processes involved in fabrication of DSCs (**Figure 1.23**) in the present thesis work are elaborated in this section. The basic steps include preparation of the electrodes (i.e. photoanode and counter electrode), their assembling, preparation of electrolyte solution and its filling into the assembled system. The devices were fabricated using our semi-automated DSC fabrication facility shown in **Figure 1.24(a)**.

(a) Photoanode fabrication. In general, the photoanode fabrication for a DSC includes the following steps:

- (i)* The FTO coated glass substrate (TEC 15 or TEC 10) is cut into square piece of required dimension (say 1.6 cm x 1.6 cm).
- (ii)* The cut FTO substrate is cleaned using an ultrasonic bath by sequentially dipping in soap solution, de-ionized water, isopropanol, and acetone for specific time periods (~ 30 min).
- (iii)* The cleaned substrate is subjected to step-wise annealing in a muffle furnace. The furnace temperature is ramped slowly to reach 150 °C, which is maintained for 10 min, then slowly ramped to 300 °C (for 10 min), then to 350 °C (for 10 min), 450 °C (for 10 min) and finally to 500 °C (for 30 min), followed by slow cooling.

- (iv) The substrate is then undergone UV/ozone treatment for 15 min.
- (v) TiO₂ pre-blocking layer is deposited over the cleaned FTO substrate via TiCl₄ bath deposition method. Herein, the substrate is immersed in 50 mM TiCl₄ aqueous solution and heated at 75 °C for 30 minutes, followed by step-wise annealing as mentioned in step (iii).
- (vi) The semiconductor layer is deposited over the above substrate using doctor blade method or by screen printing technique. Doctor blade method is mainly used throughout this thesis work, as it is the simplest among the deposition techniques and the required layer thickness could be acquired using a single step. The thickness and area of the deposited layer was controlled by using a custom-made mask having a specific thickness and aperture area. Mesoporous TiO₂ active layer is obtained by coating commercial 18NR-T titania (particle size ~ 20 nm) paste, while TiO₂ scattering layer is obtained by coating commercial 18NR-AO titania (particle size ~ 350 - 400 nm) paste. Typically, a ~ 6 μm thick active layer and ~ 6 μm thick scattering layer is deposited. In case of ZnO based DSCs ~15 μm thick ZnO layer is obtained by utilizing a homemade ZnO paste (with various particle size and morphology). The DSC electrode with multiple semiconductor layers are subjected to annealing at 100 °C for 10 min after the deposition of each intermediate layers. This is followed by step-wise annealing up to 500 °C, as mentioned in step (iii).
- (vii) The TiO₂ post-blocking layer (optional) is deposited over the mesoporous semiconductor layer via TiCl₄ bath deposition method (given in step v) or by screen printing (or spin coating) of the commercial blocking layer solution. Finally, the electrode was annealed in a step-wise manner (step (iii)).
- (viii) Dye solution is prepared by dissolving the required amount of organic dye/dyes in a 1:1 mixture of acetonitrile : tert-butanol solvents. Then the annealed electrode is cooled down slowly to about 80 °C and soaked in the prepared dye solution and kept still in the dark for 16 hours, so that the dye molecules penetrate into the semiconductor matrix and get adsorbed on the semiconductor surface forming a semi-conformal monolayer.

(b) Counter electrode preparation. The counter electrode is prepared as described below:

- (i) The FTO coated glass substrate (TEC 7 or TEC 8) is cut into square piece (of dimension 1.6 cm x 1.6 cm) and two holes are drilled on it to facilitate electrolyte

filling. The distance between the holes is such that they fall just outside the active area of the DSC (~0.5 cm in our case).

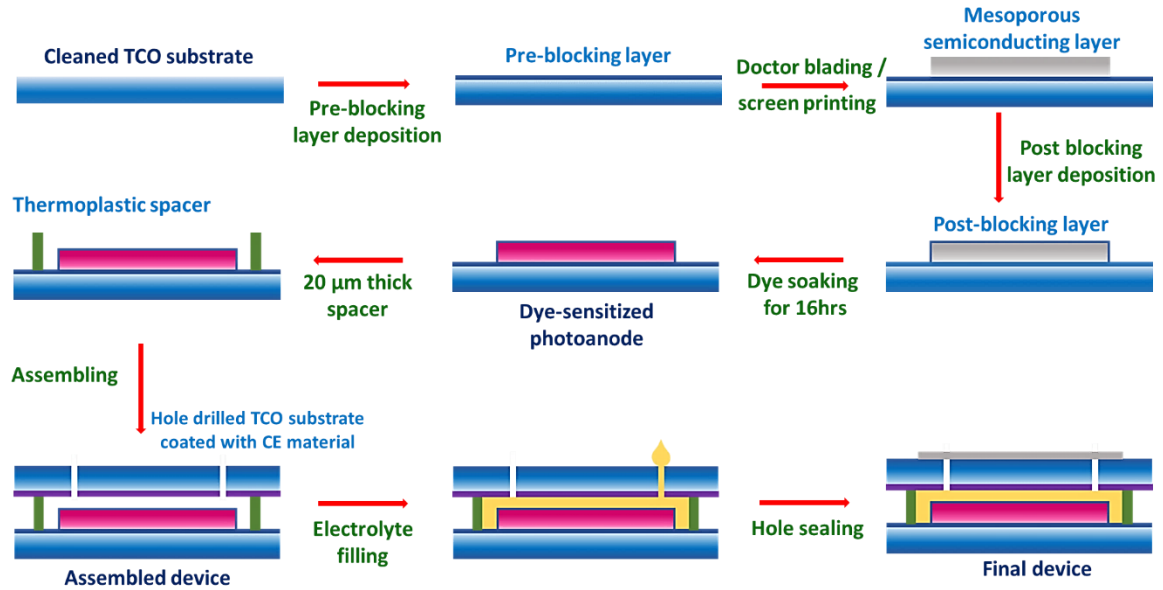


Figure 1.23. Various standard steps involved in the fabrication of DSCs.

- (ii) The hole drilled FTO substrate is cleaned using an ultrasonic bath by sequentially dipping in soap solution, de-ionized water, and ethanol for a period 45 minutes, each.
- (iii) The cleaned substrate is subjected to step-wise annealing (step (iii)) and UV/ozone treatment (step (iv)).
- (iv) The conducting polymer viz. poly (3,4-ethylene dioxythiophene) (PEDOT) is deposited on the FTO substrate via galvanostatic electrochemical polymerization technique using a two electrode system (**Figure 1.24(b)**). In this method, micellar aqueous solution of the monomer, ethylene dioxythiophene (EDOT, 0.01M) and the surfactant, sodium dodecyl sulfate (SDS, 0.1M) is used as the supporting electrolyte solution, the FTO substrate (prepared in step *xi*) on which the polymer film needs to be deposited is taken as the working electrode (electrode 1) and another FTO substrate or a metal substrate as the reference electrode (electrode 2). The electrodes 1 and 2 were immersed in the above electrolyte solution and a current of ~13 mA is passed for about 1.5 seconds using an external source (Metrohm Autolab workstation) in galvanostatic mode. Consequently, a thin porous PEDOT film is deposited on the electrode 1, which is dried at room temperature to be utilized as the CE for DSC.

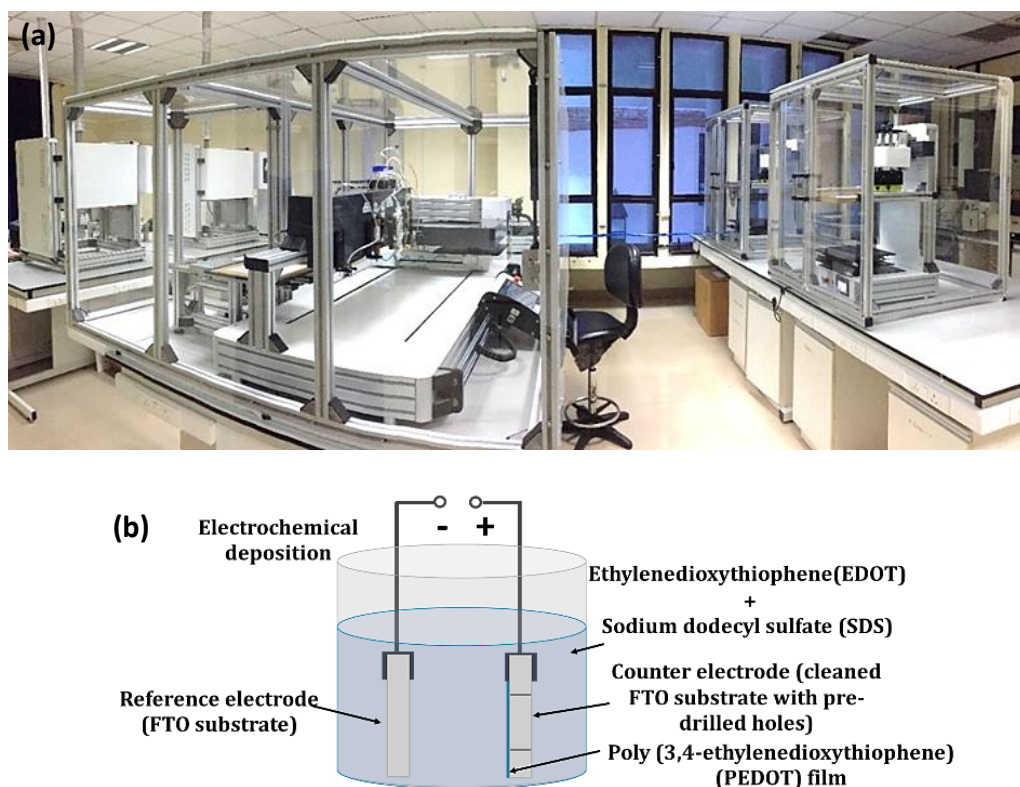


Figure 1.24. (a) The semi-automated facility used for fabrication of dye-sensitized PV cells / modules (DSC / DSM), (b) Electrochemical deposition of PEDOT on the CE.

(c) **Assembling of photoanode and counter electrode.** The dye-sensitized photoanode and the CE prepared in the above steps are conjoined either using a thermoplastic sealant (xiii) or by using a UV epoxy (xiv), which also act as a spacer between the two electrodes. The assembling is done in such a way that the holes are aligned above the active region of the photoanode.

- (v) For assembling the electrodes using thermoplastic material (Surllyn, 25 μm thick), it is cut into square piece (1.4 cm x 1.4 cm) and then a sealing gasket is formed by punching a hole (slightly bigger than the active area of photoanode) in the middle of the square piece of thermoplastic. This piece is placed above the photoanode such that its active area falls within the hole in the gasket. The CE is placed above this arrangement, with its conducting side facing downwards. The whole system is hot-pressed at ~ 120 $^{\circ}\text{C}$, such that the thermoplastic melts and joins the two electrodes.
- (vi) In order to assemble the prepared electrodes using UV epoxy, precise narrow lines of the epoxy are deposited around the active area of the photoanode (using the semi-automated fabrication facility shown in **Figure 1.24**) and the CE is placed

over it with its conducting side facing downwards. The whole arrangement is then transferred to a UV curing chamber, where UV light is irradiated for about 5 minutes. This hardens the UV epoxy and sticks the electrodes together.

The former method (xiii) is used for assembling the device throughout the thesis work unless stated otherwise.

(d) Electrolyte preparation and filling. The final step in DSC fabrication is the preparation and filling of electrolyte into the assembled device.

(vii) The electrolyte is prepared by first dissolving 0.1M Lithium bis(trifluoromethane)sulfonimide (LiTFSI) into the acetonitrile solvent containing 0.6 M 4-tert-Butylpyridine (TBP) in it, followed by the addition of the reduced and oxidized species of copper dimethyl phenanthroline complex, i.e., 0.2 M of $[\text{Cu}(\text{dmp})_2]^{1+}$ and 0.04 M of $[\text{Cu}(\text{dmp})_2]^{2+}$, respectively. The solution is mixed well so that all the additives are completely dissolved.

(viii) The prepared electrolyte solution is then injected into the inter-electrode spacing via the holes in the CE.

(ix) Finally, the holes in the CE are sealed using a thermoplastic piece and cover glass to prevent solvent evaporation and leakage.

1.8.2. Basic characterization techniques for DSCs

(a) Current density versus voltage (*J-V*) characterization. The current density against voltage (*J-V*) characteristic curve of a DSC can be used to assess its photovoltaic performance. Typically, the *J-V* curves are acquired via linear sweep voltammetry by varying the external load from zero (short circuit condition) to infinity (open circuit condition). The *J-V* curve and the corresponding power density versus voltage (*P-V*) curve obtained for a DSC under the standard illumination condition is shown in **Figure 1.25(a)**. The *J-V* curve can be used to determine variables such as V_{OC} , J_{SC} , and P_{max} , which is the product of the voltage (V_{max}) and current density (J_{max}) corresponding to the maximum power point (MPP). These parameters can be used to estimate the *FF* and *PCE* of the DSC as given in equations 1.9 and 1.10, respectively.

$$FF = \frac{V_{max} J_{max}}{V_{OC} J_{SC}} \quad (1.9)$$

$$PCE = \frac{P_{max}}{P_{in}} = \frac{V_{OC} J_{SC} FF}{P_{in}} \quad (1.10)$$

In the present work, J - V characterizations of the fabricated devices are performed under one sun condition (AM 1.5G simulated solar irradiation, 100 mW/cm^2) as well as under various indoor illumination conditions (CFL and LED light, 200 - 4000 lux) (corresponding irradiance spectra are shown in **Figure 1.25(b,c)**). J - V characterization is also done under dark condition, which gave information about recombination at the semiconductor/electrolyte and TCO/electrolyte interfaces.

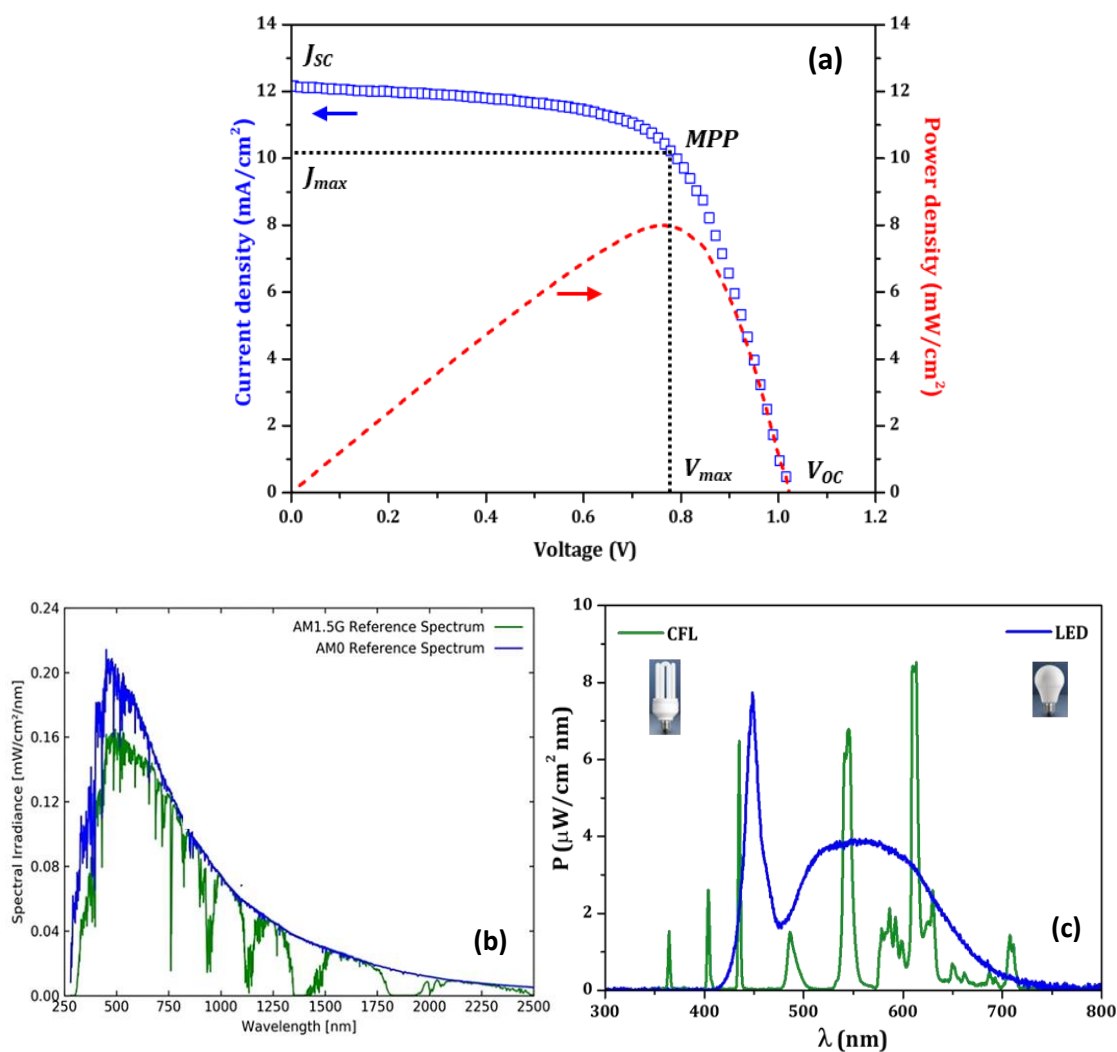


Figure 1.25. (a) Typical J - V curve along with P - V curve obtained for a DSC under AM 1.5G solar irradiation, (b) irradiance spectrum of AM 1.5G solar light and (c) irradiance spectra indoor light sources (1000 lux CFL and 1000 lux LED) usually used for J - V characterization.

(b) Incident photon-to-current conversion efficiency (IPCE) measurement. The incident photon-to-current efficiency (IPCE) or the external quantum efficiency (EQE) of a solar cell can be defined as the number photoelectrons generated per incident photon of specific

wavelength (λ). It is a measure of how efficiently a given wavelength of light is converted to electrical current. For determining the *IPCE*, the fabricated DSCs are irradiated with monochromatic light and the output J_{SC} is measured at different wavelengths. Then, the *IPCE* can be estimated using equation 1.11 as,

$$IPCE = \frac{J_{SC}(\lambda)}{q \varphi(\lambda)} = \frac{hc}{\lambda} \frac{J_{SC}(\lambda)}{q P_{in}(\lambda)} \quad (1.11)$$

where φ is photon flux density (calibrated using a photodetector), h is the Planck's constant, c is the speed of light and P_{in} is the incident photon power density. The *IPCE* spectrum (**Figure 1.26**) can be integrated to obtain the theoretical value of J_{SC} as,

$$J_{SC} = \int (q IPCE(\lambda) \varphi(\lambda)) d\lambda \quad (1.12)$$

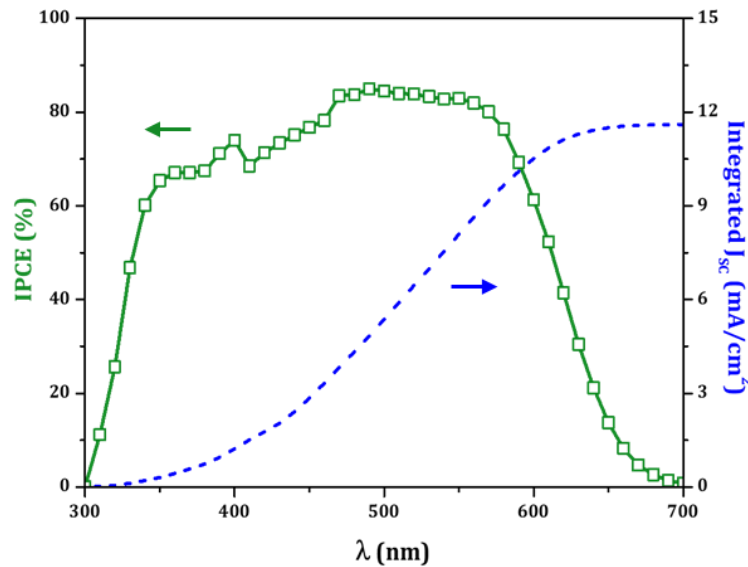


Figure 1.26. Typical *IPCE* curve for DSCs along with the integrated current density.

1.8.3. Detailed interfacial charge transfer analysis in DSCs

There are several steady state measurements as well as small amplitude modulation measurements involved in probing the interfacial electron transfer dynamics at the dye/semiconductor/electrolyte interfaces within DSCs. Steady state measurements or DC measurements, such as open circuit voltage decay, charge extraction, current transients etc. are carried out using large perturbations, wherein the system is maintained at an equilibrium. Whereas the small amplitude modulation techniques can be executed with small perturbations, either in pulse mode (e.g. transient photovoltage and photocurrent decay measurements) or AC mode (e.g. impedance measurements, intensity modulated photovoltage and photocurrent measurements).

(a) **Open circuit voltage decay measurement.** The open circuit voltage decay (OCVD) measurement is a steady state measurement using a light perturbation. In this measurement, the device is connected under open circuit condition and exposed to a constant light illumination, so that the photoelectrons are generated and injected into the semiconducting layer, hence populating its conduction band. In the meantime, since the DSC is in open circuit condition, the conduction band electrons recombine with the oxidized electrolyte species. A steady state open circuit voltage (V_{OC}) is obtained when an equilibrium is established between the injection and recombination processes under the constant illumination. After some time, when the steady state is attained, the light perturbation is switched off and the voltage decay is recorded, while the DSC is still under open circuit (Figure 1.27(a)).

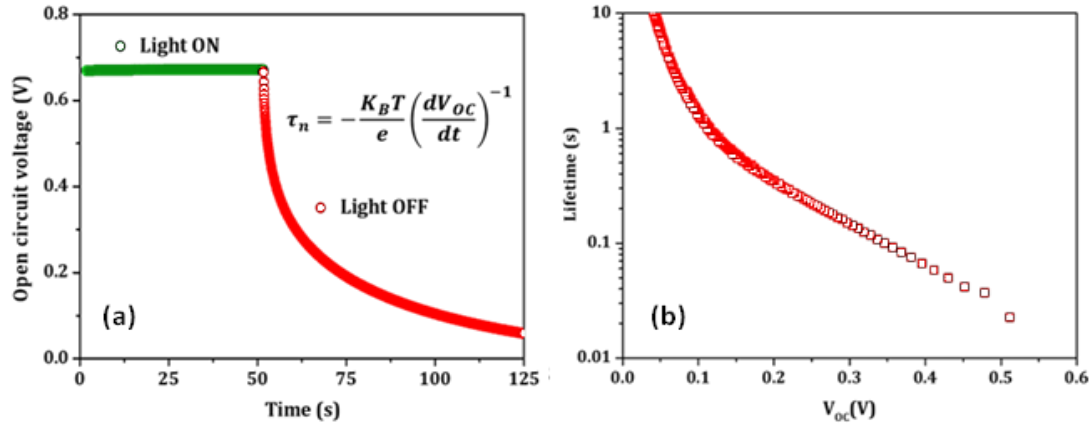


Figure 1.27. Typical (a) voltage transient and (b) lifetime versus voltage curves of DSCs obtained from open circuit voltage decay (OCVD) measurement.

Under open circuit condition, the voltage decay can occur only via charge recombination at semiconductor/electrolyte interface. Hence, the recombination time constant or electron lifetime, τ_n , can be derived from open circuit voltage transients as,^[218]

$$\tau_n = -\frac{k_B T}{q} \left(\frac{dV_{OC}}{dt} \right)^{-1} \quad (1.13)$$

where k_B is the Boltzmann's constant and T is the absolute temperature. A typical τ_n versus V_{OC} curve is shown in Figure 1.27(b).

(b) **Charge extraction (CE) measurement.** The charge extraction (CE) measurement is yet another optical perturbation based steady state measurement, used for estimating the concentration of excess charge carriers in the device at a steady state operating condition (open circuit or short circuit conditions). By observing the dependence of the charge extracted at open circuit on the semiconductor Fermi level, we can predict the conduction

band position in DSC photoanodes. For extracting charges at open circuit condition, the device was illuminated with a constant intensity light for about 10 seconds, so that the semiconductor's conduction band is populated with photoelectrons, until a steady state is attained (when V_{OC} saturates). Then, the light perturbation is switched off, while the device is short circuited so as to extract all the charges accumulated in the semiconducting layer. The charge (Q_{ext}) extracted during the process can be determined by integrating the short circuit current (j) flowing through the external circuit as,^[219]

$$Q_{ext} = - \int j dt \quad (1.14)$$

Figure 1.28. shows the typical charge extraction curves obtained for a DSC. The charge extracted can be used to calculate the concentration of electrons trapped in the device as a function of potential. This data can be used to identify any shift in the conduction band edge of the device with respect to other devices.

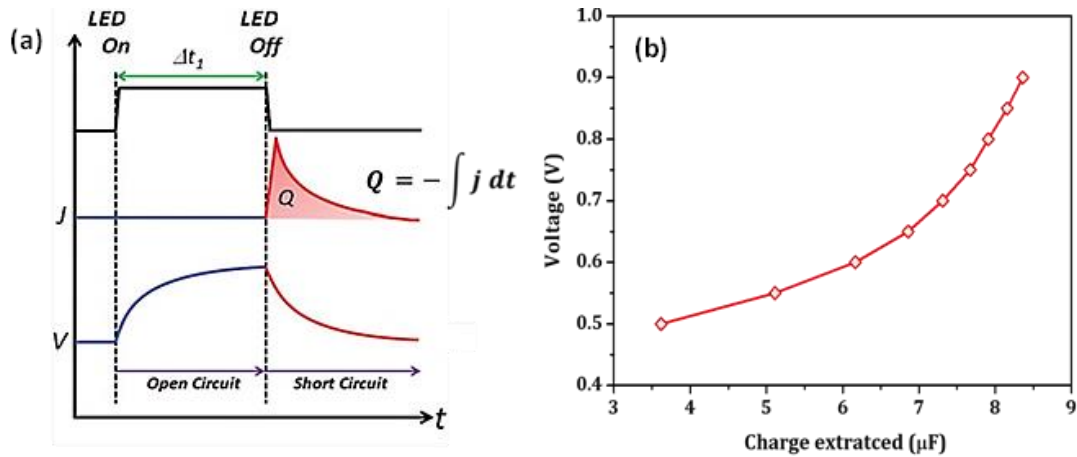


Figure 1.28. (a) Transient curves obtained from charge extraction (CE) measurement,^[40] and (b) typical plot of extracted charge against the potential for DSCs.

(c) **Transient photovoltage decay measurement.** Transient photovoltage decay (TVD) measurement is a small modulation transient technique, in which a small amplitude light pulse is used as the perturbation to probe the system maintained at steady-state open circuit condition. The steady state is attained by illuminating the device at open circuit with a constant light intensity (from LED 1), while the perturbation in the form of a small amplitude light pulse is induced by a secondary light source (LED 2). The photovoltage response following the light perturbation is recorded (**Figure 1.29**) and fitted using a single exponential decay as,^[220]

$$\Delta V_{OC}(t) = \Delta V e^{-t/\tau_n} \quad (1.15)$$

where $\Delta V_{oc}(t)$ is the photovoltage at time t , ΔV is the pre-exponential factor that signifies the amplitude of the change in photovoltage induced by the secondary light pulse, while τ_n is the time constant for the photovoltage decay which correspond to the electron recombination lifetime.

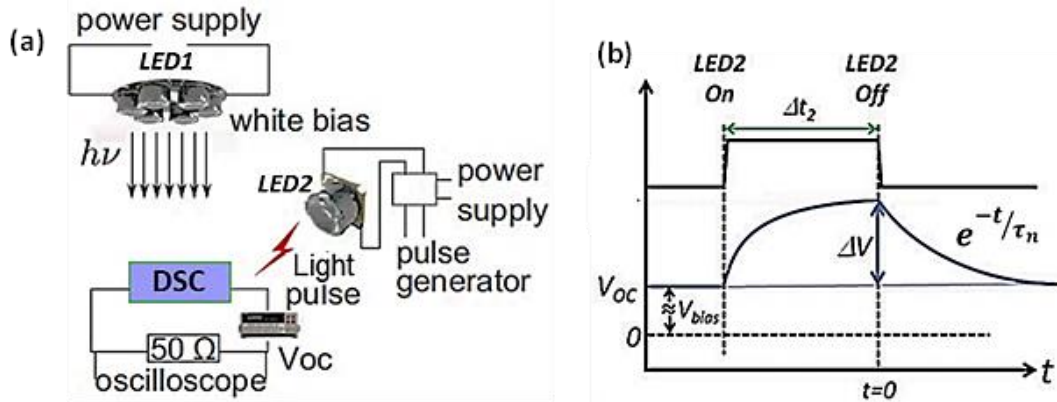


Figure 1.29. (a) Experimental setup for transient photovoltage decay (TVD) measurement,^[220] and (b) voltage transients obtained from the TVD measurement.^[40]

(d) **Transient photocurrent decay measurement.** Transient photocurrent decay (TCD) measurement is used to determine the electron transport time (τ_d), by implementing a small amplitude light perturbation on the system maintained at steady-state short circuit condition. For attaining the steady state, the device is connected in short circuit and illuminated with a constant light coming from the primary source (LED 1). The small amplitude light pulse coming from the secondary light source (LED 2) is used as the perturbation (Figure 1.30(a)).

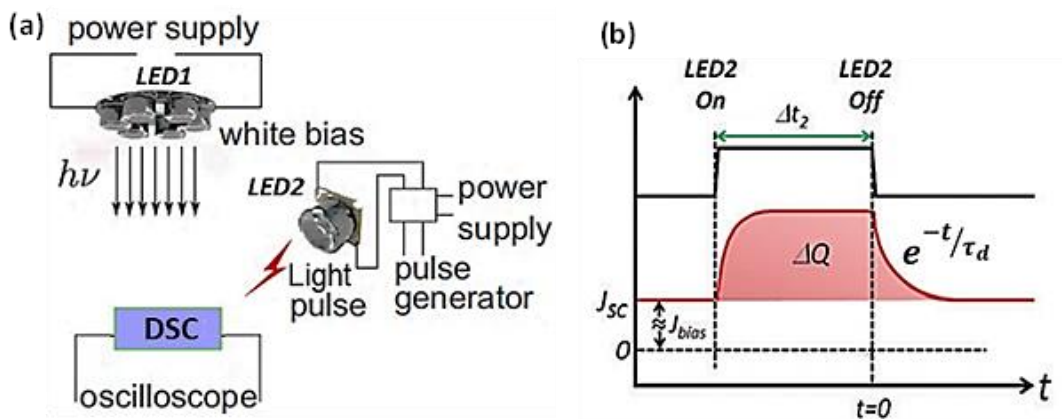


Figure 1.30. (a) Experimental setup for transient photocurrent decay (TCD) measurement,^[220] and (b) current transients obtained from the TCD measurement.^[40]

The resulting photocurrent decay curve is (**Figure 1.30(b)**) fitted using a first order kinetics as,^[220]

$$\Delta J_{SC}(t) = \Delta J e^{-t/\tau_d} \quad (1.16)$$

where $\Delta J_{SC}(t)$ is the photocurrent at time t , ΔJ is the pre-exponential factor that indicates the amplitude of the photocurrent change brought about by the optical perturbation, while τ_d is the time constant for the photocurrent decay which corresponds to the time constant for charge collection or the electron transport time.

(e) Current transient measurement. Current transient (CT) measurement is a large optical perturbation technique used for tracking the diffusion limitations in DSCs. For this, the device under short circuit is illuminated with a constant intensity light for about 20-30 seconds to attain a steady state, while the current output of the device is monitored and plotted with respect to time. A typical current transient curve for a mass transport limited DSC employing bulky electrolyte species is provided in **Figure 1.31**.

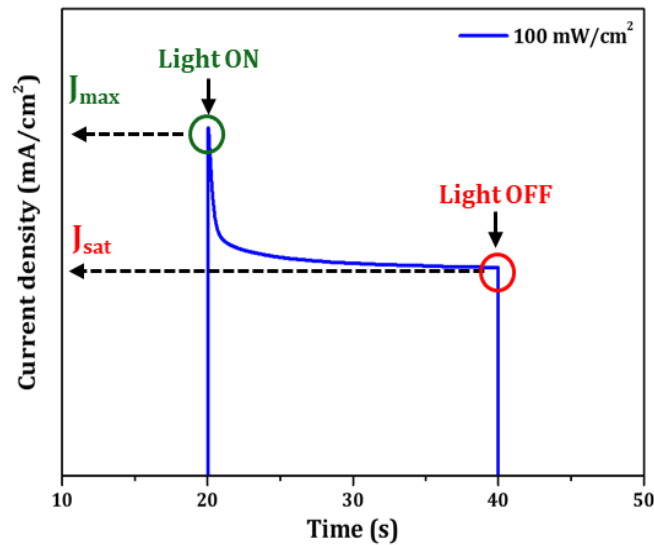


Figure 1.31. Typical current transients (CT) curve for a mass transport limited DSC.

Initially, when the light is switched on, a spike is observed in the current transient spectra (J_{max}) corresponding to the rapid regeneration of oxidized dye molecules by the nearby reduced electrolyte species. Afterwards, as the light absorption and regeneration processes continue, the number of reduced electrolyte species in the vicinity of the sensitizers are decreased, whereas the diffusion of reduced electrolyte species towards the photoanode is slower due to its bulkiness. This in turn slows down the regeneration of dye molecules, which subsequently affect the entire photovoltaic process. As a result, the current is seen to decrease gradually, and saturates (J_{sat}) after a while, when an equilibrium is established

between the diffusion and the regeneration processes. The regeneration efficiency of the DSC can be approximated by estimating the ratio of J_{sat} to J_{max} . For DSCs without any diffusion limitations, the ratio of J_{sat} to J_{max} will be equal to one ($J_{sat}/J_{max} = 1$) indicating a 100% regeneration efficiency. Whereas, this ratio will be less than one ($J_{sat}/J_{max} < 1$) for mass transport limited systems.^[221]

(f) Electrochemical impedance spectroscopy. Electrochemical impedance spectroscopy (EIS) is a small amplitude modulation technique, wherein the system maintained at a steady state operating condition (by applying a DC bias voltage, V_{dc}) is probed using an AC electrical perturbation (δV) with amplitude as small as 0.1% of the bias voltage and frequency, typically varying from 100 mHz to 100 kHz. EIS is based on frequency response analysis and can be used to resolve the electron transfer processes and charge accumulation at various interfaces within the electrochemical device, and to determine the corresponding impedances. The total voltage input given to the system, during EIS measurement, can be expressed as,

$$V(\omega t) = V_{dc} + \delta V = V_{dc} + \delta V_0 e^{i(\omega t)} \quad (1.17)$$

where δV_0 is the amplitude and ω is the angular frequency of the AC perturbation signal.

The corresponding output current density is given by,

$$J(\omega t + \theta) = J_{dc} + \delta J = J_{dc} + \delta J_0 e^{i(\omega t + \theta)} \quad (1.18)$$

where J_{dc} is the steady state output current density, while δJ is the modulation in output current induced by the perturbation. δJ_0 is the amplitude, ω is the angular frequency and θ is the phase shift of the AC component of output signal. The impedance of the system is determined by the ratio of modulation voltage (δV) to the corresponding current response (δJ) as,^[40]

$$Z = \frac{\delta V}{\delta J} = \frac{\delta V_0}{\delta J_0} e^{-i\theta} = Z_0 e^{-i\theta} = Z' + i Z'' \quad (1.19)$$

where $Z' = Z_0 \cos \theta$ and $Z'' = -Z_0 \sin \theta$, respectively, gives the real and imaginary part of the resultant impedance of the electrochemical system, while $\theta = \tan^{-1}(Z''/Z')$ gives the phase difference between the input AC voltage signal and the corresponding output current response. We obtain the Nyquist plot, also known as the complex impedance plot by plotting Z' , Z'' and ω against one another in the three-dimensional space. A projection of the Nyquist plot in the $Z'-Z''$ plane (which is an argand plane) gives us the polar diagram or phase diagram, in which each point represents a particular frequency (ω). Typically, the Nyquist plot for DSC (as shown in **Figure 1.32**) consists of three semicircles (or arcs) corresponding to the impedance of three major charge transfer processes. The arc at the

higher frequency range (> 1 kHz) corresponds to the charge transfer resistance at the counter electrode/electrolyte interface (R_{CE}), the arc at the mid-frequency range (~ 1 -100 Hz) represents the charge transfer resistance at the nanoporous semiconductor (R_{SC}), whereas the one at the low frequency region (< 1 Hz) depicts the diffusion resistance of the redox species in the electrolyte (R_t). Hence, by fitting the Nyquist plot using suitable electrical circuit models, we can determine the impedances corresponding to various electrochemical processes within the device.

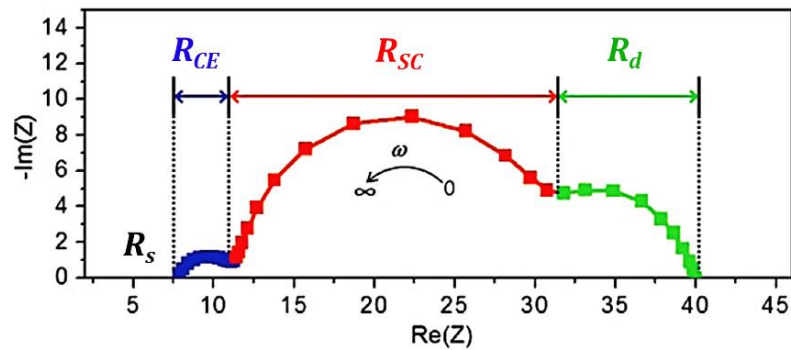


Figure 1.32. Typical Nyquist plot obtained by EIS measurement for DSC.

A transmission line model equivalent circuit, shown in **Figure 1.33(a)**, can be appropriately used to model the impedance spectra of DSCs. The circuit elements of this model include the total series resistance (R_s), a number of parallel RC circuits to represent the charge transfer resistance or recombination resistance (r_{ct}) and chemical capacitance (c_μ) at the various semiconducting particle/electrolyte interfaces, a number of resistance elements to represent the charge transport or diffusion resistance (r_t) at various interfaces or boundaries within the semiconductor matrix (assuming r_{ct} and r_t are uniformly distributed), a parallel RC network consisting of the charge transfer resistance (R_{CE}) and double layer capacitance (C_{CE}) at the counter electrode/electrolyte interface, and another one indicating the charge transfer resistance (R_{TCO}) and double layer capacitance (C_{TCO}) at the TCO/electrolyte interface, and finally the Warburg impedance (Z_d) corresponding to the diffusion of redox species in the electrolyte. Given the semiconducting layer of thickness d , the total charge transfer resistance (R_{ct}), total diffusion resistance (R_t) and total chemical capacitance (C_μ) at the semiconductor/dye/electrolyte interfaces can be estimated as, $R_{ct} = r_{ct}/d$, $R_t = r_t \times d$, and $C_\mu = c_\mu \times d$, respectively. R_t represents the diffusion of electrons in the semiconducting layer, which can be described by multiple trapping/detrapping mechanism, whereas the charge recombination behaviour is represented by R_{ct} , which can be affected by intrinsic nature of the semiconductor and adso-

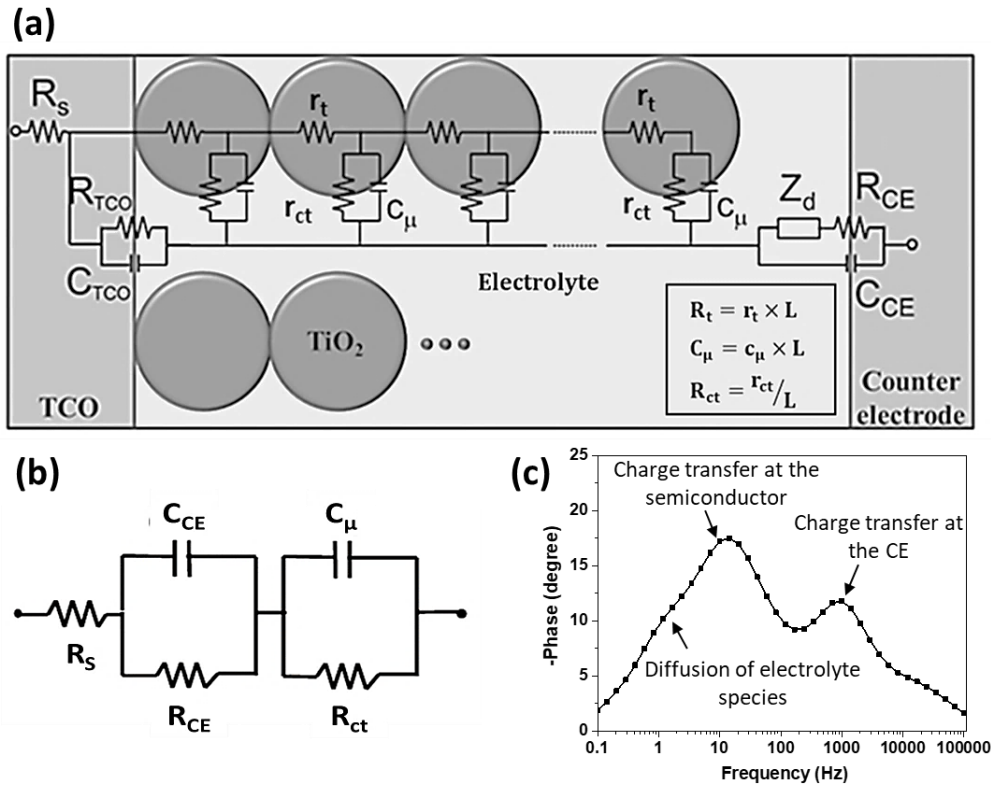


Figure 1.33. (a) Transmission line equivalent circuit and (b) Randle's circuit for impedance fitting. (c) Typical Bode phase plot obtained from EIS measurement.

-rbed dye, semiconductor morphology, additives in the electrolyte etc.^[222,223] Meanwhile, C_μ represents the total impedance of the charge accumulation in the semiconductor layer corresponding to its density of states. R_t and R_{ct} are extracted by fitting the semicircle (corresponding to R_{SC}) at the mid-frequency region of the Nyquist diagram. Assuming rapid electron diffusion through the semiconductor matrix, i.e. $R_d < R_{ct}$, the total resistance of the semiconducting layer can be expressed as,

$$R_{SC} = \frac{1}{3}R_t + R_{ct} \quad (1.20)$$

In this case, the semicircle corresponding to R_{SC} is constituted by a straight line similar to Warburg diffusion (at the high frequency end) indicating electron transport (R_d) and a semicircle (at the low frequency end) representing charge recombination (R_{ct}). Subsequently, the values of the circuit elements acquired by fitting the impedance spectra can be used for determining various device parameters as,

$$\tau_n = R_{ct} C_\mu \quad (1.21)$$

$$\tau_d = R_t C_\mu \quad (1.22)$$

$$D_n = \frac{d^2}{R_t C_\mu} \quad (1.23)$$

$$L_n = L \sqrt{R_{ct}/R_t} \quad (1.24)$$

Hence, the expression for η_{cc} (from equation 1.6) becomes

$$\eta_{cc} = \frac{1}{1 + R_t/R_{ct}} \quad (1.25)$$

A simplified Randle's circuit constituting R_s , R_{CE} , R_{ct} , C_{CE} and C_μ (assuming negligible R_t), shown in **Figure 1.33(b)**, can also serve the purpose of fitting a DSC's Nyquist plot. In addition to the Nyquist plot, we can obtain the Bode phase diagram from the EIS measurement, by plotting the phase shift (θ) against the applied frequency ($f=1/(2\pi\omega)$), as shown in **Figure 1.33(c)**. The Bode plot reveals three peaks similar to the three semicircles (or arcs) in the Nyquist plot. The frequency (f_{max}) corresponding to the peak in the mid-frequency ($\sim 1 - 100$ Hz) region can be used to deduce the recombination time constant as,

$$\tau_n = 1/(2\pi f_{max}) \quad (1.26)$$

(g) Intensity modulated photovoltage and photocurrent spectroscopy. The intensity modulated photovoltage spectroscopy (IMVS) and intensity modulated photocurrent spectroscopy (IMPS) are frequency domain measurement techniques based on small amplitude light perturbation techniques. In these measurements, the DSC (either in open circuit or short circuit condition) is illuminated with a constant bias light of intensity I_o to establish a steady state and the light coming from a sinusoidally modulated lamp, with intensity δI (with amplitude about $< 10\%$ of the bias) and frequency typically ranging from 0.1 Hz to 10 kHz, is used as the AC light perturbation. In case of IMVS, the modulated light is superimposed on the bias light illuminating the DSC under open circuit condition (**Figure 1.34(a)**), and the corresponding frequency dependent signal is recorded as,

$$H_{IMVS} = \frac{\delta V}{\delta I} \quad (1.27)$$

where δV is the voltage response of the device when the light modulation (δI) is applied. On the other hand, the device is short circuited in case of IMPS measurement (**Figure 1.34(b)**) and the corresponding frequency dependent signal is recorded as,

$$H_{IMPS} = \frac{\delta J}{\delta I} \quad (1.28)$$

where δJ is the change in the output current density up on introduction of the perturbation (δI). In both the cases, the frequency response signal (H) can be, expressed as,

$$H = H' + i H'' \quad (1.29)$$

where H' and H'' respectively, gives the real and imaginary part of the signal. The corresponding Bode plots are obtained by plotting H'' against the applied frequency. The

Bode plot for IMVS (**Figure 1.34(c)**) depicts the peak corresponding to the charge transfer at the semiconductor/electrolyte interface, whereas that for IMPS (**Figure 1.34(d)**) shows a peak corresponding to the electron diffusion within the semiconducting layer. Hence, the respective Bode plots can be used to estimate the lifetime and transport time as,

$$\tau_n = 1/(2\pi f_{IMVS}) \quad (1.30)$$

$$\tau_d = 1/(2\pi f_{IMPS}) \quad (1.31)$$

where f_{IMVS} and f_{IMPS} are the frequencies corresponding to the peak in the Bode plots for IMVS and IMPS measurements, respectively.

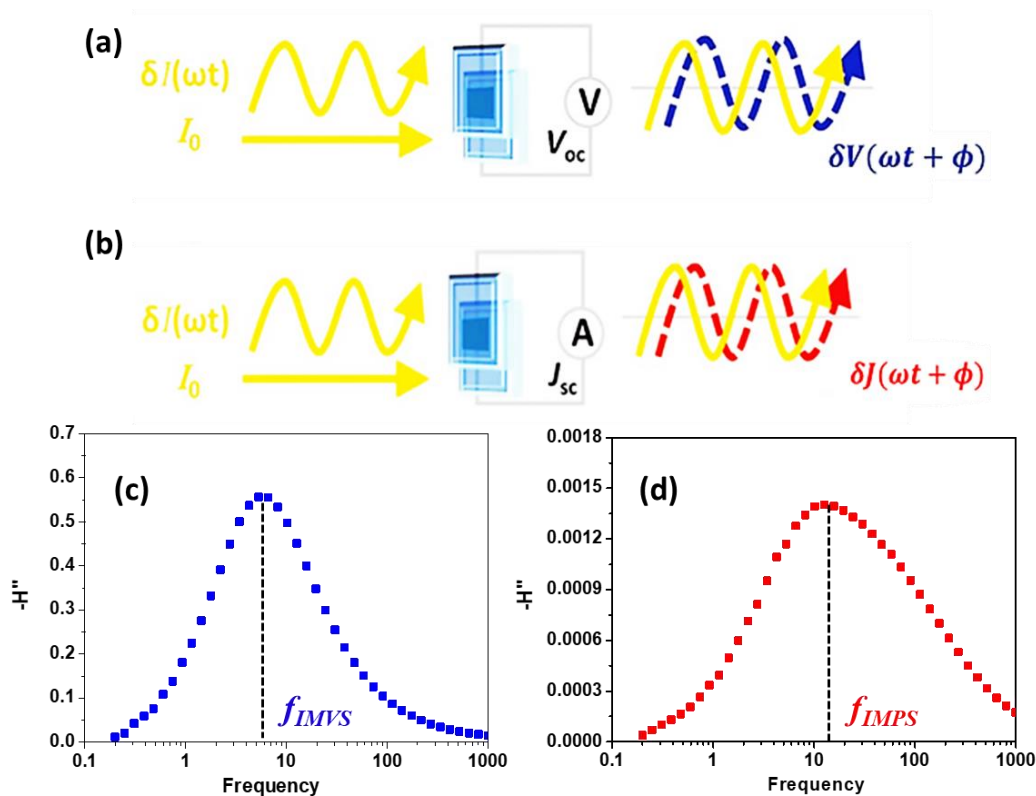


Figure 1.34. Schematic representation of operating principle of (a) IMVS and (b) IMPS measurements.^[40] Typical Bode plots obtained from (c) IMVS and (d) IMPS measurements of DSCs.

1.8.4. Mott-Schottky analysis of the semiconductor/electrolyte interface

The semiconductor/electrolyte interface is vital for DSC operation. When a semiconductor comes in contact with an electrolyte system containing redox species, electron transfer occurs across the interface to establish an equilibrium between the two phases. The electrochemical potential or Fermi level of electrons in both the phases must be same at equilibrium. The electrochemical potential of electrons in the semiconductor is given by its Fermi level (E_F), which depends on the energy band edges and the

concentration of electrons in the semiconductor. Whereas the electrochemical potential of electrons in the electrolyte is given by its redox Fermi energy (E_{redox}), which relies on the standard reduction potential of the redox couple and the concentration of the oxidized and the reduced species. The relative position of the Fermi levels of the semiconductor and the electrolyte determines the electron transfer at their interface.

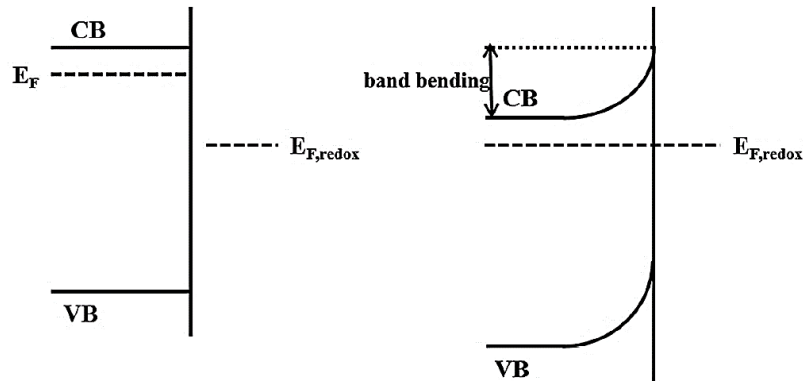


Figure 1.35. Band bending in n-type semiconductor when they are immersed in an electrolyte.^[224]

When an n-type semiconductor, such as ZnO or TiO₂, is immersed in an electrolyte, with E_{redox} lying below the E_F , the electrons flow from the semiconductor to the electrolyte till the equilibrium is attained. Consequently, a space charge region or depletion region is created at the semiconductor side of the interface, which penetrates to about 100 - 1000 Å into the semiconductor surface. The space charge region is associated with its own electric field, which result in a parabolic variation in electric potential across the region. This variation in electric potential appears as band bending of semiconductor at the semiconductor/electrolyte interface, as shown in **Figure 1.35**. The band bending will be equal to the difference between the Fermi levels of the semiconductor and the electrolyte, before they are in contact with each other.^[224] The formation of space charge region in n-type semiconductor, by immersing it in a redox electrolyte, has the effect of positively charging the semiconductor surface. The positive charges in the space charge region at the semiconductor surface is counter balanced by a layer of negative charges in the electrolyte, hence forming an electrical double layer, known as Helmholtz layer. Hence the total capacitance at the semiconductor/electrolyte interface is a combination of the space charge capacitance (C_{SC}) on the semiconductor side, which is given by the variation of space charge with respect to the potential drop across the depletion region and the Helmholtz capacitance (C_H) at the electrolyte side of the interface as,^[226]

$$\frac{1}{C} = \frac{1}{C_{SC}} + \frac{1}{C_H} \quad (1.32)$$

Since C_H is very large, its contribution to the total capacitance (C) can be neglected.

The equilibrium between the Fermi levels of the semiconductor and electrolyte can be disrupted by applying an external potential to the semiconductor. As a result, the Fermi levels are separated and the band bending is reduced. The applied potential at which the space charge region (and the band bending) completely disappears is known as the flat-band potential (V_{fb}) of the semiconductor. V_{fb} gives the extend of band bending at the semiconductor/electrolyte interface and can be evaluated by using Mott-Schottky analysis. The Mott-Schottky equation gives the relation between the interfacial capacitance (C) and the applied potential (V) as,^[225]

$$\frac{1}{C^2} = \frac{2}{\epsilon\epsilon_0 A^2 q N_d} \left(V - V_{fb} - \frac{k_B T}{q} \right) \quad (1.33)$$

where A is the geometrical area (cm^2) of semiconductor which is exposed to the electrolyte, N_d is donor density or free carrier concentration (cm^{-3}), q is electronic charge (1.6×10^{-19} C), ϵ is relative permittivity, ϵ_0 is permittivity of free space (8.85×10^{-12} F m^{-1}), k_B is the Boltzmann constant (1.381×10^{-23} J K^{-1}), and T is the absolute temperature (298 K).

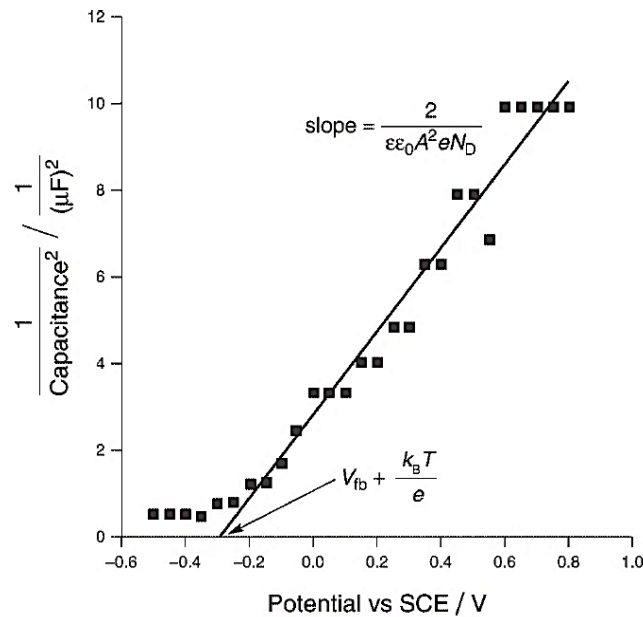


Figure 1.36. A typical Mott-Schottky plot.^[225]

For determining the V_{fb} of the semiconductor at the semiconductor/electrolyte interface of the DSC, a device is fabricated using unsensitized semiconducting layer as photoanode, by keeping the other components like electrolyte and counter electrode same as that of the conventional DSC. The device is subjected to EIS at a range of applied

potentials. For each potential, the impedance spectra of the device at a particular frequency, say 100 Hz, is fitted using appropriate circuit to extract the capacitance (C) at the semiconductor/electrolyte interface. A plot of $1/C^2$ vs. V , known as the Mott-Schottky plot (MS plot) is drawn as shown in **Figure 1.36**. From the MS plot the V_{fb} of the semiconductor can be determined by extrapolating the linear region to intercept the V axis, while N_d of the semiconductor can be estimated from its slope.

References

- [1] IEA, *Net Zero by 2050 - A Roadmap for the Global Energy Sector* **2021**.
- [2] T. Ahmad, D. Zhang, *Energy Reports* **2020**, *6*, 1973.
- [3] O. B. Awodumi, A. O. Adewuyi, *Energy Strategy Reviews* **2020**, *27*, 100434.
- [4] U. J. Banday, R. Aneja, *International Journal of Energy Sector Management* **2020**, *14*, 248.
- [5] J.-P. Rodrigue, *The Geography of Transport Systems*, 5th Edition, Routledge, **2020**.
- [6] V. Kashyap, S. Sakunkaewkasem, M. D. Marquez, T. R. Lee, H. Ghasemi, P. Jafari, M. Nazari, B. Eslami, S. Nazifi, P. Irajizad, *Joule* **2019**, *3*, 3100.
- [7] M. Vasiliev, M. Nur-E-Alam, K. Alameh, *Energies* **2019**, *12*, 1080.
- [8] A. Mohammadnia, A. Rezania, B. M. Ziapour, F. Sedaghati, L. Rosendahl, *Energy Convers Manag* **2020**, *205*, 112352.
- [9] S. Ahmed, Z. Li, M. S. Javed, T. Ma, *Mater Today Energy* **2021**, *21*, 100776.
- [10] M. A. Green, *Progress in Photovoltaics: Research and Applications* **2001**, *9*, 123.
- [11] M. A. Green, *Physica E Low Dimens Syst Nanostruct* **2002**, *14*, 65.
- [12] W. C. Sinke, *Renew Energy* **2019**, *138*, 911.
- [13] A. Aslam, U. Mehmood, M. H. Arshad, A. Ishfaq, J. Zaheer, A. Ul Haq Khan, M. Sufyan, *Solar Energy* **2020**, *207*, 874.
- [14] J. Gubbi, R. Buyya, S. Marusic, M. Palaniswami, *Future Generation Computer Systems* **2013**, *29*, 1645.
- [15] M. Mohammadi, A. Al-Fuqaha, *IEEE Communications Magazine* **2018**, *56*, 94.
- [16] S. Yun, Y. Zhang, Q. Xu, J. Liu, Y. Qin, *Nano Energy* **2019**, *60*, 600.
- [17] H. Ryu, H.-J. Yoon, S.-W. Kim, H. Ryu, H.-J. Yoon, S.-W. Kim, *Advanced Materials* **2019**, *31*, 1802898.
- [18] H. Elahi, K. Munir, M. Eugeni, S. Atek, P. Gaudenzi, *Energies* **2020**, *13*, 5528.
- [19] H. Liu, H. Fu, L. Sun, C. Lee, E. M. Yeatman, *Renewable and Sustainable Energy Reviews* **2021**, *137*, 110473.
- [20] A. Venkateswararao, J. K. W. Ho, S. K. So, S. W. Liu, K. T. Wong, *Materials Science and Engineering: Reports* **2020**, *139*, 100517.
- [21] A. S. Teran, J. Wong, W. Lim, G. Kim, Y. Lee, D. Blaauw, J. D. Phillips, *IEEE Trans Electron Devices* **2015**, *62*, 2170.

- [22] S. Biswas, H. Kim, *Polymers* **2020**, *12*, 1338.
- [23] M. Freitag, J. Teuscher, Y. Saygili, X. Zhang, F. Giordano, P. Liska, J. Hua, S. M. Zakeeruddin, J. E. Moser, M. Grätzel, A. Hagfeldt, *Nature Photonics* **2017**, *11*, 372.
- [24] G. Gokul, S. C. Pradhan, S. Soman, *Energy, Environment, and Sustainability* **2019**, 281.
- [25] A. Aslam, U. Mehmood, M. H. Arshad, A. Ishfaq, J. Zaheer, A. Ul Haq Khan, M. Sufyan, *Solar Energy* **2020**, *207*, 874.
- [26] H. Michaels, M. Rinderle, R. Freitag, I. Benesperi, T. Edvinsson, R. Socher, A. Gagliardi, M. Freitag, *Chem Sci* **2020**, *11*, 2895.
- [27] I. Mathews, S. N. Kantareddy, T. Buonassisi, I. M. Peters, *Joule* **2019**, *3*, 1415.
- [28] B. O'Regan, M. Grätzel, *Nature* **1991**, *353*, 737.
- [29] Y. Ren, D. Zhang, J. Suo, Y. Cao, F. T. Eickemeyer, N. Vlachopoulos, S. M. Zakeeruddin, A. Hagfeldt, M. Grätzel, *Nature* **2023**, *613*, 60.
- [30] S. M. Meethal, S. C. Pradhan, J. Velore, S. Varughese, R. S. Pillai, F. Sauvage, A. Hagfeldt, S. Soman, *J Mater Chem A* **2024**, *12*, 1081.
- [31] M. Grätzel, *Nature* **2001**, *414*, 338.
- [32] A. Hagfeldt, G. Boschloo, L. Sun, L. Kloo, H. Pettersson, *Chem Rev* **2010**, *110*, 6595.
- [33] C. C. Raj, R. Prasanth, *J Power Sources* **2016**, *317*, 120.
- [34] S. H. Nam, K. H. Lee, J. H. Yu, J. H. Boo, *Applied Science and Convergence Technology* **2019**, *28*, 194.
- [35] S. Thomas, T. G. Deepak, G. S. Anjusree, T. A. Arun, S. V. Nair, A. S. Nair, *J Mater Chem A* **2014**, *2*, 4474.
- [36] X. Wang, B. Zhao, W. Kan, Y. Xie, K. Pan, *Adv Mater Interfaces* **2022**, *9*, 2101229.
- [37] J. Wu, Z. Lan, J. Lin, M. Huang, Y. Huang, L. Fan, G. Luo, *Chem Rev* **2015**, *115*, 2136.
- [38] M. Grätzel, *J Photochem Photobiol A Chem* **2004**, *164*, 3.
- [39] M. Pazoki, U. B. Cappel, E. M. J. Johansson, A. Hagfeldt, G. Boschloo, *Energy Environ Sci* **2017**, *10*, 672.
- [40] L. L. Li, Y. C. Chang, H. P. Wu, E. W. G. Diau, *Int Rev Phys Chem* **2012**, *31*, 420.
- [41] R. A. Marcus, N. Sutin, *Biochimica et Biophysica Acta (BBA) - Reviews on Bioenergetics* **1985**, *811*, 265.
- [42] S. E. Koops, B. C. O'Regan, P. R. F. Barnes, J. R. Durrant, *J Am Chem Soc* **2009**, *131*, 4808.
- [43] J. Bisquert, A. Zaban, *Appl Phys A Mater Sci Process* **2003**, *77*, 507.
- [44] A. Y. Anderson, P. R. F. Barnes, J. R. Durrant, B. C. O'regan, *Journal of Physical Chemistry C* **2011**, *115*, 2439.
- [45] K. C. D. Robson, K. Hu, G. J. Meyer, C. P. Berlinguette, *J Am Chem Soc* **2013**, *135*, 1961.
- [46] Q. Zhang, G. Cao, *Nano Today* **2011**, *6*, 91.
- [47] B. Hu, Q. Tang, B. He, L. Lin, H. Chen, *J Power Sources* **2014**, *267*, 445.

- [48] M. Pazoki, N. Taghavinia, A. Hagfeldt, G. Boschloo, *Journal of Physical Chemistry C* **2014**, *118*, 16472.
- [49] S. H. Hwang, J. Yun, J. Jang, *Adv Funct Mater* **2014**, *24*, 7619.
- [50] M. Grätzel, *Inorg Chem* **2005**, *44*, 6841.
- [51] K. Fan, J. Yu, W. Ho, *Mater Horiz* **2017**, *4*, 319.
- [52] M. Ge, C. Cao, J. Huang, S. Li, Z. Chen, K. Q. Zhang, S. S. Al-Deyab, Y. Lai, *J Mater Chem A* **2016**, *4*, 6772.
- [53] D. Joshy, S. B. Narendranath, Y. A. Ismail, P. Periyat, *Nanoscale Adv* **2022**, *4*, 5202.
- [54] W. Zhang, Y. Xie, D. Xiong, X. Zeng, Z. Li, M. Wang, Y. B. Cheng, W. Chen, K. Yan, S. Yang, *ACS Appl Mater Interfaces* **2014**, *6*, 9698.
- [55] N. Liu, K. Lee, P. Schmuki, *Electrochem commun* **2012**, *15*, 1.
- [56] W. Q. Wu, Y. F. Xu, C. Y. Su, D. Bin Kuang, *Energy Environ Sci* **2014**, *7*, 644.
- [57] Y. Cao, Y. J. Dong, H. L. Feng, H. Y. Chen, D. Bin Kuang, *Electrochim Acta* **2016**, *189*, 259.
- [58] S. Ni, D. Wang, F. Guo, S. Jiao, Y. Zhang, J. Wang, B. Wang, L. Yuan, L. Zhang, L. Zhao, *J Cryst Growth* **2019**, *505*, 62.
- [59] P. Gnida, P. Jarka, P. Chulkin, A. Drygala, M. Libera, T. Tański, E. Schab-Balcerzak, *Materials* **2021**, *14*, 1633.
- [60] S. Chatterjee, W. A. Webre, S. Patra, B. Rout, G. A. Glass, F. D'Souza, S. Chatterjee, *J Alloys Compd* **2020**, *826*, 154188.
- [61] M. Shobana, P. Balraju, P. Senthil Kumar, N. Muthukumarasamy, R. Yuvakkumar, D. Velauthapillai, *Sustainable Energy Technologies and Assessments* **2022**, *52*, 102295.
- [62] L. Feng, J. Jia, Y. Fang, X. Zhou, Y. Lin, *Electrochim Acta* **2013**, *87*, 629.
- [63] J. Gu, J. Khan, Z. Chai, Y. Yuan, X. Yu, P. Liu, M. Wu, W. Mai, *J Power Sources* **2016**, *303*, 57.
- [64] W. Q. Wu, H. L. Feng, H. Y. Chen, D. Bin Kuang, C. Y. Su, *J Mater Chem A* **2017**, *5*, 12699.
- [65] Z. Zhao, G. Liu, B. Li, L. Guo, C. Fei, Y. Wang, L. Lv, X. Liu, J. Tian, G. Cao, *J Mater Chem A* **2015**, *3*, 11320.
- [66] L. Xu, C. Aumaitre, Y. Kervella, G. Lapertot, C. Rodríguez-Seco, E. Palomares, R. Demadrille, P. Reiss, *Adv Funct Mater* **2018**, *28*, 1706291.
- [67] J. A. Anta, E. Guillén, R. Tena-Zaera, *Journal of Physical Chemistry C* **2012**, *116*, 11413.
- [68] A. K. Chandiran, M. Abdi-Jalebi, M. K. Nazeeruddin, M. Grätzel, *ACS Nano* **2014**, *8*, 2261.
- [69] E. Guillén, L. M. Peter, J. A. Anta, *Journal of Physical Chemistry C* **2011**, *115*, 22622.
- [70] K. Keis, J. Lindgren, S. E. Lindquist, A. Hagfeldt, *Langmuir* **2000**, *16*, 4688.
- [71] L. Ke, S. Bin Dolmanan, L. Shen, P. K. Pallathadk, Z. Zhang, D. M. Ying Lai, H. Liu, *Solar Energy Materials and Solar Cells* **2010**, *94*, 323.
- [72] S. Ghosh, R. Sartape, J. Chakraborty, *Journal of Materials Science: Materials in Electronics* **2020**, *31*, 2202.

- [73] M. Biçer, M. Gökçen, E. Orhan, *Opt Mater* **2022**, *131*, 112691.
- [74] V. Kadam, C. Jagtap, T. Alshahrani, P. Lokhande, A. Al-Ahmed, S. P. Patole, F. Khan, H. Pathan, *Journal of Materials Science: Materials in Electronics* **2023**, *34*, 1.
- [75] A. H. Javed, N. Shahzad, M. A. Khan, M. Ayub, N. Iqbal, M. Hassan, N. Hussain, M. I. Rameel, M. I. Shahzad, *Solar Energy* **2021**, *230*, 492.
- [76] C. Y. Lin, Y. H. Lai, H. W. Chen, J. G. Chen, C. W. Kung, R. Vittal, K. C. Ho, *Energy Environ Sci* **2011**, *4*, 3448.
- [77] Y. He, J. Hu, Y. Xie, *Chemical Communications* **2015**, *51*, 16229.
- [78] F. Yuliasari, A. Aprilia, R. Hidayat, *Mater Today Proc* **2022**, *52*, 248.
- [79] R. Grover, N. Gupta, O. Nanda, K. Saxena, In *Advances in Solar Power Generation and Energy Harvesting*, Springer, Singapore, **2020**, 9–16.
- [80] A. K. Rajan, L. Cindrella, *Ceram Int* **2020**, *46*, 8174.
- [81] K. Wijeratne, J. Bandara, *Electrochim Acta* **2014**, *148*, 302.
- [82] R. Vittal, K. C. Ho, *Renewable and Sustainable Energy Reviews* **2017**, *70*, 920.
- [83] J. Fan, Y. Hao, A. Cabot, E. M. J. Johansson, G. Boschloo, A. Hagfeldt, *ACS Appl Mater Interfaces* **2013**, *5*, 1902.
- [84] D. Barpuzary, A. S. Patra, J. V. Vaghasiya, B. G. Solanki, S. S. Soni, M. Qureshi, *ACS Appl Mater Interfaces* **2014**, *6*, 12629.
- [85] W. Peng, L. Han, Z. Wang, *Chemistry – A European Journal* **2014**, *20*, 8483.
- [86] S. Yang, S. Sha, H. Lu, J. Wu, J. Ma, D. Wang, Z. Sheng, *Colloids Surf A Physicochem Eng Asp* **2020**, *594*, 124665.
- [87] P. Nandi, D. Das, *Solar Energy Materials and Solar Cells* **2022**, *243*, 111811.
- [88] R. L. Milot, G. F. Moore, R. H. Crabtree, G. W. Brudvig, C. A. Schmuttenmaer, *Journal of Physical Chemistry C* **2013**, *117*, 21662.
- [89] B. N. Dimarco, R. N. Sampaio, E. M. James, T. J. Barr, M. T. Bennett, G. J. Meyer, *ACS Appl Mater Interfaces* **2020**, *12*, 23923.
- [90] H. Cheema, J. H. Delcamp, *Chemistry – A European Journal* **2019**, *25*, 14205.
- [91] B. N. Nunes, L. A. Faustino, A. V. Muller, A. S. Polo, A. O. T. Patrocínio, In *Nanomaterials for Solar Cell Applications*, Elsevier, **2019**, pp. 287–322.
- [92] R. Panetta, A. Latini, I. Pettiti, C. Cavallo, *Mater Chem Phys* **2017**, *202*, 289.
- [93] A. Latini, R. Panetta, *Energies* **2018**, *11*, 975.
- [94] H. Zhang, Y. Wang, P. Liu, S. L. Chou, J. Z. Wang, H. Liu, G. Wang, H. Zhao, *ACS Nano* **2016**, *10*, 507.
- [95] W. Khan, S. B. Betzler, O. Šipr, J. Ciston, P. Blaha, C. Scheu, J. Minar, *Journal of Physical Chemistry C* **2016**, *120*, 23329.
- [96] M. M. Rashad, A. E. Shalan, *Appl Phys A Mater Sci Process* **2014**, *116*, 781.
- [97] S. S. Patil, R. M. Mane, K. V. Khot, S. S. Mali, C. Kook Hong, P. N. Bhosale, *Solar Energy* **2021**, *220*, 371.
- [98] K. Deevi, V. S. R. Imma Reddy, *Mater Lett* **2021**, *283*, 128848.

- [99] K. Al-Attafi, F. H. Jawdat, H. Qutaish, P. Hayes, A. Al-Keisy, K. Shim, Y. Yamauchi, S. X. Dou, A. Nattestad, J. H. Kim, *Nano Energy* **2019**, *57*, 202.
- [100] K. Pugazhendhi, V. B. Lenin, D. J. Sharmila, J. K. Agnes, B. Praveen, J. M. Shyla, *AIP Conf Proc* **2019**, *2115*.
- [101] S. Mahalingam, H. Abdullah, *Renewable and Sustainable Energy Reviews* **2016**, *63*, 245.
- [102] K. Aravinthkumar, I. John Peter, G. Anandha Babu, M. Navaneethan, S. Karazhanov, C. Raja Mohan, *Mater Lett* **2022**, *319*, 132284.
- [103] M. Younas, M. A. Gondal, M. A. Dastageer, K. Harrabi, *Solar Energy* **2019**, *188*, 1178.
- [104] M. Younas, M. A. Gondal, *Solar Energy* **2022**, *245*, 37.
- [105] A. S., N. Abraham, V. S. Babu, B. S., *ECS Journal of Solid State Science and Technology* **2022**, *11*, 061011.
- [106] S. Vijayanath, K. Janaki, R. Gopal, C. Ragupathi, B. Rangasamy, M. M. Alam, *Journal of Solid State Electrochemistry* **2023**, *27*, 183.
- [107] Y. Kusumawati, S. Koussi-Daoud, T. Pauporté, *J Photochem Photobiol A Chem* **2016**, *329*, 54.
- [108] S. A. Kazmi, S. Hameed, A. S. Ahmed, M. Arshad, A. Azam, *J Alloys Compd* **2017**, *691*, 659.
- [109] S. Mahalingam, F. W. Low, A. Omar, A. Manap, N. A. Rahim, C. H. Tan, H. Abdullah, C. H. Voon, M. Rokhmat, E. Wibowo, C. S. Oon, *Int J Energy Res* **2022**, *46*, 7082.
- [110] A. C. Celline, A. Y. Subagja, S. Suryaningsih, A. Aprilia, L. Safriani, *Materials Science Forum* **2021**, *1028*, 151.
- [111] R. Ramamoorthy, V. Eswaramoorthi, M. Sundararajan, M. Boobalan, A. D. Sivagami, R. V. Williams, *Journal of Materials Science: Materials in Electronics* **2019**, *30*, 12966.
- [112] S. Khan, S. A. Kazmi, A. J. Ansari, *IEEE International Students' Conference on Electrical, Electronics and Computer Science, SCEECS* **2022**.
- [113] B. Boro, B. Gogoi, B. M. Rajbongshi, A. Ramchiary, *Renewable and Sustainable Energy Reviews* **2018**, *81*, 2264.
- [114] A. G. Thate, K. S. Pakhare, S. S. Patil, V. M. Bhuse, *Research on Chemical Intermediates* **2023**, *49*, 147.
- [115] P. Arul, B. Balraj, C. Siva, C. Vivek, *Chemical Papers* **2023**, *77*, 7527.
- [116] M. Ismail, C. Olivier, T. Toupance, *Journal of Materials Science: Materials in Electronics* **2023**, *34*, 1.
- [117] S. Vibavakumar, K. D. Nisha, V. S. Manikandan, J. Archana, M. Navaneethan, S. Harish, *Opt Mater* **2023**, *140*, 113828.
- [118] Z. H. Bakr, Q. Wali, J. Ismail, N. K. Elumalai, A. Uddin, R. Jose, *Electrochim Acta* **2018**, *263*, 524.
- [119] M. Ashfaq, N. Talreja, N. Singh, D. Chauhan, *Electronics* **2023**, *12*, 570.
- [120] J. Xu, G. Wang, J. Fan, B. Liu, S. Cao, J. Yu, *Journal of Power Sources*. Elsevier January 15, **2015**, 77–84.
- [121] C. Wu, L. Qi, Y. Chen, Q. Ouyang, C. Li, *Research on Chemical Intermediates* **2016**, *42*, 5653.

- [122] D. O. Miles, C. S. Lee, P. J. Cameron, D. Mattia, J. H. Kim, *J Power Sources* **2016**, 325, 365.
- [123] L. Jiang, L. Sun, D. Yang, J. Zhang, Y. J. Li, K. Zou, W. Q. Deng, *ACS Appl Mater Interfaces* **2017**, 9, 9576.
- [124] C. Dall’Agnese, Y. Dall’Agnese, B. Anasori, W. Sugimoto, S. Mori, *New Journal of Chemistry* **2018**, 42, 16446.
- [125] X. Wang, Y. Xiang, B. Zhou, Y. Zhang, J. Wu, R. Hu, L. Liu, J. Song, J. Qu, *J Colloid Interface Sci* **2019**, 534, 1.
- [126] Y. Xu, X. Wang, M. Jin, G. Zhou, L. Shui, *J Mater Sci* **2020**, 55, 5499.
- [127] D. Krishnamoorthy, A. Prakasam, *Inorg Chem Commun* **2020**, 118, 108016.
- [128] H. Menon, G. Gopakumar, V. Sankaranarayanan Nair, S. V. Nair, M. Shanmugam, *ChemistrySelect* **2018**, 3, 5801.
- [129] D. Krishnamoorthy, A. Prakasam, *J Clust Sci* **2021**, 32, 621.
- [130] J. Yu, J. Fan, K. Lv, *Nanoscale* **2010**, 2, 2144.
- [131] J. Ferber, J. Luther, *Solar Energy Materials and Solar Cells* **1998**, 54, 265.
- [132] Q. Zhang, D. Myers, J. Lan, S. A. Jenekhe, G. Cao, *Physical Chemistry Chemical Physics* **2012**, 14, 14982.
- [133] J. Yu, Q. Li, Z. Shu, *Electrochim Acta* **2011**, 56, 6293.
- [134] M. J. Jeng, Y. L. Wung, L. B. Chang, L. Chow, *International Journal of Photoenergy* **2013**, 2013.
- [135] M. Balu, K. G. Baiju, M. R. Subramaniam, D. Kumaresan, *Electrochim Acta* **2019**, 319, 339.
- [136] T. G. Deepak, G. S. Anjusree, S. Thomas, T. A. Arun, S. V. Nair, A. Sreekumaran Nair, *RSC Adv* **2014**, 4, 17615.
- [137] Y. P. Que, J. Weng, L. H. Hu, J. H. Wu, S. Y. Dai, *J Power Sources* **2016**, 307, 138.
- [138] W. Lekphet, T. C. Ke, C. Su, S. Kathirvel, P. Sireesha, S. B. Akula, W. R. Li, *Appl Surf Sci* **2016**, 382, 15.
- [139] Z. Q. Li, L. E. Mo, W. C. Chen, X. Q. Shi, N. Wang, L. H. Hu, T. Hayat, A. Alsaedi, S. Y. Dai, *ACS Appl Mater Interfaces* **2017**, 9, 32026.
- [140] Y. Feng, J. Zhu, J. Jiang, W. Wang, G. Meng, F. Wu, Y. Gao, X. Huang, *RSC Adv* **2014**, 4, 12944.
- [141] G. Wang, W. Xiao, J. Yu, *Energy* **2015**, 86, 196.
- [142] Z. A. Garmaroudi, M. R. Mohammadi, *J Solgel Sci Technol* **2015**, 76, 666.
- [143] D. Guo, S. Xiao, K. Fan, J. Yu, *ACS Sustain Chem Eng* **2017**, 5, 1315.
- [144] X. D. Gao, X. M. Li, X. Y. Gan, Y. Q. Wu, R. K. Zheng, C. L. Wang, Z. Y. Gu, P. He, *J Mater Chem* **2012**, 22, 18930.
- [145] S. Son, S. H. Hwang, C. Kim, J. Y. Yun, J. Jang, *ACS Appl Mater Interfaces* **2013**, 5, 4815.
- [146] S. Hore, P. Nitz, C. Vetter, C. Prahl, M. Niggemann, R. Kern, *Chemical Communications* **2005**, 2011.

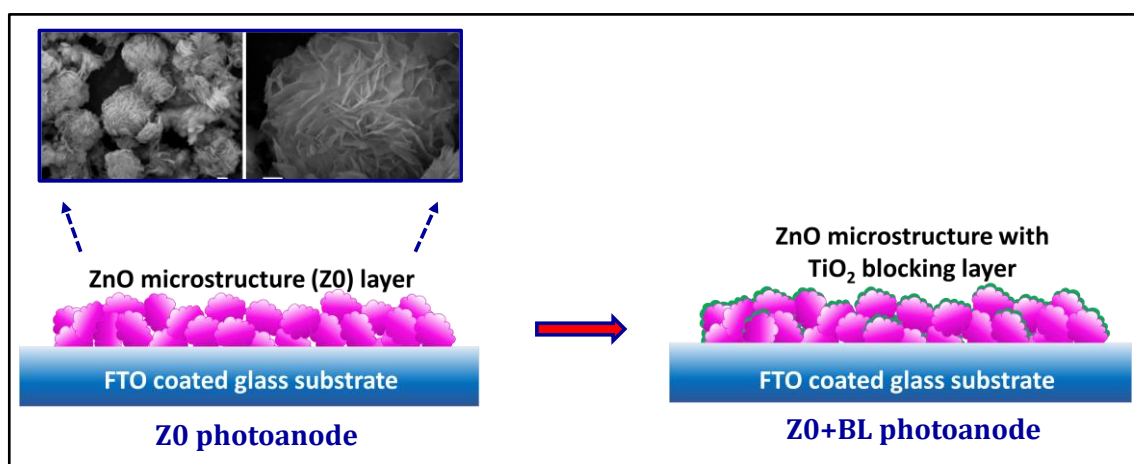
- [147] J. W. Lee, J. H. Moon, *Nanoscale* **2015**, 7, 5164.
- [148] G. Yang, J. Zhang, P. Wang, Q. Sun, J. Zheng, Y. Zhu, *Current Applied Physics* **2011**, 11, 376.
- [149] S. H. Han, S. Lee, H. Shin, H. S. Jung, *Adv Energy Mater* **2011**, 1, 546.
- [150] T. T. T. Pham, N. Mathews, Y. M. Lam, S. Mhaisalkar, *J Electron Mater* **2017**, 46, 3801.
- [151] T. T. T. Pham, N. Mathews, Y. M. Lam, S. Mhaisalkar, *Physica B Condens Matter* **2018**, 532, 225.
- [152] S. Sasidharan, S. C. Pradhan, A. Jagadeesh, B. N. Nair, A. A. P. Mohamed, N. U. Narayanan, S. Soman, U. N. S. Hareesh, *ACS Appl Energy Mater* **2020**, 3, 12584.
- [153] S. Sasidharan, A. Jagadeesh, S. C. Pradhan, B. N. Nair, A. Azeez Peer Mohamed, K. N. Narayanan Unni, S. Soman, U. Nair Saraswathy Hareesh, *Solar Energy* **2021**, 226, 214.
- [154] P. Mulvaney, *Langmuir* **1996**, 12, 788.
- [155] N. C. Jeong, C. Prasittichai, J. T. Hupp, *Langmuir* **2011**, 27, 14609.
- [156] N. Yang, In *The Preparation of Nano Composites and Their Applications in Solar Energy Conversion*, Springer, Berlin, Heidelberg, **2017**, pp. 81–91.
- [157] P. Nbelayim, G. Kawamura, W. Kian Tan, H. Muto, A. Matsuda, *Scientific Reports* **2017**, 7, 1.
- [158] S. P. Lim, A. Pandikumar, N. M. Huang, H. N. Lim, *RSC Adv* **2014**, 4, 38111.
- [159] Q. Liu, Y. Wei, M. Z. Shahid, M. Yao, B. Xu, G. Liu, K. Jiang, C. Li, *J Power Sources* **2018**, 380, 142.
- [160] H. Dong, Z. Wu, A. El-Shafei, B. Xia, J. Xi, S. Ning, B. Jiao, X. Hou, *J Mater Chem A* **2015**, 3, 4659.
- [161] S. P. Lim, Y. S. Lim, A. Pandikumar, H. N. Lim, Y. H. Ng, R. Ramaraj, D. C. S. Bien, O. K. Abou-Zied, N. M. Huang, *Physical Chemistry Chemical Physics* **2017**, 19, 1395.
- [162] M. S. Wu, R. S. Yang, *J Alloys Compd* **2018**, 740, 695.
- [163] S. Suresh, G. E. Unni, M. Satyanarayana, A. S. Nair, V. P. M. Pillai, *Dalton Transactions* **2018**, 47, 4685.
- [164] S. B. Wategaonkar, V. G. Parale, R. P. Pawar, S. S. Mali, C. K. Hong, R. R. Powar, A. V. Moholkar, H. H. Park, B. M. Sargar, R. K. Mane, *Ceram Int* **2021**, 47, 25580.
- [165] D. Dahlan, M. I. A. Umar, S. N. Sadikin, J. Ridwan, A. A. Umar, *Opt Mater* **2022**, 133, 112976.
- [166] A. Atilgan, A. Yildiz, *Int J Energy Res* **2022**, 46, 14558.
- [167] N. Kanjana, W. Maiaugree, P. Poolcharuansin, P. Laokul, *Materials Science and Engineering: B* **2021**, 271, 115311.
- [168] H. Esgin, Y. Caglar, M. Caglar, *J Alloys Compd* **2022**, 890, 161848.
- [169] F. Khojasteh, M. R. Mersagh, H. Hashemipour, *J Alloys Compd* **2022**, 890, 161709.
- [170] V. A. Tran, T. T. Truong, T. A. P. Phan, T. N. Nguyen, T. Van Huynh, A. Agresti, S. Pescetelli, T. K. Le, A. Di Carlo, T. Lund, S. N. Le, P. T. Nguyen, *Appl Surf Sci* **2017**, 399, 515.

- [171] W. Y. Rho, H. S. Kim, H. M. Kim, J. S. Suh, B. H. Jun, *New Journal of Chemistry* **2016**, *41*, 285.
- [172] E. Gurgur, S. S. Oluyamo, A. O. Adetuyi, O. I. Omotunde, A. E. Okoronkwo, M. G. Famogun, *Bulletin of Materials Science* **2022**, *45*, 1.
- [173] L. O. A. Salim, M. Z. Muzakkar, A. Zaeni, M. Maulidiyah, M. Nurdin, S. N. Sadikin, J. Ridwan, A. A. Umar, *Journal of Physics and Chemistry of Solids* **2023**, *175*, 111224.
- [174] T. Raguram, K. S. Rajni, *Mater Today Proc* **2020**, *33*, 2110.
- [175] I. P. Liu, W. H. Lin, C. M. Tseng-Shan, Y. L. Lee, *ACS Appl Mater Interfaces* **2018**, *10*, 38900.
- [176] Y.-C. Chen, Y.-C. Chang, C.-M. Chen, *J Electrochem Soc* **2018**, *165*, F409.
- [177] H. Choi, C. Nahm, J. Kim, J. Moon, S. Nam, D. R. Jung, B. Park, *Current Applied Physics* **2012**, *12*, 737.
- [178] J. H. Yang, C. W. Bark, K. H. Kim, H. W. Choi, *Materials* **2014**, *7*, 3522.
- [179] K. Fan, J. Yu, W. Ho, *Mater Horiz* **2017**, *4*, 319.
- [180] A. K. Chandiran, N. Tetreault, R. Humphry-Baker, F. Kessler, E. Baranoff, C. Yi, M. K. Nazeeruddin, M. Grätzel, *Nano Lett* **2012**, *12*, 3941.
- [181] G. K. L. Goh, H. Q. Le, T. J. Huang, B. T. T. Hui, *J Solid State Chem* **2014**, *214*, 17.
- [182] G. Shang, J. Wu, S. Tang, L. Liu, X. Zhang, *Journal of Physical Chemistry C* **2013**, *117*, 4345.
- [183] W. Song, Y. Gong, J. Tian, G. Cao, H. Zhao, C. Sun, *ACS Appl Mater Interfaces* **2016**, *8*, 13418.
- [184] P. M. Sommeling, B. C. O'Regan, R. R. Haswell, H. J. P. Smit, N. J. Bakker, J. J. T. Smits, J. M. Kroon, J. A. M. Van Roosmalen, *Journal of Physical Chemistry B* **2006**, *110*, 19191.
- [185] B. C. O'Regan, J. R. Durrant, P. M. Sommeling, N. J. Bakker, *Journal of Physical Chemistry C* **2007**, *111*, 14001.
- [186] I. P. Liu, W. H. Lin, C. M. Tseng-Shan, Y. L. Lee, *ACS Appl Mater Interfaces* **2018**, *10*, 38900.
- [187] S. C. Pradhan, J. Velore, S. M. Meethal, S. Soman, *Energies* **2023**, *16*, 6913.
- [188] E. Tanaka, H. Michaels, M. Freitag, N. Robertson, *J Mater Chem A* **2020**, *8*, 1279.
- [189] J. M. Ji, H. Zhou, Y. K. Eom, C. H. Kim, H. K. Kim, *Adv Energy Mater* **2020**, *10*, 2000124.
- [190] Y. Cao, Y. Liu, S. M. Zakeeruddin, A. Hagfeldt, M. Grätzel, *Joule* **2018**, *2*, 1108.
- [191] D. Zhang, M. Stojanovic, Y. Ren, Y. Cao, F. T. Eickemeyer, E. Socie, N. Vlachopoulos, J. E. Moser, S. M. Zakeeruddin, A. Hagfeldt, M. Grätzel, *Nat Commun* **2021**, *12*, 1.
- [192] K. Hara, Y. Dan-Oh, C. Kasada, Y. Ohga, A. Shinpo, S. Suga, K. Sayama, H. Arakawa, *Langmuir* **2004**, *20*, 4205.
- [193] S. Zhang, X. Yang, C. Qin, Y. Numata, L. Han, *J Mater Chem A* **2014**, *2*, 5167.
- [194] H. Shen, H. Lin, Y. Liu, X. Li, J. Zhang, N. Wang, J. Li, *Electrochim Acta* **2011**, *56*, 2092.
- [195] V. S. Manthou, E. K. Pefkianakis, P. Falaras, G. C. Vougioukalakis, *ChemSusChem* **2015**, *8*, 588.

- [196] Y. G. Lee, S. Park, W. Cho, T. Son, P. Sudhagar, J. H. Jung, S. Wooh, K. Char, Y. S. Kang, *Journal of Physical Chemistry C* **2012**, *116*, 6770.
- [197] S. Venkatesan, W. H. Lin, T. H. Hsu, H. Teng, Y. L. Lee, *ACS Sustain Chem Eng* **2022**, *10*, 2473.
- [198] C. Hora, F. Santos, M. G. F. Sales, D. Ivanou, A. M. Mendes, *ACS Appl Energy Mater* **2022**, *2022*, 14846.
- [199] F. Santos, C. Hora, D. Ivanou, A. M. Mendes, *ACS Appl Energy Mater* **2021**, *4*, 5050.
- [200] I. P. Liu, W. H. Lin, C. M. Tseng-Shan, Y. L. Lee, *ACS Appl Mater Interfaces* **2018**, *10*, 38900.
- [201] S. C. Pradhan, A. Hagfeldt, S. Soman, *J Mater Chem A* **2018**, *6*, 22204.
- [202] S. Hattori, Y. Wada, S. Yanagida, S. Fukuzumi, *J Am Chem Soc* **2005**, *127*, 9648.
- [203] Y. Bai, Q. Yu, N. Cai, Y. Wang, M. Zhang, P. Wang, *Chemical Communications* **2011**, *47*, 4376.
- [204] Y. Saygili, M. Söderberg, N. Pellet, F. Giordano, Y. Cao, A. B. Munoz-García, S. M. Zakeeruddin, N. Vlachopoulos, M. Pavone, G. Boschloo, L. Kavan, J. E. Moser, M. Grätzel, A. Hagfeldt, M. Freitag, *J Am Chem Soc* **2016**, *138*, 15087.
- [205] T. Higashino, H. Imahori, *ACS Energy Lett* **2022**, *7*, 1926.
- [206] A. Grobelny, Z. Shen, F. T. Eickemeyer, N. F. Antariksa, S. Zapotoczny, S. M. Zakeeruddin, M. Grätzel, A. Grobelny, Z. Shen, F. T. Eickemeyer, N. F. Antariksa, S. M. Zakeeruddin, M. Grätzel, S. Zapotoczny, *Advanced Materials* **2023**, *35*, 2207785.
- [207] Y. Liu, Y. Cao, W. Zhang, M. Stojanovic, M. I. Dar, P. Péchy, Y. Saygili, A. Hagfeldt, S. M. Zakeeruddin, M. Grätzel, *Angewandte Chemie* **2018**, *130*, 14321.
- [208] M. Freitag, Q. Daniel, M. Pazoki, K. Sveinbjörnsson, J. Zhang, L. Sun, A. Hagfeldt, G. Boschloo, *Energy Environ Sci* **2015**, *8*, 2634.
- [209] M. Freitag, F. Giordano, W. Yang, M. Pazoki, Y. Hao, B. Zietz, M. Grätzel, A. Hagfeldt, G. Boschloo, *Journal of Physical Chemistry C* **2016**, *120*, 9595.
- [210] A. Jagadeesh, G. Veerappan, P. S. Devi, K. N. N. Unni, S. Soman, *J Mater Chem A* **2023**, *11*, 14748.
- [211] A. Glinka, J. Kubicki, M. Ziółek, *Energies* **2021**, *14*, 407.
- [212] J. Li, X. Yang, Z. Yu, G. G. Gurzadyan, M. Cheng, F. Zhang, J. Cong, W. Wang, H. Wang, X. Li, L. Kloo, M. Wang, L. Sun, *RSC Adv* **2017**, *7*, 4611.
- [213] H. Jiang, Y. Ren, W. Zhang, Y. Wu, E. C. Socie, B. I. Carlsen, J.-E. Moser, H. Tian, S. M. Zakeeruddin, W.-H. Zhu, M. Grätzel, *Angewandte Chemie* **2020**, *132*, 9410.
- [214] H. Wu, G. Wang, B. X. Lei, *ACS Appl Energy Mater* **2022**, *5*, 9962.
- [215] A. Survila, *Electrochemistry of Metal Complexes* **2015**, 33.
- [216] J. Velore, S. Chandra Pradhan, T. W. Hamann, A. Hagfeldt, K. N. N. Unni, S. Soman, *ACS Appl Energy Mater* **2022**, *5*, 2647.
- [217] Y. Ren, D. Zhang, J. Suo, Y. Cao, F. T. Eickemeyer, N. Vlachopoulos, S. M. Zakeeruddin, A. Hagfeldt, M. Grätzel, *Nature* **2022**, *613*, 60.
- [218] A. Zaban, M. Greenshtein, J. Bisquert, de Wild, S. Berner, H. Suzuki, H. Yanagi, D. Schlettwein, S. Ivan, H. Guentherodt, T. A. Jung, J. V Barth, J. Weckesser, C. Cai, O.

- Jeandupeux, K. Kern, A. De Vita, P. Rev Lett, P. Wu, Q. D. Zeng, S. D. Xu, C. Wang, S. X. Yin, C. L. Bai, H. B. Yu, C. S. Jiang, P. Ebert, X. D. Wang, J. M. White, Q. Niu, Z. Zhang, X. H. Qiu, B. Xu, H. N. Wang, C. J. Li, S. L. Xu, Y. H. Qiao, L. J. Wan, A. Zaban, M. Greenshtein, J. Bisquert, *ChemPhysChem* **2003**, *4*, 859.
- [219] P. R. F. Barnes, K. Miettunen, X. Li, A. Y. Anderson, T. Bessho, M. Gratzel, B. C. O'regan, P. R. F. Barne, K. Miettunen, X. Li, A. Y. Anderson, B. C. O'regan, T. Bessho, M. Gratzel, *Advanced Materials* **2013**, *25*, 1881.
- [220] X. Wang, S. Karanjit, L. Zhang, H. Fong, Q. Qiao, Z. Zhu, *Appl Phys Lett* **2011**, *98*.
- [221] H. S. Kim, S. B. Ko, I. H. Jang, N. G. Park, *Chemical Communications* **2011**, *47*, 12637.
- [222] M. Adachi, M. Sakamoto, J. Jiu, Y. Ogata, S. Isoda, *Journal of Physical Chemistry B* **2006**, *110*, 13872.
- [223] F. Fabregat-Santiago, J. Bisquert, E. Palomares, L. Otero, D. Kuang, S. M. Zakeeruddin, M. Grätzel, *Journal of Physical Chemistry C* **2007**, *111*, 6550.
- [224] L. M. Peter, *RSC Energy and Environment Series* **2016**, *2016 January*, 3.
- [225] K. Gelderman, L. Lee, S. W. Donne, *J Chem Educ* **2007**, *84*, 685.
- [226] W. J. Albery, G. J. O'Shea, A. L. Smith, *Journal of the Chemical Society, Faraday Transactions* **1996**, *92*, 4083.

ZnO microstructures as photoanode materials in copper electrolyte based dye-sensitized photovoltaic cells



Abstract: *TiO₂ has been extensively explored as the photoanode material for dye-sensitized photovoltaic cells (DSCs), because of its favourable energy band structure and electron transfer properties. Till date, majority of the reports showcasing exceptional DSC performances use standard TiO₂ photoanodes. Owing to its abundance, ease of synthesis with wide variety of morphologies available, better electron mobility compared to TiO₂, as well as similar energy levels and charge transfer kinetics as of TiO₂, ZnO is considered as one of the most suitable alternative materials to replace TiO₂ in conventional DSC photoelectrodes. In the present chapter, we synthesized hierarchical microspheres made up of ZnO nanoflake aggregates, using a simple wet chemical synthesis method. A mesoporous layer of the ZnO microspheres sensitized with an organic dye (Y123) was utilized as the DSC photoanode along with two different electrolytes, viz. conventional iodine based and new generation copper complex based electrolytes. Detailed investigation of the various interfacial charge transfer processes in these devices were carried out. Further, the effect of introducing a TiO₂ post blocking layer over the mesoporous ZnO layer, on the DSC performance under outdoor as well as indoor light illumination, was investigated.*

2A.1. Introduction

Photoanode or working electrode is a critical component in DSCs, as majority of the performance determining processes such as generation of photoelectrons by dye excitation, charge separation, electron diffusion, recombination and dye regeneration occurs at the photoanode. Typically, DSC photoanodes are made up of a mesoporous layer of semiconducting metal oxide sensitized with one or more dye molecules coated over a transparent conductive oxide (TCO) substrate.^[1-3] The TCO substrate is often deposited with a pre-blocking layer of semiconducting oxide, to enhance the adhesion of the mesoporous layer and to prevent the electron back transfer from the TCO.^[4-8] Deposition of a post blocking layer by surface treatment of the mesoporous photoanode layer is another method for suppressing the charge recombination at the photoanode and to enhance the adsorption of dye molecules on the semiconductor surface.^[9-13] Titania (TiO_2) has been recognized as the most suitable candidate to be used as DSC photoanode material.^[14,15] Till date, majority of the outstanding performance reported in DSCs employ standard TiO_2 photoanode, constituted by an active layer of nano-sized TiO_2 particles (20-30 nm) and an additional scattering over layer made up of larger sized TiO_2 nanoparticles (200-400 nm).^[16-23] The highest power conversion efficiency (*PCE*) reported in DSC under standard AM 1.5G simulated solar irradiation (15.2%) and 1000 lux fluorescent light illumination (35.6%), were both accomplished using the standard TiO_2 photoanode, co-sensitized with various organic dyes having complementary absorption and by using copper based redox electrolyte.^[24,25]

Besides TiO_2 , several other metal oxide semiconductors like ZnO , SnO_2 , Nb_2O_5 , WO_3 , In_2O_3 , etc. were also explored as DSC photoanode materials, to have a better understanding on the electron transport, charge recombination and charge collection mechanisms.^[26] Zinc oxide (ZnO) is the most prominent candidate among them, owing to its similarities with TiO_2 , such as energy band structure, charge transfer, trap state distribution, etc.^[27] Moreover, ZnO possess some advantages over TiO_2 , such as ease of synthesizing various morphologies, higher electron mobility, etc.^[28-30] Consequently, ZnO has been utilized in the form of mesoporous semiconducting layer as well as blocking layer in DSC photoanodes.^[31-35] Despite its favourable properties, the performance of ZnO based DSCs are considerably lower when compared to that of TiO_2 based devices. The possible reason for this reduced *PCE* of ZnO based DSCs are poor dye adsorption on ZnO surface, faster dye degradation and desorption from the ZnO surface, lower chemical

stability of ZnO under electrolyte environment, and lower dielectric constant of ZnO which hinders the charge separation and higher recombination kinetics when compared to TiO₂.^{[36][37]} The poor electrochemical stability of ZnO not only affects the photovoltaic (PV) performance but also the long-term stability of ZnO based DSCs. When the ZnO based photoanode is soaked in dye solution, which is acidic in nature, the ZnO dissociates into Zn²⁺ ions, which forms aggregates with the dye molecules and get deposited on the ZnO surface.^[38] This inhibits the injection process even when the dye loading on the ZnO surface seems to increase due to dye aggregation.^[28] Another stability limiting mechanism in ZnO based DSC is the photodegradation of ZnO in the presence of electrolyte solution.^[39] This causes desorption of dye molecules from the ZnO surface, in addition to formation of surface defects on them. These degradation processes affect the short circuit current density (J_{SC}) of the device, thereby reducing the overall *PCE*. Some of the efficient methods to suppress these associated bottlenecks of ZnO based DSCs include reduction of dye soaking time and usage of blocking layers.^[28,40] By utilizing suitable dye-electrolyte combinations and by employing interfacial treatments to retard the unwanted back electron transfer processes, further enhancement in PV performance of ZnO based DSCs can be achieved. Consequently, a wide variety of ZnO nanostructures and microstructures prepared via facile hydrothermal synthesis techniques have been studied for improving the performance of DSCs.^[41–44] He *et. al.* reported a remarkable *PCE* of 8.03% under one sun condition using ZnO nanoparticles based DSCs employing iodide/triiodide electrolyte.^[45] However, there is only one report showing the compatibility of ZnO based DSC photoanode with copper electrolyte, to the best of our knowledge.^[46] In the present chapter, we synthesized ZnO microstructures using a simple wet chemical method and utilized them as photoanode material in DSCs along with different electrolyte systems, *viz.* conventional iodide/triiodide (I⁻/I₃⁻) electrolyte and bis(2,9-dimethyl-1,10-phenanthroline copper(II/I)bis(trifluoromethanesulfonyl)imide ([Cu(dmp)₂]^{2+/+}) electrolyte. The effect of TiO₂ post blocking layer on the performance of copper electrolyte based ZnO DSCs were also investigated in detail which was an effective method to improve both the performance and stability of ZnO based DSCs.

2A.2. Experimental procedures

2A.2.1. Material synthesis and characterization

The ZnO hierarchical microstructure was synthesized using a simple wet chemical method (**Figure 2A.1**) described elsewhere.^[47] This method involves the synthesis of zinc

carbonate hydroxide or hydrozincite (HZC) using zinc nitrate hexahydrate (ZN, Merck) as the precursor and urea (Merck) as the precipitant. In a typical synthesis, a 0.02 M aqueous solution of zinc nitrate hexahydrate was added drop by drop to a beaker containing 1.0 M aqueous solution of urea under continuous stirring at 500 rpm. The reaction mixture in the beaker was then continuously stirred at 1000 rpm for one hour at room temperature. The beaker was then transferred to a furnace and heated at 90 °C for 24 hours. After 24 hours of heating, the beaker was cooled down to room temperature and the white precipitate (HZC formed during the reaction) which was settled at the bottom and walls of the beaker were filtered and transferred to a centrifuge tube. The precipitates were then centrifuged and washed with DI water and ethanol, and dried at 60 °C for 12 hours in a vacuum oven. The as-synthesized sample (HZC) was utilized for DSC photoanode fabrication, during which it is annealed at 500 °C to obtain the ZnO microstructures.

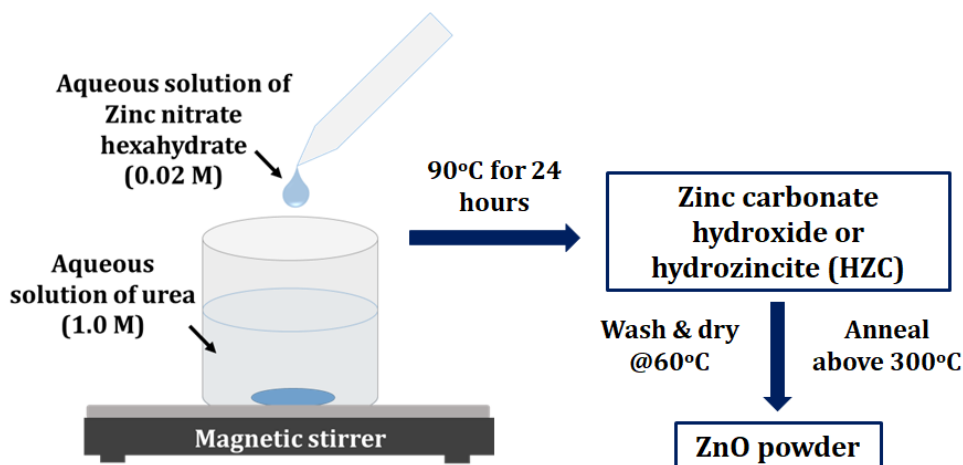


Figure 2A.1. Schematic illustration of the wet chemical synthesis of ZnO microstructure.

The crystallinity and phase of the as-synthesized (HZC) as well as the annealed (ZnO) samples were characterized using the X-ray diffraction patterns recorded by a Malvern PANalytical B.V. X-ray diffractometer in the 2θ range 20° to 80° with a slow scan mode. The specific surface area of as-synthesized and the annealed samples were estimated from the Brunauer-Emmett-Teller (BET) model, using the standard N_2 adsorption-desorption technique (using Tristar II, Micrometrics surface area analyser) after degassing at 200°C for 2h. The morphological features and particle size of the annealed sample was analysed using the micrographs obtained from Scanning Electron Microscope (SEM), Zeiss EVO 18 cryo-SEM Special Ed, at an acceleration voltage of 15.0 kV. The crystallite size and orientation of the annealed samples were also studied using High-Resolution Transmission Electron Micrograph (HR-TEM) and the corresponding selected area

electron diffraction (SAED) patterns acquired using JEOL JEM F 200 EELS STEM and EDS. ImageJ software was used for analyzing the micrographs acquired using the SEM and TEM. The Infrared (IR) spectroscopy studies of the annealed sample coated on a glass substrate was done using PerkinElmer UATR Two instrument over the range 500-2000 cm^{-1} . The diffuse reflectance spectra (DRS) of annealed sample coated on a glass substrate was acquired using Shimadzu UV-vis spectrophotometer (UV-2700i).

2A.2.2. Photoanode preparation and characterization

Photoanodes for DSCs were prepared by following the steps described in **section 1.8.1** of **Chapter 1**. The TEC 10 FTO glass substrate (Merck) was cut into small square pieces of dimension 1.6 cm x 1.6 cm and cleaned systematically using soap solution (for 30 minutes), de-ionized water (for 30 minutes), isopropanol (for 15 minutes) and acetone (for 15 minutes) in an ultrasonic bath, followed by stepwise annealing up to 500 °C. The cleaned substrates were undergone UV/ozone treatment (for 15 minutes) and TiCl_4 treatment as detailed in **section 1.8.1**, using a 50 mM aqueous solution of TiCl_4 , followed by stepwise annealing up to 500 °C. For preparing the paste for depositing the active layer, a 1:6 (wt%) mixture of ethyl cellulose (Sigma Aldrich) and α -terpineol (Sigma Aldrich) was heated at 100 °C for 10 minutes, till the ethyl cellulose completely dissolves and blends with the terpineol. The above mixture was then added to the as-synthesized HZC powder

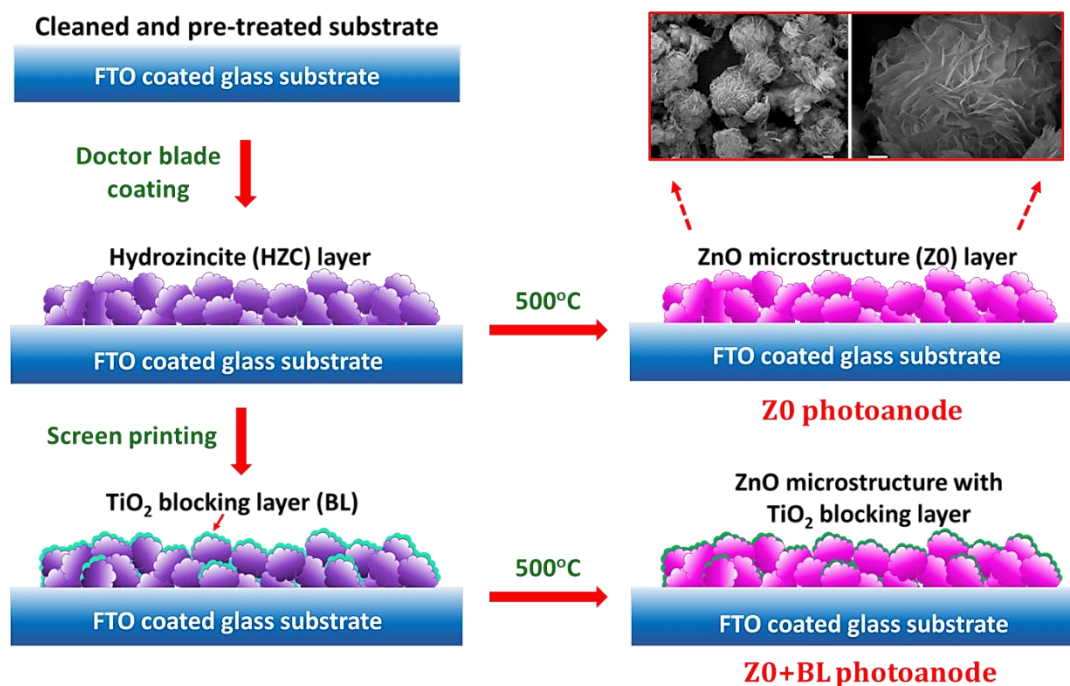


Figure 2A.2. Schematic representation of the preparation of ZnO photoanodes, namely Z0 and Z0+BL.

sample (30 wt%) and grounded well in a mortar for 10-20 minutes to obtain a uniform paste. The paste was coated over the pre-treated FTO substrate via blade coating, followed by systematic programmed annealing up to 500 °C, which results in ZnO based photoanode (**Figure 2A.2**). To fabricate the ZnO based photoanodes with blocking layer, the commercial TiO₂ blocking layer solution (Dyesol) was applied over the ZnO layer via screen printing, followed by the annealing process.

The crystallographic studies of unsensitized ZnO photoanodes were done by observing the XRD patterns acquired by a Malvern PANalytical B.V. X-ray diffractometer, in the 2θ range 20° to 70°. The surface morphology, thickness and elemental composition of ZnO photoanodes (with and without blocking layer) were analyzed using SEM and Energy dispersive X-ray (EDX) (Zeiss EVO 18 cryo-SEM Special Ed, Carl Zeiss, Germany). The unsensitized ZnO based photoanodes, with and without blocking layer, were further characterized using X-ray Photoelectron Spectroscopy (XPS, SPECS Surface Nano Analysis GmbH, Germany). XPS spectra was recorded using SpecsLab2 software, with a monochromatic Al source, Al-Kα (at 1486.7 eV and 350 W), with a beam diameter of 1 mm. The obtained XPS peaks corresponding to the energy states of various elements were fitted using the MultiPak spectrum software. The photoluminescence of the ZnO layer with and without TiO₂ blocking layer were obtained using a SPEX Fluorolog spectrofluorometer coupled with a calibrated integrating sphere. The dye loading studies of the ZnO photoanodes were performed as described below. A 0.01 mM stock solution of the Y123 dye was prepared in a 1:1 mixture of acetonitrile and tert-butanol. The stock solution of dye was divided into two equal portions, say D1 and D2. The ZnO photoanode was immersed in D2 and kept in dark for about 16 hrs, after which the solution D2 was retrieved. The photoanode was washed with 1 mL of acetonitrile to desorb the weakly bonded dye molecules, which was also added to D2. The same amount of acetonitrile (1 mL) was added to D1 also. Then, the solution state absorption spectra of D1 and D2 were acquired using the UV-Visible spectrophotometer (Shimadzu model 2100). The maximum absorbance for D1 and D2 were recorded as abs_1 and abs_2 , respectively. The amount of dye adsorbed per unit area, D (mol/cm²) of the ZnO active layer was calculated as,

$$D = ((abs_1 - abs_2)V)/\epsilon sl \quad (2A.1)$$

where V is the volume of the solution, ϵ is the molar extinction coefficient of the dye, s is the geometrical active area of ZnO photoanode, and l is the path length of the incident light in the solution, which is equal to the width of the quartz cuvette used.

2A.2.3. DSC fabrication and characterization

DSCs were fabricated as detailed in **section 1.8.1** of **Chapter 1**. The prepared photoanodes (as described in **section 2A.2.2**) were dye-sensitized by soaking them in 0.1mM solution of Y123 dye (using 1:1 mixture of acetonitrile and tert-butanol as solvent) for 16 hours. The counter electrode was (CE) was prepared by electro-polymerization of ethylene dioxythiophene (EDOT, Merck), along with the surfactant sodium dodecyl sulphate (SDS, Sigma Aldrich), on cleaned FTO plates (TEC7, GreatcellSolar, Australia) to obtain a conducting polymer *viz.* poly(3,4-ethylenedioxythiophene) (PEDOT). Prior to PEDOT deposition, the TEC7 FTO substrates (cut into 1.6 cm x 1.6 cm sizes) were drilled with two holes and were undergone ultrasonic cleaning using soap solution, de-ionized water and ethanol (45 minutes each), followed by step-wise programmed annealing up to 500 °C. Subsequently, the photoanode and the CE were joined together using a 25 µm thick thermoplastic spacer (Surlyn, GreatcellSolar, Australia) by hot pressing at 120 °C and the inter-electrode spacing was filled with the electrolyte solution through the holes in the CE, which were then sealed to prevent solvent evaporation and leakage. In the case of copper electrolyte based DSCs, the electrolyte was prepared by dissolving bis(2,9-dimethyl-1,10-phenanthroline copper(I) bis(trifluoromethanesulfonyl) imide (0.2 M of $[\text{Cu}(\text{dmp})_2]^{1+}$) and bis(2,9-dimethyl-1,10-phenanthroline copper(II) bis(trifluoromethanesulfonyl)imide chloride (0.04 M of $[\text{Cu}(\text{dmp})_2]^{2+}$) (both purchased from Dyenamo A.B., Sweden), in acetonitrile solvent (Merck) along with 0.1 M bis(trifluoro methane)sulfonimide lithium salt (LiTFSI) and 0.6 M 4-tert-butylpyridine (TBP) (Merck). Whereas, in the case of iodine electrolyte based devices, the commercial high performing electrolyte (HPE, GreatcellSolar, Australia) was utilized.

The fabricated DSCs were undergone various characterizations under ambient conditions (25 °C and 50% humidity). The basic current density *vs.* voltage (J - V) characteristics were obtained using a Keithley source meter or by using a Dyenamo AE05 potentiostat. The J - V curves under one sun condition as well as under various indoor light illuminations were acquired. The standard one sun condition (100 mWcm^{-2} , AM 1.5G) was simulated using a class AAA solar simulator (Oriel Sol3A, Model PVIV-94043A, Newport), whose light intensity was calibrated using a certified reference silicon solar cell coupled with a power meter. J - V characterizations under indoor light conditions were carried out inside a custom-made indoor light measurement setup using a compact fluorescent lamp, CFL (Osram, 14W/2700K) and light emitting diode, LED (Osram,

4W/6500K) as light sources. The irradiance intensity of these indoor light sources was calibrated using a highly sensitive photodetector coupled with a UV-Vis-NIR spectrometer (Ocean optics, DH-2000-BAL). A 250 W Xenon lamp coupled with a monochromator was used to carry out the incident photon-to-current conversion efficiency (*IPCE*) measurement of the DSCs. The advanced characterizations such as Open Circuit Voltage Decay (OCVD), Charge Extraction (CE), Electrochemical Impedance Spectroscopy (EIS), Intensity Modulated Photovoltage Spectroscopy (IMVS) and Intensity Modulated Photocurrent Spectroscopy (IMPS) were performed using the electrochemical workstation (Autolab-PGSTAT 302 N, Metrohm) attached to the electrical and light perturbation units. The OCVD and CE measurements were done using the Autolab work station coupled with LED driver and a white LED as the source of illumination. EIS was carried out under dark, by providing a bias voltage in the range 0.74 V- 0.84 V, using the PGSTAT 302N coupled with the frequency response analyzer (FRA). The electric perturbation of amplitude ~10 mV and frequency ranging from 100mHz to 100kHz was superimposed on the bias potential, and the corresponding current response was recorded. In a similar fashion, IMVS and IMPS was performed using the PGSTAT 302N in FRA mode, along with the LED driver and the white LED source. A light perturbation of small amplitude (< 10% of the steady state illumination) and frequency ranging from 0.1 Hz to 10 kHz was applied and the corresponding response was recorded.

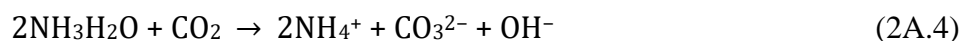
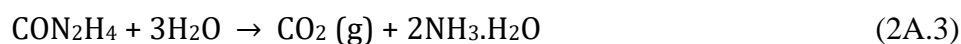
2A.3. Results and discussions

2A.3.1. Effect of redox mediator on the performance of ZnO based DSCs

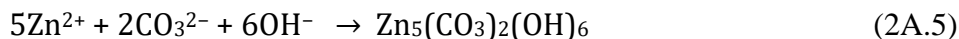
(a) Synthesis and characterization of ZnO hierarchical microstructures. The synthesis of hierarchical microstructures of zinc hydrozincite (HZC) was carried out by the reaction between zinc nitrate hexahydrate (ZN) and urea.^[48] A schematic diagram illustrating the various synthesis stages are shown in **Figure 2A.1**. When ZN is dissolved in water, it liberates Zn²⁺ ions (equation 2A.2),



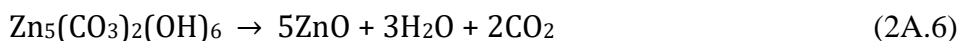
When urea is dissolved in water and heated above 60°C, it undergoes hydrolysis and generates carbonate (CO₃²⁻) and hydroxyl (OH⁻) ions (equation 2A.4).



When the aqueous solution of Zn is added to that of urea and heated at 90°C, the Zn²⁺, CO₃²⁻ and OH⁻ ions present in the reaction mixture react to form HZC (equation 2A.5),



This reaction is favoured by the basic pH of the reaction mixture owing to the presence of OH⁻ ions. Subsequent heating of the as-synthesized sample above 300 °C (500 °C in our case), results in decomposition of HZC (equation 2A.6),



Hence, pure ZnO microstructures are obtained.

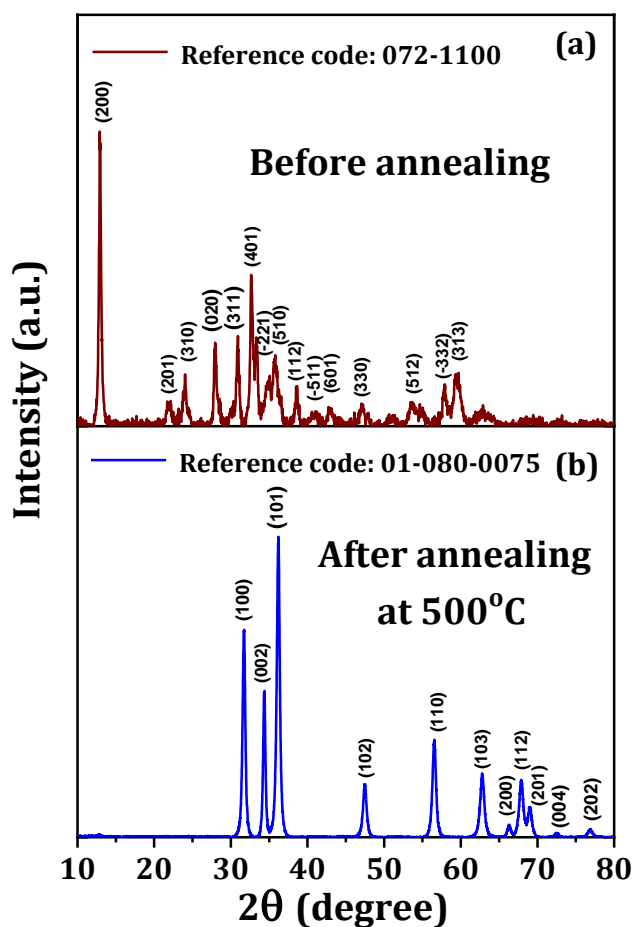


Figure 2A.3. XRD patterns of the synthesized sample (a) before annealing, and (b) after annealing at 500 °C.

The crystalline structure of the as-synthesized sample and the annealed sample were studied using the XRD. The XRD patterns of the respective samples are shown in **Figure 2A.3**. It is seen that before annealing, the XRD peaks correspond to that of monoclinic phase of HZC, Zn₅(CO₃)₂(OH)₆ (ICDD No. 072-1100), with a layered structure having large interlayer spacing, as indicated by the diffraction maximum at the 2θ angle of 13°. [49]

On the other hand, the XRD peaks of the annealed sample was completely transformed to that of pure ZnO with wurtzite phase and hexagonal crystal structure (ICDD No. 01-080-0075). The diffraction peaks observed at 31.8°, 34.5°, 36.3°, 47.6°, 56.7°, 62.9°, 66.5°, 68.1°, 69.2°, 72.7°, and 77.1° correspond to the characteristic planes of ZnO wurtzite structure, *viz.* [100], [002], [101], [102], [110], [103], [200], [112], [201], [004], and [202] respectively. By taking the diffraction peak corresponding to a particular plane $[hkl]$, we can calculate the crystallite size (D_{hkl}) of the sample, using the Debye–Scherrer equation as,^[50,51]

$$D_{hkl} = \frac{K\lambda}{\beta_{hkl} \cos\theta} \quad (2A.7)$$

where K is a unitless constant (with typical value 0.9), λ is the wavelength of X-ray used (1.5418 Å), β_{hkl} is the full width at half maximum of the diffraction peak corresponding to the $[hkl]$ plane, and θ is half of the corresponding diffraction angle (known as the Bragg angle). We estimated the average crystallite size (D_{avg}) of the annealed ZnO sample by considering the three most intense peaks [101], [002], and [100]. The corresponding crystallite sizes were found to be 26.8 nm (D_{101}), 37.8 nm (D_{002}) and 24.9 nm (D_{100}), respectively, resulting in a D_{avg} of 29.8 nm.

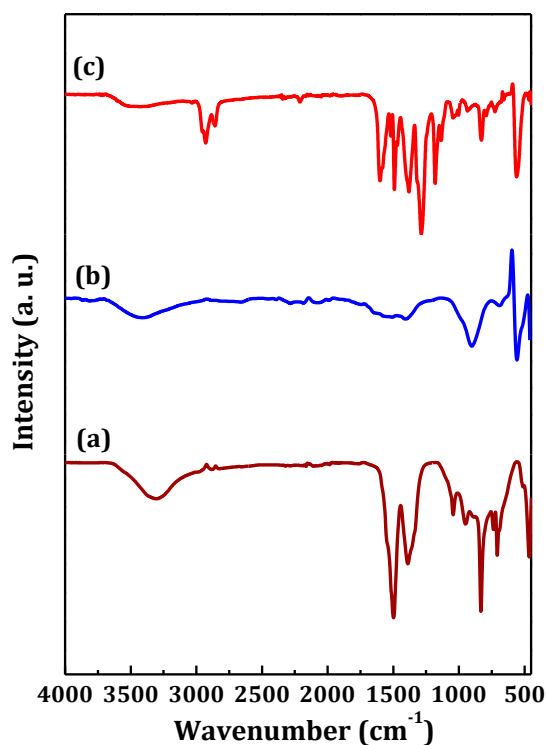


Figure 2A.4. IR spectra of the (a) as-synthesized sample (hydrozincite), (b) sample annealed at 500 °C (ZnO), and (c) Y123 dye-sensitized ZnO sample.

Further, IR spectroscopic analysis was used to confirm the formation of HZC ($\text{Zn}_5(\text{CO}_3)_2(\text{OH})_6$) and ZnO. **Figure 2A.4(a)** shows the IR spectrum of the as-synthesized sample, with absorption peaks at 464 cm^{-1} , 708 cm^{-1} , 832 cm^{-1} , 948 cm^{-1} , 1045 cm^{-1} , 1388 cm^{-1} , and 1500 cm^{-1} correspond to the characteristic vibrations in pure HZC.^[52] The broad absorption band centered at around 3308 cm^{-1} represents the stretching vibration of the disassociated hydroxyl in HZC. Adsorbed water molecules also contribute to this band. The band at 1388 cm^{-1} can be assigned to lattice vibrations (asymmetric stretching) of carbonate ion (CO_3^{2-}), while the peaks at 1500 cm^{-1} and 1045 cm^{-1} represent the C-O bond, whereas the bands at 832 cm^{-1} and 708 cm^{-1} correspond to asymmetric and phase bending vibrations of O-C-O, respectively.^[52-54] On the other hand, the IR spectrum of the annealed sample (**Figure 2A.4(b)**) shows an absorption band centred at 558 cm^{-1} range, corresponding to Zn-O stretching vibrations, while a weak band at 904 cm^{-1} corresponding to Zn-OH stretching.^[51,55] The bands corresponding to carbonate and hydroxyl groups are seen to be suppressed after the annealing, due to decomposition of HZC and associated loss of CO_2 and H_2O from the sample. This confirms the formation of ZnO after annealing. The IR spectrum of the annealed ZnO sample adsorbed with the organic dye Y123 is provided in **Figure 2A.4(c)**. The IR bands at 826 cm^{-1} (C-S stretching), 1180 cm^{-1} (C-H bending), $1289\text{-}1322\text{ cm}^{-1}$ (C-N stretching, C-N-C bending, phenyl ring twisting and C-H bending), $1383\text{-}1409\text{ cm}^{-1}$ (C-C stretching in benzene ring), $1491\text{-}1595\text{ cm}^{-1}$ (vibration modes of phenyl ring and alkyls), 1603 cm^{-1} (C-C stretching in thiophene ring), and $2857\text{-}2955\text{ cm}^{-1}$ (C-H stretching vibrations) could be attributed to the organic dye, Y123.^[56-58] Meanwhile, the peak corresponding to the Zn-O bond is slightly shifted to 563 cm^{-1} which might be due to the chemisorption of dye molecules on the ZnO surface.

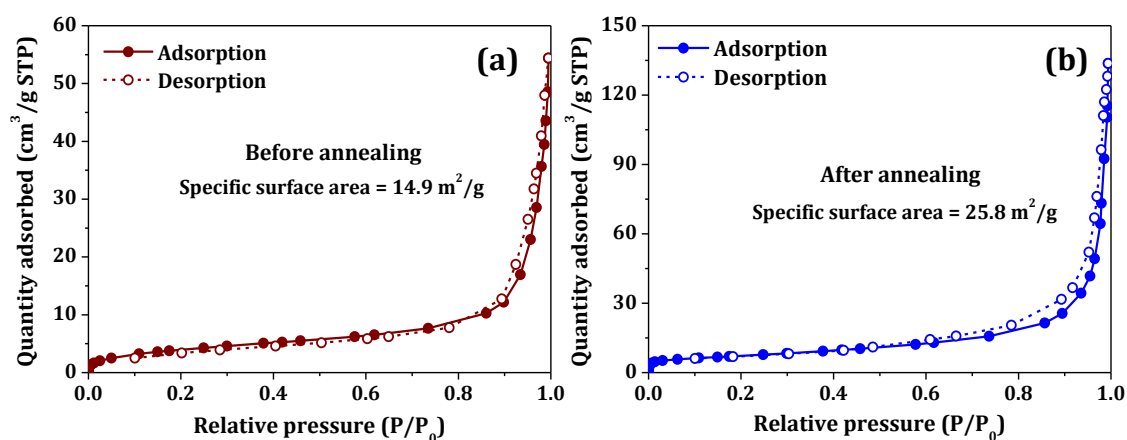


Figure 2A.5. The N_2 adsorption-desorption isotherms obtained for (a) the as-synthesized sample (before annealing), and (b) sample annealed at $500\text{ }^\circ\text{C}$.

The specific surface area of the sample before and after annealing was determined using the standard N₂ adsorption-desorption technique by applying the BET model. The obtained adsorption-desorption isotherms, given in **Figure 2A.5**, are type IV isotherms corresponding to the capillary condensation in the mesopores of the samples, which affirm the mesoporous nature of the samples before and after annealing. Moreover, the BET surface area for the as-synthesized sample (14.9 m²/g) was observed to be less when compared to that of the annealed one (25.8 m²/g). When the HZC sample is annealed above 300 °C, it decomposes and releases carbon dioxide and water (equation 2A.6), as a result of which there is an increase in porosity and hence specific surface area of the annealed ZnO sample, which will be designated as Z0 hereafter.

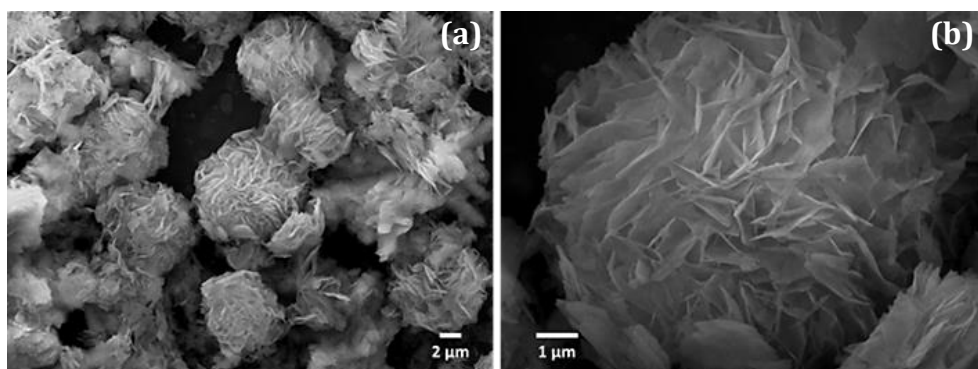


Figure 2A.6. SEM images of ZnO samples annealed at 500 °C showing hierarchical microsphere morphology, under (a) lower magnification, and (b) higher magnification.

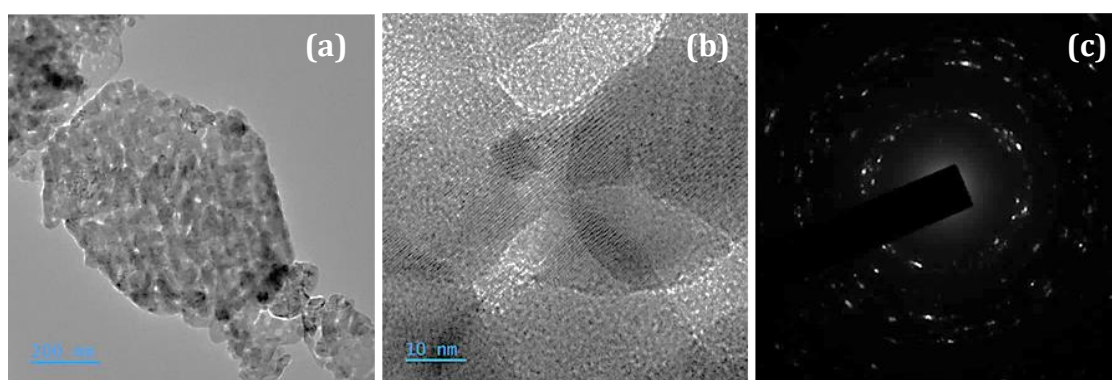


Figure 2A.7. The HRTEM images of ZnO (Z0) sample (annealed at 500 °C) (a) under low magnification, (b) under higher magnification and (c) corresponding SAED patterns.

The morphology of the Z0 sample was analysed using SEM micrographs shown in **Figure 2A.6**. The SEM images revealed a hierarchical microsphere morphology for the Z0 sample with an average particle size of ~ 9.7 μm, which was formed by the aggregation of ~ 1.8 μm sized ZnO nanoflakes. The crystallography of Z0 was further examined using

TEM analysis. The high-resolution TEM images and the corresponding SAED patterns are displayed in **Figure 2A.7**. It is clearly seen from **Figure 2A.7(a)** that the ZnO nanoflakes are made up of numerous nanoparticles with average crystallite size of 30.5 nm, which is close to that obtained from XRD analysis. At higher magnifications (**Figure 2A.7(b)**), it is observed that the crystallographic axes of various nanocrystallites are oriented in random directions. This suggests that the nanoflakes growth occurs by a heterogenous nucleation and coalescence mechanism, while the hierarchical microstructure is obtained by the diffusion-limited cluster-cluster aggregation of the nanoflakes.^[59] The SAED patterns in **Figure 2A.7(c)** confirm the crystallinity of the annealed samples.

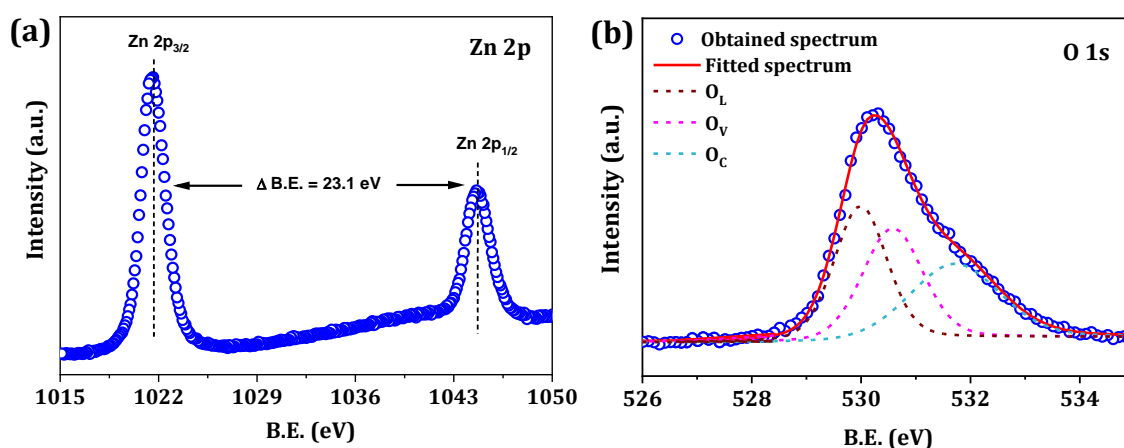


Figure 2A.8. The peaks corresponding to core level (a) Zn 2p, and (b) O 1s states in the XPS spectrum of ZnO sample (annealed at 500 °C).

Further, the formation of ZnO was confirmed by studying the surface composition using XPS analysis of the annealed sample coated over the FTO substrate. XPS spectrum of the annealed sample (Z0) was recorded and the binding energies (B.E.) were calibrated by using the peak corresponding to C 1s state (with B. E. of 284.6 eV) as the reference. It was seen that the peak corresponding to the core level Zn 2p state was split into two (**Figure 2A.8(a)**), Zn 2p_{3/2} and Zn 2p_{1/2}, with binding energies 1021.58 eV and 1044.71 eV, respectively, owing to spin-orbit coupling.^[60] A ~ 23.1 eV difference between the B.E.s of these peaks indicate the presence of Zn atoms in the Zn²⁺ valence state.^[61] On the other hand, the broad peak corresponding to the core level O 1s state could be deconvoluted into three sub-peaks centred at 529.99 eV, 530.57 eV and 531.71 eV (**Figure 2A.8(b)**).^[62] The O 1s peak at the low B. E. (529.99 eV) correspond to the lattice oxygen (or the Zn-O bond) in the wurtzite structure of hexagonal ZnO (O_L). Whereas, the peaks at middle B. E. (530.57 eV) and high B.E. (531.71 eV) region represent the O²⁻ ions in oxygen deficient regions,

such as oxygen vacancies (O_v) and interstitial oxygen atoms which are weakly attached to the ZnO surface, such as a weakly bound $-CO_3$, chemisorbed water molecule or oxygen molecule, dissociated hydroxyl species etc. (O_i or O_c), respectively.^[63,64]

The UV-visible diffuse reflectance spectra (**Figure 2A.9(a)**) was used for estimating the bandgap of Z0 sample. By modifying Tauc's relation using Kubelka-Munk function ($F(R)$), we obtain^[65,66]

$$(F(R)h\nu)^{1/\gamma} = A(h\nu - E_g) \quad (2A.8)$$

where h is the Planck's constant, ν is the frequency of incident radiation, A is a constant, E_g is the bandgap of the material and γ is the factor that indicates the nature of electron transition in the material. For materials with direct transition band gaps such as ZnO, γ is equal to $1/2$ and for indirect ones it is equal to 2. Here, the Kubelka-Munk function ($F(R_d)$) can be calculated from the diffuse reflectance (R_D) as,^[67]

$$F(R) = \frac{K}{S} = \frac{(1-R_D)^2}{2R_D} \quad (2A.9)$$

where K and S are the absorption and scattering coefficients of the material, respectively. The Kubelka-Munk function vs. energy ($h\nu$) plot for Z0 is shown in **Figure 2A.9(b)**. The point of intersection of the linear portion of the absorption edge of the curve with the energy axis, gave us the E_g of our Z0 sample as 3.29 eV, which is close to the previously reported value for ZnO.^[68-70]

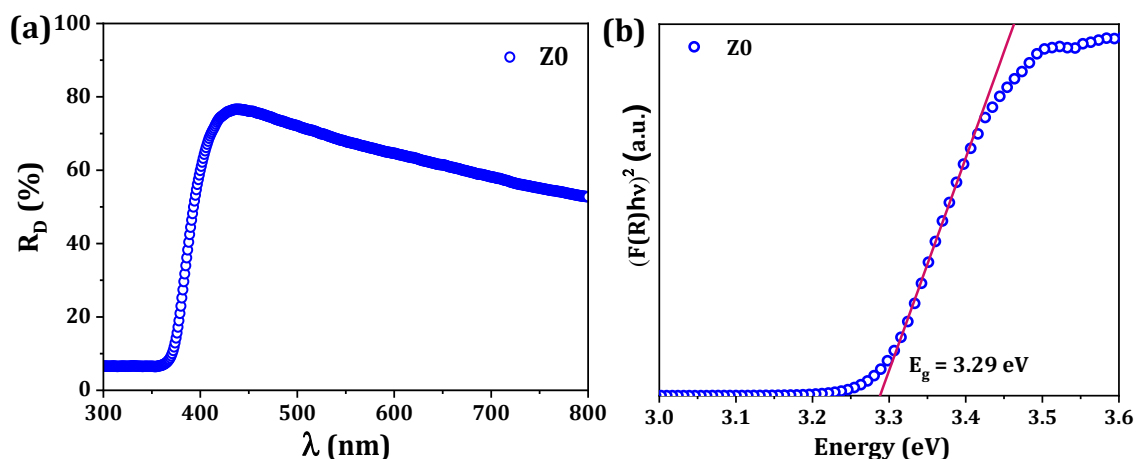


Figure 2A.9. (a) UV-visible diffuse reflectance spectra and (b) modified Tauc's plot (using Kubelka-Munk function) of Z0 sample coated on glass substrate after annealing at 500 °C.

(b) *Characterization of ZnO based DSCs using different redox mediators.* The energy level diagram and molecular structures of the components used in various ZnO (Z0) based

DSCs are shown in **Figure 2A.10(a)**. The photovoltaic (PV) performance of the DSCs utilizing Z0 based photoanodes sensitized with Y123 dye in conjunction with two different redox mediators, *viz.* iodide/triiodide (I^-/I_3^-) and $[Cu(dmp)_2]^{2+/+}$ were evaluated under one sun irradiation. The corresponding J - V characteristics and PV parameters are provided in **Figure 2A.10(b)** and **Table 2A.1** respectively. The best performing I^-/I_3^- electrolyte based device (Z0/I) delivered a V_{OC} of 0.63 V, J_{SC} of 3.52 mA/cm², FF of 45% and PCE of 1.01%, whereas the device fabricated using copper based redox electrolyte (Z0/Cu) exhibited 0.86 V V_{OC} , 4.14 mA/cm² J_{SC} , 57% FF, contributing to 2.02% PCE . The Z0/Cu DSC possessed better V_{OC} , J_{SC} as well as FF, accounting to a PCE double as that of Z0/I device.

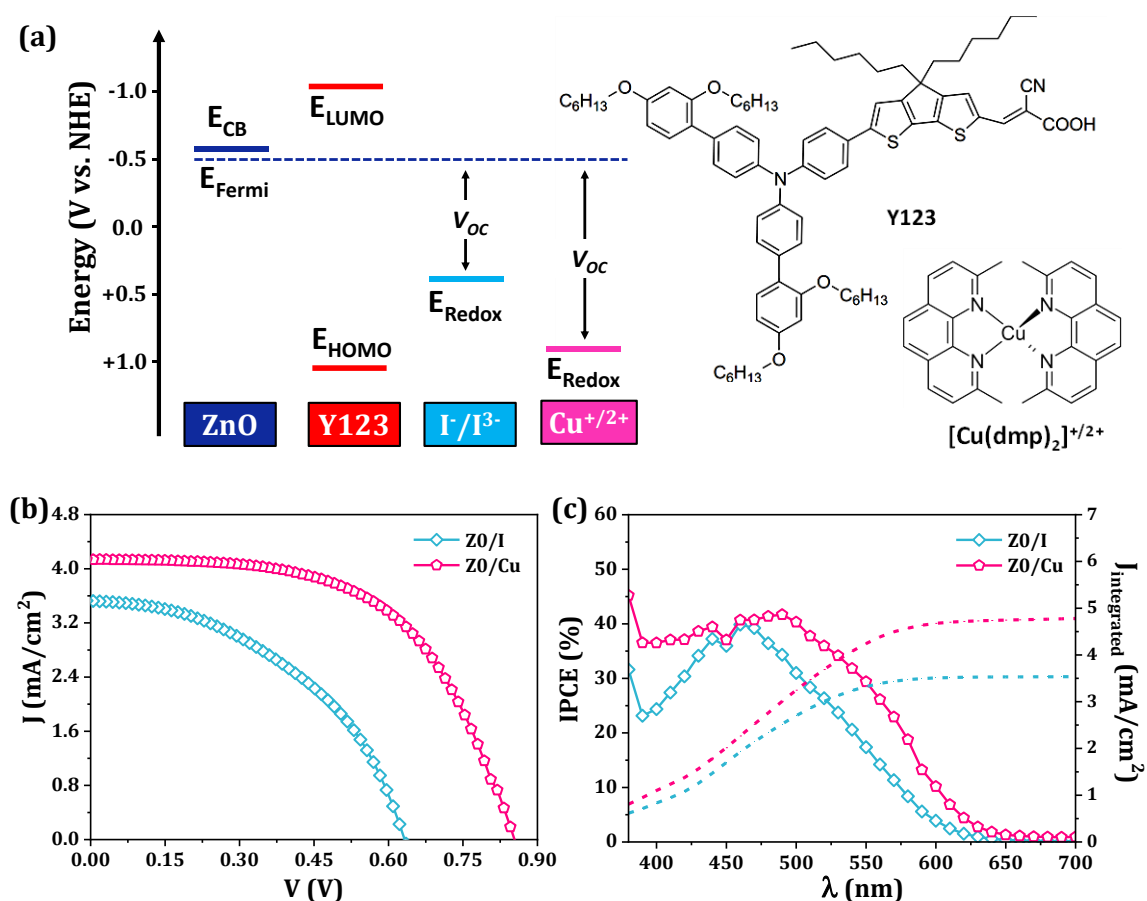


Figure 2A.10. (a) Energy level diagram and molecular structures of various device components, (b) J - V characteristics and (c) $IPCE$ spectra of DSCs employing Y123 dye-sensitized ZnO (Z0) photoanode along with iodine (I^-/I_3^-) and copper $[Cu(dmp)_2]^{2+/+}$ electrolytes.

Table 2A.1. Photovoltaic parameters of the DSCs employing Y123 sensitized ZnO photoanode using I/I₃⁻ and [Cu(dmp)₂]^{2+/+} electrolytes.

Device Code	V_{OC}^a (V)	J_{sc}^a (mA/cm ²)	FF^a	PCE^a (%)	Integrated J_{sc}^b (mA/cm ²)	n
Z0/I	0.63 (0.63 ± 0.01)	3.52 (3.46 ± 0.14)	0.45 (0.45 ± 0.01)	1.01 (0.98 ± 0.04)	3.53	1.19
Z0/Cu	0.86 (0.84 ± 0.01)	4.14 (4.01 ± 0.14)	0.57 (0.59 ± 0.02)	2.02 (1.99 ± 0.03)	4.78	2.31

^aObtained from *J-V* characterization of 3 devices (minimum) under one sun condition. The parameters corresponding to the champion cell are provided, along with the average value ± standard deviation in the parantheses.

^bObtained by integration of *IPCE* spectra.

The improved J_{SC} for Z0/Cu device could be ascribed to its better *IPCE* profile as shown in **Figure 2A.10(c)**. While, the *IPCE* relies on the light harvesting, injection, charge collection and regeneration efficiencies (equation 1.2). The difference in *IPCE* between the devices Z0/I and Z0/Cu may be caused by the variation in any of these parameters due to the influence of the different electrolyte systems used in them. The theoretical J_{SC} obtained by integrating the *IPCE* spectra (**Figure 2A.10(c)**) for Z0/I and Z0/Cu devices (listed in **Table 2A.1**) match with the J_{SC} measured under one sun condition. A 13.4% decrease in obtained J_{SC} when compared to the theoretical J_{SC} is observed for Z0/Cu device, which can be attributed to the mass transport limitation of the bulky copper species in the electrolyte system. The mass transport issues in Z0/Cu device relative to Z0/I device can be clearly observed from the current transient plots (**Figure 2A.11(a)**). In spite of this drawback, the copper electrolyte based device delivered the highest J_{SC} .

The variation of V_{OC} with incident light intensity (ϕ) was recorded for Z0/I and Z0/Cu devices as shown in **Figure 2A.11(b)**. The slope of the V_{OC} vs. ϕ curve was used for finding the ideality factor (n) of the devices as,

$$n = \frac{q}{2.3k_B T} \left(\frac{dV_{OC}}{d \log \phi} \right) \quad (2A.10)$$

where q is the electronic charge, k_B is the Boltzmann's constant, and T is the absolute temperature. A slope of ~ 59.8 mV will yield ideal n value of 1, corresponding to linear recombination kinetics. The n values obtained for Z0/I and Z0/Cu devices are given in **Table 2A.1**. It is observed that ideality factor for Z0/Cu device (2.31) is more deviating from the ideal value, when compared to Z0/I device (1.19), indicating that the charge

transfer mechanism in copper electrolyte based DSCs is more deviating from the first order kinetics. This provides indication that DSCs employing copper electrolytes are more prone to trap state mediated recombination, even in case of ZnO based photoanodes.^[71] Nonetheless, the V_{OC} of copper electrolyte based device is higher compared to its iodine counterpart. Since the V_{OC} of DSC mainly depends on the energy gap between redox potential of electrolyte (E_{redox}) and Fermi level of the semiconductor (E_F), the improved V_{OC} in Z0/Cu device could readily be attributed to the more positive E_{redox} of the copper redox species when compared to the iodide/triiodide electrolyte (as shown in **Figure 2A.10(a)**). The more positive E_{redox} leads to reduced overpotential loss for dye regeneration, which as well contributes to higher V_{OC} of Z0/Cu devices.

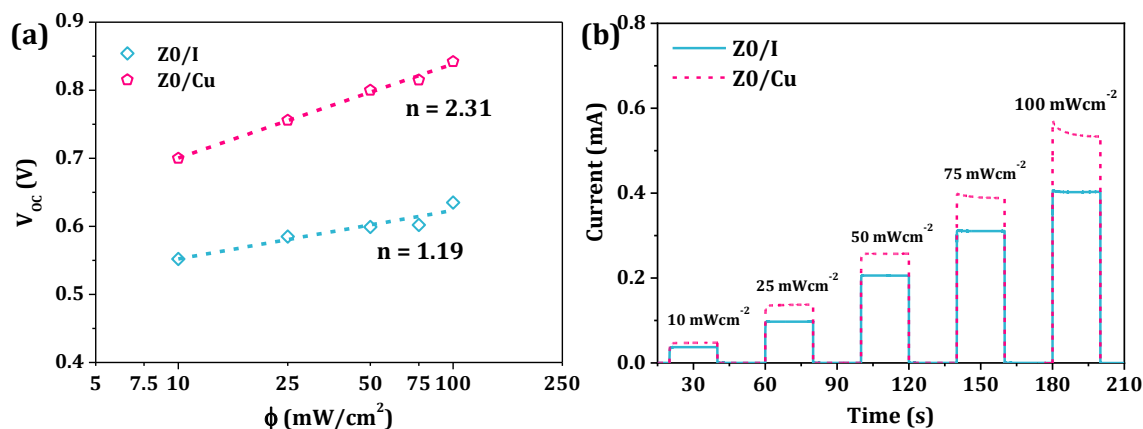


Figure 2A.11. (a) V_{OC} vs. ϕ plot, and (b) Current transient curves acquired for DSCs employing Y123 dye-sensitized ZnO (Z0) photoanode along with I^-/I_3^- and $[\text{Cu}(\text{dmp})_2]^{2+/+}$ electrolytes.

The variation in $IPCE$ and hence J_{SC} between the Z0/I and Z0/Cu devices may be attributed to the shift in ZnO conduction band (CB) edge induced by different surrounding environment, i.e. electrolyte systems. The influence of the surrounding electrolyte on the CB of the Z0 photoanode material was studied by analyzing the charge extracted vs. V_{OC} plots (**Figure 2A.12(a)**). The iodine electrolyte tends to shift the CB of ZnO to a more negative position when compared to the copper based electrolyte. This negatively shifted CB of the Z0/I device might have affected the driving force for injection, hence suppressing its J_{SC} . IMVS and IMPS studies were utilized to investigate the effect of the two electrolytes on the charge collection in ZnO based DSCs. The lifetime (τ_n) and transport time (τ_d) of electrons in the Z0 photoanode, obtained from the respective measurements, were plotted against the LED current, which is directly related to the intensity of the LED illumination

(Figure 2A.12(b)). It was observed that the Z0/I device possess better τ_n when compared to Z0/Cu device. This is in agreement with our previous observation that copper electrolyte based device has more chances of trap state mediated recombination, which will obviously affect the electron lifetime in the Z0 photoanode. Meanwhile, the electron transport in Z0/Cu devices seemed to be faster than that in Z0/I device (Figure 2A.12(b)). It is well known that the electron transport within the mesoporous semiconductor layer occurs via a diffusion mechanism involving the CB states and shallow trap-states (surface states).^[72] The injection of photoelectrons into the semiconductor layer shifts its Fermi level and

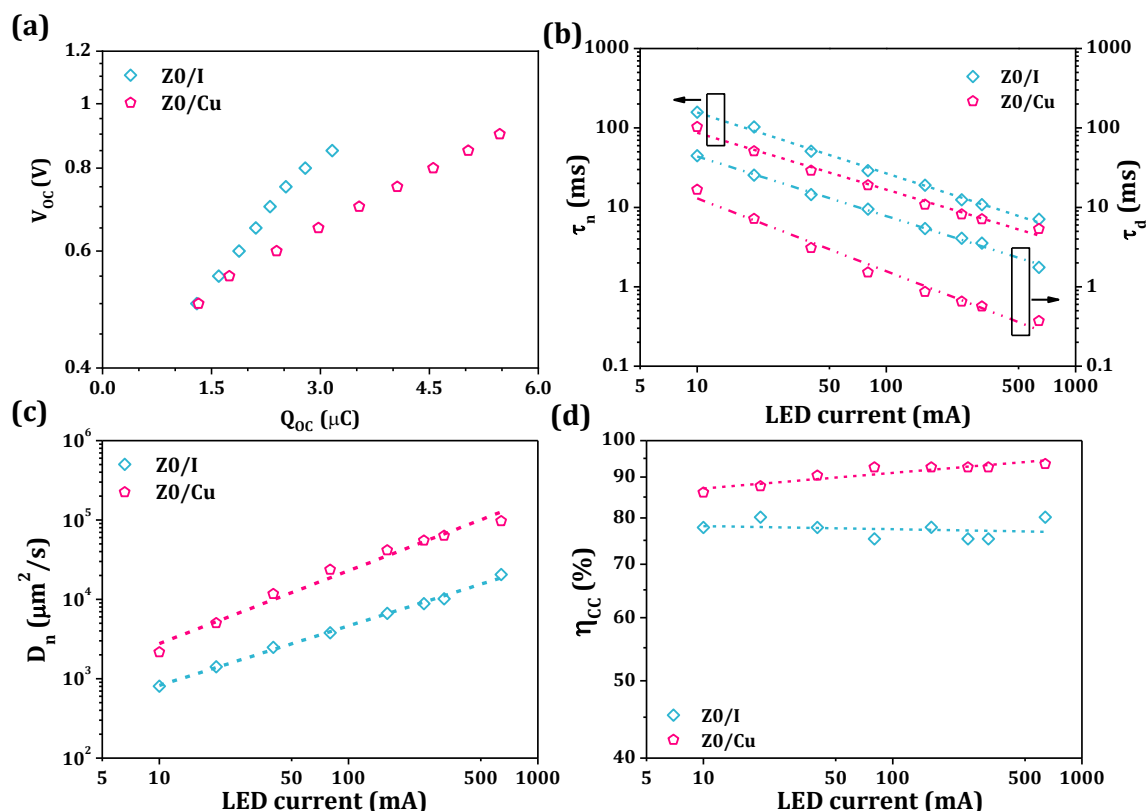


Figure 2A.12. (a) Charge extracted vs. V_{oc} plots obtained from CE measurement; (b) electron lifetime (τ_n) and transport time (τ_d), (c) electron diffusion coefficient (D_n) and (d) charge collection efficiency (η_{CC}), as a function of LED current obtained from IMVS and IMPS measurements, for DSCs employing Y123 dye-sensitized ZnO photoanodes using I^-/I_3^- and $[\text{Cu}(\text{dmp})_2]^{2+/+}$ electrolytes.

creates a potential gradient within the nanoparticles, which serves as the driving force for electron diffusion.^[73,74] In other words, when more electrons are injected into a nanoparticle, the existing electron in the particle will be forced out, leading to electron migration. In our case, the Z0/Cu device with better injection rates can create higher electron concentration gradients when compared to the Z0/I device. Consequently, Z0/Cu

device possess higher driving force for charge diffusion which lead to better diffusion coefficient (D_n) and charge collection efficiency (η_{CC}) (**Figure 2A.12(c,d)**). Altogether, copper electrolyte is observed to be more suitable for ZnO based DSCs, owing to the favourable redox potential, better injection and faster charge collection properties endowed by them.

2A.3.2. Effect of TiO₂ post blocking layer on the performance of ZnO based DSCs.

(a) Characterization of ZnO based photoanodes with and without TiO₂ blocking layer.

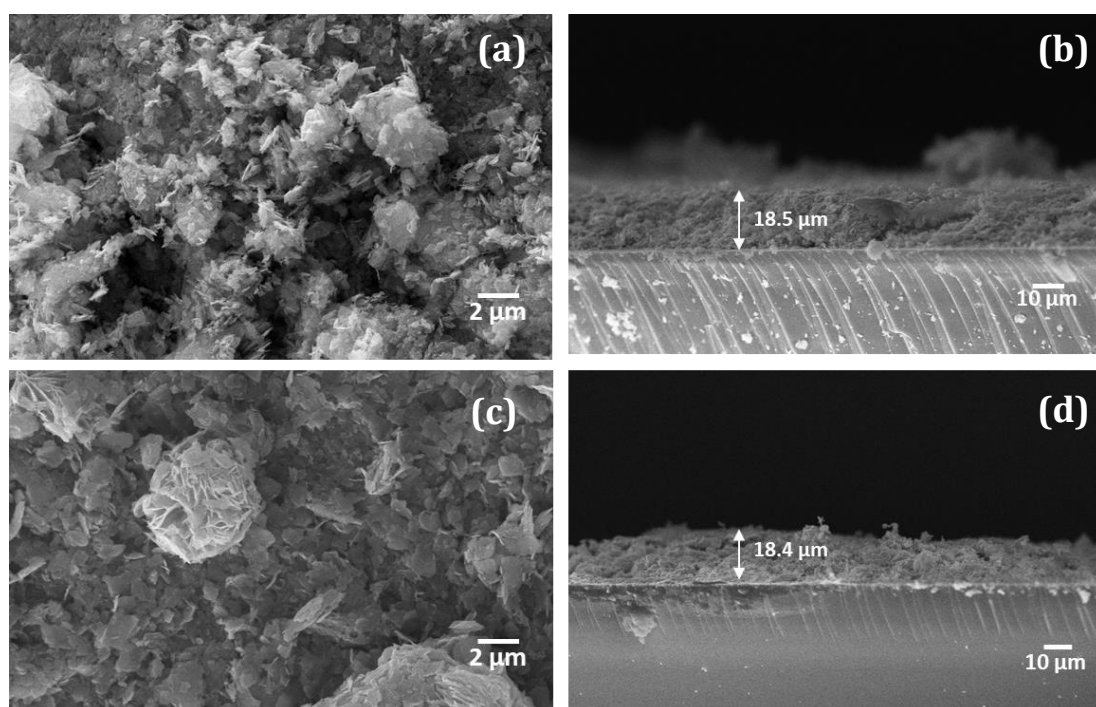


Figure 2A.13. SEM images of (a) surface and (b) cross-section of Z0 photoanode; and (c) surface and (d) cross-section of Z0+BL photoanode.

The photoanode without blocking layer (BL), labelled as Z0, was prepared by coating the paste of HZC on the FTO substrate followed by a programmed annealing up to 500 °C. During the annealing, the HZC decomposes and forms pure ZnO. While in case of the photoanode with BL, designated as Z0+BL, the BL solution is deposited over the HZC layer before the annealing process. During the annealing process, the HZC transforms to ZnO microstructures, while an ultra-thin compact layer of TiO₂ gets coated over the microparticles. The SEM micrographs showing the surface and cross-sectional profile of the unsensitized Z0 photoanodes with and without TiO₂ BL are presented in **Figure 2A.13**. The surface morphology and thickness of the Z0 films were seen to be unaffected by the deposition of the BL. However, the surface of the Z0+BL film appears smoother when

compared to that of the bare Z0 film (**Figure 2A.13(a,c)**). Both the films exhibited similar thickness of $\sim 18.5 \mu\text{m}$, as could be observed from the cross-sectional SEM image (**Figure 2A.13(b,d)**). The EDX spectra and elemental mapping of the surface of the films, shown in **Figure 2A.14**, confirm the presence of TiO_2 (0.3 wt%) in the Z0+BL photoanode. The DRS (**Figure 2A.15(a)**) of the unsensitized Z0+BL photoanode was used to obtain the corresponding Kubelka-Munk function (equation 2A.9). Subsequently, the band gap energy of the Z0+BL was determined to be 3.27 eV, from the $(F(R)hv)^2$ vs. hv plot (**Figure 2A.15(b)**). A slight decrease in E_g for Z0+BL layer was observed when compared to the Z0 photoanode, which is indicative of a possible shift in CB, owing to the modification of surface states upon BL deposition.

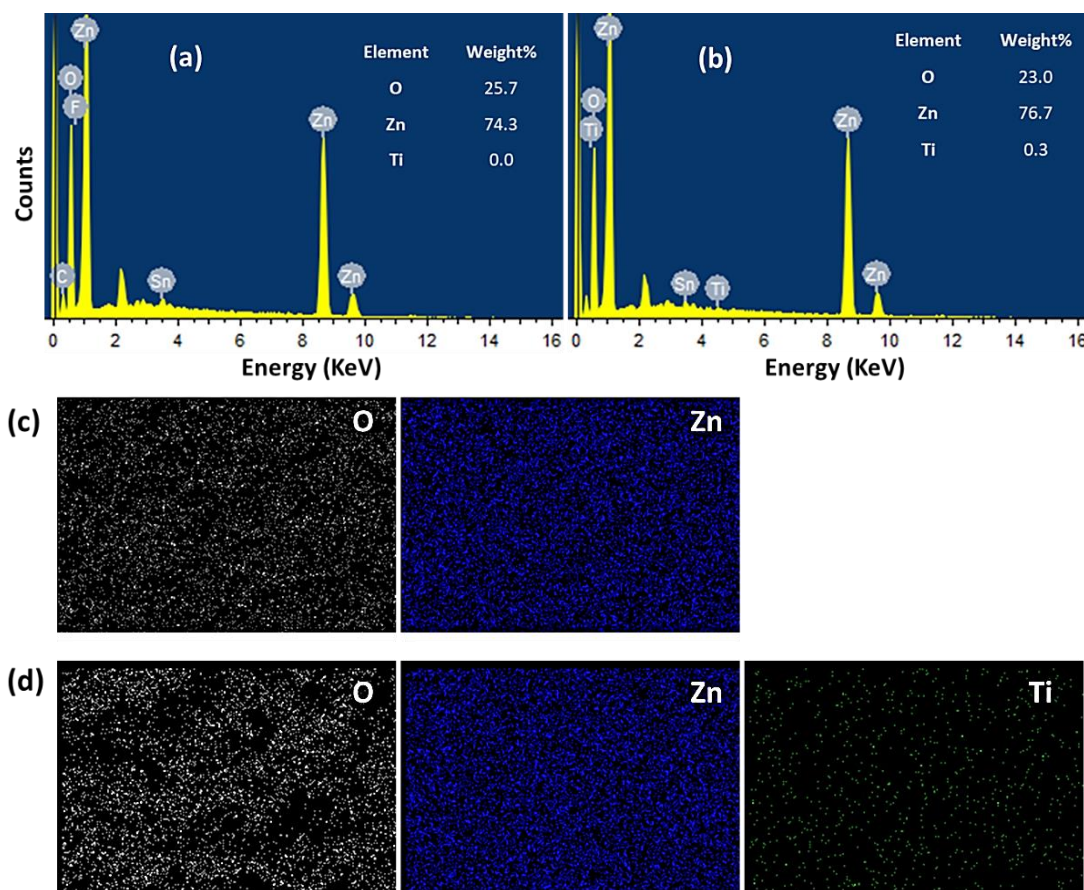


Figure 2A.14. EDX spectra of (a) Z0 and (b) Z0+BL photoanode; Elemental mapping of (c) Z0 and (d) Z0+BL photoanode.

The PL spectra acquired for the unsensitized Z0 and Z0+BL photoanodes were compared, as shown in **Figure 2A.16**. The PL was recorded at an excitation wavelength of 330 nm and two emission peaks were observed in the visible range, one centered at ~ 464 nm and another one at ~ 535 nm. The high temperature annealing of Z0 photoanode might lead to the dissociation of Zn-O bonds, thereby inducing several surface defects such as

oxygen vacancies, Zn vacancies etc.^[75] The weak and broad peak at the lower wavelength range correspond to the emissions originating from deep level oxygen vacancies or interstitial Zn²⁺ ions, while the strong and sharp green emission band at green wavelength range emerges from the singly ionized surface level oxygen vacancies localized in the depletion region, which act as recombination centers.^[76,77] The green emission is further influenced

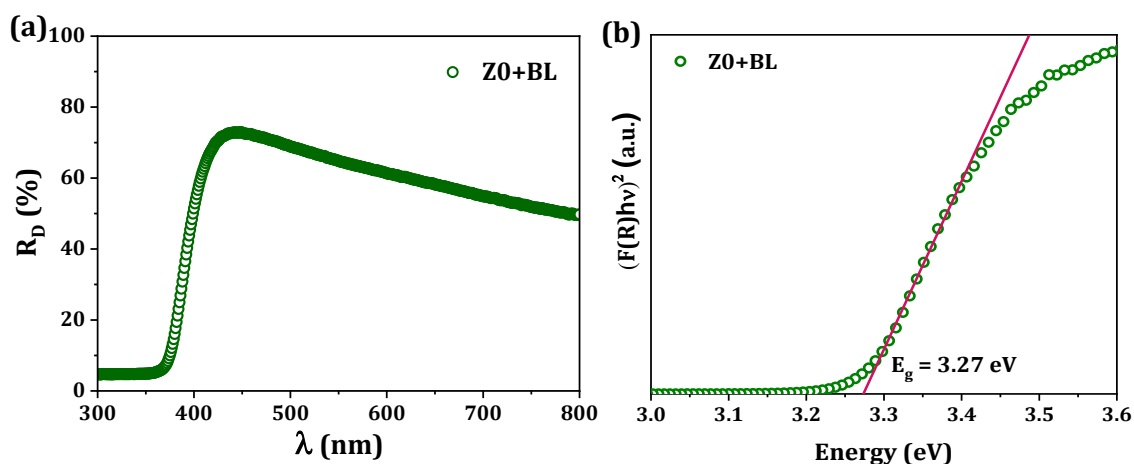


Figure 2A.15. (a) UV-visible diffuse reflectance spectra and (b) modified Tauc's plot (using Kubelka-Munk function) of Z0+BL sample coated on glass substrate.

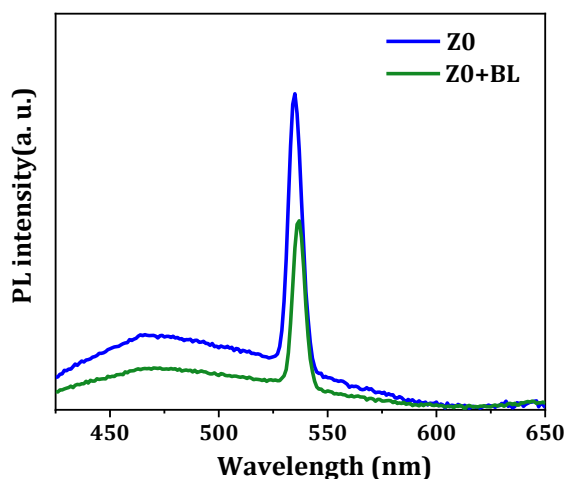


Figure 2A.16. PL spectra of Z0 and Z0+BL photoanode

by the chemisorbed oxygen at the ZnO surface, which causes upward band bending and creates a surface depletion layer, which further facilitates ionization of oxygen vacancies.^[78] These surface level oxygen vacancies in Z0 photoanodes act as surface trap states that contribute towards electron back transfer, thereby affecting the DSC performance. On comparing the PL emissions of Z0 and Z0+BL samples, it is observed

that the deposition of TiO₂ BL over the ZnO layer suppresses both the peaks. The reduction of the green emission peak indicates that the BL effectively passivate the ZnO layer against surface chemisorption, hence retarding the charge recombination.^[13,79,80] In addition, there is a chance that the O₂⁻ ions, created by the dissociation of the TiO₂ in the BL solution at high temperature (above 400 °C), to diffuse within the ZnO layer and substitute the oxygen vacancies.^[81] This results in the quenching of the lower wavelength peak. Consequently, the BL can effectively passivate the surface trap states in ZnO layer and retard the electron back transfer process in ZnO based DSCs.

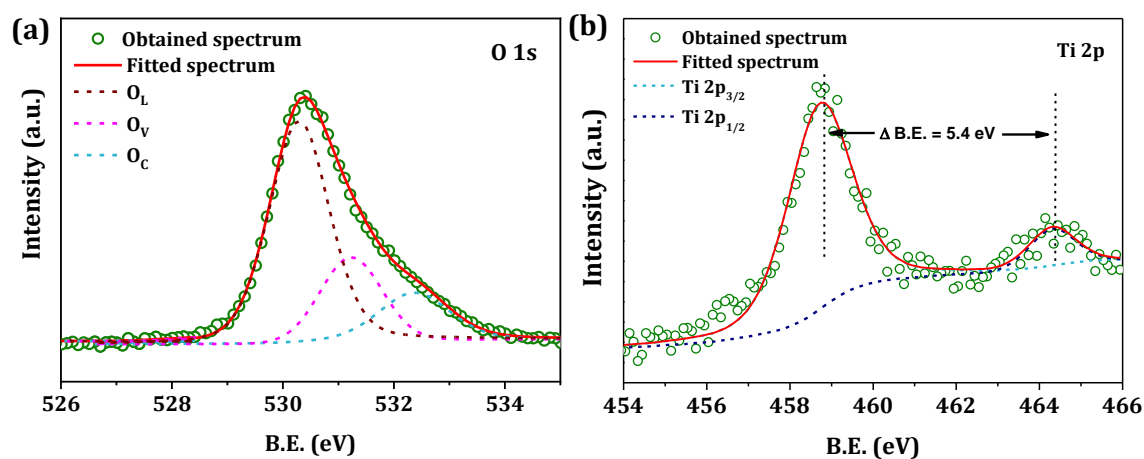


Figure 2A.17. The peak corresponding to (a) O 1s, and (b) Ti 2p states in the XPS spectrum of Z0+BL photoanode.

Table 2A.2. Peak area and atomic percentage of different components of the O 1s peak in the XPS spectra.

Photo-anode	Peak area			Atomic percentage (%)		
	O _L	O _V	O _C	O _L	O _V	O _C
Z0	4688	4736	5070	32.3	32.7	35.0
Z0+BL	9190	3187	2272	62.7	21.7	15.6

The defects formed by the high temperature annealing of Z0 film might enhance the hydrophilicity and wettability of the ZnO surface, by chemisorption of dissociative water species or other environmental oxide species.^[75] This could be observed from the deconvoluted core level O 1s peak of the XPS spectra of Z0 photoanode (**Figure 2A.8(b)**). On comparing the fitted O 1s core level peaks for Z0+BL film with that of Z0 film, it was observed that in case of Z0+BL photoanode, there is a lowering of the components corresponding to surface chemisorbed oxygen, O_C (532.37 eV) and oxygen vacancies, O_V (531.23 eV) respect to that of the lattice oxygen, O_L (530.29 eV) (**Figure 2A.17(a)**). To

study the effect of BL deposition on the number of lattice oxygen, interstitial oxygen (from the chemisorbed species) and oxygen vacancies on the surface of ZO film, the atomic percentage of each component was estimated from the corresponding peak area (**Table 2A.2**). After deposition of BL, the atomic weight percent of oxygen vacancies and chemisorbed oxygen species on the ZO film surface seemed to decrease drastically, from 32.7% to 21.7% and 35% to 15.6%, respectively. Whereas the percentage of lattice oxygen was almost double for ZO+BL film. This further substantiate the notion that the surface passivation of ZnO based photoanode is effectively accomplished using TiO₂ BL. Furthermore, the presence of TiO₂ in the ZO+BL could be confirmed using the XPS peaks at ~ 458.74 eV and ~ 464.44 eV, respectively, corresponding to the Ti 2p doublets, Ti 2p_{3/2} and Ti 2p_{1/2}, with a peak separation of 5.7 eV.^[82]

(b) PV performance of ZnO based DSCs with and without TiO₂ blocking layer. The PV performance of DSCs utilizing ZO and ZO+BL photoanodes, along with Y123 dye and [Cu(dmp)₂]^{2+/+} redox mediator, were analyzed under various light conditions. Under one sun condition, the V_{OC} , J_{SC} , FF and PCE of the champion device employing ZO+BL photoanode are respectively, 0.82 V, 8.85 mA/cm², 0.53 and 3.74%. The corresponding J - V characteristics and parameters are given in **Figure 2A.18(a)** and **Table 2A.3**, respectively. The ZO+BL devices exhibited better J_{SC} , which led to improved PCE for these devices when compared to ZO based DSCs. The improved J_{SC} for ZO+BL devices can be directly correlated to its better $IPCE$, as seen from **Figure 2A.18(c)**.

Table 2A.3. Photovoltaic parameters of the DSCs employing Y123 sensitized ZnO photoanodes without (ZO) and with TiO₂ blocking layer (ZO+BL), along with [Cu(dmp)₂]^{2+/+} electrolyte, under standard one sun irradiation (AM 1.5G, 100 mW/cm²).

Device Code	V_{OC}^a (V)	J_{SC}^a (mA/cm ²)	FF^a	PCE^a (%)	Integrated J_{SC}^b (mA/cm ²)	Dye loading (x10 ⁻⁸ mol/cm ²)
ZO	0.84 (0.84 ± 0.01)	4.15 (4.01 ± 0.14)	0.57 (0.56 ± 0.02)	2.01 (1.99 ± 0.03)	4.84	2.1
ZO+BL	0.82 (0.82 ± 0.01)	8.85 (8.61 ± 0.22)	0.53 (0.54 ± 0.02)	3.74 (3.67 ± 0.08)	8.73	1.8

^a Obtained from J - V characterization of 3 devices (minimum) under one sun condition. The parameters corresponding to the champion cell are provided, along with the average value ± standard deviation in the parantheses.

^b Obtained by integration of $IPCE$ spectra.

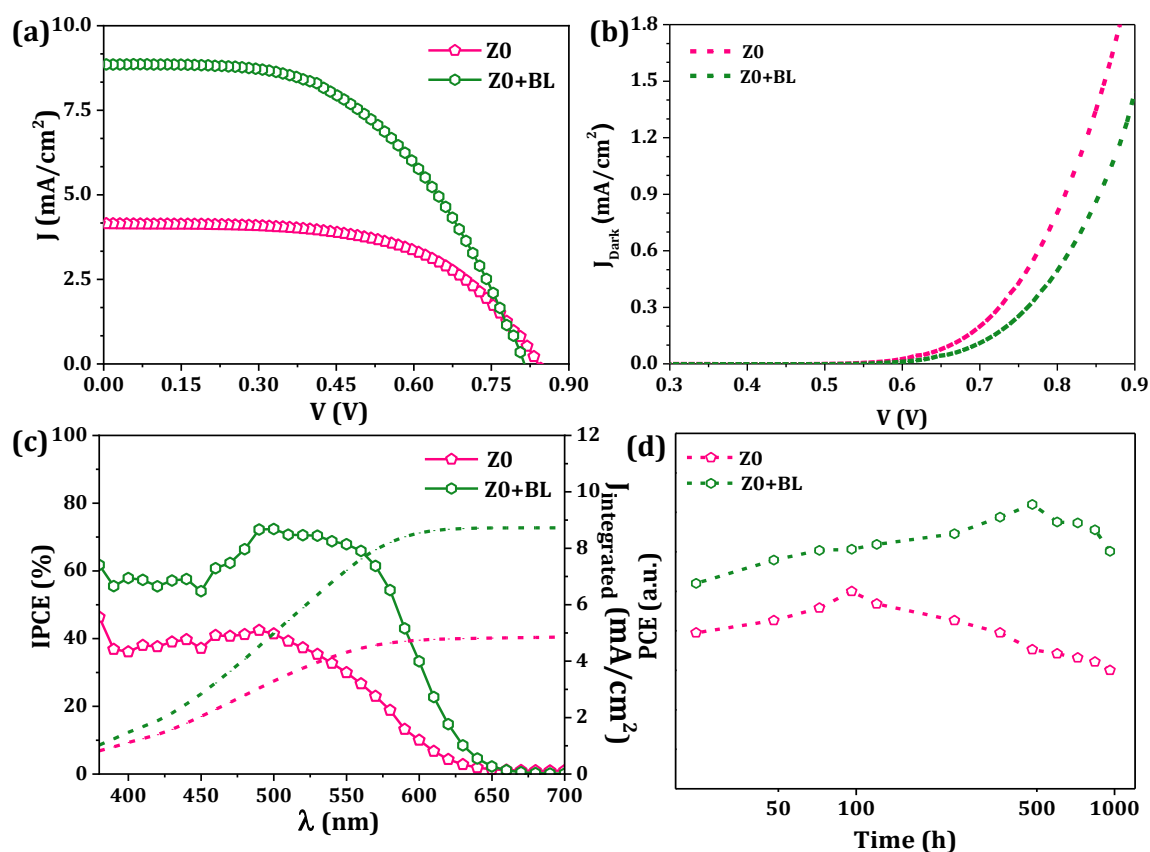


Figure 2A.18. (a) J - V characteristics under one sun illumination (AM 1.5G, 100 mW/cm²), (b) J - V characteristics under dark condition, (c) IPCE spectra, and (d) stability plot for DSCs employing Y123 sensitized ZnO photoanodes without (Z0) and with TiO₂ blocking layer (Z0+BL), along with [Cu(dmp)₂]^{2+/+} electrolyte.

The integrated J_{SC} obtained from the IPCE spectra are matching with the J_{SC} obtained by J - V plots acquired under one sun condition (Table 2A.3). The J - V characteristics of the Z0 and Z0+BL devices under dark condition is shown in Figure 2A.18(b). It is seen that the device without BL has higher dark current than the one with BL, indicating that the back electron transfer is suppressed in case of the Z0+BL device, owing to the passivation of trap states by the deposition of BL. This can contribute to the improved J_{SC} of the Z0+BL device under illuminated condition. Apparently, the BL deposition has, to some extent, also aided in preventing the degradation of ZnO during dye soaking and light exposure in the presence of electrolyte. Also, the BL helped in reducing formation of Zn²⁺/dye aggregates, as a result of which the Z0+BL based device could endure enhanced J_{SC} under illumination, despite the reduction in dye loading (which indicates reduced dye aggregation) (Table 2A.3).^[40] In addition to this, the degradation of the ZnO photoanode under prolonged

exposure to the electrolyte environment and light irradiation was also slowed down in the case of Z0+BL device. This could be observed from the stability curves (**Figure 2A.18(d)**). The performance of Z0 device started decreasing after 100 hours, while that of Z0+BL started decreasing only after about 500 hours. There was an increase in *PCE* of the Z0+BL device for the first 450 hours after electrolyte filling. This could be attributed to the deeper infiltration of the electrolyte into the mesoporous ZnO layer, facilitating more dye regeneration. After ~ 450 hours of electrolyte exposure, even the Z0+BL devices also started to show a trend suggesting lower performance owing to the penetration of electrolyte to the inner regions of ZnO mesopores which are unprotected by the BL, which results in decreased *PCE*.

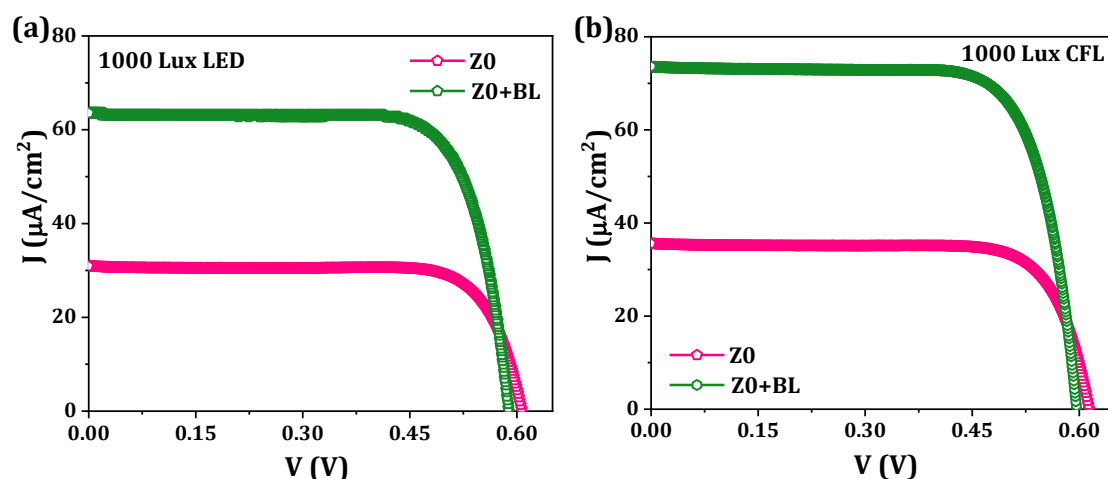


Figure 2A.19. *J-V* characteristics of DSCs employing Y123 sensitized ZnO photoanodes without (Z0) and with TiO₂ blocking layer (Z0+BL), along with [Cu(dmp)₂]^{2+/+} electrolyte, (a) under 1000 lux LED illumination and (b) under 1000 lux CFL illumination.

The *J-V* characterization of the Z0 and Z0+BL devices were done under indoor light conditions, as well. The corresponding characteristic curves are shown in **Figure 2A.19** and PV parameters are provided in **Table 2A.4**. Under 1000 lux LED illumination, with an incident intensity of 0.312 mW/cm², the champion Z0 device delivered a *V_{OC}*, *J_{SC}*, *FF* and *PCE* of 0.61 V, 31 μA/cm², 77% and 4.67%, respectively, while the Z0+BL device gave 0.60 V, 63.6 μA/cm², 76% and 9.13%, respectively. Similarly, under 1000 lux CFL (0.306 mW/cm²) illumination, the Z0+BL device exhibited better *PCE* of 10.82%, with 0.60 V *V_{OC}*, 73.6 μA/cm² *J_{SC}*, and 76% *FF* for the best performing device, while the Z0 device under the same illumination delivered a lower *PCE* of 5.47%, with 0.61 V *V_{OC}*, 35.6 μA/cm² *J_{SC}*, and 77% *FF*. The Z0+BL device exhibited an improvement in *PCE* of 95.5% and 97.8%, respectively, under LED and CFL light, when compared to Z0. In both the

indoor illumination conditions, the better performance of Z0+BL based DSC was predominantly attributed to its higher J_{SC} relative to the Z0 device, while the V_{OC} remained almost same for both devices.

Table 2A.4. Tabulated photovoltaic parameters of DSCs employing Y123 sensitized ZnO photoanodes without (Z0) and with TiO₂ blocking layer (Z0+BL), along with [Cu(dmp)₂]^{2+/+} electrolyte, under 1000 lux LED and 1000 lux CFL illumination.

Indoor light source and intensity ^a	Device Code	V_{OC}^b (V)	J_{sc}^b ($\mu\text{A}/\text{cm}^2$)	FF^b	PCE^b (%)	% Improvement in PCE
1000 lux LED (0.312 mW/cm^2)	Z0	0.61 (0.60 ± 0.01)	31.0 (31.7 ± 1.2)	0.77 (0.76 ± 0.01)	4.67 (4.55 ± 0.10)	95.5
	Z0+BL	0.60 (0.6 ± 0.01)	63.6 (62.3 ± 1.9)	0.76 (0.75 ± 0.01)	9.13 (8.98 ± 0.15)	
1000 lux CFL (0.306 mW/cm^2)	Z0	0.61 (0.61 ± 0.01)	35.6 (34.6 ± 1.3)	0.77 (0.76 ± 0.01)	5.47 (5.29 ± 0.17)	97.8
	Z0+BL	0.60 (0.61 ± 0.01)	73.6 (71.0 ± 2.8)	0.76 (0.77 ± 0.01)	10.82 (10.70 ± 0.14)	

^aObtained by integration of irradiance spectra of the corresponding indoor light source.

^bObtained from J - V characterization of 3 devices under different indoor illumination. The parameters corresponding to the champion cell are provided, along with the average value ± standard deviation in the parantheses.

(c) **Detailed interfacial charge transfer analysis.** The suppressed electron recombination in Z0+BL based DSCs are reflected in their electron lifetime (τ_n) values. Hence, the τ_n vs. V_{OC} plot (**Figure 2A.20(a)**) obtained from OCVD measurements, using equation 1.13, shows that Z0+BL devices have better lifetime when compared to the Z0 device. A similar observation was made from EIS measurement as well. A representative Nyquist plot for Z0 and Z0+BL devices, at an applied bias voltage ($V_{applied}$) of 0.8V is shown in **Figure 2A.20(b)**. The impedance plot for both devices exhibit three arcs in the high (HF), mid (MF) and low frequency (LF), each corresponding to charge transfer at CE/electrolyte interface, charge transfer at ZnO/dye/electrolyte interface and diffusion of electrolyte species, respectively. The MF arc for the Z0+BL device is seen to be wider when compared to that of Z0, indicating that the deposition of BL has endowed a higher resistance for charge recombination at the ZnO/electrolyte interface, owing to the surface passivation. This is again reflected in the τ_n vs. $V_{applied}$ plot (**Figure 2A.20(d)**), where τ_n is obtained from

the frequency corresponding to the peak in the Bode phase plot (**Figure 2A.20(c)**), using equation 1.26.

Even though the back electron transfer is reduced in case of the Z0+BL device, a slight decrease in V_{OC} is observed for the device using Z0+BL photoanode, under both the indoor as well as the outdoor illumination conditions. The reason for this reduction in V_{OC} was investigated using charge extraction measurements. From the extracted charge vs. V_{OC} plot (**Figure 2A.21(a)**), it is evident that the device using BL suffers a positive shift in ZnO CB edge, which justifies the lowered E_g of Z0+BL photoanode (**Figure 2A.15(b)**). This positively shifted CB of Z0+BL photoanode reduces the maximum attainable V_{OC} for the

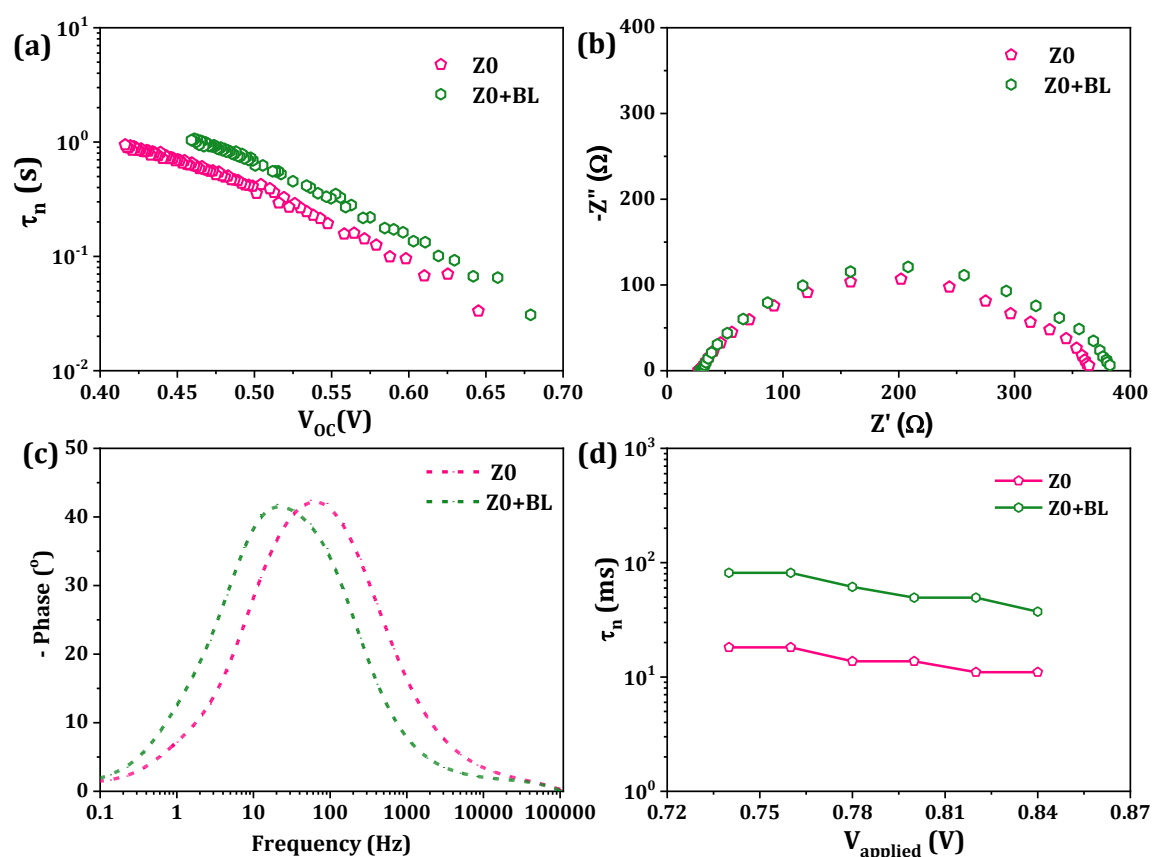


Figure 2A.20. (a) Lifetime (τ_n) vs. voltage plot obtained from OCVD measurement, (b) representative Nyquist plot (at 0.8 V), (c) corresponding Bode phase plot and (d) τ_n vs. voltage plot, obtained from EIS measurement for DSCs employing Y123 sensitized Z0 and Z0+BL photoanodes along with $[\text{Cu}(\text{dmp})_2]^{2+/+}$ electrolyte.

DSCs employing them. However, this downward shift in CB of ZnO upon BL deposition is advantageous for enhancing the J_{SC} of the DSCs using Z0+BL photoanodes, in terms of increased driving force for injection and electron transport within the Z0 layer. Moreover, since the charge transport within the ZnO layer takes place via multiple trapping-detrapping

mechanism, the passivation of surface trap states by the BL enables faster diffusion of electrons.^[83] This is observed from the τ_d vs. LED current plot (**Figure 2A.21(b)**) obtained using IMPS measurement. The better lifetime of electrons in Z0+BL device is again confirmed using the τ_n vs. LED current plot (**Figure 2A.21(b)**) obtained from IMVS measurement. The combined effect of faster electron diffusion and reduced charge recombination resulted in a longer diffusion length (L_n) for electrons in the Z0+BL photoanode (**Figure 2A.21(c)**), leading to better charge collection efficiency for the DSCs utilizing them (**Figure 2A.21(d)**). This might have further contributed towards the enhancement in *IPCE* and thereby improved J_{SC} in Z0+BL based DSCs.

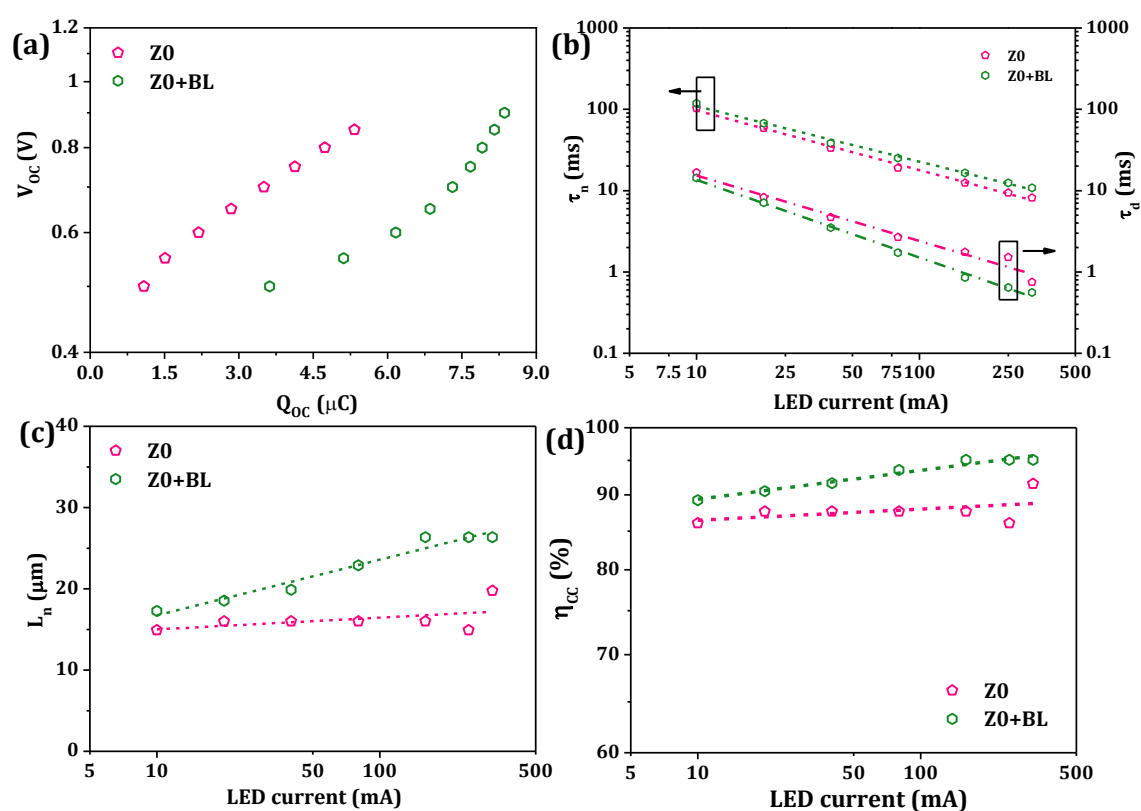


Figure 2A.21. (a) Charge extraction plot; (b) electron lifetime (τ_n) and transport time (τ_d), (c) electron diffusion length (L_n) and (d) charge collection efficiency (η_{cc}), as a function of LED current obtained from IMVS and IMPS measurements, for DSCs employing Y123 sensitized Z0 and Z0+BL photoanodes along with $[\text{Cu}(\text{dmp})_2]^{2+/+}$ electrolyte.

2A.4. Conclusions

ZnO based photoanode sensitized with the organic Y123 dye was utilized in DSC, and its compatibility with conventional iodine (I^-/I_3^-) and copper complex ($[\text{Cu}(\text{dmp})_2]^{2+/+}$) based electrolytes were evaluated in detail. It was observed that the ZnO based DSC using $[\text{Cu}(\text{dmp})_2]^{2+/+}$ electrolyte could deliver better performance compared to I^-/I_3^- electrolyte.

The more positive redox potential of $[\text{Cu}(\text{dmp})_2]^{2+/+}$ redox mediator rendered the corresponding device with enhanced V_{OC} . Further the ZnO based device using copper electrolyte was able to deliver improved J_{SC} , owing to its better electron injection and diffusion rates. Hence, the Z0/Cu device delivered better PCE relative to Z0/I device. However, the performance of copper electrolyte based device was observed to be limited by trap-state mediated recombination. This could be rectified to some extent by the introduction of an ultrathin layer of TiO_2 blocking layer (BL) over the ZnO mesoporous layer. The BL could effectively passivate the surface trap-states, which are essentially the oxygen vacancies, which not only act as the recombination centres but also limit the diffusion of electrons within the ZnO matrix. This was substantiated by the PL and XPS spectra of the ZnO photoanode before and after deposition of the BL. It was observed that after BL deposition, the recombination was suppressed (i.e. τ_n improved), while the electron diffusion length (L_n) was improved in the corresponding DSC, leading to enhanced performance. The best ZnO based device with BL (Z0+BL) could deliver a PCE of 3.74% under one sun illumination and 10.82% under 1000 lux CFL illumination.

References

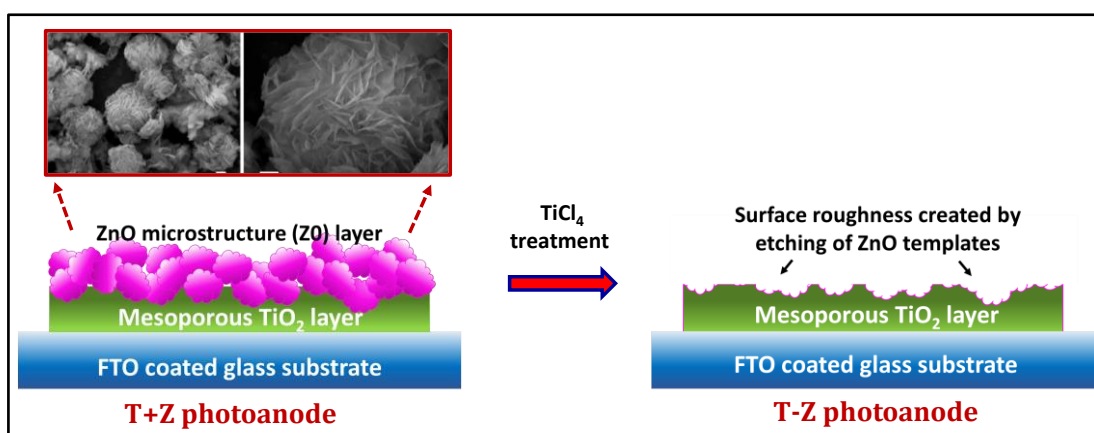
- [1] M. Grätzel, *Nature* **2001**, *414*, 338.
- [2] M. Grätzel, *Inorg Chem* **2005**, *44*, 6841.
- [3] B. O'Regan, M. Grätzel, *Nature* **1991**, *353*, 737.
- [4] B. Yoo, K. J. Kim, S. Y. Bang, M. J. Ko, K. Kim, N. G. Park, *J. Electroanal Chem* **2010**, *638*, 161.
- [5] M. H. Abdullah, M. Rusop, *J Alloys Compd* **2014**, *600*, 60.
- [6] Y. S. Jin, K. H. Kim, W. J. Kim, K. U. Jang, H. W. Choi, *Ceram Int* **2012**, *38*, S505.
- [7] I. P. Liu, W. H. Lin, C. M. Tseng-Shan, Y. L. Lee, *ACS Appl Mater Interfaces* **2018**, *10*, 38900.
- [8] H. Yu, S. Zhang, H. Zhao, G. Will, P. Liu, *Electrochim Acta* **2009**, *54*, 1319.
- [9] E. Palomares, J. N. Clifford, S. A. Haque, T. Lutz, J. R. Durrant, *J Am Chem Soc* **2003**, *125*, 475.
- [10] S. W. Lee, K. S. Ahn, K. Zhu, N. R. Neale, A. J. Frank, *J. Phys. Chem. C* **2012**, *116*, 21285.
- [11] J. H. Yang, C. W. Bark, K. H. Kim, H. W. Choi, *Materials* **2014**, *7*, 3522-3532.
- [12] K. Fan, J. Yu, W. Ho, *Mater Horiz* **2017**, *4*, 319.
- [13] A. R. Pascoe, L. Bourgeois, N. W. Duffy, W. Xiang, Y. B. Cheng, *J. Phys. Chem. C* **2013**, *117*, 25118.
- [14] B. Hu, Q. Tang, B. He, L. Lin, H. Chen, *J Power Sources* **2014**, *267*, 445.
- [15] B. O'Regan, M. Grätzel, *Nature* **1991**, *353*, 737.

- [16] A. Aslam, U. Mehmood, M. H. Arshad, A. Ishfaq, J. Zaheer, A. Ul Haq Khan, M. Sufyan, *Sol. Energy* **2020**, *207*, 874.
- [17] M. Freitag, J. Teuscher, Y. Saygili, X. Zhang, F. Giordano, P. Liska, J. Hua, S. M. Zakeeruddin, J. E. Moser, M. Grätzel, A. Hagfeldt, *Nat Photonics* **2017**, *11*, 372.
- [18] D. Zhang, M. Stojanovic, Y. Ren, Y. Cao, F. T. Eickemeyer, E. Socie, N. Vlachopoulos, J. E. Moser, S. M. Zakeeruddin, A. Hagfeldt, M. Grätzel, *Nat Commun* **2021**, *12*, 1.
- [19] Y. Bai, Q. Yu, N. Cai, Y. Wang, M. Zhang, P. Wang, *ChemComm* **2011**, *47*, 4376.
- [20] M. Freitag, Q. Daniel, M. Pazoki, K. Sveinbjörnsson, J. Zhang, L. Sun, A. Hagfeldt, G. Boschloo, *Energy Environ Sci* **2015**, *8*, 2634.
- [21] E. Tanaka, H. Michaels, M. Freitag, N. Robertson, *J Mater Chem A* **2020**, *8*, 1279.
- [22] J. M. Ji, H. Zhou, Y. K. Eom, C. H. Kim, H. K. Kim, *Adv Energy Mater* **2020**, *10*, 2000124.
- [23] Y. Cao, Y. Liu, S. M. Zakeeruddin, A. Hagfeldt, M. Grä, M. Grä Tzel, *Joule* **2018**, *2*, 1108.
- [24] Y. Ren, D. Zhang, J. Suo, Y. Cao, F. T. Eickemeyer, N. Vlachopoulos, S. M. Zakeeruddin, A. Hagfeldt, M. Grätzel, *Nature* **2023**, *613*, 60.
- [25] S. M. Meethal, S. C. Pradhan, J. Velore, S. Varughese, R. S. Pillai, F. Sauvage, A. Hagfeldt, S. Soman, *J Mater Chem A* **2024**, *12*, 1081.
- [26] Q. Zhang, G. Cao, *Nano Today* **2011**, *6*, 91.
- [27] J. A. Anta, E. Guillén, R. Tena-Zaera, *J Phys Chem C* **2012**, *116*, 11413.
- [28] K. Keis, C. Bauer, G. Boschloo, A. Hagfeldt, K. Westermark, H. Rensmo, H. Siegbahn, *J Photochem Photobiol A Chem* **2002**, *148*, 57.
- [29] T. Ling, J. G. Song, X. Y. Chen, J. Yang, S. Z. Qiao, X. W. Du, *J Alloys Compd* **2013**, *546*, 307.
- [30] R. Vittal, K. C. Ho, *Renew Sustain Energy Rev* **2017**, *70*, 920.
- [31] C. Y. Lin, Y. H. Lai, H. W. Chen, J. G. Chen, C. W. Kung, R. Vittal, K. C. Ho, *Energy Environ Sci* **2011**, *4*, 3448.
- [32] R. Ruess, J. Horn, A. Ringleb, D. Schlettwein, *J Phys Chem C* **2019**, *123*, 22074.
- [33] E. Kouhestanian, S. A. Mozaffari, M. Ranjbar, H. S. Amoli, *Org Electron* **2020**, *86*, 105915.
- [34] A. Zatirostami, *Optik* **2020**, *207*, 164419.
- [35] M. E. Yeoh, K. Y. Chan, *J Electron Mater* **2019**, *48*, 4342.
- [36] A. K. Chandiran, M. Abdi-Jalebi, M. K. Nazeeruddin, M. Grätzel, *ACS Nano* **2014**, *8*, 2261.
- [37] E. Guillén, L. M. Peter, J. A. Anta, *J Phys Chem C* **2011**, *115*, 22622.
- [38] K. Keis, J. Lindgren, S. E. Lindquist, A. Hagfeldt, *Langmuir* **2000**, *16*, 4688.
- [39] L. Ke, S. Bin Dolmanan, L. Shen, P. K. Pallathadk, Z. Zhang, D. M. Ying Lai, H. Liu, *Sol. Energy Mater Sol Cells* **2010**, *94*, 323.
- [40] C. Kim, J. Kim, H. Choi, C. Nahm, S. Kang, S. Lee, B. Lee, B. Park, *J Power Sources* **2013**, *232*, 159.
- [41] S. Ghosh, R. Sartape, J. Chakraborty, *J Mater Sci: Mater Electron* **2020**, *31*, 2202.
- [42] M. Biçer, M. Gökçen, E. Orhan, *Opt Mater* **2022**, *131*, 112691.

- [43] V. Kadam, C. Jagtap, T. Alshahrani, P. Lokhande, A. Al-Ahmed, S. P. Patole, F. Khan, H. Pathan, *J Mater Sci: Mater Electron* **2023**, *34*, 1.
- [44] A. H. Javed, N. Shahzad, M. A. Khan, M. Ayub, N. Iqbal, M. Hassan, N. Hussain, M. I. Rameel, M. I. Shahzad, *Sol Energy* **2021**, *230*, 492.
- [45] Y. He, J. Hu, Y. Xie, *ChemComm* **2015**, *51*, 16229.
- [46] C. A. Gonzalez-Flores, D. Pourjafari, R. Escalante, E. J. Canto-Aguilar, A. V. Poot, J. M. Andres Castán, Y. Kervella, R. Demadrille, A. J. Riquelme, J. A. Anta, G. Oskam, *ACS Appl Energy Mater* **2022**, *5*, 14092.
- [47] S. Sasidharan, A. Jagadeesh, S. C. Pradhan, B. N. Nair, A. Azeez Peer Mohamed, K. N. Narayanan Unni, S. Soman, U. Nair Saraswathy Hareesh, *Sol Energy* **2021**, *226*, 214.
- [48] F. S. Husairi, S. M. Ali, A. Azlinda, M. Rusop, S. Abdullah, *J Nanomater* **2013**, *2013*.
- [49] M. Y. Nassar, M. M. Moustafa, M. M. Taha, *RSC Adv* **2016**, *6*, 42180.
- [50] P. Bindu, S. Thomas, *J. Theor. Appl. Phys.* **2014**, *8*, 123.
- [51] A. Koodziejczak-Radzimska, E. Markiewicz, T. Jesionowski, *J Nanomater* **2012**, *2012*.
- [52] M. Y. Nassar, M. M. Moustafa, M. M. Taha, *RSC Adv* **2016**, *6*, 42180.
- [53] Z. Liu, F. Teng, *ChemistrySelect* **2018**, *3*, 8886.
- [54] M. Shamsipur, S. M. Pourmortazavi, S. S. Hajimirsadeghi, M. M. Zahedi, M. Rahimi-Nasrabadi, *Ceram Int* **2013**, *39*, 819.
- [55] N. Jayarambabu, B. Siva Kumari, K. Venkateswara Rao, Y. T. Prabhu, *Int. J. Adv. Multidiscip. Res.* **2015**, *2*, 273.
- [56] M. U. Munshi, G. Berden, J. Martens, J. Oomens, *Phys. Chem. Chem. Phys.* **2017**, *19*, 19881.
- [57] Y. Wang, R. Ma, R. Xiao, L. Hao, Q. Wu, C. Wang, Z. Wang, *Microchimica Acta* **2018**, *185*, 1.
- [58] B. C. Smith, *Spectroscopy* **2016**, *31*, 36.
- [59] N. T. K. Thanh, N. Maclean, S. Mahiddine, *Chem Rev* **2014**, *114*, 7610.
- [60] Y. Lai, Y. Wang, S. Cheng, J. Yu, *J Electron Mater* **2014**, *43*, 2676.
- [61] R. Ahmad, N. Tripathy, M. Y. Khan, K. S. Bhat, M. S. Ahn, Y. B. Hahn, *RSC Adv* **2016**, *6*, 54836.
- [62] H. H. Kim, D. O. Kumi, K. Kim, D. Park, Y. Yi, S. H. Cho, C. Park, O. M. Ntwaeaborwa, W. K. Choi, *RSC Adv* **2019**, *9*, 32066.
- [63] S. Ilican, M. Caglar, S. Aksoy, Y. Caglar, *J Nanomater* **2016**, *2016*.
- [64] A. Sahai, N. Goswami, *Ceram Int* **2014**, *40*, 14569.
- [65] B. Philips-Invernizzi, D. Dupont, C. Caze, *Opt Eng* **2001**, *40*, 1082.
- [66] P. Makuła, M. Pacia, W. Macyk, *J Phys Chem Lett* **2018**, *9*, 6814.
- [67] M. Nowak, B. Kauch, P. Szperlich, *Rev Sci Instrum* **2009**, *80*, 46107.
- [68] V. Srikant, D. R. Clarke, *J Appl Phys* **1998**, *83*, 5447.
- [69] R. E. Marotti, D. N. Guerra, C. Bello, G. Machado, E. A. Dalchiele, *Sol Energy Mater Sol Cells* **2004**, *82*, 85.

- [70] R. Rusdi, A. A. Rahman, N. S. Mohamed, N. Kamarudin, N. Kamarulzaman, *Powder Technol* **2011**, *210*, 18.
- [71] P. Salvador, M. G. Hidalgo, A. Zaban, J. Bisquert, *J Phys Chem B* **2005**, *109*, 15915.
- [72] B. Van Der Zanden, A. Goossens, *J Phys Chem B* **2000**, *104*, 7171.
- [73] V. Thavasi, V. Renugopalakrishnan, R. Jose, S. Ramakrishna, *Mater Sci Eng, R* **2009**, *63*, 81.
- [74] D. Cahen, G. Hodes, M. Grätzel, J. F. Guillemoles, I. Riess, *J Phys Chem B* **2000**, *104*, 2053.
- [75] D. S. Park, H. Wang, S. K. Vasheghani Farahani, M. Walker, A. Bhatnagar, D. Seghier, C. J. Choi, J. H. Kang, C. F. McConville, *Sci Rep* **2016**, *6*, 1.
- [76] J. K. Salem, T. M. Hammad, R. R. Harrison, *J Mater Sci: Mater Electron* **2013**, *24*, 1670.
- [77] L. Saikia, D. Bhuyan, M. Saikia, B. Malakar, D. K. Dutta, P. Sengupta, *Appl Catal A Gen* **2015**, *490*, 42.
- [78] D. Wang, N. Reynolds, *ISRN Condens Matter Phys.* **2012**, *2012*, 1.
- [79] X. Li, Y. Tu, S. Pace, U. Anselmi-Tamburini, J. Briscoe, *J Phys D Appl Phys* **2021**, *54*, 255107.
- [80] H. Zhao, Q. Jing, Q. Wu, J. Hou, H. Cao, R. Wu, Z. Liu, *Sci China Mater* **2017**, *60*, 239.
- [81] Y. Mizuno, F. K. King, Y. Yamauchi, T. Homma, A. Tanaka, Y. Takakuwa, T. Momose, *J Vac Sci Technol A* **2002**, *20*, 1716.
- [82] L. Zhu, Q. Lu, L. Lv, Y. Wang, Y. Hu, Z. Deng, Z. Lou, Y. Hou, F. Teng, *RSC Adv* **2017**, *7*, 20084.
- [83] T. Pauporté, C. Magne, *Thin Solid Films* **2014**, *560*, 20.

Addressing mass transport issue in copper electrolyte based dye-sensitized photovoltaic cells using surface textured photoanodes



Abstract: Owing to their better scattering properties, surface textured TiO₂ films were previously reported to be successfully implemented as photoanodes in iodine electrolyte based dye-sensitized photovoltaic cells (DSCs), leading to enhanced charge collection and short circuit current density (J_{sc}), thereby achieving better performance both under outdoor as well as indoor illumination conditions. In the present chapter, we adopted a similar strategy to fabricate surface textured TiO₂ photoanodes by using ZnO micro-particles as a template layer. The resultant photoanode when employed in DSC, in conjugation with a copper complex based redox shuttle, which is mass transport limited, could deliver better photovoltaic performance comparative to the standard TiO₂ photoanode based DSC. The better performance of DSCs utilizing surface textured photoanode is predominantly related to the improvement in J_{sc} owing to reduced mass transport limitation and faster charge collection. Additionally, the presence of trace amounts of ZnO within the surface textured TiO₂ layer not only hindered charge recombination but also induced a negative shift in the TiO₂ conduction band leading to improved open circuit potential (V_{oc}).

2B.1. Introduction

Numerous photoanode engineering strategies are being adopted extensively for improving the performance of dye-sensitized photovoltaic cells (DSCs). This includes photoanode modifications to enhance light harvesting properties by improving surface area for dye loading using hierarchical nanostructures.^[1-6] Another strategy for amplifying the light harvesting involves improving light scattering properties of DSC photoanode with the inclusion of scattering particles, plasmonic nanoparticles, voids, surface roughness etc.^[7-13] The energy bands of the semiconductor material used as photoanode could be tuned and the surface traps, like oxygen vacancies could be compensated by doping various ions, thereby improving the interfacial charge transfer properties within DSCs.^[14-20] Nanocomposites of various semiconductors, or those of semiconductors with carbonaceous materials, like graphene, reduced graphene oxide, carbon nanotubes etc., were also employed as DSC photoanode for faster electron transport and reduced charge recombination.^[21-30] Another method of photoanode engineering for improving DSC performance was done by deposition of blocking layers to suppress back transfer of electrons.^[31-37] Currently, co-sensitization strategy and surface treatments using organic molecules are being adopted to achieve better dye coverage on the semiconductor surface, thereby improving both light harvesting as well as suppressing the recombination process, leading to better device performance.^[38-41]

Majority of the works based on photoanode modifications in DSCs were carried out using conventional iodine electrolyte. Presently, metal complex based redox shuttles, like copper (Cu(II/I)) and cobalt (Co(III/II)) redox mediators, are gaining more importance in the form of electrolytes for DSCs, owing to their advantages like abundance, less corrosive nature, more positive redox potential, reduced over potential loss for dye regeneration, compatibility with organic sensitizers etc., compared to the conventional iodine based electrolyte system. Among these alternative redox shuttles, copper complex based mediators are more prominent for DSCs considering its environment friendly nature, reduced cost, lower toxicity, faster diffusion, positive redox potentials, and lower recombination kinetics compared to the cobalt systems which were used before.^[42,43] Because of the lower reorganization energy and faster electron transfer kinetics in case of the Cu(II/I) electrolytes, only very small driving force (even < 0.1 eV) is sufficient for effective dye regeneration. Hence, even though the Cu(II/I) electrolyte has a positive redox potential close to the HOMO level of most of the sensitizers, the regeneration efficiency is

close to 100%.^[38,44] The more positive redox potential enables Cu(II/I) electrolyte based DSCs to achieve better photovoltage when compared to conventional iodine electrolyte and Co(III/II) electrolyte based DSCs. Also the less bulky nature of copper species being four coordinate species in comparison to cobalt species which is six coordinate, enables Cu(II/I) electrolyte to achieve better current density when compared to Co(III/II) electrolyte based devices, accounting for the lower mass transport issues associated with the former.^[45] Consequently, the copper electrolyte based DSCs could outclass the other redox shuttles, paving way for a new generation of DSCs with remarkable performances not only under outdoor, but also under indoor illumination conditions.^[45-47] Majority of the recent reports on DSCs realizing remarkable PV performances with open circuit voltage (V_{oc}) above 1V and PCE surpassing 10% under simulated one sun irradiation (AM 1.5G, 100 mW/cm²), use Cu(II/I) redox mediators along with organic sensitizers.^[39,47-49] Nonetheless, the Cu(II/I) redox electrolyte still suffer from mass transport issues, which limits them from attaining the maximum possible short circuit current densities (J_{sc}) and power conversion efficiencies (PCE).^[50]

Previously, we have successfully demonstrated a novel surface texturing technique to improve light harvesting efficiency of TiO₂ photoanodes using ZnO sacrificial layers, in order to elevate the PCE of iodine electrolyte base DSCs.^[12,51] In this chapter, we adopted the similar surface engineering strategy for developing DSC photoanodes in order to attain appreciable light scattering effects without increasing the TiO₂ layer thickness. The surface texturing was carried out using ZnO microparticles as templates. The surface roughness, diffuse reflectance and light harvesting properties of the surface textured TiO₂ film (T-Z) was compared to that of unmodified TiO₂ film (T). The surface textured film was employed as photoanode in DSC along with copper electrolyte and the interfacial charge transfer within the film was analyzed by advanced characterization techniques like impedance spectroscopy, transient photocurrent/voltage decay measurements and so on. The influence of the surface textured TiO₂ layer on the mass transport of electrolyte species in DSC, at various light intensities was also investigated in detail.

2B.2. Experimental procedures

2B.2.1. Surface texturing of TiO₂ photoanodes using ZnO microstructure as templates

ZnO hierarchical microspheres were synthesized as described in **Chapter 2A** (section **2A.2.1**) to be utilized as templates for creating roughness on the surface of TiO₂ nanoporous layer. Briefly, 0.02 M aqueous solution of zinc nitrate hexahydrate (Merck)

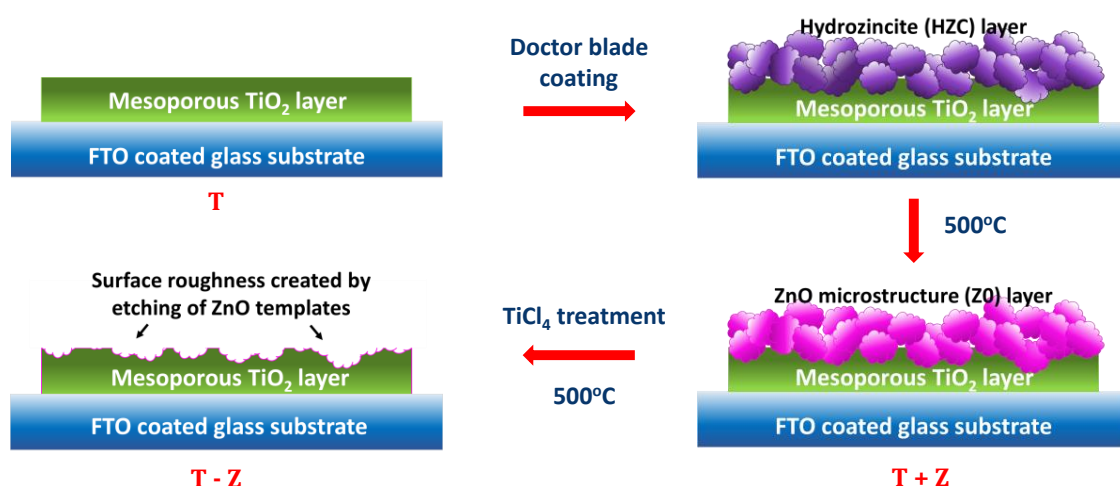


Figure 2B.1. Schematic illustration of the fabrication of surface textured TiO₂ (T-Z) photoanode.

was added dropwise into 1.0 M aqueous solution of urea (Merck) under constant stirring. The reaction mixture was stirred at 1000 rpm for one hour at room temperature, and then heated at 90 °C for 24 hours. The white precipitate of hydroxide zinc carbonate or hydrozincite (HZC) obtained after the reaction was then washed with DI water and ethanol and vacuum dried at 60 °C for 12 hours. The as-synthesized HZC sample was converted to paste by adding a mixture of ethyl cellulose and terpineol heated at 100 °C and grinding in a mortar (as described in section 2A.2.2). The FTO substrates (TEC 10, Merck) cut into required dimensions, 1.6 cm x 1.6 cm, were cleaned using detergent solution, distilled water, acetone and isopropanol, in an ultrasonic bath. TiO₂ pre-blocking layers were deposited by a 50 mM TiCl₄ treatment at 70 °C for 30 minutes. The substrates were then annealed at 500 °C for 30 min by following a step-wise heating programme. The active layer (AL) was deposited on the FTO plate using the commercial TiO₂ paste (18-NRT, GreatcellSolar, Australia). The photoanode using unmodified or bare TiO₂ active layer (without surface texturing) is designated as T, hereafter. The standard TiO₂ photoanode (designated as Std) is constructed by depositing a scattering layer (SL) of commercial 18NR-AO paste (GreatcellSolar, Australia), consisting of larger TiO₂ particles over the TiO₂ AL. Hence, the Std photoanode is an AL/SL bilayer photoanode constituted by an AL containing ~ 20 nm TiO₂ particles and an SL made up of ~ 400 nm TiO₂ particles. For fabricating the surface textured TiO₂ photoanodes, initially a TiO₂/ZnO bilayer photoanode (labelled as T+Z) is prepared by coating the HZC paste over the TiO₂ active layer (**Figure 2B.1**). All the above-mentioned depositions were done using blade coating method. After

depositing these semiconductor layers, the substrate is subjected to programmed annealing up to 500 °C for 30 min. The next step in the photoanode fabrication process is the TiCl₄ treatment, wherein the FTO plates coated with the semiconductor oxides are immersed in a 40 mM aqueous solution of TiCl₄ and heated at 70 °C for 30 minutes. In case of the T and Std photoanodes, the TiCl₄ post treatment deposits a compact TiO₂ blocking layer over the mesoporous semiconducting layer. However, carrying out TiCl₄ post treatment on the TiO₂/ZnO bilayer photoanode (T+Z), etches off the ZnO particles in the over layer, in addition to blocking layer deposition. This leaves behind a surface textured TiO₂ photoanode, which is named as T-Z hereafter. Finally, after the deposition of all the semiconducting layers, the photoanodes were annealed in a step wise manner up to 500 °C.

2B.2.2. Characterization of the TiO₂ photoanodes

The surface morphology, thickness and ZnO content in different photoanodes were analyzed using scanning electron microscope (SEM) images and energy dispersive X-ray (EDX) spectra acquired by Zeiss EVO 18 cryo-SEM Special Ed (Carl Zeiss, Germany). The elemental compositions of different photoanodes were confirmed using X-ray Photoelectron Spectroscopy (XPS, SPECS Surface Nano Analysis GmbH, Germany), using a monochromatic source, Al-K α (1486.7 eV and 350 W), with a beam diameter of 1 mm. The XPS spectrum was recorded using SpecsLab2 software and MultiPak spectrum software was used to fit the obtained XPS peaks. The thickness and surface roughness of different photoanode samples were measured using a Bruker Dektak XT profilometer. The surface roughness of different films were compared using atomic force microscopy (AFM) as well. The AFM images were acquired using an AFM-Bruker Multitop Nanoscope V instrument operating under tapping mode. The surface roughness of the TiO₂ layers were calculated from the corresponding AFM images, using Nanoscope Analysis 1.5 software. The scattering properties of the photoanode films were studied from their diffuse reflectance spectra (DRS) acquired using UV-visible spectrophotometer (Shimadzu, UV-2700i) with an integrating sphere. The light absorbance of the various photoanodes after dye sensitization were also determined using Shimadzu UV-visible spectrophotometer (UV-2700i). The amount of dye adsorbed per unit area of the various photoanode layers were determined as described in **section 2A.2.2**, using the equation 2A.1. For this, the absorbance of the dye solution (0.01 mM) before and after photoanode immersion was obtained using the UV-visible spectrometer (Shimadzu model 2100).

2B.2.3. DSC fabrication and characterization

The different TiO₂ photoanodes prepared in the previous **section 2B.2.1** were used for fabricating DSCs as described below. The photoanodes were immersed in a dye solution containing 0.1 mM Y123 dye and kept in darkness for 16 hours, to obtain the dye-sensitized photoanodes. The counter electrodes were prepared by coating poly(3,4-ethylenedioxythiophene) (PEDOT) on cleaned FTO substrates (TEC7, GreatcellSolar, Australia) with pre-drilled holes, by electro-polymerization of ethylene dioxythiophene (EDOT, Merck), along with the surfactant sodium dodecyl sulphate (SDS, Sigma Aldrich). The photoanodes and corresponding counter electrodes were assembled using a 25 μm thick thermoplastic spacer (Surlyn, GreatcellSolar), using hot pressing (at 120 °C) method. The inter-electrode gap was filled with the copper electrolyte, made up of 0.2 M bis(2,9-dimethyl-1,10-phenanthroline copper(I)bis(trifluoromethanesulfonyl)imide ([Cu(dmp)₂]¹⁺, Dyenamo A.B, Sweden) and 0.04 M bis(2,9-dimethyl-1,10-phenanthroline copper(II)bis(trifluoro methanesulfonyl)imide chloride ([Cu(dmp)₂]²⁺, Dyenamo A.B, Sweden), 0.1 M Bis(trifluoro methane)sulfonimide lithium salt (LiTFSI, Merck) and 0.6 M 4-tert-butylpyridine (TBP, Merck), in acetonitrile solvent (Merck). Finally, the holes in the counter electrode were sealed using a thermoplastic sealant and glass slide to avoid electrolyte leakage and solvent evaporation.

The photovoltaic performance of the fabricated DSCs were evaluated using photocurrent-voltage (*J-V*) measurements and incident photon-to-current conversion efficiency (*IPCE*) measurements. *J-V* characterization under one sun condition (100 mW/cm², AM 1.5G) was done using class AAA solar simulator (Oriel 3A, Model PVIV-94043A, Newport) coupled with a source meter (Keithley 2440). The intensity of the simulated light was calibrated using a certified reference silicon solar cell (Newport) coupled with a power meter (Newport). The *IPCE* measurements were carried out using a 250 W Xenon lamp as light source along with a monochromator set-up (Newport). The performance of the device under indoor light conditions was studied by carrying out the *J-V* measurement using the AE05 potentiostat (Dyenamo AB, Sweden) in a custom-made set up with a daylight compact fluorescent lamp, CFL (Osram, 14W/6500K) as light source. The irradiance intensity of these indoor light sources were calibrated using a highly sensitive photodetector coupled with a UV-vis-NIR spectrometer (Ocean optics, DH-2000-BAL). The interfacial charge transfer studies of the devices were carried out using advanced characterization techniques such as open circuit voltage decay (OCVD), charge

extraction (CE), transient photovoltage decay (TVD) and photocurrent decay (TCD), intensity modulated photovoltage spectroscopy (IMVS), intensity modulated photocurrent spectroscopy (IMPS), and electrochemical impedance spectroscopy (EIS) measurements. OCVD measurements were done using the electrochemical workstation (Autolab-PGSTAT 302N, Metrohm) with a white LED as illumination source. EIS, IMVS and IMPS were performed using the Autolab-PGSTAT 302N coupled with a Frequency Response Analyzer (FRA32M). The CE, TVD and TCD measurements were carried out using Toolbox setup (Dyename AB, Sweden). Mott-Schottky (MS) plots were obtained from the impedance spectra (acquired using a Biologic electrochemical workstation (VMP3), in the frequency range 100 Hz to 100 KHz) of the devices fabricated with unsensitized photoanodes, along with PEDOT counter electrode and $[\text{Cu}(\text{dmp})_2]^{2+/+}$ electrolyte.

2B.3. Results and discussions

2B.3.1. Characterization of surface textured TiO_2 photoanode

(a) *Effect of surface texturing on light harvesting efficiency of TiO_2 photoanode.* The light harvesting efficiency (*LHE*) is a property of the dye-sensitized photoanode film,

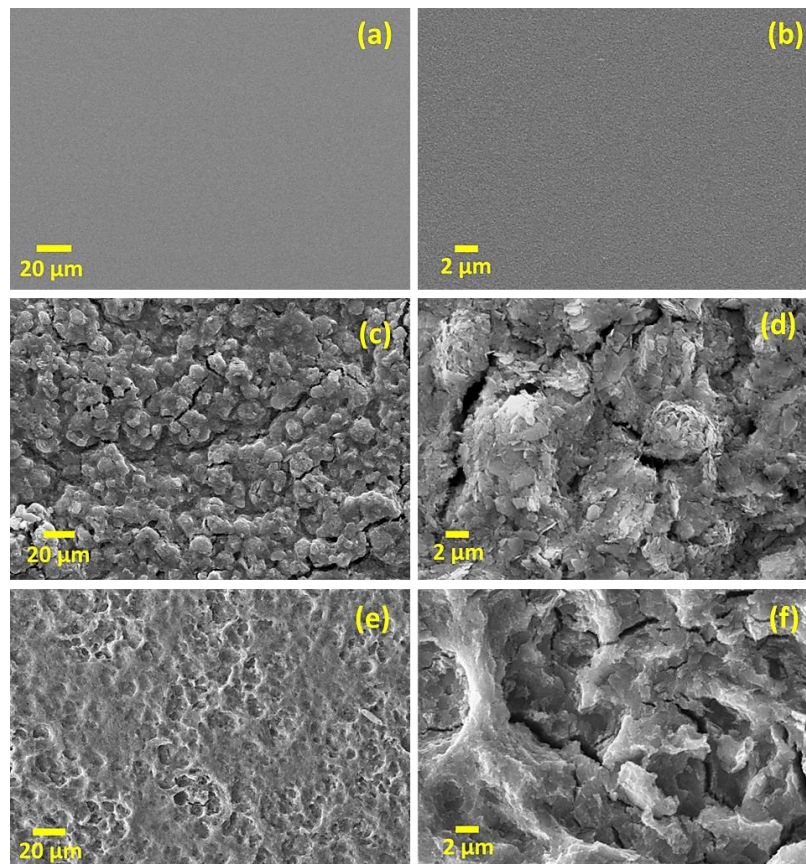


Figure 2B.2. SEM images of surface morphology of (a,b) unmodified TiO_2 photoanode (T), (c,d) TiO_2/ZnO bilayer (T+Z), and (e,f) surface textured TiO_2 photoanode (T-Z).

which describes how efficiently the photoanode absorbs the incident light. It is determined by various factors like thickness of the semiconducting layer, amount of dye adsorbed on the semiconductor, absorption coefficient, absorption profile of the adsorbed dye molecules, and path length of light within the active layer which can be increased by inclusion of scattering entities like scattering particles, voids, surface roughness, etc. The present work involves surface engineering of TiO_2 photoanodes for improving their scattering property, thereby enhancing the *LHE*. The schematic diagram for the preparation of surface textured photoanodes (T-Z) is provided in **Figure 2B.1**. The SEM micrographs showing the surface morphology of different semiconductor layers, T, T+Z and T-Z, coated over the FTO substrates are given in **Figure 2B.2**. **Figure 2B.2(a,b)** shows the smooth surface of the bare TiO_2 film, T, while the surface of the T+Z film (**Figure 2B.2(c,d)**) reveals the ZnO microsphere aggregates over the TiO_2 layer. The SEM image of the T-Z film, given in **Figure 2B.2(e,f)**, displays TiO_2 film surface with grooves/imprints created by etching off ZnO microspheres from the T+Z film. This makes the TiO_2 surface of the T-Z film rougher when compared to the T film. The improvement in roughness of the TiO_2 films after surface treatment was validated using the profilometer and AFM techniques. The root means square roughness (R_q) of the unmodified (T) and surface textured (T-Z)

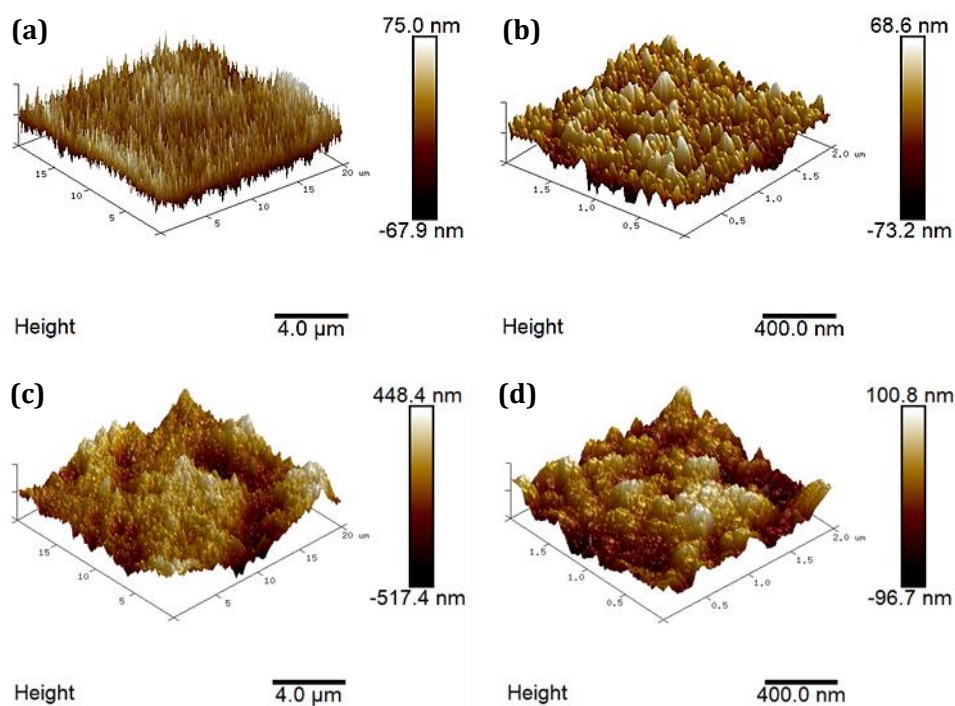


Figure 2B.3. AFM images of surface of (a,b) unmodified TiO_2 (T) photoanode and (c,d) surface textured TiO_2 (T-Z) photoanode.

TiO₂ films estimated using profilometer, with a scan length of 1600 μm, is listed in **Table 2B.1**. The three dimensional surface profiles of the T and T-Z films acquired using AFM is provided in **Figure 2B.3**. The R_q of the films were determined from the AFM profiles, for different scan areas (*viz.* 2 μm × 2 μm and 20 μm × 20 μm), and the corresponding values are listed in **Table 2B.1**. It is observed that there was a considerable improvement in R_q of the films after surface texturing.

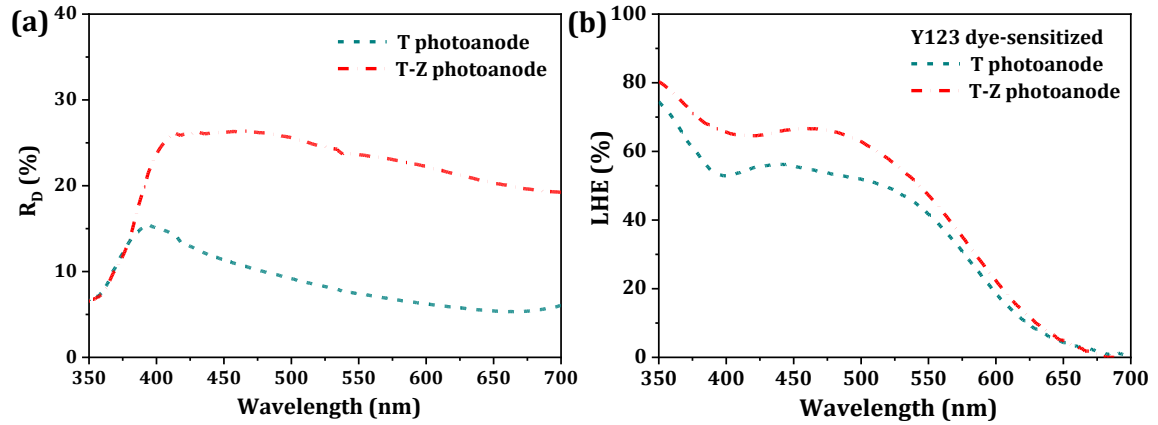


Figure 2B.4. (a) Diffuse reflectance (R_D), and (b) Light harvesting efficiency (LHE) of unmodified (T) and surface textured (T-Z) TiO₂ photoanodes as a function of wavelength.

Table 2B.1. The roughness (R_q), diffuse reflectance (R_D), dye loading and light harvesting efficiency (LHE) of unmodified (T) and surface textured (T-Z) TiO₂ photoanode films.

Photo-anode	Thickness ^a (μm)	Dye loading (x10 ⁻⁸ mol /cm ²)	Root means square roughness		R_D at 475 nm (%)	LHE at 475 nm (%)
			R_q^a (nm)	R_q^b (nm)		
T	6.7	2.6	64	20.1 (19.8)	10.2	53.8
T-Z	6.4	2.5	189	135.0 (29.5)	26.2	66.1

^a Obtained from profilometer measurement over a scan length of 1600 μm.

^b Obtained from AFM analysis over a scan area of 20 μm × 20 μm (and a scan area of 2 μm × 2 μm in parathesis).

The improved surface roughness of T-Z films was advantageous for attaining better light scattering properties for these surface modified films. This could be observed from the DRS of the un-sensitized films given in **Figure 2B.4(a)**. When compared to the bare TiO₂ layer, the surface textured TiO₂ layer displayed more than 2.5 times improvement in diffuse reflectance (R_D), at a wavelength of 475 nm, corresponding to the maximum absorption wavelength (λ_{max}) of the standard Y123 organic dye. The dye loading of the

Y123 sensitized T and T-Z layers were found to be almost similar, as given in **Table 2B.1**, since they have similar layer thickness. The absorbance of the Y123 sensitized films was obtained and utilized for determining their *LHE* in the visible range, using the equation 1.3 (**Chapter 1**), which was then plotted against the wavelength as given in **Figure 2B.4(b)**. The *LHE* of the surface textured TiO₂ photoanode was found to be better when compared to the unmodified one, though both of them exhibited similar dye loading using the same dye. Hence, the improvement in *LHE* of TiO₂ photoanodes after surface texturing could be attributed to its improved light scattering owing to higher surface roughness.

(b) Presence of ZnO in surface textured TiO₂ photoanodes. During the TiCl₄ post-treatment, the bilayer photoanode (T+Z) is immersed in the TiCl₄ solution and heated at 70 °C. During this process, the ZnO over layer undergoes degradation and gets etched off from the TiO₂ surface leaving imprints or grooves which lead to enhanced TiO₂ surface

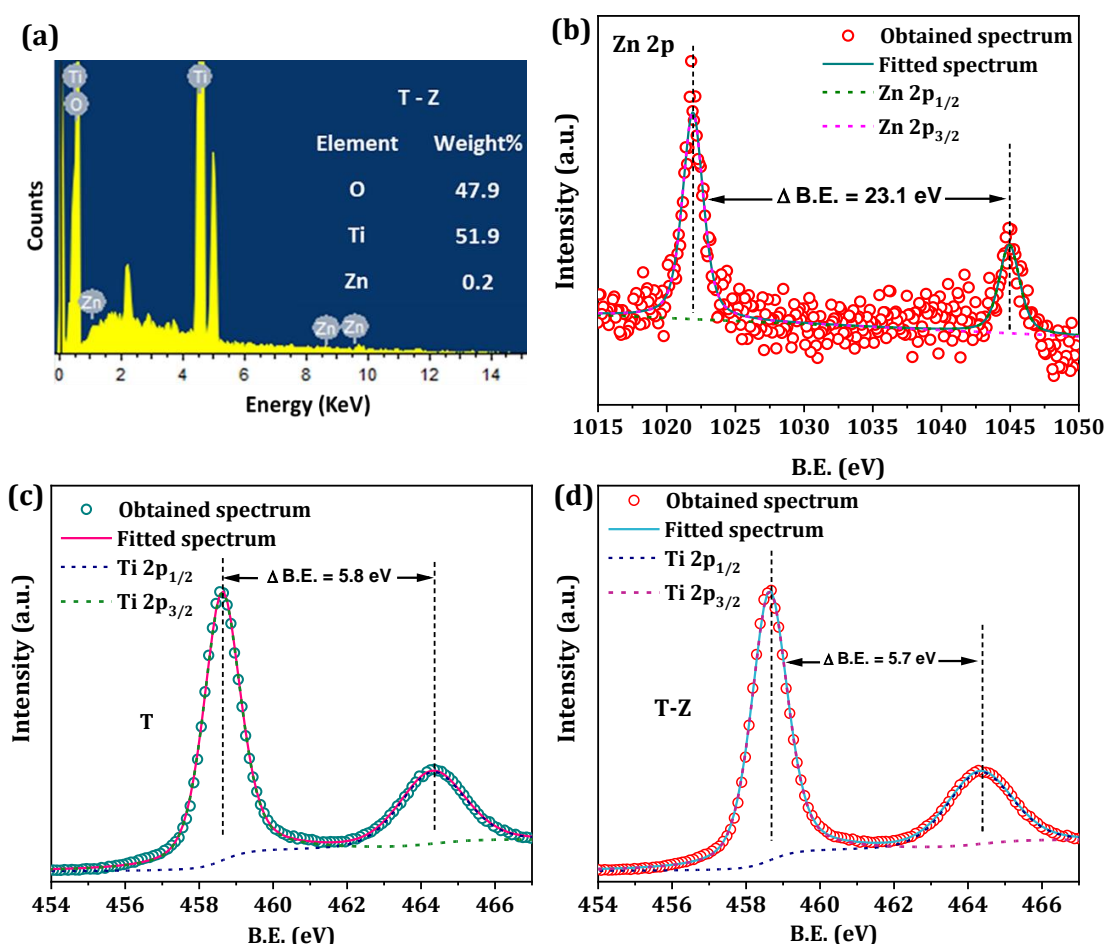


Figure 2B.5. (a) Energy dispersive X-ray (EDX) spectra; X-ray photoelectron spectroscopy (XPS) peak corresponding to (b) Zn 2p energy levels of T-Z photoanode, (c) Ti 2p energy levels of T photoanode, and (d) Ti 2p energy levels of T-Z photoanode.

roughness. Moreover, the TiCl_4 treatment deposits a compact TiO_2 blocking layer over the mesoporous TiO_2 layer, which passivates the surface trap states in the nanoporous network.^[31] In addition to these, another possible mechanism that can happen during the TiCl_4 post treatment of T+Z photoanode is that the Zn^{2+} ions generated by the degradation of ZnO may intercalate into the mesoporous matrix of the TiO_2 photoanode and get deposited as ZnO during the post annealing process (500 °C), along with the TiO_2 post-blocking layer. The presence of ZnO in the surface textured T-Z films, obtained as a result of TiCl_4 treatment of T+Z films, was verified using EDX and XPS measurements. The EDX spectra (**Figure 2B.5(a)**) of T-Z photoanode shows the presence of small amounts of Zn (0.2 wt%), in addition to elemental Ti and O. XPS spectra given in **Figure 2B.5(b)**, also shows two less intense, but specific peaks at binding energies (B.E.) 1021.78 eV and 1044.88 eV, corresponding to Zn $2p_{3/2}$ and Zn $2p_{1/2}$ states, with a separation of ~23.1 eV, which indicate the presence of ZnO in the T-Z films, even after the etching process.^[52,53] The XPS peaks corresponding to the Ti 2p core levels for the T and T-Z films are given in **Figure 2B.5(c,d)**, which are in agreement with the previous reports for TiO_2 .^[54] The Ti $2P_{3/2}$ peaks for T and T-Z photoanodes are respectively present at the B.E. 458.55 eV and 458.68 eV. The 0.13 eV shift in the Ti $2P_{3/2}$ peak of the T-Z film, towards the higher B.E. could be attributed to the presence of ZnO.^[55]

2B.3.2. Effect of surface textured TiO_2 photoanodes on the DSC performance

(a) Basic photovoltaic and mass transport studies. The photovoltaic (PV) performance of copper electrolyte ($[\text{Cu}(\text{dmp})_2]^{2+/+}$) based DSCs fabricated using Y123 sensitized surface textured TiO_2 photoanode (T-Z photoanode depicted in **Figure 2B.6(a)**) was analyzed under standard simulated one sun irradiation (AM 1.5G, 100 mW/cm^2). The J - V parameters of T-Z devices were compared to that of DSCs prepared using standard TiO_2 photoanode (Std photoanode depicted in **Figure 2B.6(b)**), constituting the AL/SL bilayer structure, sensitized with Y123 dye along with $[\text{Cu}(\text{dmp})_2]^{2+/+}$ electrolyte. The corresponding J - V curves are shown in **Figure 2B.6(c)**. The PV parameters of the champion devices along with the average and error taken for three devices of similar architecture, are listed in **Table 2B.2**. The best T-Z based device delivered a PCE of 8.04%, with a V_{OC} , J_{SC} , and fill factor (FF) of 1.04 V, 12.27 mA/cm^2 , and 63%, respectively. On the other hand, the best Std device could only deliver a PCE of 6.81%, with a V_{OC} of 0.97 V, J_{SC} of 11.70 mA/cm^2 , and FF of 60%. The lower performance of the Std device when compared to the T-Z device can be directly correlated to its lower V_{OC} and J_{SC} .

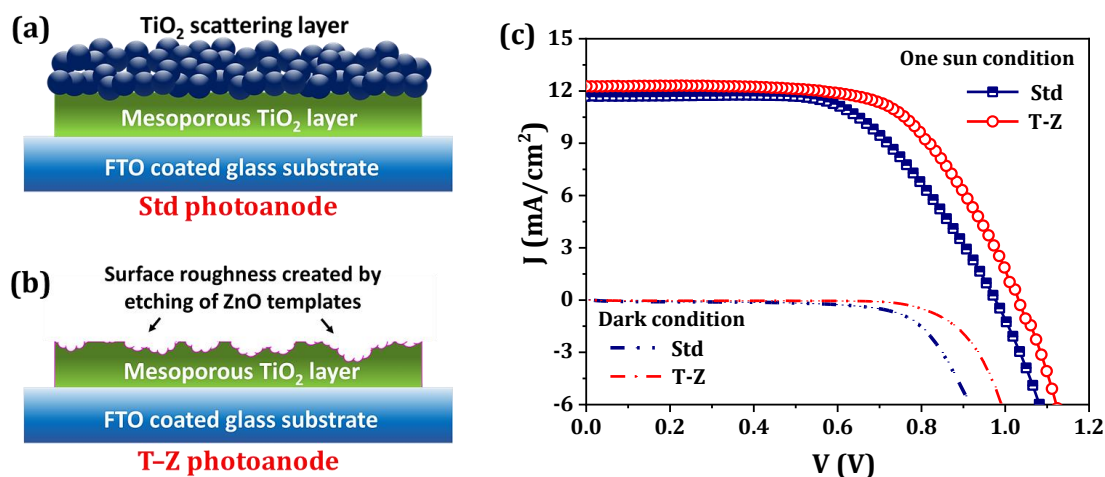


Figure 2B.6. The schematic representation of structure of (a) standard bilayer TiO₂ photoanode (Std) and (b) surface textured TiO₂ photoanode (T-Z); (c) J - V characteristic curves of DSCs utilizing Y123 sensitized Std and T-Z photoanodes, along with [Cu(dmp)₂]^{2+/+} redox mediator, under one sun condition and under dark.

Table 2B.2. Photovoltaic parameters of the DSCs employing standard bilayer (Std) and surface textured (T-Z) TiO₂ photoanodes using Y123 dye and [Cu(dmp)₂]^{2+/+} electrolyte.

Device Code	V_{OC}^a (V)	J_{sc}^a (mA/cm ²)	FF^a	PCE^a (%)	$J_{integrated}^b$ (mA/cm ²)
Std	0.97 (0.96 ± 0.01)	11.70 (10.84 ± 0.76)	0.60 (0.61 ± 0.01)	6.81 (6.39 ± 0.39)	12.3
T-Z	1.04 (1.03 ± 0.02)	12.27 (12.19 ± 0.20)	0.63 (0.61 ± 0.01)	8.04 (7.68 ± 0.24)	12.5

^aObtained from J - V characterization of 3 devices under one sun condition. The parameters corresponding to the champion cell are provided, along with the average value ± standard deviation in the parentheses.

^bObtained by integration of IPCE spectra.

The J - V curves obtained under dark condition reveals that the Std device exhibits higher dark current when compared to T-Z device, which indicates lower shunt resistance offered by the Std device. This might be due to the higher layer thickness of the Std photoanode giving rise to more recombination sites, which is reflected in the lower V_{OC} of Std device. To attain further insight into the difference in PV parameters, the dye loading, R_D and LHE of the T-Z photoanodes were compared to those of Std photoanode. It was found that the Std photoanode with higher layer thickness (~ 10.4 μm), as observed from the cross-sectional SEM images (**Figure 2B.7(a,b)**), could adsorb more amount of dye molecules

(3.2×10^{-8} mol/cm²) compared to the T-Z film (2.5×10^{-8} mol/cm²). Also, owing to the presence of overlayer with larger sized scattering particles, the Std photoanode possessed better R_D ($\sim 43.7\%$ at 475 nm) as well (**Figure 2B.7(c)**). Taking into account of its better dye loading and light scattering properties, the Std photoanode could achieve better LHE in the visible region ($\sim 81.3\%$ at 475 nm), compared to the T-Z photoanode (**Figure 2B.7(d)**). The LHE of Y123 sensitized Std photoanode was found to be $\sim 23\%$ higher than that of T-Z, at the wavelength of 475nm (where Y123 dye has its maximum absorbance). Yet, the J_{SC} of Std device under one sun irradiation is observed to be lower than that of T-Z device. This could be attributed to the higher mass transport limitation in Std device while used with copper metal complex redox mediators, as a result of the higher layer thickness of the Std TiO₂ photoanode, which consists of a scattering layer in addition to the active layer. Whereas, in case of T-Z photoanode, only one layer of surface textured TiO₂ is present, as a result of which the mass transport issues are significantly reduced.

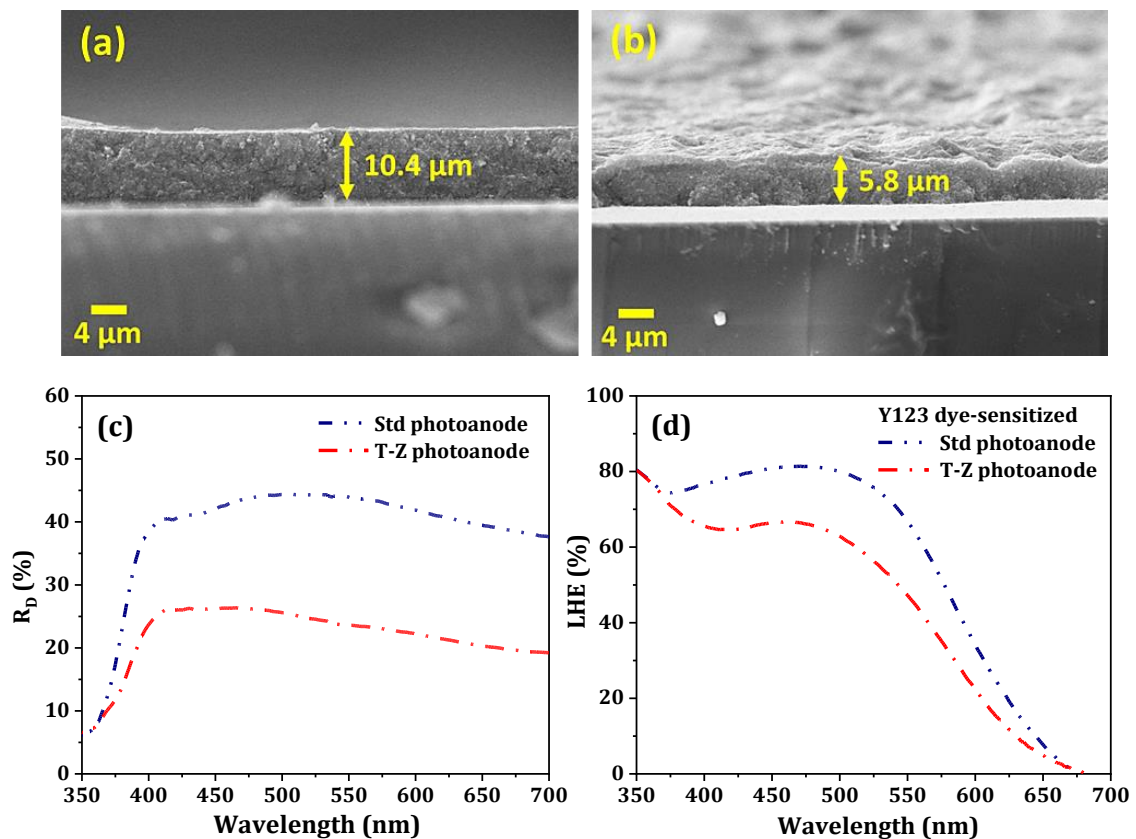


Figure 2B.7. Cross-sectional SEM images of (a) standard (Std) and (b) surface textured (T-Z) TiO₂ photoanodes. The plot of (c) diffuse reflectance (R_D), and (d) light harvesting efficiency (LHE) of Std and T-Z photoanodes as a function of wavelength.

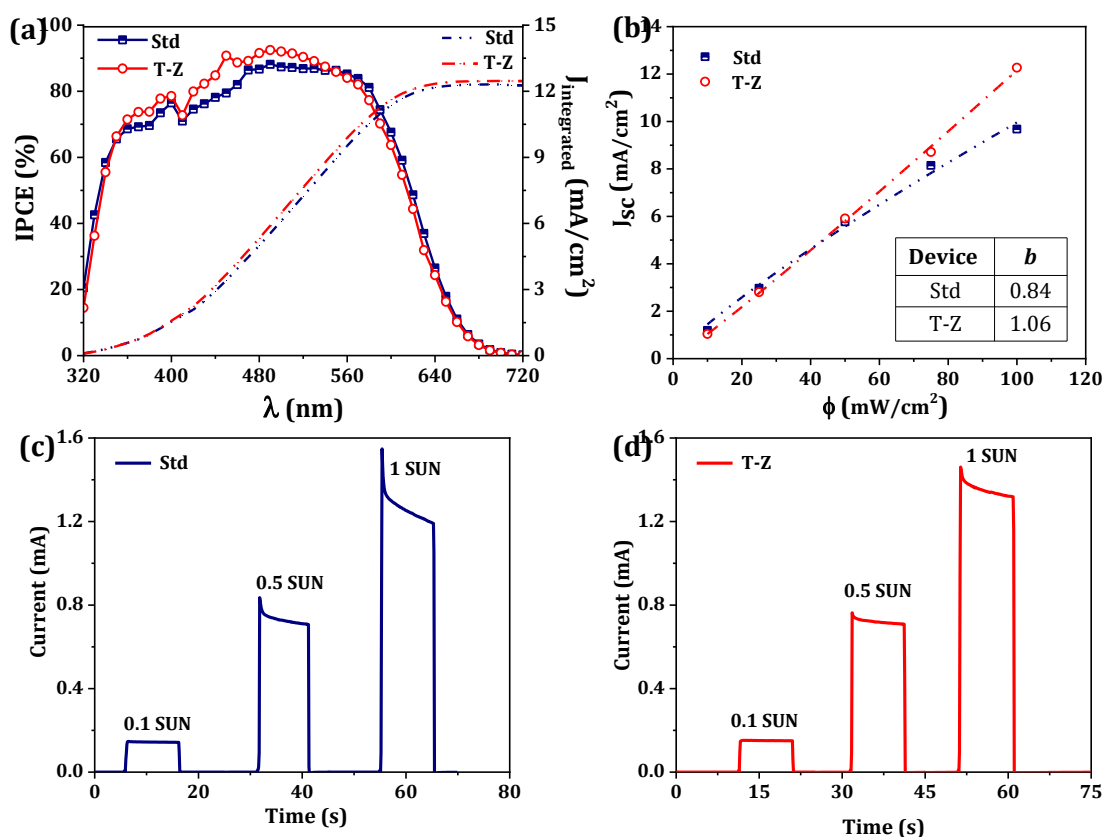


Figure 2B.8. (a) *IPCE* spectra and (b) J_{SC} versus light intensity plot, and (c,d) current transient (CT) plots of DSCs employing Y123 sensitized standard (Std) and surface textured (T-Z) TiO₂ photoanodes, along with [Cu(dmp)₂]^{2+/+} redox mediator.

The mass transport issue in Std device can be further verified using *IPCE* spectra (Figure 2B.8(a)). The theoretical values of J_{SC} for the DSCs, obtained by integration of the corresponding *IPCE* spectra, are tabulated in Table 2B.2. It is found that the theoretical J_{SC} for the T-Z device was matching with the J_{SC} obtained under one sun condition, however, the theoretical J_{SC} of Std device is lower than that obtained under one sun condition. This mismatch between the J_{SC} acquired from *J-V* measurement and that obtained by integrating *IPCE* spectra can be attributed to the mass transport limitations exhibited by the copper electrolyte based DSCs using thicker Std photoanode.^[50] Since the *IPCE* measurements are done under lower intensity monochromatic light illumination, the mass transport problem in the Std device becomes insignificant, whereas it overpowers at one sun irradiation causing a discrepancy in the obtained J_{SC} . The mass transport limitation in Std device is also obvious from the J_{SC} vs. light intensity (ϕ) plots (Figure 2B.8(b)). The J_{SC} vs. ϕ plots are fitted using the equation,

$$J_{SC} = a\phi^b \quad (2B.1)$$

where a and b are constants. In ideal systems free from mass transport limitations, the value of b is unity, signifying a linear relationship between J_{SC} and ϕ . However, in our case, since the copper redox electrolyte based DSCs are mass transport limited, the value of b deviates from unity, for both the devices. The b value for Std photoanode based DSC deviates more from ideal value of unity, compared to the T-Z device (inset, **Figure 2B.8(b)**). The mass transport in Std and T-Z devices can also be compared using the current transient (CT) curves (**Figure 2B.8(c,d)**). Clearly, the rate of reduction in current density is lesser in case of T-Z device, symbolizing lower mass transport limitation. All these observations confirm that the surface textured TiO₂ photoanode (T-Z) is more suitable to be employed in DSCs using diffusion limited new generation metal complex electrolytes. Moreover, the *PCE* of the T-Z device observed to be stable even after a shelf-life of ~ 600 hrs (**Figure 2B.9(a)**).

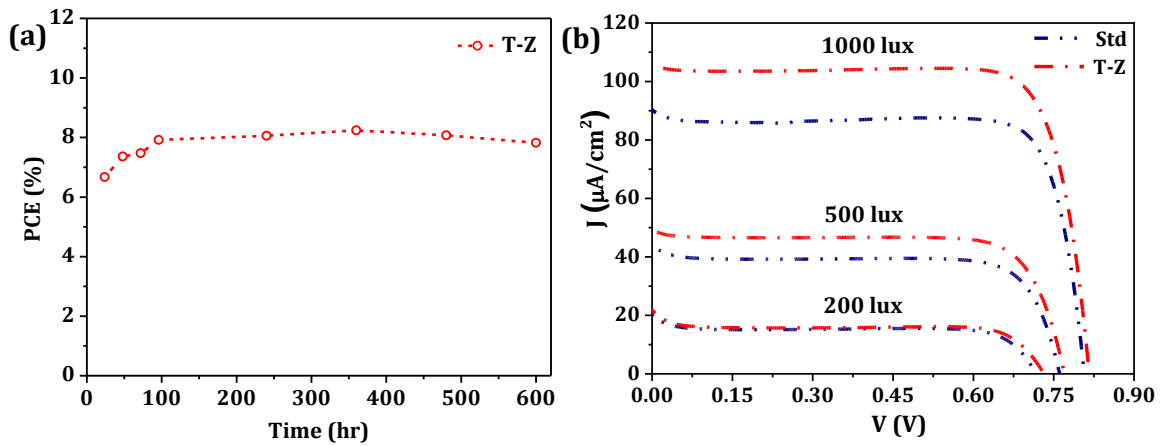


Figure 2B.9. (a) Stability curve under one sun condition, and (b) The $J-V$ characteristic curves under different indoor light (CFL) illuminations, for DSCs employing Y123 sensitized standard bilayer (Std) photoanode and surface textured (T-Z) TiO₂ photoanode, along with $[\text{Cu}(\text{dmp})_2]^{2+/+}$ electrolyte.

The PV performance of the Std and T-Z devices were evaluated under indoor light conditions as well (**Figure 2B.9(b)** and **Table 2B.3**). Under 1000 lux CFL illumination, the best Std device exhibited a V_{OC} of 0.80 V, J_{SC} of 90.1 $\mu\text{A}/\text{cm}^2$, FF of 79%, PCE of 18.6% and a maximum output power density (P_{max}) of 57.1 $\mu\text{W}/\text{cm}^2$, whereas the best T-Z device delivered a V_{OC} of 0.82 V, J_{SC} of 105.7 $\mu\text{A}/\text{cm}^2$, FF of 79%, PCE of 22.3% and P_{max} of 68.2 $\mu\text{W}/\text{cm}^2$. Under 500 lux CFL illumination, the champion cell among the Std devices delivered a PCE of 15.6% and P_{max} of 23.8 $\mu\text{W}/\text{cm}^2$, with a V_{OC} , J_{SC} , and FF of 0.76 V, 44.0 $\mu\text{A}/\text{cm}^2$, and 71%, respectively, whereas the champion T-Z device gave a PCE of 18.7% and P_{max} of 28.4 $\mu\text{W}/\text{cm}^2$, with a V_{OC} , J_{SC} , and FF of 0.77 V, 49.1 $\mu\text{A}/\text{cm}^2$, and 75%,

respectively. Similarly, under 200 lux CFL illumination, the best performing T-Z device exhibited a better PCE of 16.5% and P_{max} of $9.7 \mu\text{W}/\text{cm}^2$, with a V_{OC} of 0.73 V, J_{SC} of $21.3 \mu\text{A}/\text{cm}^2$, and FF of 62%, when compared to the Std device giving the best PCE of 15.4% and P_{max} of $8.9 \mu\text{W}/\text{cm}^2$, with a V_{OC} , J_{SC} , and FF of 0.72 V, $20.2 \mu\text{A}/\text{cm}^2$, and 62%, respectively.

Table 2B.3. Photovoltaic parameters of the DSCs employing Y123 sensitized standard bilayer (Std) and surface textured (T-Z) TiO_2 photoanodes, along with $[\text{Cu}(\text{dmp})_2]^{2+/+}$ electrolyte, under CFL illumination.

CFL illumination	P_{in}^a ($\mu\text{W}/\text{cm}^2$)	Device code	V_{oc}^b (V)	J_{sc}^b ($\mu\text{A}/\text{cm}^2$)	FF^b	PCE^b (%)	P_{max}^b ($\mu\text{W}/\text{cm}^2$)
1000 lux	306	Std	0.80 (0.80 ± 0.01)	90.1 (88.1 ± 2.6)	0.79 (0.78 ± 0.01)	18.6 (17.9 ± 0.7)	57.1 (54.8 ± 2.3)
		T-Z	0.82 (0.82 ± 0.01)	105.7 (103.2 ± 3.0)	0.79 (0.79 ± 0.01)	22.3 (21.8 ± 0.6)	68.2 (66.6 ± 1.8)
500 lux	152	Std	0.76 (0.75 ± 0.01)	44.0 (41.6 ± 2.8)	0.71 (0.69 ± 0.02)	15.6 (14.3 ± 1.5)	23.8 (21.7 ± 2.2)
		T-Z	0.77 (0.77 ± 0.01)	49.1 (48.5 ± 1.9)	0.75 (0.72 ± 0.03)	18.7 (17.6 ± 1.0)	28.4 (26.8 ± 1.5)
200 lux	58	Std	0.72 (0.71 ± 0.01)	20.2 (19.9 ± 1.0)	0.62 (0.60 ± 0.02)	15.4 (14.6 ± 1.1)	8.9 (8.4 ± 0.6)
		T-Z	0.73 (0.72 ± 0.01)	21.3 (21.1 ± 0.5)	0.62 (0.61 ± 0.01)	16.5 (16.0 ± 0.7)	9.7 (9.3 ± 0.4)

^aObtained by integration of irradiance spectra of the CFL under different illumination intensities.

^bObtained from J - V characterization of 3 devices under CFL illumination. The parameters corresponding to the champion cell are provided, along with the average value \pm standard deviation in the parentheses.

It is well known that, for DSCs, the mass transport limitations are not significant under low intensity light conditions. In our case, this is evident from the CT under 0.1 sun for Std device (**Figure 2B.8(d)**). As previously reported, thicker photoanodes have shown enhanced efficiency under indoor lighting conditions.^[50] Thus, we anticipated the Std device, having higher layer thickness along with superior dye loading and LHE to deliver higher PCE under indoor illumination. Surprisingly, the T-Z device consistently

outperformed the Std device across all the indoor lighting scenarios used in the present study. This superior performance of T-Z devices is primarily attributed to the enhanced voltage and current density, possibly arising from the presence of smaller proportions of ZnO within the T-Z films which may have influenced recombination kinetics at the TiO₂/electrolyte interface, which was investigated in detail using comprehensive charge transfer measurements.

(b) Detailed interfacial electron transfer studies. The presence of ZnO in the surface textured TiO₂ (T-Z) photoanode was detected using EDX and XPS measurements (**Figure 2B.5**). Detailed investigation of interfacial electron transfer dynamics was carried out to understand the effect of ZnO present in the T-Z photoanodes on photovoltaic performance of the corresponding DSCs. For this, DSCs were fabricated using the Std, T and T-Z photoanodes sensitized with Y123 dye along with [Cu(dmp)₂]^{2+/+} electrolyte. Here, a comparison between the T and T-Z based devices are included to study the effect of the TiO₂ layer (having similar thickness) before and after surface texturing, respectively, on the charge transfer kinetics. EIS measurements were performed on these devices (labelled as Std, T and T-Z) under darkness, and the corresponding Nyquist plots and Bode phase plots obtained at various bias potentials ($V_{applied}$) are shown in **Figure 2B.10**. The impedance plot for all the three devices consisted of three arcs, representing the impedance corresponding to three crucial processes within the DSCs. The width of the arc at the higher frequency region gives the resistance to charge transfer at the CE/electrolyte interface (R_{CE}), while that of the mid-frequency arc represents a combination of transport resistance within the TiO₂ layer (R_{tr}) and the charge transfer resistance (R_{ct}) at the TiO₂/dye/electrolyte interface. The arc at low frequency range corresponds to resistance to diffusion of electrolyte species (R_d). Assuming faster electron diffusion within the TiO₂ layer ($R_{tr} \ll R_{ct}$), the width of the mid-frequency arc in Nyquist plot can be used to determine the R_{ct} of different devices at various applied bias potentials, as shown in **Figure 2B.11(a)**. It is observed that, the T-Z photoanode based DSC is having better R_{ct} when compared to the device employing T photoanode, which is having similar thickness and porosity. The higher R_{ct} in T-Z device could be ascribed to the presence of ZnO, which might have become a part of the post blocking layer, deposited during the TiCl₄ treatment.^[56] The Std device is having even lower R_{ct} when compared to T device, which could be attributed to the higher layer thickness of the Std photoanode film. Resultantly, the lifetime (τ_n) of electrons in these devices decrease in the order T-Z > T > Std, as can be seen from the τ_n vs. $V_{applied}$ plot

(Figure 2B.11(b)) obtained from the peak frequencies of the Bode plot, using the equation 1.27 (Chapter 1).

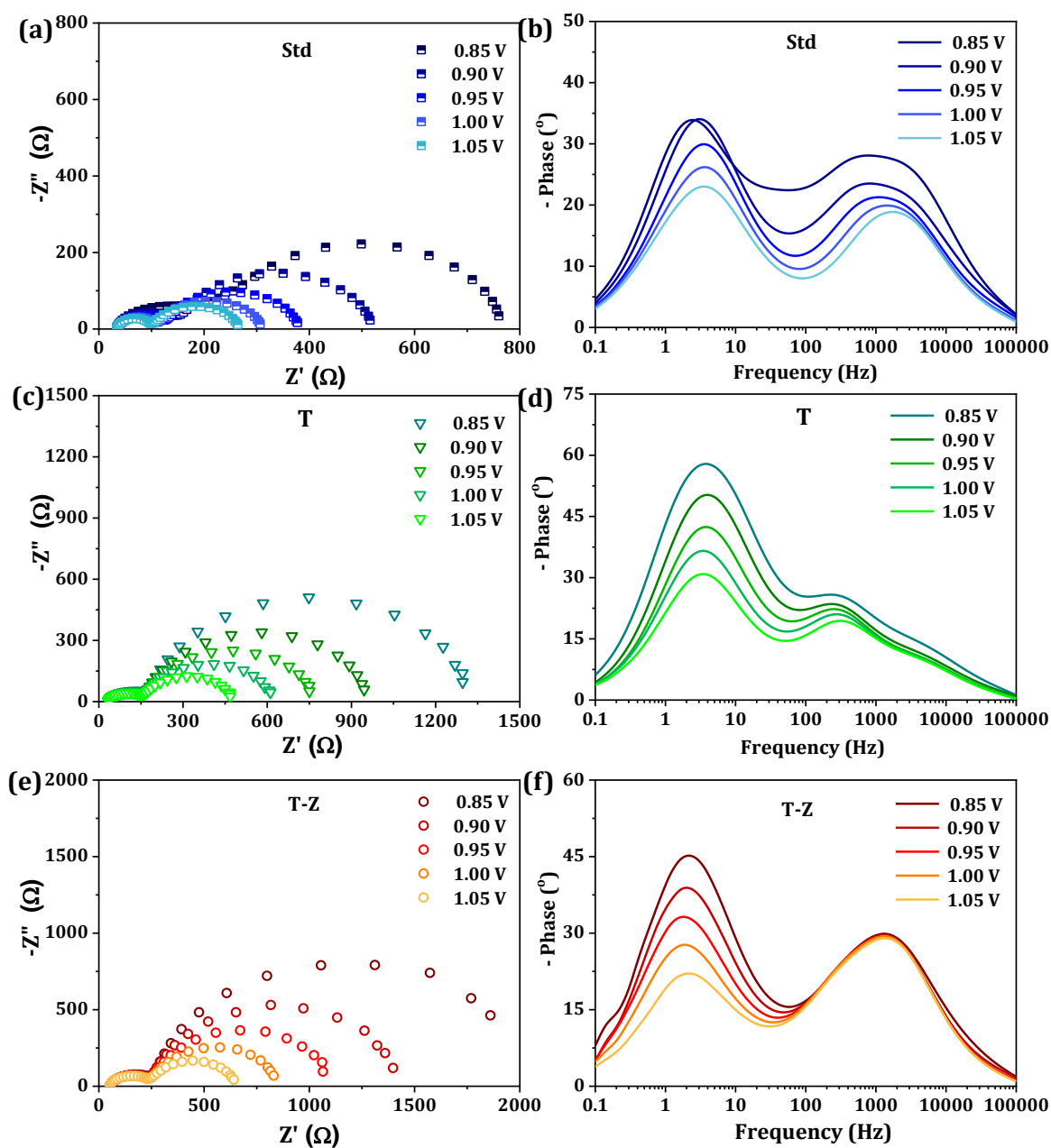


Figure 2B.10. (a,c,e) The Nyquist plots, and (b,d,f) the corresponding Bode phase plots of the devices utilizing standard (Std) bilayer, unmodified (T) and surface textured (T-Z) TiO_2 photoanodes, acquired using EIS measurement under dark condition, at various applied bias potentials ($V_{applied}$).

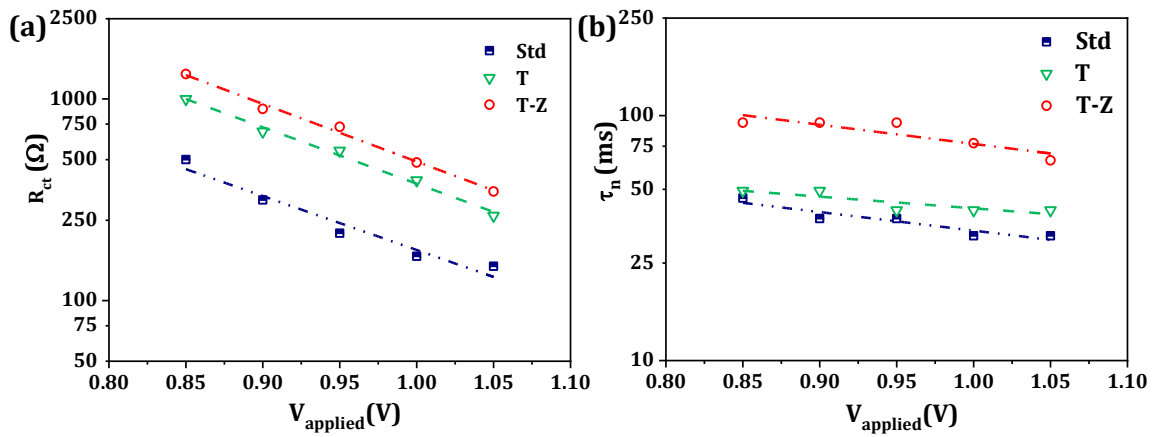


Figure 2B.11. (a) The charge transfer resistance (R_{ct}), and (b) the electron lifetime (τ_n), obtained using EIS analysis, plotted against the applied bias ($V_{applied}$), for devices utilizing standard bilayer (Std), unmodified TiO_2 layer (T) and surface textured TiO_2 layer (T-Z) based photoanodes.

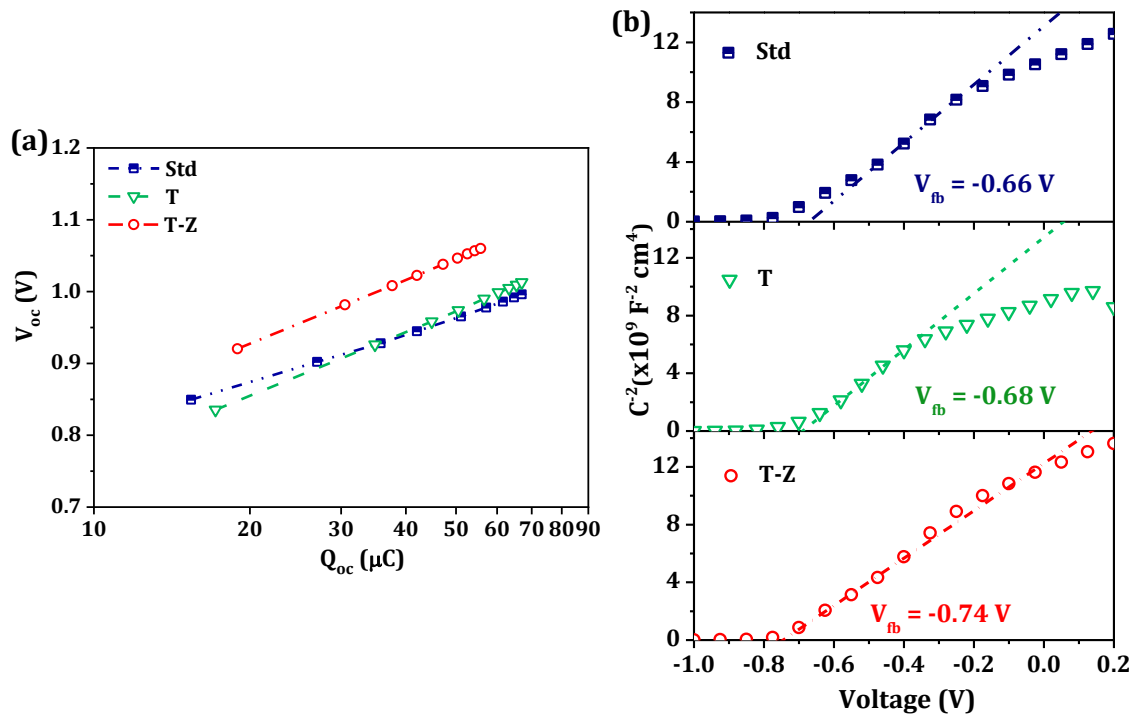


Figure 2B.12. (a) The charge extraction (CE) plot, and (b) Mott-Schottky (MS) plots obtained for devices using standard bilayer (Std), unmodified TiO_2 layer (T) and surface textured TiO_2 layer (T-Z) based photoanodes.

Hence the T-Z based devices possess lower recombination kinetics at the TiO_2 /electrolyte interface, which might be attributed to the presence of ZnO within the T-Z layer.^[56] The extracted charge vs. voltage plot obtained from CE measurement (**Figure 2B.12(a)**) showed $\sim 50 - 100 \text{ mV}$ negative shift in CB edges of TiO_2 in T-Z device with respect to Std

device as well as the T device, which again could be attributed to the presence of ZnO in the T-Z layer.^[56,57] This could be further confirmed using MS analysis. The flat band potential (V_{fb}) attained by extrapolating the MS plot to intersect the voltage axis, is seen to be more negative for T-Z when compared to the Std and T devices (**Figure 2B.12(b)**).

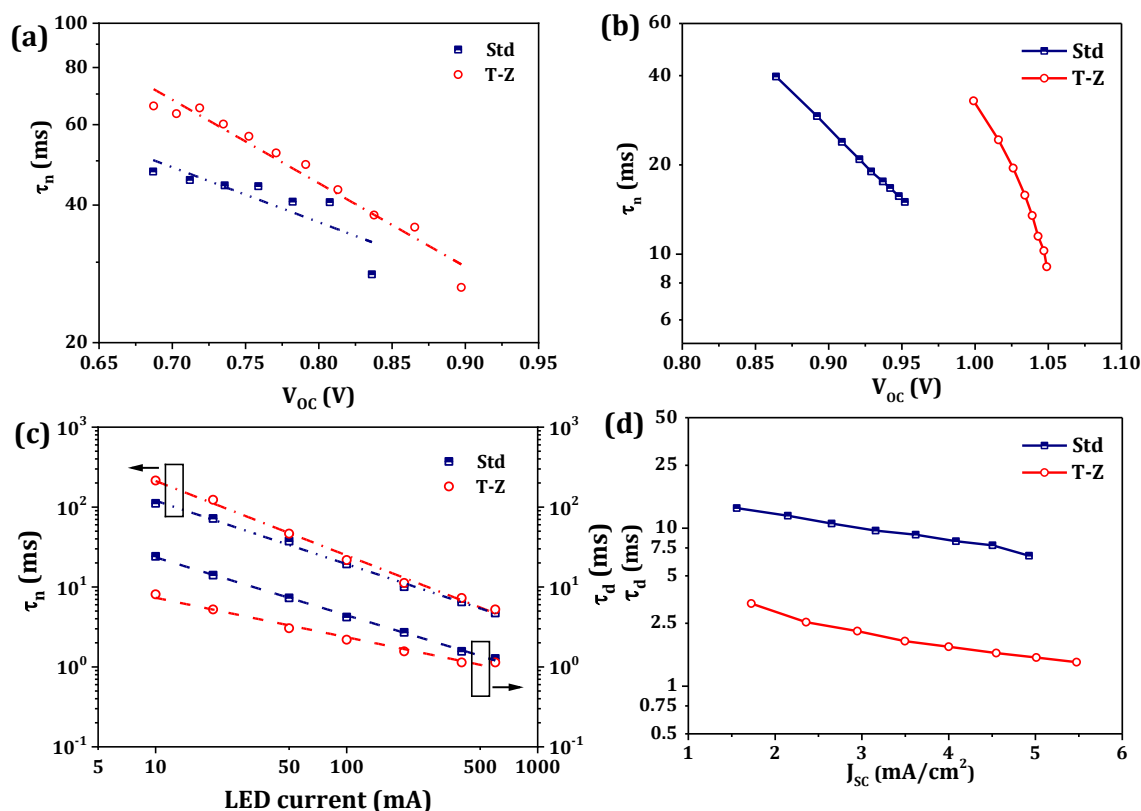


Figure 2B.13. The lifetime (τ_n) versus open circuited voltage (V_{OC}) plots obtained using (a) open circuit voltage decay (OVCD), and (b) transient photovoltage decay (TVD) measurements, (c) electron lifetime (τ_n) and diffusion time (τ_d), obtained from intensity modulated photovoltage and photocurrent spectroscopies (IMVS and IMPS), respectively, plotted against LED current, and (d) τ_d acquired using transient photocurrent decay (TCD) measurement, plotted against short circuit current density (J_{SC}).

Hence the presence of ZnO in the T-Z film helps in attaining better V_{OC} (outdoors as well as indoors) for the T-Z device, by inducing a negative shift in TiO_2 CB, in addition to the higher resistance to recombination. The improved lifetime for T-Z device with respect to the Std device, owing to the reduced recombination can be clearly seen from the plots obtained using OCVD, TVD and IMVS measurements as well (**Figure 2B.13(a-c)**). The J_{SC} of DSCs is a cumulative effect of how efficiently the light harvesting, injection, regeneration and charge collection processes are occurring at various interfaces. Hence the

reason for better J_{SC} exhibited by the T-Z device, in spite of its lower LHE when compared to Std device, can be understood by exploring the kinetics of other interfacial charge transfer processes within the devices. The plots of electron transport time or diffusion time (τ_d), obtained from IMPS and TCD measurements (**Figure 2B.13(c,d)**) illustrate that the diffusion of electrons through the T-Z photoanode is faster when compared to that of Std electrode. This may be attributed to the lower thickness of the T-Z layer, which reduces the path length for electron diffusion. Additionally, the presence of ZnO in the T-Z film might have helped in improving the mobility of electrons within the TiO_2 layer, as can be observed from the diffusion coefficient (D_n) plots obtained using IMPS and TCD measurements (**Figure 2B.14(a,b)**). Besides, the ZnO deposition within the T-Z layer might also have contributed towards the passivation of surface trap states, which as well can lead to smoother pathways for electron diffusion.^[31,58] All these factors pave the way for faster diffusion of electrons within the T-Z films. The faster electron diffusion along with enhan-

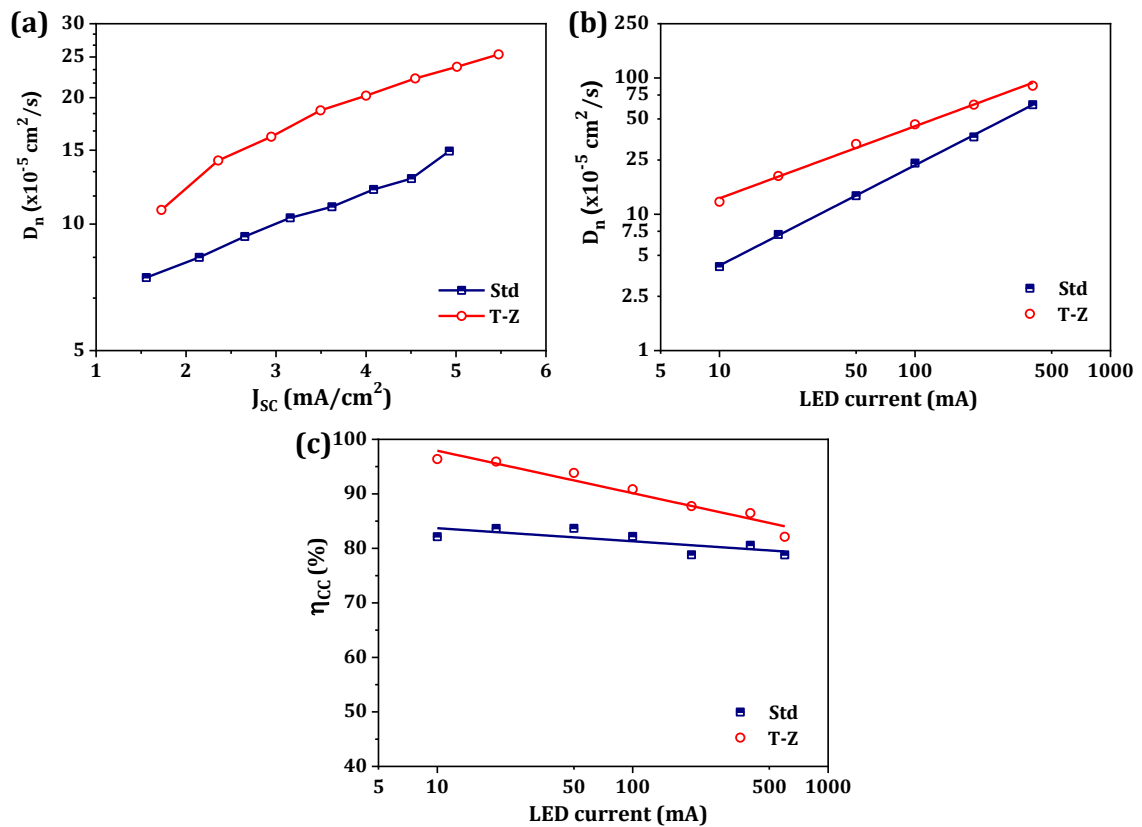


Figure 2B.14. The plot of diffusion coefficient (D_n) of electrons obtained from (a) transient photocurrent decay (TCD) measurement, and (b) intensity modulated photocurrent spectroscopy (IMPS). (c) Charge collection efficiency (η_{CC}) of DSCs utilizing standard bilayer (Std) and surface textured TiO_2 (T-Z) photoanodes.

-ced lifetime endows the T-Z devices with better charge collection efficiency (η_{CC}), comparative to the Std device (**Figure 2B.14(c)**). Thus, better charge collection, improved lifetime and higher regeneration kinetics, owing to lower mass transport limitation, helped T-Z device to achieve enhanced J_{SC} under one sun condition despite its lower LHE compared to Std device. Under indoor illumination, though the mass transport is similar in both the devices, the faster charge offered by the T-Z photoanodes enabled the corresponding device to attain better J_{SC} than the Std photoanode based DSC. In summary, the surface textured TiO_2 photoanode is a viable alternative to the standard AL/SL bilayer TiO_2 photoanodes, particularly in DSCs employing diffusion limited electrolyte systems. Additionally, the reduction in number of semiconductor layers, in case of T-Z photoanodes, enables reduction in cost and improves the transparency collection of the photoanode, which in turn make suitable for building-integrated photovoltaics (BIPV) applications when utilized along with iodine or cobalt based electrolytes.

2B.4. Conclusions

Surface textured TiO_2 (T-Z) photoanodes were fabricated using ZnO hierarchical microspheres as template particles. After surface modification using ZnO particles, there was $\sim 23\%$ improvement in the light harvesting efficiency of the TiO_2 films. The Y123 sensitized T-Z film was successfully employed as photoanode in DSC along with copper complex ($[Cu(dmp)_2]^{2+/+}$) based electrolyte, to achieve a PCE of 8.04% under one sun irradiation and 22.3% under standard 1000 lux CFL illumination. It was observed that, when compared to the DSC employing standard TiO_2 photoanode (Std) having a bilayer structure constituted by an active layer and a scattering layer, the device using T-Z photoanode with lower layer thickness and appreciable scattering property could achieve better J_{SC} . Under one sun condition, the enhanced J_{SC} for the T-Z device could be attributed to reduced mass transport issues owing to lower layer thickness, while under lower intensities and indoor conditions the faster electron transport and lower recombination facilitated more effective charge collection in T-Z device, leading to its higher J_{SC} . The faster electron transport in T-Z device was in turn ascribed to the presence of small amount of ZnO within the mesoporous TiO_2 layer of the T-Z electrodes. This further contributed towards better V_{OC} for T-Z device under both outdoor as well as indoor light, owing to a negative shift in TiO_2 CB and improved lifetime. Altogether, the ZnO templated surface textured TiO_2 films could act as an effective photoanode for copper electrolyte based DSCs, by effectively controlling mass transport issues under higher illumination intensities, and

by providing a smoother pathway for electron diffusion under higher as well as lower light intensities. This photoanode architecture opens up an opportunity for developing cost-effective, semi-transparent dye-sensitized PV modules that can be implemented for building-integrated photovoltaic (BIPV) as well as indoor photovoltaic (IPV) applications.

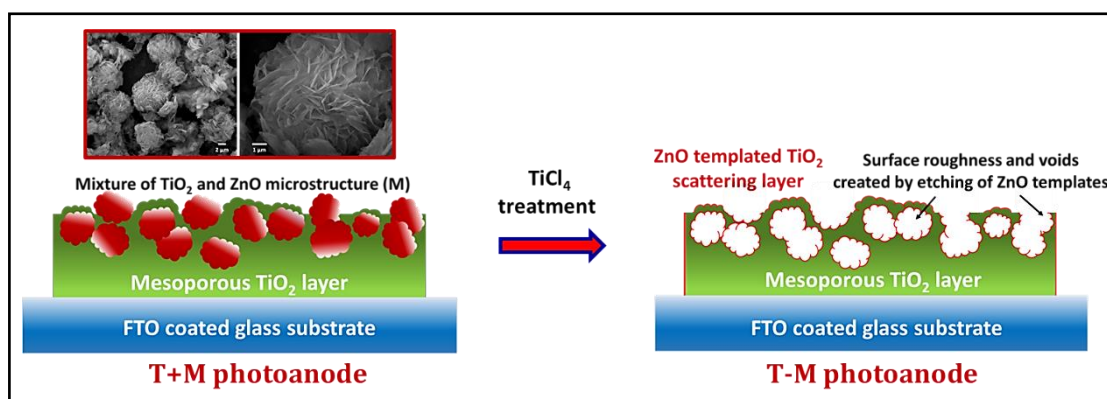
References

- [1] D. Guo, S. Xiao, K. Fan, J. Yu, *ACS Sustain Chem Eng* **2017**, *5*, 1315.
- [2] Z. Q. Li, L. E. Mo, W. C. Chen, X. Q. Shi, N. Wang, L. H. Hu, T. Hayat, A. Alsaedi, S. Y. Dai, *ACS Appl Mater Interfaces* **2017**, *9*, 32026.
- [3] H. Y. Chen, D. Bin Kuang, C. Y. Su, *J Mater Chem* **2012**, *22*, 15475.
- [4] Y. T. Kim, J. Park, S. Kim, D. W. Park, J. Choi, *Electrochim Acta* **2012**, *78*, 417.
- [5] A. H. Javed, N. Shahzad, M. A. Khan, M. Ayub, N. Iqbal, M. Hassan, N. Hussain, M. I. Rameel, M. I. Shahzad, *Sol Energy* **2021**, *230*, 492.
- [6] K. Fan, J. Yu, W. Ho, *Mater Horiz* **2017**, *4*, 319.
- [7] B. D. Choudhury, C. Lin, S. M. A. Z. Shawon, J. Soliz-Martinez, H. Huq, M. J. Uddin, *Sci Rep* **2021**, *11*, 1.
- [8] S. Saravanan, R. Kato, M. Balamurugan, S. Kaushik, T. Soga, *J. Sci.: Adv. Mater. Devices* **2017**, *2*, 418.
- [9] S. Hore, P. Nitz, C. Vetter, C. Prahl, M. Niggemann, R. Kern, *Chem Comm* **2005**, 2011.
- [10] T. T. T. Pham, N. Mathews, Y. M. Lam, S. Mhaisalkar, *J Electron Mater* **2017**, *46*, 3801.
- [11] F. Huang, D. Chen, X. L. Zhang, R. A. Caruso, Y. B. Cheng, *Adv Funct Mater* **2010**, *20*, 1301.
- [12] S. Sasidharan, A. Jagadeesh, S. C. Pradhan, B. N. Nair, A. Azeez Peer Mohamed, K. N. Narayanan Unni, S. Soman, U. Nair Saraswathy Hareesh, *Sol Energy* **2021**, *226*, 214.
- [13] L. Xu, C. Aumaitre, Y. Kervella, G. Lapertot, C. Rodríguez-Seco, E. Palomares, R. Demadrille, P. Reiss, *Adv Funct Mater* **2018**, *28*, 1706291.
- [14] X. Zhang, F. Liu, Q. L. Huang, G. Zhou, Z. S. Wang, *J Phy Chem C* **2011**, *115*, 12665.
- [15] K. Subalakshmi, J. Senthilselvan, *Sol Energy* **2018**, *171*, 914.
- [16] S. B. Wategaonkar, V. G. Parale, R. P. Pawar, S. S. Mali, C. K. Hong, R. R. Powar, A. V. Moholkar, H. H. Park, B. M. Sargar, R. K. Mane, *Ceram Int* **2021**, *47*, 25580.
- [17] T. Raguram, K. S. Rajni, *Int J Hydrogen Energy* **2022**, *47*, 4674.
- [18] H. Esgin, Y. Caglar, M. Caglar, *J Alloys Compd* **2022**, *890*, 161848.
- [19] L. O. A. Salim, M. Z. Muzakkar, A. Zaeni, M. Maulidiyah, M. Nurdin, S. N. Sadikin, J. Ridwan, A. A. Umar, *J Phy Chem Solids* **2023**, *175*, 111224.
- [20] Y. Tabari-Saadi, M. R. Mohammadi, *J. Mater. Sci.: Mater. Electron.* **2015**, *26*, 8863.
- [21] B. Boro, B. Gogoi, B. M. Rajbongshi, A. Ramchiary, *Renew. Sustain. Energy Rev.* **2018**, *81*, 2264.

- [22] Z. H. Bakr, Q. Wali, J. Ismail, N. K. Elumalai, A. Uddin, R. Jose, *Electrochim Acta* **2018**, 263, 524.
- [23] B. Praveen, K. Pugazhendhi, J. Sahaya Selva Mary, S. Padmaja, E. Merlin Arnold, J. Madhavan, J. Merline Shyla, *Mater Today Proc* **2019**, 8, 239.
- [24] S. Bykkam, D. N. Prasad, M. R. Maurya, K. K. Sadasivuni, J. J. Cabibihan, *Sustainability* **2021**, 13, 7685.
- [25] N. Abraham, C. Unni, D. Philip, *J. Mater. Sci.: Mater. Electron.* **2018**, 29, 21002.
- [26] S. A. Kazmi, S. Hameed, A. S. Ahmed, M. Arshad, A. Azam, *J Alloys Compd* **2017**, 691, 659.
- [27] E. Nouri, M. R. Mohammadi, P. Lianos, *Electrochim Acta* **2016**, 219, 38.
- [28] S. Z. Siddick, C. W. Lai, J. C. Juan, S. B. Hamid, *Curr Nanosci* **2017**, 13.
- [29] S. Aseena, N. Abraham, V. S. Babu, *Ceram Int* **2020**, 46, 28355.
- [30] M. Younas, M. A. Gondal, M. A. Dastageer, K. Harrabi, *Sol Energy* **2019**, 188, 1178.
- [31] S. W. Lee, K. S. Ahn, K. Zhu, N. R. Neale, A. J. Frank, *J Phy Chem C* **2012**, 116, 21285.
- [32] J. H. Yang, C. W. Bark, K. H. Kim, H. W. Choi, *Materials* **2014**, 7, 3522.
- [33] S. Sasidharan, S. Soman, S. C. Pradhan, K. N. N. Unni, A. A. P. Mohamed, B. N. Nair, H. U. N. Saraswathy, *New J Chem* **2017**, 41, 1007.
- [34] I. P. Liu, W. H. Lin, C. M. Tseng-Shan, Y. L. Lee, *ACS Appl Mater Interfaces* **2018**, 10, 38900.
- [35] C. Kim, J. Kim, H. Choi, C. Nahm, S. Kang, S. Lee, B. Lee, B. Park, *J Power Sources* **2013**, 232, 159.
- [36] A. R. Pascoe, L. Bourgeois, N. W. Duffy, W. Xiang, Y. B. Cheng, *J Phy Chem C* **2013**, 117, 25118.
- [37] K. K. Tehare, S. T. Navale, F. J. Stadler, Z. He, H. Yang, X. Xiong, X. Liu, R. S. Mane, *Mater Res Bull* **2018**, 99, 491.
- [38] M. Freitag, J. Teuscher, Y. Saygili, X. Zhang, F. Giordano, P. Liska, J. Hua, S. M. Zakeeruddin, J. E. Moser, M. Grätzel, A. Hagfeldt, *Nat Photonics* 2017 11:6 **2017**, 11, 372.
- [39] H. Michaels, M. Rinderle, R. Freitag, I. Benesperi, T. Edvinsson, R. Socher, A. Gagliardi, M. Freitag, *Chem Sci* **2020**, 11, 2895.
- [40] E. Tanaka, H. Michaels, M. Freitag, N. Robertson, *J Mater Chem A* **2020**, 8, 1279.
- [41] Y. Ren, D. Zhang, J. Suo, Y. Cao, F. T. Eickemeyer, N. Vlachopoulos, S. M. Zakeeruddin, A. Hagfeldt, M. Grätzel, *Nature* **2023**, 613, 60.
- [42] M. Freitag, Q. Daniel, M. Pazoki, K. Sveinbjörnsson, J. Zhang, L. Sun, A. Hagfeldt, G. Boschloo, *Energy Environ Sci* **2015**, 8, 2634.
- [43] Y. Saygili, M. Söderberg, N. Pellet, F. Giordano, Y. Cao, A. B. Munoz-García, S. M. Zakeeruddin, N. Vlachopoulos, M. Pavone, G. Boschloo, L. Kavan, J. E. Moser, M. Grätzel, A. Hagfeldt, M. Freitag, *J Am Chem Soc* **2016**, 138, 15087.
- [44] M. Freitag, F. Giordano, W. Yang, M. Pazoki, Y. Hao, B. Zietz, M. Grätzel, A. Hagfeldt, G. Boschloo, *J Phy Chem C* **2016**, 120, 9595.
- [45] S. C. Pradhan, A. Hagfeldt, S. Soman, *J Mater Chem A* **2018**, 6, 22204.

- [46] T. Higashino, H. Imahori, *ACS Energy Lett* **2022**, 7, 1926.
- [47] A. Grobelny, Z. Shen, F. T. Eickemeyer, N. F. Antarksa, S. Zapotoczny, S. M. Zakeeruddin, M. Grätzel, A. Grobelny, Z. Shen, F. T. Eickemeyer, N. F. Antarksa, S. M. Zakeeruddin, M. Grätzel, S. Zapotoczny, *Adv Mater* **2023**, 35, 2207785.
- [48] Y. Cao, Y. Liu, S. M. Zakeeruddin, A. Hagfeldt, M. Grätzel, *Joule* **2018**, 2, 1108.
- [49] D. Zhang, M. Stojanovic, Y. Ren, Y. Cao, F. T. Eickemeyer, E. Socie, N. Vlachopoulos, J. E. Moser, S. M. Zakeeruddin, A. Hagfeldt, M. Grätzel, *Nat Comm* **2021**, 12, 1.
- [50] J. Velore, S. Chandra Pradhan, T. W. Hamann, A. Hagfeldt, K. N. N. Unni, S. Soman, *ACS Appl Energy Mater* **2022**, 5, 2647.
- [51] S. Sasidharan, S. C. Pradhan, A. Jagadeesh, B. N. Nair, A. A. P. Mohamed, N. U. Narayanan, S. Soman, U. N. S. Hareesh, *ACS Appl Energy Mater* **2020**, 3, 12584.
- [52] Y. Lai, Y. Wang, S. Cheng, J. Yu, *J Electron Mater* **2014**, 43, 2676.
- [53] R. Ahmad, N. Tripathy, M. Y. Khan, K. S. Bhat, M. S. Ahn, Y. B. Hahn, *RSC Adv* **2016**, 6, 54836.
- [54] L. Zhu, Q. Lu, L. Lv, Y. Wang, Y. Hu, Z. Deng, Z. Lou, Y. Hou, F. Teng, *RSC Adv* **2017**, 7, 20084.
- [55] S. H. Kang, J. Y. Kim, Y. Kim, H. S. Kim, Y. E. Sung, *J Phy Chem C* **2007**, 111, 9614.
- [56] W. Ahmad, U. Mehmood, A. Al-Ahmed, F. A. Al-Sulaiman, M. Z. Aslam, M. S. Kamal, R. A. Shawabkeh, *Electrochim Acta* **2016**, 222, 473.
- [57] S. Borbón, S. Lugo, D. Pourjafari, N. Pineda Aguilar, G. Oskam, I. López, *ACS Omega* **2020**, 5, 10977.
- [58] T. Pauporté, C. Magne, *Thin Solid Films* **2014**, 560, 20.

ZnO templated scattering layers for enhanced performance in copper electrolyte based dye-sensitized photovoltaic cells



Abstract: In this chapter, we fabricated a bilayer photoanode comprising of conventional TiO₂ active layer and an innovative TiO₂ scattering layer having voids created by utilizing ZnO hierarchical microstructures as template particles. These electrodes were then co-sensitized with organic dyes (D35 and XY1b) having complementary absorption, and utilized in dye-sensitized photovoltaic cells (DSCs) along with a copper complex based electrolyte, bis (2,9 dimethyl-1,10-phenanthroline copper (I/II) bis (trifluoromethanesulfonyl) imide ([Cu(dmp)₂]^{2+/+}). The DSCs based on the new photoanode architecture outperformed the devices using surface textured TiO₂ photoanodes (presented in chapter 2B) under indoor/ambient illuminations. Nevertheless, when subjected to AM 1.5G solar irradiation, DSCs employing the novel bilayer photoanode along with [Cu(dmp)₂]^{2+/+} encountered challenges related to mass transport, primarily attributed to the increased thickness of the semiconductor layer. The performance of bilayer photoanode based DSCs could further be enhanced by optimizing the weight percentage of ZnO templates used in the scattering layer. Utilizing 20 wt% of ZnO template particles resulted in a notable enhancement of DSC performance to achieve 10.1% under AM 1.5G sunlight and 33.8% under 1000 lux CFL illumination.

3.1. Introduction

Though iodine based electrolytes marked the beginning of well performing dye-sensitized photovoltaic cells (DSCs) in 1991, its widespread usage was limited by several disadvantages like corrosive nature, competitive light absorption, intricate dye regeneration mechanism and higher regeneration overpotential loss.^[1-4] This created a need for exploring alternative options like the one-electron outer sphere redox systems based on transition metal complexes (such as cobalt and copper complexes), with more positive redox potentials that significantly reduce the dye regeneration overpotential loss.^[5-10] In recent years, copper complex (Cu(II/I)) based electrolytes have garnered more significance in DSCs owing to their abundance, cost-effectiveness, reduced toxicity, favorable redox potential, accelerated ion diffusion rates, and compatibility with organic sensitizers.^[11,12] Moreover, the redox potential of the copper complexes can be finely controlled through ligand substitutions, facilitating the optimization of open circuit voltage (V_{OC}). For instance, Saygili *et al.* synthesized three copper bipyridyl based redox shuttles using three different ligands, *viz.* tetramethyl bipyridine (tmby), dimethyl phenanthroline (dmp) and dimethyl bipyridine (dmby) and achieved redox potentials of 0.87 V, 0.93 V and 0.97 V, respectively, with respect to SHE.^[13] Due to the lower reorganization energy and rapid charge transfer rate in copper complexes, only a minimal driving force of less than 0.1-0.2 eV is sufficient for efficient dye regeneration using these redox systems. Hence, the more positive redox potentials of copper species renders higher voltage without compromising the regeneration efficiency.^[14,15] Multiple studies indicate that under simulated sunlight, small area DSCs using copper complex redox mediators can achieve V_{OC} above 1V and power conversion efficiencies (PCE) exceeding 10%.^[13,16,17] Additionally, they also deliver state-of-the-art performance under ambient/indoor illumination compared to the rest of available PV technologies.^[18-20] Copper complex based electrolytes, particularly Cu(II/I)(4,4',6,6'-tetramethyl-2,2'-bipyridine) ($[Cu(tmby)_2]^{2+/+}$), used in conjugation with organic sensitizers paved the way for the paradigm shift of DSCs into indoor photovoltaic applications.^[19,21-24] Recently, Ren *et al.* realized DSCs with PCE of 15.2% under one sun and Zhang *et al.* achieved an efficiency of 34.5% under 1000 lux fluorescent light (CFL) using the $[Cu(tmby)_2]^{2+/+}$ redox mediator.^[23,24] Using a TiO_2/ZnO bilayer photoanode and an electrolyte based on the copper(II/I) bis (2,9-dimethyl-1,10-phenanthroline) ($[Cu(dmp)_2]^{2+/+}$) complex, Jagadeesh *et al.* recently developed DSCs that exhibited an outstanding V_{OC} of 1.27 V under one sun and 1.02 V under 1000 lux CFL illumination.^[25]

Subsequently, a record efficiency of 35.6% under 1000 lux CFL illumination was realized by utilizing a modified $[\text{Cu}(\text{dmp})_2]^{2+/+}$ complex synthesized using the novel concept of asymmetric dual species copper electrolyte.^[26]

Given the relatively lower mass transport issues observed in copper complexes comparative to cobalt complex based electrolytes, coupled with their more positive redox potential, DSCs utilizing Cu(II/I) electrolytes exhibit enhanced current and voltage. This, in turn, results in improved *PCEs* for Cu(II/I) electrolyte based DSCs when compared to cobalt and iodine electrolyte based ones.^[27] Despite its advantages, the dye regeneration and diffusion process in copper electrolyte based DSC is constrained by slow mass transport of bulky redox species, impacting the maximum achievable output current density. It has been identified that the thickness and structure of the semiconductor layer, along with the nature of dye molecules, can significantly influence the mass transport of redox species within the photoanode matrix^[28,29]. Majority of the breakthrough research contributions in Cu(II/I) electrolyte based DSCs focused on designing novel copper complexes with appropriate redox potentials and developing new sensitizers with better extinction coefficient and broader absorption window. Effective strategies like co-sensitization and semiconductor surface treatment with organic molecules were also explored to ensure the formation of a closely packed monolayer made up of well-ordered dye molecules, to facilitate panchromatic light absorption and to minimize recombination at the semiconductor/electrolyte interface.^[18,20,30] Almost all of these literature reports use standard TiO_2 photoanodes constituted by an active layer (20-30 nm TiO_2 nanoparticles) and a scattering layer (200-400 nm TiO_2 nanoparticles). Till date, no new photoanode architectures were employed in copper electrolyte based DSCs, to the best of our knowledge. Since the photoanode architecture determines its porosity and thickness, it plays a pivotal role in controlling the diffusion of redox species within the device. So, it is desirable to explore novel photoanode architectures with modified semiconductor materials compatible with copper complex based electrolytes to minimize the reduction in current resulting from mass transport issues. So far, many studies on enhancing the performance of iodine electrolyte based DSCs by photoanode modifications have been done. The possibility of enhancing light scattering by introducing voids within the TiO_2 photoanodes are being presented in many previous literature reports.^[31-36] Pham *et. al.* demonstrated the capability of such a photoanode architecture in compensating the mass transport issues of bulky cobalt based electrolytes.^[37] Previously, we have demonstrated a novel surface

texturing method using ZnO sacrificial layers to increase the light harvesting efficiency (*LHE*) of TiO₂ photoanodes which improves the *PCE* of iodine electrolyte based DSCs.^[38,39] The same technique was adopted in the **Chapter 2B** to address mass transport limitation in copper electrolyte based DSC, in addition to the enhancement in *LHE*. In the present chapter, we introduce a novel bilayer photoanode architecture to be used in copper electrolyte based DSCs. These bilayer photoanodes employed conventional TiO₂ as active layer and a scattering layer made up of TiO₂ layer with voids, created by using hierarchical ZnO microstructures as templates. This novel photoanode was co-sensitized using two organic sensitizers (D35 and XY1b) having complementary absorption and utilized in DSC along with [Cu(dmp)₂]^{2+/+} electrolyte to realize a *PCE* of 8.9% under one sun and 32.3% under 1000 lux CFL illumination. By finely adjusting the light harvesting capability of the bilayer photoanode through optimization of the weight percentage (wt%) of ZnO template particles in the scattering layer, the photovoltaic performance was further elevated to 10.1% under one sun and 33.8% under 1000 lux CFL illumination.

3.2. Experimental procedures

3.2.1. Preparation and characterization of ZnO templated TiO₂ photoanodes

The template particles used in this study were the ZnO hierarchical microspheres, which were synthesized as detailed in **Chapter 2A (section 2A.2.1)**. Briefly, a reaction mixture containing 0.02 M aqueous solution of zinc nitrate hexahydrate (Merck) and 1.0 M aqueous solution of urea (Merck) was stirred at 1000 rpm in a beaker for one hour at room temperature. The beaker was then heated at 90 °C for 24 hours and the obtained white precipitate was then washed with DI water and ethanol, and vacuum dried at 60 °C for 12 hours. The as-synthesized sample (hydroxide zinc carbonate or hydrozincite, HZC) was converted to a paste by adding ethyl cellulose and terpineol (mixed and heated at 100 °C) and ground in a mortar. In addition, commercial TiO₂ paste (18-NRT) was mixed with different weight percentage of the as-synthesized HZC powder (10 wt%, 20 wt% and 40 wt%) and ground well in a mortar to obtain uniformly mixed pastes, designated as M10, M20 and M40, respectively. The FTO substrates (TEC 10, Merck) were cut into small pieces of dimensions, 1.6 cm x 1.6 cm, and were cleaned in an ultrasonic bath, using detergent solution, distilled water, acetone and isopropanol. TiO₂ pre-blocking layers were deposited by dipping the substrates in a 50 mM TiCl₄ solution at 70 °C for 30 minutes. The substrates were then annealed at 500 °C for 30 min. The surface textured TiO₂ photoanodes were prepared as described in **section 2B.2.1 of Chapter 2B**. The fabrication steps for the

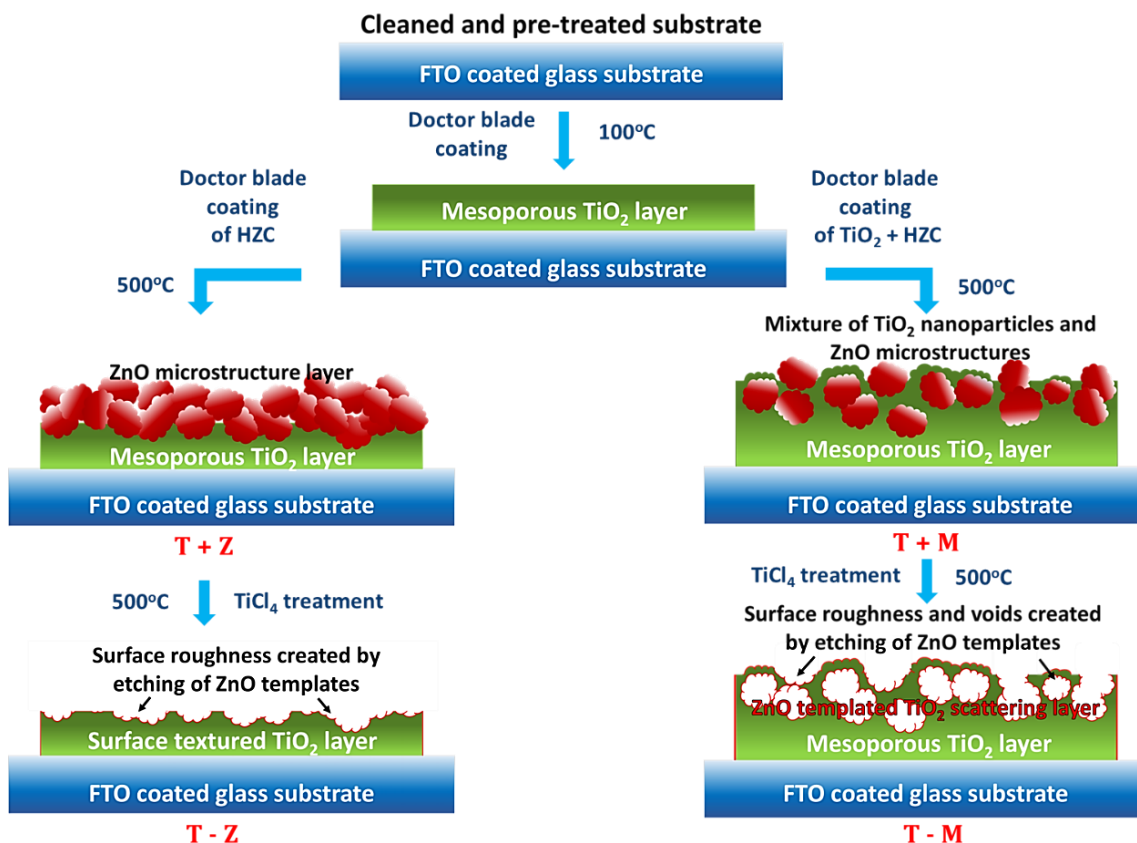


Figure 3.1. Schematic illustration of the fabrication of surface textured TiO₂ (T-Z) photoanode and bilayer TiO₂ photoanode with ZnO templated scattering layer with voids (T-M).

same are depicted in **Figure 3.1** and briefly described below. The commercial TiO₂ paste (18-NRT, GreatcellSolar, Australia) was coated on the FTO substrate via blade coating technique, to form the active layer (AL). The HZC paste was then deposited over the AL by blade coating. This result in a TiO₂/ZnO bilayer photoanode, which is designated as T+Z. In order to obtain the surface textured TiO₂ photoanode (labelled as T-Z), TiCl₄ post-treatment was carried out on the bilayer photoanode, wherein the T+Z photoanodes were immersed in 40 mM TiCl₄ solution and heated at 70 °C for 30 minutes. TiO₂ photoanodes with ZnO templated scattering layers (designated as T-M10, T-M20 and T-M40) were prepared in a similar manner (as illustrated in **Figure 3.1**). Firstly, a bilayer photoanode film was fabricated by coating the M10 paste, which is a mixture of 18-NRT paste and 10 wt% of the as-synthesized HZC powder over the TiO₂ AL. This photoanode is designated as T+M10 or simply T+M. This bilayer electrode was then post-treated with 40 mM TiCl₄ solution (at 70 °C for 30 min) to obtain the T-M or T-M10 photoanode. Similarly for

fabricating T-M20 and T-M40 photoanodes, the mixture pastes M20 and M40, respectively containing 20 wt% and 40 wt% of HZC sample, is coated over the AL (to obtain T+M20 and T+M40 films), followed by post TiCl_4 treatment. In all the above cases, the TiCl_4 post-treatment leads to dissolution of ZnO template particles from the respective films, leaving imprints on the surface or voids within the TiO_2 layer. The final photoanodes were slowly annealed to 500 °C (for 30 min).

The scanning electron microscopy (SEM) images and energy dispersive X-ray (EDX) spectra generated by using Zeiss EVO 18 cryo-SEM Special Ed (Carl Zeiss, Germany) instrument, were used to analyze the surface morphology, thickness, and ZnO content in various photoanodes. A Bruker Dektak XT profilometer was used to measure the thickness and surface roughness of various photoanode samples. Atomic force microscopy (AFM) was also used to compare the surface roughness of various films. An AFM-Bruker Multitop Nanoscope V device in tapping mode was used to capture the AFM images, which were then utilized to estimate the surface roughness of the various TiO_2 photoanode layers with the aid of Nanoscope Analysis 1.5 software. Using an integrating sphere alongside a UV-visible spectrophotometer (Shimadzu, UV-2700i), the diffuse reflectance spectra (DRS) of the photoanode films were obtained in order to study their scattering properties. After dye sensitization, the light absorbance of the different photoanodes were measured using UV-vis spectrophotometer. The amount of dye adsorbed per unit area of the different photoanode layers were calculated using equation 2A.1, as discussed in **section 2A.2.2 (Chapter 2A)**. Shimadzu model 2100 UV-visible spectrometer was used to determine the absorbance of the dye solution (0.01mM) both prior to and following photoanode immersion.

3.2.2. DSC fabrication and characterization

The various TiO_2 photoanodes prepared in the preceding **section 3.2.1** were utilized to fabricate DSCs. To fabricate dye-sensitized photoanodes, the prepared films were submerged in a cocktail dye solution containing D35:XY1b (1:1) mixture and left in the dark for 16 hours. Poly(3,4-ethylenedioxythiophene) (PEDOT) coated counter electrodes, were prepared by electro-polymerization of ethylenedioxythiophene (EDOT, Merck) along with sodium dodecyl sulphate (SDS, Sigma Aldrich) on cleaned FTO substrates (TEC7, GreatcellSolar, Australia) with pre-drilled holes. Using a 25 μm thick thermoplastic (Surlyn, GreatcellSolar, Australia) as spacer, the photoanodes and counter electrodes were assembled by hot pressing (at 120 °C) and the space between the electrodes was filled with

copper complex based redox mediator through the holes in the counter electrode, which were then sealed to prevent electrolyte leakage and solvent evaporation. The copper complex based electrolyte solution was prepared by dissolving 0.2 M of bis(2,9-dimethyl-1,10-phenanthroline copper(I) bis(trifluoromethanesulfonyl) imide ($[\text{Cu}(\text{dmp})_2]^{1+}$, Dyenamo A.B., Sweden) and 0.04 M of bis(2,9-dimethyl-1,10-phenanthroline copper(II) bis(trifluoromethane sulfonyl)imidechloride ($[\text{Cu}(\text{dmp})_2]^{2+}$, Dyenamo A.B., Sweden), 0.1 M of bis(trifluoromethane) sulfonimide lithium salt (LiTFSI, Merck) and 0.6 M of 4-tert-butylpyridine (TBP, Merck), in acetonitrile solvent (Merck).

The photovoltaic performance of the fabricated DSCs was assessed using photocurrent-voltage (J - V) measurements. The J - V characterization under simulated solar irradiation (100 mW/cm^2 , AM 1.5G) was done using class AAA solar simulator (Oriel 3A, Model PVIV- 94043A, Newport, USA) integrated with a source meter (Keithley 2440). The incident photon-to-current conversion efficiency ($IPCE$) measurements were carried out using a 250 W Xenon lamp as light source along with a monochromator set-up (Newport, USA). The AE05 potentiostat (Dyenamo A.B., Sweden) was used for measuring J - V characteristics under indoor light conditions with a custom-made set up equipped with compact fluorescent lamp, CFL (Osram, 14W/2700K) and light emitting diode, LED (Osram, 4W/6500K) as light sources (light intensity calibrated using a UV-vis-NIR spectrometer, Ocean optics, DH-2000-BAL). The interfacial charge transfer kinetics was investigated using several advanced characterization techniques. Large perturbation techniques such as charge extraction (CE), transient photovoltage decay (TVD) and transient photocurrent decay (TCD) were carried out using the Toolbox setup (Dyenamo A.B., Sweden). Further, small amplitude AC perturbation techniques such as electrochemical impedance spectroscopy (EIS), intensity modulated photovoltage spectroscopy (IMVS) and intensity modulated photocurrent spectroscopy (IMPS) were performed using the electrochemical workstation (Autolab-PGSTAT 302N, Metrohm) coupled with a Frequency Response Analyzer (FRA32M). The current transients (CT) data under different illumination intensities were obtained using Autolab-PGSTAT 302N to investigate the mass transport limitations in DSCs employing various photoanodes and to study its influence in the dye regeneration rates.

3.3. Results and discussions

3.3.1. ZnO templated TiO₂ photoanodes for DSCs

(a) *Characteristics of ZnO templated photoanodes.* The light harvesting efficiency (*LHE*) stands as one among the most prominent characteristic property required for an efficient dye-sensitized photoanode film. *LHE* depends on several parameters including the thickness of the semiconducting layer (*d*), amount of dye adsorbed, light absorption coefficient, absorption profile of the dye molecules and the path length of light within the active layer. The introduction of surface roughness and scattering voids in TiO₂ photoanode films can be used as effective strategies to elongate the path length of light within the photoanode. The present work involves the T-Z photoanodes with surface roughness as

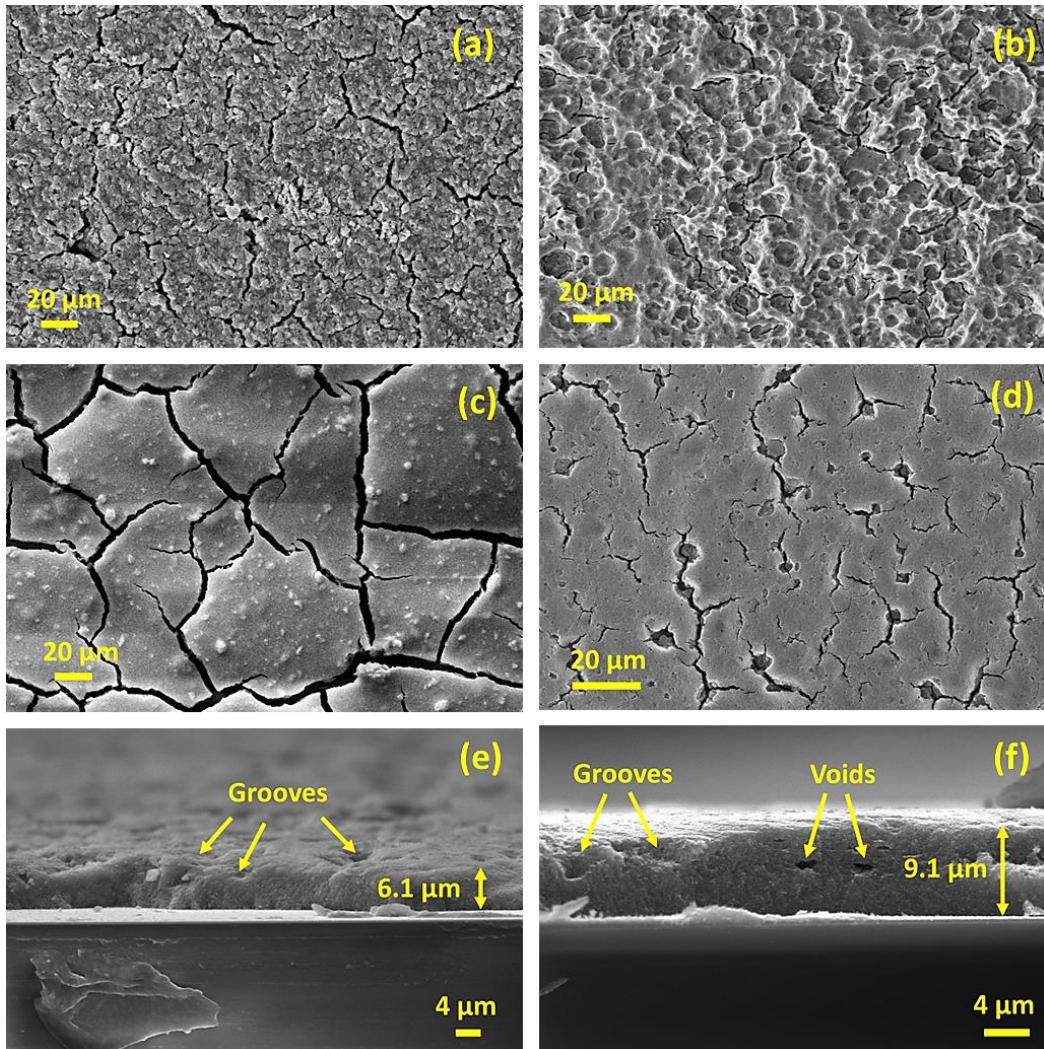


Figure 3.2. SEM images of surface morphology of (a) T+Z bilayer photoanode (b) T-Z surface textured photoanode, (c) T+M bilayer photoanode, and (d) T-M bilayer photoanode with templated scattering layer; cross section of (e) T-Z and (f) T-M photoanodes.

well as T-M photoanodes having voids within the TiO₂ layer. The **Figure 3.2(a-d)** show the SEM micrographs of surface morphology of the T+Z, T-Z, T+M and T-M photoanode films, while **Figure 3.2(e,f)** show the cross sectional SEM images of T-Z and T-M films. It is observed that in case of T-Z film, the surface of TiO₂ layer contains numerous grooves/imprints (**Figure 3.2(b,e)**), which was formed as a result of etching off the ZnO overlayer from T+Z film (**Figure 3.2(a)**). On the other hand, the T-M film not only exhibited surface grooves but also voids within the TiO₂ layer (**Figure 3.2(d,f)**) created by etching off the ZnO microstructure template particles which were present within the TiO₂ scattering overlayer of T+M film (**Figure 3.2(c)**). The T-M layer with higher thickness ($d \sim 9 \mu\text{m}$) holds more dye molecules ($9.9 \times 10^{-8} \text{ mol/cm}^2$) compared to T-Z layer with $d \sim 6 \mu\text{m}$ ($8.9 \times 10^{-8} \text{ mol/cm}^2$), as provided in **Figure 3.2(e,f)** and **Table 3.1**. The EDX spectra of the surface of the various photoanode films, T+Z, T-Z, T+M, and T-M, are shown in **Figure 3.3**. The surface of T+Z photoanode consisted of Zn as the major component (**Figure 3.3(a)**), while that of T-Z (which is obtained by TiCl₄ treatment of T+Z) has only minimal amount of Zn atoms (**Figure 3.3(b)**), which indicates that the ZnO layer is etched off from

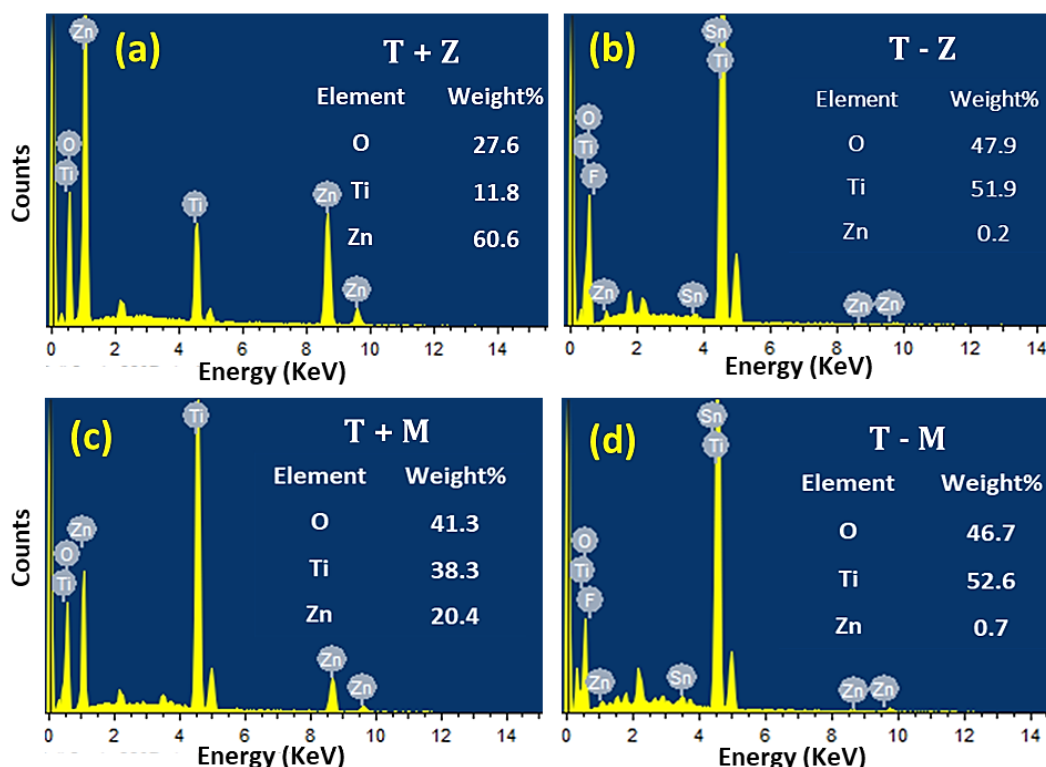


Figure 3.3. EDX spectra of the surface of (a) T+Z, (b) T-Z, (c) T+M, and (d) T-M photoanodes.

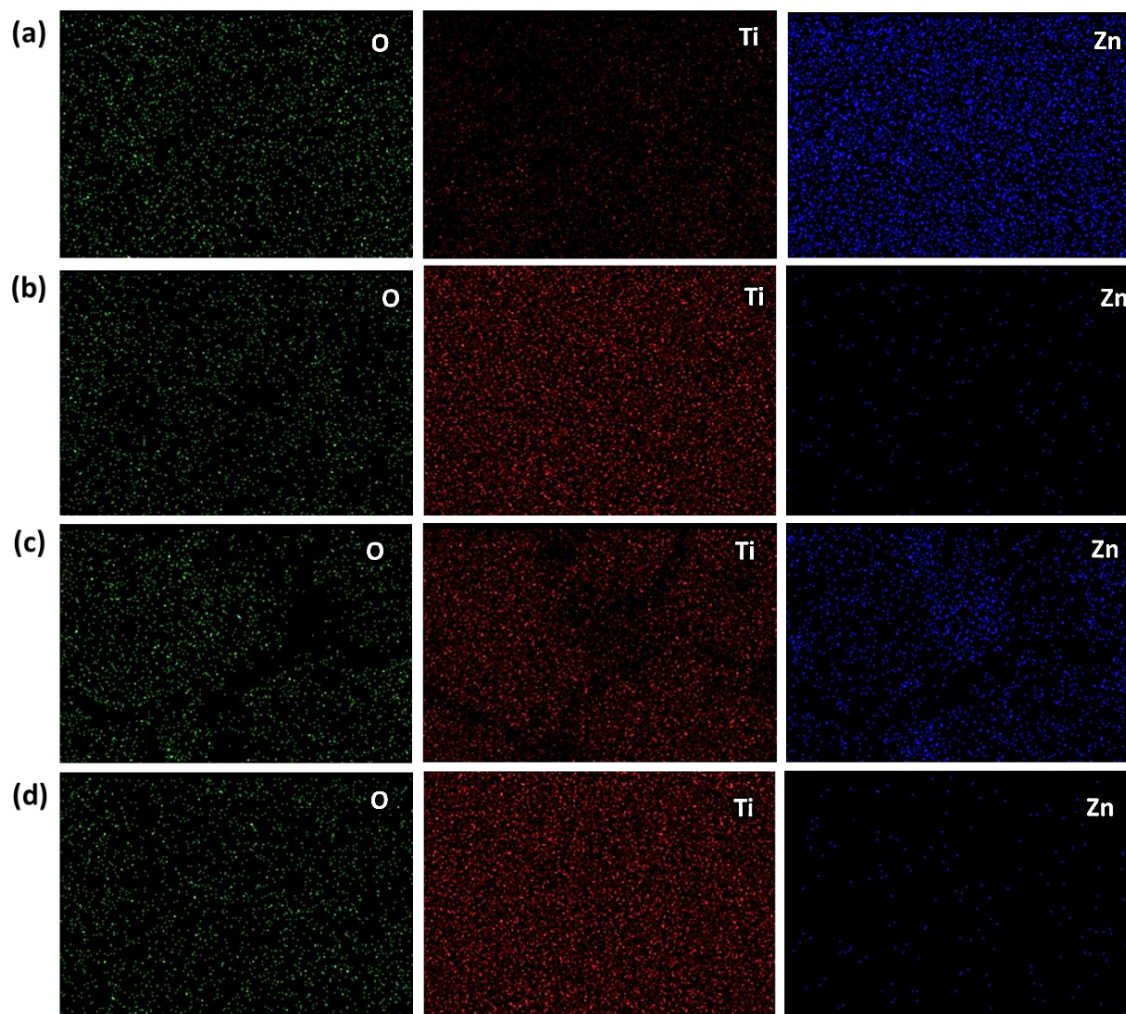


Figure 3.4. Elemental mapping on the surface of (a) T+Z, (b) T-Z, (c) T+M, and (d) T-M photoanodes.

the surface of TiO_2 layer. A similar observation was seen for the T+M and T-M photoanodes as well. EDX spectra of the T+M photoanode surface showed the presence of about 20 wt% of Zn atoms (**Figure 3.3(c)**), which was reduced to 0.7 wt% in the case of T-M photoanode films (**Figure 3.3(d)**) obtained after TiCl_4 treatment. It was also observed that the presence of Zn atoms in T-M photoanodes with voids (**Figure 3.3(b)**) were slightly higher than that of the T-Z film having surface roughness (**Figure 3.3(d)**). This could be attributed to the fact that in case of T+M photoanode from which T-M was fabricated, the ZnO is deposited within the TiO_2 layer, which might have caused more Zn atoms to be trapped within the T-M layer compared to the T-Z layer. **Figure 3.4** shows the elemental mapping of the surfaces of T+Z, T-Z, T+M and T-M photoanode films. The surface mapping of T+Z film (**Figure 3.4(a)**) shows Zn as the prominent elemental composition, whereas, from the elemental mapping shown in **Figure 3.4(b)**, it is observed that only trace

amounts of Zn atoms existed in the T-Z film surface, after TiCl_4 treatment of T+Z film. The elemental mapping of T+M and T-M films also revealed similar behaviour (**Figure 3.4(c,d)**). The T+M film showed the presence of Zn atoms, which was considerably reduced in case of T-M film.

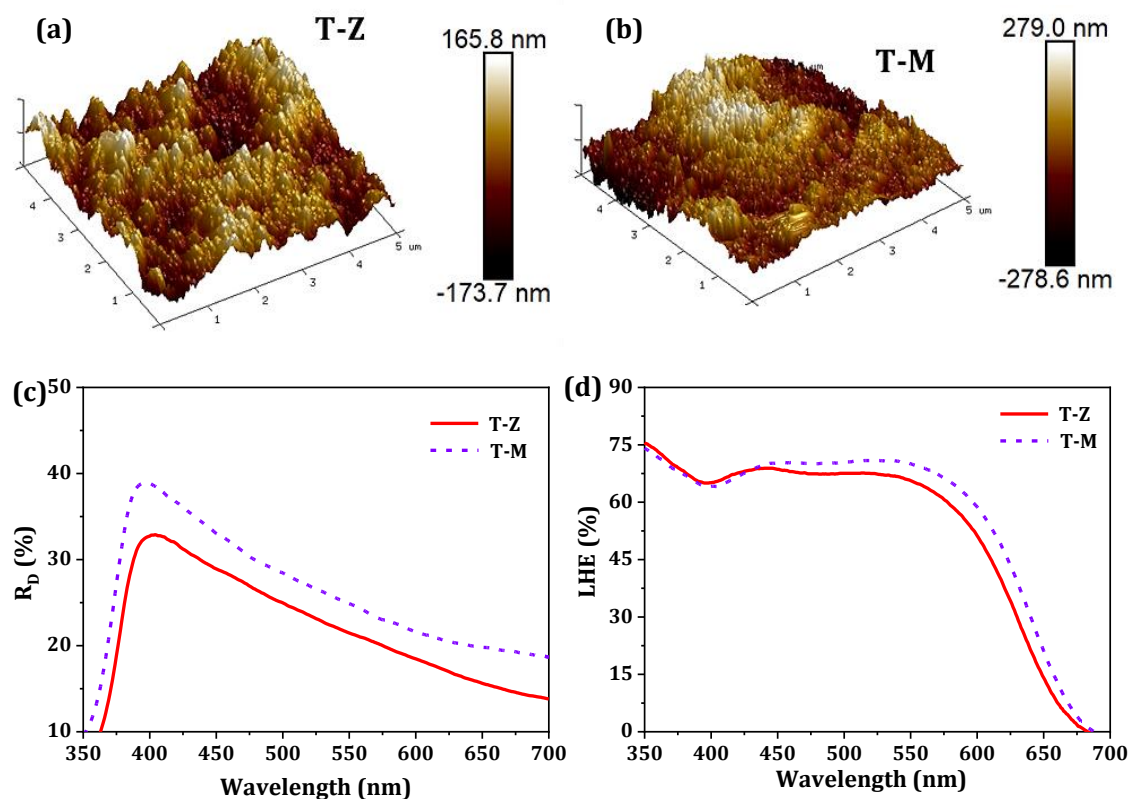


Figure 3.5. AFM images of the surface of (a) T-Z and (b) T-M photoanode films. (c) Diffuse reflectance (R_D) of unsensitized photoanode films and (d) light harvesting efficiency (LHE) of the photoanode films sensitized with D35:XY1b (1:1) dye.

The scattering properties of the photoanode layers are significantly influenced by both the roughness of the film and the presence of scattering centers like voids or scattering particles. Surface roughness of the T-Z and T-M films were determined using AFM as well as profiler analysis. The AFM images acquired for T-Z and T-M photoanodes, with a scan area of $5\mu\text{m} \times 5\mu\text{m}$, are provided in **Figure 3.5(a,b)** and the corresponding root means square roughness (R_q) is listed in **Table 3.1**. It is observed that T-M film was about 1.6 times more rough when compared to the T-Z film. Similar observations were obtained from profilometer measurements (with scan length of $1600\mu\text{m}$) as well (**Table 3.1**). Consequently, the T-M photoanode displayed better diffuse reflectance (R_D) compared to T-Z photoanode (**Figure 3.5(c) and table 3.1**), which indicate better light scattering by the T-M film. Enhanced light scattering within the photoanode film contribute towards longer

path length for light within the photoanode, leading to better light absorption. Owing to the better dye loading and light scattering capabilities of the T-M film, the corresponding dye-sensitized photoanode exhibited improved *LHE* compared to that of T-Z electrode (**Figure 3.5(d) and table 3.1**).

Table 3.1. The photoanode layer thickness (d), dye loading (DL), roughness (R_q), diffuse reflectance (R_D), and light harvesting efficiency (*LHE*) of surface textured TiO₂ photoanode film (T-Z) and bilayer TiO₂ photoanode film with templated scattering layer (T-M).

Photo-anode	d^a (μm)	DL ($\times 10^{-8}$ mol/cm ²)	Root means square roughness		R_D at 530 nm (%)	<i>LHE</i> at 530 nm (%)
			R_q^a (nm)	R_q^b (nm)		
T-Z	6.2	8.9	189	49	22.8	67.1
T-M	9.1	9.9	305	79	26.3	70.8

^a Obtained from profilometer measurement over a scan length of 1600 μm .

^b Obtained from AFM analysis over a scan area of 5 $\mu\text{m} \times 5 \mu\text{m}$.

(b) Photovoltaic performance and mass transport studies. The *J-V* characteristics of DSCs fabricated using T-Z and T-M photoanodes, co-sensitized with D35:XY1b (1:1) dyes in conjugation with [Cu(dmp)₂]^{2+/+} redox mediators, were acquired under outdoor illumination (**Figure 3.6(a)**) and the corresponding parameters are listed in **Table 3.2**. Under standard outdoor illumination (AM 1.5G) having incident intensity of 100 mW/cm², the champion T-Z device could showcase a power conversion efficiency (*PCE*) of 9.45% (with a V_{OC} of 1.01 V, J_{SC} of 13.95 mA/cm², and fill factor (*FF*) of 67%), whereas the best T-M device exhibited a lower *PCE* of 8.95% (with a V_{OC} of 1.00 V, J_{SC} of 12.98 mA/cm²,

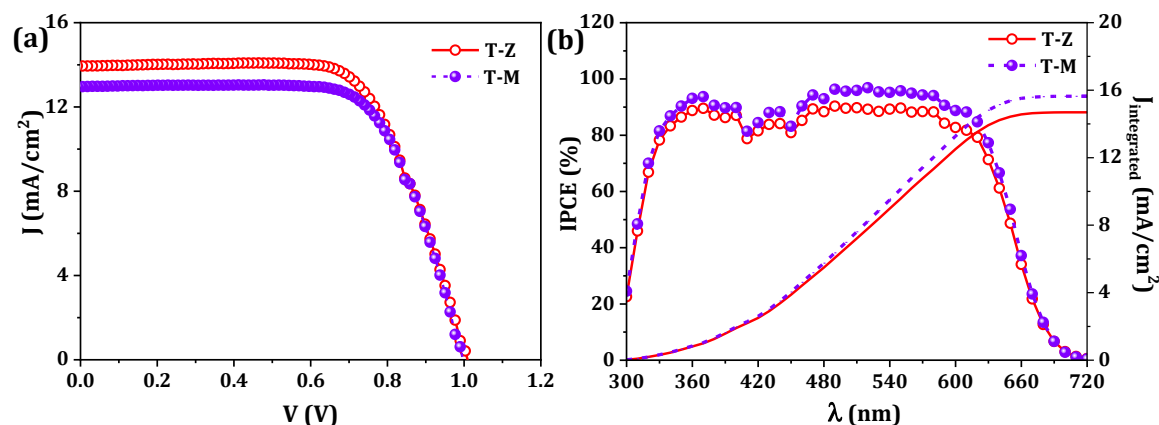


Figure 3.6. (a) *J-V* characteristic curves obtained under one sun (AM 1.5G) illumination, and (b) corresponding *IPCE* spectra for DSCs employing T-Z and T-M photoanodes co-sensitized with D35:XY1b (1:1) dyes and along with [Cu(dmp)₂]^{2+/+} electrolyte.

Table 3.2. PV parameters of DSCs employing T-Z and T-M photoanodes co-sensitized with D35:XY1b (1:1) dyes along with $[\text{Cu}(\text{dmp})_2]^{2+/+}$ electrolyte, under one sun irradiation.

Device Code	V_{oc}^a (V)	J_{sc}^a (mA/cm ²)	FF^a	PCE^a (%)	$J_{integrated}^b$ (mA/cm ²)	J_{max}^c (mA/cm ²)	J_{sat}^c (mA/cm ²)	ΔJ^c (%)
T-Z	1.01 (1.01± 0.01)	13.95 (13.56 ± 0.34)	0.67 (0.67± 0.01)	9.45 (9.31± 0.16)	14.68	14.9	14.0	6.0
T-M	1.00 (0.99± 0.01)	12.98 (12.65 ± 0.46)	0.69 (0.68± 0.01)	8.95 (8.69± 0.30)	15.64	17.0	13.0	23.5

^aObtained from J - V characterization of 3 devices under one sun condition ($AM\ 1.5G$). The parameters corresponding to the champion cell are provided, along with the average value \pm standard deviation in the parantheses.

^bTheoretical J_{SC} obtained by integration of $IPCE$ spectra.

^cmaximum J_{SC} (J_{max}), saturated J_{SC} (J_{sat}) and reduction in J_{SC} (ΔJ) obtained from current transient curves at 100 mW/cm².

and FF of 69%). It is observed that even though the T-M photoanode exhibited better LHE compared to T-Z, the fabricated DSCs utilizing the former could not attain better photovoltaic performance under one sun illumination, due to its lower J_{SC} . However, the $IPCE$ of T-M device (**Figure 3.6(b)**) is observed to be better than that of T-Z, which is reflected in the theoretical J_{SC} values ($J_{integrated}$) obtained by integrating the $IPCE$ curves of these devices (**Table 3.2**). For both the T-Z and T-M devices, the J_{SC} obtained under one sun condition (with light intensity of 100 mW/cm²), is reduced when compared to the $J_{integrated}$ obtained from $IPCE$, which is done at a much lower illumination intensity. This shows that both the devices are mass transport limited. However, the extend of this reduction in current density is significantly higher for the T-M device suggesting higher mass transport of redox species offered by the thicker photoanode layer, despite its higher LHE and $IPCE$.^[28] This is also evident from the current transient (CT) results obtained as shown in **Figure 3.7(a,b)**. Under higher intensities of 50-100 mW/cm², the current output of T-M device shows a significant decay before it saturates, while that of T-Z device shows minimal decay. At an incident light intensity of 100 mW/cm², the T-M device reached to a maximum J_{SC} (J_{max}) of 17.0 mA/cm², which saturated to a J_{SC} of 13.0 mA/cm² (J_{sat}) after 30 seconds. This suggests that if the device was free from diffusion limitations and mass transport, a current of 17.0 mA/cm² could have been achieved. On the other hand, T-Z exhibited a lower J_{max} of 14.9 mA/cm² but a higher J_{sat} of 14.0 mA/cm², when compared to T-M device, under 100 mW/cm² light intensity. A 23.5% reduction in J_{SC} (ΔJ) for T-M

device compared to a ΔJ of 6.0% for T-Z device clearly indicate higher mass transport limitation in T-M, owing to its thicker photoanode layer. However, at lower intensities, both T-M and T-Z devices show negligible decay in output current density, indicating that mass transport limitations are not significant at lower light intensities. This is also visible from the J_{SC} vs. light intensity (ϕ) curves (**Figure 3.7(c)**), which shows a linear relationship at lower intensities and deviates from linearity at higher intensities. The extend of deviation of J_{SC} vs. ϕ curves from linearity for T-Z and T-M devices can be evaluated by fitting the corresponding curves using the equation, $J_{SC} = a\phi^b$, where a and b are constant values. The value of b is more deviating from unity for T-M device (0.78) than for T-Z device (0.93), which indicates more non-linearity for T-M device, which in turn confirms its higher mass transport.

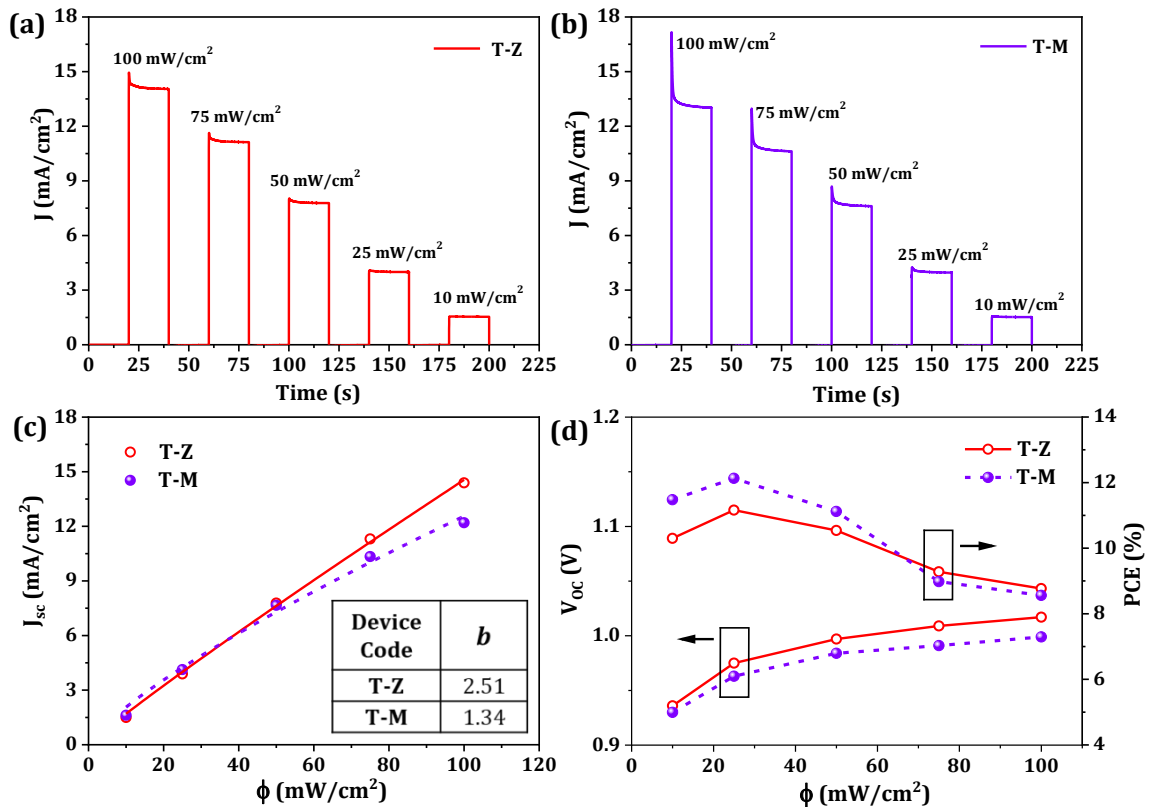


Figure 3.7. Current transient curves of (a) T-Z, and (b) T-M devices; Plots of (c) J_{SC} , (d) V_{OC} and PCE as a function of incident light intensity (ϕ), for T-Z and T-M devices. The T-Z and T-M devices employed D35:XY1b (1:1) dyes along with $[\text{Cu}(\text{dmp})_2]^{2+/+}$ electrolytes.

The variation of V_{OC} and PCE of the devices with incident light intensity is presented in **Figure 3.7(d)**. It is seen that the V_{OC} of T-M device is lower than that of T-Z device at all light intensities. Meanwhile, the PCE of T-M device is lower than T-Z only at higher intensities. This can be attributed to the variation in J_{SC} with intensity under the

influence of mass transport and diffusion limitation. At lower intensities, when mass transport becomes insignificant, the J_{SC} is determined by the other factors like *LHE*, electron collection efficiency etc. Hence the T-M device with better *LHE* possess better J_{SC} under such low intensity conditions leading to better *PCE*. Resultantly, the efficiency trend is reversed under indoor light illuminations having lower light intensities (**Figure 3.8** and **Table 3.3**). Under 1000 lux LED, the T-Z device gave a *PCE* of 21.8% (with a V_{OC} of 0.85 V, J_{SC} of 108.9 $\mu\text{A}/\text{cm}^2$, and *FF* of 74%), while the T-M device exhibited an improved *PCE* of 28.0% (with a V_{OC} of 0.83 V, J_{SC} of 130.1 $\mu\text{A}/\text{cm}^2$, and *FF* of 78%). Similarly, under 1000 lux CFL, while the *PCE* of T-Z device was only 25.3% (with a V_{OC} of 0.86 V, J_{SC} of 123.3 $\mu\text{A}/\text{cm}^2$, and *FF* of 73%), the T-M device showcased a higher *PCE* of 32.3% (with a V_{OC} of 0.84 V, J_{SC} of 136.5 $\mu\text{A}/\text{cm}^2$, and *FF* of 79%). The improved performance of T-M DSCs under indoor conditions in spite of their reduced V_{OC} could be predominantly attributed to their improved J_{SC} owing to better *LHE*.

Table 3.3. Photovoltaic parameters of the DSCs employing T-Z and T-M photoanodes co-sensitized with D35:XY1b (1:1) dyes along with $[\text{Cu}(\text{dmp})_2]^{2+/+}$ electrolyte, under standard indoor LED and CFL illuminations.

Indoor light source	P_{in}^a ($\mu\text{W}/\text{cm}^2$)	Device code	V_{oc}^b (V)	J_{sc}^b ($\mu\text{A}/\text{cm}^2$)	<i>FF</i> ^b	<i>PCE</i> ^b (%)	P_{max}^b ($\mu\text{W}/\text{cm}^2$)
1000 lux LED	306	T-Z	0.85 (0.84 ± 0.01)	108.9 (103.1 ± 5.1)	0.74 (0.75 ± 0.01)	21.8 (21.4 ± 0.6)	68 (65 ± 3)
		T-M	0.83 (0.84 ± 0.01)	130.1 (128.4 ± 1.9)	0.78 (0.76 ± 0.02)	28.0 (27.1 ± 0.9)	85 (82 ± 3)
1000 lux CFL	283	T-Z	0.86 (0.85 ± 0.01)	123.3 (115.7 ± 6.6)	0.73 (0.75 ± 0.02)	25.3 (24.7 ± 0.6)	72 (70 ± 2)
		T-M	0.84 (0.84 ± 0.01)	136.5 (134.3 ± 3.4)	0.79 (0.78 ± 0.01)	32.3 (31.3 ± 1.3)	91 (88 ± 3)

^aObtained by integration of irradiance spectra of the LED and CFL light.

^bObtained from *J-V* characterization of 3 devices under different indoor illuminations. The parameters corresponding to the champion cell are provided, along with the average value ± standard deviation in the parantheses.

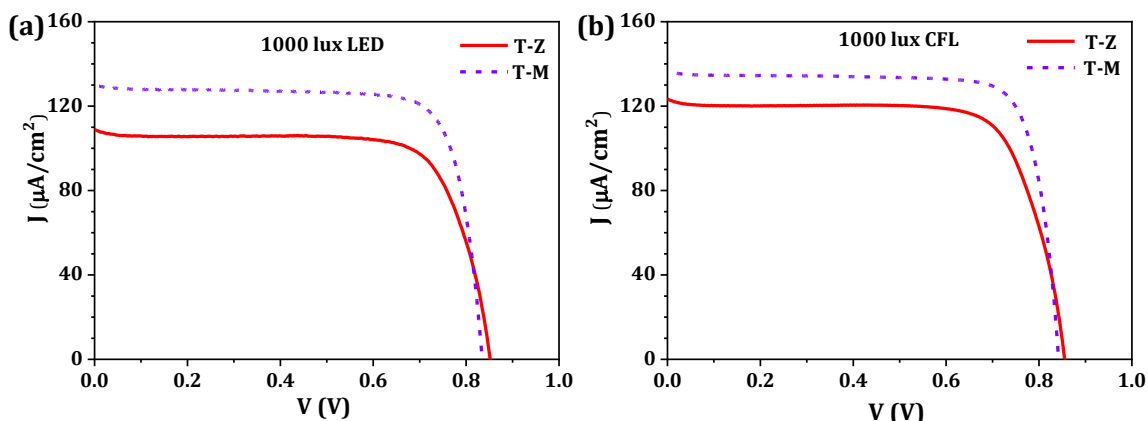


Figure 3.8. The J - V characteristics of DSCs employing T-Z and T-M photoanodes co-sensitized with D35:XY1b (1:1) dyes, along with $[\text{Cu}(\text{dmp})_2]^{2+/+}$ electrolyte, under (a) 1000 lux LED ($0.306 \text{ mW}/\text{cm}^2$), and (b) 1000 lux CFL ($0.283 \text{ mW}/\text{cm}^2$) illumination.

(c) **Advanced characterizations for interfacial charge transfer studies.** Interfacial charge transfer dynamics at various interfaces within DSCs were analyzed using advanced characterization tools and techniques. The small amount of ZnO that got deposited in the T-Z and T-M photoanode films, during TiCl_4 treatment, might influence the charge transfer characteristics within the device. It is presumed that during the TiCl_4 post treatment process of T+Z and T+M electrodes, the ZnO template particles in the photoanode films got dissolved into the TiCl_4 solution, intercalated in the TiO_2 films of the photoanodes, and got deposited within the TiO_2 layer along with the ultrathin TiO_2 post blocking layer. The presence of ZnO in T-M photoanode films was found to be slightly higher, as the ZnO template particles are deposited within the TiO_2 film of T+M photoanode, and hence can

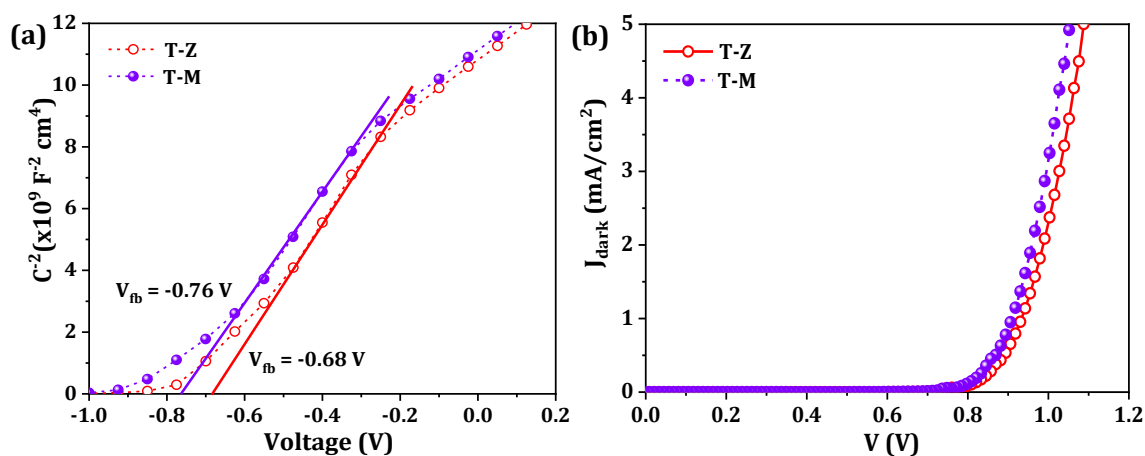


Figure 3.9. (a) The Mott-Schottky (MS) plots, and (b) J - V characteristics under dark, obtained for devices using T-Z and T-M photoanodes.

get trapped within the film even after TiCl_4 treatment. On the contrary, the ZnO template particles are deposited as an over layer in T+Z films and can be easily etched off during TiCl_4 treatment, hence the presence of ZnO in the T-Z films is slightly lower. The presence of ZnO contributed towards a slight negative shift in conduction band (CB) of TiO_2 in the T-M film as compared to the T-Z photoanode based devices. This is again validated using the Mott-Schottky (MS) plot shown in **Figure 3.9(a)**. By extrapolating the linear portion of the MS plot corresponding to T-Z and T-M photoanodes to intersect the voltage axis, we obtained the respective flat band potentials (V_{fb}) to be -0.68 V and -0.76 V relative to the copper electrolyte's redox potential, respectively. The more negatively shifted V_{fb} for T-M comparative to T-Z photoanodes correlates with a higher amount of ZnO particles deposited within the T-M film.

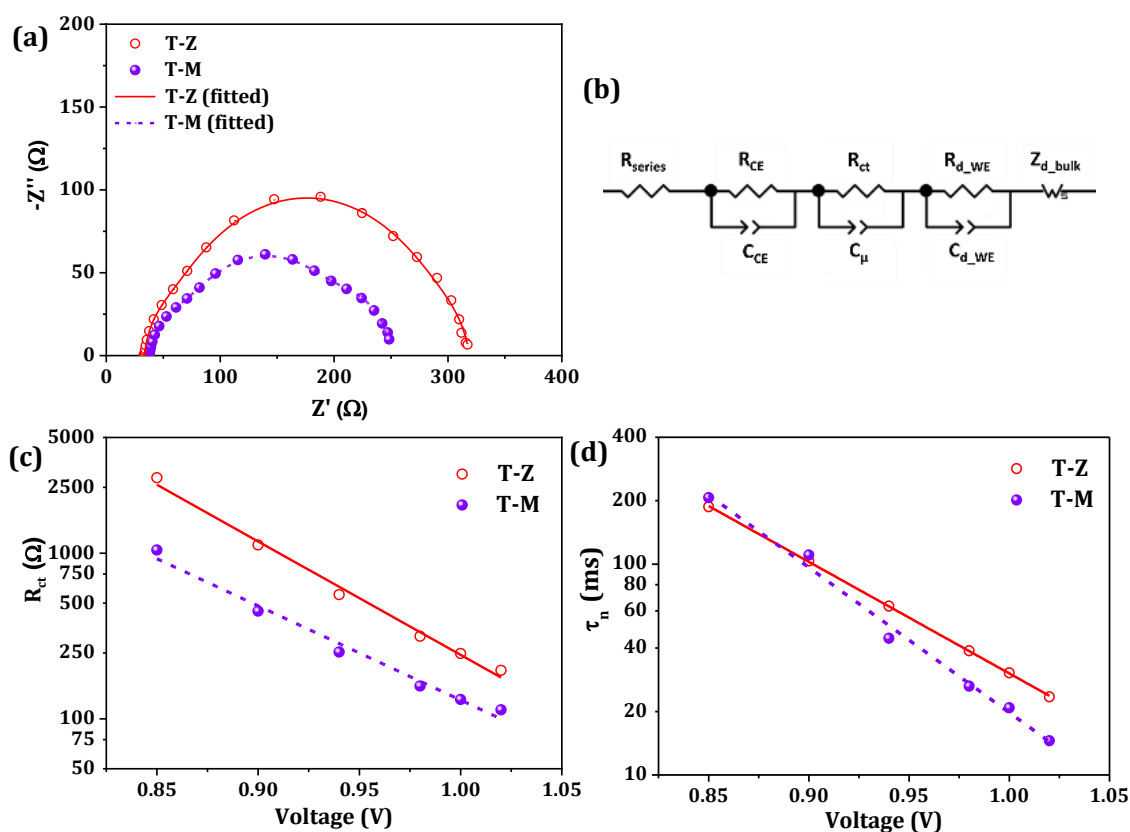


Figure 3.10. (a) Nyquist plots obtained from EIS measurement at applied bias of 1.0 V, (b) equivalent circuit used for fitting the Nyquist plots, (c) charge transfer resistance (R_{ct}) obtained by fitting the Nyquist plot, and (d) electron lifetime plotted against the potential, obtained for T-Z and T-M devices.

The EIS spectra obtained at an applied bias voltage of 1.0 V is shown in **Figure 3.10(a)**. Both the devices, T-Z and T-M, exhibited a characteristic impedance spectrum with three semicircles corresponding to the charge transfer at various interfaces in the fabricated devices using the respective photoanodes. It is clearly seen that the semicircle corresponding to T-Z device is appreciably larger compared to the T-M device. This indicates reduced charge transfer resistance at the semiconductor/electrolyte interface for T-M device. This is further quantified by fitting the EIS spectra using the equivalent circuit model as shown in the **Figure 3.10(b)**. The equivalent circuit consists of the series resistance (R_{series}), charge transfer resistance (R_{CE}) and capacitance (C_{CE}) at the counter electrode/electrolyte interface, charge transfer resistance (R_{ct}) and capacitance (C_{μ}) at the semiconductor/electrolyte interface, a Warburg's diffusion resistance corresponding to the diffusion of ions in the bulk of the electrolyte (Z_d) and resistance to the diffusion of electrolyte species within the semiconductor matrix of the working electrode (R_{WE}). The R_{ct} obtained by fitting the impedance spectra were plotted against the applied potential as shown in **Figure 3.10(c)**. As observed from the Nyquist plot, the R_{ct} for T-M was found to be lower compared to the T-Z device. Contrary to our observation in the previous chapter, where the presence of ZnO in TiO₂ film enhanced its R_{ct} , we observed a lower R_{ct} value for T-M device despite its higher ZnO content compared to T-Z. This could be attributed to the higher thickness of the T-M photoanode film.^[40,41] Owing to this lower resistance to interfacial charge transfer, the lifetime of electrons in the T-M film based DSC was comparatively less than that seen in T-Z device (**Figure 3.10(d)**). This is again confirmed

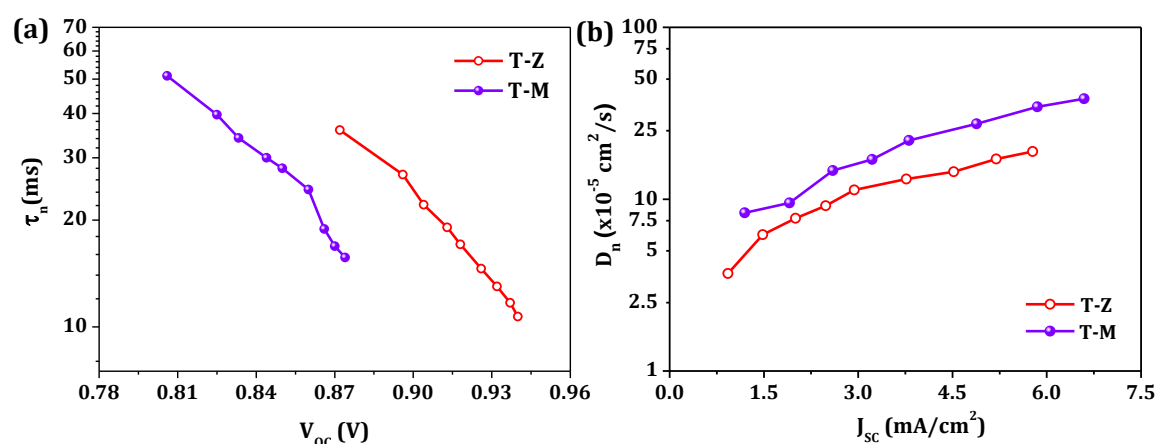


Figure 3.11. (a) Lifetime (τ_n) acquired from TVD measurement, and (b) Diffusion coefficient (D_n), acquired using TCD measurement, for T-Z and T-M devices.

using TVD measurements as well (**Figure 3.11(a)**). This indicates more recombination in thicker T-M photoanode based DSCs, which is also visible from the higher dark current observed for T-M based device (**Figure 3.9(b)**). Limited by higher recombination, the T-M based device failed to attain higher V_{OC} compared to T-Z device, even though the T-M photoanode is having the advantage of more negatively positioned TiO_2 CB. However, the presence of more ZnO content in T-M layer had a positive impact on the diffusion of electrons within the TiO_2 layer, as could be seen from the diffusion coefficient (D_n) plot obtained from TCD measurement (**Figure 3.11(b)**). Higher D_n contributed to improved J_{SC} for T-M device under low intensity light conditions. However, under high intensity illuminations, the mass transport limitation has overruled this improvement in electron mobility.

3.3.2. Optimizing the weight percentage of ZnO templates for enhanced DSC performance

T-M photoanodes were fabricated with different weight percentage (wt%) of ZnO template particles (10%, 20% and 40%) in the scattering layer, and the respective photoanodes were designated as T-M10, T-M20 and T-M40. The impact of the variation in number of voids in the scattering layer on *LHE* and *PCE* of the corresponding DSCs was investigated in detail and is described in the following sections.

(a) Effect of ZnO content on the LHE of templated photoanodes. The SEM images revealing the surface and cross-section of T-M10, T-M20 and T-M40 photoanode films are provided in **Figure 3.12**. It is observed that with the increase in wt% of ZnO template particles, there is a considerable increase in the number of grooves, cracks and voids formed in the TiO_2 layer (**Figure 3.12(a-c)**). This resulted in an increase in surface roughness (R_q) of the films with increase in the template content, while the thickness of all the photoanode films were found to be similar (**Figure 3.12(d-f)** and **Table 3.4**). However, the dye loading (DL) of the photoanode films decreased in the order T-M10 > T-M20 > T-M40. With the increase in wt% of template particles, the number of TiO_2 particles in the scattering layer got reduced, which in turn affected the number of dye molecules adsorbed on the respective photoanodes (**Table 3.4**). The diffuse reflectance (R_D) spectra for unsensitized T-Z and T-M photoanode films were provided in **Figure 3.13(a)**. It is observed that the R_D of the films increased in the order T-M10 < T-M20 < T-M40.

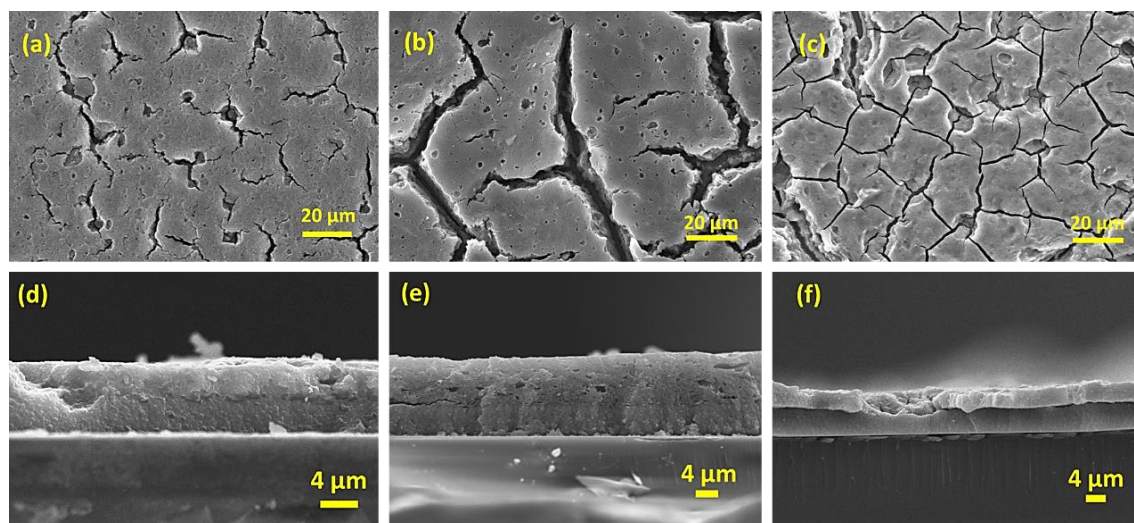


Figure 3.12. SEM images revealing the surface morphology of (a) T-M10, (b) T-M20, and (c) T-M40 photoanodes, and cross-section of (d) T-M10, (e) T-M20, and (f) T-M40 photoanodes.

Table 3.4. Photoanode layer thickness (d), dye loading (DL), root means square surface roughness (R_q), diffuse reflectance (R_D), and light harvesting efficiency (LHE) of T-Z and T-M photoanodes.

Photo-anode	wt% of ZnO in scattering layer	d^a (μm)	DL ($\times 10^{-8}$ mol/cm 2)	R_q^b (nm)	R_D at 530 nm (%)	LHE at 530 nm (%)
T-M10	10	10.5	10.0	331	26.3	70.8
T-M20	20	11.6	9.8	415	35.1	74.3
T-M40	40	11.4	9.5	538	49.0	64.3

^a Obtained from cross-sectional SEM.

^b Obtained from profilometer measurement over a scan length of 1600 μm .

As expected, the T-M40 film with the highest R_q value (538 nm) exhibited the highest R_D of 49.0% at a wavelength of 530 nm (which is the maximum absorption wavelength (λ_{max}) for the XY1b dye), followed by T-M20 (35.1%) and then T-M10 (26.3%) as listed in **Table 3.4**. A combined effect of the dye loading and scattering property of the photoanode films determine their LHE . The T-M10 photoanode with the highest dye loading possessed the least R_D , whereas the T-M40 photoanode with the highest R_D could hold only lower amount of dye molecules. Thus, the T-M20 films with optimum dye loading and scattering effects exhibited the highest LHE among the three templated photoanodes (**Figure 3.13(b)**).

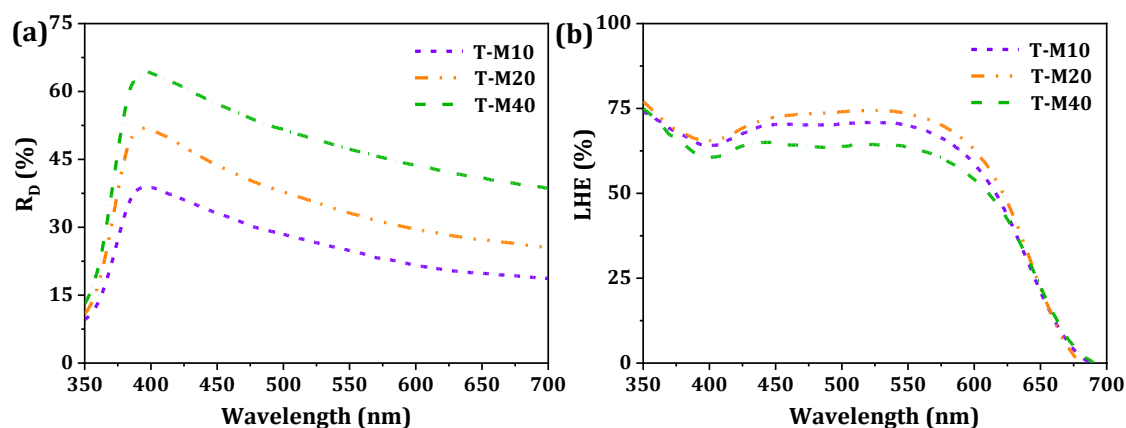


Figure 3.13. (a) Diffuse reflectance (R_D) of unsensitized T-M10, T-M20 and T-M40 photoanode films, and (b) light harvesting efficiency (LHE) of the T-M10, T-M20 and T-M40 photoanode films sensitized with D35:XY1b (1:1) co-sensitized dyes.

(b) *Photovoltaic performance evaluation under various light conditions and interfacial charge dynamics studies.* The J - V characteristics of the Cu(II/I) electrolyte ($[\text{Cu}(\text{dmp})_2]^{2+/+}$) based DSCs fabricated using T-M10, T-M20 and T-M40 photoanodes co-sensitized with D35:XY1b dyes, under AM 1.5G irradiation (100 mW/cm^2), 1000 lux CFL illumination and under dark condition are shown in **Figure 3.14**. Under standard AM 1.5G simulated sunlight (**Figure 3.14(a)**), the champion device (T-M20), with 20 wt% ZnO templates, delivered the highest PCE of 10.12%, with V_{OC} of 1.0 V, J_{SC} of 15.16 mA/cm^2 ,

Table 3.5. PV parameters of DSCs employing T-M10, T-M20 and T-M40 photoanodes co-sensitized with D35:XY1b (1:1) dyes, along with $[\text{Cu}(\text{dmp})_2]^{2+/+}$ electrolytes, under one sun (AM 1.5G) irradiation.

Device Code	V_{OC}^a (V)	J_{SC}^a (mA/cm^2)	FF^a	PCE^a (%)	$J_{integrated}^b$ (mA/cm^2)
T-M10	0.99 (0.99 ± 0.01)	12.86 (12.70 ± 0.28)	0.68 (0.67 ± 0.01)	8.65 (8.48 ± 0.17)	15.72
T-M20	1.00 (1.00 ± 0.01)	15.16 (14.99 ± 0.19)	0.67 (0.66 ± 0.01)	10.12 (9.99 ± 0.13)	16.15
T-M40	1.01 (1.01 ± 0.01)	12.09 (11.58 ± 0.44)	0.65 (0.65 ± 0.01)	7.92 (7.61 ± 0.37)	14.58

^aObtained from J - V characterization of 3 devices. The parameters corresponding to the champion cell are provided, along with the average value \pm standard deviation in the parentheses.

^bTheoretical J_{SC} obtained by the integration of IPCE spectra.

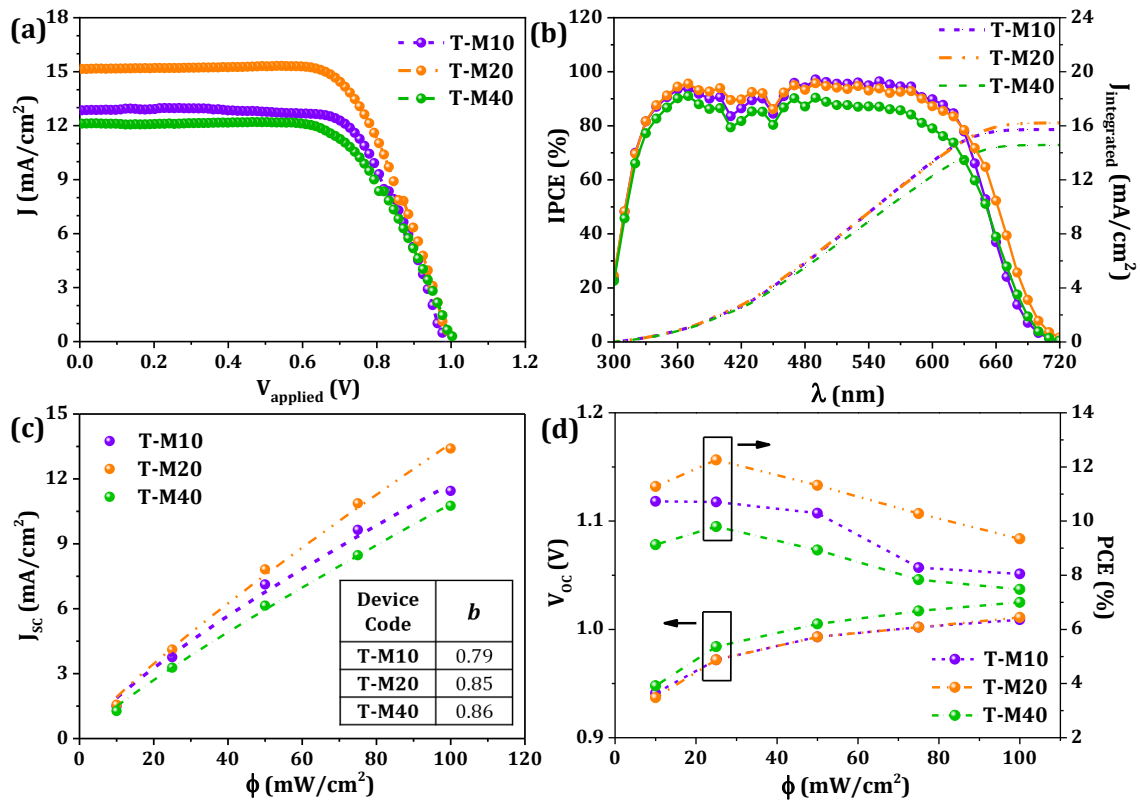


Figure 3.14. (a) J - V characteristics under AM 1.5G simulated sunlight (100 mW/cm²) and (b) corresponding $IPCE$ spectra for DSCs employing T-M10, T-M20 and T-M40 photoanodes co-sensitized with D35:XY1b (1:1) dyes, along with [Cu(dmp)₂]^{2+/+} electrolyte; plots of (c) J_{sc} , (d) V_{oc} and PCE of the DSCs as a function of incident light intensity (ϕ).

and FF of 67%. Corresponding $IPCE$ spectra are given in **Figure 3.14(b)** and the J_{sc} values obtained by integrating $IPCE$ curves are provided in **Table 3.5**. It is observed that the theoretical value of J_{sc} obtained for all the devices are higher when compared to the J_{sc} obtained under one sun irradiation. This could be attributed to the mass transport limitation present in these devices, as commonly observed in DSCs fabricated using the bulky Cu(II/I) metal complex redox electrolytes. The mass transport issues in T-M10, T-M20 and T-M40 devices were examined using their J_{sc} vs. ϕ plots (**Figure 3.14(c)**). From the value of the constant b for T-M10, T-M20 and T-M40 devices, it is observed that as the wt% of ZnO templates is increased, the mass transport issues are diminished. This might be attributed to the increase in the number of voids within the scattering layer paving the way for easy diffusion of bulky Cu(II/I) electrolyte species. An improvement in PCE was observed for all the devices with decrease in illumination intensity (**Figure 3.14(d)**), which might be attributed to the reduced mass transport problems under lower light intensities, which is

clear from the current transient (CT) curves shown in **Figure 3.15(a-c)**. The best T-M20 device exhibited the highest *PCE* of 12.26% under simulated sunlight with lower intensity of 25 mW/cm² with a *V_{OC}* of 0.97 V, *J_{SC}* of 4.11 mA/cm², and *FF* of 77%.

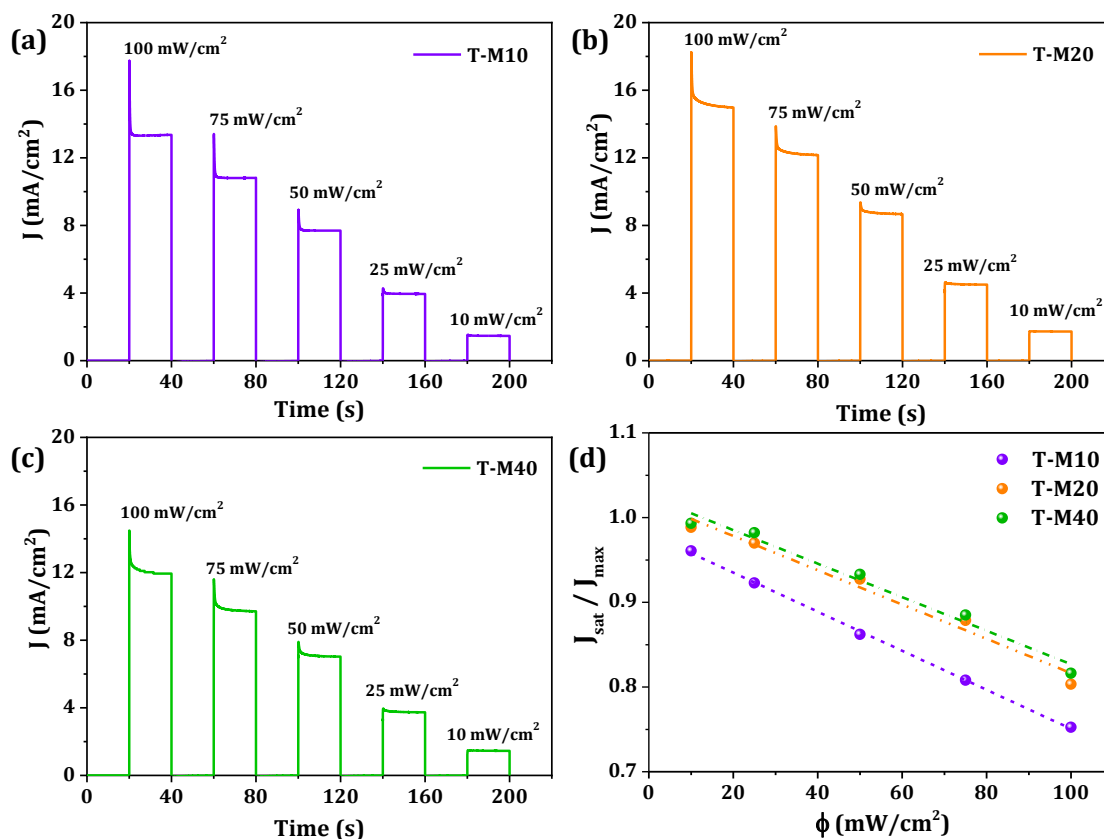


Figure 3.15. Current transient curves for (a) T-M10, (b) T-M20, (c) T-M40 devices employing D35: XY1b (1:1) dyes along with [Cu(dmp)₂]^{2+/+} electrolyte, and (d) *J_{sat}/J_{max}* ratio of these devices plotted against the incident intensity (ϕ).

The regeneration efficiency (η_{reg}) in DSC is mainly determined by the energy level distribution of the dye and the electrolyte system. Moreover, in case of DSCs using bulky electrolyte systems, the η_{reg} can be influenced by the mass transport properties of the electrolyte species, and hence can be correlated to the *J_{sat}/J_{max}* ratio, obtained from the corresponding CT curves.^[42] In our case, all the devices (T-M10, T-M20, and T-M40) employ the same set of dyes and electrolyte. Hence the difference in mass transport properties of the devices can lead to a variation in their η_{reg} . For an ideal system with no mass transport limitation, the *J_{sat}/J_{max}* ratio ought to be unity (ideal value), which leads to a η_{reg} of 100%. Whereas for systems with mass transport limitation, like the copper electrolyte based DSCs, the *J_{sat}/J_{max}* ratio deviates from ideal value (<1) and hence the η_{reg}

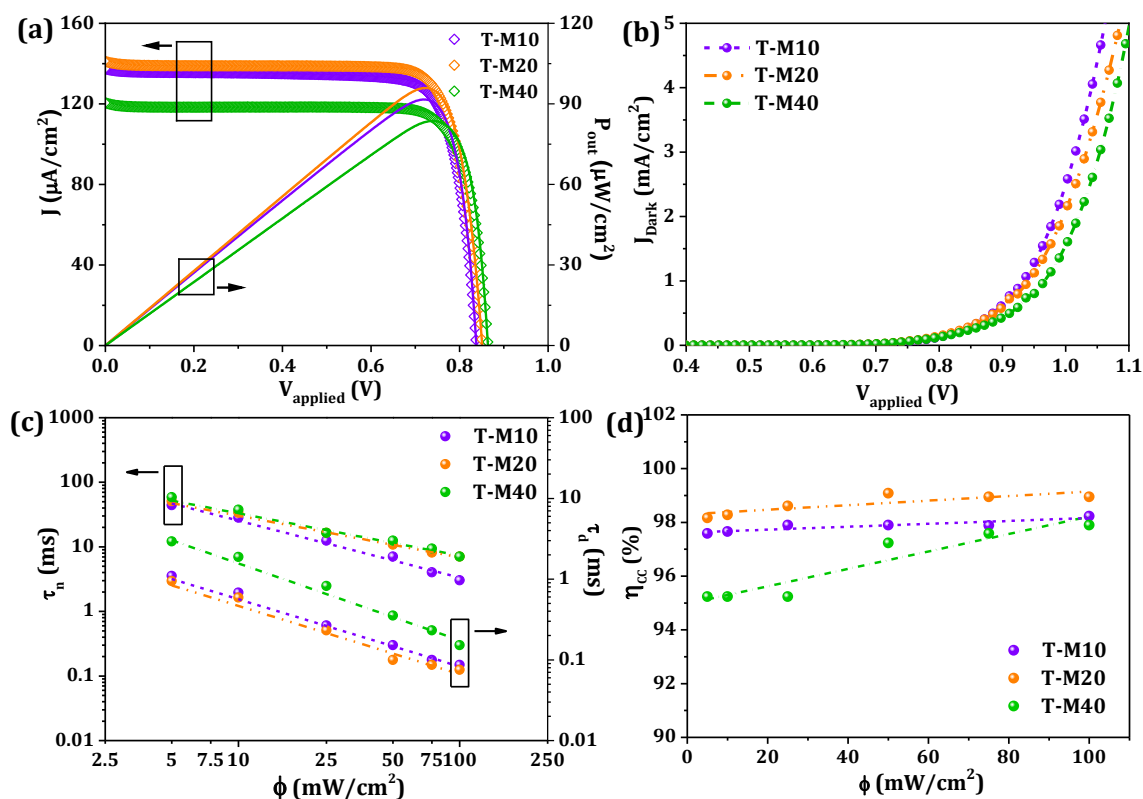


Figure 3.16. J - V characteristics under (a) 1000 lux CFL illumination, and (b) dark condition; (c) lifetime (τ_n) and diffusion time (τ_d), acquired respectively using IMVS and IMPS measurements, and (d) the charge collection efficiency (η_{CC}) of T-M10, T-M20 and T-M40 based DSCs, as a function of incident light intensity.

is less than 100%. The $J_{\text{sat}}/J_{\text{max}}$ ratio for T-M10, T-M20 and T-M40 devices were estimated at different illumination intensities (shown in **Figure 3.15(d)**). The deviation of $J_{\text{sat}}/J_{\text{max}}$ ratio from unity was highest for T-M10 and the least for T-M40 device. Because, T-M40 photoanodes were endowed with more number of vacant spaces or voids through which the electrolyte species could smoothly diffuse, as discussed before. As a result, the η_{reg} of the devices can be expected to be increasing in the order T-M10 < T-M20 < T-M40. It is observed that, even though T-M20 device was limited by mass transport issues, it could attain better J_{SC} and PCE when compared to the T-M40 device with the least mass transport limitation. This might be explained by the superior LHE of the T-M20 photoanode film, which could compensate for the decrease in J_{SC} induced by mass transport limitation. The T-M20 device could outperform even the T-Z device, not only under one sun but also under indoor light illumination (**Figure 3.16(a)** and **Table 3.6**). Under 1000 lux CFL illumination, the T-M20 device exhibited the highest PCE of 33.8% among all the devices

with a V_{OC} of 0.85 V, J_{SC} of 141.1 $\mu\text{A}/\text{cm}^2$, and FF of 80%, and P_{max} of 91 $\mu\text{W}/\text{cm}^2$. In all the illumination conditions, there was a slight increase in V_{OC} when changing the ZnO template content from 10 to 40%. This could be attributed to the reduction in electron recombination at the $\text{TiO}_2/\text{electrolyte}$ interface, because the number of TiO_2 particles decreased with the increase in weight percentage of the ZnO template particles. This is evident from the J - V curve obtained under dark (**Figure 3.16(b)**), in which the T-M10 device exhibits the highest dark current while the T-M40 gives the lowest.

Table 3.6. PV parameters for DSCs fabricated with T-M10, T-M20 and T-M40 co-sensitized with D35: XY1b (1:1) dyes along with $[\text{Cu}(\text{dmp})_2]^{2+/+}$ electrolyte, under standard 1000 lux CFL illumination.

Device Code	V_{oc}^a (V)	J_{sc}^a ($\mu\text{A}/\text{cm}^2$)	FF^a	PCE^a (%)	P_{max}^a ($\mu\text{W}/\text{cm}^2$)
T-M10	0.84 (0.84 \pm 0.01)	137.5 (136.4 \pm 1.3)	0.80 (0.77 \pm 0.03)	32.3 (31.1 \pm 1.2)	91 (88 \pm 3)
T-M20	0.85 (0.85 \pm 0.01)	141.1 (137.6 \pm 4.3)	0.80 (0.80 \pm 0.01)	33.8 (32.8 \pm 0.9)	95 (92 \pm 3)
T-M40	0.86 (0.86 \pm 0.01)	120.5 (117.6 \pm 2.6)	0.80 (0.80 \pm 0.01)	29.5 (28.6 \pm 1.0)	83 (81 \pm 2)

^aObtained from J - V characterization of 3 devices. The parameters corresponding to the champion cell are provided, along with the average value \pm standard deviation in the parentheses.

The time constants, i.e., electron lifetime (τ_n) and diffusion time (τ_d), acquired respectively using IMVS and IMPS measurements, were plotted against the incident intensity as shown in **Figure 3.16(c)**. The device using T-M40 photoanode with the lowest number of $\text{TiO}_2/\text{electrolyte}$ interface available for recombination exhibited the highest τ_n , followed by T-M20 and then T-M10. However, the lowest τ_d value was given by the T-M20 device indicating faster electron diffusion in the corresponding photoanode. This could be attributed to the higher electron concentration gradients created in the T-M20 photoanode layer because of its better *LHE* as compared to other photoanodes. The faster diffusion of electrons along with appreciable lifetime led to better charge collection efficiency (η_{CC}) in T-M20 devices (**Figure 3.16(d)**), which further contributed to better J_{SC} , not only under one sun but also under indoor illumination conditions. A single T-M20 device with an active area of $\sim 0.24 \text{ cm}^2$ when irradiated with the standard simulated sunlight ($100 \text{ mW}/\text{cm}^2$) could power a temperature sensor (ACETEQ DC-2) as shown in **Figure 3.17(a)**. However, under 1000 lux CFL illumination, two such devices needed to

be connected in series to achieve the threshold voltage (> 1.0 V) required for powering the same temperature sensor (**Figure 3.17(b)**). **Figure 3.17(c)** shows the stability of the best performing T-M20 device under 1000 lux CFL illumination. This unwraps the prospect of application of small area DSCs employing copper electrolytes using innovative photoanode architectures for powering smart electronics and IoT devices in the forthcoming years.

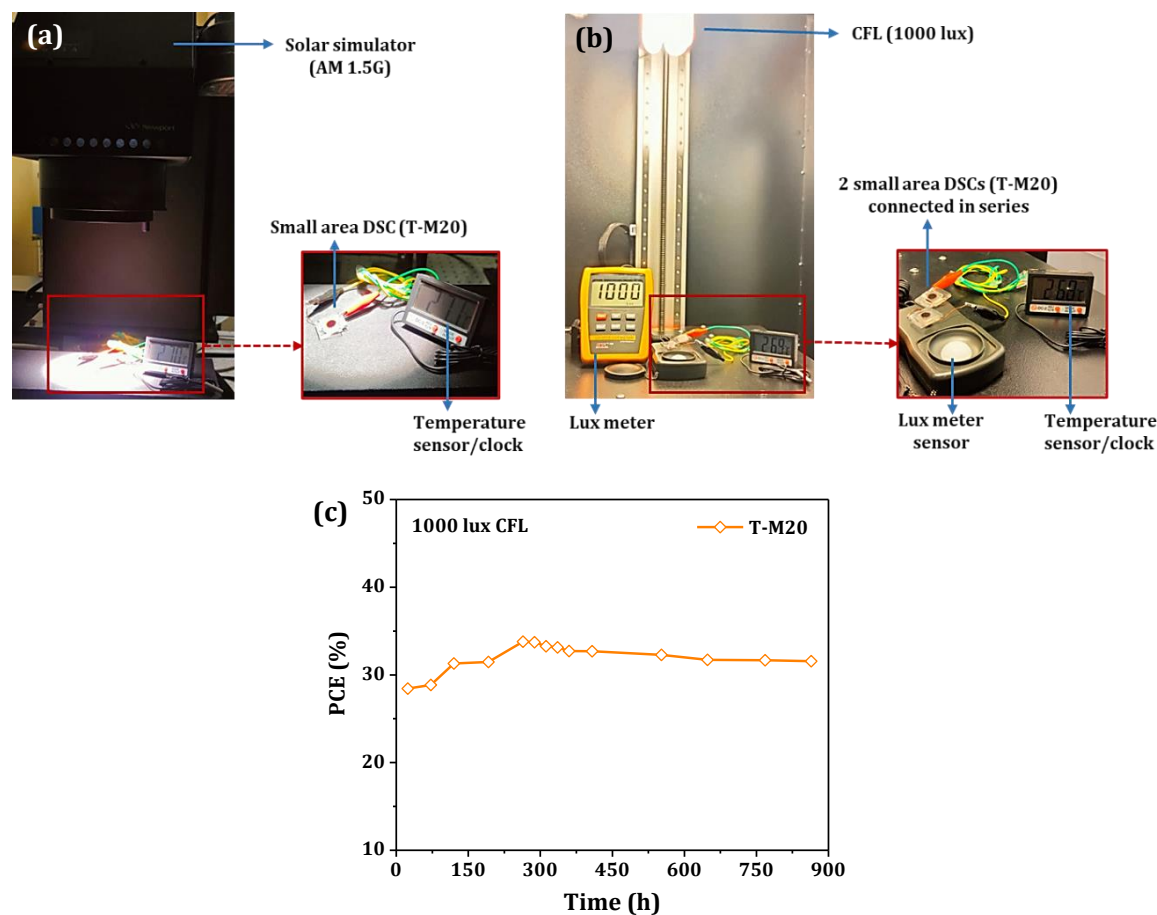


Figure 3.17. Powering a temperature sensor (ACETEQ DC-2) **(a)** using a single small area DSC, T-M20, illuminated under AM 1.5G simulated sunlight, and **(b)** using two T-M20 DSCs connected in series and illuminated under 1000 lux CFL; **(c)** Stability curve for T-M20 device under 1000 lux CFL illumination.

3.4. Conclusions

ZnO hierarchical microstructures were employed as templates to create TiO₂ photoanodes with novel architectures, namely surface textured photoanode (T-Z) and photoanode with templated scattering layers with voids (T-M), for copper electrolyte based DSCs. These photoanodes were co-sensitized using two organic dyes, D35 and XY1b,

having complementary absorption, and employed in DSCs along with $[\text{Cu}(\text{dmp})_2]^{2+/+}$ electrolyte. The T-M photoanode based DSCs were found to be diffusion limited under higher intensity illuminations. Nonetheless, the T-M devices outperformed the T-Z devices under low intensity and indoor/artificial light illuminations, owing to the higher light harvesting efficiency and faster charge transport in T-M electrodes. The performance of T-M photoanode based DSCs under outdoor as well as indoor conditions were further refined by optimizing the weight percentage (wt%) of the ZnO template particles used for creating the voids/scattering centers in the scattering layer. The T-M photoanode prepared using 20 wt% of ZnO template content, designated as T-M20, could attain an optimum light harvesting efficiency of $\sim 74\%$ (at 530 nm) and the corresponding DSC could deliver a higher charge collection efficiency ($\sim 98\%$) compared to other devices. The T-M20 based DSCs could realize a *PCE* of 10.1% under solar irradiation of intensity 100 mW/cm^2 (AM 1.5G) and 12.3% under a lower intensity of 25 mW/cm^2 . The same devices delivered a *PCE* of 33.8% under standard 1000 lux CFL illumination. The potential of using these innovative indoor light harvesting DSCs with modified photoanodes were successfully demonstrated by powering a temperature sensor by serially interconnecting two T-M20 devices (with active area of $\sim 0.24 \text{ cm}^2$ each) illuminated under 1000 lux CFL. Moreover, a single T-M20 device could power the sensor under high intensity one sun condition. Integration of such small area DSCs with electronic devices such as sensors and actuators can realize the development of self-powered IoT systems for future applications.

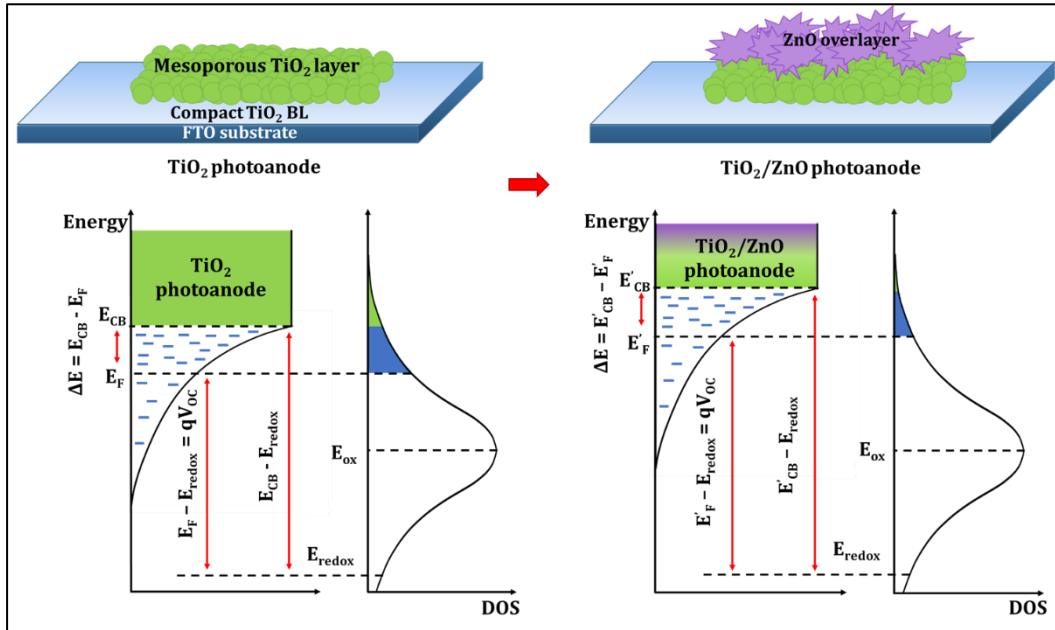
References

- [1] Y. Shozo, Y. Youhai, M. Kazuhiro, *Acc Chem Res* **2009**, *42*, 1827.
- [2] G. Boschloo, A. Hagfeldt, *Acc Chem Res* **2009**, *42*, 1819.
- [3] G. Boschloo, A. Hagfeldt, *Acc Chem Res* **2009**, *42*, 1819.
- [4] A. Hagfeldt, M. Gratzel, *Chem. Rev* **1995**, *95*, 49.
- [5] G. Oskam, B. V. Bergeron, G. J. Meyer, P. C. Searson, *Journal of Physical Chemistry B* **2001**, *105*, 6867.
- [6] M. Wang, N. Chamberland, L. Breau, J. E. Moser, R. Humphry-Baker, B. Marsan, S. M. Zakeeruddin, M. Grätzel, *Nature Chemistry* **2010**, *2*, 385.
- [7] Z. Zhang, P. Chen, T. N. Murakami, S. M. Zakeeruddin, M. Grätzel, *Adv Funct Mater* **2008**, *18*, 341.
- [8] S. A. Sapp, C. M. Elliott, C. Contado, S. Caramori, C. A. Bignozzi, *J Am Chem Soc* **2002**, *124*, 11215.

- [9] H. Nusbaumer, J. E. Moser, S. M. Zakeeruddin, M. K. Nazeeruddin, M. Grätzel, *Journal of Physical Chemistry B* **2001**, *105*, 10461.
- [10] H. Nusbaumer, S. M. Zakeeruddin, J. E. Moser, M. Grätzel, *Chemistry – A European Journal* **2003**, *9*, 3756.
- [11] Y. Bai, Q. Yu, N. Cai, Y. Wang, M. Zhang, P. Wang, *Chemical Communications* **2011**, *47*, 4376.
- [12] S. Hattori, Y. Wada, S. Yanagida, S. Fukuzumi, *J Am Chem Soc* **2005**, *127*, 9648.
- [13] Y. Saygili, M. Söderberg, N. Pellet, F. Giordano, Y. Cao, A. B. Munoz-García, S. M. Zakeeruddin, N. Vlachopoulos, M. Pavone, G. Boschloo, L. Kavan, J. E. Moser, M. Grätzel, A. Hagfeldt, M. Freitag, *J Am Chem Soc* **2016**, *138*, 15087.
- [14] S. C. Pradhan, J. Velore, A. Hagfeldt, S. Soman, *J Mater Chem C* **2022**, *10*, 3929.
- [15] T. Higashino, H. Imahori, *ACS Energy Lett* **2022**, *7*, 1926.
- [16] M. Freitag, F. Giordano, W. Yang, M. Pazoki, Y. Hao, B. Zietz, M. Grätzel, A. Hagfeldt, G. Boschloo, *Journal of Physical Chemistry C* **2016**, *120*, 9595.
- [17] A. Grobelny, Z. Shen, F. T. Eickemeyer, N. F. Antariksa, S. Zapotoczny, S. M. Zakeeruddin, M. Grätzel, A. Grobelny, Z. Shen, F. T. Eickemeyer, N. F. Antariksa, S. M. Zakeeruddin, M. Grätzel, S. Zapotoczny, *Advanced Materials* **2023**, *35*, 2207785.
- [18] E. Tanaka, H. Michaels, M. Freitag, N. Robertson, *J Mater Chem A Mater* **2020**, *8*, 1279.
- [19] H. Michaels, M. Rinderle, R. Freitag, I. Benesperi, T. Edvinsson, R. Socher, A. Gagliardi, M. Freitag, *Chem Sci* **2020**, *11*, 2895.
- [20] M. Freitag, J. Teuscher, Y. Saygili, X. Zhang, F. Giordano, P. Liska, J. Hua, S. M. Zakeeruddin, J. E. Moser, M. Grätzel, A. Hagfeldt, *Nature Photonics* **2017**, *11*, 372.
- [21] Y. Liu, Y. Cao, W. Zhang, M. Stojanovic, M. I. Dar, P. Péchy, Y. Saygili, A. Hagfeldt, S. M. Zakeeruddin, M. Grätzel, *Angewandte Chemie* **2018**, *130*, 14321.
- [22] Y. Cao, Y. Liu, S. M. Zakeeruddin, A. Hagfeldt, M. Grä, M. Grä Tzel, *Joule* **2018**, *2*, 1108.
- [23] D. Zhang, M. Stojanovic, Y. Ren, Y. Cao, F. T. Eickemeyer, E. Socie, N. Vlachopoulos, J. E. Moser, S. M. Zakeeruddin, A. Hagfeldt, M. Grätzel, *Nature Communications* **2021**, *12*, 1.
- [24] Y. Ren, D. Zhang, J. Suo, Y. Cao, F. T. Eickemeyer, N. Vlachopoulos, S. M. Zakeeruddin, A. Hagfeldt, M. Grätzel, *Nature* **2023**, *613*, 60.
- [25] A. Jagadeesh, G. Veerappan, P. S. Devi, K. N. N. Unni, S. Soman, *J Mater Chem A* **2023**, *11*, 14748.
- [26] S. M. Meethal, S. C. Pradhan, J. Velore, S. Varughese, R. S. Pillai, F. Sauvage, A. Hagfeldt, S. Soman, *J Mater Chem A* **2023**, *6*, 1081.
- [27] S. C. Pradhan, A. Hagfeldt, S. Soman, *J Mater Chem A* **2018**, *6*, 22204.

- [28] J. Velore, S. Chandra Pradhan, T. W. Hamann, A. Hagfeldt, K. N. N. Unni, S. Soman, *ACS Appl Energy Mater* **2022**, *5*, 2647.
- [29] M. Pazoki, N. Taghavinia, A. Hagfeldt, G. Boschloo, *Journal of Physical Chemistry C* **2014**, *118*, 16472.
- [30] J. M. Ji, H. Zhou, Y. K. Eom, C. H. Kim, H. K. Kim, *Adv Energy Mater* **2020**, *10*, 2000124.
- [31] S. Hore, P. Nitz, C. Vetter, C. Prah, M. Niggemann, R. Kern, *Chemical Communications* **2005**, 2011.
- [32] J. W. Lee, J. H. Moon, *Nanoscale* **2015**, *7*, 5164.
- [33] G. Yang, J. Zhang, P. Wang, Q. Sun, J. Zheng, Y. Zhu, *Current Applied Physics* **2011**, *11*, 376.
- [34] S. H. Han, S. Lee, H. Shin, H. S. Jung, *Adv Energy Mater* **2011**, *1*, 546.
- [35] T. T. T. Pham, N. Mathews, Y. M. Lam, S. Mhaisalkar, *J Electron Mater* **2017**, *46*, 3801.
- [36] T. T. T. Pham, N. Mathews, Y. M. Lam, S. Mhaisalkar, *Physica B Condens Matter* **2018**, *532*, 225.
- [37] T. T. Trang Pham, T. M. Koh, K. Nonomura, Y. M. Lam, N. Mathews, S. Mhaisalkar, *ChemPhysChem* **2014**, *15*, 1216.
- [38] S. Sasidharan, A. Jagadeesh, S. C. Pradhan, B. N. Nair, A. Azeez Peer Mohamed, K. N. Narayanan Unni, S. Soman, U. Nair Saraswathy Hareesh, *Solar Energy* **2021**, *226*, 214.
- [39] S. Sasidharan, S. C. Pradhan, A. Jagadeesh, B. N. Nair, A. A. P. Mohamed, N. U. Narayanan, S. Soman, U. N. S. Hareesh, *ACS Appl Energy Mater* **2020**, *3*, 12584.
- [40] R. Escalante, R. García-Rodríguez, B. E. Heredia-Cervera, M. A. Aguilar-Frutis, N. Gómez-Ortíz, J. Villanueva-Cab, G. Oskam, *Energy and Environment Focus* **2014**, *2*, 280.
- [41] R. García-Rodríguez, J. Villanueva-Cab, J. A. Anta, G. Oskam, *Materials* **2016**, *9*, 33.
- [42] H. S. Kim, S. B. Ko, I. H. Jang, N. G. Park, *Chemical Communications* **2011**, *47*, 12637.

Synergetic effect of TiO₂/ZnO bilayer photoanodes realizing exceptionally high V_{OC} in DSCs under outdoor and indoor illuminations



Abstract: Energy harvesting and managing circuits in smart internet of thing (IoT) devices demand higher open circuit potentials (V_{OC}). However, recombination losses often reduce the V_{OC} in DSCs, particularly when lit indoors. We introduce a novel TiO₂/ZnO bilayer architecture that can achieve higher V_{OC} by controlling the position of the conduction band (CB) and minimizing the recombination losses. We were able to obtain a record V_{OC} of 1.27 V from a single junction device under 100 mW/cm² solar irradiation and 1.295 V under higher intensity LED light (200 mW/cm²) by utilizing this novel bilayer electrodes in conjunction with MS5 dye and [Cu(dmp)₂]^{2+/+} redox mediator. Additionally, under 1000 lux light-emitting diode (LED) and 1000 lux compact fluorescent light (CFL) illumination, these bilayer devices showed an impressive V_{OC} of 1.025 V. This work emphasizes the possibility of altering semiconductor and device architecture to achieve higher V_{OC} in DSCs opening possibilities to integrate these devices with smart IoT gadgets making them autonomous and sustainable.

4.1. Introduction

In the smart world of connected technologies fueled by fourth industrial revolution (industry 4.0), the use of automation and digitization through the integration of the Internet of Things (IoT), Artificial Intelligence (AI), cloud computing, and Machine Learning (ML) into our daily activities continues to rise in popularity.^{1,2} In order to achieve continuous communication between these diverse devices and guarantee their effective utilization in this intelligent connected ecosystem, a significant quantity of battery-operated electronic sensors and actuator nodes are needed. The frequent replacement of batteries in billions of these communication devices adds to the burden of the carbon economy and sustainability, which may eventually pose a threat to the environment. This makes battery-free energy-harvesting Internet of Things imperative.³⁻⁵ These low-power electronic devices, which are mostly used indoors, can become self-sufficient by using state-of-the-art indoor/ambient light harvesting dye-sensitized photovoltaic cells (DSCs) to augment their energy needs.⁶⁻¹⁰ Furthermore, the application possibilities and market penetration of DSCs are further enhanced by the use of environmentally friendly materials, less energy-intensive manufacturing process, ability to fabricate these devices on flexible substrates like metal and plastic, and compliance for recycling and reusing.¹¹⁻¹⁵ In the Internet of Things (IoT) ecosystem, electronic communication devices only require lower current (μA to mA range) but, a higher threshold voltage ($>1\text{V}$) to operate continuously.¹⁶⁻¹⁸ This necessitates development of DSCs that can deliver higher voltage, preferably above 1V , under ambient or indoor lighting, from single small area DSC. This will ultimately lower the requirement for interconnection of multiple DSCs to achieve the desired voltage, which reduces the carbon footprint and ownership costs of the device. Using alternate redox shuttles based on cobalt and copper metal complexes turned out to be an effective and successful strategy among the many used.^{8-10,19-24} Since cobalt complexes are bulky and have limited mass transport, they have problems with recombination and regeneration, which lowers the values for short circuit current density (J_{SC}) and open circuit voltage (V_{OC}) of DSCs employing these complexes as electrolyte.²⁵ Zhang *et al.* recently achieved a V_{OC} of 1.24 V under one sun (100 mW/cm^2) and 0.98 V under 1000 lux fluorescent light (CFL) illumination by using copper redox mediators ($[\text{Cu}(\text{tmby})_2]^{2+/+}$) in combination with a custom-designed organic dye (MS5).²⁶ In the present chapter, we are introducing an innovative material engineering approach to further improve the V_{OC} of DSCs under both

outdoor and indoor illumination and to further extend it by demonstrating its potential application powering a temperature sensor.

Since the semiconductor layer regulates the charge transport and recombination at the dye/electrolyte interfaces, it plays a crucial role in determining the V_{OC} in DSCs. Titania (TiO₂) nanoporous films are widely used in DSCs because of their favourable band gap, conduction band (CB) edge, high surface area, low defect count, chemical stability, affordability, and ease of availability.^{12,27} Zinc oxide (ZnO), with comparable band edges to TiO₂ and superior electron mobility, is considered as a promising candidate for the development of efficient DSCs.^{27–29} The application of 3D structures and hierarchical ZnO aggregates in DSCs helped in improving dye loading and scattering, which ultimately contributed to the enhancement in J_{SC} .^{30–32} In order to prevent recombination at the semiconductor/dye/electrolyte and FTO/electrolyte interfaces, compact ZnO blocking/buffer layers were also used.^{33,34} However, poor dye adsorption, rapid dye degradation, and increased recombination lower performance in ZnO-based DSCs resulting from delayed charge separation at the ZnO/dye/electrolyte interface.^{35–37} Here we present a complementary photoanode engineering approach that takes advantage of both materials, i.e. TiO₂ and ZnO, to deliver higher V_{OC} by precisely controlling the CB position and minimizing recombination losses at the semiconductor/electrolyte junction. For this, ZnO microstructures are utilized as overlayers above TiO₂ nanoporous layer. With this new architecture, a higher V_{OC} of 1.13 V was achieved using standard Y123 organic sensitizer in conjunction with [Cu(dmp)₂]^{2+/+} electrolyte, as opposed to 1.02 V for the control device with TiO₂ layer alone. The effect was more noticeable under indoor lighting (CFL and LED). With this novel TiO₂/ZnO bilayer stacked photoanode architecture, we were able to achieve a V_{OC} of 1.0 V at 1000 lux illumination. Further, the introduction of an ultrathin TiO₂ blocking layer (BL) over the TiO₂/ZnO bilayer could potentially address stability issues resulting from ZnO degradation in the presence of electrolytes.³⁸ We accomplished a record V_{OC} of 1.27 V under full sun (100 mW/cm²) irradiation, 1.295 V under higher intensity LED light (200 mW/cm²), and 1.025 V under 1000 lux CFL as well as LED illuminations by sensitizing the new TiO₂/ZnO bilayer photoanodes with MS5 dye instead of Y123. As of date, this is the highest recorded V_{OC} under standard indoor lighting conditions of 1000 lux using a single junction DSC. Finally, we have demonstrated the development of a battery-free, self-powered temperature sensor by integrating it with a single bilayer DSC (0.24 cm² active area). This illustrates how these high V_{OC} DSCs can

be used in real-world situations to reduce the need for batteries and hence minimize carbon emissions.

4.2. Experimental procedure

4.2.1. Synthesis and characterization of ZnO hierarchical structures

A simple process using zinc nitrate hexahydrate (Merck) as the precursor and urea (Merck) as the precipitant was used for the synthesis of ZnO hierarchical structures, as detailed in chapter 2A (section 2A.2.1), by varying the concentration of urea in the reaction mixture. During the standard synthesis procedure, a concentrated aqueous urea solution was stirred continuously and vigorously while an aqueous solution of zinc nitrate hexahydrate was added dropwise into it. Zn^{2+} ions are produced when zinc nitrate hexahydrate ($\text{Zn}(\text{NO}_3)_2 \cdot 6\text{H}_2\text{O}$) dissolves in water [equation (2A.2)]. Simultaneously, urea (CON_2H_4) hydrolyses and breaks down in water at temperatures higher than 60°C , releasing hydroxyl (OH^-) and carbonate (CO_3^{2-}) ions [equations (2A.3) and (2A.4)]. Zn^{2+} ions react with CO_3^{2-} and OH^- ions in the reaction mixture to form hydroxide zinc carbonate (HZC, $\text{Zn}_5\text{CO}_3(\text{OH})_6 \cdot \text{H}_2\text{O}$) when the OH^- ions raise the pH of the reaction mixture to provide a favourable reaction condition [equation (2A.5)]. Pure ZnO is obtained from HZC when it is annealed above 300°C , after losing H_2O and CO_2 [equation (2A.6)]. Three reaction mixtures were made with three different concentrations of urea (0.03 M, 0.08 M, and 0.8 M) and the same concentration of zinc nitrate hexahydrate (0.02 M) in order to synthesize three distinct samples, labelled as Z1, Z2 and Z3. After an hour of agitation at 1000 rpm, the reaction mixtures were placed in the furnace and maintained at 90°C for 24 hours. After being cleaned with ethanol and DI water, the white precipitates (HZC) obtained were vacuum dried for 8 hours at 60°C . The as-synthesized samples were used for fabricating DSC photoanodes, during which the samples get converted to ZnO by annealing at 500°C .

Using a Zeiss EVO 18 cryo-SEM Special Ed scanning electron microscope (at an acceleration voltage of 15.0 kV), the morphology of the as-synthesised samples were examined. The specific surface area of the samples were determined using the Brunauer-Emmett-Teller (BET) model based on data acquired from the standard N_2 adsorption technique using a surface area analyser (Tristar II, Micrometrics). A high-resolution transmission electron microscope (JEOL JEM F 200 EELS STEM, EDS) was used to further analyze the morphological characteristics, crystallite size, and crystallographic orientation of the samples annealed at 500°C . ImageJ software was used to analyze the

images obtained using SEM and TEM, and to estimate the of the particle size and crystallite size from the corresponding micrographs. Using the X-ray diffraction patterns captured by an X-ray diffractometer (Malvern PANalytical B.V.) in the 2θ range of 20° to 80° (in slow scan mode), the crystallinity and phase of the annealed samples were verified. X'pert Highscore software was used to analyze the XRD patterns and determine the crystal size and phase of the samples.

4.2.2. Photoanode preparation and characterization

The as-synthesized HZC samples (Z1, Z2, and Z3) were ground into a paste in a mortar both before and after adding a heated mixture (100°C) of 60 wt% α -terpineol (Merck) and 10 wt% ethyl cellulose (Merck). Glass substrates coated with fluorine doped tin oxide, FTO (TEC 10, Merck) was used as the conducting substrate to prepare photoanodes for DSCs. The FTO substrates were cut to small pieces measuring 1.6 cm x 1.6 cm, which were then thoroughly cleaned in an ultrasonic bath for 30 minutes using a soap solution, 30 minutes using de-ionized water, 15 minutes using isopropanol, and 15 minutes using acetone. Finally, they were annealed for 30 minutes at 500°C . After the cleaned FTO glasses were treated with UV/ozone for 15 minutes, the electrodes were submerged in a 50 mM aqueous solution of TiCl_4 at 75°C for 30 minutes to deposit TiO_2 pre-blocking layer. The FTO substrates deposited with pre-blocking layer were then subjected to a step-by-step annealing process, which involved slow heating and maintenance of the temperature at 150°C for 10 minutes, 300°C for 10 minutes, 350°C for 10 minutes, 450°C for 10 minutes, and finally 500°C for 30 minutes, before slow cooling. The standard TiO_2 photoanode (T) was created by depositing a commercial titania paste (18NR-T, GreatcellSolar, Australia) over an active area of 0.24 cm^2 on the FTO substrate. The TiO_2/ZnO bilayer photoanodes (T+Z) were fabricated by coating an additional layer of HZC paste over the TiO_2 active layer after drying the active layer at 100°C for 10 minutes. Finally, the electrodes were put to a step-by-step annealing procedure up to 500°C for 30 minutes. **Figure 4.1(a)** shows the fabrication scheme for the bilayer TiO_2/ZnO devices. For electrodes that used blocking layers (BL), screen printing was used to deposit a commercial TiO_2 BL solution (GreatcellSolar, Australia) over the TiO_2/ZnO stacked photoanodes before annealing at 500°C .

The morphological and crystallographic features of unsensitized photoanode films were examined using FESEM and XRD analysis. FESEM images were acquired using Zeiss Gemini 500 and were analyzed using ImageJ software to determine the surface

morphology and film thickness. The XRD patterns of the films were captured in the 2θ range of 20° to 70° using a Malvern PANalytical B.V. X-ray diffractometer. Using a Biologic electrochemical workstation (VMP3), Mott Schottky analysis was performed on the dummy cells made with unsensitized photoanodes. The dye loading studies of the photoanode films were carried out as described in chapter 2A (section 2A.2.2). Briefly, the unsensitized photoanodes were immersed in a 0.01 mM dye solution for 16 hrs. The maximum absorbance of the dye solution before (abs1) and after (abs2) the immersion of photoanodes were obtained using the UV-Visible spectrometer (Shimadzu model 2100) and the amount of dye adsorbed per unit area (mol/cm^2) of the photoanode film was determined using equation (2A.1).

4.2.3 Fabrication and characterization of DSCs

DSCs were fabricated as described in the previous chapters. The photoanodes that were prepared as per the previous section 4.2.2. were subjected to a 16 hour immersion in a 0.1 mM dye solution that was prepared using a 1:1 mixture of acetonitrile and tert-butanol. As counter electrodes for our devices, we used the conducting polymer poly (3,4-ethylene dioxythiophene) (PEDOT) electro-polymerized using the electrochemical workstation (Autolab, Metrohm) on cleaned 1.6 cm x 1.6 cm FTO substrates (TEC7, GreatcellSolar, Australia). The FTO glass plates were drilled with holes, ultrasonically cleaned for 45 minutes with soap solution, 45 minutes with de-ionized water, and 45 minutes with ethanol, then annealed at 500°C for 30 minutes followed by UV/ozone treatment for 15 minutes, prior to the PEDOT deposition. The dye-sensitized photoanode and the counter electrode were then joined together by hot pressing at 120°C by utilizing a 25 μm thermoplastic spacer (Surlyn, GreatcellSolar Australia). The copper dimethyl phenanthroline complex electrolyte, bis(2,9-dimethyl-1,10-phenanthroline copper (II/I) bis(trifluoromethanesulfonyl)imide (Dyename A.B, Sweden) ($0.2\text{ M } [\text{Cu}(\text{dmp})_2]^{1+}$ and $0.04\text{ M } [\text{Cu}(\text{dmp})_2]^{2+}$) were dissolved in acetonitrile solvent along with 0.1 M bis(trifluoromethane)sulfonimide lithium salt, LiTFSI (Merck) and 0.6 M 4-tert-butylpyridine, TBP (Merck) as additives to prepare the electrolyte. Ultimately, the electrolyte solution was introduced in the inter-electrode spacing in the assembled device through the counter electrode's holes, which were sealed to avoid solvent evaporation and leakage. **Figure 4.1(b)** shows the chemical structures of the copper redox mediator and organic sensitizers used for fabricating the DSCs in the present work.

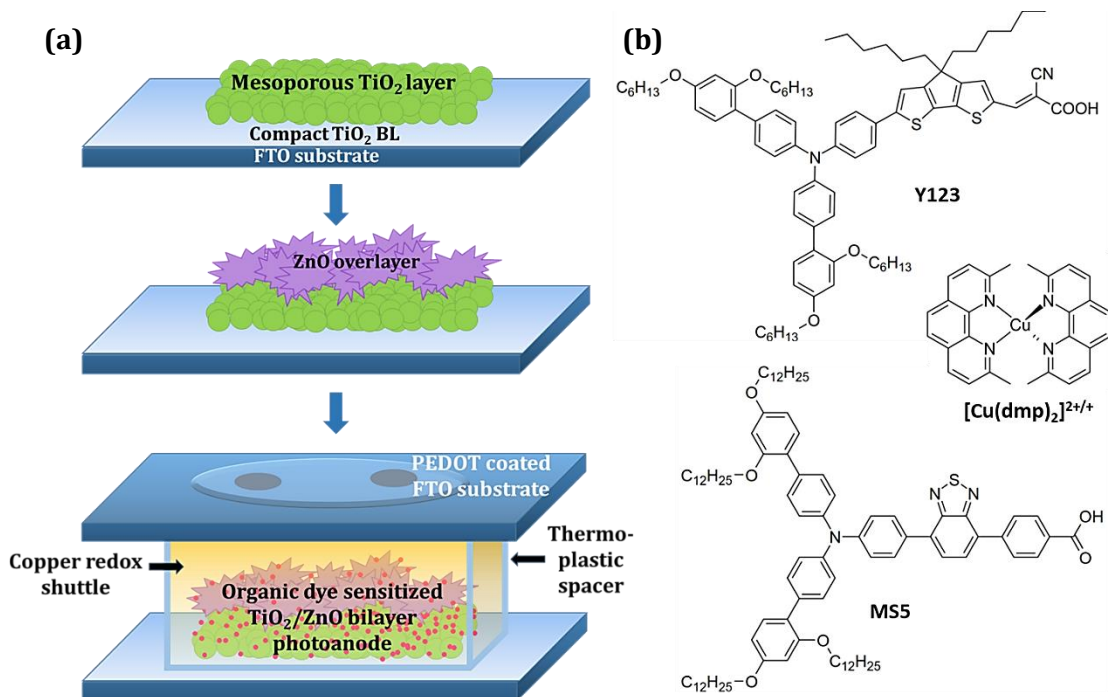


Figure 4.1. (a) Fabrication scheme and device architecture of DSCs employing bilayer TiO₂/ZnO photoanodes. (b) Chemical structure of the organic sensitizers (Y123 and MS5) and the redox mediator ([Cu(dmp)₂]^{2+/+}) used for the fabrication of DSCs.

The fabricated DSCs were subjected to photovoltaic characterization under standard one sun condition (AM 1.5G, 100 mWcm⁻²) using a class AAA solar simulator (Model PVIV-94043A, Newport) and a source meter (Keithley) with a scan rate of 100 mV/s. The devices were undergone a stability test while being kept in an ambient environment with a temperature of 27°C and 80% humidity. Using a Dyenamo AE 05 potentiostat and a custom made indoor light measurement setup, *J-V* characterization under indoor light conditions was performed. The light sources used were a warm white compact fluorescent lamp (CFL; Osram, 14W/2700K) and a daylight emitting diode (LED; Osram, 4W/6500K). The CFL and LED irradiance spectra and incident power density were measured using a highly sensitive photodetector in conjunction with a UV-Vis-NIR spectrometer (Ocean optics, DH-2000-BAL). This measurement was cross-checked using a certified irradiance measuring unit from Dyenamo AB (DN-AE06). *J-V* measurements were conducted under one sun using a black mask with a circular aperture of 0.11 cm², and indoor measurements were conducted with a larger aperture of 0.34 cm². A 250 W Xenon lamp connected to a monochromator was used to measure incident photon-to-current conversion efficiency (*IPCE*). The electrochemical workstation (Autolab, Metrohm) was used to measure intensity modulated photovoltage spectroscopy (IMVS), open circuit voltage decay

(OCVD), and electrochemical impedance spectroscopy (EIS). EIS was performed in the absence of light, with a bias voltage between 0.8 V and 1.1 V and a frequency ranging from 0.1 Hz to 100 kHz. The ZView software was utilized to fit the impedance plots acquired from EIS and derive several parameters, including chemical capacitance (C_{μ}) and charge transfer resistance (R_{ct}). The same workstation, an LED driver, and a white LED were used for IMVS measurements, with a frequency range of 1 Hz to 10 kHz applied. A white LED was used to illuminate the cells during open circuit conditions in order to perform OCVD measurements. Measurements of transient photovoltaic and photocurrent decay (TVD and TPD) were performed with the Dyenamo toolbox. An LED source was used for the measurements, and the modulation amplitude was consistently kept below 10% of the steady-state value.

4.3. Results and Discussion

4.3.1. Characterization of materials and photoanodes

Various morphologies of hierarchical microstructures were synthesized by varying the concentration of urea in the reaction mixture. The growth of hierarchical microstructures with three distinct morphologies - mimosa flower-like (Z1), dandelion flower-like (Z2), and rose flower-like (Z3) - was controlled using three different urea concentrations, 0.03 M, 0.08 M, and 0.8 M. **Figure 4.2(a-f)** shows the SEM images of Z1, Z2, and Z3, whereas **Table 4.1** provides details on particle size, crystallite size, and BET surface area. The HRTEM images of annealed Z1, Z2, and Z3 samples (**Figure 4.2(g-l)**) indicate that these microstructures were formed by the aggregation of oval-shaped nanoparticles with average sizes of 32.9 nm, 33.9 nm, and 33.9 nm, respectively. Additionally, the randomly oriented nanocrystallites with varying crystallographic alignments (**Figure 4.2(h,j,l)**) imply a heterogeneous nucleation and coalescence mechanism for particle growth, which is followed by a diffusion-limited cluster-cluster aggregation to form hierarchical structures.⁴⁰ The nano-sized crystallites undergo coalescence to produce nanofibers at a lower concentration of urea (0.03 M) in the reaction mixture. These nanofibers then aggregate to form the hierarchical structure resembling a mimosa flower. As the concentration of urea increases to 0.08 M, the nanoparticles coalesce in a manner that results in a decrease in the length of the nanofiber and an increase in its width. This creates 2D nanoribbons, which group together to form microstructures resembling dandelion flowers. The length of the nanoribbon is further reduced while its

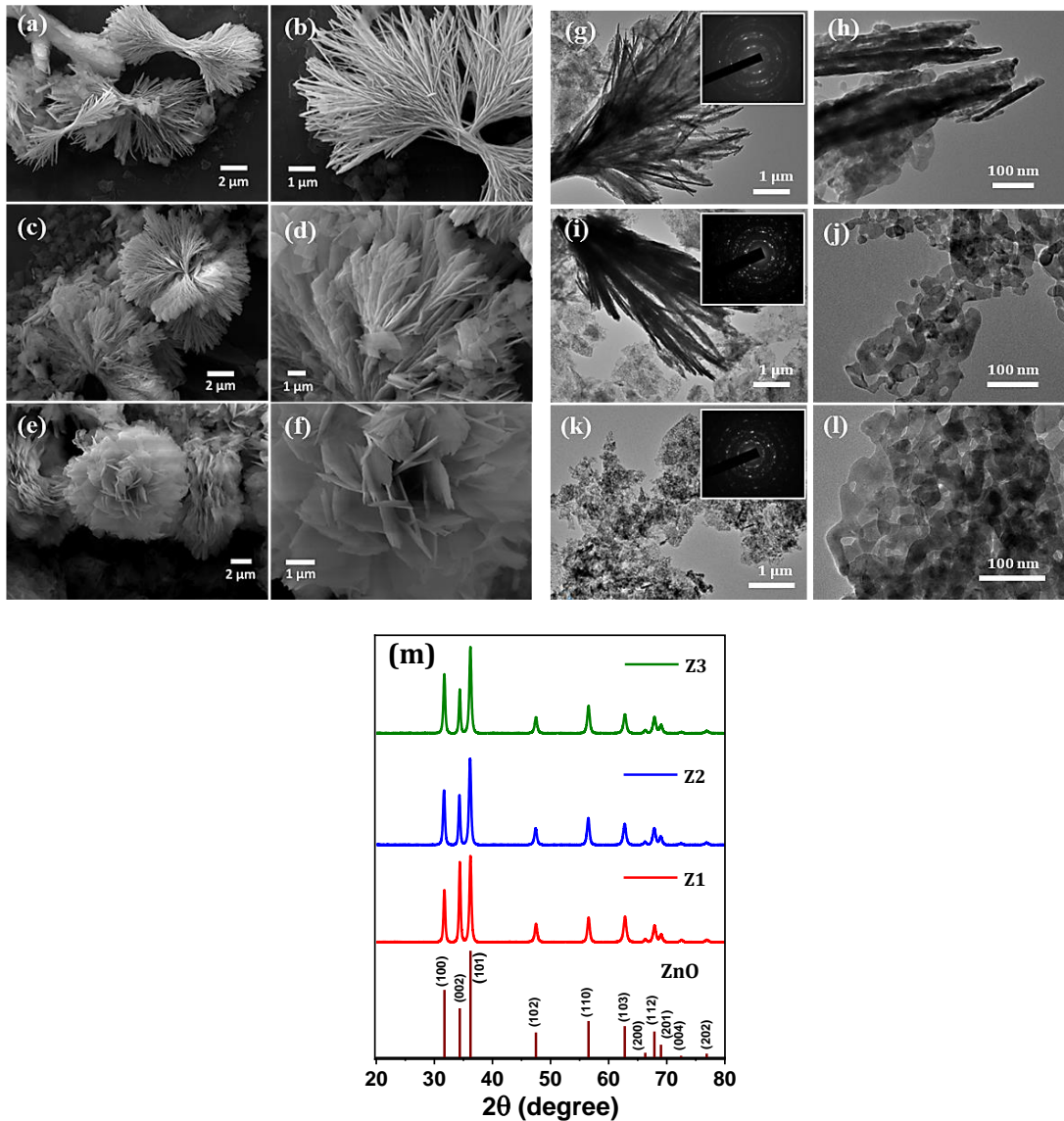


Figure 4.2. SEM micrographs of as-synthesized samples of (a,b) Z1, (c,d) Z2, and (e,f) Z3; TEM images of annealed samples (500 °C) of (g,h) Z1, (i,j) Z2, and (k,l) Z3; (m) XRD patterns of Z1, Z2 and Z3 samples annealed at 500 °C.

width increases with a tenfold increase in urea concentration (0.8 M), creating 2D nanoflakes that come together to form rose flower-like microstructures. The annealed samples of Z1, Z2, and Z3 are confirmed to be crystalline by the selected area electron diffraction (SAED) patterns displayed in the inset of **Figure 4.2(g,i,k)**. The XRD patterns of ZnO samples obtained after 500 °C annealing (**Figure 4.2(m)**) demonstrate that all of the samples are crystalline, displaying a hexagonal crystal structure in the wurtzite phase (JCPDS No. 01-080-0074). By considering the [100], [002], and [101] directions, the average crystallite sizes of Z1, Z2, and Z3 microflowers were found to be 34.7 nm, 35.5 nm, and 31.8 nm, respectively.

Table 4.1. Particle size, crystallite size and surface area obtained for the ZnO samples (Z1, Z2 and Z3).

ZnO sample	Average particle size from SEM (μm)	Average crystallite size from XRD (nm)	Average crystallite size from HRTEM (nm)	BET surface area (m^2/g)
Z1	11.5 ± 1.0	34.7 ± 3.3	33.9 ± 6.9	81.7
Z2	10.1 ± 1.3	35.5 ± 4.9	33.9 ± 1.5	58.3
Z3	9.6 ± 2.5	31.8 ± 4.5	33.0 ± 2.2	35.3

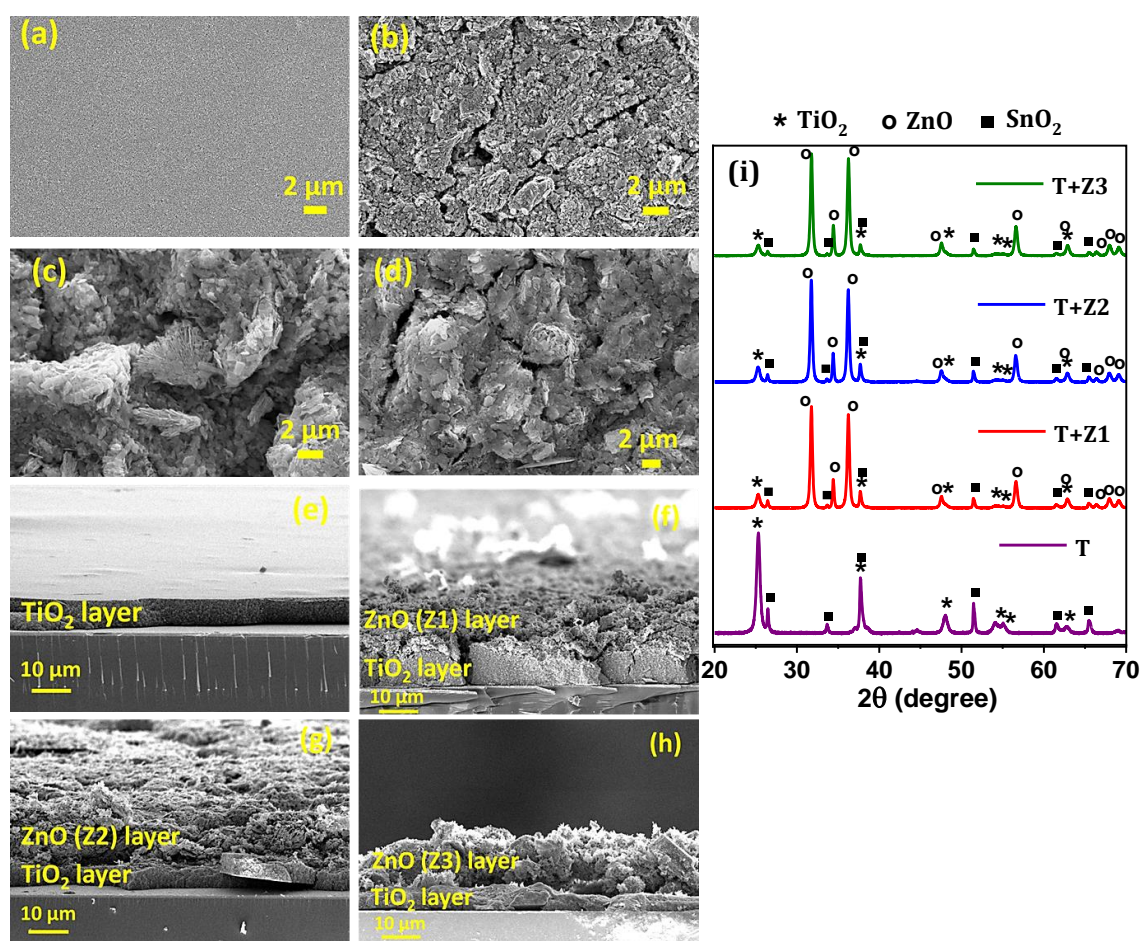
**Figure 4.3.** SEM images showing the surface of the photoanodes (a) T, (b) T+Z1, (c) T+Z2, and (d) T+Z3; SEM images showing the cross-section of the photoanodes (e) T, (f) T+Z1, (g) T+Z2, and (h) T+Z3; (i) XRD spectra of T, T+Z1, T+Z2 and T+Z3 photoanodes.

Figure 4.3(a) shows the SEM images of the top and cross-sectional views of the T, T+Z1, T+Z2, and T+Z3 electrodes. The cross-sectional SEM was used to estimate the approximate thickness of each layer, which is presented in **Table 4.2**. The ZnO over layers were observed to be slightly distorted following the blade coating (**Figure 4.3(a)**), resulting in an average thickness of approximately $15 \mu\text{m}$, while the thickness of the TiO_2 layer was

approximately 6 μm . Peaks corresponding to anatase TiO₂ and wurtzite ZnO (JCPDS Nos. 21–1272 and 01-075–1526) can be seen in the XRD pattern of the TiO₂/ZnO bilayer stacks (**Figure 4.3(a)**). **Table 4.2** lists the dye loading for each of the three photoanodes (T, T+Z1, T+Z2, and T+Z3). When compared to the T electrode, the bilayer photoanodes have slightly superior dye loading that could be explained by their higher film thickness. Using TiO₂ and TiO₂/ZnO bilayer electrodes, DSCs were fabricated using Y123, a standard organic dye, and copper redox mediator [Cu(dmp)₂]^{2+/+}.

4.3.2. Photovoltaic and advanced characterization of DSCs

The current density versus voltage (*J-V*) curves for the TiO₂/ZnO bilayer devices (T+Z1, T+Z2, and T+Z3) and the standard device (T), measured under AM 1.5G simulated solar irradiation (100 mW/cm²) is shown in **Figure 4.4(a)**. **Table 4.2** summarizes the corresponding photovoltaic parameters. A *V_{OC}* of 1.02 V was shown by the control device with a single layer of TiO₂ (T). The *V_{OC}* increased to 1.13 V, 1.11 V, and 1.09 V for T+Z1, T+Z2, and T+Z3 devices, respectively, with the addition of a ZnO layer on top of TiO₂.

Table 4.2. Photovoltaic parameters of TiO₂ (T) and TiO₂/ZnO bilayer (T+Z1, T+Z2 and T+Z3) DSCs employing Y123 sensitizer and [Cu(dmp)₂]^{2+/+} redox electrolyte under AM 1.5G one sun (100 mW/cm²) irradiation along with average semiconductor layer thickness (d), dye loading (DL), and theoretical *J_{SC}* (*J_{integrated}*) values acquired by integrating the *IPCE* spectra.

Device Code	<i>d</i> ^a (μm)	DL ($\times 10^{-7}$ mol/cm ²)	<i>V_{OC}</i> ^b (V)	<i>J_{SC}</i> ^b (mA/cm ²)	<i>FF</i> ^b	<i>PCE</i> ^b (%)	<i>J_{integrated}</i> ^c (mA/cm ²)
T	6.3	0.94	1.02 (1.03 \pm 0.01)	12.24 (12.01 \pm 0.35)	0.64 (0.64 \pm 0.01)	8.00 (7.92 \pm 0.09)	11.60
T+Z1	20.3	1.48	1.13 (1.13 \pm 0.01)	9.88 (9.74 \pm 0.20)	0.68 (0.68 \pm 0.01)	7.61 (7.48 \pm 0.16)	9.90
T+Z2	21.5	1.43	1.11 (1.11 \pm 0.01)	8.91 (9.04 \pm 0.18)	0.67 (0.65 \pm 0.02)	6.67 (6.60 \pm 0.08)	9.60
T+Z3	20.3	1.36	1.09 (1.09 \pm 0.01)	8.63 (8.58 \pm 0.12)	0.63 (0.62 \pm 0.01)	5.96 (5.85 \pm 0.13)	8.60

^aAverage semiconductor layer thickness obtained from cross-sectional SEM analysis.

^b*J-V* parameters of champion cells with averages taken over five sets of samples \pm mean deviation in parentheses.

^c*J_{SC}* obtained by integrating the *IPCE* spectra.

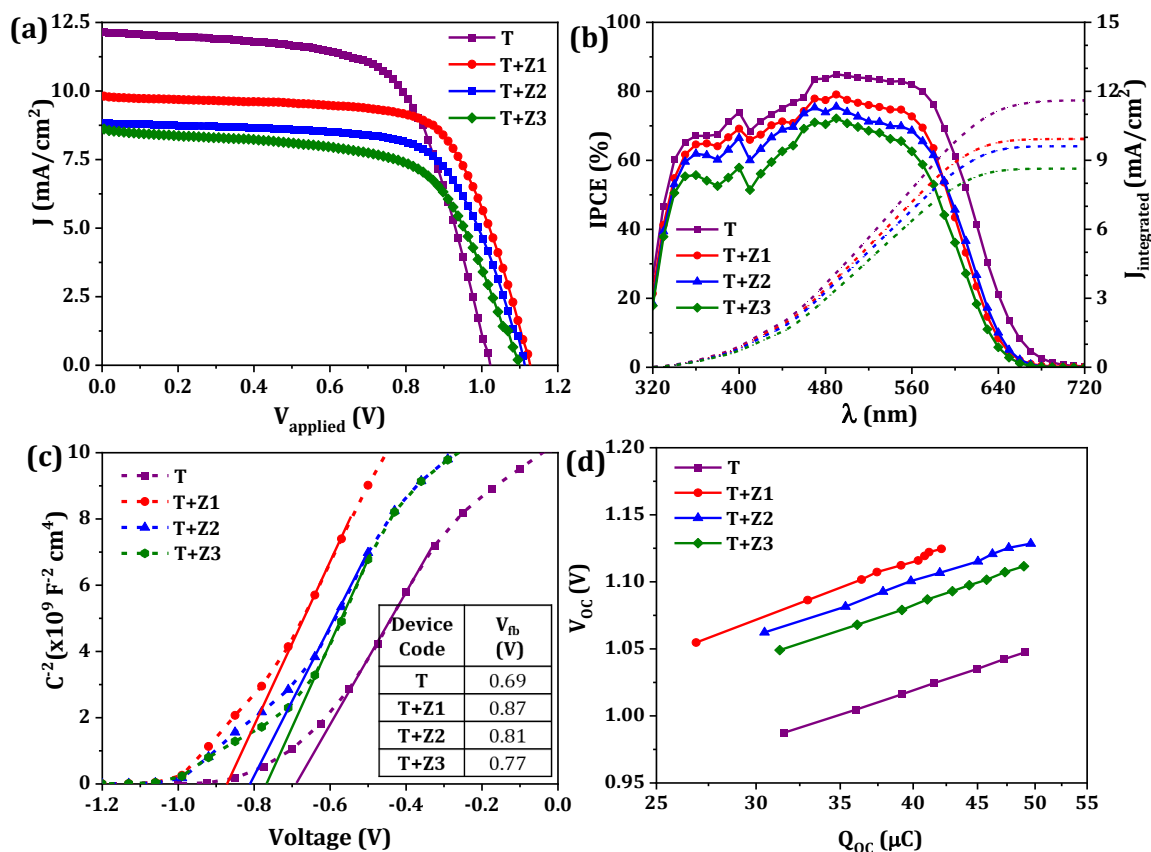


Figure 4.4. (a) The J - V characteristics under AM 1.5G (100 mW/cm^2) irradiation, (b) $IPCE$ spectra (the dotted line represents integrated photocurrent density calculated from the $IPCE$ and the standard solar emission spectrum), (c) Mott-Schottky (MS) plots, and (d) charge extraction (CE) plots of the DSCs fabricated using T, T+Z1, T+Z2 and T+Z3 photoanodes employing Y123 sensitizer and $[\text{Cu}(\text{dmp})_2]^{2+/+}$ redox electrolyte.

T+Z1 outperformed the other two bilayer devices in terms of photovoltaic performance, achieving 7.61%, with superior V_{OC} (1.13 V), J_{SC} (9.88 mA/cm^2), and FF (0.68). The $IPCE$ spectra of the devices showed comparable trends in J_{SC} (Figure 4.4(b)), with values for integrated J_{SC} obtained from $IPCE$ and J_{SC} from J - V measurements (Table 4.2) matching within allowed error limits. By extending the linear region of the Mott-Schottky (MS) plots, as shown in Figure 4.4(c) to intersect the voltage axis, the flat band potentials (V_{fb}) of the semiconductor used in various devices were determined.^{41–44} In comparison to the standard T device, it is observed that the obtained V_{fb} values for T+Z1, T+Z2, and T+Z3 are shifted towards more negative potentials (Table 4.2). This shift indicates that the CB is shifted towards more negative potentials in the bilayer devices, specifically with the addition of a ZnO layer on top of the TiO_2 . It is well known that ZnO has a CB edge that is positioned more negatively than TiO_2 . Besides, based on cyclic voltametric studies, S.-S. Kim *et al.*

have reported that ZnO addition to TiO₂ results in a negative shift in CB edge of TiO₂.⁴⁵ It could be assumed that the apparent charging of the ZnO layer as a result of the band alignment at the TiO₂/ZnO interface contribute to this upward shift in CB.^{46,47} Charge extraction (CE) plots (**Figure 4.4(d)**), which shows an approximate 50-100 mV negative shift upon the introduction of ZnO layers, were used to further verify the negative shift in the CB for the TiO₂/ZnO bilayer devices. This CB shift in the negative direction could potentially lead to increased V_{OC} in TiO₂/ZnO bilayer devices.

To further explore the recombination losses and the charge carrier concentration in bilayer devices, the EIS measurements were performed. **Figure 4.5(a)** shows the Nyquist plots of T, T+Z1, T+Z2 and T+Z3 devices fabricated using Y123 sensitizer and [Cu(dmp)₂]^{2+/+} electrolyte obtained from EIS measurement under dark condition (at a bias of 1.0 V). The modified Randle's circuit used for fitting them is given in the inset of **Figure**

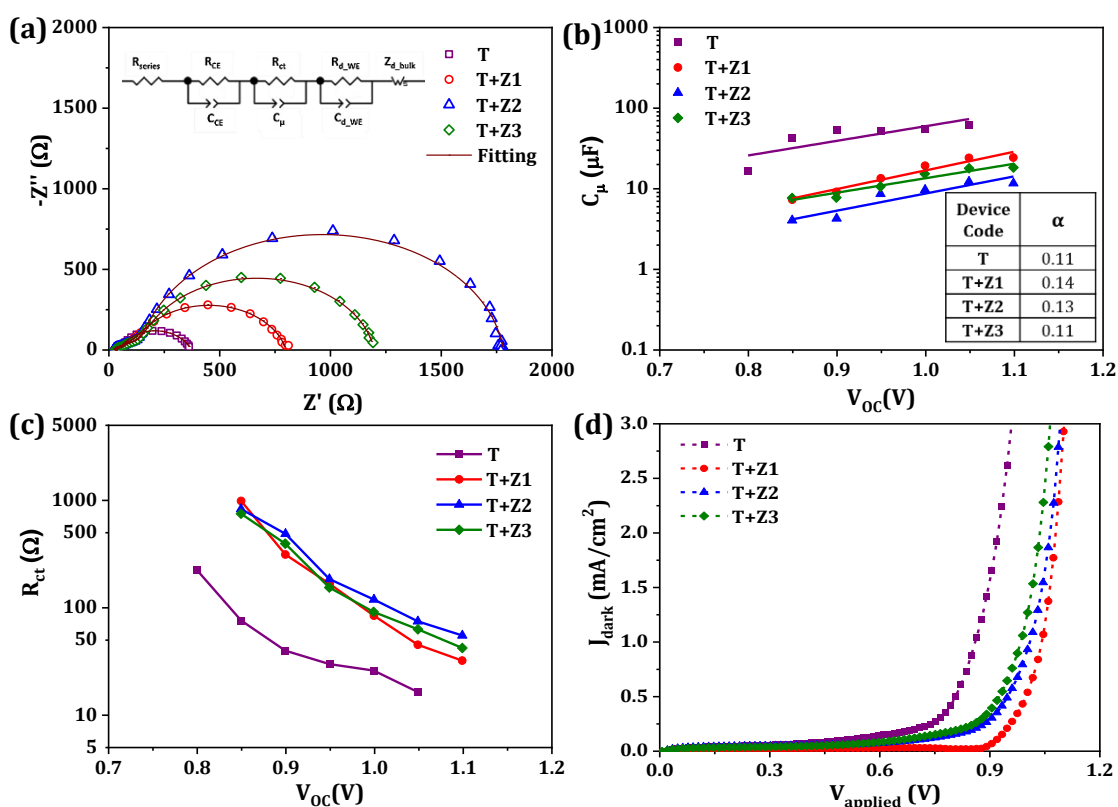


Figure 4.5. (a) Nyquist plots obtained from EIS measurement under dark condition (at a bias of 1.0 V) along with the modified Randle's circuit used for fitting them (in inset); (b) Chemical capacitance (C_{μ}) and (c) charge transfer resistance (R_{ct}), determined by fitting Nyquist plots, plotted against V_{OC} ; (d) J - V curves obtained under dark condition, for T, T+Z1, T+Z2 and T+Z3 devices fabricated using Y123 sensitizer and [Cu(dmp)₂]^{2+/+} redox electrolyte.

Table 4.3. Parameters obtained by fitting the corresponding Nyquist plots for T, T+Z1, T+Z2 and T+Z3 devices obtained from EIS carried out at a bias of 1.0 V employing Y123 sensitizer and $[\text{Cu}(\text{dmp})_2]^{2+/+}$ redox electrolyte.

Parameters	T	T+Z1	T+Z2	T+Z3
R_{ct}	29.92 Ω	84.47 Ω	119.3 Ω	91.57 Ω
C_{μ}	55 μF	19.3 μF	9.69 μF	15.3 μF
R_{d-WE}	286.9 Ω	649.7 Ω	1597 Ω	1032 Ω
R_{d-bulk}	22.21 Ω	21.56 Ω	22.43 Ω	17.15 Ω

4.5(a), in which R_{series} , R_{ct} and R_{CE} symbolize the series resistance, charge transfer resistance at $\text{TiO}_2/\text{dye}/\text{electrolyte}$ interface and counter electrode interface respectively, whereas C_{μ} and C_{CE} respectively specify the chemical capacitance and capacitance due to charge accumulation at the counter electrode/electrolyte interface. The Warburg diffusion element (Z_{d-bulk}) corresponds to resistance (R_{d-bulk}) for the diffusion of redox species in the bulk of the electrolyte, while R_{d-WE} corresponds to the diffusion of charged species within the mesoporous semiconductor layer.⁴⁸ **Table 4.3** lists the corresponding fitted parameters obtained at a bias of 1.0 V. A negative shift in the CB position for bilayer devices is also seen in the chemical capacitance (C_{μ}), calculated from the EIS analysis, plotted as a function of V_{OC} , as seen in **Figure 4.5(b)**. This shift was previously noted from the MS and CE analysis. C_{μ} and V_{OC} have an exponential relationship, as shown by the equation,^{46,49}

$$C_{\mu} = C_o \exp\left(\frac{\alpha q V_{OC}}{k_B T}\right) \quad (4.1)$$

where T is the absolute temperature, q is the electronic charge, k_B is the Boltzmann's constant, α is the trap states distribution parameter in the semiconductor layer, and C_o is a parameter that is explicitly dependent on α , the CB edge (E_{CB}), the trap state density (n_t) in the semiconductor, and the electrolyte's redox potential (E_{redox}). The slope of the $\log C_{\mu}$ vs. V_{OC} plot (**Figure 4.5(b)**) was used to estimate the α values for the various devices, and the results indicated a negligible difference between the standard and bilayer devices. Thus, the change in C_{μ} can be directly connected to the shift in CB edges according to the relationship,

$$C_o = \frac{q^2 n_t \alpha}{k_B T} \exp\left(-\frac{\alpha(E_{CB} - E_{redox})}{k_B T}\right) \quad (4.2)$$

The lower C_{μ} values for the bilayer devices (**Figure 4.5(b)** and **Table 4.3**) provide additional empirical evidence supporting the negative shift in CB.

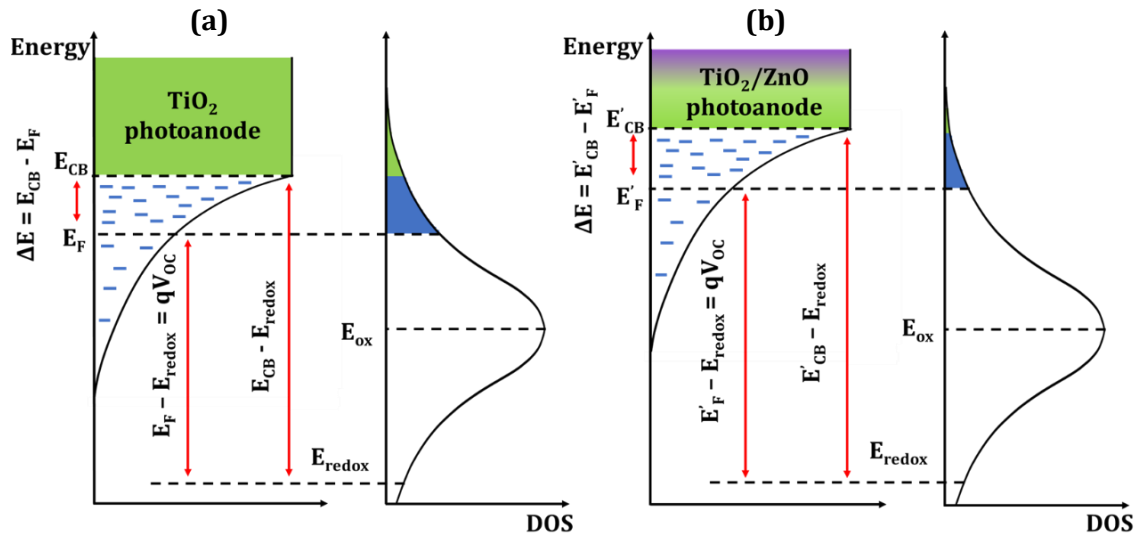


Figure 4.6. Alignment of energy levels of the semiconductor layer and electrolyte in **(a)** T and **(b)** T+Z devices. A negative shift in the conduction band edge (E_{CB}) of TiO_2/ZnO electrodes results in reduced overlapping between the oxidized energy states of the electrolyte with the CB states (shaded in green) and the gap states (shaded in blue).

The negative shift in CB for the bilayer devices concurrently minimizes the overlap between the oxidized states of the redox mediator and the CB states and sub-bandgap states of the semiconductor, which inhibits electron transfer from the semiconducting layer to the electrolyte (**Figure 4.6**).^{50,51} This can be seen in the reduced dark current (**Figure 4.5(d)**) and increased recombination resistance, R_{ct} (**Figure 4.5(c)**, **Table 4.3**) for the TiO_2/ZnO bilayer devices. The formation of an energy barrier at the TiO_2/ZnO interface, caused by the higher CB energy of ZnO, can also be ascribed to the increased R_{ct} in the bilayer devices.⁵² Collectively, these results demonstrate that, in comparison to the conventional TiO_2 device, the TiO_2/ZnO bilayer devices exhibit a greater capacity to inhibit charge recombination at the semiconductor/electrolyte interface. By conducting transient photovoltage decay (TVD) measurements, the charge carrier recombination losses were investigated further, and **Figure 4.7(a)** displays the variation of the corresponding lifetime (τ_n) as a function of V_{OC} . The bilayer devices showed longer lifetimes than the TiO_2 alone device, which again suggests effective recombination suppression. Interestingly, we also noticed the same trend in lifetimes of these devices when we measured their intensity modulated photovoltaic spectroscopy (IMVS) (**Figure 4.7(b)**). In addition, intensity-dependent V_{OC} measurements were used to investigate the role of trap states in the recombination (**Figure 4.7(c)**). The equation, which estimates the ideality factor (n) of the

devices, is derived from the slope of the semi-logarithmic plot of V_{OC} versus illumination intensity (ϕ) as given in the equation,^{25,53}

$$\frac{d V_{OC}}{d \log \phi} = \frac{2.3 n k_B T}{q} \quad (4.3)$$

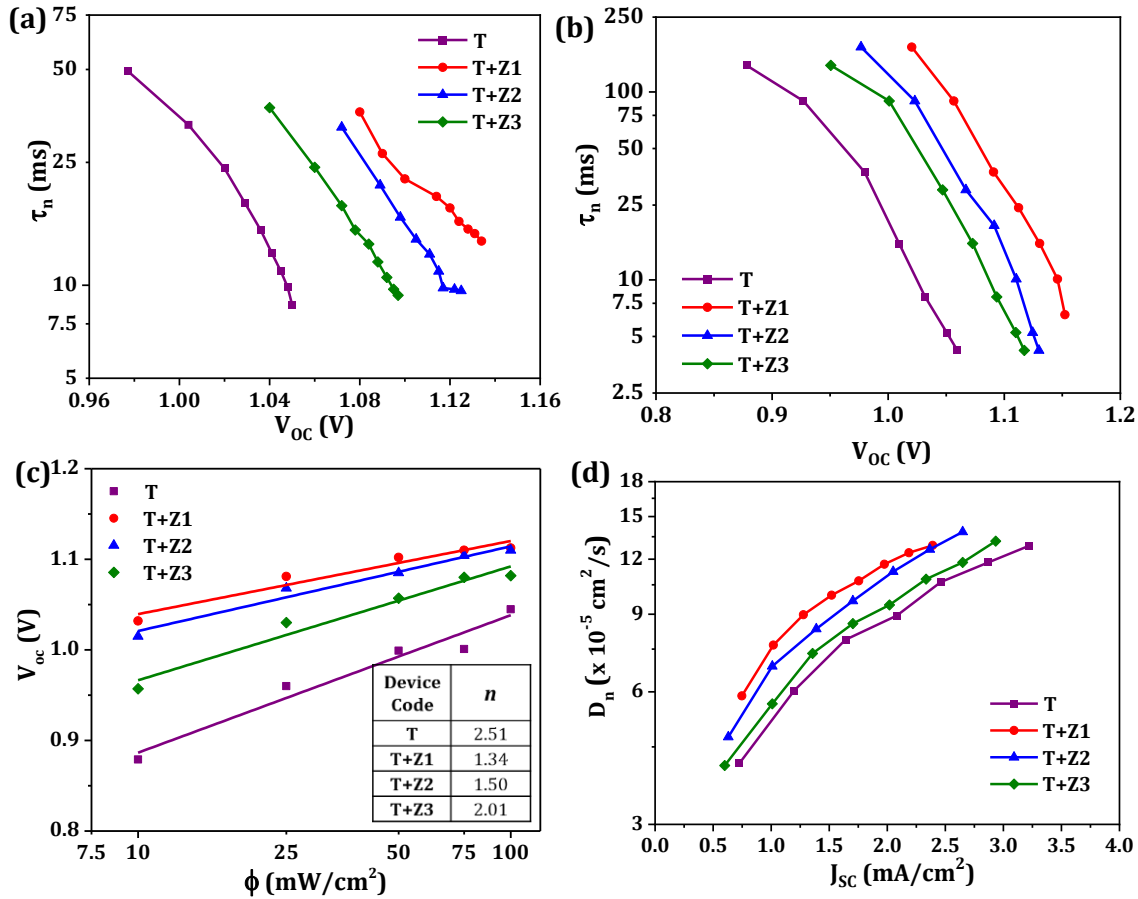


Figure 4.7. Lifetime as a function of V_{OC} obtained from (a) transient photovoltage decay (TVD) and (b) Intensity modulated photovoltage spectroscopy (IMVS) measurements; (c) V_{OC} as a function of intensity; (d) Electron diffusion coefficient (D_n) as a function of J_{SC} obtained from transient photocurrent decay (TCD) measurement, for T, T+Z1, T+Z2 and T+Z3 devices fabricated using Y123 sensitizer and $[\text{Cu}(\text{dmp})_2]^{2+/+}$ redox electrolyte.

Non-linear recombination kinetics resulting from the trap state-mediated recombination cause n to deviate from the ideal value of unity. It is evident from the obtained values of n that the bilayer devices exhibit less trap state-assisted recombination. In particular, the T+Z1 device has a n value that is closer to unity. This confirms the previously discussed concept that the negatively shifted CB in bilayer devices reduces the electron transfer from the sub bandgap states - basically the trap states - to the electrolyte. Therefore, it is possible

to attribute the observed rise in V_{OC} for the TiO₂/ZnO bilayer devices primarily to the combined effects of CB shift and suppressed recombination.

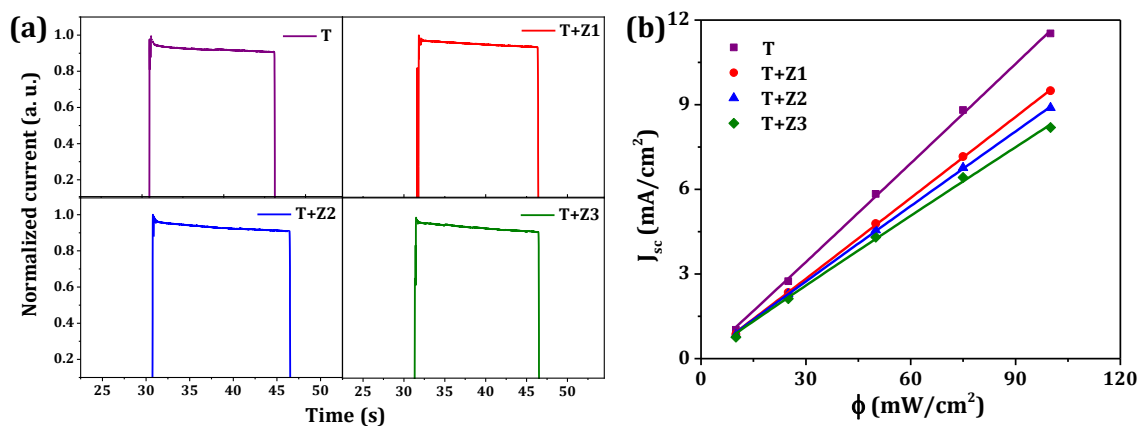


Figure 4.8. (a) Current transients (CT) and (b) J_{SC} vs. ϕ curves obtained for T, T+Z1, T+Z2 and T+Z3 devices fabricated using Y123 sensitizer and $[\text{Cu}(\text{dmp})_2]^{2+/+}$ redox electrolyte.

Furthermore, ZnO can function as a superior electron transport layer in DSC owing to its notable electron mobility. As a result, in comparison to the T device, the T+Z devices with ZnO over layers have superior diffusion coefficients (D_n) (**Figure 4.7(d)**). The resistance to redox species diffusion in the bulk of the electrolyte (R_{d-bulk}) is similar for all of the devices, but since the TiO₂/ZnO devices have thicker layers, the resistance to redox species diffusion within the mesoporous layer (R_{d-WE}) is more than three times higher for them (**Table 4.3**). It has been reported that the electrolyte systems based on copper complexes have limited mass transport. Nonetheless, at 100 mW/cm² illumination, the current transient (CT) curves for T and T+Z devices are similar (**Figure 4.8(a)**), and the J_{SC} versus ϕ plots (**Figure 4.8(b)**) for the T+Z devices are linear, suggesting that mass transport has little effect in these systems even with the thicker layers. This might be explained by the ZnO over layer's considerable porosity. In spite of the better D_n and negligible mass transport limitation, the J_{SC} of T+Z devices is smaller than that of T devices, which could be attributed to the lower injection driving force induced by the upward-shifted CB edges in bilayer devices. Moreover, the injection difficulties seen in TiO₂/ZnO bilayer devices may also be related to the presence of Zn²⁺/dye aggregates within the ZnO layer as a result of ZnO degradation in acidic environments.^{54,58,59} The above-mentioned extensive study, which includes various interfacial charge transfer studies in standard and bilayer devices, clearly correlates with the disparities in photovoltaic parameters between the two device configurations.

4.3.3. Effect of ZnO layer thickness and TiO₂ blocking layers on the performance of bilayer DSCs

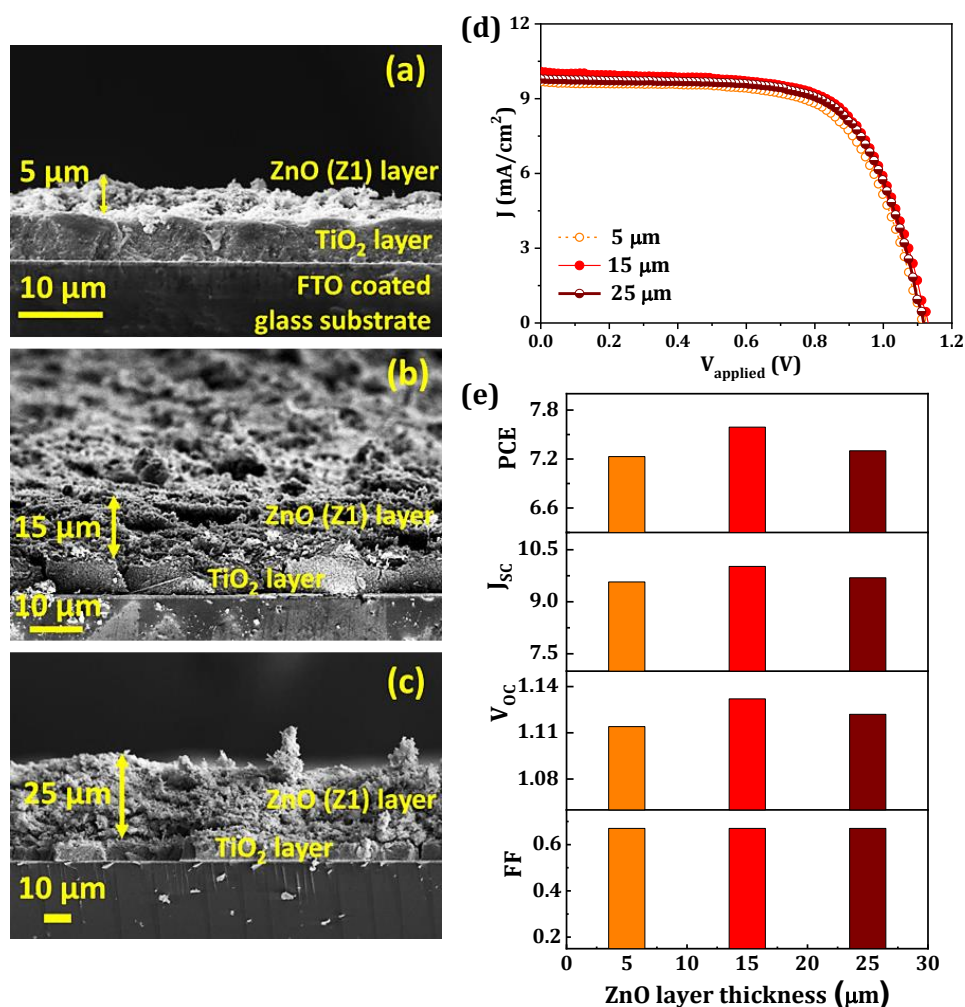


Figure 4.9. SEM images showing the cross-section of the T+Z1 photoanodes with ZnO layer thickness of (a) 5 μm, (b) 15 μm, and (c) 25 μm; (d) J - V characteristic curves of the corresponding devices under AM 1.5G (100 mW/cm²) irradiation and (e) Comparison of photovoltaic parameters (J_{sc} , V_{oc} , FF and PCE) of T+Z1 devices with different ZnO layer thickness (5 μm, 15 μm and 25 μm).

The bilayer T+Z1 showcased the best performance among all the bilayer devices, with a ZnO (Z1) layer over TiO₂ that was about 15 μm thick. To further explore the impact of ZnO layer thickness on device performance, T+Z1 devices were fabricated by varying the ZnO thickness, with an average Z1 layer thickness of 5 μm, 15 μm, and 25 μm (**Figure 4.9(a-c)**). **Figure 4.9(d)** displays the obtained J - V curves of the T+Z1 devices with different ZnO layer thickness, under AM 1.5G 100 mW/cm² illumination, and **Table 4.4** summarizes the corresponding photovoltaic parameters. The photovoltaic parameters were not

significantly affected by changes in the thickness of the ZnO layer (**Figure 4.9(e)**); however, a thickness of 15 μm was found to be optimal, providing the highest *PCE*.

Table 4.4. Photovoltaic parameters of DSCs employing T+Z1 photoanodes with different ZnO layer thicknesses (5 μm , 15 μm and 25 μm), sensitized with Y123 dye, and $[\text{Cu}(\text{dmp})_2]^{2+/+}$ redox electrolyte under AM 1.5G (100 mW/cm^2) irradiation.

ZnO layer thickness (μm)	V_{oc}^a (V)	J_{sc}^a (mA/cm^2)	FF^a	PCE^a (%)
5	1.11 (1.11 \pm 0.01)	9.66 (9.65 \pm 0.05)	0.66 (0.67 \pm 0.01)	7.12 (7.10 \pm 0.02)
15	1.13 (1.13 \pm 0.01)	10.06 (10.07 \pm 0.01)	0.66 (0.66 \pm 0.01)	7.54 (7.49 \pm 0.05)
25	1.12 (1.12 \pm 0.01)	9.79 (9.82 \pm 0.02)	0.68 (0.67 \pm 0.01)	7.42 (7.38 \pm 0.04)

^a *J-V* parameters of champion cells with averages taken over five sets of samples \pm mean deviation in parentheses.

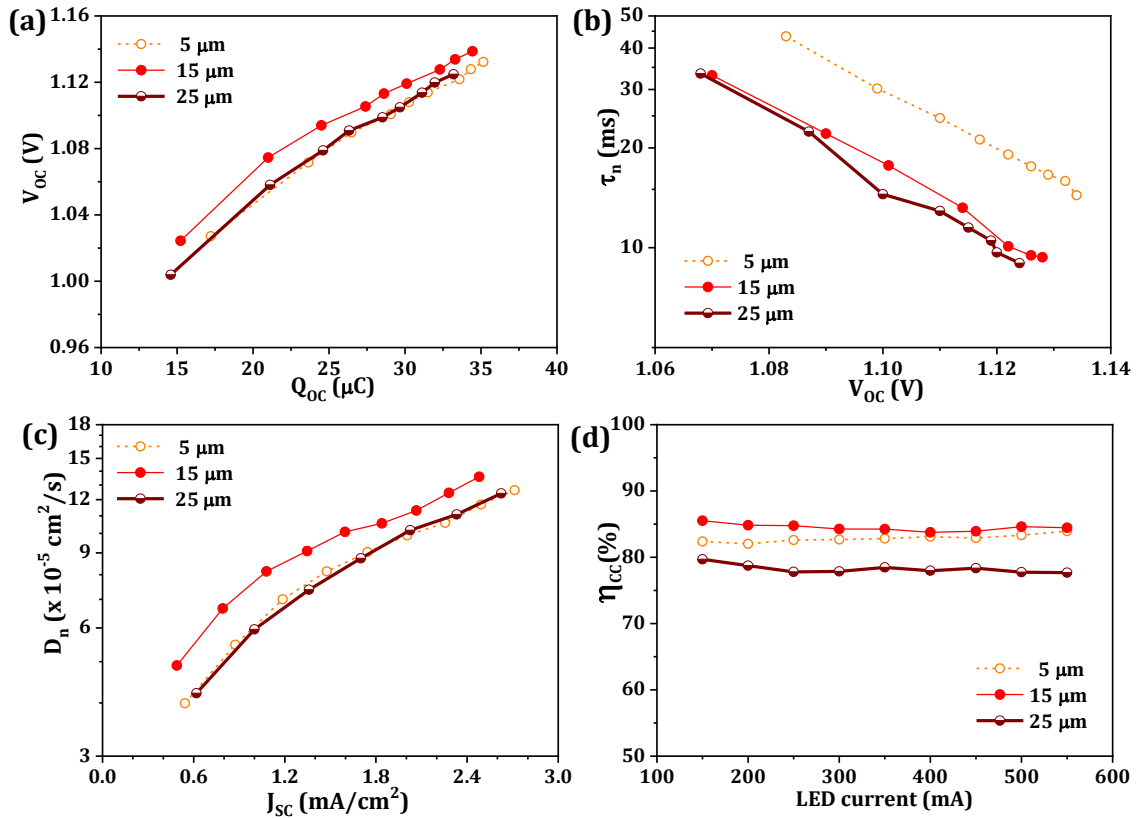


Figure 4.10. (a) Charge extraction (CE) plot, (b) lifetime plot (τ_n) obtained by TVD measurement, (c) electron diffusion coefficient (D_n) obtained from TCD measurement, and (d) charge collection efficiency (η_{cc}) plot obtained from IMVS and IMPS measurements, for devices fabricated with T+Z1 photoanodes having different ZnO layer thicknesses (5 μm , 15 μm and 25 μm).

Better performance of T+Z1 device with a 15 μm thick Z1 layer was attributed to its optimal V_{OC} and J_{SC} when compared to the other devices. The better V_{OC} of 15 μm thick Z1 layer based T+Z1 DSCs could be ascribed to its more negatively shifted CB edge (**Figure 4.10(a)**) despite the lower τ_n (**Figure 4.10(b)**). Whereas, the better J_{SC} of this device is explained by its higher D_n (**Figure 4.10(c)**) leading to higher η_{CC} (**Figure 4.10(d)**).

It is already reported that compact blocking layers (BLs) are essential for eliminating leakage/recombination in DSCs using bulky alternate metal complex redox mediators.^{55,56} The ZnO overlayers are harmed by the traditional method of depositing TiO_2 BLs via TiCl_4 treatment. Consequently, using a commercial BL solution as detailed in the experimental section, an ultrathin TiO_2 BL was introduced over the bilayer architecture. The J - V curves and IPCE spectra of the DSCs using Y123 sensitized bilayer photoanodes without and with BL (T+Z1 and T+Z1+BL, respectively) along with $[\text{Cu}(\text{dmp})_2]^{2+/+}$ redox electrolyte are shown in **Figure 4.11(a,b)**. The T+Z1+BL device delivered 8.16% PCE , 1.12 V V_{OC} , 10.29 mA/cm^2 J_{SC} , and 0.70 FF under AM 1.5G 100 mW/cm^2 illumination (**Figure 4.11(a)**, **Table 4.5**). When comparing the T+Z1+BL device to T+Z1, slightly better J_{SC} and FF were achieved along with a slight decrease in V_{OC} . As shown by the dark J - V plot in **Figure 4.11(c)**, the addition of BL effectively reduced electron leakage at the FTO/electrolyte interface, improving FF . However, a positive shift in CB following the introduction of BLs was observed from the CE plot (**Figure 4.11(d)**), which in turn led to a decrease in V_{OC} . This downward shift in CB increases the overlap of CB states with the oxidized states in the redox system, which leads to more recombination as observed from TVD, OCVD and IMVS measurements (**Figure 4.12(a-c)**). Multiple trapping-detrapping events are known to slow down charge carrier diffusion in semiconducting films.⁵⁷ **Figure 4.12(d)** shows that the BL effectively enhanced the D_n , which could be attributed to the faster electron diffusion owing to the passivation surface traps in the TiO_2/ZnO bilayer devices. The faster diffusion of electrons in T+Z1+BL device result in better charge collection efficiencies (η_{CC}) for this device (**Figure 4.12(e)**), which in turn leads to its improved J_{SC} and hence higher PCE . This is reflected in the IPCE plot (**Figure 4.11(b)**) and corresponding integrated J_{SC} ($J_{integrated}$) values (**Table 4.5**).

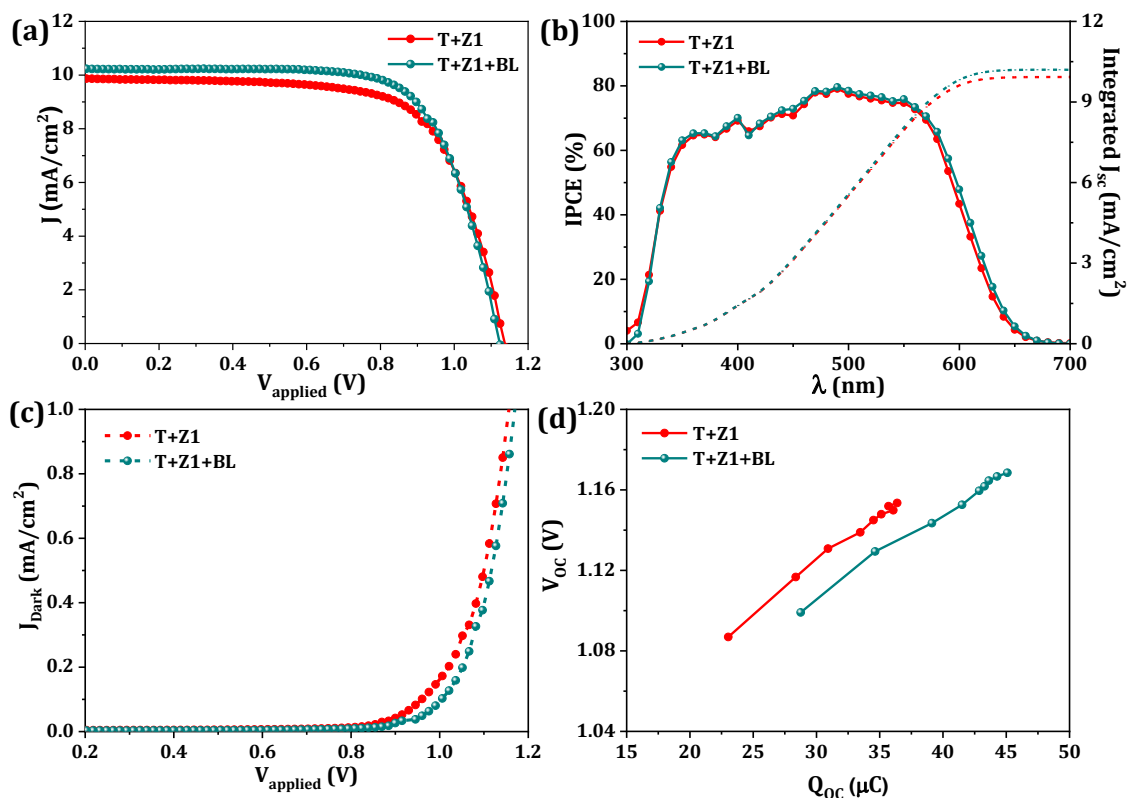


Figure 4.11. (a) J - V curves measured under AM 1.5G sunlight (100 mW/cm²), (b) corresponding IPCE spectra, (c) J - V curves measured under darkness, and (d) charge extraction (CE) plots obtained for DSCs employing TiO_2/ZnO bilayer photoanodes (T+Z1 and T+Z1+BL) sensitized with Y123 dye along with $[Cu(dmp)_2]^{2+/+}$ redox shuttle.

Table 4.5. Comparison of photovoltaic parameters of DSCs employing TiO_2/ZnO bilayer photoanodes (T+Z1 and T+Z1+BL) sensitized with Y123 sensitizer along with $[Cu(dmp)_2]^{2+/+}$ electrolyte measured under AM 1.5G solar (100 mW/cm²) irradiation.

Device Code	V_{oc} ^a (V)	J_{sc} ^a (mA/cm ²)	FF ^a	PCE ^a (%)	$J_{integrated}$ ^b (mA/cm ²)
T+Z1	1.13 (1.13 ± 0.01)	9.90 (9.84 ± 0.05)	0.68 (0.68 ± 0.01)	7.67 (7.63 ± 0.04)	9.90
T+Z1+BL	1.12 (1.12 ± 0.01)	10.29 (10.33 ± 0.06)	0.70 (0.70 ± 0.01)	8.16 (8.12 ± 0.04)	10.20

^a J - V parameters of champion cells with averages taken over five sets of samples ± mean deviation in parentheses.

^b J_{sc} obtained by integrating the IPCE spectra.

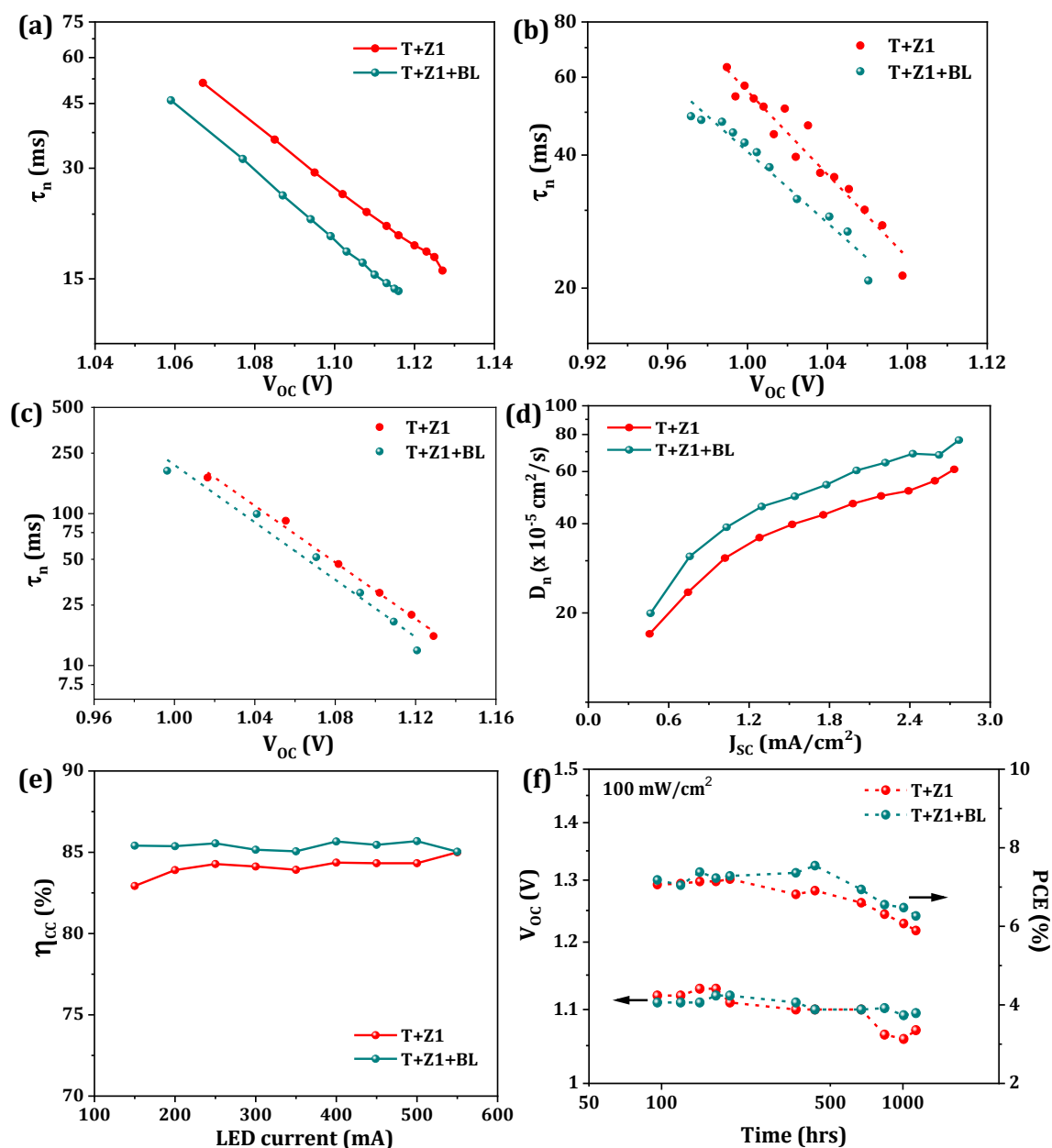


Figure 4.12. The lifetime plot (τ_n) obtained by (a) TVD, (b) OCVD, and (c) IMVS measurements; (d) Electron diffusion coefficient (D_n) obtained from TCD measurement; (e) charge collection efficiency (η_{cc}) as a function of LED current (which is proportional to the intensity of the incident light used in TVD and TCD studies); (f) Stability curves obtained under AM 1.5G simulated sunlight, for T+Z1 and T+Z1+BL devices employing Y123 sensitizer along with $[\text{Cu}(\text{dmp})_2]^{2+/+}$ redox electrolyte.

Wider bandgap and higher electron mobility are two benefits of ZnO, as was highlighted in the introduction section. However, the presence of defects and trap states, combined with its lower electrochemical stability under solar cell operating conditions,

lead to increased recombination and decrease in the long-term stability of ZnO based devices. The decrease in ZnO based DSC performance results from two main degradation mechanisms. First, Zn²⁺ ions from the ZnO surface dissolve in the acidic dye solution when ZnO electrodes are submerged in it for dye adsorption. This creates Zn²⁺/dye aggregates that accumulate in the pores of the ZnO matrix. This lowers the J_{SC} of the device by restricting electron injection.⁵⁸ Secondly, in the presence of electrolyte, ZnO degrades chemically when exposed to light, releasing Zn²⁺ and O²⁻ ions into the electrolyte along with desorbed dye molecules.⁵⁹ As a result, there are fewer dye molecules adsorbed, defects form on the ZnO surface, and the dye aggregates, which lowers the J_{SC} and PCE of the device. By covering the ZnO film with the TiO₂ BL, we were able to effectively address the initial degradation process in our investigation. The J_{SC} improvement of the T+Z1+BL device over the T+Z1 device, even with a lower dye loading (1.2×10^{-7} mol/cm²) of the T+Z1+BL film (which suggests less dye aggregation), is indicative of this. Furthermore, as shown by the stability curves (**Figure 4.12(f)**), the addition of the BL decreased the rate of the second degradation process as well. The T+Z1+BL device kept about 98% of the original V_{OC} even after 1000 hours, whereas the bare T+Z1 device saw a decline in both the V_{OC} and PCE after 200 hours. But after 400 hours, the T+Z1+BL device's PCE started to drop. To determine the changes that occurred in the bilayer photoanode films throughout the stability test, SEM and XRD analyses were performed.

Figure 4.13(a-f) displays the SEM images of the T+Z1 and T+Z1+BL electrodes after over 1000 hours of electrolyte exposure. These images show that there are more cracks in these electrode surfaces than there were on the freshly prepared electrode. Furthermore, both films showed a smoother surface than the fresh T+Z1 films after prolonged contact with the electrolyte. The reason for this is the selective dissolution of ZnO from the film surface.⁶⁰ **Figure 4.13(g)** displays the XRD patterns of the T+Z1 and T+Z1+BL electrodes that were adsorbed with Y123 dye after soaking in electrolyte for 1000 hours. Although some peak intensities, like [100], [101], and [110], were lower in the corroded ZnO films than in the fresh T+Z1 films, the films were still crystalline. Nevertheless, the XRD spectra of the degraded films showed no change in peak positions or the emergence of new peaks. Therefore, prolonged exposure to the electrolyte does not alter the crystallinity of the ZnO films; instead, it modifies the film surface as a result of ZnO degradation in both the bilayer electrodes with and without the BL.⁶¹ In conclusion, the prolonged exposure of bilayer films to the electrolyte system and frequent illumination

probably caused ZnO and dye to dissolve into the electrolyte, which may have decreased the J_{SC} and, consequently, the PCE of the T+Z1+BL devices after 400 hours (as shown in **Figure 4.12(f)**).

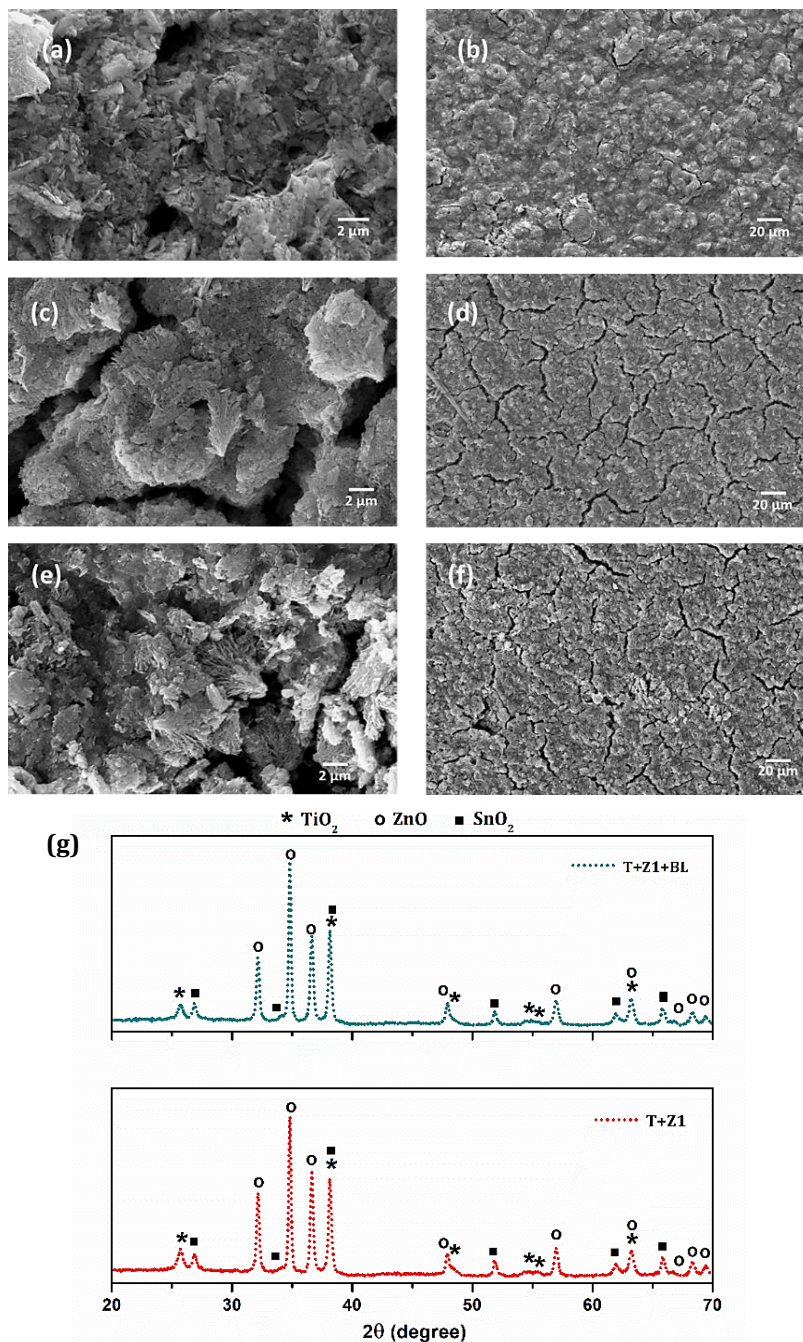


Figure 4.13. SEM images of (a,b) freshly prepared T+Z1 film (without dye adsorption and electrolyte exposure), (c,d) Y123 dye adsorbed T+Z1 films after 1000 h of electrolyte exposure, (e,f) Y123 dye adsorbed T+Z1+BL films after 1000 h of electrolyte exposure; (g) XRD patterns of Y123 dye adsorbed T+Z1 and T+Z1+BL films after 1000 h of electrolyte exposure.

Table 4.6. Indoor photovoltaic parameters of TiO₂/ZnO bilayer DSCs (T, T+Z1 and T+Z1+BL) employing Y123 dye and [Cu(dmp)₂]^{2+/+} redox electrolyte measured under different intensities (1000 lux and 500 lux) of CFL and LED illumination.

Source	Illuminance (P_{in}^a)	Device Code	V_{oc}^b (V)	J_{sc}^b ($\mu\text{A}/\text{cm}^2$)	FF^b	PCE^b (%)	P_{max}^b ($\mu\text{W}/\text{cm}^2$)
CFL	1000 lux (283 $\mu\text{W}/\text{cm}^2$)	T	0.82 (0.81 \pm 0.01)	103.9 (102.5 \pm 1.2)	0.70 (0.70 \pm 0.01)	21.2 (21.0 \pm 0.2)	60.1 (59.6 \pm 0.4)
		T+Z1	1.00 (0.99 \pm 0.01)	78.7 (82.6 \pm 3.2)	0.75 (0.73 \pm 0.02)	20.9 (20.5 \pm 0.4)	59.3 (58.1 \pm 1.2)
		T+Z1+ BL	0.99 (0.98 \pm 0.01)	87.4 (86.4 \pm 1.0)	0.70 (0.70 \pm 0.01)	21.3 (21.1 \pm 0.2)	60.3 (59.7 \pm 0.5)
	500 lux (143 $\mu\text{W}/\text{cm}^2$)	T	0.79 (0.78 \pm 0.01)	46.0 (45.4 \pm 0.7)	0.60 (0.60 \pm 0.01)	15.2 (14.8 \pm 0.4)	21.9 (21.1 \pm 0.6)
		T+Z1	0.97 (0.97 \pm 0.01)	36.6 (35.8 \pm 0.5)	0.65 (0.64 \pm 0.01)	16.2 (15.8 \pm 0.4)	23.2 (22.5 \pm 0.5)
		T+Z1+ BL	0.96 (0.95 \pm 0.01)	40.8 (40.6 \pm 0.2)	0.63 (0.63 \pm 0.01)	17.5 (17.0 \pm 0.5)	25.8 (24.3 \pm 0.5)
LED	1000 lux (313 $\mu\text{W}/\text{cm}^2$)	T	0.83 (0.83 \pm 0.01)	106.7 (107.2 \pm 0.5)	0.70 (0.70 \pm 0.01)	19.9 (19.8 \pm 0.1)	62.2 (61.9 \pm 0.2)
		T+Z1	1.00 (1.00 \pm 0.01)	77.1 (76.4 \pm 0.5)	0.76 (0.76 \pm 0.01)	18.8 (18.6 \pm 0.2)	58.9 (58.2 \pm 0.7)
		T+Z1+ BL	0.99 (0.99 \pm 0.01)	84.6 (84.1 \pm 0.1)	0.73 (0.72 \pm 0.01)	19.7 (19.3 \pm 0.4)	61.6 (60.3 \pm 1.5)
	500 lux (156 $\mu\text{W}/\text{cm}^2$)	T	0.76 (0.76 \pm 0.01)	46.3 (45.6 \pm 0.5)	0.60 (0.60 \pm 0.01)	13.6 (13.4 \pm 0.2)	21.2 (21.1 \pm 0.6)
		T+Z1	0.98 (0.97 \pm 0.01)	33.5 (33.3 \pm 0.2)	0.67 (0.65 \pm 0.02)	14.0 (13.6 \pm 0.4)	21.8 (21.2 \pm 0.7)
		T+Z1+ BL	0.95 (0.95 \pm 0.01)	36.9 (37.3 \pm 0.2)	0.66 (0.63 \pm 0.02)	14.9 (14.4 \pm 0.5)	23.3 (22.4 \pm 0.6)

^a Power density of incident light obtained by integrating the spectral irradiance of the various light sources.

^b J-V parameters of champion cells with averages taken over five sets of samples \pm mean deviation in parentheses.

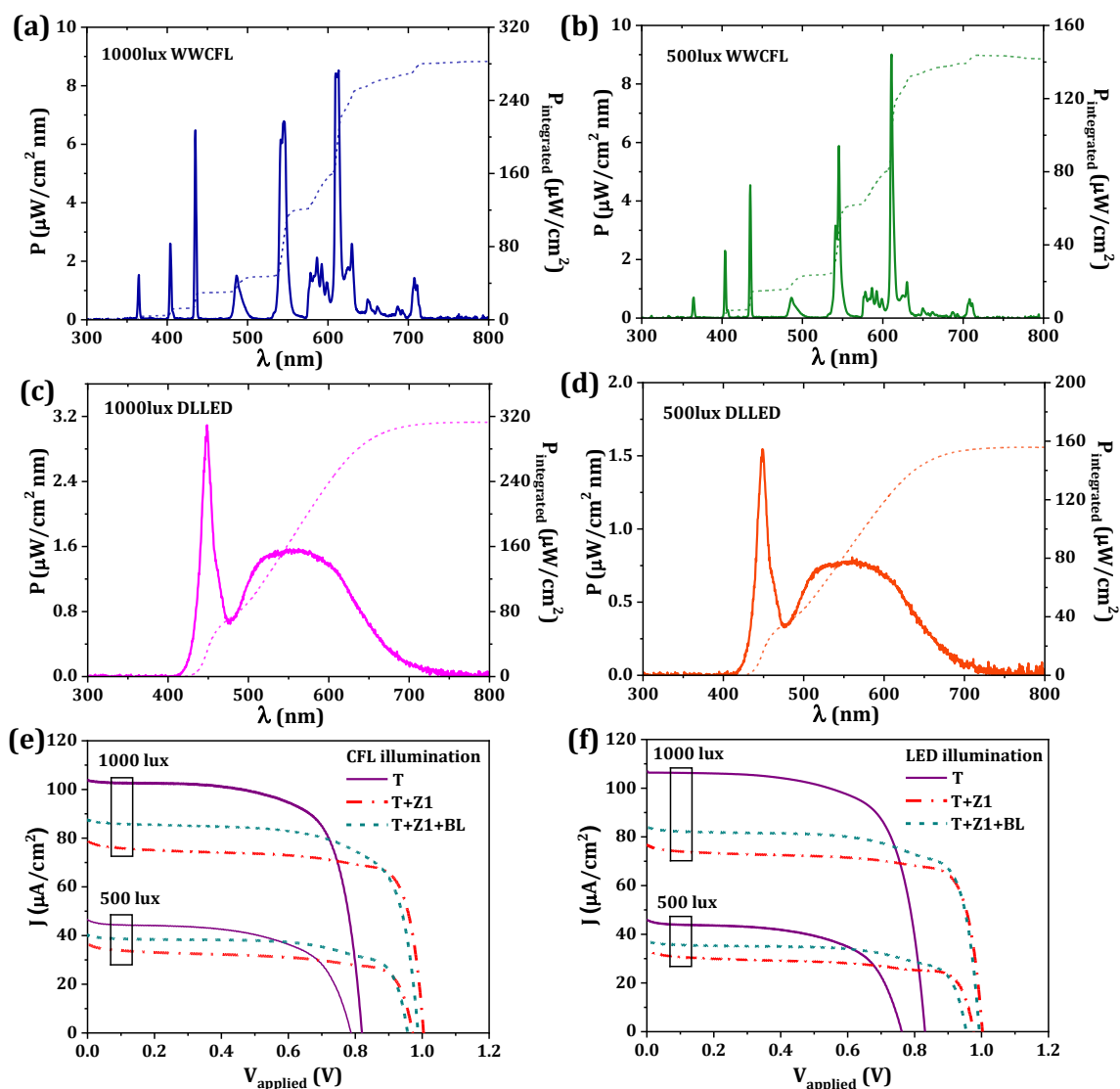


Figure 4.14. The spectral irradiance and integrated power as function of wavelength for (a) 1000 lux CFL light, (b) 500 lux CFL light, (c) 1000 lux LED light, and (d) 500 lux LED light; J - V characteristic curves of T, T+Z1 and T+Z1+BL DSCs employing Y123 sensitizer along with $[\text{Cu}(\text{dmp})_2]^{2+/+}$ redox electrolyte measured under different (e) CFL, and (f) LED illuminations.

DSCs have been demonstrated to be one of the most effective indoor/ambient light harvesting photovoltaic systems available. The potential of the newly developed bilayer devices was evaluated in warm white CFL and daylight LED lighting. The spectral irradiance and integrated power under 1000 lux and 500 lux CFL and LED illuminations are displayed in **Figure 4.14(a-d)**. In most IoT smart device applications, the circuits for energy harvesting and management require larger open circuit potentials. We were able to achieve improvements in V_{oc} under both CFL and LED illuminations by utilizing the

TiO₂/ZnO bilayer architecture in conjunction with Y123 dye and [Cu(dmp)₂]^{2+/+} (**Figure 4.14(e,f), Table 4.6**). The T+Z1 device had a V_{OC} of 1.0 V under 1000 lux CFL illumination (with a J_{SC} of 78.7 μA/cm², FF of 0.75, PCE of 20.9%, and a maximum power output (P_{max}) of 59.3 μW/cm²). In contrast, the standard T device had only a V_{OC} of 0.82 V (with a J_{SC} of 103.9 μA/cm², FF of 0.70, PCE of 21.2%, and P_{max} of 60.1 μW/cm²). The current density was further raised by carefully using BLs, without sacrificing the FF. Consequently, T+Z1+BL devices produced a 20.7% improvement in V_{OC} (0.99 V) and nearly comparable PCE (21.3%) and P_{max} (60.3 μW/cm²) to the control T device. Under lower CFL illumination intensity also similar trends were observed. Under 500 lux illuminances, the V_{OC} of T was 0.79 V, which improved to 0.96 V for T+Z1+BL device, in addition to the rise in PCE (17.5%) and P_{max} (25.2 mW/cm²). The T+Z1 device produced a V_{OC} of 1.0 V under 1000 lux LED illumination (with a J_{SC} of 77.1 μA/cm², FF of 0.76, PCE of 18.8% and P_{max} of 58.9 μW/cm²), when compared to the standard T device, which produced a V_{OC} of 0.83 V (with a J_{SC} of 106.7 μA/cm², FF of 0.70, PCE of 19.9% and P_{max} of 62.2 μW/cm²). Using T+Z1+BL, the current density was further improved in order to achieve a P_{max} (61.6 μW/cm²) similar to that of T device, but with 19.3% increased V_{OC} (0.99 V). Under lower intensity LED illumination of 500 lux, a similar photovoltaic performance was observed for the devices. The T device exhibited a V_{OC} of 0.76 V which got elevated to 0.98 V for T+Z1 device. Meanwhile, T+Z1+BL device could further improve the J_{SC}, leading to improved P_{max} (14.9 mW/cm²) and PCE (23.3%), without compromising much on the V_{OC}.

4.3.4. Achieving record V_{OC} by using TiO₂/ZnO bilayer photoanodes

Finally, under AM 1.5G solar illumination, we were able to realize a record V_{OC} of 1.27 V (previous best: 1.24 V) with a J_{SC} of 6.75 mA/cm², FF of 0.73, and PCE of 6.23% by sensitizing our best-optimized bilayer architecture (T+Z1+BL) with MS5 dye (**Figure 4.15(a), Table 4.7**).²⁶ The observed J_{SC} is within allowable error limits from the theoretical J_{SC}, 7.30 mA/cm², obtained by integrating the corresponding IPCE spectrum (**Figure 4.15(b)**). The use of MS5 instead of the traditional Y123 dye resulted in a couple orders of magnitude improvement in lifetime (**Figure 4.15(c)**) and a negative shift in CB (**Figure 4.15(d)**). This was because the long alkyl chains in the MS5 sensitizer retarded recombination. A V_{OC} of 1.295 V could also be attained by the MS5 sensitized T+Z1+BL bilayer device when exposed to 200 mW/cm² of higher intensity LED illumination (**Figure 4.15(e)**). Under indoor lighting, the performance of T+Z1+BL devices that used MS5 dye

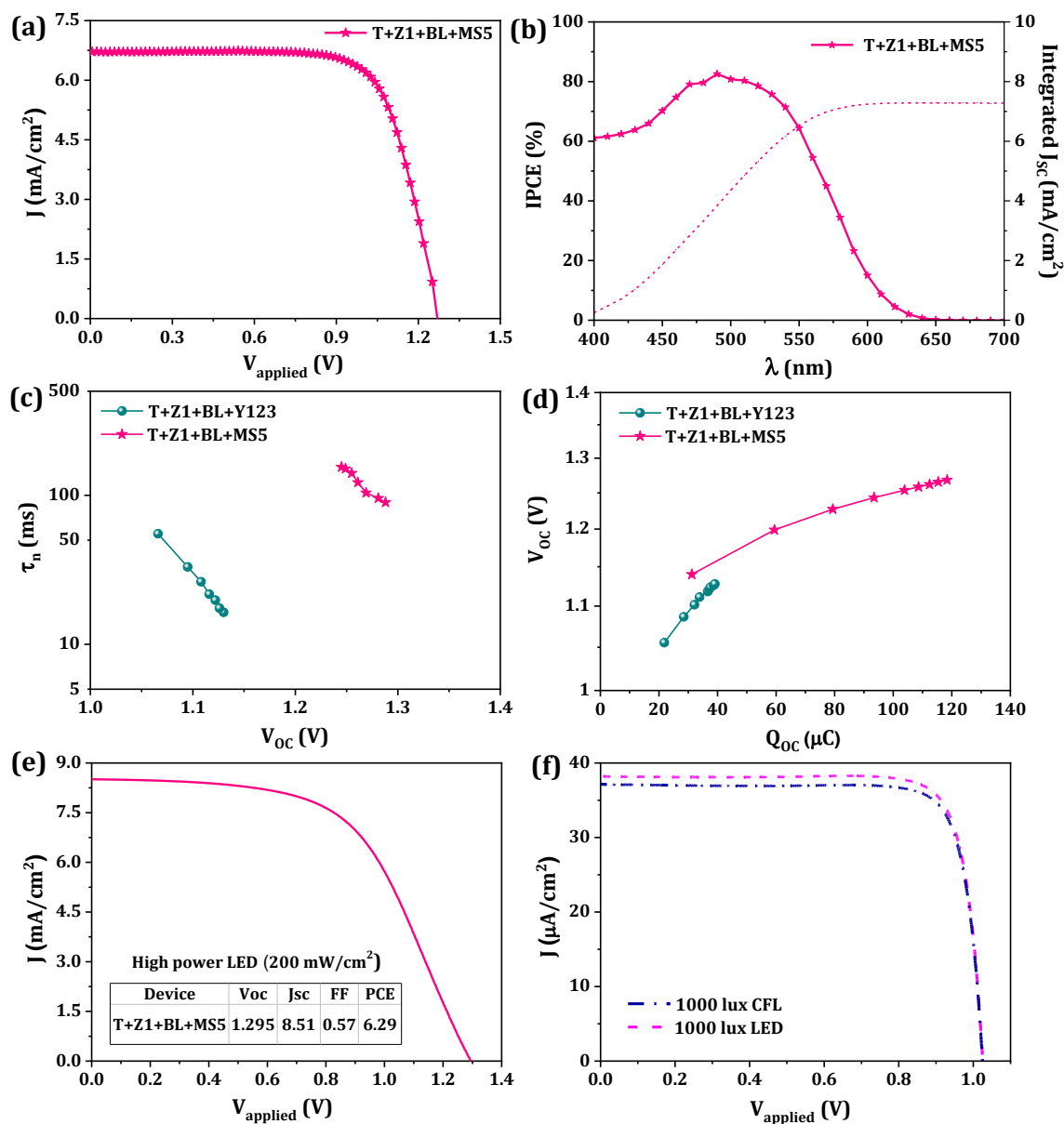


Figure 4.15. (a) J - V curves measured under AM 1.5G sunlight, and (b) corresponding IPCE spectra obtained for T+Z1+BL device employing MS5 sensitizer and $[\text{Cu}(\text{dmp})_2]^{2+/+}$ redox shuttle, and comparison of (e) charge extraction (CE) plots, and (f) lifetime plots (obtained from TVD) of this DSC with the corresponding device employing Y123 sensitizer. J - V curves measured under (c) high intensity LED light (200 mW/cm²), and (d) indoor illuminations (1000 lux CFL and 1000 lux LED) obtained for the MS5 based T+Z1+BL device.

4.15(e). Under indoor lighting, the performance of T+Z1+BL devices that used MS5 dye and $[\text{Cu}(\text{dmp})_2]^{2+/+}$ electrolyte were assessed. When illuminated by 1000 lux LED and CFL, these DSCs realized a record V_{oc} of 1.025 V (Figure 4.15(f), Table 4.8). However,

the *PCE* of the MS5 sensitized device was lower when compared to the devices using Y123 dye, which could be attributed to the loss in *J_{SC}* owing to the narrower absorption window of MS5 dye. The *V_{OC}* of MS5 dye-sensitized T+Z1+BL device reported in this work, i.e. 1.27 V under full sun, 1.295 V under higher intensity (200 mW/cm²) LED light, and 1.025 V under 1000 lux CFL and LED illuminations, are the highest reported open circuit potentials in DSC so far. Finally, we could demonstrate the importance of this work by powering a temperature sensor (ACETEQ DC-2) using a single DSC (of active area ~ 0.24 cm²) **employing the TiO₂/ZnO bilayer photoanodes sensitized with MS5 dye and [Cu(dmp)₂]^{2+/+} electrolyte**, under outdoor as well as indoor lighting conditions (Figure 4.16). The present design methodology has proven effective in creating indoor DSCs with more compact footprints, which lowers costs and increases open circuit potentials, improving integration opportunities and enabling self-powered IoT device realization.

Table 4.7. Photovoltaic parameters of T+Z1+BL based DSCs employing MS5 dye and [Cu(dmp)₂]^{2+/+} redox electrolyte measured under AM 1.5G solar irradiation.

Illumination condition	V_{OC}^a (V)	J_{SC}^a (mA/cm²)	FF^a	PCE^a (%)	J^{integrated}^b (mA/cm²)
AM 1.5G sunlight	1.27 (1.26 ± 0.01)	6.75 (6.70 ± 0.05)	0.73 (0.72 ± 0.01)	6.23 (6.08 ± 0.15)	7.30

^a *J-V* parameters of champion cells with averages taken over five sets of samples ± mean deviation in parentheses.

^b *J_{SC}* obtained by integrating the IPCE spectra.

Table 4.8. Photovoltaic parameters of T+Z1+BL based DSCs employing MS5 dye and [Cu(dmp)₂]^{2+/+} redox electrolyte measured under various indoor illumination conditions.

Illumination condition	V_{OC}^a (V)	J_{SC}^a (μA/cm²)	FF^a	PCE^a (%)	P_{max}^a (μW/cm²)
1000 lux CFL (0.283 mW/cm²)	1.025 (1.020 ± 0.005)	37.1 (35.9 ± 1.5)	0.82 (0.81 ± 0.01)	11.1 (10.8 ± 0.4)	31.33 (30.9 ± 0.4)
1000 lux LED (0.313 mW/cm²)	1.025 (1.016 ± 0.008)	38.2 (38.5 ± 2.5)	0.82 (0.81 ± 0.01)	10.3 (10.1 ± 0.3)	32.28 (32.1 ± 0.3)

^a *J-V* parameters of champion cells with averages taken over five sets of samples ± mean deviation in parentheses.

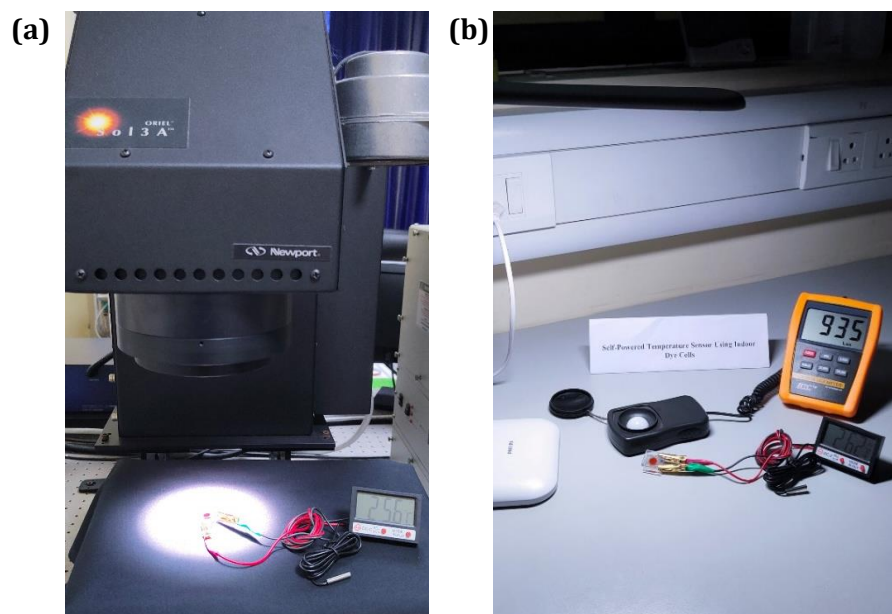


Figure 4.16. A temperature sensor (ACETEQ DC-2) powered using a single TiO_2/ZnO bilayer DSC (active area 0.24 cm^2) fabricated using MS5 dye and $[\text{Cu}(\text{dmp})_2]^{2+/+}$ redox electrolyte under (a) AM1.5 G simulated sunlight ($100 \text{ mW}/\text{cm}^2$) and (b) an indoor LED reading lamp (935 lux LED light).

4.4. Conclusions

To sum up, we introduced a new photoanode architecture for dye-sensitized photovoltaic cells (DSCs) that consists of a layer of ZnO hierarchical microstructures over the traditional TiO_2 active layer to realize TiO_2/ZnO bilayer photoanodes. Our photoanode design seeks to improve the open circuit voltage (V_{OC}) of DSCs in both indoor and outdoor lighting scenarios. We succeeded in achieving an impressive V_{OC} of 1.27 V under AM 1.5G one sun illumination and 1.295 V under a higher intensity LED light of $200 \text{ mW}/\text{cm}^2$ using this optimized bilayer electrode with a blocking layer (T+Z1+BL) in combination with the MS5 sensitizer and $[\text{Cu}(\text{dmp})_2]^{2+/+}$ redox electrolyte. These are the highest V_{OC} reported to date from a single junction DSC. Comprehensive investigations into interfacial charge transfer have demonstrated that the bilayer structure results in an improved lifetime and a negatively shifted CB, both of which greatly contribute to the enhanced V_{OC} . Additionally, by utilizing an MS5 sensitizer and a $[\text{Cu}(\text{dmp})_2]^{2+/+}$ redox electrolyte with the TiO_2/ZnO bilayer photoanode (T+Z1+BL), which lowers recombination losses, we were able to achieve a V_{OC} of 1.025 V under 1000 lux CFL and LED illumination. These encouraging findings motivated us to develop a battery-free temperature sensor powered using a DSC with $\sim 0.24 \text{ cm}^2$ active area under indoor lighting. Ultimately, when combined with the

right blend of dyes and electrolytes, this work offers useful material and device engineering strategies that can be used to realize higher V_{OC} in DSCs. In order to efficiently operate cutting-edge self-powered electronic applications, achieving higher V_{OC} is imperative. Most of the energy harvesting and management circuits in these smart devices have lower current requirements (in μA) but require higher voltage. This indicates that V_{OC} must be taken into account while designing DSCs for indoor photovoltaic applications, in addition to current and efficiency. Additionally, by minimizing the device's size without sacrificing voltage, innovative and creative ways to incorporate indoor DSCs in lieu of batteries to promote sustainability and carbon neutrality can be realized.

References

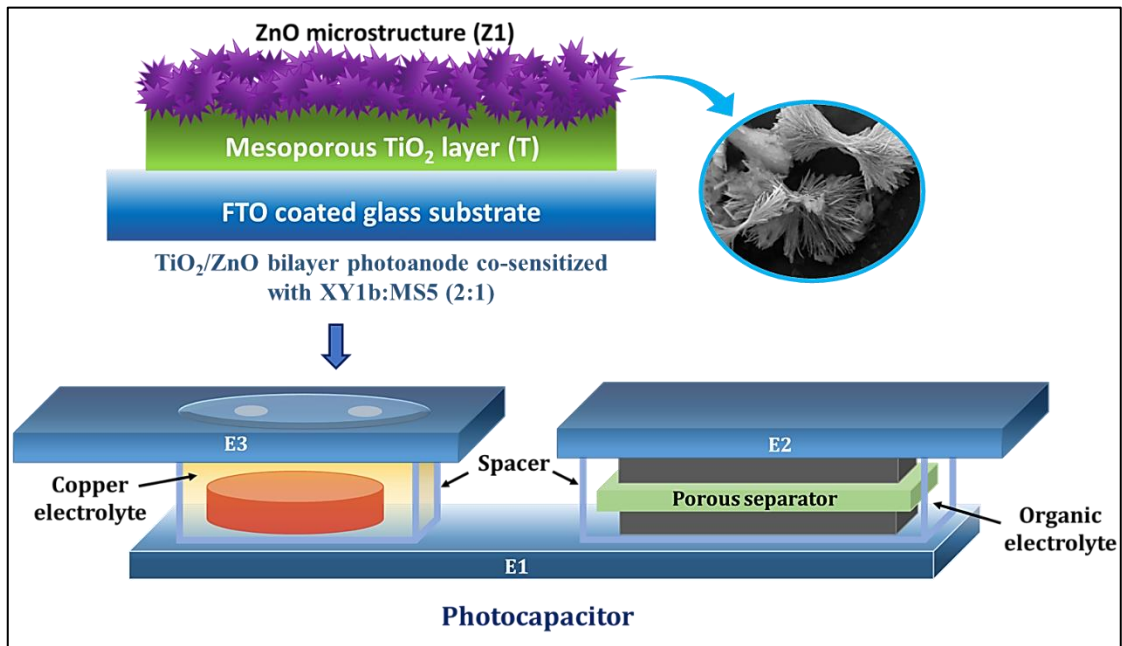
- [1] J. Gubbi, R. Buyya, S. Marusic and M. Palaniswami, *Future Generation Computer Systems*, **2013**, 29, 1645–1660.
- [2] M. Mohammadi and A. Al-Fuqaha, *IEEE Communications Magazine*, **2018**, 56, 94–101.
- [3] D. Ma, G. Lan, M. Hassan, W. Hu and S. K. Das, *IEEE Communications Surveys and Tutorials*, **2020**, 22, 1222–1250.
- [4] J. Hester and J. Sorber, *Proceedings of the 15th ACM Conference on Embedded Networked Sensor Systems*, Association for Computing Machinery, **2017**.
- [5] H. Elahi, K. Munir, M. Eugeni, S. Atek and P. Gaudenzi, *Energies*, **2020**, 13, 5528.
- [6] A. Aslam, U. Mehmood, M. H. Arshad, A. Ishfaq, J. Zaheer, A. Ul Haq Khan and M. Sufyan, *Solar Energy*, **2020**, 207, 874–892.
- [7] G. Gokul, S. C. Pradhan and S. Soman, *Energy, Environment, and Sustainability*, **2019**, 281–316.
- [8] Y. Cao, Y. Liu, S. M. Zakeeruddin, A. Hagfeldt and M. Grätzel, *Joule*, **2018**, 2, 1108–1117.
- [9] H. Michaels, M. Rinderle, R. Freitag, I. Benesperi, T. Edvinsson, R. Socher, A. Gagliardi and M. Freitag, *Chem Sci*, **2020**, 11, 2895–2906.
- [10] M. Freitag, J. Teuscher, Y. Saygili, X. Zhang, F. Giordano, P. Liska, J. Hua, S. M. Zakeeruddin, J. E. Moser, M. Grätzel and A. Hagfeldt, *Nat Photonics*, **2017**, 11, 372–378.
- [11] B. O'Regan and M. Grätzel, *Nature*, **1991**, 353, 737–740.
- [12] A. Hagfeldt, G. Boschloo, L. Sun, L. Kloo and H. Pettersson, *Chem Rev*, **2010**, 110, 6595–6663.
- [13] A. R. Yugis, R. F. Mansa and C. S. Sipaut, *IOP Conf Ser Mater Sci Eng*, **2015**, 78, 012003.
- [14] F. Schoden, A. K. Schnatmann, E. Davies, D. Diederich, J. L. Storck, D. Knefelkamp, T. Blachowicz and E. Schwenzfeier-Hellkamp, *Materials*, **2021**, 14, 6622.

- [15] F. Schoden, A. K. Schnatmann, T. Blachowicz, H. Manz-Schumacher and E. Schwenzfeier-Hellkamp, *Sustainability*, **2022**, 14, 15280.
- [16] A. Dewan, S. U. Ay, M. N. Karim and H. Beyenal, *J Power Sources*, **2014**, 245, 129–143.
- [17] H. Jayakumar, K. Lee, W. S. Lee, A. Raha, Y. Kim and V. Raghunathan, *Proceedings of the International Symposium on Low Power Electronics and Design*, **2015**, 375–380.
- [18] X. Cao, Y. Xiong, J. Sun, X. Zhu, Q. Sun and Z. L. Wang, *Adv Funct Mater*, **2021**, 31, 210298.
- [19] S. M. Feldt, G. Wang, G. Boschloo and A. Hagfeldt, *Journal of Physical Chemistry C*, **2011**, 115, 21500–21507.
- [20] J. H. Yum, E. Baranoff, F. Kessler, T. Moehl, S. Ahmad, T. Bessho, A. Marchioro, E. Ghadiri, J. E. Moser, C. Yi, M. K. Nazeeruddin and M. Grätzel, *Nat Commun*, **2012**, 3, 631.
- [21] Y. Saygili, M. Söderberg, N. Pellet, F. Giordano, Y. Cao, A. B. Muñoz-García, S. M. Zakeeruddin, N. Vlachopoulos, M. Pavone, G. Boschloo, L. Kavan, J. E. Moser, M. Grätzel, A. Hagfeldt and M. Freitag, *J Am Chem Soc*, **2016**, 138, 15087–15096.
- [22] Y. Saygili, M. Stojanovic, H. Michaels, J. Tjepelt, J. Teuscher, A. Massaro, M. Pavone, F. Giordano, S. M. Zakeeruddin, G. Boschloo, J. E. Moser, M. Grätzel, A. B. Muñoz-García, A. Hagfeldt and M. Freitag, *ACS Appl Energy Mater*, **2018**, 1, 4950–4962.
- [23] Y. Ren, D. Zhang, J. Suo, Y. Cao, F. T. Eickemeyer, N. Vlachopoulos, S. M. Zakeeruddin, A. Hagfeldt and M. Grätzel, *Nature*, **2023**, 613, 60–65.
- [24] A. Grobelny, Z. Shen, F. T. Eickemeyer, N. F. Antariksa, S. Zapotoczny, S. M. Zakeeruddin and M. Grätzel, *Advanced Materials*, **2023**, 35, 2207785.
- [25] S. C. Pradhan, A. Hagfeldt and S. Soman, *J Mater Chem A*, **2018**, 6, 22204–22214.
- [26] D. Zhang, M. Stojanovic, Y. Ren, Y. Cao, F. T. Eickemeyer, E. Socie, N. Vlachopoulos, J. E. Moser, S. M. Zakeeruddin, A. Hagfeldt and M. Grätzel, *Nat Commun*, **2021**, 12, 1777.
- [27] Q. Zhang and G. Cao, *Nano Today*, **2011**, 6, 91–109.
- [28] J. A. Anta, E. Guillén and R. Tena-Zaera, *Journal of Physical Chemistry C*, **2012**, 116, 11413–11425.
- [29] C. C. Raj and R. Prasanth, *J Power Sources*, **2016**, 317, 120–132.
- [30] S. H. Ko, D. Lee, H. W. Kang, K. H. Nam, J. Y. Yeo, S. J. Hong, C. P. Grigoropoulos and H. J. Sung, *Nano Lett*, **2011**, 11, 666–671.
- [31] R. Gao, Z. Liang, J. Tian, Q. Zhang, L. Wang and G. Cao, *Nano Energy*, **2013**, 2, 40–48.
- [32] W. Peng, L. Han and Z. Wang, *Chemistry – A European Journal*, **2014**, 20, 8483–8487.
- [33] S. Sasidharan, S. Soman, S. C. Pradhan, K. N. N. Unni, A. A. P. Mohamed, B. N. Nair and H. U. N. Saraswathy, *New Journal of Chemistry*, **2017**, 41, 1007–1016.
- [34] N. Memarian, I. Concina, A. Braga, S. M. Rozati, A. Vomiero and G. Sberveglieri, *Angewandte Chemie*, **2011**, 123, 12529–12533.

- [35] A. K. Chandiran, M. Abdi-Jalebi, M. K. Nazeeruddin and M. Grätzel, *ACS Nano*, **2014**, 8, 2261–2268.
- [36] E. Guillén, L. M. Peter and J. A. Anta, *Journal of Physical Chemistry C*, **2011**, 115, 22622–22632.
- [37] K. Keis, J. Lindgren, S. E. Lindquist and A. Hagfeldt, *Langmuir*, 2000, 16, 4688–4694.
- [38] M. Quintana, T. Marinado, K. Nonomura, G. Boschloo and A. Hagfeldt, *J Photochem Photobiol A Chem*, **2009**, 202, 159–163.
- [39] S. Sasidharan, A. Jagadeesh, S. C. Pradhan, B. N. Nair, A. Azeez Peer Mohamed, K. N. Narayanan Unni, S. Soman and U. Nair Saraswathy Hareesh, *Solar Energy*, **2021**, 226, 214–224.
- [40] N. T. K. Thanh, N. Maclean and S. Mahiddine, *Chem Rev*, **2014**, 114, 7610–7630.
- [41] K. Gelderman, L. Lee and S. W. Donne, *J Chem Educ*, **2007**, 84, 685–688.
- [42] A. Gopalraman, S. Karuppuchamy and S. Vijayaraghavan, *RSC Adv*, **2019**, 9, 40292–40300.
- [43] J. Zhang and H. Yu, *J Mater Chem A*, **2021**, 9, 4138–4149.
- [44] J. Zhang, Y. Sun, C. Huang, B. Yu and H. Yu, *Adv Energy Mater*, **2022**, 12, 2202542.
- [45] S. S. Kim, J. H. Yum and Y. E. Sung, *Solar Energy Materials and Solar Cells*, **2003**, 79, 495–505.
- [46] S. Borbón, S. Lugo, D. Pourjafari, N. Pineda Aguilar, G. Oskam and I. López, *ACS Omega*, **2020**, 5, 10977–10986.
- [47] K. Shen, K. Wu and D. Wang, *Mater Res Bull*, **2014**, 51, 141–144.
- [48] R. Ruess, S. Haas, A. Ringleb and D. Schlettwein, *Electrochim Acta*, **2017**, 258, 591–598.
- [49] F. Fabregat-Santiago, G. Garcia-Belmonte, I. Mora-Seró and J. Bisquert, *Physical Chemistry Chemical Physics*, **2011**, 13, 9083–9118.
- [50] S. Rühle, M. Greenshtein, S. G. Chen, A. Merson, H. Pizem, C. S. Sukenik, D. Cahen and A. Zaban, *Journal of Physical Chemistry B*, **2005**, 109, 18907–18913.
- [51] P. Siva Gangadhar, A. Jagadeesh, A. S. George, G. Reddy, S. Prasanthkumar, S. Soman and L. Giribabu, *Mol Syst Des Eng*, **2021**, 6, 779–789.
- [52] K. E. Kim, S. R. Jang, J. Park, R. Vittal and K. J. Kim, *Solar Energy Materials and Solar Cells*, **2007**, 91, 366–370.
- [53] P. Salvador, M. G. Hidalgo, A. Zaban and J. Bisquert, *Journal of Physical Chemistry B*, **2005**, 109, 15915–15926.
- [54] K. Keis, E. Magnusson, H. Lindström, S. E. Lindquist and A. Hagfeldt, *Solar Energy Materials and Solar Cells*, **2002**, 73, 51–58.
- [55] H. Yu, S. Zhang, H. Zhao, G. Will and P. Liu, *Electrochim Acta*, **2009**, 54, 1319–1324.

- [56] I. P. Liu, W. H. Lin, C. M. Tseng-Shan and Y. L. Lee, *ACS Appl Mater Interfaces*, **2018**, 10, 38900–38905.
- [57] T. Pauporté and C. Magne, *Thin Solid Films*, **2014**, 560, 20–26.
- [58] K. Keis, J. Lindgren, S. E. Lindquist and A. Hagfeldt, *Langmuir*, **2000**, 16, 4688–4694.
- [59] L. Ke, S. Bin Dolmanan, L. Shen, P. K. Pallathadk, Z. Zhang, D. M. Ying Lai and H. Liu, *Solar Energy Materials and Solar Cells*, **2010**, 94, 323–326.
- [60] E. J. Canto-Aguilar, M. Rodríguez-Pérez, R. García-Rodríguez, F. I. Lizama-Tzec, A. T. De Denko, F. E. Osterloh and G. Oskam, *Electrochim Acta*, **2017**, 258, 396–404.
- [61] S. Ghosh, R. Sartape and J. Chakraborty, *Journal of Materials Science: Materials in Electronics*, **2020**, 31, 2202–2220.

Dye-sensitized TiO₂/ZnO bilayer photoanode based photocapacitors for outdoor/indoor light harvesting and storage applications



Abstract: Dye-sensitized photovoltaic cells (DSCs) demonstrate significant light harvesting capabilities under both outdoor (AM 1.5G simulated sunlight) and indoor (LED or CFL light) illuminations, offering higher open-circuit potential (V_{OC}) and short circuit current density (J_{SC}). In the present chapter, we achieved enhanced DSC performance of 8.3% under AM 1.5G irradiation and 39.5% under 6000 lux illumination, by employing a TiO₂/ZnO bilayer photoanode architecture co-sensitized with organic dyes (XY1b and MS5) along with $[Cu(dmp)_2]^{2+/+}$ redox mediator. As discussed in the previous chapter, conventional use of DSCs to power sensor/clock has revealed a notable limitation; the clock reset each time the light is turned off. To overcome this challenge, we propose integrating the light harvester (DSC) with an energy storage device, specifically an electric double-layer capacitor (EDLC) utilizing activated carbon. This integration resulted in a novel photocapacitor (PC) exhibiting an impressive overall photoelectric conversion and storage efficiency (OPCSE) of 4.1% under one sun conditions and 15.5% under 6000 lux CFL illumination.

5.1. Introduction

Dye-sensitized photovoltaic cells (DSCs) are enormously pursued to be applied as an alternative to conventional batteries, in a wide variety of outdoor as well as indoor applications, owing to their environmental friendliness, ease of recycling and appreciably long lifetimes. The outdoor applications include building integrated photovoltaics (BIPV) or transportation integrated photovoltaics (TIPV) in which DSCs are integrated to the windows, roofs etc. of various infrastructures or vehicles.^[1-4] Meanwhile, DSCs proved to be the best candidates for indoor photovoltaic (IPV) applications for powering smart electronic devices, such as smart watches, earphones and for powering the sensors and actuators associated with emerging technologies like Internet of Things (IoTs) and machine-to-machine communication systems.^[4-9] In the previous chapter (**Chapter 4**), we developed a novel TiO₂/ZnO bilayer photoanode based small area DSC that could deliver appreciable voltage output, enough for powering a temperature sensor/digital clock (ACETEQ DC-2) under 1000 lux CFL illumination. It is anticipated that the performance of this bilayer DSC can be further improved by optimizing the thickness of the TiO₂ layer. Several studies shows that the short circuit current density (J_{SC}) and open circuit voltage (V_{OC}) of DSCs depend on the semiconductor layer thickness.^[10,11] Generally, V_{OC} of DSCs experiences decrease with the increase in layer thickness, due to the enhanced surface area available for recombination. Meanwhile, J_{SC} is seen to increase with increase in layer thickness, taking advantage of the higher dye loading. However, after an optimum thickness, J_{SC} also starts decreasing with further increase in thickness, which might be due to the dominance of the recombination process over the photoelectron generation. In case of DSCs devices utilizing metal complex based redox shuttles, like copper or cobalt based electrolytes, J_{SC} is further influenced by the mass transport limitation, particularly under higher intensity illuminations.^[12,13] Higher the layer thickness, more will be the resistance to the diffusion of the bulky electrolyte species, hence affecting the J_{SC} . However, under low intensity or indoor light illuminations, the J_{SC} of the DSC utilizing bulky redox species are not limited by the layer thickness, which may be attributed to the less influence of mass transport issues under low intensity light conditions.

Energy storage is a primary concern that is directly associated with photovoltaic (PV) technologies. The intrinsic variations in solar light caused by weather, day cycles, and location necessitate the integration of PV devices with storage systems for continuous operation. Additionally, the potential of third generation PV technologies to generate

electricity from diffuse light and indoor/artificial illuminations, makes the integration of energy harvesting and storage technologies even more alluring.^[4,14] The external integration of PV device with rechargeable storage device may reduce the overall performance of the system, due to the nonunitary efficiency of each component causing energy mismatch between them.^[15,16] Moreover, such systems exhibit higher device footprint and ohmic losses due to the external connection and power management electronic components. In this regard, many studies on the monolithic integration of PV cells with storage units are being carried out, in which the two devices use one or more shared electrodes resulting in 2-terminal or 3-terminal systems.^[17–21] Supercapacitors (SCs), particularly electrochemical double-layer capacitors (EDLCs) are a promising option for storage, as they can withstand larger number of charge/discharge cycles without significantly altering the capacitance nominal value.^[22–24] In addition, when compared to the rechargeable batteries, EDLCs are less susceptible to the output voltage of the photovoltaic devices being used.^[25,26] An EDLC is an electrochemical storage device, typically made up of two parallel electrodes coated with high surface area active materials sandwiched with a non-conductive porous separator impregnated with an electrolyte. The capacitance of EDLC arises due to the adsorption of both anions and cations at the electrode/electrolyte interface and hence is determined by the specific surface area and pore-size distribution of the electrode materials.^[27–29] Carbon-based porous materials with high specific surface area and good conductivity, like graphene, xerogels, carbon nanotubes (CNTs), activated carbon, etc., typically exhibit EDLC type behavior.^[30,31] The integration of SCs or EDLCs with PV devices to produce photo-chargeable supercapacitors or photocapacitors (PCs) have been reported previously.^[32–36] The PCs are built based on the fundamental idea of a self-charging capacitor that has the ability to generate electrical energy from light and store it simultaneously, making them suitable for a large number of futuristic smart applications.^[37–41] The use of PCs eliminates the need for two physically distinct devices for photoelectric conversion and energy storage, which lowers the cost, weight, and space requirements, while improving the overall efficiency of the system.^[42]

The third generation PV technologies, including DSC, perovskite solar cells (PSC), organic solar cell (OSC), quantum dot sensitized solar cell (QDSC), etc., are observed to be the most suitable candidates for developing PCs, as they can be fabricated in a wide variety of architectures and range of substrates.^[35,36,43–45] Also, the application of such PCs utilizing third generation PV cells and EDLCs can be extended to smart electronics

(portable and wearable ones) and IoT devices, as they can be fabricated on any type of conducting substrates (rigid as well as flexible ones). The simple design, facile fabrication steps, abundant and non-toxic materials used, tunable optical properties, etc., make DSC a prominent choice for developing PCs.^[37,44,46] Earlier in 2004, Miyasaka *et. al.* explored a 2-terminal PC device directly combining an activated carbon (AC) based EDLC with N719 based DSC.^[45] However, they could attain a maximum achievable potential (V_m) of only 0.4 V under simulated one sun irradiation with an incident intensity of 100 mW/cm². One year later, the same group developed a 3-terminal stacked architecture for PCs by introducing an intermediate platinum electrode between the AC based EDLC and the N719 based DSC, thereby attaining a V_m of 0.8V under one sun condition.^[47] Later on in 2010, this stacked 3-terminal PC architecture was utilized by Hsu *et. al.*, to achieve a V_m of 0.75 V under 100 mW/cm² irradiation with a discharge energy density of 22 μ Wh/cm².^[48] The SC was a poly(3,3-diethyl-3,4-dihydro-2H-thieno-[3,4-b][1,4]dioxepine) (PProDOT) polymer based one with symmetric structure and the DSC utilized N3 sensitized photoanodes along with iodide/triiodide (I^-/I_3^-) electrolyte. An overall photoelectric conversion and storage efficiency (*OPCSE*) of 5.12% with a V_m of 0.72 V was reported by Yang *et. al.* by utilizing an all solid-state PC device employing N719-based DSC with a gel electrolyte and multi-walled carbon nanotube (MWCNT) array based EDLC.^[49] Later on, V_m of 0.89 V and maximum *OPCSE* of 0.8% under one sun was realized by integrating a D35 dye based solid-state DSC and ruthenium oxide based SC, with silver electrode as the intermediate electrode.^[50] In a similar design, Xu *et. al.* stacked DSC and SC, both made up of one-dimensional anodic titanium oxide (ATO) nanotube arrays to form a 3-terminal PC with Ti foil as the intermediate electrode, to achieve a V_m and *OPCSE* of 0.61 V and 1.64%, respectively.^[51] They could further realize a V_m of 2.5 V by interconnecting four such PC devices in series. Scalia *et. al.* could attain a V_m of 2.45 V under one sun from a single PC device, by integrating a single AC based EDLC using an ionic liquid as electrolyte integrated to a W-type dye-sensitized PV module (DSM) using Z907 dye and iodine based electrolyte.^[52] However, they utilized a 4-terminal stacked architecture, wherein the PV section and storage section were fabricated separately on different FTO substrates and then connected externally, thereby attaining a maximum *OPCSE* of 1.83%.

In all the aforementioned reports of 3-terminal monolithic PCs, a stacked architecture was adopted, in which the active material of the SC and the CE material of the DSC part was coated on the two sides of an intermediate electrode, which served as a

common terminal for both photoconversion and storage part of the device. However, a new design for 3-terminal PCs was opted by Speranza *et. al.*, wherein the active electrode materials of both the SC and DSC part were deposited on the same side of a conducting substrate, but on different portions.^[53] Let us call it the parallel architecture for 3-terminal PC fabrication. They integrated a W-type large area DSM (composed of N719 dye and iodide/triiodide electrolyte) with AC based EDLC. They reported a maximum *OPCSE* of 1.6% under one sun illumination and 9.7% under indoor illumination with a maximum storage potential of ~ 3 V. In the present chapter, we explored the possibility of integrating activated carbon electrode based EDLC with copper electrolyte based DSCs (with active area ~ 0.24 cm²) made up of TiO₂/ZnO bilayer photoanodes, in a parallel architecture to obtain V_m above 1V under simulated solar light and above 0.9 V under indoor light irradiation. The resulting PC could achieve a maximum *OPCSE* of 4.1%, with V_m of ~ 1.1 V, under one sun irradiation. It could also exhibit a remarkably high maximum *OPCSE* of 8.2% (with V_m ~ 0.95 V), 11.4% (with V_m ~ 0.98 V) and 15.5% (with V_m ~ 1.01 V), under CFL illumination of 2000 lux, 4000 lux and 6000 lux, respectively.

5.2. Experimental procedure

5.2.1. Dye sensitized photovoltaic cell fabrication and characterization

The photoanode for DSCs or DSCs in this work consisted of a TiO₂/ZnO bilayer (designated as T+Z1), made up of a TiO₂ layer (18NR-T, GreatcellSolar, Australia with ~ 20 nm particle size and an over layer of ZnO microparticles (Z1) with ~ 10 μm particle size (synthesized as described in **Chapter 4**). The photoanodes were fabricated on the FTO substrate (TEC 10, Merck) cut into small pieces (1.6 cm x 1.6 cm) and cleaned in an ultrasonic bath using soap solution (for 30 minutes), de-ionized water (for 30 minutes), isopropanol (for 15 minutes), and acetone (for 15 minutes), followed by annealing at 500 °C for 30 minutes. Pre-blocking layers were deposited on the cleaned FTO plates by submerging them in a 50 mM aqueous solution of TiCl₄ at 75 °C for 30 minutes. The substrates were then subjected to a step-by-step annealing process, which involved slow heating and maintenance of the temperature at 150°C for 10 minutes, 300°C for 10 minutes, 350°C for 10 minutes, 450°C for 10 minutes, and finally 500 °C for 30 minutes. The active layer (area 0.24 cm²) of commercial TiO₂ paste (18NR-T) and the Z1 over layer was deposited on the substrate via blade coating method, with intermediate heating at 100°C for 10 minutes. Finally, the electrodes were subjected to the previously described step-wise programme annealing procedure. Screen printing was used to deposit a commercial TiO₂

BL solution (GreatcellSolar, Australia) over the TiO₂/ZnO stacked photoanodes for electrodes that used post blocking layers (BL), before the programmed annealing. The next step involved immersing the photoanodes for 16 hours in dye solution prepared using a 1:1 acetonitrile to tert-butanol mixture as solvent. We utilized cleaned 1.6 cm x 1.6 cm FTO substrates (TEC7, GreatcellSolar, Australia) electrochemically polymerized with the conducting polymer poly (3,4-ethylene dioxythiophene) (PEDOT) as the counter electrodes for our devices. After that, a 25 μm thermoplastic spacer (Surlyn, GreatcellSolar, Australia) was used to hot press (at 120°C) the dye-sensitized photoanode and counter electrode together. To prepare the electrolyte, the copper dimethyl phenanthroline species, bis (2,9-dimethyl-1,10-phenanthroline copper(I/II) bis(trifluoromethanesulfonyl)imide (Dyename A.B, Sweden) (0.2 M [Cu(dmp)₂]¹⁺ and 0.04 M [Cu(dmp)₂]²⁺) were added to the solution of 0.1 M bis(trifluoromethane)sulfonimide lithium salt, LiTFSI (Merck), and 0.6 M 4-tert-butylpyridine, TBP (Merck). All of these substances were dissolved in acetonitrile solvent. Finally, holes in counter electrode were used to introduce the electrolyte solution into the inter-electrode spacing in the assembled device. The holes were sealed to prevent solvent evaporation and leakage. The initial optimization of the TiO₂ layer thickness in bilayer photoanode based devices were performed using T+Z1 bilayers without BL and sensitized with Y123 dye (using 0.1 mM dye solution). The final devices with optimum performance was acquired using T+Z1 bilayers with BL and co-sensitized with XY1b:MS5 (2:1) cocktail dye.

A class AAA solar simulator (Model PVIV-94043A, Newport) and a source meter (Keithley) were used to characterize the photovoltaic performance of the fabricated DSCs under AM 1.5G sunlight (100 mW/cm²). After being stored in an ambient environment with a temperature of 27°C and 80% humidity, the devices underwent a stability test. The current density versus voltage (*J-V*) and output power density versus voltage (*P-V*) characterizations of the DSCs were carried out in the indoor light environment using a Dyename AE 05 potentiostat and a specially designed indoor light measurement setup. A warm white compact fluorescent lamp (CFL; Osram, 14W/2700K) was used as the source of light. Using a UV-Vis-NIR spectrometer (Ocean optics, DH-2000-BAL) and a highly sensitive photodetector, the CFL irradiance spectra and incident power density was measured. *J-V* measurements were performed under outdoor condition with a black mask having a circular aperture of 0.11 cm², and indoors with a larger aperture of 0.34 cm². The incident photon-to-current conversion efficiency (*IPCE*) was measured using a 250 W

Xenon lamp that was connected to a monochromator. Advanced characterizations of the DSCs were done by electrochemical impedance spectroscopy (EIS) using the electrochemical workstation (Autolab, Metrohm). EIS was carried out at a frequency of 0.1 Hz to 100 kHz and a bias voltage between 0.95 V and 1.14 V in the absence of light. The ZView software was employed to fit the impedance plots obtained from EIS and determine various parameters such as charge transfer resistance (R_{ct}) and chemical capacitance (C_{μ}) corresponding to the interfacial charge transfer within the electrochemical device. The mass transport limitation in the DSCs were studied using current transient (CT) measurements at various illumination intensities. This was done using the Autolab workstation (Metrohm) coupled with an LED driver and a white LED as the light source. The transient photovoltaic and photocurrent decay (TVD and TPD) measurements of the DSCs were carried out using the toolbox set-up (Dyename A. B., Sweden), with an LED as light source.

5.2.2. Photocapacitor fabrication and characterization

The photocapacitor (PC) was fabricated in a three-terminal mode, in which the DSC part and EDLC part share a common FTO substrate (E1) for supporting the respective working electrodes. Whereas, the second working electrode (E2) of the EDLC and the counter electrode (E3) of the DSC were fabricated on two separate FTO plates. The E1 electrode was deposited with the dye-sensitized photoanode (or working electrode) layer of the DSC and the active material for the EDLC. The photoanode of DSC was made up of a TiO₂/ZnO bilayer architecture co-sensitized with two organic dyes (XY1b and MS5 in 2:1 proportion), as described in the previous **section 5.2.1**. While, the active material of EDLC was made up of a mixture of activated carbon and polyvinylidene fluoride (PVDF). For fabricating the working electrodes (or active electrodes) of the EDLC, the mixture of activated carbon and PVDF (9:1) was dispersed in ethanol and sonicated for 1-2 hours. The resulting dispersion was drop-casted on the FTO substrates (E1 and E2) over an area of 1 cm², followed by drying at room temperature for 15 minutes. Then the substrates were undergone an overnight heating at 120°C. The two working electrodes of the EDLC were fused together using a UV epoxy. The active layers in the working electrodes were infiltrated with an organic electrolyte containing 1M lithium perchlorate (LiOCl₄) in propylene carbonate, before joining the electrodes. Also, a porous separator (Celgard 2500) was placed between them. The DSC part was completed by combining the photoanode in E1 with a PEDOT coated counter electrode (E3) using the UV epoxy and filling the inter-

electrode gap with $[\text{Cu}(\text{dmp})_2]^{2+/+}$ electrolyte (prepared in the previous section 5.2.1). The steps involved in the fabrication of the PC is depicted in **Figure 5.1**.

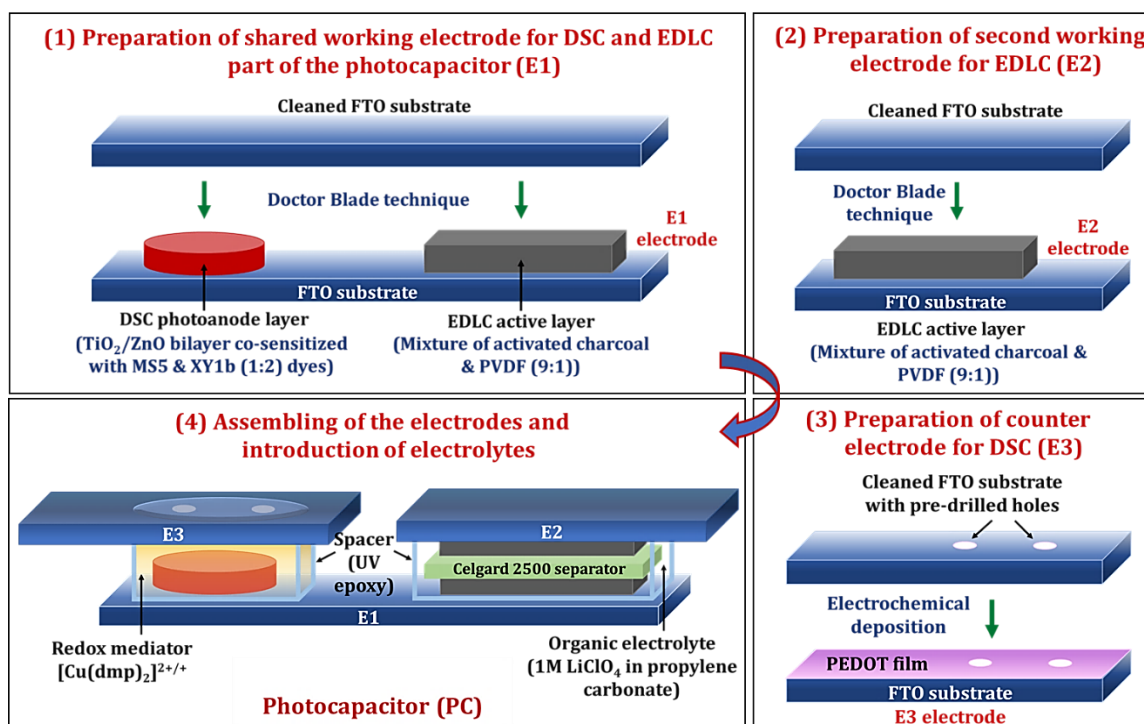


Figure 5.1. The steps involved in the fabrication of the photocapacitor (PC).

Initially, the performance of the EDLC part alone was tested using EIS, cyclic voltammetry (CV) and galvanostatic charge-discharge (GCD) measurements, using a potentiostat (BioLogic VMP3). The CV was performed at different scan rates ranging from 10 to 200 mV/s. For the GCD studies, the EDLC was charged up to a voltage of 1.1 V at a constant current and then allowed to discharge (up to 0 V) at the same rate. This was carried out at different constant currents ranging from 0.1 - 1.0 mA. The CV and GCD curves were used to determine the specific capacitance (C_s) of the EDLC. The integrated PC device was characterized by performing a photocharge/constant-current discharge test both under simulated AM1.5 G sunlight (simulated by a AAA solar simulator, Model PVIV-94043A, Newport) and under different CFL (Osram, 14W/2700K) illuminations. The measurements were carried using the electrochemical workstation (Autolab, Metrohm). During the photocharging step, the PC was connected in the charging mode by connecting the E2 and E3 electrodes (**Figure 5.2**), such that the DSC and EDLC are connected in parallel, and exposed to the light source, and the voltage across the EDLC was measured until the V_m is reached. Immediately after photocharging, the PC is connected in discharging mode, by disconnecting the E2 and E3 terminals (**Figure 5.2**). The discharge profile of the EDLC

was then recorded at a constant current value, while measuring its voltage. From the measurement, the *OPCSE* was calculated.

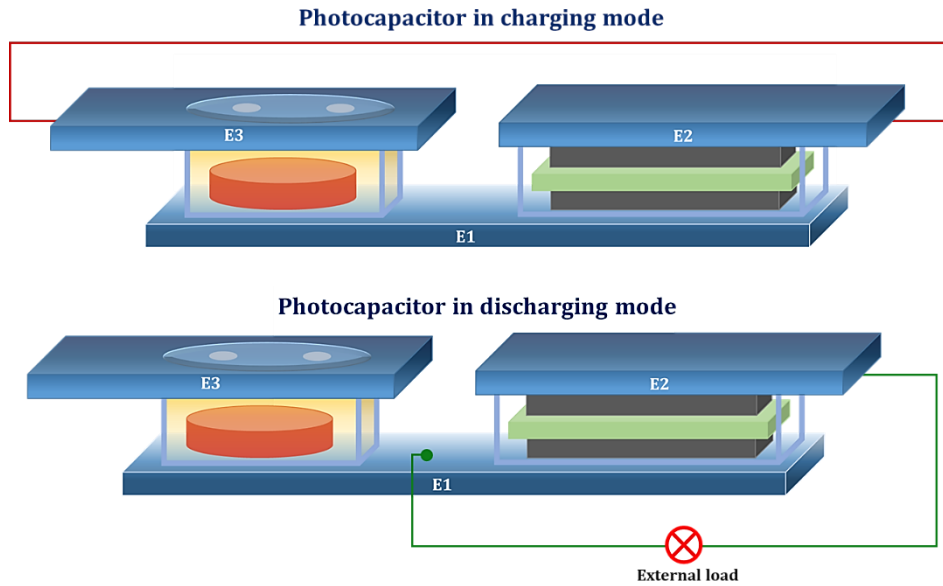


Figure 5.2. Photocapacitor (PC) connected in (a) charging mode, and (b) discharging mode.

5.3. Results and Discussion

5.3.1. Optimizing the TiO₂ layer thickness for dye sensitized light harvesters

In the initial studies, the TiO₂ layer thickness in the TiO₂/ZnO bilayer photoanodes of T+Z1 devices using Y123 dye and copper redox mediator ([Cu(dmp)₂]^{2+/+}) were optimized. The TiO₂ layer thickness in the T+Z1 electrodes were varied from 3 to 12 μm and the performance of the corresponding DSCs under various indoor light conditions were observed. Figure 5.3(a) shows the current density versus voltage (*J-V*) characteristics for the T+Z1 devices with various TiO₂ layer thicknesses, measured under AM 1.5G simulated sunlight (100 mW/cm²). The corresponding photovoltaic parameters are summarized in **Table 5.1**. It is observed that the dye loading in the photoanode films increased with the increase in TiO₂ layer thickness. This was obviously due to the higher number of TiO₂ particles available for dye adsorption in thicker films. However, the *J_{SC}* of the devices first increased with the increase in TiO₂ layer thickness, up to the optimum thickness of 6 μm. Then it started decreasing with further increase in layer thickness. This trend in variation of *J_{SC}* with TiO₂ thickness was not matching with the theoretical *J_{SC}* (*J_{integrated}*) acquired by integrating the *IPCE* spectra (**Figure 5.3(b)**). *J_{integrated}* was observed to be proportional to the dye loading values. This discrepancy in *J_{SC}* values observed under one sun condition

and those calculated from *IPCE* spectra, could be attributed to the mass transport limitation associated with copper species based electrolyte system.^[12] The increase in mass transport issues with increase in layer thickness might have resulted in lowering of J_{SC} in the respective DSCs. Consequently, the device with an optimum TiO_2 film thickness of 6 μm exhibited the highest *PCE* of 7.50% with a V_{OC} of 1.14 V, J_{SC} of 9.67 mA/cm^2 , and fill factor (*FF*) of 0.68.

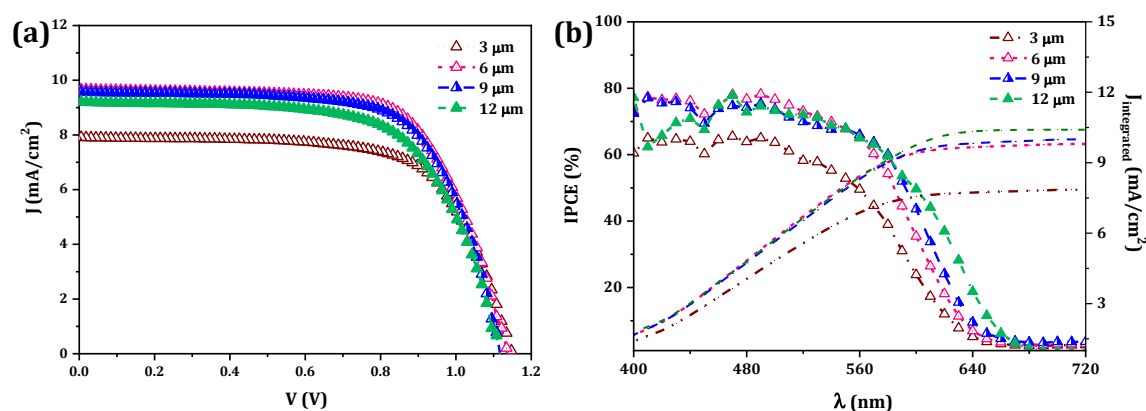


Figure 5.3. (a) *J-V* characteristics under one sun condition, and (b) *IPCE* spectra obtained for TiO_2/ZnO (T+Z1) bilayer device employing Y123 dye and $[\text{Cu}(\text{dmp})_2]^{2+/+}$ electrolyte, with different TiO_2 layer thickness.

Table 5.1. Photovoltaic parameters of DSCs employing TiO_2/ZnO bilayer (T+Z1) photoanodes with different TiO_2 layer thicknesses (d), sensitized with Y123 dye in conjugation with $[\text{Cu}(\text{dmp})_2]^{1+/2+}$ redox electrolyte, under AM 1.5G solar irradiation, along with dye loading (DL), and theoretical J_{SC} ($J_{\text{integrated}}$) values.

TiO_2 layer thickness ^a (μm)	DL ($\times 10^{-7}$ mol/cm ²)	V_{oc} ^b (V)	J_{sc} ^b (mA/cm ²)	<i>FF</i> ^b	<i>PCE</i> ^b (%)	$J_{\text{integrated}}$ ^c (mA/cm ²)
3	3.7	1.15 (1.14 \pm 0.01)	7.91 (7.70 \pm 0.20)	0.68 (0.68 \pm 0.02)	6.19 (5.95 \pm 0.36)	7.85
6	3.9	1.14 (1.13 \pm 0.01)	9.67 (9.64 \pm 0.11)	0.68 (0.67 \pm 0.02)	7.50 (7.31 \pm 0.20)	9.80
9	4.2	1.12 (1.12 \pm 0.01)	9.59 (9.58 \pm 0.10)	0.67 (0.66 \pm 0.02)	7.29 (7.25 \pm 0.20)	9.97
12	4.3	1.11 (1.11 \pm 0.01)	9.22 (9.28 \pm 0.57)	0.66 (0.64 \pm 0.02)	6.77 (6.62 \pm 0.32)	10.01

^a Average TiO_2 layer thickness obtained from profilometer measurement.

^b *J-V* parameters of champion cells with averages taken over three sets of samples \pm mean deviation (in parentheses).

^c Theoretical J_{SC} obtained by integrating the *IPCE* spectra.

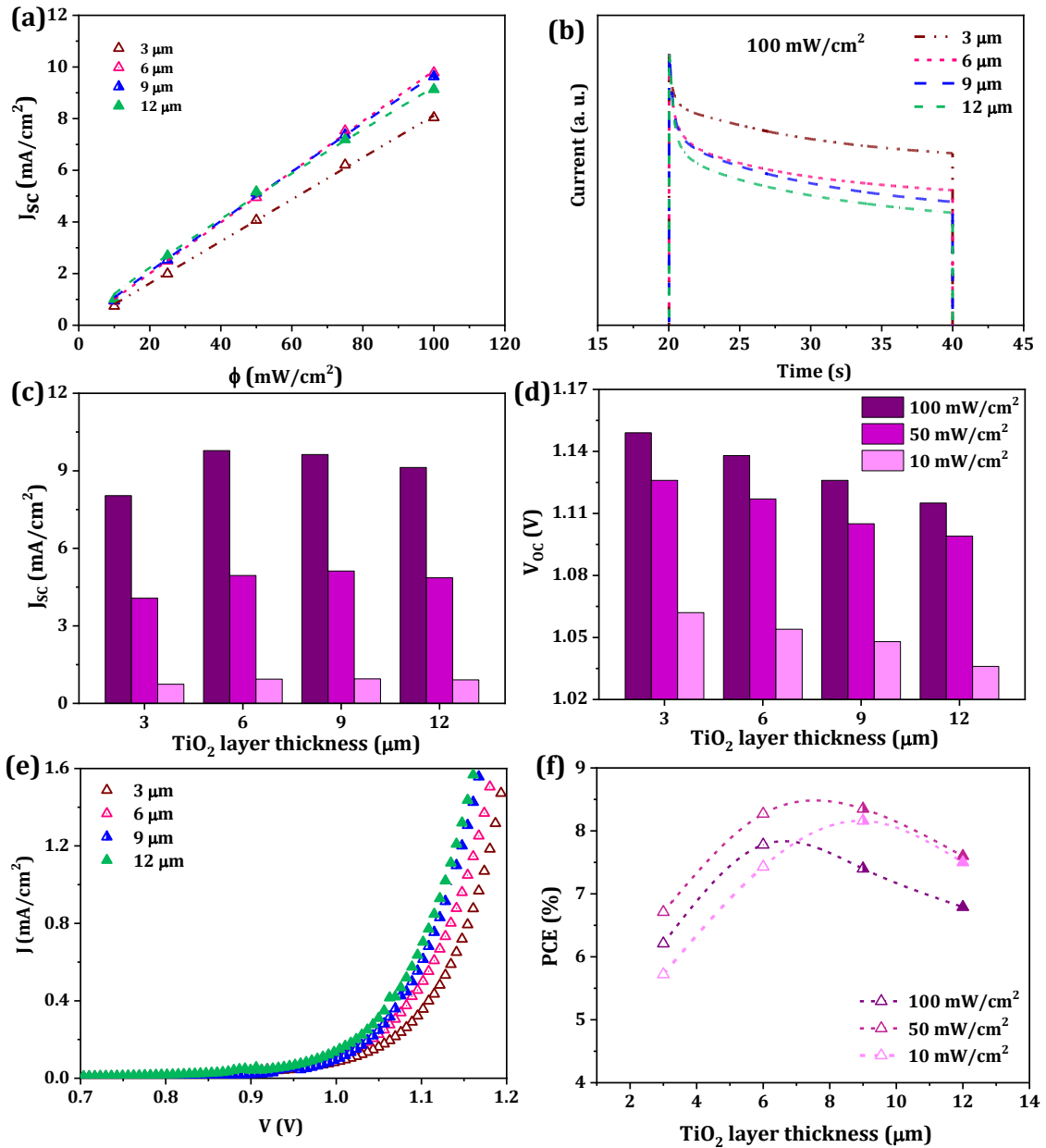


Figure 5.4. (a) J_{SC} vs. intensity plot; (b) current transient (CT) curves obtained at an incident light intensity of 100 mW/cm²; (c) V_{OC} , and (d) J_{SC} as a function of TiO₂ layer thickness, under various light intensities; (e) J - V characteristic curves obtained under dark condition; and (h) PCE as a function of TiO₂ layer thickness, under various light intensities for TiO₂/ZnO (T+Z1) bilayer devices employing Y123 dye and [Cu(dmp)₂]^{2+/+} electrolyte.

The influence of TiO₂ layer thickness on the mass transport of electrolyte species in the bilayer DSCs could be further verified using J_{SC} versus intensity plots and current transient curves. The J_{SC} versus intensity plot deviates more from linearity as the TiO₂ layer thickness increases (as shown in **Figure 5.4(a)**), indicating the dominance of diffusion limitation at higher thickness. This is further affirmed by the current transient curves

obtained at an incident intensity of 100 mW/cm^2 (**Figure 5.4(b)**), from which the reduction in output current of the devices due to mass transport limitation is seen to be increasing with the increase in TiO_2 layer thickness. However, the mass transport problem was observed to be minimized at lower light intensities. This was reflected in the J_{SC} of the DSCs under lower intensities (**Figure 5.4(c)**). At 50 mW/cm^2 light intensity, the optimum J_{SC} was obtained for the TiO_2 thickness of $9 \mu\text{m}$ with better dye loading, owing to the decreased mass transport problem. While at 10 mW/cm^2 , the J_{SC} was almost similar for all the devices despite the variation in dye loading. The variation in V_{OC} for T+Z1 devices with change in TiO_2 layer thickness is given in **Figure 5.4(d)**. At all intensities, the V_{OC} of the devices seem to decrease with increase in layer thickness. This might be attributed to the observation that with the increased layer thickness there was an increase in leakage current (observed from $J-V$ under darkness, (**Figure 5.4(e)**), pertaining to the increase in $\text{TiO}_2/\text{electrolyte}$ interface available for electron back transfer processes. Ultimately, the T+Z1 device with $6 \mu\text{m}$ thick TiO_2 layer exhibited the highest PCE under higher intensity (100 mW/cm^2), while that with with $9 \mu\text{m}$ thick TiO_2 layer showcased the maximum PCE under low intensity (10 mW/cm^2) (**Figure 5.4(f)**).

The interfacial charge transfer kinetics in T+Z1 devices with various TiO_2 layer thicknesses were investigated using EIS, TVD and TCD analysis. The representative Nyquist diagram obtained using EIS measurement at an applied bias of 1.0 V is shown in **Figure 5.5(a)** and the equivalent circuit used for fitting them is provided in **Figure 5.5(b)**. The resistance element R_{series} represents the series resistance of the device. R_{ct} and C_{μ} respectively specify the charge transfer resistance and chemical capacitance due to charge accumulation at the $\text{TiO}_2/\text{dye}/\text{electrolyte}$ interface. Whereas, R_{CE} and C_{CE} denote the chemical capacitance and capacitance due to charge accumulation at the counter electrode/electrolyte interface. Z_{d-bulk} corresponds to the Warburg diffusion of the redox species in the bulk of the electrolyte, while R_{d-WE} correspond to that within the mesoporous semiconductor matrix of the working electrode. The R_{ct} obtained by fitting the Nyquist plot was plotted against the V_{OC} , as shown in **Figure 5.5(c)**. As inferred before, with increase in layer thickness, there was a decrease in R_{ct} , resulting in higher electron recombination kinetics at the $\text{TiO}_2/\text{electrolyte}$ interface. Moreover, the C_{μ} versus V_{OC} plot obtained from EIS analysis displays a positive shift in conduction band (CB) of the semiconductor layer with increase in TiO_2 layer thickness (**Figure 5.5(d)**). This positive shift in CB with higher

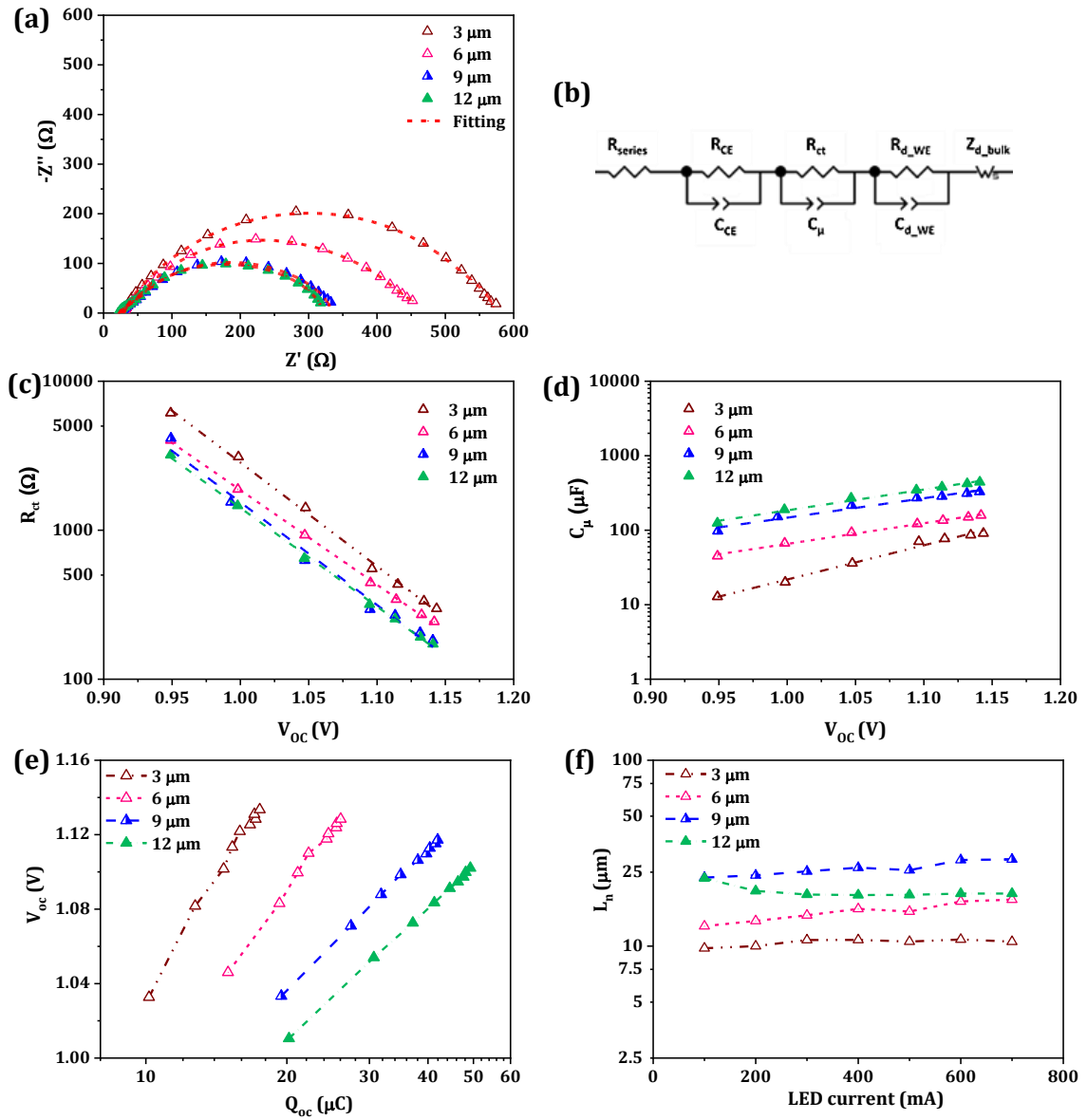


Figure 5.5. (a) Representative Nyquist plots obtained from EIS measurement under dark, at a bias potential of 1.0 V and corresponding fitted curves (red dotted line), and (b) Modified Randle's circuit used for them; (c) Charge transfer resistance (R_{ct}), and (d) chemical capacitance (C_{μ}) obtained by fitting the Nyquist plots as a function of V_{OC} ; (e) Charge extraction (CE) plot, and (f) Diffusion length (L_n) obtained from TVD and TCD measurements obtained using Toolbox setup.

TiO₂ thickness was confirmed using the charge extraction (CE) plots as well (Figure 5.5(e)). This downward shift, as described in the previous chapter (Chapter 4), causes an increased overlap between CB states or sub- bandgap states of the semiconductor with the oxidized states of the redox mediator, leading to more electron recombination rates. The electron diffusion time (τ_d) and lifetime (τ_n), obtained from TCD and TVD measurements,

respectively, were used to estimate the diffusion length (L_n) of electrons within the semiconducting layer of the DSCs, using the equation,

$$L_n = d \times \sqrt{(\tau_n/\tau_d)} \quad (5.1)$$

where d is the layer thickness of the bilayer photoanode. The obtained L_n was plotted against the LED current (which is proportional to the light intensity emanating from the LED source used for TVD and TCD measurements) as shown in **Figure 5.5(f)**. It is observed that at all incident intensities, the T+Z1 device with 9 μm thick TiO_2 layer exhibited the highest L_n of $\sim 25 \mu\text{m}$, followed by the device with 12 μm thick TiO_2 layer ($\sim 20 \mu\text{m}$), with 6 μm thick TiO_2 layer ($\sim 15 \mu\text{m}$) and finally the one with 3 μm thick TiO_2 layer ($\sim 10 \mu\text{m}$). L_n seemed to increase with increase in TiO_2 thickness from 3 μm to 9 μm , and afterwards it decreased for the device with 12 μm thick TiO_2 layer. The initial increase in L_n with increase in TiO_2 thickness might be ascribed to the greater number of photogenerated electrons created in the thicker semiconducting layer. However, further increase in thickness paved way for increasing the rate of the competing electron recombination process, which might have resulted in lowering the L_n for the device with thicker TiO_2 layer. The higher L_n for T+Z device with 9 μm thick TiO_2 layer might also have helped it in achieving better J_{SC} and hence better PCE under low intensity illumination conditions. The J - V characteristic curves for the T+Z1 devices with various TiO_2 layer thicknesses (3 to 12 μm) sensitized with Y123 dye and using $[\text{Cu}(\text{dmp})_2]^{2+/+}$ based electrolyte, measured under 1000 lux CFL illumination are shown in **Figure 5.6** and the corresponding parameters are given in **Table 5.2**. As expected, the device with 9 μm thick

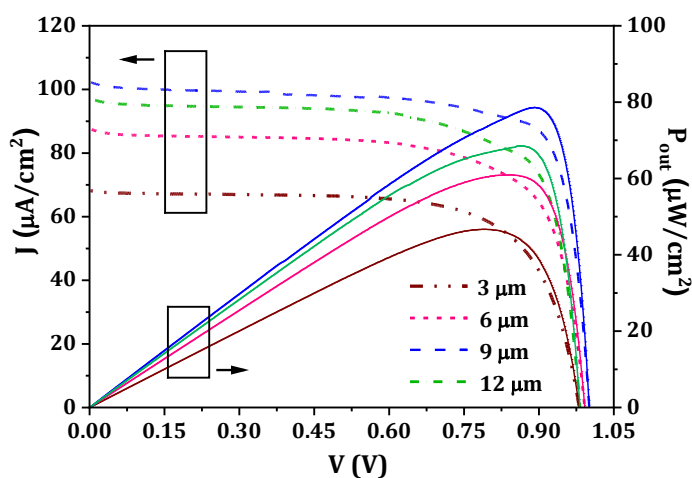


Figure 5.6. J - V characteristics under of TiO_2/ZnO (T+Z1) bilayer device employing Y123 dye and $[\text{Cu}(\text{dmp})_2]^{2+/+}$ electrolyte, with different TiO_2 layer thickness under 1000 lux CFL illumination.

Table 5.2. Photovoltaic parameters of DSCs employing TiO₂/ZnO bilayer (T+Z1) photoanodes having different TiO₂ layer thicknesses (*d*), sensitized using Y123 dye along with [Cu(dmp)₂]^{2+/+} redox electrolyte, under 1000 lux CFL illumination.

TiO ₂ layer thickness ^a (μm)	V _{oc} ^b (V)	J _{sc} ^b (μW/cm ²)	FF ^b	PCE ^b (%)	P _{max} ^b (μW/cm ²)
3	0.98 (0.97 ± 0.01)	68.2 (64.1 ± 5.3)	0.70 (0.69 ± 0.02)	16.5 (15.1 ± 1.8)	46.8 (42.7 ± 5.1)
6	0.99 (0.98 ± 0.01)	87.7 (86.5 ± 1.1)	0.70 (0.68 ± 0.02)	21.5 (20.5 ± 1.0)	60.8 (57.9 ± 2.5)
9	1.00 (0.99 ± 0.01)	102.4 (98.0 ± 3.9)	0.77 (0.76 ± 0.01)	27.9 (26.1 ± 1.8)	78.8 (74.0 ± 4.3)
12	0.98 (0.97 ± 0.01)	97.2 (95.1 ± 1.8)	0.72 (0.71 ± 0.01)	24.2 (23.1 ± 1.0)	68.6 (65.4 ± 2.8)

^aAverage TiO₂ layer thickness obtained from profilometer measurement.

^bJ-V parameters of champion cells with averages taken over three sets of samples ± mean deviation (in parentheses).

TiO₂ layer delivered the highest PCE of 27.9%, with a V_{OC} of 1.0 V, J_{SC} of 102.4 μA/cm², FF of 0.77, and maximum output power density (P_{max}) of 78.8 μW/cm² under 1000 lux CFL illumination.

Further, the performance of the device with 9 μm thick TiO₂ layer under various illumination conditions was evaluated by co-sensitizing the bilayer device using MS5: XY1b (1:2) dye combination. Under simulated AM 1.5G (100 mW/cm²) irradiation, the co-sensitized device using [Cu(dmp)₂]^{2+/+} based electrolyte could achieve a PCE of 8.3%, with a V_{OC} of 1.13 V, J_{SC} of 10.8 mA/cm², and FF of 0.68 (**Figure 5.7(a) and Table 5.3**). The corresponding IPCE spectrum is provided in **Figure 5.7(b)** and the J_{integrated} obtained from it is 10.9 mA/cm². Under 1000 lux CFL irradiation, the co-sensitized device delivered a PCE of 34.5%, with a V_{OC} of 1.00 V, J_{SC} of 114.8 μA/cm², FF of 0.85, and P_{max} of 97.6 μW/cm² (**Figure 5.7(c) and Table 5.4**). Hence, the co-sensitization strategy could effectively improve the J_{SC} of the T+Z1 bilayer DSC without compromising its V_{OC}, both under outdoor as well as indoor lighting conditions. The performance of the device under higher CFL intensities, such as 2000 lux, 4000 lux and 6000 lux, were also studied. With increase in CFL intensity, the V_{OC} as well as J_{SC} of the device got enhanced, resulting in an enhanced PCE. Hence, under 6000 lux CFL illumination, the co-sensitized device delivered a maximum PCE of 39.5%, (with 1.07 V V_{OC}, 762.5 μA/cm² J_{SC}, 0.82 FF, and 669.0 μW/cm² P_{max}), while under 4000 lux it exhibited 38.8% PCE (with 1.05 V V_{OC}, 510.1 μA/cm² J_{SC}, 0.82 FF, and 439.2 μW/cm² P_{max}) and under 2000 lux, it gave 37.3% PCE

(with 1.02 V V_{oc} , 246.7 $\mu\text{A}/\text{cm}^2$ J_{sc} , 0.84 FF , and 211.4 $\mu\text{W}/\text{cm}^2$ P_{max}) (Figure 5.7(c) and Table 5.4).

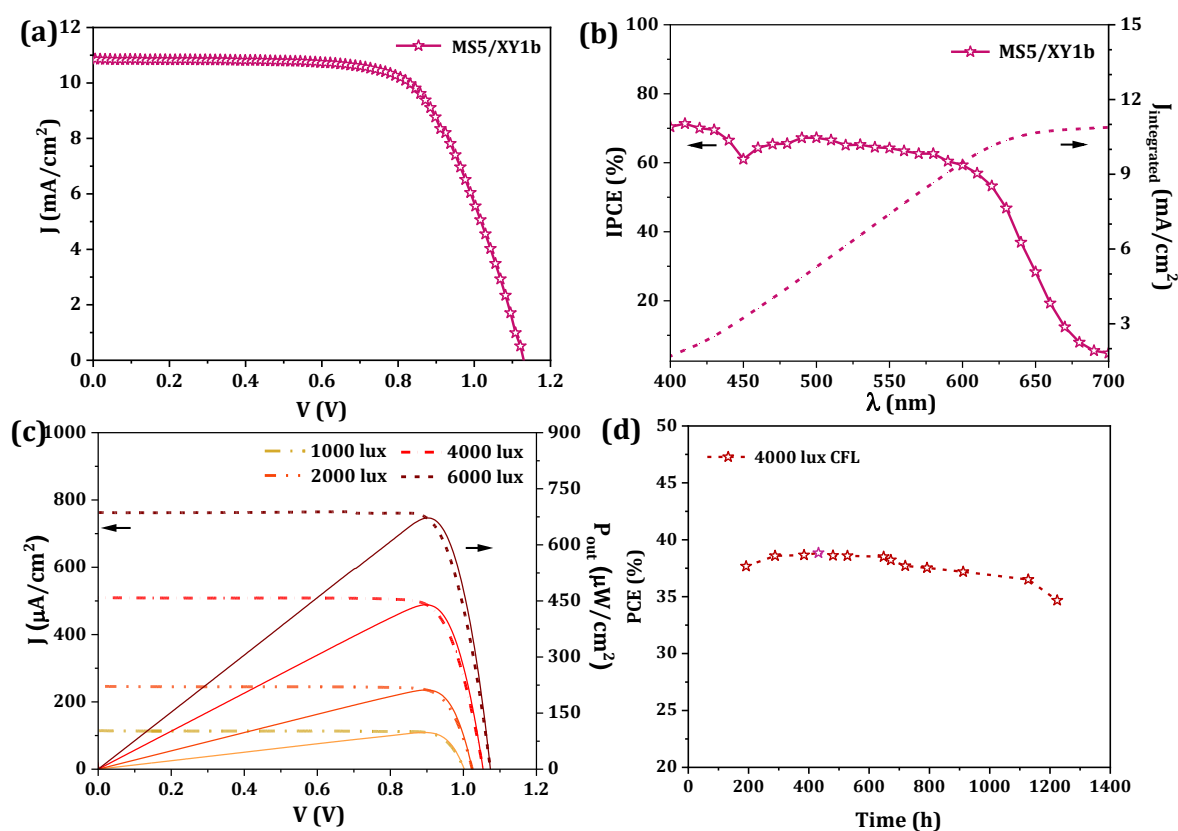


Figure 5.7. (a) J - V characteristics under one sun condition and (b) corresponding $IPCE$ spectrum; (c) J - V characteristics under various CFL illumination intensities, and (d) stability curve under 4000 lux CFL irradiation, obtained for T+Z1 bilayer device employing XY1b:MS5 dye and $[\text{Cu}(\text{dmp})_2]^{2+/+}$ electrolyte, with 9 μm thick TiO_2 layer.

Table 5.3. Photovoltaic parameters of DSCs employing T+Z1 bilayer photoanodes with 9 μm thick TiO_2 layer, co-sensitized with XY1b:MS5 dye system in conjugation with $[\text{Cu}(\text{dmp})_2]^{2+/+}$ redox electrolyte, under AM 1.5G solar irradiation.

P_{in}^a (mW/cm^2)	V_{oc}^b (V)	J_{sc}^b (mA/cm^2)	FF^b	PCE^b (%)	$J_{integrated}^c$ (mA/cm^2)
100	1.13 (1.13 ± 0.01)	10.80 (10.76 ± 0.56)	0.68 (0.65 ± 0.03)	8.30 (7.88 ± 0.52)	10.88

^a Intensity of the incident light from the solar simulator.

^b J - V parameters of champion cells with averages taken over three sets of samples ± mean deviation (in parentheses).

^c Theoretical J_{sc} obtained by integrating the $IPCE$ spectra.

The stability of the co-sensitized device was tested under 4000 lux CFL irradiation and the corresponding stability curve is shown in **Figure 5.7(d)**. Even after 1000 hours, the device could retain a *PCE* of 36.5%, which is ~ 94% of the maximum *PCE* obtained under 4000 lux CFL. The co-sensitized bilayer T+Z1 device could power a temperature sensor/digital clock under outdoor as well as indoor lighting (even under lower intensity of 500 lux CFL), as shown in **Figure 5.8**, giving rise to a battery-free self-powered electronic device. However, a major drawback of this system was that, whenever the light was turned off the digital clock also stopped working and when the light was on, the clock reset to 12:00 disrupting the proper working of the clock. A feasible solution for such a situation is to incorporate a storage device to the system. In this work, we integrated the DSC device with an activated carbon based EDLC device for realizing efficient photocapacitor (PC) for outdoor as well as indoor light energy harvesting and storing application.

Table 5.4. Photovoltaic parameters of DSCs employing TiO₂/ZnO bilayer (T+Z1) photoanodes with 9 μm thick TiO₂ layer, co-sensitized with XY1b:MS5 dye system in conjugation with [Cu(dmp)₂]^{2+/+} redox electrolyte, under different CFL illumination intensities.

Illuminance	P_{in}^a (μW/cm ²)	V_{oc}^b (V)	J_{sc}^b (μW/cm ²)	FF^b	PCE^b (%)	P_{max}^b (μW/cm ²)
1000 lux	283	1.00 (0.99 ± 0.01)	114.8 (117.6 ± 2.6)	0.85 (0.81 ± 0.04)	34.5 (33.3 ± 1.6)	97.6 (94.3 ± 4.6)
2000 lux	566	1.02 (1.02 ± 0.01)	246.7 (244.8 ± 1.7)	0.84 (0.81 ± 0.03)	37.3 (36.1 ± 1.2)	211.4 (204.1 ± 6.9)
4000 lux	1132	1.05 (1.05 ± 0.01)	510.1 (517.9 ± 8.9)	0.82 (0.80 ± 0.02)	38.8 (38.2 ± 1.0)	439.2 (433.1 ± 9.2)
6000 lux	1698	1.07 (1.07 ± 0.01)	762.5 (772.3 ± 9.5)	0.82 (0.80 ± 0.01)	39.5 (39.0 ± 0.5)	669.0 (661.7 ± 7.9)

^a Intensity of the incident CFL light.

^b *J-V* parameters of champion cells with averages taken over three sets of samples ± mean deviation (in parentheses).

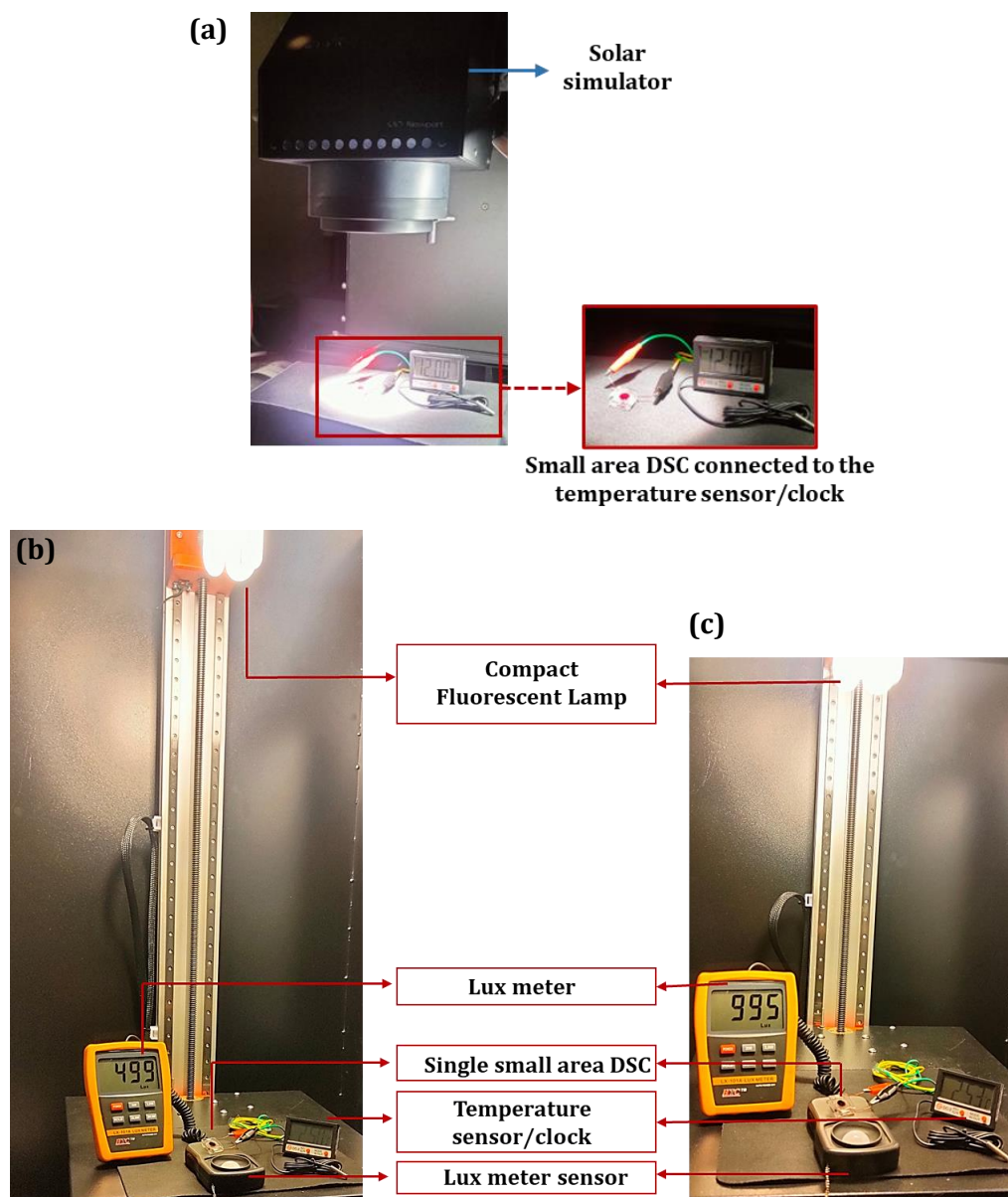


Figure 5.8. Powering a temperature sensor/digital clock (ACETEQ DC-2) using a small area DSC (T+Z1) employing XY1b:MS5 dye and $[\text{Cu}(\text{dmp})_2]^{2+/+}$ electrolyte, under (a) outdoor condition (AM 1.5G irradiation), and indoor conditions (b) 499 lux CFL, and (c) 995 lux CFL illumination.

5.3.2. Characterization of the EDLC

The electrochemical behaviour of the storage part of the integrated PC device was evaluated using EIS, CV, and GCD measurements. The Nyquist plot of the EDLC obtained from EIS is shown in **Figure 5.9(a)**. A large solution resistance of $\sim 47 \Omega$ and a semicircle corresponding to the FTO/carbon interface was observed for the EDLC. The higher series resistance could be attributed to the large sheet resistance of the FTO coated current

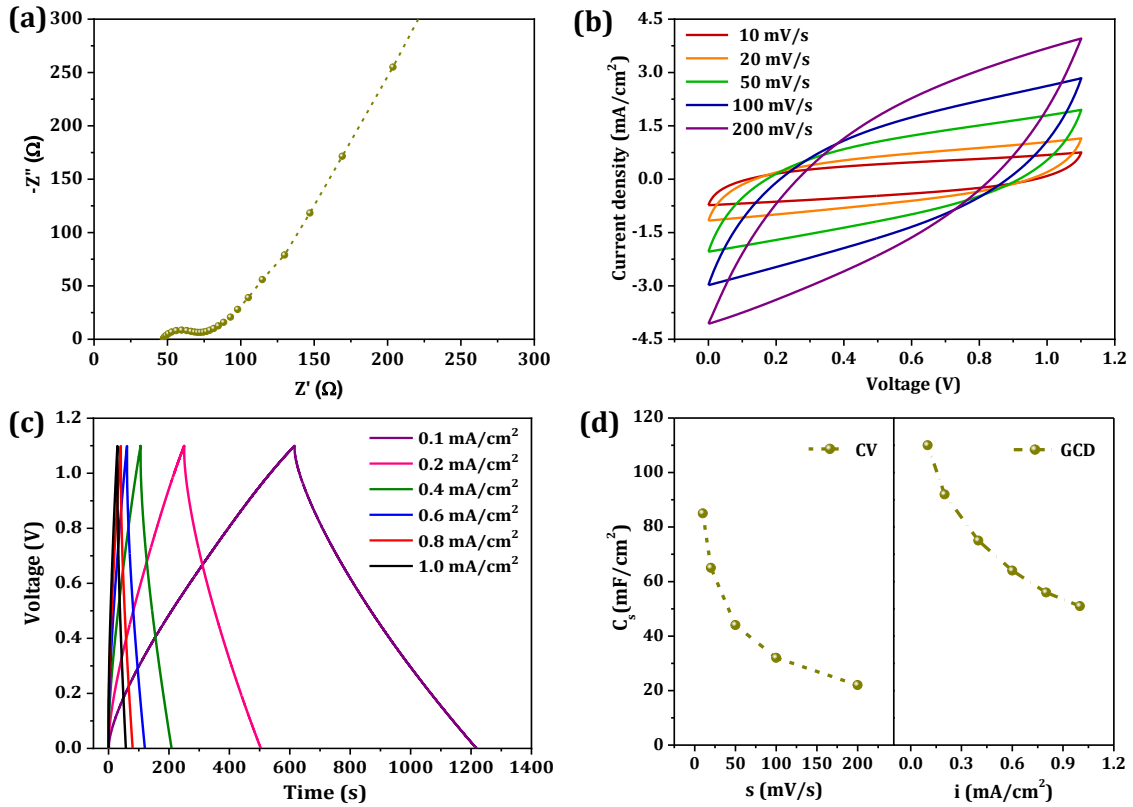


Figure 5.9. (a) Impedance plot obtained from EIS, (b) CV plots obtained at different scan rates, (c) GCD curves obtained at different current densities, and (d) specific capacitance (C_s , estimated from CV and GCD plots) of EDLC device employing activated carbon based working electrodes and an organic electrolyte.

collector and the bulk resistance of the organic electrolyte.^[52] The CV curves obtained at different scan rates (10 - 200 mV/s) in a fixed operating voltage of 1.1 V are shown in **Figure 5.9(b)**. The CV curves were deformed from the ideal rectangular shape expected for ideal EDLCs owing to the high series resistance. The deformation increased with increase in the scan rate (s). Similarly, the GCD curves also showed a deviation from the ideal triangular behaviour. The GCD curves were obtained up to a maximum voltage of 1.1 V at various applied constant current densities (i) ranging from 0.1 - 1.0 mA/cm², as shown in **Figure 5.9(c)**. A maximum voltage of 1.1 V for EDLC was chosen corresponding to the maximum achievable voltage, i.e. V_{OC} , of the DSC (1.13 V) under AM 1.5G solar light. The specific capacitance (C_s) of the EDLC section was estimated from the CV curves using the equation,

$$C_s = \frac{\int I dV}{s \times \Delta V \times A} \quad (5.2)$$

where $\int I dV$ is the area enclosed by the CV curve, s is the scan rate in V/s, ΔV is the voltage window in V and A is the active area of the working electrode (1 cm^2). The obtained C_s from CV data are plotted against the scan rate as shown in **Figure 5.9(d)**. At the scan rate of 10 mV/s the EDLC exhibited C_s of 85 mF/cm², while it reduced to 22 mF/cm² at the higher scan rate of 200 mV/s. The C_s was also estimated using the GCD curves using the equation,

$$C_s = \frac{2 \times i}{A \times (dV/dt)} \quad (5.3)$$

where i is the galvanostatic discharge current (in mA) and dV/dt is the slope of the linear region of the discharge curve (in V/s). From the GCD measurement at a discharge current density of 0.1 mA/cm², the C_s of EDLC was estimated to be 110 mF/cm², while at 1 mA/cm² it was 51 mF/cm².

5.3.3. Photocapacitor characterization and application

The light harvesting and storage capacity of the integrated PC device was assessed using photocharge/discharge measurements under various lighting conditions, such as outdoor and indoor light irradiations. The photocharge/discharge profile of the PC is obtained by plotting the photocharged voltage (V_{PC}) across the PC against the photocharging time (t_{PC}). The maximum achievable V_{PC} of the PC and the corresponding t_{PC} under a particular irradiation condition may be denoted as V_m and t_m , respectively. Under simulated AM 1.5G sunlight, the PC was charged up to a V_m of 1.1 V in ~ 3 minutes (t_m), as shown in **Figure 5.10(a)**. The observed variation in the slope of the photocharging curve suggest that the DSC charged the EDLC with a non-constant current determined by the J - V response of the DSC. At V_{PC} closer to the V_{OC} of the DSC, the photocharging current (i_{PC}) might be too small, which result in a plateau in the photocharging curve. The photocharge/discharge profiles of the PC under various CFL illumination intensities (2000 lux, 4000 lux, and 6000 lux) are shown in **Figure 5.10(b)**. Under 6000 lux CFL illumination, the PC could only charge up to a V_m of 1.01 V in ~ 18 minutes, after which the photocharging curve formed a plateau. Similarly, under 4000 lux CFL, it took ~ 28 minutes for the PC to achieve a V_m of 0.98 V, after which it got saturated. Under 2000 lux CFL, the V_{PC} could reach only up to a maximum of 0.95 V in ~ 40 minutes. The V_m of the PC was seen to be decreasing with decrease in intensity of the incident radiation, since the V_{OC} of the DSC is reduced at lower light intensities. Also, the photocharging time, t_m , required for achieving the corresponding V_m were observed to be higher at lower light

intensities. This could in turn be attributed to the lower current output (I_{SC}) of DSC under low intensity conditions. Also, during the photocharging process of the PC, the i_{PC} is

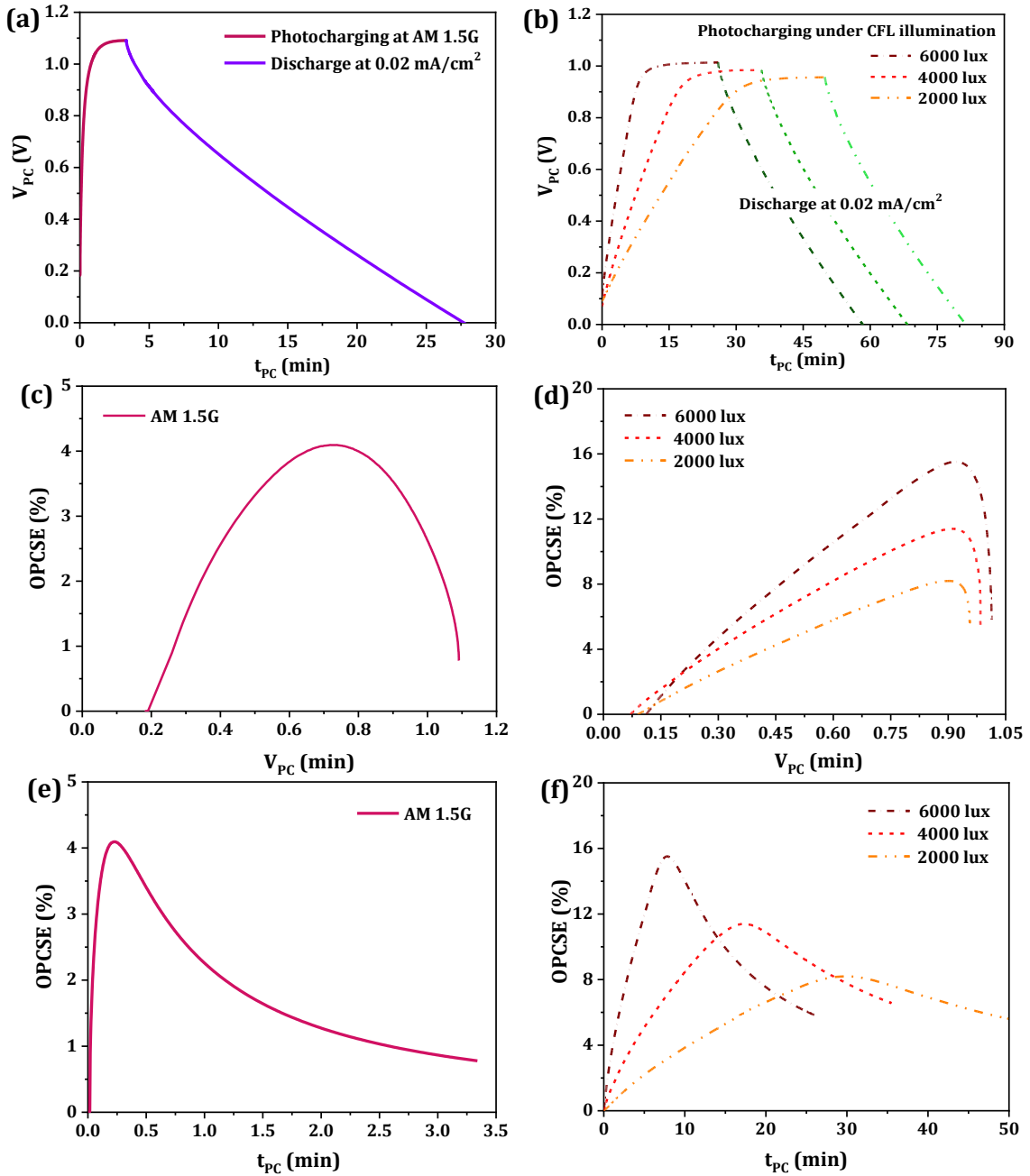


Figure 5.10. Photocharge/discharge curves of the integrated PC device under (a) AM 1.5G simulated sunlight (100 mW/cm²), and (b) different CFL illumination intensities (2000 lux, 4000 lux and 6000 lux); OPCSE of the PC device as a function of photocharged voltage (V_{PC}) obtained under (c) AM 1.5G simulated sunlight, and (d) CFL illumination; OPCSE as a function of photocharging time (t_{PC}) obtained under (e) AM 1.5G simulated sunlight, and (f) CFL illumination.

observed to be reducing with the increase in V_{PC} . At higher V_{PC} , the i_{PC} becomes as low as the self-discharging current of the EDLC, so that the V_m of PC get saturated at a value lower than the V_{OC} of the DSC and a plateau is formed in the photocharging profiles. Under all illumination conditions, the discharge curves of the EDLC section were recorded at a current rate of 0.02 mA/cm^2 , and it was observed that the PC took about 30 min to discharge completely.

The overall performance of the integrated PC was quantified by estimating the *OPCSE* of the device from the photo-charging curve using equation,

$$OPCSE = \frac{1/2 \times C \times (V - V_i)^2}{P_{in} \times t \times S} \quad (5.4)$$

where P_{in} is the power density of incident radiation (mW/cm^2), t is the photocharging time (in s), S is the DSC active area (0.24 cm^2), V is the voltage across the EDLC at time t , V_i is the initial voltage across the EDLC. The *OPCSE* of integrated PC device can further be expressed as,

$$OPCSE = PCE \times SE \quad (5.5)$$

where *PCE* is the power conversion efficiency of the DSC part and *SE* is the storage efficiency of the EDLC part. The *OPCSE* of the PC illuminated by various lighting conditions were plotted against the photocharging time (t_{pc}) and the photocharged voltage of the device, as shown in **Figure 5.10(c-f)**. Under AM 1.5G irradiation, the *OPCSE* of the PC was observed to initially increase with the photocharge voltage and then it started decreasing after an optimum voltage. The maximum *OPCSE* of 4.09% was achieved at an optimum photocharge voltage (V_{OPCSE}) of 0.74 V, which is $\sim 67\%$ of the corresponding V_m . Correspondingly, this maximum *OPCSE* was achieved at an optimum t_{pc} of 0.2 min (t_{OPCSE}). The *OPCSE* of the PC device was further enhanced under indoor (CFL) illuminations. In this case, the *OPCSE* first increased with the V_{PC} , up to an optimum V_{OPCSE} listed in **Table 5.5**, and then started decreasing. The highest maximum *OPCSE* of 15.5% was achieved by the PC under 6000 lux CFL illumination, at a V_{OPCSE} of 0.93 V, which is $\sim 92\%$ of the corresponding V_m , with t_{OPCSE} of 7.7 min. Whereas, under CFL irradiation of 4000 lux, the maximum *OPCSE* of 11.4% was realized at 0.92 V ($t_{OPCSE} = 17.5 \text{ min}$) and under 2000 lux, it was 8.2% at 0.90 V ($t_{OPCSE} = 30.4 \text{ min}$). From the *OPCSE* versus t_{pc} curves, it was observed that under high intensity outdoor illumination, the *OPCSE* rises to maximum within a few seconds, while under indoor condition the maximum *OPCSE* is reached after few minutes. The PC device exhibited better *OPCSE* and higher V_{OPCSE} at

lower intensity light conditions when compared to the standard one sun condition. According to equation (5.5), the better *OPCSE* could be attributed to the better *PCE* of the DSC part under indoor conditions. However, the lower i_{PC} offered by the DSC under low intensity condition result in reduction of V_m of the device and elongates the time (t_m) required for achieving the same. Meanwhile, the higher V_{OPCSE} at indoor light conditions could be ascribed to the better charging of the EDLC part at such low i_{PC} .

Table 5.5. Various parameters of the PC during the photocharging under various illuminations: The maximum photovoltage attained (V_m) and the photo-charging time (t_m) required to attain the same, the maximum *OPCSE* attained along with the voltage (V_{OPCSE}) and photo-charging time (t_{OPCSE}) at which the maximum *OPCSE* is acquired.

illumination condition	V_m (V)	t_m (min)	Maximum <i>OPCSE</i> (%)	V_{OPCSE} (V)	t_{OPCSE} (min)
AM 1.5G sunlight	1.10	3	4.1	0.74	0.2
6000 lux CFL	1.01	18	15.5	0.93	7.7
4000 lux CFL	0.98	28	11.4	0.92	17.5
2000 lux CFL	0.95	40	8.2	0.90	30.4

Finally, we applied this PC device to rectify the drawback described in the previous section 5.3.1. We connected the same temperature sensor/digital clock to the new PC device and observed its operation under AM 1.5G solar irradiation and 4000 lux CFL illumination, as shown in **Figure 5.11**. Under AM 1.5G condition, the digital clock was switched on after few seconds of charging the PC. After a few minutes (~ 3 min), the light was switched off and the PC was connected in discharging mode by removing the connection between the DSC and the EDLC part. It was observed that the clock continued to work for ~ 30 min, even after the light was turned off. A similar behaviour was observed under 4000 lux CFL illumination as well. However, the PC required to be charged for ~ 30 min, so that it could achieve the V_m , before it was connected to the temperature sensor/digital clock. The clock was switched on immediately when the photocharged PC was connected to it. After about 5 minutes, the CFL was switched off and the active area of the DSC was covered with a black mask to rule out the possibility of illumination from the stray light. The clock continued to work for ~ 25 min, even after the light was cut-off. The time for which the PC could power the device was longer in case of outdoor irradiation condition. This was

because the V_m achieved under simulated sunlight was $\sim 12\%$ higher than the one at 4000 lux CFL illumination.

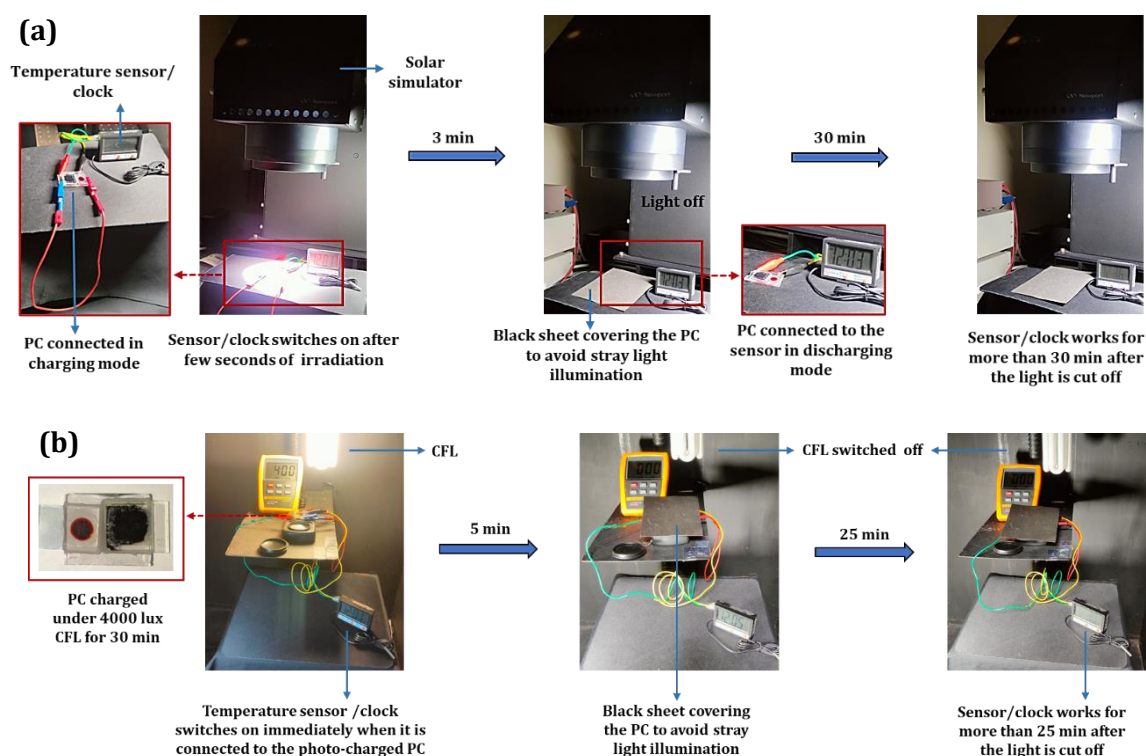


Figure 5.11. Powering the temperature sensor/digital clock (ACETEQ DC-2) using the PC device under (a) AM 1.5G simulated sunlight (100 mW/cm^2), and (b) 4000 lux CFL illumination.

5.4. Conclusions

In the present chapter, TiO_2 layer thickness in TiO_2/ZnO bilayer photoanode (T+Z1) based dye-sensitized photovoltaic cell (DSC) using copper electrolyte ($[\text{Cu}(\text{dmp})_2]^{2+/+}$), was optimized to obtain the best performance with optimum open circuit voltage (V_{OC}), both under one sun (AM 1.5G, 100 mW/cm^2) and indoor (CFL illumination) conditions. Co-sensitization strategy was implemented to further enhance the power conversion efficiency (PCE) of T+Z1 based DSC device, by improving its short circuit current (J_{SC}) without compromising its V_{OC} . The best optimized light harvester (using T+Z1 bilayer photoanode co-sensitized with XY1b:MS5 dye mixture (2:1)) was integrated with a standard activated carbon based electrochemical double layer capacitor (EDLC) to realize a photocapacitor (PC), which could attain a maximum overall photoelectric conversion and storage efficiency ($OPCSE$) of 4.1%, with a maximum storage voltage (V_m) of 1.1 V, under AM 1.5G simulated sunlight. Meanwhile, the PC achieved the highest $OPCSE$ of 15.5%

with a V_m of 1.01 V, under 6000 lux CFL illumination. Finally, the pertinency of this hybrid device in IoT applications was demonstrated by powering a temperature sensor/digital clock using the PC, both under simulated solar irradiation as well as CFL illumination. The PC could power this sensor/clock for more than 20 minutes, even after the light was switched off, hence overcoming the drawback of systems utilizing DSC alone for powering such electronic devices. To the best of our knowledge, this work presents the first report on photocapacitor employing an EDLC integrated with a copper electrolyte based DSC, achieving such a remarkable *OPCSE* under indoor light conditions.

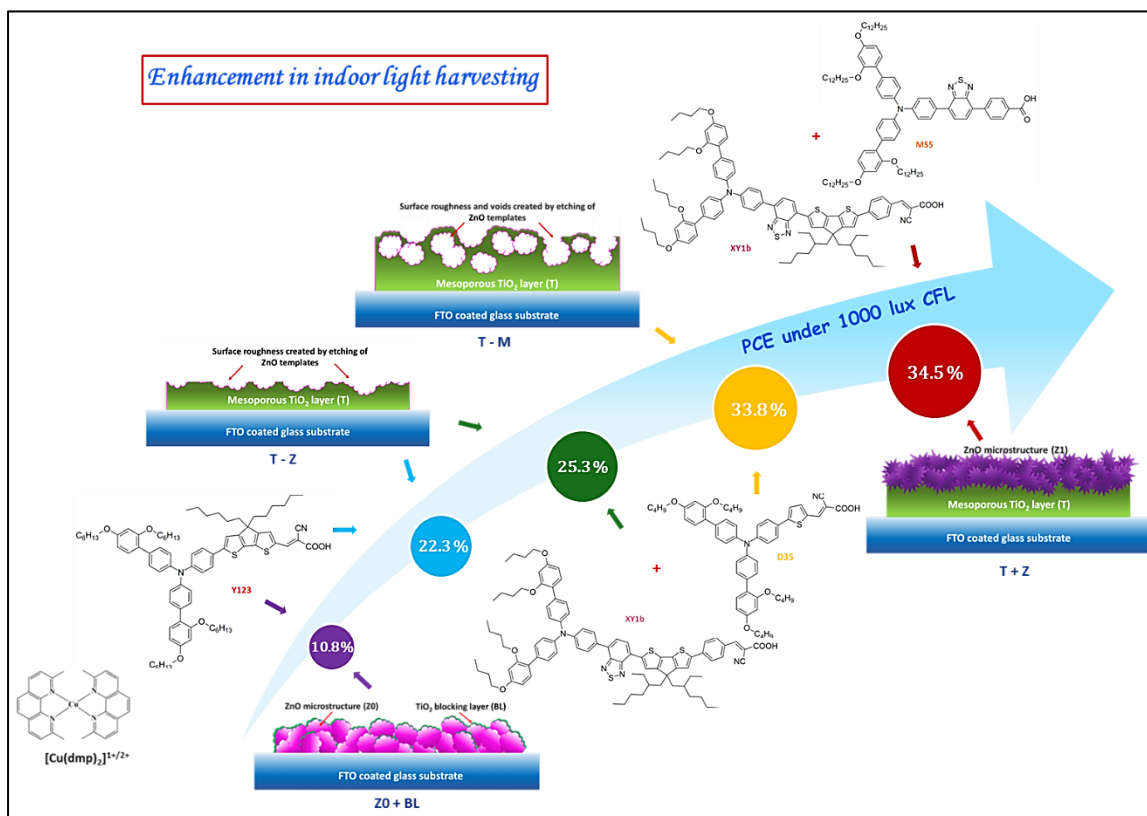
References

- [1] M. Saifullah, J. Gwak, J. H. Yun, *J Mater Chem A* **2016**, *4*, 8512.
- [2] A. K. Shukla, K. Sudhakar, P. Baredar, *Energy Build* **2016**, *128*, 99.
- [3] K. A.V, S. Bashir, S. Ramesh, K. Ramesh, *Ionics (Kiel)* **2022**, *28*, 4065.
- [4] G. Gokul, S. C. Pradhan, S. Soman, *Energy, Environment, and Sustainability* **2019**, 281.
- [5] S. Mishra, S. Ghosh, B. Boro, D. Kumar, S. Porwal, M. Paul, H. Dixit, T. Singh, *Energy Advances* **2022**, *1*, 761.
- [6] H. Michaels, M. Rinderle, R. Freitag, I. Benesperi, T. Edvinsson, R. Socher, A. Gagliardi, M. Freitag, *Chem Sci* **2020**, *11*, 2895.
- [7] D. Devadiga, M. Selvakumar, P. Shetty, M. S. Santosh, *J Electron Mater* **2021**, *50*, 3187.
- [8] A. Aslam, U. Mehmood, M. H. Arshad, A. Ishfaq, J. Zaheer, A. Ul Haq Khan, M. Sufyan, *Solar Energy* **2020**, *207*, 874.
- [9] J. Barichello, P. Mariani, L. Vesce, D. Spadaro, I. Citro, F. Matteocci, A. Bartolotta, A. Di Carlo, G. Calogero, *J Mater Chem C* **2024**, *12*, 2317.
- [10] R. Escalante, R. García-Rodríguez, B. E. Heredia-Cervera, M. A. Aguilar-Frutis, N. Gómez-Ortíz, J. Villanueva-Cab, G. Oskam, *Energy and Environment Focus* **2014**, *2*, 280.
- [11] R. García-Rodríguez, J. Villanueva-Cab, J. A. Anta, G. Oskam, *Materials* **2016**, *9*, 33.
- [12] J. Velore, S. Chandra Pradhan, T. W. Hamann, A. Hagfeldt, K. N. N. Unni, S. Soman, *ACS Appl Energy Mater* **2022**, *5*, 2647.
- [13] S. C. Pradhan, A. Hagfeldt, S. Soman, *J Mater Chem A Mater* **2018**, *6*, 22204.
- [14] A. Scalia, F. Bella, A. Lamberti, S. Bianco, C. Gerbaldi, E. Tresso, C. F. Pirri, *J Power Sources* **2017**, *359*, 311.
- [15] F. Yuan, Q. T. Zhang, S. Jin, H. Zhu, *IEEE Trans Wirel Commun* **2015**, *14*, 698.
- [16] R. Wang, H. Liu, Y. Zhang, K. Sun, W. Bao, R. Wang, H. Liu, Y. Zhang, W. Bao, K. Sun, *Small* **2022**, *18*, 2203014.
- [17] Y. Sun, X. Yan, *Solar RRL* **2017**, *1*, 1700002.

- [18] A. Scalia, F. Bella, A. Lamberti, C. Gerbaldi, E. Tresso, *Energy* **2019**, *166*, 789.
- [19] Y. Wu, C. Li, Z. Tian, J. Sun, *J Power Sources* **2020**, *478*, 228762.
- [20] Q. Zeng, Y. Lai, L. Jiang, F. Liu, X. Hao, L. Wang, M. A. Green, *Adv Energy Mater* **2020**, *10*, 1903930.
- [21] D. Schmidt, M. D. Hager, U. S. Schubert, D. Schmidt, M. D. Hager, U. S. Schubert, *Adv Energy Mater* **2016**, *6*, 1500369.
- [22] T. Chen, L. Qiu, Z. Yang, Z. Cai, J. Ren, H. Li, H. Lin, X. Sun, H. Peng, *Angewandte Chemie* **2012**, *124*, 12143.
- [23] M. Skunik-Nuckowska, K. Grzejszczyk, P. J. Kulesza, L. Yang, N. Vlachopoulos, L. Häggman, E. Johansson, A. Hagfeldt, *J Power Sources* **2013**, *234*, 91.
- [24] C. H. Ng, H. N. Lim, S. Hayase, I. Harrison, A. Pandikumar, N. M. Huang, *J Power Sources* **2015**, *296*, 169.
- [25] W. Raza, F. Ali, N. Raza, Y. Luo, K. H. Kim, J. Yang, S. Kumar, A. Mehmood, E. E. Kwon, *Nano Energy* **2018**, *52*, 441.
- [26] N. Flores-Diaz, F. De Rossi, A. Das, M. Deepa, F. Brunetti, M. Freitag, *Chem Rev* **2023**, *123*, 9327.
- [27] N. R. Chodankar, H. D. Pham, K. Nanjundan, J. F. S. Fernando, K. Jayaramulu, D. Golberg, Y.-K. Han, D. P. Dubal, N. R. Chodankar, Y.-K. Han, H. D. Pham, J. F. S. Fernando, D. Golberg, D. P. Dubal, A. K. Nanjundan, K. Jayaramulu, *Small* **2020**, *16*, 2002806.
- [28] J. W. Long, D. Bélanger, T. Brousse, W. Sugimoto, M. B. Sassin, O. Crosnier, *MRS Bull* **2011**, *36*, 513.
- [29] G. Wang, L. Zhang, J. Zhang, *Chem Soc Rev* **2012**, *41*, 797.
- [30] J. Castro-Gutiérrez, A. Celzard, V. Fierro, *Front Mater* **2020**, *7*, 560362.
- [31] T. Li, R. Ma, J. Lin, Y. Hu, P. Zhang, S. Sun, L. Fang, *Int J Energy Res* **2020**, *44*, 2426.
- [32] Z. Song, J. Wu, Y. Tu, L. Sun, T. Zhu, G. Li, X. Wang, Y. Du, C. Deng, Q. Chen, W. Sun, M. Huang, L. Fan, Y. Huang, Y. Wei, Y. Xie, Y. Lin, H. Chen, J. Lin, L. Zhan, P. Gao, M. K. Nazeeruddin, W. Huang, *Energy Environ Sci* **2022**, *15*, 4247.
- [33] Z. Song, J. Wu, L. Sun, T. Zhu, C. Deng, X. Wang, G. Li, Y. Du, Q. Chen, W. Sun, L. Fan, H. Chen, J. Lin, Z. Lan, *Nano Energy* **2022**, *100*, 107501.
- [34] A. P. Cohn, W. R. Erwin, K. Share, L. Oakes, A. S. Westover, R. E. Carter, R. Bardhan, C. L. Pint, *Nano Lett* **2015**, *15*, 2727.
- [35] C. T. Chien, P. Hiralal, D. Y. Wang, I. S. Huang, C. C. Chen, C. W. Chen, G. A. J. Amaratunga, *Small* **2015**, *11*, 2929.
- [36] N. Flores-Diaz, F. De Rossi, A. Das, M. Deepa, F. Brunetti, M. Freitag, *Chem Rev* **2023**, *123*, 9327.
- [37] T. N. Murakami, N. Kawashima, T. Miyasaka, *Chemical Communications* **2005**, 3346.
- [38] R. Liu, Y. Liu, H. Zou, T. Song, B. Sun, *Nano Res* **2017**, *10*, 1545.

- [39] S. Sahoo, S. Ratha, C. S. Rout, S. K. Nayak, *Journal of Materials Science* **2022**, *57*, 4399.
- [40] N. K., C. S. Rout, *J Mater Chem A Mater* **2021**, *9*, 8248.
- [41] Y. Sun, X. Yan, *Solar RRL* **2017**, *1*, 1700002.
- [42] J. Kim, S. M. Lee, Y. H. Hwang, S. Lee, B. Park, J. H. Jang, K. Lee, *J Mater Chem A* **2017**, *5*, 1906.
- [43] T. Berestok, C. Diestel, N. Ortlieb, J. Buettner, J. Matthews, P. S. C. Schulze, J. C. Goldschmidt, S. W. Glunz, A. Fischer, *Solar RRL* **2021**, *5*, 2100662.
- [44] X. Zhang, X. Huang, C. Li, H. Jiang, *Advanced Materials* **2013**, *25*, 4093.
- [45] T. Miyasaka, T. N. Murakami, *Appl Phys Lett* **2004**, *85*, 3932.
- [46] N. Bagheri, A. Aghaei, M. Y. Ghotbi, E. Marzbanrad, N. Vlachopoulos, L. Häggman, M. Wang, G. Boschloo, A. Hagfeldt, M. Skunik-Nuckowska, P. J. Kulesza, *Electrochim Acta* **2014**, *143*, 390.
- [47] T. N. Murakami, N. Kawashima, T. Miyasaka, *Chemical Communications* **2005**, 3346.
- [48] C. Y. Hsu, H. W. Chen, K. M. Lee, C. W. Hu, K. C. Ho, *J Power Sources* **2010**, *195*, 6232.
- [49] Z. Yang, L. Li, Y. Luo, R. He, L. Qiu, H. Lin, H. Peng, *J Mater Chem A Mater* **2012**, *1*, 954.
- [50] M. Skunik-Nuckowska, K. Grzejszczyk, P. J. Kulesza, L. Yang, N. Vlachopoulos, L. Häggman, E. Johansson, A. Hagfeldt, *J Power Sources* **2013**, *234*, 91.
- [51] J. Xu, H. Wu, L. Lu, S. F. Leung, D. Chen, X. Chen, Z. Fan, G. Shen, D. Li, *Adv Funct Mater* **2014**, *24*, 1840.
- [52] A. Scalia, A. Varzi, A. Lamberti, E. Tresso, S. Jeong, T. Jacob, S. Passerini, *Sustain Energy Fuels* **2018**, *2*, 968.
- [53] R. Speranza, P. Zaccagnini, A. Sacco, A. Lamberti, *Solar RRL* **2022**, *6*, 2200245.

Summary & Future Perspectives



In summary, the present thesis encompasses different photoanode designs for dye-sensitized photovoltaic cells (DSCs) to achieve efficient light energy harvesting not only under standard one sun irradiation (AM 1.5G, 100 mW/cm²) but also under indoor light illuminations (CFL with incident intensity less than 1 mW/cm²). The photovoltaic parameters of the best performing DSCs presented in each of the working chapters are listed in Table 6.1. In chapter 2A, we synthesized a ZnO microstructure (designated as Z0), which could effectively be utilized as the photoanode material in DSCs employing copper electrolyte ([Cu(dmp)₂]^{2+/+}) along with an organic sensitizer (Y123). By introducing a TiO₂ blocking layer over the Z0 based photoanode (the resulting photoanode was labelled as Z0+BL), we could realize a power conversion efficiency (PCE) of 3.7 % under one sun condition and 10.8 % under 1000 lux CFL illumination (~ 0.3 mW/cm²). In the succeeding work, chapter 2B, we adopted a novel strategy for designing surface textured TiO₂ photoanodes by utilizing the ZnO microstructures (Z0) as a sacrificial over layer. This was accomplished by depositing a layer of ZnO microstructures over the TiO₂ active layer and

Table 6.1. Photovoltaic parameters (obtained under one sun condition and 1000 lux CFL illumination) of the best performing DSCs fabricated in the present thesis work.

Working chapter	Photoanode design	Sensitizer	PCE (%) under AM 1.5G irradiation			PCE (%) under 1000 lux CFL illumination		
			V_{oc} (V)	J_{sc} (mA/cm ²)	PCE (%)	V_{oc} (V)	J_{sc} (μA/cm ²)	PCE (%)
2A	Z0+BL	Y123	0.82	8.85	3.74	0.60	73.6	10.8
2B	T-Z0	Y123	1.04	12.27	8.04	0.82	105.7	22.3
3	T-Z0	XY1b/D35	1.01	13.95	9.45	0.86	123.3	25.3
	T-M20		1.00	15.16	10.12	0.85	141.1	33.8
4	T+Z1	Y123	1.12	10.29	8.16	0.99	87.4	21.3
		MS5	1.27	6.75	6.23	1.02	37.1	31.3
5	T+Z1	XY1b/MS5	1.13	10.80	8.30	1.00	114.8	34.5

then treating the resulting bilayer electrode with 40 mM aqueous solution of $TiCl_4$ to etch off the ZnO particles, leaving behind grooves or imprints on the surface of the TiO_2 active layer. The surface texturing of TiO_2 layer resulted in increased surface roughness which led to improved light scattering and hence enhanced light harvesting efficiency in the corresponding dye-sensitized photoanodes. Also, this surface textured TiO_2 photoanode (T-Z0) could minimize the mass transport limitations showcased by conventional bilayer photoanode based DSCs using copper electrolyte. As a result, the DSCs utilizing T-Z0 photoanodes, sensitized with Y123 dye along with $[Cu(dmp)_2]^{2+/+}$ based redox shuttle could achieve better short circuit current density (J_{sc}) and hence better PCE (8.0 % under one sun condition and 22.3 % under 1000 lux CFL illumination). In chapter 3, the performance of this T-Z0 based DSCs were further improved by adopting co-sensitization strategy using a 1:1 mixture of D35:XY1b dyes, and a PCE of 9.5 % under one sun condition and 25.3 % under 1000 lux CFL irradiation was achieved. Chapter 3 also presents another novel photoanode architecture which employs ZnO templated scattering layer containing light scattering voids for achieving improved light harvesting. The light scattering voids were incorporated in the TiO_2 photoanodes by coating a mixture of TiO_2 paste and the Z0 microstructure over the conventional TiO_2 active layer, followed by $TiCl_4$ treatment, which etches off the ZnO particles leaving behind voids in the TiO_2 over layer.

The resulting photoanode (T-M20), using an optimum weight percentage of ZnO template particles (20 wt%), was sensitized using D35:XY1b (1:1) dyes and utilized in $[\text{Cu}(\text{dmp})_2]^{2+/+}$ electrolyte based DSC to achieve an appreciable PCE of 10.1 % under AM 1.5G irradiation and 33.8 % under 1000 lux CFL illumination. The enhanced performance of T-M20 based DSC could be attributed to its better light harvesting efficiency (*LHE*) which led to enhance J_{SC} , owing to the improved light scattering and dye loading in the respective photoanode.

Chapter 4 and chapter 5 entails a novel TiO_2/ZnO bilayer photoanode architecture which could render higher open circuit voltage (V_{OC}) for small area DSCs, under outdoor as well as indoor light conditions. In chapter 4, three different ZnO microstructures, namely mimosa flower-like (Z1), dandelion flower-like (Z2) and rose flower-like (Z3) microstructures were synthesized and utilized as an additional layer over the conventional TiO_2 active layer to obtain the bilayer photoanodes, labelled as T+Z1, T+Z2 and T+Z3, respectively. Among these, T+Z1 photoanode based DSC, employing Y123 dye and $[\text{Cu}(\text{dmp})_2]^{2+/+}$ electrolyte delivered the best *PCE* of 7.61% with a V_{OC} of 1.13 V. This V_{OC} was ~100 mV higher than that of standard T device (consisting TiO_2 active layer only). The improvement in V_{OC} of bilayer DSCs was attributed to the negative shift in CB edge and lower recombination rate in these devices when compared to the standard device. Further, we achieved a record V_{OC} of 1.27 V under one sun irradiation and 1.025 V under indoor illuminations (1000 lux CFL and LED) by sensitizing the T+Z1 photoanode with MS5 dye. These promising results inspired us to develop a battery-free temperature sensor / digital clock that can be powered autonomously by a single bilayer DSC of ~ 0.24 cm^2 active area, even under indoor illuminations. However, this battery-free sensor/clock device could be operated only under illuminated conditions. Under darkness or very low intensity conditions, the DSC could not power the device, which affected its continuous operation. In order to resolve such problems, in chapter 5, we proposed the development of a photocapacitor (PC) by integrating the DSC with an activated charcoal based electrochemical double layer capacitor (EDLC). For this, we utilized $[\text{Cu}(\text{dmp})_2]^{2+/+}$ electrolyte based DSC employing our best optimized TiO_2/ZnO bilayer photoanode architecture (T+Z1) with an optimum TiO_2 layer thickness of ~ 9 μm , co-sensitized with a 2:1 mixture of XY1b:MS5 dyes, which could deliver a PCE of 8.3% under one sun irradiation, 34.5% under 1000 lux CFL and 39.5% under 6000 lux CFL illumination. The corresponding PC showcased a maximum overall photoelectric conversion and storage

efficiency (*OPCSE*) of 4.1%, with a maximum achievable voltage (V_m) of ~ 1.1 V, under one sun irradiation. Under CFL illumination of 2000 lux, 4000 lux and 6000 lux, the PC could exhibit a remarkably high maximum *OPCSE* of 8.2% ($V_m \sim 0.95$ V), 11.4% ($V_m \sim 0.98$ V) and 15.5% ($V_m \sim 1.01$ V), respectively. The PC was able to power the temperature sensor/digital clock device both under outdoor as well as indoor illumination, and continued to power it for more than 20 minutes even after the illumination was cut-off.

The present thesis work encloses some DSC photoanode design strategies for efficient indoor light harvesting, which can be effectively implemented in internet of things (IoT) technologies for developing self-powered sensors, actuators, and more. Furthermore, reducing the device's footprint without compromising the output voltage opens up possibilities for integrating DSCs as a replacement for primary batteries contributing towards carbon neutrality and sustainability. For achieving long term stability, various copper electrolyte based DSCs discussed in this thesis work can be further optimized to develop solid state devices. Further, fabrication of these DSCs on flexible substrates can open up opportunities for integrating them with wearable and portable electronic devices like smartwatches and headsets. The semi-transparent nature of ZnO-templated photoanodes, combined with transparent electrolytes like cobalt-based ones, enables the development of bifacial dye-sensitized modules (DSMs) for building-integrated photovoltaics (BIPV) applications. The ZnO templated TiO₂ photoanodes and TiO₂/ZnO bilayer photoanodes can also be used for fabricating large area DSCs and DSMs, that can deliver higher output power for operating various high power consuming devices.

ABSTRACT

Name of the Student: **Ms. Anooja J.**
Faculty of Study: Physical Sciences
AcSIR academic centre/CSIR Lab: CSIR-National
Institute for Interdisciplinary Science
and Technology (CSIR-NIIST)

Registration No.: 10PP17A39032
Year of Submission: 2024

Name of the supervisor: Dr. Suraj Soman
Name of the co-supervisor: Dr. Narayanan Unni K. N.

Title of the thesis: **Photoanode engineering of dye-sensitized photovoltaic cells using zinc oxide microstructures for efficient light harvesting applications**

Chapter 1 provides a brief introduction to dye-sensitized photovoltaic cells (DSCs), their fabrication and characterization techniques, along with various photoanode modification strategies reported so far for improving their performance.

Chapter 2A includes the synthesis method and characterization of a ZnO hierarchical microstructure (designated as Z0) and its application as the photoanode active layer material in DSC utilizing standard organic dye Y123 and two different electrolyte systems (iodide/triiodide $[I/I_3^-]$ and copper dimethyl phenanthroline $[Cu(dmp)_2]^{2+/+}$ based redox mediators). The Z0 based device using I/I_3^- electrolyte system (Z0/I) obtained a power conversion efficiency (PCE) of 1.01%, which was enhanced to 2.02% by employing $[Cu(dmp)_2]^{2+/+}$ (Z0/Cu). The improved PCE of Z0/Cu device was associated with the improvement in both open circuit voltage (V_{OC}) and short circuit current density (J_{SC}). The improvement in V_{OC} could be attributed to the more positive redox potential for the copper electrolyte which eliminates the over potential loss prevailing in iodine electrolyte system. Meanwhile the improvement in J_{SC} emerges from the faster electron transport in the copper electrolyte based devices, which results in better diffusion coefficient (D_n) and charge collection efficiency (η_{CC}). The PCE of Z0/Cu device was further enhanced to 3.7% by the introduction of a TiO_2 blocking layer (BL) over the Z0 microstructures. This could be ascribed to the suppression of back electron transfer by the TiO_2 BL, leading to better electron lifetime and faster electron diffusion.

Chapter 2B depicts the utilization of the aforementioned ZnO microstructure (Z0) as a sacrificial layer for surface texturing the conventional TiO_2 photoanodes for improved light harvesting in DSCs. This was achieved by depositing ZnO layer over the TiO_2 active layer, followed by a $TiCl_4$ treatment which etched off the ZnO particles, leaving grooves/imprints on the TiO_2 surface. It was observed that surface texturing of TiO_2 layer resulted in increased surface roughness which led to improved light scattering in these modified electrodes. The DSCs utilizing the surface textured TiO_2 photoanodes (T-Z0) sensitized with Y123 dye along with $[Cu(dmp)_2]^{2+/+}$ based redox shuttle outperformed the corresponding standard device (Std) employing the conventional bilayer photoanode consisting of TiO_2 active layer and TiO_2 scattering overlayer. The T-Z0 based DSCs exhibited a maximum PCE of 8.04% under one sun condition and 22.3% under 1000 lux CFL illumination.

Chapter 3 introduces a novel photoanode architecture employing ZnO templated scattering layer containing light scattering voids for achieving improved light harvesting, particularly under indoor light illumination. Light scattering voids were incorporated in the TiO_2 photoanodes by coating a mixture of TiO_2 paste and the ZnO (Z0) microstructure over the conventional TiO_2 active layer, followed by $TiCl_4$ treatment. As a result, the ZnO particles are etched off leaving behind voids in the TiO_2 over layer. The resulting photoanode is designated as T-M. The T-Z and T-M photoanodes were co-sensitized with 1:1 mixture of D35:XY1b dyes and utilized in DSC along with $[Cu(dmp)_2]^{2+/+}$ based electrolyte. Under one sun irradiation, T-M device suffer from mass transport limitation owing to its higher layer thickness, which in turn reduces its J_{SC} and PCE. Hence, the T-Z device (PCE ~ 9.5%) performs better than the T-M device (PCE ~ 8.9%). However, under 1000 lux CFL illumination, when the mass transport issues are insignificant, the T-M device (PCE ~ 32.3%) outperforms the T-Z device (PCE ~ 25.3%), which could be attributed to its better light harvesting efficiency (LHE) owing to better light scattering and dye loading. The PCE of T-M device under 1000 lux CFL illumination could be further elevated to 33.8% by using an optimum weight percentage of ZnO template particles (20 wt%) for preparing the scattering layer with voids.

Chapter 4 presents a novel TiO_2/ZnO bilayer photoanode architecture which could render higher V_{OC} for small area DSCs, under outdoor as well as indoor illumination conditions. For this, we synthesized three different ZnO microstructures, namely mimosa flower-like (Z1), dandelion flower-like (Z2) and rose flower-like (Z3) microstructures and deposited them as an additional layer over the conventional TiO_2 active layer to obtain T+Z1, T+Z2 and T+Z3 DSC photoanode, respectively. Among these, T+Z1 photoanode based DSC, employing Y123 dye and $[Cu(dmp)_2]^{2+/+}$ electrolyte delivered the best PCE of 7.61% with a V_{OC} of 1.13 V. This V_{OC} was ~100 mV higher than that of standard T device (consisting TiO_2 active layer only). The improvement in V_{OC} of bilayer DSCs was attributed to the negative shift in CB edge and lower recombination rate in these devices when compared to the standard device. Further, we achieved a record V_{OC} of 1.27 V under one sun irradiation and 1.025 V under indoor illuminations (1000 lux CFL and LED) by sensitizing the T+Z1 photoanode with MS5 dye. These promising results inspired us to develop a battery-free temperature sensor that can be powered autonomously by a single bilayer DSC of ~0.24 cm² active area under indoor illuminations.

Chapter 5 entails the development of a photocopacitor (PC) by integrating an activated charcoal based electric double layer capacitor (EDLC) device with DSC employing our best optimized TiO_2/ZnO bilayer photoanode architecture (T+Z1). Using an optimum TiO_2 layer thickness (~9 μm) in the T+Z1 photoanode and co-sensitizing it using 2:1 mixture of XY1b:MS5 dyes, we could achieve a PCE of 8.3% under one sun, 34.5% under 1000 lux CFL and 39.5% under 6000 lux CFL illumination. The PC integrated with this optimized photoanode could achieve a maximum overall photoelectric conversion and storage efficiency (OPCSE) of 4.1%, with a maximum achievable voltage (V_m) of ~1.1 V, under one sun irradiation. Under CFL illumination of 2000 lux, 4000 lux and 6000 lux, the PC could exhibit a remarkably high maximum OPCSE of 8.2% ($V_m \sim 0.95$ V), 11.4% ($V_m \sim 0.98$ V) and 15.5% ($V_m \sim 1.01$ V), respectively. Finally, we powered a temperature sensor/digital clock device by using the PC, under outdoor as well as indoor illumination. The PC was able to power the device for more than 20 min even after the illumination was cut-off.

Overall, the present work encompasses effective photoanode design for indoor DSCs for self-powered IoT applications. Furthermore, reducing the device's footprint without compromising the voltage opens up possibilities for integrating DSCs as a replacement for primary batteries contributing towards carbon neutrality and sustainability.

List of Publications Emanating from the Thesis

1. **Anooja Jagadeesh**, Ganapathy Veerappan, P. Sujatha Devi, K. N. Narayanan Unni and Suraj Soman*, Synergetic effect of TiO₂/ZnO bilayer photoanodes realizing exceptionally high V_{oc} for dye-sensitized solar cells under outdoor and indoor illumination, *J. Mater. Chem. A*, **2023**, 11, 14748-14759. DOI: 10.1039/D3TA02698A
2. **Anooja Jagadeesh**, K. N. Narayanan Unni and Suraj Soman*, ZnO microstructures based photoanode for DSCs: Effect of electrolyte system and blocking layers. (*Manuscript under preparation*)
3. **Anooja Jagadeesh**, K. N. Narayanan Unni and Suraj Soman*, TiO₂ photoanode surface textured using ZnO sacrificial layer for tackling mass transport issues in copper electrolyte based DSCs. (*Manuscript under preparation*)
4. **Anooja Jagadeesh**, K. N. Narayanan Unni and Suraj Soman*, Novel TiO₂ photoanode architectures employing ZnO microstructures templated scattering layers for improved DSC performance under indoor conditions. (*Manuscript under preparation*)
5. **Anooja Jagadeesh**, Visakh V. Mohan, K. N. Narayanan Unni, Rakhi R. B.* and Suraj Soman*, Photocapacitors based on small area DSCs for efficient light energy harvesting and storage under outdoor as well as indoor conditions. (*Manuscript under preparation*)

List of Publications not Related to the Thesis Work

1. Swetha Sasidharan, Sourava Chandra Pradhan, **Anooja Jagadeesh**, Balagopal N. Nair, Abdul Azeez Peer Mohamed, Narayanan Unni K. N, Suraj Soman*, and Unnikrishnan Nair Saraswathy Hareesh*, Bifacial dye-sensitized solar cells with enhanced light scattering and improved power conversion efficiency under full sun and indoor light conditions, *ACS Appl. Energy Mater.*, **2020**, 3, 12, 12584–12595, DOI: <https://doi.org/10.1021/acsaem.0c02500>
2. Koffi A. Kamenan[‡], **Anooja Jagadeesh**[‡], N'guessan Raymond Kre, Edja Florentin Assanvo, Suraj Soman*, and K. N. Narayanan Unni*, Natural rubber (*Hevea Brasiliensis*)-based quasi-solid electrolyte as a potential candidate for arresting recombination and improving performance in aqueous dye-sensitized solar cells, *J Mater Sci: Mater Electron.*, **2021**, 32, 14207–14216, DOI: 10.1007/s10854-021-05979-3
3. Koteswar Devulapally, Govind Reddy, Seelam Prasanthkumar, **Anooja Jagadeesh**, Suraj Soman* and Lingamallu Giribabu*, Effect of auxiliary acceptor on D-π-A based porphyrin sensitizers for dye sensitized solar cells, *J. Porphyrins Phthalocyanines*, **2021**, DOI: 10.1142/S1088424621500127
4. Palivela Siva Gangadhar[‡], **Anooja Jagadeesh**[‡], Andrew Simon George, Govind Reddy, Seelam Prasanthkumar, Suraj Soman* and Lingamallu Giribabu*, An investigation into the origin of variations in photovoltaic performance using D-D-π-A and D-A-π-A triphenylimidazole dyes with a copper electrolyte[‡], *Syst. Des. Eng.*, **2021**, DOI: 10.1039/d1me00073j
5. Swetha Sasidharan[‡], **Anooja Jagadeesh**[‡], Sourava C. Pradhan, Balagopal N. Nair,

Abdul Azeez Peer Mohamed, K.N. Narayanan Unni Suraj Soman* and Unnikrishnan Nair Saraswathy Hareesh*, ZnO hierarchical structures as sacrificial inclusions for enhanced performance under full sun and indoor light in bifacial dye sensitized solar cells, *Solar Energy*, **2021**, 226, 214–224, DOI: 10.1016/j.solener.2021.08.030

6. Palivela Siva Gangadhar‡, **Anooja Jagadeesh**‡, Manne Naga Rajesh, Andrew Simon George, Seelam Prasanthkumar, Suraj Soman* and Lingamallu Giribabu*, Role of π -spacer in regulating the photovoltaic performance of copper electrolyte dye-sensitized solar cells using triphenylimidazole dyes, *Mater. Adv.*, **2022**, 3, 1231, DOI: 10.1039/d1ma00852h
7. Palivela Siva Gangadhar‡, **Anooja Jagadeesh**‡, Andrew Simon George, Suraj Soman* and Lingamallu Giribabu*, Triphenylimidazole based Dye-Sensitized Solar Cells for efficient solar and artificial light conversion using iodide/triiodide redox electrolyte, *J. Chem. Sci.*, **2022**, 134:91, DOI: 10.1007/s12039-022-02088-4
8. **Anooja Jagadeesh** and Suraj Soman*, Dye-sensitized cells: Powerhouses for ambient light harvesting, *Encyclopedia of Renewable Energy, Sustainability and the Environment*, **2023**, DOI: 10.1016/b978-0-323-93940-9.00120-1 (**Book chapter**)

‡ Equal contribution

List of conference presentations

1. **Anooja Jagadeesh**, Sourava Chandra Pradhan, Lingamoorthy S, Pooja Chandran, Syamika Sunil, Narayanan Unni*, Suraj Soman* and Thomas W. Hamann, *Understanding Charge Transfer Properties in Thiocyanate-free Cyclo-metalated Ru dyes*, 3rd International Conference on Optoelectronic and Nano Materials for Advanced Technology (icONMAT 2019), Cochin University of Science and Technology (CUSAT), Kochi, January 2019.
2. **Anooja Jagadeesh**, Swetha Sasidharan, Sourava Chandra Pradhan, Unnikrishnan Nair Saraswathy Hareesh, Narayanan Unni K. N, and Suraj Soman*, *Photoanode Engineering in DSSC Leading to Improved Power Conversion Efficiency under Natural/Artificial Light Conditions*, 3rd International Conference on Advanced Functional Materials (ICAFM 2019), CSIR-National Institute for Interdisciplinary Science & Technology (CSIR-NIIST), Thiruvananthapuram, December 2019.
3. **Anooja Jagadeesh**, Sreelekshmy M. R., Sourava Chandra Pradhan, Narayanan Unni K. N., and Suraj Soman*, *Realizing Record V_{oc} of 1.25 V Under Full Sun and 1V Under 1000 Lux from Single Junction DSCs through Photoanode Modification*, International Conference on Chemistry and Applications of Soft Materials (CASM 2022), CSIR-National Institute for Interdisciplinary Science & Technology (CSIR-NIIST), Thiruvananthapuram, July 2022.
4. **Anooja Jagadeesh**, Visakh V. Mohan, K. N. Narayanan Unni, Rakhi R. B.* and Suraj Soman*, *Efficient Photoelectric Energy Conversion and Storage using Dye-Sensitized TiO_2/ZnO Bilayer Photoanode Based Photocapacitor for Indoor Application*, International Conference on Emerging Advanced Materials (ICEAM- 2024), Centre for Nanoscience and Technology (CNST), Anna University, Chennai-25, March 2024. (**secured second prize for oral presentation**)

Abstracts for Conference Presentations

1. *International Conference on Optoelectronic and Nano Materials for Advanced Technology (icONMAT 2019), Cochin University of Science and Technology (CUSAT), Kochi, January 2019*

Understanding Charge Transfer Properties in Thiocyanate-free Cyclometalated Ru dyes

Anooja Jagadeesh^{a,b}, Sourava Chandra Pradhan^{a,b}, Lingamoorthy S^a, Pooja Chandran^a, Syamika Sunil^a, Narayanan Unni *^{a,b}, Suraj Soman*^{a,b} and Thomas W. Hamann^c

^a *Photosciences and Photonics Section, Chemical Sciences and Technology Division, CSIR-National Institute for Interdisciplinary Science and Technology, Thiruvananthapuram, 695019 Kerala, India*

^b *Academy of Scientific and Innovative Research (AcSIR), Ghaziabad 201002, India*
E-mail address: suraj@niist.res.in, unni@niist.res.in

^c *Department of Chemistry, Michigan State University, East Lansing, MI, USA.*
E-mail address: hamann@chemistry.msu.edu

Since its invention by Grätzel and coworkers in 1991, Dye-sensitized solar cells (DSSC) evolved as an attractive technology in the domain of renewable energy, in particular photovoltaics, owing to their low manufacturing cost, ease of fabrication, modifiable aesthetic features (like colour and transparency) and admirable performance under ambient light conditions.^{1,2} Till date, DSSC could achieve a maximum power conversion efficiency of about 14% under 1 sun (100 mW/cm²) illumination and 32% under low light/indoor light harvesting conditions.^{1,3} The sensitizer or dye constitutes the key component in DSSC. The unfavorable reactions of SCN ligand, present in conventional Ru dyes (e.g. N719 dye, N3 dye) used in DSSCs, with electrolyte, affect the chemical stability of these dyes. In addition to this, the incompatibility of these dyes with alternate redox shuttles have persuaded researchers to look for alternative structurally engineered design possibilities, the most prominent being the replacement of labile thiocyanate ligands with cyclometalated groups which retains the ground and excited state electron distribution. Cyclometalated ruthenium complexes gained much significance in this aspect because of the flexibility to tune their ground states by judicious substitutions on the cyclometalating ligand, thereby making them compatible with alternate redox mediators (cobalt electrolytes). The influence of cyclometalation on dye regeneration has been extensively studied, however, its effect on the charge injection and collection, is yet to be explored. As a debut into the detailed study of electron transfer dynamics within the DSSCs utilizing thiocyanate-free cyclometalated ruthenium complexes, we have chosen three cyclometalated Ru dyes (labelled as RC1, RC2 and RC3 in the present work) and employed them in DSSCs along with iodide/triiodide electrolyte.⁴⁻⁶ The photovoltaic characteristics revealed improvement in performance of devices endowed with RC2 and RC3 which relied not only on the increment in the short circuit current (J_{sc}) but also on the elevation in the open circuited voltage (V_{oc}) of the devices. Advanced characterization techniques, including small perturbation techniques like electrochemical impedance spectroscopy (EIS), intensity modulated photovoltage spectroscopy (IMVS), and intensity modulated photocurrent spectroscopy (IMPS), were utilized in a way to unveil the origin for this enhancement in J_{sc} and V_{oc} .

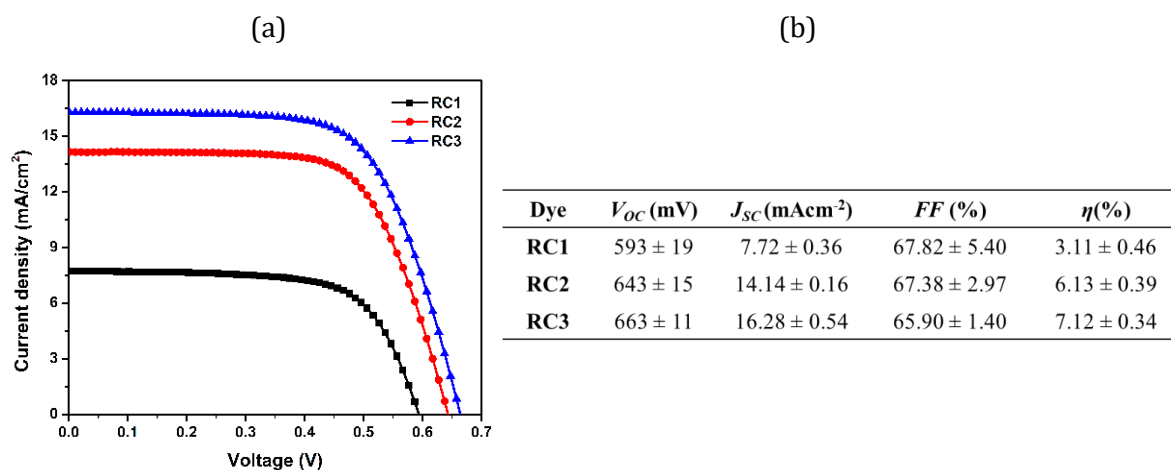


FIGURE 1. (a) J - V characteristics & (b) J - V parameters for the devices fabricated using the Cyclometalated Ru complexes as sensitizers.

References

1. Y. Cao, Y. Liu, M. Zakeeruddin, A. Hagfeldt, Y. Cao, Y. Liu, S. M. Zakeeruddin, A. Hagfeldt and M. Gra, *Joule*, 2018, 2, 1–10.
2. M. Freitag, J. Teuscher, Y. Saygili, X. Zhang, F. Giordano, P. Liska, J. Hua, S. M. Zakeeruddin, J. Moser, M. Grätzel and A. Hagfeldt, *Nat. Photonics*, 2017, 1–8.
3. K. Kakiage, Y. Aoyama, T. Yano, K. Oya, J. Fujisawa and M. Hanaya, *Chem. Commun.*, 2015, 51, 15894–15897.
4. T. Bessho, E. Yoneda, J.-H. Yum, M. Guglielmi, I. Tavernelli, H. Imai, U. Rothlisberger, M. K. Nazeeruddin and M. Grätzel, *J. Am. Chem. Soc.*, 2009, 131, 5930–5934.
5. J. Bezdek, P. A. Schauer and C. P. Berlinguette, *Inorg Chem*, 2013, 52, 3001–3006.
6. S. Soman, Y. Xie and T. W. Hamann, *Polyhedron*, 2014, 82, 139–147.

Photoanode Engineering in DSSC Leading to Improved Power Conversion Efficiency under Natural/Artificial Light Conditions

Anooja Jagadeesh,^{1,a,b} Swetha Sasidharan,^{2,a,b} Sourava Chandra Pradhan,^{1,a,b} Unnikrishnan Nair Saraswathy Hareesh,^{2,a,b} Narayanan Unni K. N,^{1,a,b} and Suraj Soman^{*1,a,b}

¹Chemical Sciences and Technology Division, ²Materials Science and Technology Division, ^aNational Institute for Interdisciplinary Science and Technology, Council of Scientific and Industrial Research (CSIR-NIIST), Thiruvananthapuram-695019, Kerala, India

^b Academy of Scientific and Innovative Research (AcSIR), Ghaziabad 201002, India

*E-mail: suraj@niist.res.in

Dye-sensitized solar cells (DSSC) has become an attractive photovoltaic technology owing to the facile fabrication steps, cost effectiveness, environmental friendliness, appealing aesthetic features and admirable performance under ambient/diffused light conditions. Till date, DSSC could achieve a maximum power conversion efficiency of about 14% under One Sun (100 mW/cm²) condition and 32% under ambient/indoor light illumination.^{1,2} Various strategies to enhance the performance of DSSC by developing efficient photoanodes are attempted, such as use of high surface area layers, surface modification on conductive glass as well as semiconductor active layer with nanometer sized particles, insertion of scattering over layer, addition of scattering particles to the active layer, inclusion of metal nanoparticles in the active layer or as overlayer etc.^{2,3}

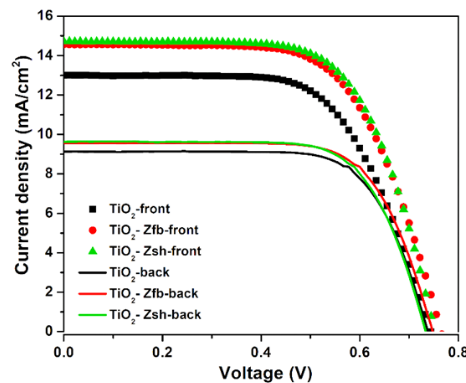


FIGURE 1. *J-V* characteristics under One Sun, for the devices employing TiO₂ photoanodes modified using sacrificial layers of ZnO fibril like aggregates (TiO₂-Zfb) and ZnO sheet like aggregates (TiO₂-Zsh), when illuminated from front and back side

Light incident on	Device	V_{oc} (mV)	J_{sc} (mAcm ⁻²)	FF (%)	η (%)
Front side of the device	TiO ₂	744	12.9	63.8	6.17
	TiO ₂ -Zfb	765	14.6	64.0	7.13
	TiO ₂ -Zsh	751	14.7	66.2	7.32
Rear side of the device	TiO ₂	738	9.1	71.2	4.79
	TiO ₂ -Zfb	749	9.5	70.5	5.03
	TiO ₂ -Zsh	733	9.6	70.1	4.96

TABLE 1. Photovoltaic parameters of the TiO₂-Zfb and TiO₂-Zsh devices, under One Sun condition, when illuminated from front and back side

In the present work, a novel strategy was developed for improving the performance of DSSCs, by utilizing the scattering effect introduced by engineering the surface texture of TiO₂ photoanodes. The surface roughness of the TiO₂ film can be manipulated by creating grooves/imprints on it. This was done by depositing a sacrificial layer of ZnO microstructures, such as microflowers (ZF), fibril like aggregates (Zfb) and sheet like aggregates (Zsh), over the conventional TiO₂ active layer, followed by etching off the over layer using suitable reagent, in this case aqueous TiCl₄ solution. Significant improvement in J_{sc} of the device was observed by following this strategy, resulting in enhanced power conversion efficiency with a little reduction in transparency, both in One Sun and low intensity light illuminations. Even though the architectural change to TiO₂ resulted in higher recombination as evident from the perturbation results, the negative shift in conduction band along with shorter transport time and longer diffusion length helped surface modified devices to achieve better charge collection efficiency. A mixture of TiO₂ nanoparticles and ZnO microstructures as overlayer also exhibited similar improvement in performance of the device.

References

1. Y. Cao, Y. Liu, M. Zakeeruddin, A. Hagfeldt, Y. Cao, Y. Liu, S. M. Zakeeruddin, A. Hagfeldt and M. Gratzel, *Joule* 2018, 2, 1–10.
2. S. Sasidharan, S. Soman, S. C. Pradhan, K. N. N. Unni, A. A. P. Mohamed, B. N. Nair, H. U. N. Saraswathy, *New Journal of Chemistry* 2017, 41, 1007-1016
3. T. G. Deepak, G. S. Anjusree, S. Thomas, T. A. Arun, S. V. Nair and A. S. Nair, *RSC Advances* 2014, 4, 17615–17638

3. *International Conference on Chemistry and Applications of Soft Materials (CASM 2022), CSIR-National Institute for Interdisciplinary Science & Technology (CSIR-NIIST), Thiruvananthapuram, July 2022.*

Realizing Record V_{OC} of 1.25 V Under Full Sun and 1V Under 1000 Lux from Single Junction DSCs through Photoanode Modification

Anooja Jagadeesh,^{1,2} Sreelekshmy M. R.,¹ Sourava Chandra Pradhan,^{1,2} Narayanan Unni K. N.,^{1,2} Suraj Soman^{1,2*}

¹ *Chemical Sciences and Technology Division, National Institute for Interdisciplinary Science and Technology, Council of Scientific and Industrial Research (CSIR-NIIST), Thiruvananthapuram-695019, Kerala, India*

² *Academy of Scientific and Innovative Research (AcSIR), Ghaziabad 201002, India*
E-mail: suraj@niist.res.in

Dye-sensitized Solar Cells (DSCs) proved to be the most suitable photovoltaic technology for indoor photovoltaic (IPV) applications. Many electronic devices (such as sensors, detectors, etc.) utilized in IoT technology and consumer electronics require ultra-small current (μA range) but higher voltage (about 1.5V - 5V) for operation. Hence, small area DSCs with voltage higher than 1V are a need of the time. Various strategies have been adopted to enhance the open circuit voltage (V_{OC}) of DSCs. Employing alternate redox shuttles based on cobalt and copper having more positive redox potentials is one of the recent methods to realize higher V_{OC} .^{1,2} Designing of dye molecules with long alkyl chains to prevent back electron transfer is another strategy being adopted for further enhancing the V_{OC} . Recently, a V_{OC} of 1.24V was realized under one sun condition by Hagfeldt and co-workers using MS5 dye and copper electrolyte.³ In the present work, we modified the DSC photoanode by utilizing ZnO nanoporous microstructures as an over layer to the standard TiO_2 active layer. The modified photoanode was sensitized with MS5 and Y123 dyes which delivered a record V_{OC} of 1.25V under one sun condition and 1V under 1000 lux indoor illumination, respectively, when employed along with copper electrolyte.

References

1. Michaels, H.; Rinderle, M.; Freitag, R.; Benesperi, I.; Edvinsson, T.; Socher, R.; Gagliardi, A.; Freitag, M. *Chemical Science*, **2020**, *11*, 2895-2906.
2. Pradhan, S. C.; Hagfeldt, A.; Soman, S. *Journal of Materials Chemistry A*, **2018**, *6*, 22204-22214
3. Zhang, D.; Stojanovic, M.; Ren, Y.; Cao, Y.; Eickemeyer, F. T.; Socie E.; Vlachopoulos, N.; Moser, J. E.; Zakeeruddin, S. M.; Hagfeldt, A.; Grätzel, M. *Nature Communications*, **2021**, *12*, 1777

Efficient Photoelectric Energy Conversion and Storage using Dye-Sensitized TiO₂/ZnO Bilayer Photoanode Based Photocapacitor for Indoor Application

Anooja Jagadeesh,^{1,2} Visakh V. Mohan,¹ K. N. Narayanan Unni,^{1,2} Rakhi R. B.^{1,2*} and Suraj Soman^{1,2*}

¹ *Centre for Sustainable Energy Technologies (C-SET), National Institute for Interdisciplinary Science and Technology, Council of Scientific and Industrial Research (CSIR-NIIST), Thiruvananthapuram-695019, Kerala, India*

² *Academy of Scientific and Innovative Research (AcSIR), Ghaziabad 201002, India*

* E-mail: suraj@niist.res.in, rakhisarath@gmail.com

Owing to their remarkable performance under low intensity light conditions, dye-sensitized photovoltaic cells (DSCs) have proved to be one of the most suitable indoor/ambient light harvesting technologies for indoor photovoltaic (IPV) applications. Majority of devices like sensors, detectors, *etc.* employed in consumer electronics and internet of things (IoT) require a higher voltage (~ 1.5 V to 5 V) but can be operated at lower current range (μA range). To address this, we focused on developing small-area DSCs to generate voltages exceeding 1V for indoor device powering. Usage of redox shuttles based on cobalt and copper complexes, endowed with more positive redox potentials is one of the methods reported to realize higher open circuit voltage (V_{OC}) for DSCs.¹⁻³ Recently, Hagfeldt and co-workers designed an organic dye, named MS5, with long alkyl chains to prevent back electron transfer in DSCs utilizing a copper bipyridyl based electrolyte, thereby realizing a V_{OC} of 1.24 V under simulated sunlight.⁴ By incorporating ZnO nanoporous microstructures as an over layer to the standard TiO₂ active layer and sensitizing it with MS5 dye, we achieved a record V_{OC} of 1.27 V under solar irradiation and 1.02 V under 1000 lux indoor illumination.⁵ Employing a co-sensitization strategy with MS5 and XY1b dyes enhanced the short-circuit current density (J_{sc}), resulting in higher power conversion efficiency (PCE) of 34.5% and 39.5% under 1000 lux and 6000 lux CFL illuminations. Integration of this DSC with an activated carbon-based electric double layer capacitor (EDLC) led to an efficient photocapacitor (PC) exhibiting a maximum overall photoelectric power conversion and storage efficiency (OPCSE) of 15.5% under 6000 lux CFL illumination. This small-area PC could successfully power a digital device with a temperature sensor and clock under indoor conditions, demonstrating its practical application. The PC continued to power the device even after the light was switched off.

References

1. Michaels, H.; Rinderle, M.; Freitag, R.; Benesperi, I.; Edvinsson, T.; Socher, R.; Gagliardi, A.; Freitag, M. *Chemical Science*, **2020**, *11*, 2895-2906.
2. Pradhan, S. C.; Hagfeldt, A.; Soman, S. *Journal of Materials Chemistry A*, **2018**, *6*, 22204-22214.
3. Meethal, S. M.; Pradhan, S. C.; Velore, J.; Varughese, S.; Pillai, R. S.; Sauvage, F.; Hagfeldt, A.; Soman, S.; *Journal of Materials Chemistry A*, **2024**, *12*, 1081-1093.
4. Zhang, D.; Stojanovic, M.; Ren, Y.; Cao, Y.; Eickemeyer, F. T.; Socie E.; Vlachopoulos, N.; Moser, J. E.; Zakeeruddin, S. M.; Hagfeldt, A.; Grätzel, M. *Nature Communications*, **2021**, *12*, 1777.
5. Jagadeesh, A.; Veerappan, G.; Devi, P. S.; Unni, K. N. N.; Soman, S. *Journal of Materials Chemistry A* **2023**, *11*, 14748.

Cite this: *J. Mater. Chem. A*, 2023, **11**, 14748

Synergetic effect of TiO₂/ZnO bilayer photoanodes realizing exceptionally high V_{OC} for dye-sensitized solar cells under outdoor and indoor illumination†

Anooja Jagadeesh,^{ab} Ganapathy Veerappan,^c P. Sujatha Devi,^{ab} K. N. Narayanan Unni^{ab} and Suraj Soman^{*ab}

Harnessing energy from the surrounding light using indoor photovoltaics has gained momentum to address the carbon footprint resulting from used and dead batteries. Dye-sensitized solar cells (DSCs) have emerged as one of the most efficient and sustainable indoor light harvesting alternatives which can significantly reduce the environmental impact of batteries. Energy harvesting and managing circuits in these devices demand higher open circuit potentials (V_{OC}). Nevertheless, recombination losses frequently lower the open-circuit potential in DSCs, especially when illuminated indoors. We present an innovative TiO₂/ZnO bilayer architecture capable of delivering higher V_{OC} by carefully controlling the conduction band (CB) position and recombination losses. By sensitizing this innovative bilayer electrode with MS5 dye and a [Cu(dmp)₂]^{1+/2+} redox mediator, we achieved a record V_{OC} of 1.27 V from a single junction device under Air Mass 1.5 Global (AM 1.5G), 100 mW cm⁻² solar irradiation and 1.295 V under higher intensity LED light (200 mW cm⁻²). These bilayer devices also demonstrated impressive V_{OC} of 1.025 V under 1000 lux compact fluorescent light (CFL) and light emitting diode (LED) illumination and could autonomously power a temperature sensor using a single device of 0.24 cm² active area. This work highlights the potential of modifying the semiconductor and device architecture to achieve higher V_{OC} in DSCs, which is essential for integrating these photovoltaic devices with smart IoT devices making them autonomous and sustainable.

Received 6th May 2023
Accepted 7th June 2023

DOI: 10.1039/d3ta02698a

rsc.li/materials-a

1. Introduction

The use of automation and digitization through the integration of the Internet of Things (IoT), Artificial Intelligence (AI), cloud computing, and Machine Learning (ML) into our everyday activities is becoming increasingly popular in the smart world of connected technologies driven by the fourth industrial revolution (industry 4.0).^{1,2} A large number of battery-operated electronic sensors and actuator nodes are required to realize uninterrupted communication between these various devices to ensure their efficient utilization in this intelligent connected ecosystem. The batteries in billions of these communication devices may eventually threaten the environment, with their frequent replacements adding an extra burden to the carbon economy and sustainability. This urges the need for battery-less

energy-harvesting IoTs.³⁻⁵ State-of-the-art indoor/ambient light harvesting Dye-sensitized Solar Cells (DSCs) can be successfully utilized to supplement the energy demands of these low-power electronic devices, which are primarily deployed in indoor spaces, enabling them to become self-powered.⁶⁻¹⁰ In addition, the use of environmentally friendly materials, less energy-intensive manufacturing process, possibilities of fabricating these devices on flexible substrates like metal and plastics and the compliance for recycling and reusing further enhance the application possibilities and market penetration of DSCs.¹¹⁻¹⁵ Electronic communication devices in the IoT ecosystem require only low current (in the μA to mA range) but a higher threshold voltage (>1 V) for continuous operation.¹⁶⁻¹⁸ This demands developing DSCs that deliver higher voltage, preferentially above 1 V under ambient/indoor illumination, from single junction devices, which will ultimately reduce the need for interconnection, thereby reducing the device's footprint and ownership cost. Of the various strategies employed, using alternate redox shuttles based on cobalt and copper metal complexes proved to be an efficient and successful method.^{8-10,19-24} Cobalt complexes, being bulky and mass transport limited, suffer from recombination and regeneration issues resulting in lower open circuit voltage (V_{OC}) and short circuit current (I_{SC}) values.²⁵ Recently, by using copper redox mediators ([Cu(tmb)₂]^{1+/2+}) in combination with a custom-

^aPhotosciences and Photonics Section, Chemical Sciences and Technology Division, CSIR-National Institute for Interdisciplinary Science and Technology (CSIR-NIIST), Thiruvananthapuram 695019, India. E-mail: suraj@niist.res.in

^bAcademy of Scientific and Innovative Research (AcSIR), Ghaziabad 201002, India

^cCentre for Solar Energy Materials, International Advanced Research Centre for Powder Metallurgy and New Materials (ARCI), Balapur, Hyderabad 500005, Telangana, India

† Electronic supplementary information (ESI) available: Experimental section, supplementary figures (Fig. S1 to S12), supplementary tables (Tables S1 to S5), and supplementary videos (Videos S1 and S2). See DOI: <https://doi.org/10.1039/d3ta02698a>

designed organic dye (MS5), Zhang *et al.* were successful in achieving a V_{OC} of 1.24 V under one sun (100 mW cm^{-2}) and 0.98 V under 1000 lux fluorescent light (CFL) illumination.²⁶ In the present work, an innovative material and device engineering strategy is being explored to further enhance the V_{OC} under full sun and indoor illumination.

The semiconductor layer is critical in determining the V_{OC} in DSCs, as it controls the charge transport and recombination at the interfaces formed with the dye and redox mediator. Nanoporous films made of titania (TiO_2) are widely used owing to their favourable band gap, conduction band (CB) edge, high surface area, minimal defects, chemical stability, low cost and ease of availability.^{12,27} Compared to other alternative metal oxides (SnO_2 , Nb_2O_5 , WO_3 , In_2O_3), zinc oxide (ZnO) with superior electron mobility and comparable band edges with TiO_2 is used as a promising candidate for developing efficient DSCs.^{27–29} Hierarchical ZnO aggregates and 3D structures were used to improve dye loading and scattering, contributing to enhanced J_{SC} .^{30–32} Compact ZnO blocking/buffer layers were also utilized to suppress recombination at the FTO/electrolyte and TiO_2 /dye/electrolyte interfaces.^{33,34} Nevertheless, ZnO-based DSCs suffer from performance losses owing to poor chemical stability, lower dye adsorption, faster dye degradation and higher recombination that retards charge separation at the ZnO/dye/electrolyte interface.^{35–37} Herein, we introduced a complementary device engineering strategy utilizing ZnO microstructures as overlayers above the TiO_2 nanoporous layer, taking advantage of both materials that can deliver higher V_{OC} by carefully controlling the conduction band (CB) position and reducing recombination losses. Using the standard Y123 organic sensitizer along with $[\text{Cu}(\text{dmp})_2]^{1+/2+}$ electrolyte, a higher V_{OC} of 1.13 V was achieved employing this new architecture compared to 1.02 V for the control device having a TiO_2 layer alone. The effect was more pronounced at indoor illumination using CFL and LED light sources, where we could accomplish a V_{OC} of 1.0 V at 1000 lux illumination using the newly introduced TiO_2 /ZnO bilayer stacked architecture. Stability issues due to the degradation of ZnO in the presence of electrolytes could also be resolved by introducing an ultrathin TiO_2 blocking layer (BL) over the TiO_2 /ZnO bilayer.³⁸ By sensitizing the new TiO_2 /ZnO bilayer photoanodes with MS5 dye instead of Y123, we succeeded in realizing a record V_{OC} of 1.27 V under full sun (100 mW cm^{-2}) irradiation, 1.295 V under higher intensity LED light (200 mW cm^{-2}) and 1.025 V under 1000 lux CFL as well as LED illumination. Remarkably, this stands as the highest reported V_{OC} under standard 1000 lux indoor lighting conditions to date. We have demonstrated the practical application of these high V_{OC} DSCs by developing a battery-free, self-powered temperature sensor using a single device with 0.24 cm^2 active area under indoor illumination, reducing reliance on batteries, thereby minimizing the carbon footprint.

2. Results and discussion

Conventional TiO_2 photoanodes (T) and bilayer TiO_2 /ZnO stacked photoanodes (denoted as T + Z1, T + Z2 and T + Z3) were fabricated as detailed in the experimental procedures, ESI.† The

TiO_2 /ZnO bilayer photoanode stacks employ the synthesized ZnO hierarchical structures (Z1, Z2 and Z3) as an overlayer above the conventional TiO_2 layer. The fabrication scheme for the bilayer TiO_2 /ZnO devices is provided in Fig. 1(A), and the chemical structures of organic sensitizers and the copper redox mediator are given in Fig. 1(B). Fig. 1(C) depicts the alignment of energy levels of the semiconductor layer and electrolyte investigated in the present study. ZnO microstructures were synthesized following a facile wet chemical route using zinc nitrate hexahydrate and urea.³⁹ Synthesis details are provided in the Experimental section, ESI.† The hierarchical microstructures of different morphologies were synthesized by changing the urea concentration in the reaction mixture. Three different concentrations of urea, *viz.* 0.03 M, 0.08 M and 0.8 M, were used to control the growth of hierarchical microstructures of three different morphologies, *viz.* mimosa flower-like (Z1), dandelion flower-like (Z2) and rose flower-like (Z3) morphologies, respectively. SEM images of Z1, Z2 and Z3 are provided in Fig. 2(A) and the particle size, crystallite size and BET surface area are detailed in Table S1, ESI.† HRTEM images of Z1, Z2 and Z3 microstructures (Fig. S1(A), ESI†) show that they are formed by the aggregation of oval-shaped nanoparticles having average sizes of 33.9 nm, 33.9 nm, and 32.9 nm, respectively. It is also seen that the nanocrystallites with different crystallographic alignments are randomly oriented, suggesting a heterogenous nucleation and coalescence mechanism for particle growth followed by a diffusion-limited cluster–cluster aggregation to form hierarchical structures.⁴⁰ At a lower concentration of urea (0.03 M) in the reaction mixture, the nano-sized crystallites undergo coalescence to give nanofibers, and these nanofibers then aggregate together to form the mimosa flower-like hierarchical structure. With the increase in urea concentration (0.08 M), the coalescence of nanoparticles occurs in such a way that the length of the nanofiber is reduced while its width is increased to obtain 2D nanoribbons, which cluster together to form dandelion flower-like microstructures. A ten times increase in urea concentration (0.8 M) further reduces the length while increasing the nanoribbon's width, forming 2D nanoflakes, which assemble to form rose flower-like morphology. The selected area electron diffraction (SAED) patterns shown in the inset of Fig. S1(A), ESI† confirm the crystalline nature of the annealed samples of Z1, Z2 and Z3. The XRD patterns of ZnO samples obtained after annealing at 500 °C (Fig. S1(B), ESI†) show that all of them are crystalline, exhibiting a wurtzite phase with a hexagonal crystal structure (JCPDS no. 01-080-0074). Along the [100], [002] and [101] directions, Z1, Z2 and Z3 exhibited average crystallite sizes of 34.7 nm, 35.5 nm and 31.8 nm. The SEM images of the top and cross-sectional views of T, T + Z1, T + Z2 and T + Z3 electrodes are provided in Fig. 2(B). The approximate thickness of each layer was determined from the cross-sectional SEM (Table 1). The TiO_2 layer thickness was *ca.* 6 μm , whereas the ZnO overlayers were seen to be slightly distorted after the blade coating (Fig. 2(B)), resulting in an average thickness of *ca.* 15 μm . The XRD pattern of the TiO_2 /ZnO bilayer stacks (Fig. 2(C)) shows peaks corresponding to anatase TiO_2 and wurtzite ZnO (JCPDS no. 21-1272 and 01-075-1526). The dye loading for the different

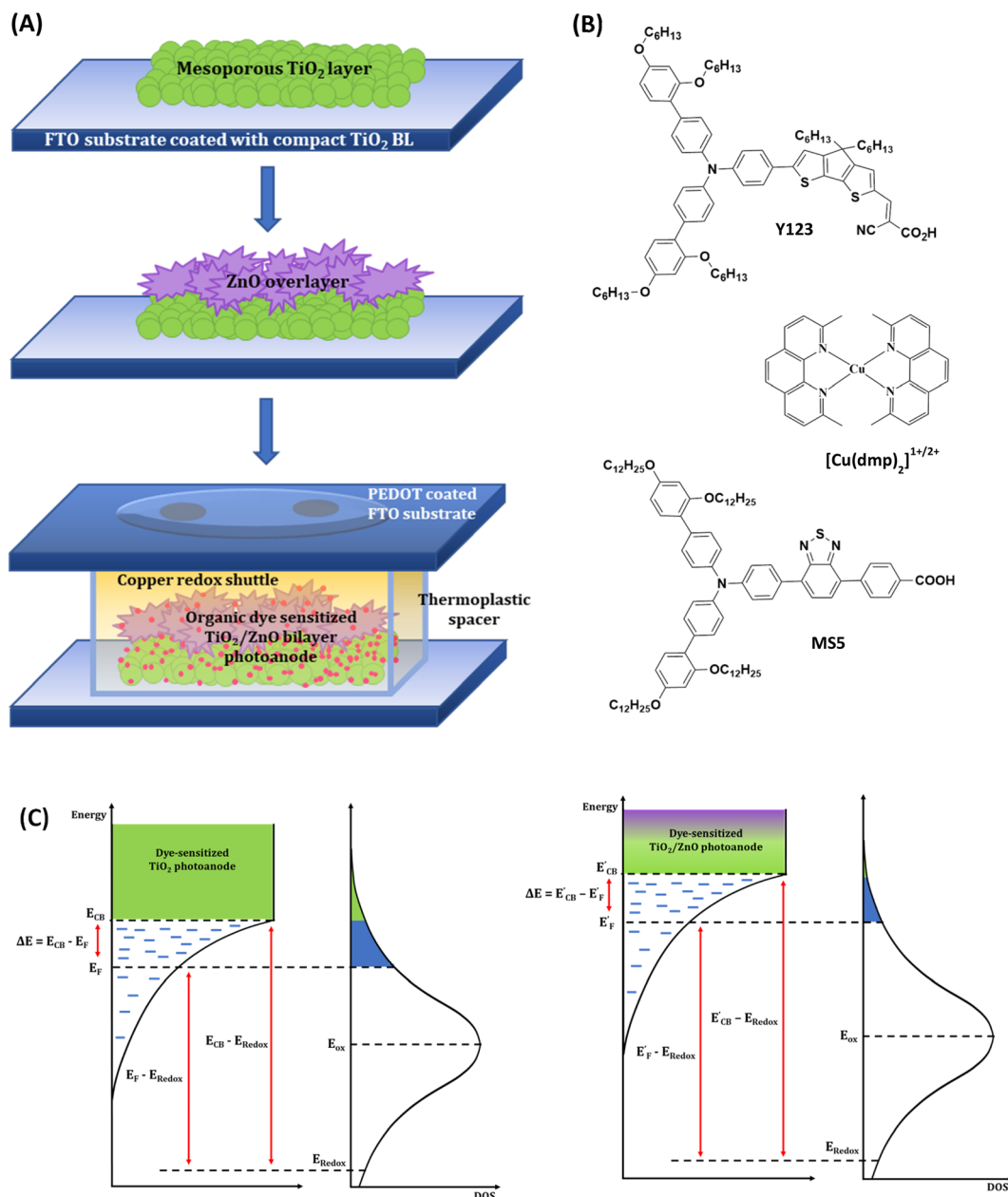


Fig. 1 (A) Fabrication scheme and device architecture of DSCs employing bilayer TiO₂/ZnO photoanodes. (B) Chemical structure of the organic sensitizers (Y123 and MS5) and the redox mediator ([Cu(dmp)₂]^{1+/2+}). (C) Alignment of energy levels of the semiconductor layer and electrolyte. A negative shift in the conduction band edge (E_{CB}) of TiO₂/ZnO electrodes results in reduced overlapping between the oxidized energy states of the electrolyte with the conduction band states (shaded in green) and the gap states (shaded in blue).

photoanodes (T, T + Z1, T + Z2, and T + Z3), determined as described in the Experimental section, ESI,[†] is listed in Table 1. The slightly better dye loading for the bilayer photoanodes may be attributed to the higher film thickness when compared to the T electrode. DSCs were initially fabricated employing standard organic dye (Y123) and a copper redox mediator ([Cu(dmp)₂]^{1+/2+}) using TiO₂ and TiO₂/ZnO bilayer electrodes. The device fabrication and characterization procedures are provided in detail in the Experimental section, ESI.[†]

The current density *versus* voltage (*J*-*V*) curves for the standard device (T) along with the TiO₂/ZnO bilayer devices (T + Z1,

T + Z2 and T + Z3), measured under AM 1.5G simulated solar irradiation (100 mW cm⁻²), are given in Fig. 3(A), and the corresponding photovoltaic parameters are summarized in Table 1. The control device T with one layer of TiO₂ exhibited a V_{OC} of 1.02 V. With the introduction of a ZnO layer on top of TiO₂, the V_{OC} increased to 1.13 V, 1.11 V and 1.09 V for the T + Z1, T + Z2 and T + Z3 devices, respectively. Among the three bilayer devices, T + Z1 delivered the best photovoltaic performance of 7.61%, with a better V_{OC} (1.13 V), J_{SC} (9.88 mA cm⁻²) and FF (0.68). The IPCE spectra of the devices followed similar J_{SC} trends (Fig. 3(B)) with matching values inside the permitted

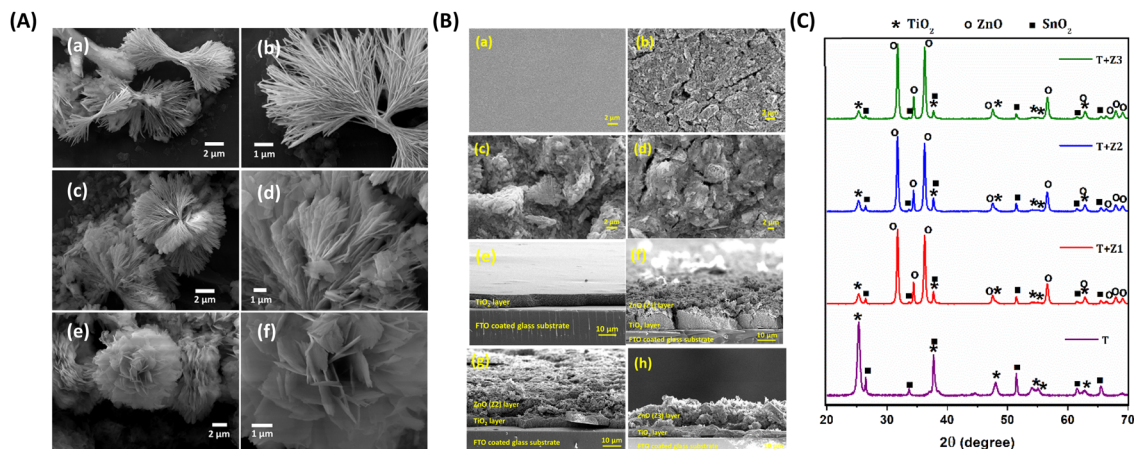


Fig. 2 (A) SEM images of the as-synthesized samples of (a and b) mimosa flower-like microstructures (Z1); (c and d) dandelion flower-like microstructures (Z2); (e and f) rose flower-like microstructures (Z3). (B) SEM images of the top view of the photoanodes: (a) T, (b) T + Z1, (c) T + Z2, (d) T + Z3; and cross-sectional view of the photoanodes: (e) T, (f) T + Z1, (g) T + Z2, (h) T + Z3; and (C) XRD patterns of T, T + Z1, T + Z2 and T + Z3 layers coated over an FTO substrate.

Table 1 Photovoltaic parameters of TiO₂ (T) and TiO₂/ZnO bilayer DSCs (T + Z1, T + Z2 and T + Z3) employing the Y123 sensitizer and [Cu(dmp)₂]^{1+/2+} redox electrolyte under AM 1.5G one sun (100 mW cm⁻²) irradiation along with average semiconductor layer thickness, dye loading, trap state distribution parameter (α), ideality factor (n) and flat band potential (V_{fb})

Device code	Average layer thickness ^a (μm)	Dye loading (mol cm ⁻²)	V_{OC} ^b (V)	J_{SC} ^b (mA cm ⁻²)	FF ^b	PCE ^b (%)	Integrated J_{SC} ^c (mA cm ⁻²)	α ^d	n ^e	V_{fb} ^f (V)
T	6.3	0.94×10^{-7}	1.02 (1.03)	12.24 (12.01)	0.64 (0.64)	8.00 (7.92)	11.60	0.11	2.51	0.69
T + Z1	20.3	1.48×10^{-7}	1.13 (1.13)	9.88 (9.74)	0.68 (0.68)	7.61 (7.48)	9.90	0.14	1.34	0.87
T + Z2	21.5	1.43×10^{-7}	1.11 (1.11)	8.91 (9.04)	0.67 (0.65)	6.67 (6.60)	9.60	0.13	1.50	0.81
T + Z3	20.3	1.36×10^{-7}	1.09 (1.09)	8.63 (8.58)	0.63 (0.62)	5.96 (5.85)	8.60	0.11	2.01	0.77

^a Average semiconductor layer thickness obtained from cross-sectional SEM analysis. ^b J - V parameters of champion cells and averages taken over five sets of samples (in parentheses) with a maximum mean deviation of ± 0.01 , ± 0.31 , ± 0.02 and ± 0.14 in V_{OC} , J_{SC} , FF and PCE respectively. ^c J_{SC} obtained by integrating the IPCE spectra. ^d Obtained from the $\log C_{\mu}$ versus V_{OC} plot. ^e Obtained from the V_{OC} versus ϕ plot. ^f Obtained from Mott-Schottky analysis.

error limits for integrated J_{SC} from IPCE, and J_{SC} obtained from J - V measurements (Table 1). The observed blue shift in the IPCE spectra of T + Z devices, compared to the T device, can be ascribed to dye aggregation within the bilayer devices. On the other hand, the difference in onset of IPCE spectra between the different bilayer devices may be attributed to the difference in scattering effects caused by the utilization of various ZnO microstructure (Z1, Z2, and Z3) overlayers with varying particle size and layer thickness.

The flat band potentials (V_{fb}) of the semiconductor utilized in different devices were determined by extrapolating the linear region of the Mott-Schottky (MS) plots, as depicted in Fig. 3(C), to intersect the voltage axis.^{41–44} The obtained V_{fb} values for T + Z1, T + Z2, and T + Z3 are observed to be shifted towards more negative potentials compared to the standard T device (Table 1). This shift indicates that in the bilayer devices, specifically with the inclusion of a ZnO layer on top of the TiO₂, the conduction band (CB) is shifted towards more negative potentials. It is well established that ZnO possesses a more negatively positioned CB edge relative to TiO₂. Moreover, S.-S. Kim *et al.* have reported, based on cyclic voltametric studies, that the addition of ZnO to

TiO₂ results in a negative shift in the CB edge of TiO₂.⁴⁵ This upward shift in the CB can be attributed to the apparent charging of the ZnO layer due to the band alignment at the TiO₂/ZnO interface.^{46,47} The negative shift in the CB for the TiO₂/ZnO bilayer devices was further verified through charge extraction (CE) plots (Fig. 3(D)), which demonstrate an approximate 50–100 mV negative shift upon the introduction of ZnO layers. This negatively shifted CB may further contribute to the enhanced V_{OC} in the TiO₂/ZnO bilayer devices.

Electrochemical Impedance Spectroscopy (EIS) measurements were carried out to further investigate the charge carrier concentration in the bilayer devices and to probe recombination losses. The obtained Nyquist plots were fitted using a modified Randles circuit (Fig. S2(A), ESI†).⁴⁸ The corresponding fitted parameters obtained at a bias of 1 V are listed in Table S2, ESI†. The chemical capacitance (C_{μ}) determined from EIS analysis plotted as a function of V_{OC} , given in Fig. S2(B), ESI†, also shows a negative shift in the CB position for bilayer devices as observed previously from the MS and CE analysis. C_{μ} has an exponential dependence on V_{OC} , as given by the relation,^{46,49}

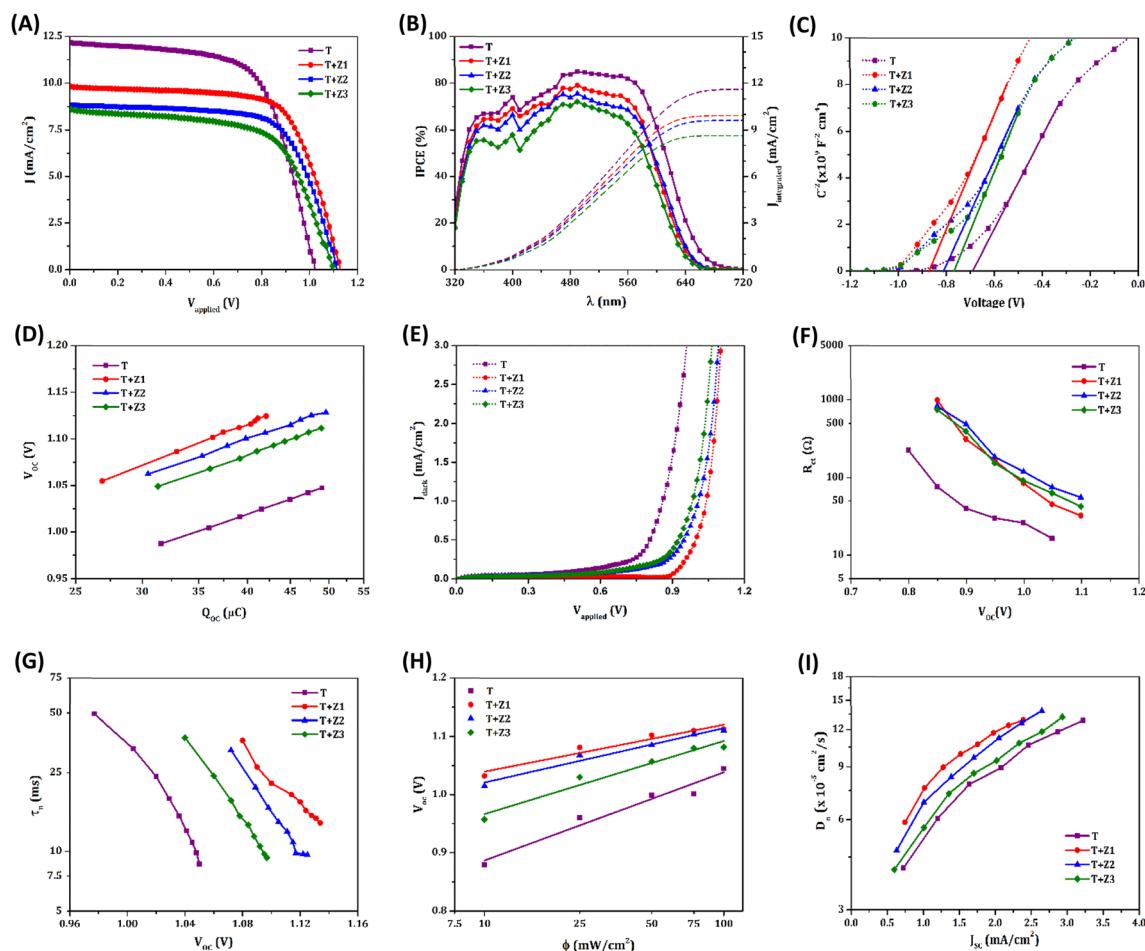


Fig. 3 (A) The J - V curves measured under AM 1.5G 1 sun illumination (100 mW cm^{-2}), (B) IPCE of the DSCs (the dotted line represents the integrated photocurrent density calculated from the IPCE and the standard solar emission spectrum), (C) Mott-Schottky (MS) plots, (D) charge extraction (CE) plots, (E) J - V curves measured in the dark, (F) charge transfer resistance (R_{ct}) measured from EIS analysis under dark conditions plotted against corrected potential, (G) lifetime (τ_n) as a function of V_{OC} obtained from transient photovoltage decay measurements, (H) intensity dependence plot of V_{OC} , the solid line represents linear fits of the data and (I) diffusion coefficient (D_n) as a function of J_{SC} .

$$C_\mu = C_o \exp\left(\frac{\alpha q V_{OC}}{k_B T}\right) \quad (1)$$

where α is the trap state distribution parameter in the semiconductor layer, q is the electronic charge, k_B is Boltzmann's constant, T is the absolute temperature, and C_o is a parameter that depends explicitly on α , the CB edge (E_{CB}), the trap state density (n_t) in the semiconductor and the redox potential of the electrolyte (E_{redox}). The α values for different devices were estimated from the slope of the $\log C_\mu$ versus V_{OC} plot (Fig. S2(B), ESI †), and the obtained values (Table 1) showed a minimal difference between the standard and the bilayer devices. Hence, the variation in C_μ can be directly correlated with the shift in CB edges as per the relation,

$$C_o = \frac{q^2 n_t \alpha}{k_B T} \exp\left(-\frac{\alpha(E_{CB} - E_{redox})}{k_B T}\right) \quad (2)$$

Empirically, the lower C_μ values for the bilayer devices (Fig. S2(B) and Table S2, ESI †) further substantiate the negative shift in CB.

The negative shift in CB for the bilayer devices concomitantly reduces the overlap of the CB states and the sub-bandgap states/trap states of the semiconductor with the redox mediator's oxidized states, thereby suppressing electron transfer from the semiconducting layer to the electrolyte (Fig. 1(C)).^{50,51} This is evident from the lower dark current (Fig. 3(E)) and higher recombination resistance, R_{ct} (Fig. 3(F) and Table S2, ESI †) for the TiO₂/ZnO bilayer devices. The increased R_{ct} in the bilayer devices can also be attributed to the formation of an energy barrier at the TiO₂/ZnO interface, owing to the higher CB energy of ZnO.⁵² Altogether, these findings highlight the superior ability of the TiO₂/ZnO bilayer devices to suppress charge recombination at the semiconductor/electrolyte interface compared to the standard TiO₂ device. The charge carrier recombination losses were further studied by performing the transient photovoltage decay measurements, and the lifetime (τ_n) obtained as a function of V_{OC} is provided in Fig. 3(G). Compared to the TiO₂ alone device, the bilayer devices exhibited improved lifetime, again indicating efficient suppression of recombination. Notably, we observed the same trend in the

lifetime for these devices by performing intensity modulated photovoltage spectroscopy (IMVS) measurements as well (Fig. S3(A), ESI†). Further, the role of trap states in the recombination was explored using intensity-dependent V_{OC} measurements (Fig. 3(H)). The slope of the semi-logarithmic plot of V_{OC} versus illumination intensity (ϕ) is used to estimate the ideality factor (n) of the devices using the equation,^{25,53}

$$\frac{d V_{OC}}{d \log \phi} = \frac{2.3nk_B T}{q} \quad (3)$$

The trap state-mediated recombination leads to non-linear recombination kinetics, which results in a deviation of n from the ideal value of unity. From the obtained values of n provided in Table 1, it is quite obvious that the trap state-assisted recombination is less for the bilayer devices; in particular, the T + Z1 device possesses an n value which is closer to unity. This explains our aforementioned notion that the negatively shifted CB in bilayer devices diminishes the electron transfer from the trap states to the electrolyte. Thus, the observed increase in V_{OC} for the TiO₂/ZnO bilayer devices can be predominantly associated with the collective effect of CB shift and suppressed recombination.

From Table S2, ESI† it is observed that the resistance to the diffusion of redox species in the bulk of the electrolyte (R_{d-bulk}) is similar for all the devices, while that within the mesoporous layer (R_{d-WE}) is increased by more than three times for the TiO₂/ZnO devices, owing to the higher layer thicknesses. In addition, the copper complex based electrolyte systems are reported to be mass transport limited. However, the similar current transient (CT) curves for T and T + Z devices under an illumination

intensity of 100 mW cm⁻² (Fig. S3(B), ESI†), and the linear nature of the J_{SC} versus ϕ plots (Fig. S3(C), ESI†) for the T + Z devices indicates minimal influence of mass transport in these systems, despite the higher layer thickness. This may be attributed to the highly porous nature of the ZnO overlayer. Moreover, ZnO, being endowed with appreciable electron mobility, can act as an excellent electron transport layer in the DSC. Resultantly, the T + Z devices having ZnO overlayers exhibit better diffusion coefficients (D_n), when compared to the T device (as shown in Fig. 3(I)). Nonetheless, the J_{SC} of T + Z devices is lower than that of T devices, which may be explained by the lower injection driving force associated with the upward-shifted CB edges in the bilayer devices. Further, the presence of Zn²⁺/dye aggregates within the ZnO layer, due to degradation of ZnO under acidic conditions, may also play a role in the injection challenges observed in the TiO₂/ZnO bilayer devices.^{54,58,59} The comprehensive investigation mentioned above, encompassing diverse interfacial charge transfer studies in both standard and bilayer devices, establishes a clear correlation between the two device configurations.

Among the bilayer devices, T + Z1 delivered the best performance with a *ca.* 15 μ m thick ZnO (Z1) layer over TiO₂ (Fig. 2B(f)). The effect of ZnO layer thickness on device performance was further investigated by fabricating T + Z1 devices with an average Z1 layer thickness of 5 μ m, 15 μ m and 25 μ m (Fig. S4, ESI†). The obtained J - V curves under AM 1.5G 100 mW cm⁻² illumination are shown in Fig. S5, ESI† and the photovoltaic parameters are summarized in Table S3, ESI†. The variation of ZnO layer thickness did not bring much difference in the photovoltaic parameters (Fig. 4(A)); however, a thickness

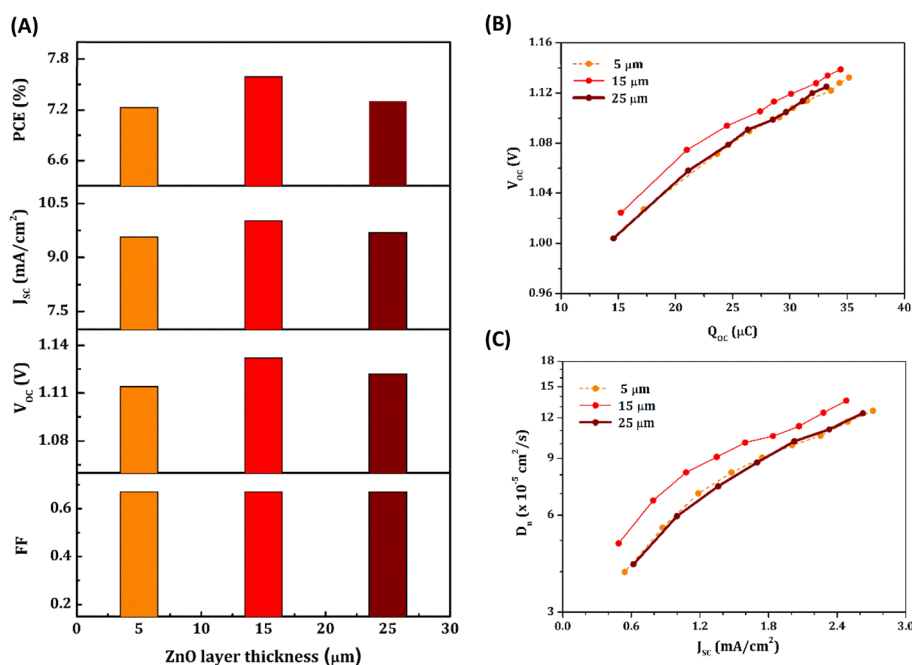


Fig. 4 (A) Comparison of photovoltaic parameters (J_{SC} , V_{OC} , FF and PCE) of T + Z1 devices with different ZnO layer thicknesses. (B) V_{OC} as a function of extracted charge and (C) diffusion coefficient (D_n) as a function of J_{SC} obtained for T + Z1 devices with different ZnO layer thicknesses.

of 15 μm was found to be optimal, giving the highest V_{OC} and optimum PCE. A more negatively shifted CB edge (Fig. 4(B)) and higher D_n (Fig. 4(C)) contributed to the better performance of T + Z1 devices with a 15 μm thick Z1 layer.

Compact blocking layers (BLs) play a critical role in inhibiting leakage/recombination in DSCs, particularly employing bulky alternate metal complex redox mediators.^{55,56} The conventional method of depositing TiO_2 BLs by TiCl_4 treatment causes damage to the ZnO overlayers. Therefore, an ultrathin TiO_2 BL was introduced over the bilayer architecture using commercial BL solution as described in the Experimental section, ESI.† Under AM 1.5G 100 mW cm^{-2} illumination, the bilayer devices with BL (T + Z1 + BL) fabricated using the Y123 sensitizer and $[\text{Cu}(\text{dmp})_2]^{1+/2+}$ redox electrolyte delivered a PCE of 8.16% with V_{OC} of 1.12 V, J_{SC} of 10.29 mA cm^{-2} and FF of 0.70 (Fig. 5(A) and Table 2). Slightly improved J_{SC} and FF were realized for the T + Z1 + BL device compared to T + Z1 (without BL) with a minor drop in V_{OC} . Introduction of BLs resulted in a positive shift in CB, as evident from the CE plot (Fig. 5(B)),

leading to a lower V_{OC} . Additionally, this increases the overlap of CB states with the oxidized states in the redox system, which results in more recombination as observed from transient photovoltage decay (Fig. 5(C)), OCVD (Fig. S6(A), ESI†) and IMVS (Fig. S6(B), ESI†) measurements. On the other hand, the introduction of BL successfully inhibited electron leakage at the FTO/electrolyte interface, as reflected in the dark J - V plot (Fig. 5(D)), leading to better FF. It is already known that multiple trapping–detrapping events slow down the diffusion of charge carriers in semiconducting films.⁵⁷ The TiO_2 BL could efficiently passivate these traps in the TiO_2/ZnO bilayer devices, reducing the transport time (τ_d) (Fig. S6(C), ESI†). This in turn contributes to enhanced D_n (Fig. 5(E)), leading to improved J_{SC} , which is reflected in the IPCE plot (Fig. S6(D), ESI†) and integrated J_{SC} values (Table 2), resulting in improved PCE for the T + Z1 + BL device.

As emphasized in the introduction section, ZnO possesses advantages such as wider bandgap and higher electron mobility. However, its lower electrochemical stability under the

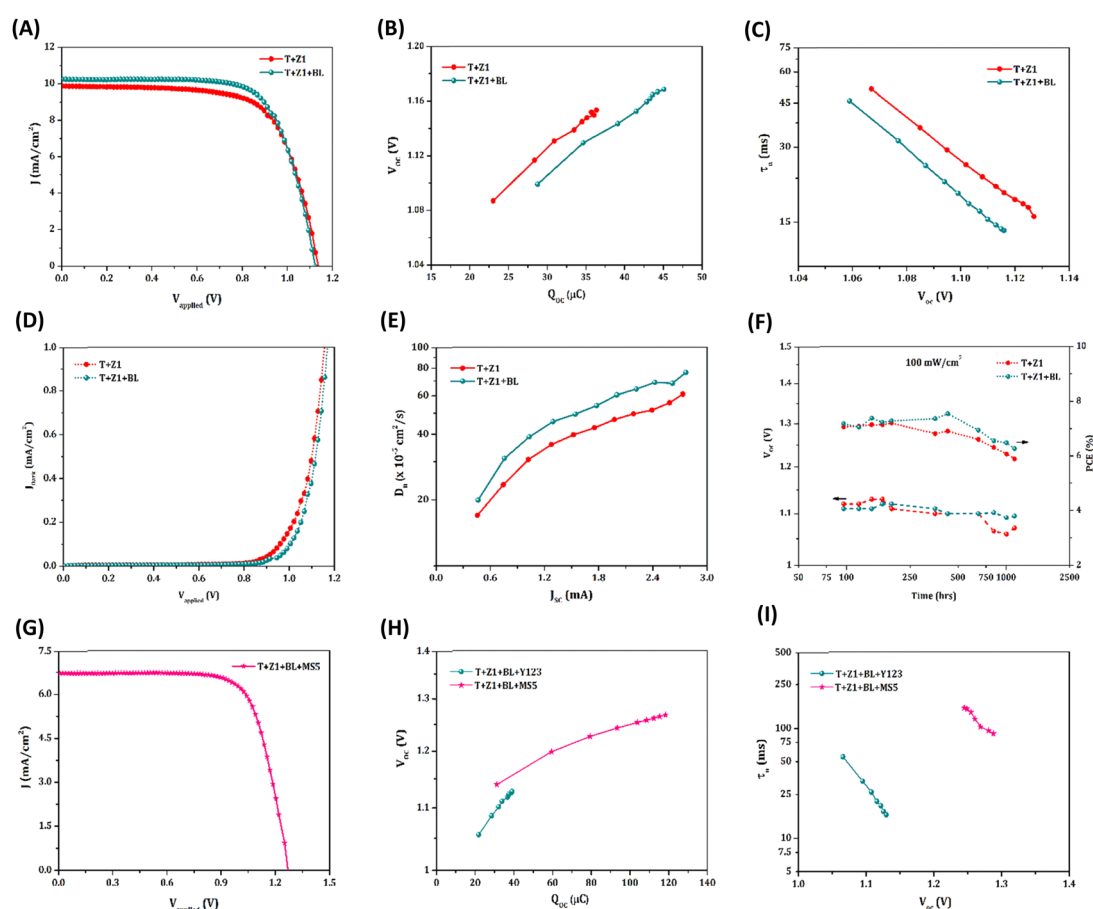


Fig. 5 (A) J - V curves measured under AM 1.5G 1 sun illumination (100 mW cm^{-2}), (B) charge extraction (CE) plots, (C) lifetime (τ_n) as a function of V_{OC} obtained from transient photovoltage decay measurements, (D) J - V characteristics obtained under dark conditions, (E) diffusion coefficient (D_n) as a function of J_{SC} obtained from transient photocurrent decay measurements and (F) stability data obtained for TiO_2/ZnO bilayer DSCs with a blocking layer (T + Z1 + BL) and without the blocking layer (T + Z1), employing the Y123 sensitizer and $[\text{Cu}(\text{dmp})_2]^{1+/2+}$ redox shuttle. (G) J - V curves measured under AM 1.5G 1 sun illumination (100 mW cm^{-2}) for TiO_2/ZnO bilayer DSCs with BL (T + Z1 + BL) employing the MS5 sensitizer and $[\text{Cu}(\text{dmp})_2]^{1+/2+}$ redox electrolyte. (H) Charge extraction (CE) and (I) lifetime (τ_n) plots, obtained for TiO_2/ZnO bilayer DSCs with BL (T + Z1 + BL) employing Y123 and MS5 sensitizers and the $[\text{Cu}(\text{dmp})_2]^{1+/2+}$ redox electrolyte.

Table 2 Photovoltaic parameters of DSCs employing TiO₂/ZnO bilayer photoanodes with the TiO₂ blocking layer (T + Z1 + BL) sensitized with Y123 and MS5 sensitizer along with [Cu(dmp)₂]^{1+/2+} redox electrolyte measured under AM 1.5G one sun (100 mW cm⁻²) irradiation

Device code	V_{OC}^a (V)	J_{SC}^a (mA cm ⁻²)	FF ^a	PCE ^a (%)	Integrated J_{SC}^b (mA cm ⁻²)
T + Z1 + BL + Y123	1.12 (1.12)	10.29 (10.33)	0.70 (0.70)	8.16 (8.12)	10.20
T + Z1 + BL + MS5	1.27 (1.26)	6.75 (6.70)	0.73 (0.72)	6.23 (6.08)	7.30

^a J - V parameters of champion cells and averages taken over five sets of samples (in parentheses) with a maximum mean deviation of ± 0.01 , ± 0.30 , ± 0.02 and ± 0.15 in V_{OC} , J_{SC} , FF and PCE, respectively. ^b J_{SC} obtained by integrating the IPCE spectra.

working conditions of the solar cell, along with the presence of defects and trap states, contributes to more recombination and reduces the long-term stability of the ZnO based devices. Two major degradation mechanisms contribute to the reduction in performance of ZnO based DSCs. Firstly, when ZnO electrodes are immersed in the acidic dye solution for dye adsorption, the Zn²⁺ ions from the ZnO surface dissolve, forming Zn²⁺/dye aggregates that become trapped within the pores of the ZnO matrix. This limits electron injection and reduces the J_{SC} of the device.⁵⁸ Secondly, ZnO undergoes chemical degradation under illumination in the presence of electrolyte, releasing Zn²⁺ and O²⁻ ions along with desorbed dye molecules into the electrolyte.⁵⁹ This leads to a reduced number of adsorbed dye molecules, formation of defects on the ZnO surface, and aggregation of the dye, thereby affecting the J_{SC} and PCE of the device. In our study, we successfully addressed the first degradation process by introducing the TiO₂ BL over the ZnO film. This is evident from the improved J_{SC} observed for the T + Z1 + BL device compared to the T + Z1 device, despite the reduced dye loading in the T + Z1 + BL film (1.2×10^{-7} mol cm⁻²), indicating reduced dye aggregation. Additionally, the introduction of the BL slowed down the rate of the second degradation process, as observed in the stability measurements (Fig. 5(F)). While the bare T + Z1 device experienced a drop in both the V_{OC} and PCE after 200 hours, the T + Z1 + BL device retained approximately 98% of the initial V_{OC} even after 1000 hours. However, the PCE of the devices began to decrease after 400 hours.

SEM and XRD analysis were carried out to identify the changes in the bilayer photoanode films during the stability test. The SEM images of T + Z1 and T + Z1 + BL electrodes after exposure to the electrolyte for over 1000 hours are presented in Fig. S7(A).† These images reveal an increased presence of cracks compared to the fresh electrode. Additionally, after prolonged contact with the electrolyte, both films exhibited a smoother surface compared to the fresh T + Z1 films. This can be attributed to the selective dissolution of ZnO from the film surface.⁶⁰ XRD patterns of the Y123 dye adsorbed T + Z1 and T + Z1 + BL electrodes after 1000 hours of electrolyte soaking are shown in Fig. S7(B).† The corroded ZnO films still exhibited a crystalline nature, although some peak intensities, such as [100], [101], and [110], were reduced compared to the fresh T + Z1 films (Fig. 2(C)). However, no shift in peak positions or appearance of new peaks was observed in the XRD spectra of the degraded films. Hence, prolonged exposure to the electrolyte does not affect the crystallinity of the ZnO films but induces changes in the film surface due to the degradation of ZnO in both the

bilayer electrodes with and without the BL.⁶¹ In conclusion, the exposure of the bilayer films to the electrolyte system for a long time, coupled with frequent illumination, likely resulted in the dissolution of ZnO and dye into the electrolyte, which might have led to a decrease in J_{SC} and hence PCE of the T + Z1 + BL devices after 400 hours (as seen in Fig. 5(F)).

Eventually, by sensitizing our best-optimized bilayer architecture (T + Z1 + BL) with MS5 dye, we could realize a record V_{OC} of 1.27 V (previous best – 1.24 V)²⁶ under AM 1.5G solar illumination with a J_{SC} of 6.75 mA cm⁻², FF of 0.73 and PCE of 6.23% (Fig. 5(G) and Table 2). The J_{SC} obtained by integrating the corresponding IPCE spectrum (Fig. S8(A), ESI†) matches the observed J_{SC} within the permitted error limits. Switching the dye from the conventional Y123 to MS5 contributed to the negative shift in CB (Fig. 5(H)) and couple of orders of magnitude improvement in lifetime (Fig. 5(I)) owing to the retardation of recombination by the long alkyl chains present in the MS5 sensitizer. The MS5 sensitized T + Z1 + BL bilayer device could also achieve a V_{OC} of 1.295 V under a higher-intensity LED illumination of 200 mW cm⁻² (Fig. S8(B), ESI†).

DSCs proved to be among the most efficient indoor/ambient light harvesting PV technologies. The potential of the newly designed bilayer devices was tested under warm white CFL, and daylight LED illumination. Fig. S10, ESI† shows the custom-designed indoor PV characterization set-up and Fig. S11, ESI† shows the spectral irradiance and integrated power under 1000 lux and 500 lux CFL/LED illumination. The energy harvesting and management circuits in most IoT smart device applications demand higher open circuit potentials. By using the TiO₂/ZnO bilayer architecture along with Y123 dye and [Cu(dmp)₂]^{1+/2+}, we were able to realize an improvement in V_{OC} both under CFL and LED illumination (Fig. 6(A, B) and Table 3). Under 1000 lux CFL illumination, the T + Z1 device exhibited a V_{OC} of 1.0 V (with a J_{SC} of 78.7 μ A cm⁻², FF of 0.75, PCE of 20.9% and a maximum power output (P_{max}) of 59.3 μ W cm⁻²) compared to a V_{OC} of 0.82 V for the standard T device (with a J_{SC} of 103.9 μ A cm⁻², FF of 0.70, PCE of 21.2% and P_{max} of 60.1 μ W cm⁻²). Careful use of BLs further increased the current density without compromising the FF. Thus T + Z1 + BL devices delivered similar PCE (21.3%) and P_{max} (60.3 μ W cm⁻²) to those of the control T device, with a 20.7% improvement in V_{OC} (0.99 V). Similar trends were observed under lower illumination intensity of 500 lux, where V_{OC} improved from 0.79 V for T to 0.96 V for T + Z1 + BL devices, along with improvement in FF, PCE and P_{max} .

Under 1000 lux LED illumination, the T + Z1 device delivered a V_{OC} of 1.0 V (J_{SC} = 77.1 μ A cm⁻², FF = 0.76, PCE = 18.8% and

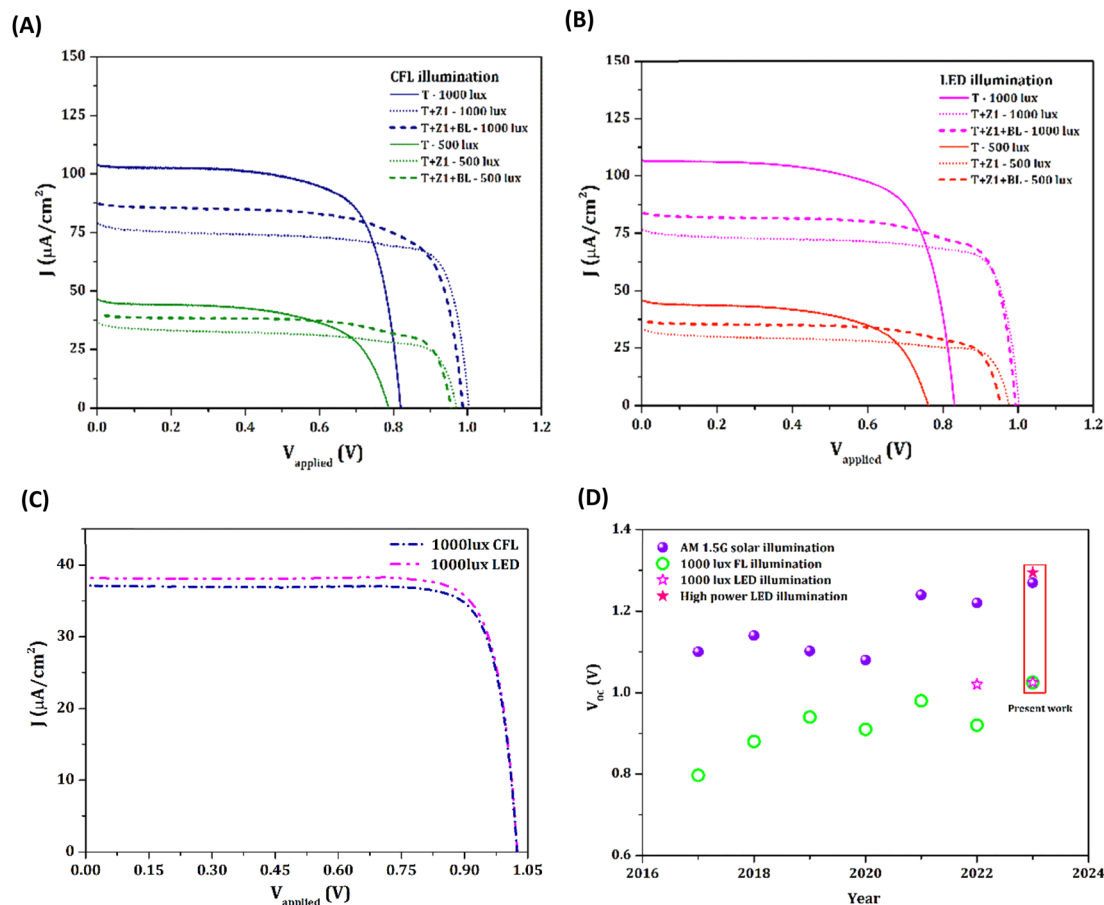


Fig. 6 (A) J - V curves measured for T, T + Z1 and T + Z1 + BL DSCs employing the Y123 sensitizer and $[\text{Cu}(\text{dmp})_2]^{1+/2+}$ redox electrolyte under 1000 lux and 500 lux CFL illumination. (B) J - V curves measured for T, T + Z1 and T + Z1 + BL DSCs employing the Y123 sensitizer and $[\text{Cu}(\text{dmp})_2]^{1+/2+}$ redox electrolyte under 1000 lux and 500 lux LED illumination. (C) J - V curves measured for T + Z1 + BL DSCs employing the MS5 sensitizer and $[\text{Cu}(\text{dmp})_2]^{1+/2+}$ redox electrolyte under 1000 lux CFL and LED illumination (obtained PV parameters are shown in the inset), and (D) representation of the highest V_{OC} values reported in the literature yearly (since 2017) for DSCs using organic dyes and copper electrolyte under outdoor and indoor illumination.

Table 3 Indoor photovoltaic parameters of TiO_2/ZnO bilayer DSCs sensitized with Y123 dye and $[\text{Cu}(\text{dmp})_2]^{1+/2+}$ redox electrolyte measured under varying intensities (1000 lux and 500 lux) using CFL and LED illumination

Illumination source	Intensity	P_{in} ($\mu\text{W cm}^{-2}$)	Device code	V_{OC}^a (V)	J_{SC}^a ($\mu\text{A cm}^{-2}$)	FF ^a	PCE ^a (%)	P_{max}^a ($\mu\text{W cm}^{-2}$)
CFL	1000 lux	283	T	0.82 (0.81)	103.9 (102.5)	0.70 (0.70)	21.2 (21.0)	60.1 (59.6)
			T + Z1	1.00 (0.99)	78.7 (82.6)	0.75 (0.73)	20.9 (20.5)	59.3 (58.1)
			T + Z1 + BL	0.99 (0.98)	87.4 (86.4)	0.70 (0.70)	21.3 (21.1)	60.3 (59.7)
	500 lux	143	T	0.79 (0.78)	46.0 (45.4)	0.60 (0.60)	15.2 (14.8)	21.9 (21.1)
			T + Z1	0.97 (0.97)	36.6 (35.8)	0.65 (0.64)	16.2 (15.8)	23.2 (22.5)
			T + Z1 + BL	0.96 (0.95)	40.8 (40.6)	0.63 (0.63)	17.5 (17.0)	25.8 (24.3)
LED	1000 lux	313	T	0.83 (0.83)	106.7 (107.2)	0.70 (0.70)	19.9 (19.8)	62.2 (61.9)
			T + Z1	1.00 (1.00)	77.1 (76.4)	0.76 (0.76)	18.8 (18.6)	58.9 (58.2)
			T + Z1 + BL	0.99 (0.99)	84.6 (84.1)	0.73 (0.72)	19.7 (19.3)	61.6 (60.3)
	500 lux	156	T	0.76 (0.76)	46.3 (45.6)	0.60 (0.60)	13.6 (13.4)	21.2 (21.1)
			T + Z1	0.98 (0.97)	33.5 (33.3)	0.67 (0.65)	14.0 (13.6)	21.8 (21.2)
			T + Z1 + BL	0.95 (0.95)	36.9 (37.3)	0.66 (0.63)	14.9 (14.4)	23.3 (22.4)

^a J - V parameters of champion cells and averages taken over five sets of samples (in parentheses) with a maximum mean deviation of ± 0.01 , ± 3.2 , ± 0.02 , ± 0.5 and ± 1.5 in V_{OC} , J_{SC} , FF, PCE and P_{max} respectively.

$P_{\text{max}} = 58.9 \mu\text{W cm}^{-2}$) compared to a V_{OC} of 0.83 V for the standard T device ($J_{\text{SC}} = 106.7 \mu\text{A cm}^{-2}$, FF = 0.70, PCE = 19.9% and $P_{\text{max}} = 62.2 \mu\text{W cm}^{-2}$). Using T + Z1 + BL, the current

density was further improved to achieve a P_{max} ($61.6 \mu\text{W cm}^{-2}$) similar to that of T, but with 19.3% increased V_{OC} (0.99 V). Under 500 lux LED illumination, V_{OC} increased from 0.76 V for T

to 0.98 V for T + Z1. The T + Z1 + BL device could further improve the J_{SC} and PCE, leading to improved power output, without compromising much on the V_{OC} . The performance of T + Z1 + BL devices employing MS5 dye and $[Cu(dmp)_2]^{1+/2+}$ electrolyte was also evaluated under indoor light, and they delivered a record V_{OC} of 1.025 V under both 1000 lux LED and 1000 lux CFL illumination (Fig. 6(C) and Table S4†). However, the PCE was lower than for the devices fabricated using the Y123 sensitizer due to the loss in J_{SC} , which could be attributed to the narrower absorption window of MS5 dye. Fig. 6(D) and Table S5† represent the highest V_{OC} values reported in the literature yearly (since 2017) for DSCs using organic dyes and copper electrolyte under outdoor and indoor illumination. The champion V_{OC} of 1.27 V under one sun, 1.295 V under higher intensity (200 mW cm^{-2}) LED light and 1.025 V under 1000 lux CFL and LED illumination are the best open circuit potentials in DSCs reported to date. Ultimately, we could highlight the significance of this work by powering a temperature sensor (ACETEQ DC-2) completely autonomously using a single DSC (of active area 0.24 cm^2) employing a TiO_2/ZnO bilayer photoanode sensitized with MS5 dye (eliminating the need for co-sensitization) and $[Cu(dmp)_2]^{1+/2+}$ electrolyte, under CFL (Video S1†) as well as LED lighting conditions (Video S2 and Fig. S12, ESI†). The present design approach has been successful in developing indoor DSCs with smaller footprints contributing to reduced costs and higher open circuit potentials that enable better integration possibilities to realize self-powered IoT devices.

3. Conclusions

In summary, we present a novel architecture for dye-sensitized solar cells (DSCs), which involves the implementation of a layer of ZnO hierarchical microstructures over the conventional TiO_2 active layer, resulting in a TiO_2/ZnO bilayer photoanode. Our design aims to enhance the open-circuit voltage (V_{OC}) of DSCs under one sun and indoor lighting conditions. Using an optimized bilayer electrode with a blocking layer (T + Z1 + BL) in combination with an MS5 sensitizer and $[Cu(dmp)_2]^{1+/2+}$ redox electrolyte, we have achieved a remarkable V_{OC} of 1.27 V under AM 1.5G one sun illumination and 1.295 V under a higher intensity LED light of 200 mW cm^{-2} , which are the highest V_{OC} reported to date for a single junction DSC. Detailed interfacial charge transfer studies have revealed that the bilayer structure leads to a negatively shifted conduction band and improved electron lifetime, contributing significantly to the enhanced V_{OC} . We have also succeeded in achieving a V_{OC} of 1.025 V under both 1000 lux CFL and LED illumination using the MS5 sensitizer and $[Cu(dmp)_2]^{1+/2+}$ redox electrolyte employing the TiO_2/ZnO bilayer photoanode (T + Z1 + BL). These promising results have inspired us to develop a battery-free temperature sensor that can be powered autonomously by a single DSC of 0.24 cm^2 active area under indoor illumination. Overall, this work provides valuable material and device engineering strategies that can be used to realize higher V_{OC} in conjunction with the appropriate combination of dyes and electrolytes. Achieving higher V_{OC} is essential for operating innovative self-powered electronic applications. The majority of the energy harvesting

and management circuits used in these smart devices require lower current (in μA) but demand higher voltage (above 1 V) for continuous operation, highlighting the fact that more than current and efficiency, V_{OC} needs to be taken into consideration while designing DSCs for indoor photovoltaic applications. Furthermore, reducing the device's footprint without compromising the voltage opens up creative and imaginative possibilities for integrating indoor DSCs as a replacement for batteries contributing to carbon neutrality and sustainability.

Author contributions

SS conceived the idea and coordinated the work. AJ synthesized the materials, carried out all of the characterization, fabricated the solar cells and conducted measurements and data analysis under one sun and indoor conditions. GV performed the SEM measurements. PSD and KNU contributed to manuscript corrections and preparation. SS wrote the manuscript with support from AJ and revisions from other co-authors. All authors commented on the manuscript.

Conflicts of interest

There are no conflicts to declare.

Acknowledgements

We acknowledge financial support from the SERB CRG project (CRG/2020/001406), CSIR-FIRST project (MLP65), DST Solar Challenge Award (DST/ETC/CASE/RE5/2023/05 (C)), CSIR-FTT project (MLP74) and CSIR-Mission Project (HCP30). GV gratefully acknowledges financial support from DST-TRC (AI/1/65/ARCI/2014). AJ acknowledges CSIR for the research fellowship. AJ acknowledges support from Mr Sourava Chandra Pradhan in optimizing the copper electrolyte-based DSCs and Ms Sreelekshmy M. R. for support with device fabrication and measurements.

References

- 1 J. Gubbi, R. Buyya, S. Marusic and M. Palaniswami, *Future Gener. Comput. Syst.*, 2013, **29**, 1645–1660.
- 2 M. Mohammadi and A. Al-Fuqaha, *IEEE Commun. Mag.*, 2018, **56**, 94–101.
- 3 D. Ma, G. Lan, M. Hassan, W. Hu and S. K. Das, *IEEE Commun. Surv. Tutor.*, 2020, **22**, 1222–1250.
- 4 J. Hester and J. Sorber, in *SensSys 2017 – Proceedings of the 15th ACM Conference on Embedded Networked Sensor Systems*, Association for Computing Machinery, Inc., 2017, vol. 2017.
- 5 H. Elahi, K. Munir, M. Eugeni, S. Atek and P. Gaudenzi, *Energies*, 2020, **13**, 5528.
- 6 A. Aslam, U. Mehmood, M. H. Arshad, A. Ishfaq, J. Zaheer, A. Ul Haq Khan and M. Sufyan, *Sol. Energy*, 2020, **207**, 874–892.
- 7 G. Gokul, S. C. Pradhan and S. Soman, *Energy Environ. Sustain.*, 2019, 281–316.

- 8 Y. Cao, Y. Liu, S. M. Zakeeruddin, A. Hagfeldt and M. Grätzel, *Joule*, 2018, **2**, 1108–1117.
- 9 H. Michaels, M. Rinderle, R. Freitag, I. Benesperi, T. Edvinsson, R. Socher, A. Gagliardi and M. Freitag, *Chem. Sci.*, 2020, **11**, 2895–2906.
- 10 M. Freitag, J. Teuscher, Y. Saygili, X. Zhang, F. Giordano, P. Liska, J. Hua, S. M. Zakeeruddin, J. E. Moser, M. Grätzel and A. Hagfeldt, *Nat. Photonics*, 2017, **11**, 372–378.
- 11 B. O'Regan and M. Grätzel, *Nature*, 1991, **353**, 737–740.
- 12 A. Hagfeldt, G. Boschloo, L. Sun, L. Kloo and H. Pettersson, *Chem. Rev.*, 2010, **110**, 6595–6663.
- 13 A. R. Yugis, R. F. Mansa and C. S. Sipaut, *IOP Conf. Ser.: Mater. Sci. Eng.*, 2015, **78**, 012003.
- 14 F. Schoden, A. K. Schnatmann, E. Davies, D. Diederich, J. L. Storck, D. Kniefelkamp, T. Blachowicz and E. Schwenzfeier-Hellkamp, *Materials*, 2021, **14**, 6622.
- 15 F. Schoden, A. K. Schnatmann, T. Blachowicz, H. Manz-Schumacher and E. Schwenzfeier-Hellkamp, *Sustainability*, 2022, **14**, 15280.
- 16 A. Dewan, S. U. Ay, M. N. Karim and H. Beyenal, *J. Power Sources*, 2014, **245**, 129–143.
- 17 H. Jayakumar, K. Lee, W. S. Lee, A. Raha, Y. Kim and V. Raghunathan, *Proceedings of the International Symposium on Low Power Electronics and Design*, 2015, pp. 375–380.
- 18 X. Cao, Y. Xiong, J. Sun, X. Zhu, Q. Sun and Z. L. Wang, *Adv. Funct. Mater.*, 2021, **31**, 210298.
- 19 S. M. Feldt, G. Wang, G. Boschloo and A. Hagfeldt, *J. Phys. Chem. C*, 2011, **115**, 21500–21507.
- 20 J. H. Yum, E. Baranoff, F. Kessler, T. Moehl, S. Ahmad, T. Bessho, A. Marchioro, E. Ghadiri, J. E. Moser, C. Yi, M. K. Nazeeruddin and M. Grätzel, *Nat. Commun.*, 2012, **3**, 631.
- 21 Y. Saygili, M. Söderberg, N. Pellet, F. Giordano, Y. Cao, A. B. Muñoz-García, S. M. Zakeeruddin, N. Vlachopoulos, M. Pavone, G. Boschloo, L. Kavan, J. E. Moser, M. Grätzel, A. Hagfeldt and M. Freitag, *J. Am. Chem. Soc.*, 2016, **138**, 15087–15096.
- 22 Y. Saygili, M. Stojanovic, H. Michaels, J. Tjepelt, J. Teuscher, A. Massaro, M. Pavone, F. Giordano, S. M. Zakeeruddin, G. Boschloo, J. E. Moser, M. Grätzel, A. B. Muñoz-García, A. Hagfeldt and M. Freitag, *ACS Appl. Energy Mater.*, 2018, **1**, 4950–4962.
- 23 Y. Ren, D. Zhang, J. Suo, Y. Cao, F. T. Eickemeyer, N. Vlachopoulos, S. M. Zakeeruddin, A. Hagfeldt and M. Grätzel, *Nature*, 2023, **613**, 60–65.
- 24 A. Grobelny, Z. Shen, F. T. Eickemeyer, N. F. Antariksa, S. Zapotoczny, S. M. Zakeeruddin and M. Grätzel, *Adv. Mater.*, 2023, **35**, 2207785.
- 25 S. C. Pradhan, A. Hagfeldt and S. Soman, *J. Mater. Chem. A*, 2018, **6**, 22204–22214.
- 26 D. Zhang, M. Stojanovic, Y. Ren, Y. Cao, F. T. Eickemeyer, E. Socie, N. Vlachopoulos, J. E. Moser, S. M. Zakeeruddin, A. Hagfeldt and M. Grätzel, *Nat. Commun.*, 2021, **12**, 1777.
- 27 Q. Zhang and G. Cao, *Nano Today*, 2011, **6**, 91–109.
- 28 J. A. Anta, E. Guillén and R. Tena-Zaera, *J. Phys. Chem. C*, 2012, **116**, 11413–11425.
- 29 C. C. Raj and R. Prasanth, *J. Power Sources*, 2016, **317**, 120–132.
- 30 S. H. Ko, D. Lee, H. W. Kang, K. H. Nam, J. Y. Yeo, S. J. Hong, C. P. Grigoropoulos and H. J. Sung, *Nano Lett.*, 2011, **11**, 666–671.
- 31 R. Gao, Z. Liang, J. Tian, Q. Zhang, L. Wang and G. Cao, *Nano Energy*, 2013, **2**, 40–48.
- 32 W. Peng, L. Han and Z. Wang, *Chem.-Eur. J.*, 2014, **20**, 8483–8487.
- 33 S. Sasidharan, S. Soman, S. C. Pradhan, K. N. N. Unni, A. A. P. Mohamed, B. N. Nair and H. U. N. Saraswathy, *New J. Chem.*, 2017, **41**, 1007–1016.
- 34 N. Memarian, I. Concina, A. Braga, S. M. Rozati, A. Vomiero and G. Sberveglieri, *Angew. Chem.*, 2011, **123**, 12529–12533.
- 35 A. K. Chandiran, M. Abdi-Jalebi, M. K. Nazeeruddin and M. Grätzel, *ACS Nano*, 2014, **8**, 2261–2268.
- 36 E. Guillén, L. M. Peter and J. A. Anta, *J. Phys. Chem. C*, 2011, **115**, 22622–22632.
- 37 K. Keis, J. Lindgren, S. E. Lindquist and A. Hagfeldt, *Langmuir*, 2000, **16**, 4688–4694.
- 38 M. Quintana, T. Marinado, K. Nonomura, G. Boschloo and A. Hagfeldt, *J. Photochem. Photobiol., A*, 2009, **202**, 159–163.
- 39 S. Sasidharan, A. Jagadeesh, S. C. Pradhan, B. N. Nair, A. Azeez Peer Mohamed, K. N. Narayanan Unni, S. Soman and U. Nair Saraswathy Hareesh, *Sol. Energy*, 2021, **226**, 214–224.
- 40 N. T. K. Thanh, N. Maclean and S. Mahiddine, *Chem. Rev.*, 2014, **114**, 7610–7630.
- 41 K. Gelderman, L. Lee and S. W. Donne, *J. Chem. Educ.*, 2007, **84**, 685–688.
- 42 A. Gopalraman, S. Karuppuchamy and S. Vijayaraghavan, *RSC Adv.*, 2019, **9**, 40292–40300.
- 43 J. Zhang and H. Yu, *J. Mater. Chem. A*, 2021, **9**, 4138–4149.
- 44 J. Zhang, Y. Sun, C. Huang, B. Yu and H. Yu, *Adv. Energy Mater.*, 2022, **12**, 2202542.
- 45 S. S. Kim, J. H. Yum and Y. E. Sung, *Sol. Energy Mater. Sol. Cells*, 2003, **79**, 495–505.
- 46 S. Borbón, S. Lugo, D. Pourjafari, N. Pineda Aguilar, G. Oskam and I. López, *ACS Omega*, 2020, **5**, 10977–10986.
- 47 K. Shen, K. Wu and D. Wang, *Mater. Res. Bull.*, 2014, **51**, 141–144.
- 48 R. Ruess, S. Haas, A. Ringleb and D. Schlettwein, *Electrochim. Acta*, 2017, **258**, 591–598.
- 49 F. Fabregat-Santiago, G. Garcia-Belmonte, I. Mora-Seró and J. Bisquert, *Phys. Chem. Chem. Phys.*, 2011, **13**, 9083–9118.
- 50 S. Rühle, M. Greenshtein, S. G. Chen, A. Merson, H. Pizem, C. S. Sukenik, D. Cahen and A. Zaban, *J. Phys. Chem. B*, 2005, **109**, 18907–18913.
- 51 P. Siva Gangadhar, A. Jagadeesh, A. S. George, G. Reddy, S. Prasanthkumar, S. Soman and L. Giribabu, *Mol. Syst. Des. Eng.*, 2021, **6**, 779–789.
- 52 K. E. Kim, S. R. Jang, J. Park, R. Vittal and K. J. Kim, *Sol. Energy Mater. Sol. Cells*, 2007, **91**, 366–370.
- 53 P. Salvador, M. G. Hidalgo, A. Zaban and J. Bisquert, *J. Phys. Chem. B*, 2005, **109**, 15915–15926.
- 54 K. Keis, E. Magnusson, H. Lindström, S. E. Lindquist and A. Hagfeldt, *Sol. Energy Mater. Sol. Cells*, 2002, **73**, 51–58.

- 55 H. Yu, S. Zhang, H. Zhao, G. Will and P. Liu, *Electrochim. Acta*, 2009, **54**, 1319–1324.
- 56 I. P. Liu, W. H. Lin, C. M. Tseng-Shan and Y. L. Lee, *ACS Appl. Mater. Interfaces*, 2018, **10**, 38900–38905.
- 57 T. Pauporté and C. Magne, *Thin Solid Films*, 2014, **560**, 20–26.
- 58 K. Keis, J. Lindgren, S. E. Lindquist and A. Hagfeldt, *Langmuir*, 2000, **16**, 4688–4694.
- 59 L. Ke, S. Bin Dolmanan, L. Shen, P. K. Pallathadk, Z. Zhang, D. M. Ying Lai and H. Liu, *Sol. Energy Mater. Sol. Cells*, 2010, **94**, 323–326.
- 60 E. J. Canto-Aguilar, M. Rodríguez-Pérez, R. García-Rodríguez, F. I. Lizama-Tzec, A. T. De Denko, F. E. Osterloh and G. Oskam, *Electrochim. Acta*, 2017, **258**, 396–404.
- 61 S. Ghosh, R. Sartape and J. Chakraborty, *J. Mater. Sci.: Mater. Electron.*, 2020, **31**, 2202–2220.